



HAL
open science

Integrity monitoring for mobile users in urban environment

Philippe Brocard

► **To cite this version:**

Philippe Brocard. Integrity monitoring for mobile users in urban environment. Signal and Image processing. INP DE TOULOUSE, 2016. English. NNT: . tel-01379632

HAL Id: tel-01379632

<https://theses.hal.science/tel-01379632>

Submitted on 11 Oct 2016

HAL is a multi-disciplinary open access archive for the deposit and dissemination of scientific research documents, whether they are published or not. The documents may come from teaching and research institutions in France or abroad, or from public or private research centers.

L'archive ouverte pluridisciplinaire **HAL**, est destinée au dépôt et à la diffusion de documents scientifiques de niveau recherche, publiés ou non, émanant des établissements d'enseignement et de recherche français ou étrangers, des laboratoires publics ou privés.



Distributed under a Creative Commons Attribution - NonCommercial - NoDerivatives 4.0 International License



THÈSE

En vue de l'obtention du

DOCTORAT DE L'UNIVERSITÉ DE TOULOUSE

Délivré par :

Institut National Polytechnique de Toulouse (INP Toulouse)

Présentée et soutenue par :

Philippe Brocard

le mercredi 30 mars 2016

Titre :

Contrôle d'intégrité pour utilisateurs mobiles en milieu urbain

Integrity monitoring for mobile users in urban environment

École doctorale et discipline ou spécialité :

ED MITT : Domaine STIC : Réseaux, Télécoms, Systèmes et Architecture

Unité de recherche :

Ecole Nationale de l'Aviation Civile (ENAC), Laboratoire TELECOM

Directeur/trice(s) de Thèse :

Olivier Julien

Christophe Macabiau

Jury :

Professeur Boris Pervan

Professeur Washington Ochieng

Professeur Emmanuel Duflos

Docteur Olivier Julien

Docteur Christophe Macabiau

Monsieur Mikael Mabilieu

ABSTRACT

Satellite navigation is a promising technology for terrestrial applications that requires the monitoring of the vehicle position thanks to costly ground infrastructures. In the rail domain, the European train control system (ETCS) relies on a combination of radio beacons (that provides information of absolute position) and odometry to propagate the position between two balises groups. The use of Global Navigation Satellite Systems (GNSS) in ETCS has been proposed in order to reduce the amount of beacons. In the road domain, the GNSS is one of the technologies recommended by the European Union directive for Electronic Toll Collection (ETC), and GNSS based ETC systems already exists for heavy good transportation in Germany (Toll Collect) and Slovakia (MYTO). For these two applications that are either safety critical (train control) or liability critical (toll collection), it is not acceptable to estimate the position of the vehicle with a large error without warning the system within a sufficiently short delay. It is firstly necessary to define the operational requirements for the navigation system for these terrestrial applications. This kind of problematic has already been handled in the context of civil aviation which is also a critical application, but currently, the operational requirements associated to GNSS are not standardized for the train control and ETC. Based on the model of civil aviation, a state of the art of possible requirements for train control and electronic toll collection is proposed. For train control, a solution based on redundant independent GNSS constellations has been proposed in order to relax the integrity risk requirements on each sub constellation. In the case of ETC, the requirements will depend on the case of study and are indirectly imposed by the toll charger. For terrestrial applications, the vehicles are likely to operate in constrained environment (including urban environment). In urban environment, the performances of GNSS are highly degraded due to multipath interference, tracking of non-line-of-sights and masking effects. These phenomena are likely to degrades the accuracy, integrity, availability and continuity of the GNSS based positioning system. It is proposed to augment the solution proposed for each application by integrating measurements from a six axis inertial measurement unit which are insensitive to the receiver surrounding environment. Integrating information from other sensors such as a track database for train control or odometry for toll collection is investigated. The nominal error models and fault modes of the sensors are then studied. The nominal error models will be used to weight the measurements in the fusion algorithm and to test the performances of the fusion algorithm by realistic simulations. In particular, the characterization of the distribution and the modelling of the errors dues to multipath and non-line-of-sights in urban environment is studied on simulator and on a data collection campaign conducted in Toulouse downtown (France) and its surroundings. The extended Kalman filter used to fuse the GNSS measurements and the measurements from other sensors are then presented. A tight coupling architecture in closed loop is presented as it is the most adapted to the cases of study. The integration of a track database in the solution is discussed in the case of train control. The extension of the solution to the multi-constellation case is also presented. The solutions have been validated and tested on a simulator as well as in real condition in Toulouse downtown. It is shown that additional sensors such as track database or wheel speed sensors enable to limit the drift of the position error in costing/degraded constellation condition. Then, it is proposed to improve the robustness and the reliability of the GNSS measurements in urban area by developing multipath detection algorithms at the signal processing level. A detection algorithm based on the real

time analysis of the correlation function is proposed. This algorithm aims at assisting the integrity monitoring algorithm upstream by protecting it against the faults due to multipath with large amplitudes. However, this algorithm does not protect against non-line-of-sights that can lead to integrity failures as this phenomenon is not associated with any abnormal distortion. Several methods based on the elevations of the satellites, the signal to noise ratio, or the coherence of the measurements based on the comparison with non GNSS sensors measurements have been studied in order to protect the solution against this phenomenon. Two snapshots integrity monitoring algorithms adapted to the Kalman filter are presented. Finally, the performances of these algorithms are tested on the data collected in Toulouse downtown and surroundings. The improvement obtained by assisting the integrity monitoring algorithm upstream by testing the quality of the measurement is quantized (with respect to a simple inflation of the nominal models in urban environments).

ACKNOWLEDGEMENTS

This work has been conducted in the SIGnal processing and NAVigation (SIGNAV) Lab at the ENAC. I warmly acknowledge ENAC and Egis for funding this thesis.

I would like to express my gratitude to my thesis directors Olivier Julien and Christophe Macabiau for their time, trust and support during these three years of labour. I also would like to thank Mikael Mabillean for his interest in my researches.

I am grateful to Washington Ochieng and Boris Pervan for reviewing the thesis and travelling to Toulouse to attend the defence. I am also grateful to Emmanuel Duflos for presiding the jury.

Finally, I would like to thank all my colleagues in SIGNAV team, with a special mention for Sébastien for making me cross ENAC carrying a SPAN on my back, Paul for helping me to conduct data collections during the hottest days of summer (without air conditioning), Amani and Jérémy for our many debates and discussion about Kalman filtering, Anne Christine for her precious advice on data fusion and badminton, Myriam for our discussions on carrier phase discriminators and Leslie for her sound advice.

TABLE OF CONTENTS

1 Introduction	23
1.1 Motivations of the work	23
1.2 Contributions	25
1.3 Outline	26
1.4 References	28
2 State of the art on GNSS and inertial navigation	29
2.1 Principle of GNSS and possible augmentations	29
2.1.1 Space segment	29
2.1.2 Control segment	33
2.1.3 User segment	33
2.1.4 Augmentation systems.....	40
2.2 Principle of inertial navigation	49
2.2.1 Introduction to inertial sensors	49
2.2.2 Frames of reference	51
2.2.3 Principles of inertial mechanization	51
2.3 Conclusion	55
2.4 References	55
3 Operational Requirements	58
3.1 Performance requirements criterion used for civil aviation	58
3.2 Derivation of performance requirements for train control	61
3.2.1 Alert limit derived from ETCS	62
3.2.2 Accuracy.....	64
3.2.3 Integrity risk	66
3.2.4 Availability	68
3.2.5 Continuity	69
3.2.6 Time to alert	69
3.2.7 Summary of the requirements of GNSS for train control	69
3.3 Derivation of performance requirements for GNSS in Electronic toll collection	70
3.3.1 Alert limit	72
3.3.2 Accuracy.....	74
3.3.3 Integrity risk	74
3.3.4 Availability.....	76
3.3.5 Continuity	76
3.3.6 Time-To-Alert	76
3.3.7 Summary	77

3.4 Conclusions	77
3.5 References	77
4 Positioning Platform Definition for Train Control and ETC.....	82
4.1 GNSS receivers' architectures.....	82
4.1.1 Train control	83
4.1.2 Electronic toll collection.....	92
4.1.3 Observations	93
4.2 Sensor augmentation and integration strategies.....	93
4.2.1 Train control	95
4.2.2 Electronic Toll Collection	96
4.3 Conclusions	96
4.4 References	97
5 Measurement models.....	99
5.1 Nominal measurement model.....	99
5.1.1 GNSS.....	99
5.1.2 Doppler error model	117
5.1.3 Other Sensors	118
5.2 Faults	121
5.2.1 Failure sources of GNSS	122
5.2.2 Sensors faults.....	123
5.3 Consideration of local effects.....	124
5.3.1 Multipath interference	124
5.3.2 Non-Line-Of-Sight GNSS errors in urban environment.....	124
5.3.3 Discussions.....	143
5.4 Conclusions	146
5.5 References	146
6 Design of the fusion algorithm	150
6.1 Design of the hybridization filter	150
6.1.1 Kalman Filter.....	150
6.1.2 Extension to the non-linear case: Extended Kalman Filter.....	152
6.1.3 Design of the basic fusion algorithm	153
6.1.4 Improving the solution	158
6.1.5 Train control	162
6.1.6 ETC	165
6.2 Validation and performance assessment on simulated data.....	166
6.2.1 Parameters of the simulations.....	166
6.2.2 Results: GPS/INS	168
6.2.3 Results: integration of the track database	171
6.2.4 Results: integration of the wheel speed sensors	174

6.2.5 Conclusions	174
6.3 Performance assessment on real data.....	175
6.3.1 Reference.....	175
6.3.2 Results: GPS/INS	176
6.3.3 Results: integration of the track database for train control	180
6.3.4 Results: dual constellation based architecture and introduction of WSS for electronic toll collection	185
6.4 Conclusions	187
6.5 References	188
7 Selection of the GNSS measurements	190
7.1 Detection of measurements affected by abnormally large errors due to multipath	191
7.1.1 Existing and proposed detection metrics	193
7.1.2 Determination of the detection thresholds for coherent metrics	194
7.1.3 Determination of the detection thresholds for non-coherent metrics.....	199
7.1.4 Sensitivity of the Detection Metrics	200
7.1.5 Performance assessment on urban channel model.....	205
7.1.6 Conclusion.....	212
7.2 Protection against NLOS errors and residual large multipath errors	213
7.2.1 Application of masks in train control	213
7.2.2 Application of masks in ETC	221
7.2.3 Innovation monitoring	225
7.3 Conclusion.....	228
7.4 References	231
8 Monitoring the integrity of the hybridized solutions.....	233
8.1 Allocation of the integrity risk between the sources of failure at the sensor level...	234
8.2 Allocation of the GNSS integrity risk and Selection of the augmentation system...	235
8.2.1 Risk allocation between the sources of GNSS failures.....	235
8.2.2 Protection against failures of SiS.....	236
8.2.3 Considerations of local effects	237
8.3 Integrity monitoring algorithm, principles and results	238
8.3.1 Discussions on the algorithm and its parameters.....	238
8.3.2 Principle	240
8.3.3 Availability results on the data set conducted in downtown Toulouse.....	248
8.3.4 Detection ability	262
8.4 Improving the measurement selection by determining the maximum tolerable bias	264
8.4.1 Concept of critical biases.....	265
8.4.2 Computation of the critical bias in the single bias case	265
8.4.3 Impact of the lifespan of the bias.....	269
8.5 Use of critical biases for monitoring the measurements	273

8.6 Monitoring integrity of the IMU measurements	278
8.6.1 Behavior of the test with respect to the different failure sources.....	280
8.7 Conclusion.....	284
8.8 References	285
<i>9 Conclusion and recommendations for future work</i>	<i>288</i>
9.1 Conclusions	288
9.2 Recommendations for future work.....	291

LIST OF TABLES

Table 1 GNSS signals specifications [RTKLIB].....	32
Table 2 SiS performance requirements [ICAO, 2006]	60
Table 3 List of projects targeting the introduction of GNSS in ETCS.....	62
Table 4 Estimated correlation time on real data	65
Table 5 Proposition for operational requirements to use GNSS for Train Position Locator in ETCS	69
Table 6 Event matrix decision: theoretic event matrix for discrete schemes [Grush et al., 2009]71	71
Table 7 Proposition for operational requirements for GNSS to be used in ETC	77
Table 8 σ_{iono}, v for Galileo E1 as in function of the geomagnetic latitude [Salos, 2012].....	104
Table 9 Weighting scheme based on estimated Doppler measurement standard deviation as a function of velocity and C/N_0	117
Table 10 IMU specifications [Landmark 01, datasheet]	118
Table 11 Parameters of the real distribution of building heights for different cities.....	126
Table 12 Characterization of the first trajectory.....	136
Table 13 Characterization of the second trajectory.....	137
Table 14 Proposed weighting scheme for pseudorange errors due to local effects (including NLOS)	142
Table 15 Proposed mixture model for LOS and NLOS	143
Table 16 Position accuracy performances of the different configurations	170
Table 17 Position accuracy performances of the different configurations which include track database measurements	173
Table 18 Position accuracy and error RMS of the different possible configurations with WSS	174
Table 19 Position accuracy performances of the different configurations combining GPS and the IMU	178
Table 20 Position accuracy performances of the different configurations combining GPS or GLONASS, the IMU and the track database.....	182
Table 21 Position accuracy performances of the different configurations combining GPS, GLONASS, the IMU and WSS.....	187
Table 22 Metrics of interest used in this thesis	194
Table 23 The white cells represents the sensitivity of the test (maximum SMR for which the detection is successful given the PMD) on GPS L1 C/A for $M1$ with an infinite front end bandwidth. The green cells represent the observed PMD	204

Table 24 The white cells represents the sensitivity of the test (maximum SMR for which the detection is successful given the <i>PMD</i>) on GPS L1 C/A for M1 with infinite front end BW with smoothing of the correlator. The green cells represent the observed <i>PMD</i>	205
Table 25 Performances of the test based on the simple ratio test.....	208
Table 26 Performance of the <i>SNR</i> monitoring.....	210
Table 27 <i>PFA</i> and <i>PMD</i> performed by monitoring the differential ratio metric.....	210
Table 28 <i>PFA</i> and <i>PMD</i> performed by monitoring the non coherent simple ratio metric	211
Table 29 Performances of the simple ratio metric for BOC(1,1)	212
Table 30 Impact of an elevation mask on the position error for the train control solutions based on GPS.....	215
Table 31 Impact of an elevation mask on the position error for the train control solutions based on GLONASS.....	215
Table 32 Impact of a <i>C/N0</i> mask on the position error for the train control solutions based on GPS	219
Table 33 Impact of a <i>C/N0</i> mask on the position error for the train control solutions based on GLONASS.....	220
Table 34 Impact of an elevation mask on the position error for the ETC solutions based on GPS and GLONASS.....	222
Table 35 Impact of a <i>C/N0</i> mask on the position error for the ETC solutions based on GPS and GLONASS.....	224
Table 36 Summary of the parameters of the integrity monitoring algorithm for train control	249
Table 37 Statistics on the position error of the two sub solutions and their combination after inflated weighting schemes.....	251
Table 38 Statistics on availability in suburban environment with inflated weighting scheme..	252
Table 39 Statistics on availability in urban environment with inflated weighting scheme	252
Table 40 Statistics on availability in suburban environment with inflated weighting scheme. (approach based on separated mechanizations).....	253
Table 41 Statistics on availability in urban environment with inflated weighting scheme. (approach based on separated mechanizations).....	253
Table 42 Statistics on the position error of the two sub solutions and their combination after measurement selection.....	254
Table 43 Statistics of availability in suburban environment with measurement selection.....	255
Table 44 Statistics of availability in urban environment with measurement selection	255

Table 45 Statistics on availability in suburban environment with measurement selection. (approach based on separated mechanizations).....	256
Table 46 Statistics on availability in urban environment with measurement selection (approach based on separated mechanizations).....	256
Table 47 Summary of the parameters of the integrity monitoring algorithm for ETC.....	257
Table 48 Statistics of availability in suburban environment with measurement selection.....	258
Table 49 Statistics of availability in urban environment with measurement selection	258
Table 50 Statistics of availability in suburban environment with inflated measurement error model	259
Table 51 Statistics of availability in urban environment with inflated measurement error model.....	259
Table 52 Statistics of availability in suburban environment with measurement selection.....	260
Table 53 Statistics of availability in urban environment with measurement selection	260
Table 54 Statistics of availability in suburban environment with measurement selection, approach based on parallel mechanizations	261
Table 55 Statistics of availability in urban environment with measurement selection, approach based on parallel mechanizations	261
Table 56 Sensitivity of the test with respect to failures to zero for a MEMS gyroscope (Landmark 01)	281
Table 57 Sensitivity of the test with respect to the additional noise fault for a MEMS gyroscope (Landmark 01)	282
Table 58 Sensitivity of the test associated with a <i>PMD</i> and <i>PFA</i>	284
Table 59 Parameters of the gamma fitting for bias due to diffraction k	299
Table 60 Parameters of the gamma fitting for bias due to diffraction θ	300
Table 61 Quality of the velocity estimation for the different configurations combining GPS and the IMU	303
Table 62 Quality of the velocity estimation for the different configurations combining GNSS, INS and the track database.....	304
Table 63 Quality of the velocity estimation for the different configurations combining GPS, GLONASS, the IMU, and a simulated WSS.....	304

LIST OF FIGURES

Figure 1 Principle of the Delay Lock Loop.....	37
Figure 2 Integrity monitoring algorithm available	40
Figure 3 Integrity monitoring algorithm unavailable	40
Figure 4 Diagram of FDE configurations [RTCA, 2006]	42
Figure 5 Selection of the detection <i>Threshold</i> to set the <i>PFA</i>	46
Figure 6 Representation of <i>PMD</i> in the faulty case	46
Figure 7 Principle of an inertial navigation processor, from [Groves, 2013].....	52
Figure 8 Correlation of position error for GPS L1 C/A receiver with Least Square position estimation algorithm.....	65
Figure 9 Generic functional fault tree of ETCS level 2 proposed in [UNISIG 3].....	68
Figure 10 Example of optimal Geo-object boundary for $D = 20$ m and $\sigma_{GNSS} = 5$ m.....	74
Figure 11 Definition of the confidence interval for train control, first configuration	85
Figure 12 Definition of the confidence interval for train control, second configuration	85
Figure 13 Distribution of <i>HPL12</i> with respect to <i>HPL1</i>	89
Figure 14 Spectra of GNSS signals.....	91
Figure 15 Basic architecture of the solution proposed for train position determination in train control	96
Figure 16 Basic architecture of the solution proposed for ETC	96
Figure 17 Street model used for the channel generation	109
Figure 18 Mean pseudorange error for the narrowband receiver processing BPSK(1).....	111
Figure 19 95th percentile of the code pseudorange error for the narrowband receiver processing BPSK(1).....	112
Figure 20 Percentage of time at which the receiver is actually tracking the signal generated by the LMS simulator.....	112
Figure 21 Signal to multipath amplitude ratio for a satellite elevation of 10°	113
Figure 22 Signal to multipath amplitude ratio for a satellite elevation of 20°	113
Figure 23 Signal to multipath amplitude ratio for a satellite elevation of 30°	113
Figure 24 Nominal multipath standard deviation for the narrowband receiver obtained after CDF overbounding.....	115
Figure 25 Nominal multipath standard deviation for the wideband receiver obtained after CDF overbounding for the BPSK(1) and CBOC(6,1,1/11,-) modulation.....	115

Figure 26 Nominal multipath standard deviation for the wideband receiver obtained after CDF overbounding for the BPSK(10) modulation.....	115
Figure 27 Distribution of the distance to the closest building.....	127
Figure 28 Probability density function for $\epsilon_{NLOS diffracted}$	128
Figure 29 Fitting $L1 + L2$ by lognormal distribution with Fenton-Wilkinson approximation .	129
Figure 30 Probabilities of occurrence of scenarios in urban environment	130
Figure 31 EP_{direct} as a function of the elevation and azimuth.....	131
Figure 32 Value of $EP_{diffracted}$ as a function of the elevation and azimuth	131
Figure 33 Value of $EP1_{reflection}$ as a function of the elevation and azimuth	131
Figure 34 Value of $EP2_{reflections}$ as a function of the elevation and azimuth.....	131
Figure 35 Distribution of NLOS error for $\vartheta = 10^\circ$	132
Figure 36 Distribution of NLOS error for $\vartheta = 30^\circ$	132
Figure 37 Distribution of NLOS error for $\vartheta = 60^\circ$	132
Figure 38 Distribution of NLOS error for $\vartheta = 90^\circ$	132
Figure 39 GNSS receiver and antenna used for the data collection	134
Figure 40 The U-blox antenna (left) and the NovAtel SPAN antenna (right).....	134
Figure 41 Power supply for the set-up (battery and inverter).....	134
Figure 42 Picture of the set-up	134
Figure 43 Data collection in Toulouse	135
Figure 44 Principle of modelling.....	140
Figure 45 Pseudorange error due to local effects in beltway environment	140
Figure 46 Pseudorange error due to local effects in suburban environment	141
Figure 47 Pseudorange error due to local effects in urban environment.....	141
Figure 48 Pseudorange error as a function of the $C/N0$ for 2h40 of data in Toulouse.....	144
Figure 49 $C/N0$ estimation in Toulouse downtown for GPS L1 C/A for Satellite 15, elevation of 40°	145
Figure 50 EKF residuals in Toulouse downtown for GPS L1 C/A for Satellite 15, elevation of 40°	145
Figure 51 Spiral viaduct near Brusio, Switzerland [bahnbilder.ch]	163
Figure 52 Portion of the tramway line number 3 in Montpellier, France.....	167
Figure 53 Skyplot of the constellation used for the simulations	168
Figure 54 Position errors in the navigation frame, single frequency L1 C/A GPS receiver (left) or dual frequency L1 C/A and L5 receiver (right) and IMU	169

Figure 55 Velocity errors in the navigation frame, single frequency L1 C/A GPS receiver (left) or dual frequency L1 C/A and L5 receiver (right) and IMU	169
Figure 56 Attitude errors, single frequency L1 C/A GPS receiver (left) or dual frequency L1 C/A and L5 receiver (right) and IMU	169
Figure 57 Accelerometer biases estimation.....	171
Figure 58 Gyroscopes biases estimation	171
Figure 59 Position errors in the navigation frame, single frequency L1 C/A GPS receiver (left) or dual frequency L1 C/A and L5 receiver (right), IMU and track database.....	172
Figure 60 Velocity errors in the navigation frame, single frequency L1 C/A GPS receiver (left) or dual frequency L1 C/A and L5 receiver (right), IMU and track database.....	172
Figure 61 Attitude errors, single frequency L1 C/A GPS receiver (left) or dual frequency L1 C/A and L5 receiver (right), IMU and track database.....	173
Figure 62 Standard deviation of the position error on the trajectory of reference as estimated by the SPAN system with inertial explorer	176
Figure 63 Number of GPS satellites being tracked as a function of time	177
Figure 64 CDF of GPS satellites being tracked as a function of the environment.....	177
Figure 65 Selection of the Threshold for the detection of the stationarity to apply the ZUPT and ZARU constraints.....	179
Figure 66 Position errors in the navigation frame, single frequency L1 C/A GPS receiver and IMU on real data.....	180
Figure 67 Velocity errors in the navigation frame, single frequency L1 C/A GPS receiver and IMU on real data.....	180
Figure 68 Attitude errors, single frequency L1 C/A GPS receiver and IMU on real data	180
Figure 69 Number of GLONASS satellites being tracked as a function of time	181
Figure 70 CDF of GLONASS satellites being tracked as a function of the environment.....	181
Figure 71 Histogram of C/N_0 in urban environment for GPS and GLONASS	181
Figure 72 Position error, single frequency GPS L1 C/A receiver, IMU and track database on real data	183
Figure 73 Position error, GLONASS L1 receiver, IMU and track database on real data	183
Figure 74 Velocity error, single frequency GPS L1 C/A receiver, IMU and track database on real data	183
Figure 75 Velocity error, GLONASS L1 receiver, IMU and track database on real data.....	183
Figure 76 Attitude error, single frequency GPS L1 C/A receiver, IMU and track database on real data	183

Figure 77 Attitude error, GLONASS L1 receiver, IMU and track database on real data	183
Figure 78 Position error after exclusion of all GPS satellites except SV 12 and SV 13 (from 50 to 200 seconds).	184
Figure 79 Horizontal position error after exclusion of all GPS and GLONASS satellites during 50 s (50 to 100 s).....	186
Figure 80 Estimation of WSS scale factor error.....	187
Figure 81 Code multipath envelope for the narrowband receiver model processing GPS L1 C/A and Galileo E1 OS.....	192
Figure 82 Code multipath envelope for the narrowband receiver model processing GPS L1 C/A and Galileo E1 OS.....	192
Figure 83 Locations allowed for the correlator used for the normalization of the metric correspond to the area above the curve	197
Figure 84 Comparaisn between the expected PFA (0.0228) and the observed PFA for $M1$..	198
Figure 85 Comparaisn between the expected PFA (0.0228) and the observed PFA for $M2$..	199
Figure 86 Approximation of the non-coherent metric probability density function with doubly non central F distribution.....	200
Figure 87 Possible scenarios that can lead to a missed detection.....	201
Figure 88 Allowed locations for the correlator used for the normalization of the metric after low pass filtering (5Hz).....	205
Figure 89 Correlation between code pseudorange error and value of the raw simple ratio metric ($M1$) for BPSK.....	207
Figure 90 Correlation between code pseudorange error and value of the simple ratio metric ($M1$) after smoothing the correlator outputs for BPSK.....	207
Figure 91 Estimation of $CN0$ with true $CN0$ set to 40dB-Hz	208
Figure 92 Correlation between code pseudorange error and estimated $C/N0$ with multipath only for BPSK	209
Figure 93 Correlation between code pseudorange error and estimated $C/N0$ with multipath and thermal noise (40 dB-Hz) for BPSK.....	209
Figure 94 Correlation between code pseudorange error and differential ratio metric ($M2$)	210
Figure 95 Correlation between code pseudorange error and non-coherent simple ratio metric ($M3$).....	211
Figure 96 Correlation between code pseudorange error and simple ratio metric for BOC(1,1) modulation.....	212
Figure 97 Percentage of time with more than 3 (left), 4 (center) and 5 (right) GPS satellites, satellite mask angle of 10°	217

Figure 98 Percentage of time with more than 3 (left), 4 (center) and 5 (right) GPS satellites, satellite mask angle of 20°	217
Figure 99 Percentage of time with more than 3 (left), 4 (center) and 5 (right) GPS satellites, satellite mask angle of 30°	217
Figure 100 Percentage of time with more than 3 (left), 4 (center) and 5 (right) GPS satellites, satellite mask angle of 40°	218
Figure 101 Impact of elevation and C/N_0 filtering on the along track error, train control (GPS/INS/Track database).....	221
Figure 102 Impact of elevation and C/N_0 filtering on the alongtrack error, train control (GLONASS/INS/Track database)	221
Figure 103 Percentage of time with more than 3 (left), 4 (center) and 5 (right) GPS/Galileo satellites, satellite mask angle of 30°	223
Figure 104 Percentage of time with more than 3, 4 and 5 GPS/Galileo satellites, satellite mask angle of 40°.....	223
Figure 105 Impact of elevation and C/N_0 filtering, ETC (GPS/GLONASS/INS/WSS)	224
Figure 106 Distribution of pseudorange residuals for satellite 22 (elevation $\cong 20^\circ$).....	227
Figure 107 Impact of innovation filtering on position error, train control (GPS/INS/track database), $mexp=1.5$	227
Figure 108 Impact of innovation filtering on position error, train control (GLONASS/INS/track database), $mexp =2$	228
Figure 109 Impact of innovation filtering on position error, ETC (GPS/GLONASS/INS/WSS), $mexp =1.5$	228
Figure 110 Reduction of the positioning error with cascaded testing, train control (GPS/INS/track database).....	229
Figure 111 Number of satellite selected, train control (GPS/INS/track database).....	229
Figure 112 Reduction of the positioning error with cascaded testing, train control (GLONASS/INS/track database).....	230
Figure 113 Number of satellite selected, train control (GLONASS/INS/track database).....	230
Figure 114 Reduction of the positioning error with innovation filtering, ETC (GPS/GLONASS/INS/WSS), $mexp =2$	230
Figure 115 Number of satellite selected, ETC (GPS/GLONASS/INS/track database).....	231
Figure 116 Allocation of the integrity risk: train control	235
Figure 117 Allocation of the integrity risk: ETC	235
Figure 118 Allocation of the integrity risk for the ETC	236

Figure 119 Principle of the solution separation algorithm in a closed loop scheme	241
Figure 120 Algorithm proposed for solution separation in a closed loop scheme	246
Figure 121 Distribution of the position error of the two sub solutions and their combination after inflated weighting scheme in urban environment ($PFA = 10^{-4}$)	250
Figure 122 Distribution of the <i>HPL</i> of the two sub solutions and their combination after inflated weighting scheme in urban environment ($PFA = 10^{-4}$)	251
Figure 123 Distribution of the <i>HPL</i> of the two sub solutions and their combination after inflated weighting scheme in urban environment (approach based on separated mechanizations with $PFA = 10^{-4}$)	253
Figure 124 Distribution of the position error of the two sub solutions and their combination after innovation filtering in suburban and urban environments ($PFA = 10^{-4}$).....	254
Figure 125 Distribution of the <i>HPL</i> of the two sub solutions and their combination after selection of the measurements in suburban and urban environments ($PFA = 10^{-4}$).....	255
Figure 126 Distribution of the <i>HPL</i> of the two sub solutions and their combination after selection of the measurements in urban environment (approach based on separated mechanizations with $PFA = 10^{-4}$)	256
Figure 127 Distribution of the <i>HPL</i> for ETC ($PFA = 10^{-4}$).....	258
Figure 128 Distribution of the <i>HPL</i> for ETC ($PFA = 10^{-4}$), solution separation using sub mechanizations for inflated measurement error model.....	259
Figure 129 Distribution of the <i>HPL</i> for ETC ($PFA = 10^{-4}$).....	260
Figure 130 Distribution of the <i>HPL</i> for ETC ($PFA = 10^{-4}$).....	261
Figure 131 Detection of a step with a magnitude of 30 m	262
Figure 132 Detection of a step with a magnitude of 100 m	262
Figure 133 Detection of a ramp failure with a magnitude of 0.1 m/s.....	263
Figure 134 Detection of a ramp failure with a magnitude of 0.5 m/s.....	263
Figure 135 Detection of a step with a magnitude of 30 m, separated mechanizations.....	264
Figure 136 Detection of a step with a magnitude of 100 m, separated mechanizations.....	264
Figure 137 Detection of a ramp failure with a magnitude of 0.1 m/s, separated mechanizations.....	264
Figure 138 Detection of a ramp failure with a magnitude of 0.5 m/s, separated mechanizations.....	264
Figure 139 Principle of the critical bias concept	265
Figure 140 Convergence of critical bias assuming a frozen constellation/vehicle scenario.	272
Figure 141 Convergence of critical bias assuming a frozen constellation/vehicle scenario (Zoomed).	272

Figure 142 Calculation of the critical bias. In this example, the source of the bias is not a threat for the integrity of the solution because: $P\epsilon NLOS > bias = Pf$ is lower than the critical bias .	275
Figure 143 Calculation of the critical bias	276
Figure 144 Principle of cascaded testing approach with real time threshold monitoring	276
Figure 145 Distribution of the lifespan of an echo in urban environment for a car [Lehner and Steingass, 2005].....	277
Figure 146 Distribution of the lifespan of an echo in urban environment in terms of KF updates for a 1 Hz GNSS receiver	278
Figure 147 Distribution of the lifespan of an echo in urban environment in terms of KF updates for a 5 Hz GNSS receiver	278
Figure 148 Detection of step failure by the WSSR monitoring algorithm (onset at the 3000 sample index).....	281
Figure 149 Detection of additional noise failure by the WSSR monitoring algorithm (onset at the 3000 sample index).....	283
Figure 150 Detection of a ramp failure by the WSSR monitoring algorithm (onset at the 3000 sample index).....	284
Figure 151 Steady state error of a first order DLL for a vehicle at a constant speed on the LMS297	
Figure 152 Steady state error of a first order PLL for a vehicle at a constant speed on the LMS297	
Figure 153 Steady state error of a second order FLL for a vehicle at a constant speed on the LMS	298
Figure 154 Stanford diagrams plotted for the two subsystems (based on GPS on the left and GLONASS on the right) after inflation of weighting scheme in suburban and urban environments. IMU and track database measurement are integrated.	311
Figure 155 Stanford diagram plotted for the combined system after inflation of weighting scheme in suburban and urban environments. IMU and track database measurement are integrated	312
Figure 156 Stanford diagrams plotted for the two subsystems (based on GPS on the left and GLONASS on the right) after inflation of weighting scheme in suburban and urban environments (approach based on separated mechanizations). IMU and track database measurement are integrated	312
Figure 157 Stanford diagram plotted for the combined system after inflation of weighting scheme in suburban and urban environments (approach based on separated mechanizations). IMU and track database measurement are integrated.	313
Figure 158 Stanford diagrams for each subsystem (based on GPS on the left and GLONASS on the right) after selection of the measurements. IMU and track database measurement are integrated.	313
Figure 159 Stanford diagram the combined system after selection of the measurements. IMU and track database measurement are integrated.	314

Figure 160 Stanford diagrams plotted for the two subsystems (based on GPS on the left and GLONASS on the right) after selection of the measurements in suburban and urban environments (approach based on separated mechanizations). IMU and track database measurement are integrated.	314
Figure 161 Stanford diagrams plotted for the combined system after selection of the measurements in suburban and urban environments (approach based on separated mechanizations). IMU and track database measurement are integrated.	315
Figure 162 Stanford diagrams plotted for the GPS/GLONASS/IMU/WSS solution with conventional solution separation algorithm. Approach based on the inflation of the weighting scheme in suburban and urban environments	315
Figure 163 Stanford diagrams plotted for the GPS/GLONASS/IMU/WSS solution with solution separation using sub mechanizations. Approach based on the inflation of the weighting scheme in suburban and urban environments	316
Figure 164 Stanford diagrams plotted for the GPS/GLONASS/IMU/WSS solution with conventional solution separation. Approach based on the selection of the measurements.	316
Figure 165 Stanford diagrams plotted for the GPS/GLONASS/IMU/WSS solution with solution separation using sub mechanizations. Approach based on the selection of the measurements.	317
Figure 166 Validation of the relation on simulated measurements	320

LIST OF ABBREVIATIONS AND ACRONYMS

AAIM	Aircraft Autonomous Integrity Monitoring
ABAS	Aircraft Based Augmentation System
AGC	Automatic Gain Control
AL	Alert Limit
AIME	Autonomous Integrity Monitoring and Extrapolation
ANPR	Automatic Number Plate Recognition
APME	A Posteriori Multipath Estimation
ATM	Air Traffic Management
BPSK	Binary Phase Shift Keying
BOC	Binary Offset Carrier
C/A	Coarse Acquisition
CBOC	Composite BOC
CDF	Cumulative Distribution Function
CDMA	Code Division Multiple Access
CNS	Communications, Navigation, and Surveillance
DCM	Direction Cosine Matrix
DLL	Delay Lock Loop
DLR	Deutsches Zentrum für Luft- und Raumfahrt
ECEF	Earth Centered Earth Fixed
EGNOS	European Geostationary Navigational Overlay Service
EKF	Extended Kalman Filter
ERA	European Railway Association
ERTMS	European Railway Traffic Management System
ETC	Electronic Toll Collection
ETCS	European Train Control System
FD	Fault Detection
FDMA	Frequency Division Multiple Access
FE	Fault Exclusion

FI	Fault Isolation
FLL	Frequency Lock Loop
FOG	Fiber Optical Gyroscope
GAGAN	GPS Aided GEO Augmented Navigation
GBAS	Ground Based Augmentation System
GEO	Geostationary Orbit
GLONASS	GLOBAL NAVIGATION Satellite System
GLR	Generalized Likelihood Ratio
GM	Gauss-Markov
GMAR	GNSS Metering Association for Road user charging
GNSS	Global Navigation Satellite System
GPS	Global Positioning System
<i>HPL</i>	Horizontal Protection Level
ICAO	International Civil Aviation Organization
IMU	Inertial Measurement Unit
INS	Inertial Navigation System
IR	Integrity Risk
KF	Kalman filter
LADGPS	Local Area Differential GPS
LMS	Land Mobile Satellite
LNA	Low Noise Amplifier
LOS	Line of Sight
LSE	Least square estimator
LSR	Least square residual
MEMS	Micro-Electro-Mechanical Systems
MSAS	MTSAT Satellite Augmentation System
MSF	Major Service Failure
MSS	Multiple Solution Separation
MTBF	Mean Time Between Failures
NHC	Non Holonomic Constraints
NLOS	Non-Line-Of-Sight

NRZ	Non Return to Zero
NTE	Not to Exceed
OBU	On Board Unit
OS	Open Service
PDF	Probability Density Function
PLL	Phase Lock Loop
PRN	Pseudo Random Noise
PRR	Pseudorange Rates
RAIM	Receiver Autonomous Integrity Monitoring
RF	Radio Frequency
RTK	Real Time Kinematic
SA	Selective Availability
SAW	Surface Acoustic Wave
SBAS	Satellite Based Augmentation System
SF	Scale Factor
SGE	Slowly Growing Error
SIS	Signal In Space
SQM	Signal Quality Monitoring
THR	Tolerable Hazard Rate
TTA	Time To Alert
TPL	Train Position Locator
URA	User Range Accuracy
URE	User Range Error
VCO	Voltage-Controlled Oscillator
WAAS	Wide Area Augmentation System
WADGPS	Wide Area Differential GPS
WLSE	Weighted Least Square Estimator
WLSR	Weighted Least Square Residuals
WSS	Wheel Speed Sensors
WSSR	Weighted Sum of Squared Residuals
ZUPT	Zero Velocity Update

ZARU Zero Angular Rate Update

1 INTRODUCTION

1.1 Motivations of the work

Due to the modernization of current Global Positioning System (GPS) and GLObal NAVigation Satellite System (GLONASS), the development of Galileo and Beidou, and the developments of augmentation systems, the fields of application that could benefit from Global Navigation Satellite Systems (GNSS) is constantly expanding.

GPS together with augmentations has been a proven technology for safety-critical applications such as civil aviation for which the GNSS use is performed in a fair environment (mostly open sky reception, controlled frequency bands, etc...). With the advent of multiple GNSS systems and the availability of signals located in different frequency bands, better performance can be expected from GNSS even in more challenging conditions. As a consequence, there is a trend to investigate the use GNSS for other critical applications taking place in locations where GNSS signal reception can be difficult (forest, light urban, urban). These applications are not necessarily safety-critical, but can be liability-critical and thus still require a certain quality of service to be maintained. This is for instance the case for terrestrial rail and road position monitoring systems, which currently requires costly ground infrastructures.

- In the rail domain, the European Train Control System (ETCS) is the automatic signaling, control and train protection system that is currently being deployed for an improved interoperability in Europe. In ETCS level 2 and 3, the vehicles have to self-monitor their position and speed based on a combination of radiobeacons (Eurobalises) installed along the railway to provide reference positions - and odometry. The density of these radiobeacons should be at least one per 2.5 km. The possible introduction of GNSS in ETCS could thus allow a significant reduction in the number of radiobeacons resulting in an important cost saving and a reduced exposition to degradations and robbery.

- In the road domain, GNSS could be used as a technology for Electronic Toll Collection (ETC) in order to replace or limit the amount of costly tolling gates necessary for other technologies. GNSS is already used for tolling of heavy good transportation in Germany (Toll Collect) and Slovakia (MYTO).

The main objective of this PhD thesis is to investigate the feasibility of using GNSS-based positioning for these two above-mentioned applications, which means understanding of its specificities, construction of a position solution and insurance of the matching of the positioning quality provided with the application requirements.

The first challenge that slows down the introduction of satellite navigation in these critical terrestrial applications is the lack of standardized requirements for the GNSS-based positioning system. This process took long years in civil aviation and is a work in process in rail and road. The first objective of the thesis is thus to investigate the foreseen operational requirements for train control and ETC.

As mentioned earlier, unlike aircrafts and ships that operate in open sky conditions, terrestrial vehicles are likely to operate in constrained environments such as forests, urban canyons and tunnels. The performances of GNSS in terms of accuracy are highly dependent on the environment in which the receiver is located. The thesis focuses on the most challenging environments which are suburban and urban environment. In urban environment, the obstacles such as buildings and vehicles usually mask several satellites and thus degrade the geometry of the constellation from the receiver point of view. In deep urban canyons and tunnels, even less than 4 satellites may be in view which leads to GNSS unavailability (depending on the dimension of positioning, e.g. 2D, 3D, 4D). As standalone GNSS can have poor availability in constrained environment, it requires the use of complementary sensors. For instance, inertial navigation provides a positioning solution by integrating angular rates and specific forces from Inertial Measurement Units (IMU). Therefore, unlike GNSS, the resulting solution is independent from the propagation environment of the vehicle. However this technology cannot be used on its own for navigation as the position error is unbounded due to integration of biases. By coupling GNSS with a 6 axis IMU, it is possible to get a solution that is more accurate than each system taken separately because of the complementarity of their error models. Other sensors or information can be available on terrestrial vehicles such as wheel speed sensors and track database for rail applications. The integration of these measurements can be used to improve the accuracy and the robustness of the whole navigation algorithm. A second objective of this PhD thesis is to propose concrete system architectures that integrate the different sensors available on board for both rail and road applications.

In order to design the sensor fusion algorithm (as well as to design an efficient integrity monitoring algorithm), it is necessary to characterize and model the measurement error associated to each sensor integrated in the solution. These errors, classified into nominal and faults (from an integrity point-of-view) and their different sources are investigated in this thesis. In particular, the distribution and magnitude of the GNSS measurement errors specific to an urban environment are of interest. In suburban and urban environments, the GNSS measurements can frequently be affected by large errors due to strong multipath. If the satellite is not in view which is likely to happen when the satellite is

masked by a building, the receiver may track a diffracted or reflected ray. This phenomenon is referred to as Non Line-Of-Sight (NLOS) reception. The range measurements that result from NLOS signals are positively biased compared to the true geometric ranges due to the non-direct trajectory of the signal. They can thus lead to erroneous positioning. Such error sources and their distributions should be investigated and modelled in order to derive realistic models. This is another objective of this thesis.

Then, another objective of this thesis is to design the data fusion algorithms and assess their performance in order to check that they are coherent with the anticipated performance requirements. This study can be conducted by simple simulations, by feeding the algorithm with measurements generated by a measurement generator that integrates the realistic sensors measurement error models developed in this thesis. Another objective of this study is to implement the proposed fusion algorithms on real data campaigns. Quantizing the benefit of integrating as much measurement and sensors as possible is of particular interest.

Then the possibility to improve the reliability of the solutions by pre selecting the GNSS measurement according to the values of different criterion is investigated. The objective is to assist the integrity monitoring algorithm by excluding from the solution the faulty-prone measurements (due to the effects of the environment). In particular, one of the motivations of this thesis is to detect abnormal measurements at the signal processing level. Moreover, the use of additional sensors appears to be a promising technique to protect against outliers among the GNSS measurement.

Finally, the positioning systems have to be augmented to fulfill the integrity requirements of the critical applications of interest. Current augmentations systems were designed to monitoring integrity of GNSS positioning in the context of civil aviation. Algorithms inspired from ABAS are deemed to be the best candidates because they are able to detect failures of the receiver. The last objective of this PhD thesis is thus to adapt integrity monitoring algorithms to the proposed GNSS/Sensors architecture and assess their true performances in real urban/sub-urban environments.

1.2 Contributions

The major contributions of this thesis are:

- A state of the art of the existing operational requirements for train control and ETC has been done.
- A realistic way to fulfill the very low integrity risk requirement for train control is proposed based on using redundant subsystems based on independent constellations
- A characterization of pseudorange error measurements due to multipath have been conducted by connecting a realistic receiver simulator to the Land Mobile Satellite channel developed by the DLR. After overbounding of the error distribution, an error model has been proposed for urban environment. The results have been published in [Brocard et al., 2014 (1)].
- New results have been found for the detection of abnormally large multipath interference by monitoring the correlation function. It includes rigorous threshold expressions to design the tests, and a theoretical way to assess the performance of such tests in terms of sensitivity. The

behavior of such metric was investigated on the tracking simulator connected to the DLR model. The results have been published in [Brocard et al., 2014 (2)].

- The measurement model of GNSS, IMU, Wheel Speed Sensors (WSS) and track database have been proposed. The models are added to the ideal sensor measurements that are generated by simulations. It is used as the reference for the validation of the system in the nominal case. Failure sources and models for each sensor are proposed in this work.
- An Extended Kalman Filter (EKF) that couples GNSS and a 6 axis IMU has been proposed, and implemented. The IMU measurements are processed by a quaternion based mechanization that has been implemented. A method for the validation of the GNSS/IMU hybridized filter is proposed. Two architectures for ETC and train control have been developed. In particular, a method to integrate the measurement from the track database is given in this thesis. Early results obtained by simulations and real signals have been published in [Brocard et al., 2015 (1)].
- A statistic NLOS error model in urban environment is proposed in the Thesis. The distribution of NLOS error is also assessed thanks to a real measurement campaign. It will be used to characterize this source of failure in urban environment. A test based on the predicted pseudorange (innovation) is used to detect the abnormally large jumps and exclude or down weight the dangerous measurements due to NLOS and residual multipath.
- A method to calculate the biases that are critical in the sense that they can make the error exceed the *HAL* is given. The output of this calculation is used as the input of the multipath detection algorithm and the innovation monitoring test.
- An integrity monitoring algorithm designed for GPS/INS architectures in civil aviation is adapted to our case of study. It aims at providing protection levels and detecting the residual faulty measurements. The results obtained with such an algorithm have been published [Brocard et al., 2015 (2)]. A reliability checking algorithm for the IMU is also proposed.
- Finally, accuracy and integrity performances of the proposed solutions are assessed in real urban environment in downtown Toulouse.

1.3 Outline

Chapter 1 contains the context and the objective of the thesis and an introduction to the chapters of the thesis.

Chapter 2 is a state of the art of GNSS and inertial navigation. It describes the GNSS signals, a basic least square navigation algorithm and the principle of an autonomous integrity monitoring algorithm through the example of receiver autonomous integrity monitoring algorithm. The second part of the chapter is an introduction to inertial navigation that describes the 3D quaternion based mechanization that has been implemented in the thesis.

Chapter 3 is a state of the art on the existing examples of requirements for the GNSS to be used in train control and ETC.

Chapter 4 discusses the choices in terms of GNSS receiver and of additional sensors that are available on board and that can be used to improve navigation. The choice of the coupling integration strategy is discussed in this chapter.

Chapter 5 contains a full description of the nominal error models for every sensor including GNSS, gyroscopes, accelerometers, wheel speed sensors and track database. These nominal error models will be used to generate simulated realistic sensor outputs and validate the navigation algorithm. They are used for modelling the error in the Extended Kalman Filter observation and propagation models. The failure sources are investigated in the second part of the chapter for GNSS and sensors. In particular, the distribution of NLOS pseudorange biases in urban environment is modelled statistically and compared to the observations real measurements.

Chapter 6 describes the implemented hybridized solution for ETC and train control. The design of the fusion algorithms are detailed in this chapter. The integration of the data from WSS and a track database in the measurement model are detailed in this chapter. Moreover, the extension of the algorithm to the dual constellation case is presented. The second part of the chapter consists in the validation and the results obtained on simulated GNSS and sensor measurements. The third part of the chapter describes the results and assesses the performances in term of accuracy of the two architectures proposed in urban environment on real receiver processing GPS and GLONASS and a MEMS 6 axis IMU. The ways to improve the accuracy of the solutions are discussed in the chapter.

Chapter 7 discusses ways to select the GNSS measurements in order to assist the integrity monitoring algorithm by excluding the measurements that are likely to be affected by large local errors. This chapter firstly describes a way to enhance integrity at the signal processing level and presents a method to design and assess the performances of signal quality monitoring indicators. These metrics quantizes the distortion of the correlation function and inform the integrity monitoring algorithm of the potentially dangerous measurements due to multipath interference. The metrics are tested on the DLR model processed by a realistic tracking simulator. Then the possibility of selecting the measurements based on other criterions such as elevation or C/N_0 is investigated.

Chapter 8 investigates the approach to monitor integrity in urban environment. The integrity risk allowed for each application is firstly allocated among the sensors that are integrated. Then the integrity risk allocated to GNSS is shared among the different failure modes. Then, the section describes the integrity monitoring algorithms for both the GNSS and IMU. The snapshot integrity monitoring algorithm used is firstly described. The performances of this integrity monitoring algorithm are assessed on a real dataset in urban environment. Then, this chapter describes an advanced way to adjust in real time the thresholds for the outlier detections algorithms (multipath detector and innovation monitoring) as a possible way to improve the integrity of the solution. Finally, the way to monitor the reliability of the inertial measurement is looked at.

Chapter 9 presents the conclusion and perspectives of this thesis

1.4 References

- [Brocard et al., 2014 (1)] Brocard, P.; Salos, D.; Julien, O.; Mabillean, M., "Performance evaluation of multipath mitigation techniques for critical urban applications based on a land mobile satellite channel model," Position, Location and Navigation Symposium - PLANS 2014, 2014 IEEE/ION , vol., no., pp.612,625, 5-8 May 2014
- [Brocard et al., 2014 (2)] Brocard, Philippe, Thevenon, Paul, Julien, Olivier, Salos, Daniel, Mabillean, Mikael, "Measurement Quality Assessment in Urban Environments Using Correlation Function Distortion Metrics," Proceedings of the 27th International Technical Meeting of The Satellite Division of the Institute of Navigation (ION GNSS+ 2014), Tampa, Florida, September 2014, pp. 2684-2697:
- [Brocard et al., 2015 (1)] Brocard, P., Julien, O., Mabillean, M., "Performance assessment of GPS/INS/Track database tight coupling for rail applications", ITS World Congress, Bordeaux, 2015
- [Brocard et al., 2015 (2)] Brocard, Philippe, Julien, Olivier, Mabillean, Mikael, "Autonomous Integrity Monitoring Proposal for Critical Rail Applications," Proceedings of the 28th International Technical Meeting of The Satellite Division of the Institute of Navigation (ION GNSS+ 2015), Tampa, Florida, September 2015, pp. 706-734

2 STATE OF THE ART ON GNSS AND INERTIAL NAVIGATION

This chapter introduces the two main technologies that are used in this thesis for the navigation, that is to say GNSS and inertial navigation. First the basic principles of GNSS are investigated. Then, the possible ways to augment the GNSS that have been developed in the context of civil aviation are presented. These augmentation systems have been used to monitor the integrity of the GNSS solution and measurements. Second, the basic principles of inertial navigation are presented. The different sensors' technologies are introduced. Then the frames of reference are defined, and finally, the way to estimate the vehicle position, velocity and attitude from inertial sensors is detailed.

2.1 Principle of GNSS and possible augmentations

The GNSS enables civil and military users to determine their positions, velocity and time anywhere in the world at any time. The GNSS that are operational are GPS developed by the USA and GLOBAL NAVIGATION SATELLITE SYSTEM (GLONASS) developed by Russia. The other GNSS that are currently under development are Galileo developed by Europe and BeiDou developed by China.

A GNSS is composed of three segments, referred to as the space segment, the control segment and the user segment. This section describes briefly these three segments successively. Then the augmentation systems that have been developed for monitoring the integrity of the GNSS measurements in the case of civil aviation are described.

2.1.1 Space segment

The space segment corresponds to the constellation of the transmitting satellites.

- The GPS system, which was declared operational in 1995 by the US Department Of Defence, is specified with a minimum of 24 Medium Earth Orbit (MEO) satellites located in 6 circular orbital planes inclined of 55° . The constellation is designed so that any user will have at least 4 satellites in view anywhere at any time. The GPS constellation currently (November 2015) consists of 30 Healthy satellites. GPS satellites are at an altitude of 20200 km.
- The GLONASS system was initially (1995) composed of 24 satellites located at an altitude 19100 km on three orbital planes inclined of approximately 65° . The GLONASS constellation currently consists of (November 2015) 23 operational satellites (on 28 satellites in orbit).
- Galileo is expected to be composed of 30 satellites (24 + 6 spares) located on 3 orbits located at an altitude of 23222 km. The orbital planes are inclined of 56° with respect to the equatorial axis.

The satellites are transmitting the GNSS signals that enable the receivers to estimate their positions. These signals are using direct sequence - spread spectrum techniques, meaning that they have three main components:

- a sinusoidal carrier. As an example, for GPS, the carrier frequencies are L1: 1575.42 MHz, L2: 1227.60 MHz, and L5: 1176.45 MHz. For GPS and Galileo, all the satellites of a given constellation transmit in the same frequency band without interfering thanks to the use of Code Division Multiple Access (CDMA). For GLONASS, each satellite transmits a signal at its own slightly shifted carrier frequency. This multiplexing method is referred to as Frequency Division Multiple Access (FDMA).
- a Pseudo Random Noise (PRN) code, also referred to as ranging code or spreading code. The PRN code is a sequence of zeros and ones that are used by the GNSS receiver to acquire and get synchronized with the received signal, thus enabling it to generate relatively accurate pseudorange measurements for each satellite. Each satellite uses its own spreading code, which is known by the receiver. The spreading codes used by GPS L1 C/A signals are Gold code which length is 1023 chips. The chip rate of the PRN code is significantly high with respect to the bit rate of the navigation message thus spreading the frequency occupation of the useful signal. This is why this type of communication is referred to as spread spectrum technique. For GPS L1 C/A, the chip rate is equal to 1.023 Mchips per second.
- The navigation message, which is a binary sequence that provides all the necessary information for the user to compute pseudorange measurements. This message is narrowband with respect to the PRN code (for GPS L1 C/A, the data rate is 50 bits per second). For GPS L1 C/A, the navigation message is periodic with a period of 12.5 minutes. In the case of GPS, the navigation message contains, among others, the satellite ephemeris, the satellite clock error model, the ionosphere delay model, the satellite health status and the constellation almanac. Some GPS and Galileo signals do not contain any navigation messages. They are referred to as pilot signals and enable more robust tracking capabilities.

The model of the signal transmitted by a GNSS satellite is the following:

$$s(t) = Ad(t)c(t) \cos(2\pi f_0 t) \quad \text{Eq. 2-1}$$

where:

- d is the materialization of the navigation message of the satellite
- c is the PRN code after pulse shaping
- f_0 is the frequency of the carrier.
- A is the amplitude of the signal

The GPS, Galileo and GLONASS satellites transmit different signals with different characteristics which are summarized in Table 1.

System	Carrier Frequency (MHz)	Signal	Band Width (MHz)	I/Q	Modulation	Spreading Code					Navigation Data			
						Primary (chips)	Second (chips)	Mcps	Period	ENC	Data	Rate (sps)	Rate (bps)	FEC
GPS	1575.42	L1C/A	2.046	Q	BPSK (1)	1,023	-	1.023	1ms	-	NAV	50	50	-
		L1P(Y)	20.46	I	BPSK (10)	1week	-	10.23	1week	(Y)	NAV	50	50	-
		L1M	N.A	N.A	BOC (10,5)	N.A	N.A	5.115	N.A	Y	N.A	N.A	N.A	N.A
		L1C	30.69	I/Q	TMBOC (6,1,4/33)	10,230	-	1.023	10ms	-	CNAV-2	100	50	1/2
						10,230	1,800	1.023	18s	-	-	-	-	
		L2P(Y)	20.46	I	BPSK (10)	1week	-	10.23	1week	(Y)	(NAV)	(50)	(50)	-
		L2M	N.A	N.A	BOC (10,5)	N.A	N.A	5.115	N.A	Y	N.A	N.A	N.A	N.A
	L2C	2.046	I/Q	BPSK (1)	10,230	-	0.5115	20ms	-	(CNAV)	(50)	(25)	1/2	
					767,250	-	0.5115	1.5s	-	-	-	-		
	1176.45	L5-I	20.46	I	BPSK (10)	10,230	10	10.23	10ms	-	CNAV	100	50	1/2
L5-Q		20.46	Q	BPSK (10)	10,230	20	10.23	20ms	-	-	-	-	-	
GLONASS	1602.00+ 0.5625K	L1C/A	1.022	I/Q	BPSK	511	-	0.511	1ms	-	NAV	50	50	-
		L1P	10.22		BPSK	5,110,000	-	5.11	1s	(Y)	NAV	50	50	-
	1246.00+ 0.4375K	L2C/A	1.022	I/Q	BPSK	511	-	0.511	1ms	-	NAV	50	50	-
		L2P	10.22		BPSK	5,110,000	-	5.11	1s	(Y)	NAV	50	50	-
	1204.704+ 0.423K	L3C/A	8.19	I	BPSK	N.A	-	4.095	N.A	N.A	N.A	N.A	N.A	N.A
		L3P	8.19	Q	BPSK	N.A	-	4.095	N.A	N.A	N.A	N.A	N.A	N.A

Galileo	1575.42	E1-A	35.805	Q	BOC (15,2.5)	N.A	N.A	2.5575	N.A	Y	G/NAV	N.A	N.A	N.A
		E1-B	24.552	I	CBOC (6,1,1/11)	4,092	-	1.023	4ms	-	I/NAV	250	125	1/2
		E1-C	24.552	Q	CBOC (6,1,1/11)	4,092	25	1.023	100ms	-	-	-	-	-
	1191.795	E5	51.15	I	8-PSK (10)	10,230	100	10.23	100ms	-	-	-	-	-
	1176.45	E5a-I	20.46	I	BPSK (10)	10,230	20	10.23	20ms	-	F/NAV	50	25	1/2
		E5a-Q	20.46	Q	BPSK (10)	10,230	100	10.23	100ms	-	-	-	-	-
	1207.14	E5b-I	20.46	I	BPSK (10)	10,230	4	10.23	4ms	-	I/NAV	250	125	1/2
		E5b-Q	20.46	Q	BPSK (10)	10,230	100	10.23	100ms	-	-	-	-	-
	1278.75	E6-A	N.A	Q	BOC (10,5)	N.A	N.A	5.115	N.A	Y	G/NAV	N.A	N.A	N.A
		E6-B	40.92	I	BPSK (5)	5,115	-	5.115	1ms	Y	C/NAV	1,000	N.A	N.A
		E6-C	40.92	I	BPSK (5)	5,115	100	5.115	100ms	Y	-	-	-	-

Table 1 GNSS signals specifications [RTKLIB]

The first step in the generation of the GNSS signal consists in mapping the two binary sequences (navigation message and the PRN code) into BPSK symbols (+1 or -1). This operation is called pulse shaping. The data symbols are shaped by a Non-Return to Zero (NRZ) waveform, defined by:

$$h_{NRZ}(t) = \begin{cases} 1 & \text{if } 0 \leq t \leq T_d \\ 0 & \text{else} \end{cases} \quad \text{Eq. 2-2}$$

where T_d represents the data bit duration.

$$d(t) = \sum_{k=0}^{N-1} d_k h_{NRZ}(t - kT_d) \quad \text{Eq. 2-3}$$

The PRN symbols can be shaped differently.

- In the case of legacy signals, such as GPS L1 C/A or GLONASS L1, the shaping waveform is also an NRZ waveform except that the time support of the waveform is the chip duration T_c (chip duration).
- Some new signals are modulated by a different waveform. For instance, Galileo E1 OS is shaped by a Composite BOC (CBOC) waveform [RTKLIB].

The shaped PRN sequence and data bits are then synchronized and multiplied. This product then modulates the carrier.

2.1.2 Control segment

Each GNSS has its own control segment which consists in a network of monitoring stations, control stations and upload stations. The control segment has to:

- monitor the quality of the transmitted signals and parameters,
- predict the satellites' orbits, clock drift with respect to GNSS time, and some other parameters,
- upload these information on each satellite.

It is thus a key element in the reliability of the system.

2.1.3 User segment

The User Segment consists in the equipment which receives and processes the GNSS signals, compute pseudoranges (and other observables), and user location and clock. The structure of a GNSS receiver is composed of an Antenna, an RF Frontend, a signal processing unit, and a data processing unit. These elements are discussed in this section.

2.1.3.1 Antenna/frontend

The receivers are equipped with an antenna to capture the GNSS signals in the L-band. GNSS antennas can be of different types (patch, helical, spiral, choke ring, phased-array), sizes, shapes, prices and therefore adapted to different types of users. The GNSS signals are transmitted from the antenna to the front-end by cable. If the antenna is located at a non-negligible distance from the receiver, the transmission may be associated with power losses. This phenomenon can be mitigated by including a low-noise amplifier in the antenna, that is then referred to as active antenna (in contrast with passive antennas). At the output of the receiver's antenna, the signal $r(t)$ from one single GNSS satellite can be modelled as:

$$r(t) = g(t) \otimes s(t) + w(t) \quad \text{Eq. 2-4}$$

where:

- g is the pulse response of the propagation channel.
- w is an additive white noise
- \otimes is the convolution product

If the channel is modelled as only adding a pure delay to the signal, the expression of $r(t)$ becomes:

$$r(t) = A(t)d(t - \tau(t))c(t - \tau(t)) \cos(2\pi ft + \phi(t)) + w(t) \quad \text{Eq. 2-5}$$

where:

- τ is the code delay
- ϕ is the time-varying carrier phase delay due to the propagation

- the amplitude A varies with time

The signal is then transmitted to the RF Front-End where it is amplified with a Low Noise Amplifier (LNA), filtered, and downconverted to an intermediate frequency denoted f_I by multiplying by the carrier generated by a local oscillator. The signal is then filtered, quantized and sampled with an Analog to Digital Converter (ADC). The processing of the signal by the RF front end induces the addition of a thermal noise to the received signal.

2.1.3.2 Signal processing unit

The samples processed by the RF frontend are then transmitted to the signal processing module of the receiver. The GNSS signal from a given satellite at the output of the RF frontend can be modelled as (the channel is considered as a delay):

$$r_f(k) = A(kT_s)d(kT_s - \tau(kT_s))c_f(kT_s - \tau(kT_s)) \cos(2\pi f_I kT_s + \phi(kT_s)) + n(kT_s) \quad \text{Eq. 2-6}$$

where:

- T_s is the sampling period of the receiver
- c_f represents the code filtered by the user's antenna and the front end filter
- $n(kT_s)$ represents the thermal noise

The receiver has to synchronize itself with this GNSS signals. This operation is necessary to demodulate the data message and to estimate the pseudorange observables. The synchronization of the receiver consists in estimating the delay of the PRN code τ and the phase offset of the carrier of the incoming signal ϕ . The synchronization is done in two consecutive steps.

- First, the receiver assesses the presence of the signal during the acquisition phase. This process is coupled with the coarse estimation of the incoming signal code delay and Doppler frequency. The principle of the acquisition is not presented here because this step is not further looked at in the thesis. However acquisition principles can be found in e.g. [Foucras, 2015].
- Then the receiver enters a tracking mode in which the code delay and carrier phase are tracked more precisely using two different control loops. The principle of tracking loops is introduced here as techniques to improve the robustness of these loops have been investigated during the thesis. In a conventional receiver, the incoming signal code delay is tracked with a Delay Locked Loop (DLL) and the incoming carrier phase is tracked by a Phase Locked Loop (PLL).

For the acquisition and both loops, the GNSS receiver needs to go through a specific signal processing step referred to as the correlation operation. This correlation operation consists in correlating the incoming GNSS signal with a local replica of this signal composed of the PRN code and the carrier over a duration T_i which is a multiple of the PRN code repetition period. For GPS L1 C/A, the integration time varies from 1ms to 20ms, which corresponds to the duration of a data bit. The local carrier is generated with a phase denoted $\hat{\phi}$ as estimated by the PLL and the local PRN code with a

delay denoted $\hat{\tau}$ that is estimated by the DLL. For the simplicity of the notations, the parameters which are time dependent are indexed by k . Assuming that the variations of the code phase delays are small during the integration time, the In-phase correlator output can be approximated by [Holmes, 2000]:

$$I_P(i) = \frac{A_k}{2} d_k K_{cc}(\tau_k - \hat{\tau}_k) \text{sinc}(\pi(f_k - \hat{f}_k)T_i) \cos(\phi_k - \hat{\phi}_k) + n_{I_P}(k) \quad \text{Eq. 2-7}$$

where:

- f_{d_k} represents the Doppler frequency of the received signal, it is such as $f_{d_k} = \left. \frac{1}{2\pi} \frac{d\phi}{dt} \right|_{t=kT_s}$ and \hat{f}_k , its estimation.
- K_{cc} represents the autocorrelation function the spreading code

It is also usual to compute the Quadra-phase correlator output by using a local carrier in quadrature-phase with the incoming signal. Its model is given by:

$$Q_P(i) = \frac{A_k}{2} d_k K_{cc}(\tau_k - \hat{\tau}_k) \text{sinc}(\pi(f_k - \hat{f}_k)T_i) \sin(\phi_k - \hat{\phi}_k) + n_{Q_P}(k) \quad \text{Eq. 2-8}$$

2.1.3.2.1 Principle of a conventional DLL

In a conventional DLL, after being multiplied by the in-phase and quadrature phase local carrier, the signal is multiplied by three versions of the code replica:

- The prompt replica which delay is the code delay estimated by the DLL ($\hat{\tau}(k)$),
- the early replica which delay is $\hat{\tau}(k) + \delta/2$, and
- the late replica which delay is $\hat{\tau}(k) - \delta/2$.

The parameter δ is referred to as the chip spacing, and is a fundamental parameter which has an impact on the performances of the DLL. This provides 6 correlator outputs as detailed in Figure 1: the in-phase prompt, early and late correlator outputs, as well as the quadrature-phase prompt, early and late correlator outputs. Their expressions are given hereafter:

$$I_E(i) = \frac{A_k}{2} d_k K_{cc} \left(\tau_k - \hat{\tau}_k + \frac{\delta}{2} \right) \text{sinc}(\pi(f_k - \hat{f}_k)T_i) \cos(\phi_k - \hat{\phi}_k) + n_{I_E}(i) \quad \text{Eq. 2-9}$$

$$Q_E(i) = \frac{A_k}{2} d_k K_{cc} \left(\tau_k - \hat{\tau}_k + \frac{\delta}{2} \right) \text{sinc}(\pi(f_k - \hat{f}_k)T_i) \sin(\phi_k - \hat{\phi}_k) + n_{Q_E}(i) \quad \text{Eq. 2-10}$$

and the two late correlator outputs are formed:

$$I_L(i) = \frac{A_k}{2} d_k K_{cc} \left(\tau_k - \hat{\tau}_k - \frac{\delta}{2} \right) \text{sinc}(\pi(f_k - \hat{f}_k)T_i) \cos(\phi_k - \hat{\phi}_k) + n_{I_L}(i) \quad \text{Eq. 2-11}$$

$$Q_L(i) = \frac{A_k}{2} d_k K_{cc} \left(\tau_k - \hat{\tau}_k - \frac{\delta}{2} \right) \text{sinc}(\pi(f_k - \hat{f}_k)T_i) \sin(\phi_k - \hat{\phi}_k) + n_{Q_L}(i) \quad \text{Eq. 2-12}$$

The correlator outputs are then combined to estimate the code delay tracking error $\varepsilon_{\tau_k} = \tau_k - \widehat{\tau}_k$. This estimation operation is referred to as discriminator function. A code discriminator is referred to as coherent when its value is dependent of the value of the carrier tracking error: $\varepsilon_{\phi_k} = \phi_k - \widehat{\phi}_k$. The Early-Minus-Late (EML) discriminator is an example of coherent discriminator. Its expression is given by:

$$D_{EML} = I_E - I_L \quad \text{Eq. 2-13}$$

For noncoherent discriminators, the estimation of the code delay is independent of the quality of the estimation of the phase delay (but still depends on the residual Doppler error between the incoming and local carriers). Non coherent discriminators are more suitable in urban environment because frequent losses of phase lock can occur, and may degrade the quality of the code measurements. The Early-Minus-Late Power (EMLP) is an example of classic non coherent discriminators:

$$D_{EMLP} = (I_E^2 + Q_E^2) - (I_L^2 + Q_L^2) \quad \text{Eq. 2-14}$$

Finally, the estimation of ε_{τ} provided by the discriminator is low-pass filtered to update the frequency of the DCO used to generate the local PRN code replica. The principle of the conventional DLL is summarized by Figure 1.

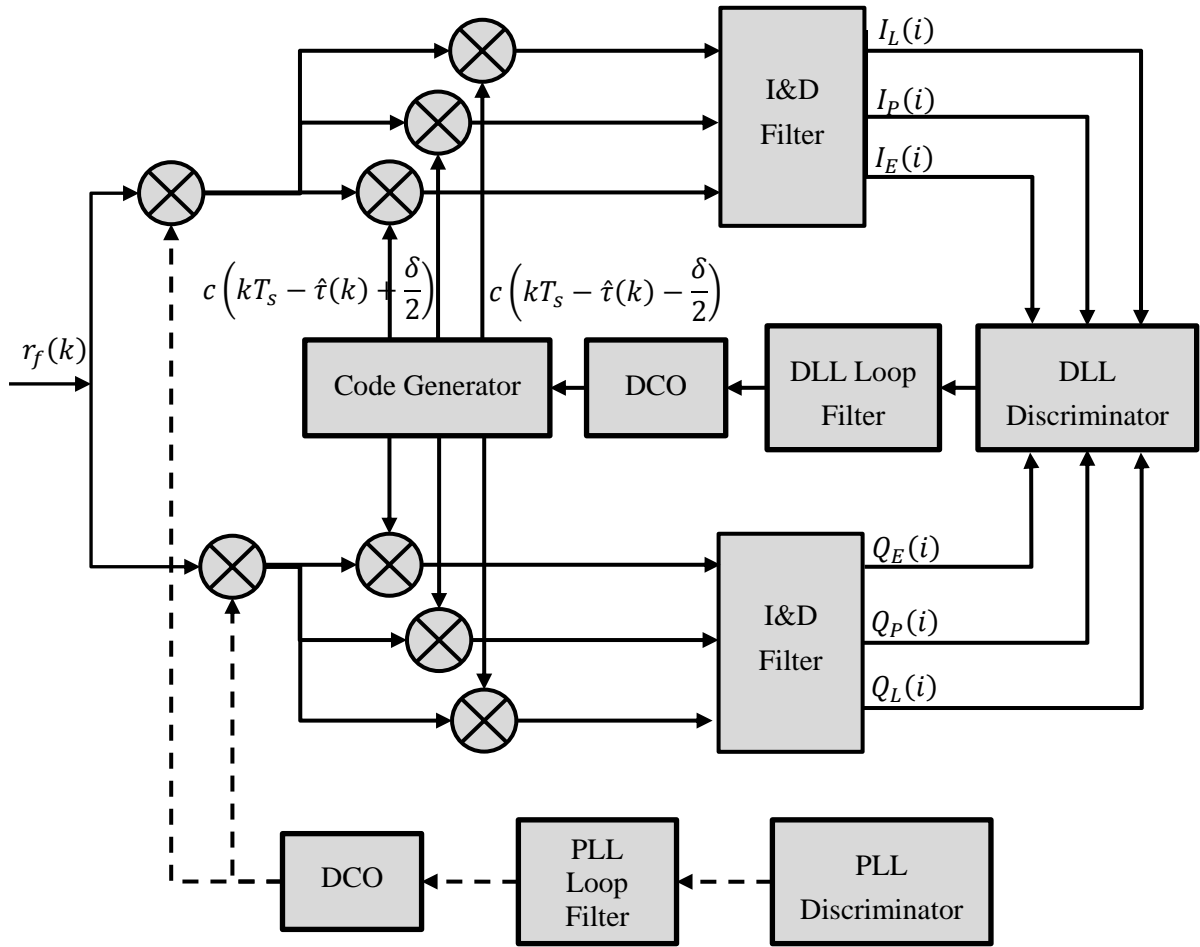


Figure 1 Principle of the Delay Lock Loop

2.1.3.2.2 Principle of a conventional PLL

The PLL consists in generating a local carrier with a DCO which frequency is adjusted so that the local carrier is in phase with the received carrier. The prompt In-phase and Quadrature phase correlator outputs are combined in a phase discriminator to estimate the phase error ε_ϕ . Several PLL discriminators can be found in the literature. The arctangent discriminator is one of them that is defined as:

$$D_{Atan} = \text{Atan}\left(\frac{Q_p}{I_p}\right) \quad \text{Eq. 2-15}$$

The phase error estimate is then low-pass filtered by the loop filter to update the phase of the local carrier.

A frequency locked loop (FLL) may be used instead of a PLL for carrier synchronization (not a phase synchronization). The principle of this control loop can be found in [Curran et al., 2012].

2.1.3.3 GNSS position estimation

The code delay and carrier phase synchronization allows to have an in-phase correlator output that can be simplified into:

$$I_P(i) = \frac{A}{2} d(i) + n_{IP}(i) \quad \text{Eq. 2-16}$$

It can thus be seen that the correlator output can then be used to demodulate the data bits as long as the signal to noise ratio is high enough.

As a consequence, when the tracking loops are locked, their outputs are:

- The navigation message bits
- The knowledge of the received time and phase of the incoming signal. This, with the knowledge of the transmit time, can be translated into raw pseudorange measurements

These raw measurements can be used to compute the user position. Prior to the estimation of the position, however, the ionospheric, tropospheric and satellite clock corrections are applied to the raw measurements. The receiver then has to estimate its position based on the following observables:

$$\begin{cases} \rho_1(t) = \sqrt{(x(t) - x_1(t))^2 + (y(t) - y_1(t))^2 + (z(t) - z_1(t))^2} + c\Delta t_u(t) + \varepsilon_1(t) \\ \vdots \\ \rho_n(t) = \sqrt{(x(t) - x_n(t))^2 + (y(t) - y_n(t))^2 + (z(t) - z_n(t))^2} + c\Delta t_u(t) + \varepsilon_n(t) \end{cases} \quad \text{Eq. 2-17}$$

where :

- ρ_i are the GNSS pseudoranges
- x, y and z are the coordinates of the receiver that have to be estimated. They are generally expressed in the Earth-Centered Earth-Fixed Frame (ECEF).
- x_i, y_i and z_i are the coordinates of satellite i in the same frame
- ε_i is the residual error on the pseudorange measured with respect to the satellite i after correction
- Δt_u is the clock offset between the receiver's internal clock and the GNSS system time

Let us denote $X(t)$ the vector which components are the four parameters to estimate: $x(t), y(t), z(t)$ and $\Delta t_u(t)$. The observable can be related to $X(t)$ with the function:

$$h_{i,t}(X(t)) = \sqrt{(x(t) - x_i(t))^2 + (y(t) - y_i(t))^2 + (z(t) - z_i(t))^2} + c\Delta t_u(t) \quad \text{Eq. 2-18}$$

The system can be written in terms of vector with:

$$Y(t) = h_t(X(t)) + \varepsilon(t) \quad \text{Eq. 2-19}$$

where:

- h_t corresponds to the concatenation of the $h_{i,t}$ functions

- $\varepsilon(t) = [\varepsilon_1 \quad \dots \quad \varepsilon_n]^T$

Different estimation methods can be used to estimate X_t such as iterative Least Squares Estimator (LSE)/Weighted Least Squares Estimator (WLSE), recursive least squares [Yuheng et al., 2010], Bancroft method [Bancroft, 1985] or Kalman filtering if the dynamic of the vehicle is modelled. The LSE/WLSE method to estimate X_t is detailed hereafter.

Let us denote $\hat{X}_0(t)$ an initial estimate of $X(t)$. The previous estimation is generally used as \hat{X}_0 . Let us denote $X(t) = \hat{X}_0(t) + \Delta X(t)$. The measurement model can be rewritten:

$$Y(t) = h_t \left(\hat{X}_0(t) + \Delta X(t) \right) + \varepsilon(t) \quad \text{Eq. 2-20}$$

The model linearized $\hat{X}_0(t)$ around becomes:

$$Y(t) \cong h_t \left(\hat{X}_0(t) \right) + \frac{\partial h_t}{\partial X} \left(\hat{X}_0(t) \right) \Delta X(t) + \varepsilon(t) \quad \text{Eq. 2-21}$$

The linearized model can be written:

$$\Delta Y(t) \cong H(t) \Delta X(t) + \varepsilon(t) \quad \text{Eq. 2-22}$$

where:

- $\Delta Y(t) = Y(t) - h_t \left(\hat{X}_0(t) \right)$
- H is the Jacobian of h_t

$$H = \begin{bmatrix} \frac{\hat{x}_0(t) - x_1(t)}{d_1} & \frac{\hat{y}_0(t) - y_1(t)}{d_1} & \frac{\hat{z}_0(t) - z_1(t)}{d_1} & 1 \\ \vdots & \vdots & \vdots & \vdots \\ \frac{\hat{x}_0(t) - x_n(t)}{d_n} & \frac{\hat{y}_0(t) - y_1(t)}{d_n} & \frac{\hat{z}_0(t) - z_1(t)}{d_n} & 1 \end{bmatrix} \quad \text{Eq. 2-23}$$

- $d_i = \sqrt{[\hat{x}_0(t) - x_i(t)]^2 + [\hat{y}_0(t) - y_i(t)]^2 + [\hat{z}_0(t) - z_i(t)]^2}$

Once the observation model has been linearized, the LSE solution to Eq. 2-22 is given by:

$$\Delta \hat{X}(t) \cong [H(t)^T H(t)]^{-1} H(t)^T \Delta Y(t) \quad \text{Eq. 2-24}$$

When the measurement error covariance matrix (denoted R) is known, the WLSE can be used. The WLSE estimation is:

$$\Delta \hat{X}(t) \cong [H(t)^T R^{-1} H(t)]^{-1} H(t)^T R^{-1} \Delta Y(t) \quad \text{Eq. 2-25}$$

2.1.4 Augmentation systems

Augmentation systems have been developed in the context of civil aviation because the performances of standalone GPS (which are specified in [GPS SPS, 2008]) were not sufficient to fulfill the integrity requirements specified by the ICAO which definitions are detailed in chapter 3 and given in Table 2. There are three sorts of existing augmentation systems which are referred to as Ground Based Augmentation Systems (GBAS), Satellite Based Augmentation Systems (SBAS) and Aircraft Based Augmentation Systems (ABAS). The augmentation systems enable the receiver to monitor the integrity of the GNSS navigation solution by computing Horizontal Protection Levels (*HPL*) and Vertical Protection Levels (*VPL*). The definitions of *HPL* and *VPL* are:

- *HPL* is the radius of a circle in the horizontal plane (the local plane tangent to the WGS-84 ellipsoid), with its center being at the true position, that describes the region assured to contain the indicated horizontal position [RTCA, 2006]. *HPL* is a horizontal region where the missed alert requirements is met for the chosen set of satellites. Missed alert occurred when the position error exceeds the protection level and there is no detection [RTCA, 2006].
- *VPL* is half the length of a segment on the vertical axis (perpendicular to the horizontal plane of the WGS-84 ellipsoid), with its center being at the true position, that describes the region assured to contain the indicated vertical position [RTCA, 2006]. *VPL* is a vertical region where the missed alert requirements is met for the chosen set of satellites.

The system is said to be available if the *PL* estimated thanks to the augmentation system are within the maximum values allowed in the operational requirements, referred to as Alert Limits (*AL*), which definitions are given in Chapter 3. This configuration is represented in Figure 2. The system is said to be unavailable if the *PL* exceeds the *AL* as illustrated in Figure 3.

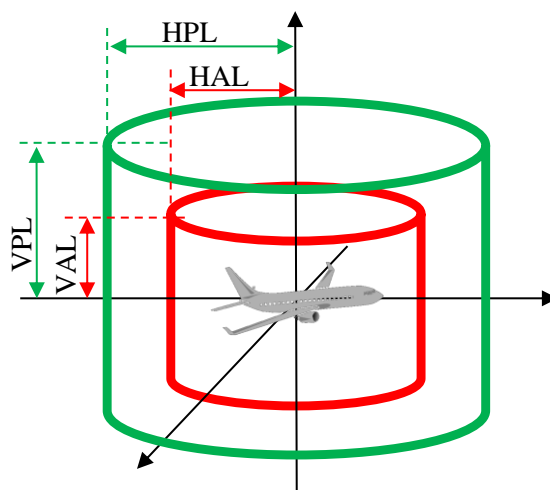
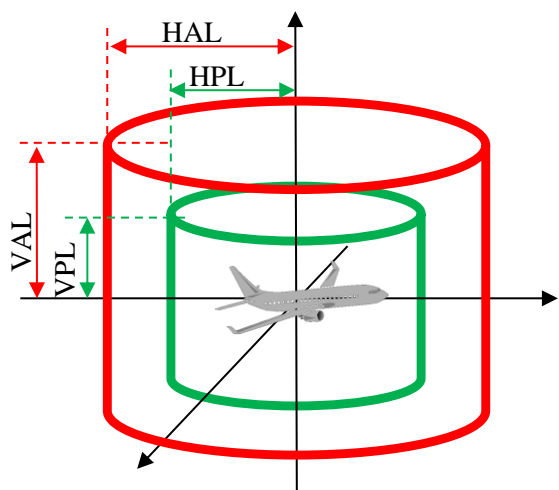


Figure 2 Integrity monitoring algorithm available

Figure 3 Integrity monitoring algorithm unavailable

2.1.4.1 Principle of GBAS

GBAS has been developed for civil aviation applications, in order to enhance the integrity and the accuracy of GNSS in the airport areas. The principle of this augmentation system is similar to the Local Area Differential GPS (LADGPS) concept, but with the provision of integrity information. GBAS systems consist of three subsystems:

- The GNSS satellite subsystem that provides ranging signal and navigation message.
- The GBAS ground system is a station settled near the airport which sends data to the aircrafts within 23 Nautical Miles (42 km), up to Flight Level 100 through a dedicated data link in the VHF frequency band (108-117 MHz). Each station uses several GNSS receivers to measure pseudoranges and compute the augmentation data.
- The Aircraft subsystem that uses the data to correct its measurements, measure its protection levels and exclude the faulty satellites from the computation.

2.1.4.2 Principle of SBAS

The principle of SBAS is similar to that of Wide Area Differential GPS (WADGPS), but with the provision of integrity information. SBAS consist of three subsystems:

- The ground subsystem which contain a network of reference stations and a master station. The stations calculate integrity information and differential corrections for each monitored satellites. The integrity information contains integrity flags and conservative bounds of the range error after application of the differential corrections. Ground transmitters are used to send the data calculated to the GEO (geostationary orbit) satellites.
- The space subsystem contains the GEO transparent satellites that broadcast the SBAS signals with a modulation that is similar to that of GPS L1 C/A.
- The user subsystem is composed of the receivers that process the SBAS data.

The satellites may broadcast additional ranging signal similarly to GNSS satellite but this service is optional. Currently, four SBAS are in an operational capability: Wide Area Augmentation System (WAAS) in North America, European Geostationary Navigation Overlay System (EGNOS) in Europe, MTSAT Satellite Augmentation System (MSAS) in Japan and GPS Aided GEO Augmented Navigation (GAGAN) in India. SBAS frequency band are identical to that of the GPS L1 signal, broadcast in the L1 band, and the signal modulation is BPSK(1).

2.1.4.3 Principle of ABAS

ABAS augment the GNSS information autonomously with information available on the aircraft. It can either employ only GNSS information or take advantage of other sensors like barometric altimeters or inertial sensors. The ABAS scheme referred to as fault detection and exclusion (FDE) enables to monitor the integrity of the position information by taking advantage of the redundancy of the measurements.

The autonomous integrity monitoring algorithms are classified as Receiver Autonomous Integrity Monitoring (RAIM) algorithm when they exclusively use GNSS information and Aircraft Autonomous Integrity Monitoring (AAIM) if they include other on-board sensors [ICAO, 2006].

2.1.4.3.1 Fault detection, Fault exclusion

Fault Detection (FD) or Fault Detection and Exclusion (FDE) are the principles of autonomous integrity monitoring algorithms performed by the receiver. The FDE consists of two distinct parts:

- The Fault Detection part detects the presence of an unacceptably large position error for a given mode of flight. This part is referred to as Receiver Autonomous Integrity Monitoring (RAIM). FD requires at least 5 satellites available to use redundancy.
- The fault exclusion follows and tries to exclude the source of the unacceptably large position error, thereby allowing navigation to return to normal performance without an interruption in service. FDE requires at least six satellites with sufficiently good geometry.

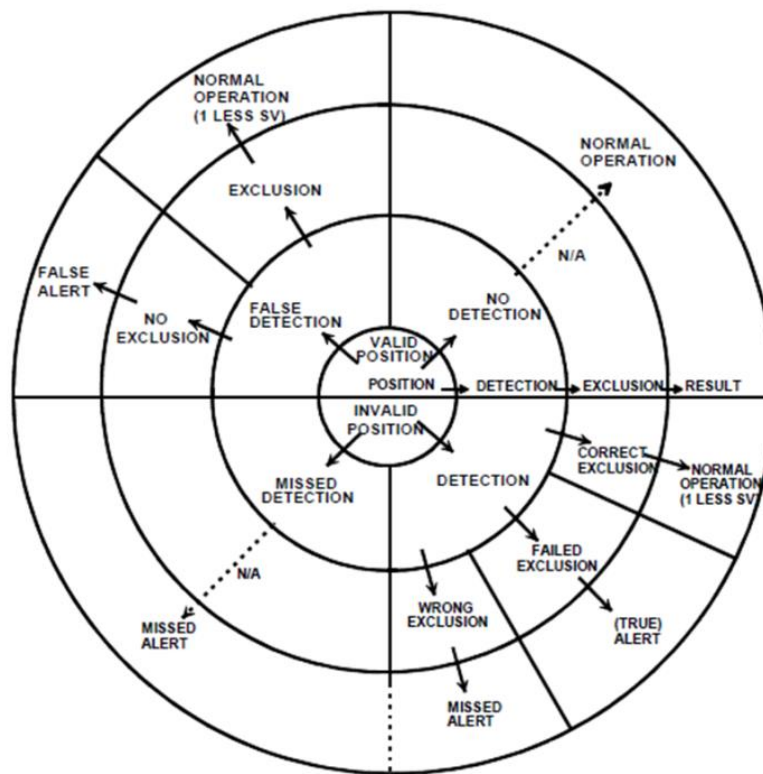


Figure 4 Diagram of FDE configurations [RTCA, 2006]

The several scenarios that can lead to the FDE events are defined in [RTCA, 2006], and summarized in Figure 4:

- A *Positioning failure* is defined to occur whenever the difference between the true position and the indicated position exceeds the applicable alert limit.
- An *Alert* is an indication provided to the receiver when the positioning does not meet the integrity requirements.

- A *False Alert* is defined to occur when a position failure is detected by the algorithm whereas no position failure actually occurred. If the equipment is not aware of the navigation mode/alert limit, a positioning failure is defined to occur whenever the difference between the true position and the indicated position exceeds the applicable protection level.
- A *Missed alert* is defined to occur when position failure is not detected within the time to alert.
- A *Missed detection* is defined to occur when a position failure is not detected
- A *Failed exclusion* is defined to occur when a true positioning failure is detected and the detection condition is not eliminated within the time-to-alert.
- A *Wrong exclusion* is defined to occur when a detection occurs, and a positioning failure exists but is undetected after exclusion, resulting in a missed alert.

RAIM algorithms are divided into “snapshot” and “sequential” depending whether the measurements used are only from the current epoch or from a time period.

2.1.4.3.2 RAIM

RAIMs are algorithms which take advantage of the redundancy of GNSS measurements to monitor integrity. In order to have redundancy:

- at least an additional range measurements with respect to the minimum required to compute the navigation solution is needed for the fault detection function,
- at least two additional range measurements are required for fault exclusion.

First, the weighted least squares residuals (WLSR) RAIM used in civil aviation is analyzed. Then, other RAIM algorithms are discussed including the solution separation (SS) RAIM.

2.1.4.3.2.1 WLSR RAIM

Least Square Residuals (LSR) and Weighted Least Square Residuals (WLSR) are two of the most used algorithms in civil aviation that are discussed in this chapter. These two types of RAIM are snapshot algorithms based on least square position estimation. LSR/WLSR RAIMS usually outperforms solution separation. The LSR RAIM that was published in [Parkinson and Axelrad, 1988] assumes that the errors are described by independent Gaussian distributions with equal variance, which was a meaningful assumption when the selective availability (SA) dominated the pseudorange error. As the SA no longer exists, this assumption is no longer valid and the pseudorange errors shall be characterized by their own variances. The WLSR RAIM which has been proposed in [Walter and Enge, 1995] addresses this case. These two algorithms provide integrity for a navigation solution obtained by applying LSE or WLSE.

Measurement model

The measurement model used for the WLSR RAIM assumes that the pseudorange errors are divided into nominal errors and faults:

- Nominal errors are assumed to follow independent, zero-mean and gaussian distribution

$$\varepsilon(t) \sim \mathcal{N}(0, R(t)) \quad \text{Eq. 2-26}$$

where:

$$R(t) = \begin{bmatrix} \sigma_1^2 & 0 & \dots & 0 \\ 0 & \sigma_2^2 & & \vdots \\ \vdots & & \ddots & 0 \\ 0 & \dots & 0 & \sigma_n^2 \end{bmatrix} \quad \text{Eq. 2-27}$$

In the case of a LSR RAIM, the $R(t)$ matrix is replaced by the identity matrix times the variance of the pseudoranges (denoted σ^2).

- Faults are biased measurements. Only one biased satellite is assumed in the LSR/WLSR RAIM assumptions

$$b = [0 \quad \dots \quad 0 \quad b_i \quad 0 \quad \dots \quad 0]^T \quad \text{Eq. 2-28}$$

Test statistics

The RAIM is a decision test. Two hypotheses to test are defined:

- H_0 : the measurements are nominal, in this case, $\varepsilon(t) \sim \mathcal{N}(0, R(t))$
- H_1 : a satellite is faulty, $\varepsilon(t) \sim \mathcal{N}(b, R(t))$

LSR/WLSR RAIM computes the test statistic processing the pseudorange residual vector, defined as the difference between the measured pseudorange vector and the pseudorange vector derived from the estimated navigation solution:

$$r(t) = \Delta Y(t) - H(t) \Delta \hat{X}(t) \quad \text{Eq. 2-29}$$

The expression of the residual vector can be rewritten by replacing $\Delta \hat{X}(t)$ by its expression:

$$r(t) = (I - B(t)) \Delta Y(t) = (I - B(t)) \varepsilon(t) \quad \text{Eq. 2-30}$$

with:

$$B(t) = H(t)[H(t)^T H(t)]^{-1} H(t)^T \quad \text{for LSR} \quad \text{Eq. 2-31}$$

$$B(t) = H(t)[H(t)^T R(t)^{-1} H(t)]^{-1} H(t)^T R(t)^{-1} \quad \text{for WSSR} \quad \text{Eq. 2-32}$$

A scalar metric called sum of the square residual errors (*SSE*) is defined in the LSR case, and the weighted sum of square error (*WSSSE*) is defined for the WLSR algorithm:

$$\frac{SSE(t)}{\sigma^2} = \frac{r(t)^T r(t)}{\sigma^2} \sim \begin{cases} \chi_k^2 & \text{if } \varepsilon(t) \sim \mathcal{N}(0, \sigma^2 I) \\ \chi_{k,\lambda}^2 & \text{if } \varepsilon(t) \sim \mathcal{N}(b, \sigma^2 I) \end{cases} \quad \text{Eq. 2-33}$$

Or

$$WSSE = r(t)^T R(t)^{-1} r(t) \sim \begin{cases} \chi_k^2 & \text{if } \varepsilon(t) \sim \mathcal{N}(0, R(t)) \\ \chi_{k,\lambda}^2 & \text{if } \varepsilon(t) \sim \mathcal{N}(b, R(t)) \end{cases} \quad \text{Eq. 2-34}$$

where:

- k is the number of degrees of freedom of the distribution
- λ is the non-centrality parameter

If the measurement errors follow independent centered normal distributions, SSE and $WSSE$ are chi-squared distributed random variables. These variables follow non-central chi-squared distributions in the faulty case and a centered chi-squared distributions in a fault-free case. The number of degrees of freedom k of the squared distribution is the number of redundant pseudorange measurements (in general the number of satellites tracked minus 4).

In the faulty case, for the WSSR, the non-centrality parameter is:

$$\lambda = b^T R(t)^{-1} (I - B(t)) b \quad \text{Eq. 2-35}$$

R must be replacted by σ^2 in Eq. 2-38 to have the expression for the LSR.

Assuming that only the satellite i is biased, the previous equation is equivalent to:

$$\lambda = \frac{(I - B)_{ii}}{\sigma_i^2} b_i^2 \quad \text{Eq. 2-36}$$

The test statistics (denoted T) for the LSR and WLSR are respectively $SSE(t)/\sigma^2$ and $WSSE$. The LSR RAIM test statistic is defined differently in [Parkinson and Axelrad, 1988] ($\sqrt{SSE/k}$). The WLSR RAIM test statistic has also been defined differently in [Walter and Enge, 1995] (\sqrt{WSSE}).

Detection thresholds

Once the decision test variable has been determined as well as its distribution, it is necessary to set the detection threshold for the test. The fault detection process consists in comparing the test statistic value to a detection threshold. If the test statistic exceeds the detection threshold, a fault detection is declared. False alarm means that there is no fault (i.e. the null hypothesis, H_0 holds) but the test statistic is over the detection threshold. As we assume that there is no fault, the test follows a chi-square distribution with k degrees of freedom.

$$P_{FA} = P(T \geq \text{Threshold} | T \sim \chi_k^2) \quad \text{Eq. 2-37}$$

Using the probability density function of the chi squared distribution, the threshold is calculated with:

$$P_{FA} = 1 - \text{cdf}_{\chi_k^2}(\text{Threshold}) \quad \text{Eq. 2-38}$$

Equivalently, from a required P_{FA} , it is possible to find the appropriate threshold.

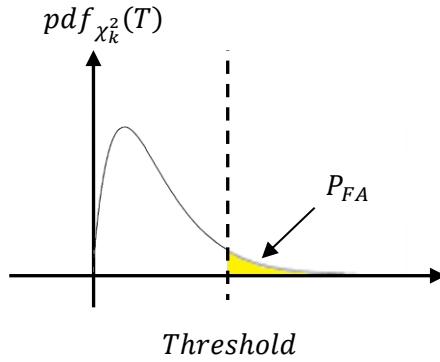


Figure 5 Selection of the detection *Threshold* to set the P_{FA}

Minimum detectable failures

The probability of non-detected failure (P_{MD}) can be derived from the integrity risk requirements and the probability of occurrence of a fault. Provided the detection *Threshold* and P_{MD} , the minimum value of the non-centrality parameter λ_{det} corresponding to a fault that can be detected with P_{MD} as illustrated in Figure 6 and so that:

$$P_{MD} = P(T \leq \text{Threshold} | T \sim \chi_{k, \lambda_{det}}^2) \quad \text{Eq. 2-39}$$

where λ_{det} is independent of the satellite.

The smallest bias that is detectable with the algorithm for each pseudorange can be derived from λ_{det} with:

$$b_{det,i} = \sigma_i \sqrt{\frac{\lambda_{det}}{(I - B_{i,i})}} \quad \text{Eq. 2-40}$$

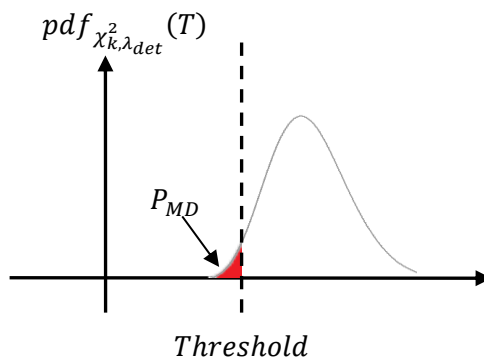


Figure 6 Representation of P_{MD} in the faulty case

Protection levels

The objective of a RAIM algorithm is to raise an alarm if the horizontal error exceeds the *HPL* within the required P_{MD} and P_{FA} . An alarm is raised when the test statistics exceeds the detection threshold. It is thus necessary to assess the impact on the position of a maximum measurement bias that would not trigger and alarm (minimum detectable fault). It is then required to relate the minimum detectable fault, the test statistic and the horizontal position error in order to bound the position error with the *HPL*. The position error and the measurement errors, in the case of a biased measurement, are related by:

$$\Delta X = X - \hat{X} = -A(t) \begin{bmatrix} 0 \\ \vdots \\ b_{det,i} \\ \vdots \\ 0 \end{bmatrix} = \begin{bmatrix} A_{N,i} \\ A_{E,i} \\ \vdots \end{bmatrix} b_{det,i} \quad \text{Eq. 2-41}$$

where $A(t) = I - B(t)$

Thus the impact of the bias $b_{det,i}$ in the horizontal plane is given by:

$$\Delta X_H = \sqrt{A_{N,i}^2 + A_{E,i}^2} b_{det,i} \quad \text{Eq. 2-42}$$

Replacing $b_{det,i}$ by its expression (Eq. 2-40):

$$\Delta X_H = \sqrt{\frac{A_{N,i}^2 + A_{E,i}^2}{(I - B_{i,i})}} \sigma_i \sqrt{\lambda_{det}} = HSLOPE_i \sqrt{\lambda_{det}} \quad \text{Eq. 2-43}$$

Denoting:

$$HSLOPE_i = \sqrt{\frac{A_{N,i}^2 + A_{E,i}^2}{(I - B_{i,i})}} \sigma_i \quad \text{Eq. 2-44}$$

The slope quantizes the coupling between the effect of a bias in the range domain (i.e. the test statistic's), and what the RAIM aims to bound (i.e. the horizontal position error). Each satellite has its own slope.

$$HSLOPE_{max} = \max_i(HSLOPE_i) \quad \text{Eq. 2-45}$$

The horizontal protection level is then defined based on to the worst satellite:

$$HPL = HSLOPE_{max} \sqrt{\lambda_{det}} \quad \text{Eq. 2-46}$$

The vertical protection levels can be computed analogously.

2.1.4.3.2.2 Examples of other RAIM algorithms

Other RAIMs algorithms that can be found in the literature are introduced in this subsection.

The maximum solution separation (MSS) RAIM which principle is described in [Brown and Mc Burney, 1988] is one of them. It is said to be outperformed by LSR RAIM [Van Graas and Farrell, 1993]. The maximum solution separation method consists in monitoring the separation between the position estimate generated by the full-set filter that processes all the satellite measurements and the position estimate generated by each possible subset filters (each using all satellite measurements except one).

These techniques can be further extended to include multiple hypotheses. Multiple Hypothesis Solution Separation (MHSS) which was proposed by [Pervan et al., 1998] for a GBAS monitoring application is a RAIM technique that comprises a protection level computation procedure that admits multiple simultaneous faulty measurements.

Novel Integrity Optimized RAIM (NIORAIM) [Hwang and Brown, 2006]. NIORAIM is a method to improve RAIM availability by weighting the pseudorange measurements in a non-linear fashion so that the integrity limits (or slopes) of the satellites become nearly equal. The non-linearly weighted measurements are then used to compute a position fix. The weights are designed to improve availability of the RAIM at the cost of accuracy.

Advanced Receiver Autonomous Monitoring (ARAIM) is based on dual frequency (L1/E1 and L5/E5a) measurements and at least two independent GNSS core constellations for civil aviation. As opposed to what indicate its name, ARAIM is not autonomous because it relies on a ground system in order to provide periodic updates of the nominal performance and fault rates [Blanch et al., 2012]. This integrity data is contained in the Integrity Support Message (ISM) that is created on the ground and broadcast to the aircrafts. ARAIM places the greatest integrity responsibility on the aircraft and the smallest burden on the ground monitors. ARAIM algorithms are developed from the Multi-Hypothesis Solution Separation (MHSS) algorithm. Unlike RAIM, ARAIM does not assume that the probability of a constellation failure is negligible.

2.1.4.3.2.3 AAIM algorithms

AAIM algorithms have been designed to monitor the integrity of the GNSS measurements on a system that integrates GNSS and inertial measurements in a tight coupling scheme (the notion of tight coupling is defined in Chapter 4). Three main integrity algorithms have been developed for tight integrated systems.

The most popular method is the Multiple Solution Separation (MSS) algorithm. MSS is a snapshot algorithm which has been developed in [Brenner, 1995]. A different version of the MSS has been proposed in [Young and McGraw, 2003] and is patented by Rockwell Collins [US7219013]. MSS for hybridized systems consists in monitoring the separation between the position estimated by a fusion filter that processes all the satellite measurements and the position estimate by sub fusion filters (each processing all satellite measurements except one).

The second AAIM algorithm is Assured Integrity monitoring by Extrapolation Method (AIME). AIME was developed by John Diesel for Litton systems in 1996. This algorithm is patented [US 5583774A] and it is certified as primary mean of navigation for up to the non-precision approach (NPA) on the Airbus 300 Series aircraft [Diesel and Dunn, 1996]. The purpose of AIME navigation is to identify the satellites whose clock drifts are within specification and to use only those satellites within specification in estimating the user's position. According to [RTCA, 2006], this algorithm provides exclusion capability for large steps, ramps and ramp rates. Moreover multiple failures can be handled. However, detection and exclusion of slow drifts or drift rate are not guaranteed by this technique. For the fault detection, the Extrapolation Method compute three test statistics that are all based on the Kalman filter innovations (i.e., measurement residuals). The first test is based on the innovation that have been averaged over the last 2.5 min duration and the others, are obtained by averaging the innovations over 10 min and 30 min. The three tests variables follow Chi-square distributions in the nominal case [Lee and O'Laughlin, 2000]. AIME is a sequential integrity monitoring algorithm because it uses measurements from several epochs (current and past).

A third method called Generalized Likelihood Ratio, which is sequential, is also introduced in this chapter. It is proven in [Giremus and Escher, 2007] that this algorithm outperforms MSS in term of protection level. Generalized Likelihood Ration (GLR) is applied in to detect possible component failure in system. This algorithm was first introduced by [Willisky, 1976] and it is applicable to any dynamical system that estimates its state using Kalman filter. This algorithm can detect multiple simultaneous failures and is robust to disturbance of small magnitude. However, since no fault-free solution is maintained, after a fault is detected, a compensation step is necessary to remove the induced errors on the Kalman filter estimates. In GLR, test statistics are the jump/ramp occurrence Likelihood Ratios (LR).

2.2 Principle of inertial navigation

Inertial navigation is used in plenty of applications such as aviation, military ships, submarines and guided weapons. Unlike GNSS, inertial sensors are not sensitive to the surrounding environment of the vehicle. This property is of particular interest for the navigation in constrained environments such as urban canyons, tunnels, and indoor. In term of position estimation, Inertial Navigation Systems (INS) have a good short term accuracy. However, the main drawback of INS is that the estimated position error slowly drifts and is not bounded. This is due to the integration of errors in the dead reckoning process. Therefore, inertial navigation is complementary to the technologies that estimate an absolute position with a bounded error such as GNSS or Wi-Fi based positioning (in indoor environments).

2.2.1 Introduction to inertial sensors

Inertial sensors comprise gyroscopes and accelerometers.

Gyroscopes generally measure angular rates (except mechanical gyroscopes) or angular increments (rates multiplied by the sampling period). There are three main technologies used for gyroscopes:

- Mechanical gyroscopes which are made of a spinning wheel mounted on two gimbals which enable it to rotate around the three axes. They directly measure the orientation of the device.
- Optical gyroscopes regroup the Fiber Optical Gyroscopes (FOG) and Ring Laser Gyroscopes. They operate by sensing the difference in propagation time between beams of light traveling in clockwise and counter-clockwise directions about a closed optical path [Stedman, 1997]. This difference is referred to as Sagnac effect. Optical gyroscopes are usually associated with high grades (tactical grade at minimum) and high costs.
- Microelectromechanical (MEMS) gyroscopes are made of silicon micromachining techniques. MEMS gyroscopes contain vibrating elements to measure the Coriolis effect. At present MEMS sensors cannot reach the accuracy level of optical devices, however, they are expected to do so in the future. Unlike Mechanical and Optical gyroscopes, MEMS gyroscopes are cheap to manufacture and therefore suitable for applications that demands low cost devices such as ETC and, to a minor extent, train control.

Accelerometers measure the specific forces (or equivalently, velocity increments). The specific force is defined as the difference between the true acceleration in space and the acceleration due to gravity [Titterton and Weston, 1997].

There are three main technologies used for accelerometers:

- A mechanical accelerometer consists of a mass suspended by springs. The displacement of the mass is measured. A signal proportional to the force acting on the mass in the direction of the input axis is generated. The acceleration of the mobile is deduced by dividing the magnitude of the force by the
- Solid state accelerometers can be classified into sub-groups, including surface acoustic wave, vibratory, silicon and quartz devices. An example of a solid-state accelerometer is the surface acoustic wave (SAW) accelerometer. Such accelerometer consists of a cantilever beam which is resonated at a particular frequency. A mass is attached to one end of the beam which is free to move whereas the other end is rigidly attached to the case. The acceleration along the input axis makes the beam bend. This causes the frequency of the surface acoustic wave to change proportionally to the applied strain. Therefore, the acceleration of the vehicle can be deduced from this change of frequency.
- MEMS accelerometers can be divided into two classes. The first class consists of mechanical accelerometers that measure the displacement of a supported mass. The second class consists of devices which measure the change in frequency of a vibrating element caused by a change of tension, similarly to SAW accelerometers.

Inertial measurement unit (IMU) are typically made of three gyroscopes, three accelerometers, a processor, a calibration-parameter store [Groves, 2013], a temperature sensor, and the power supplies. IMUs with fewer than six inertial sensors are usually referred to as partial IMUs. IMUs that include more than 6 sensors for fault-detection or isolation also exist, and referred to as Redundant IMU (RIMU). Current INS uses a strapdown architecture, in which the inertial sensors are attached to the vehicle frame. Strapdown technology has the advantage of decreasing the IMU size, power and cost

with respect to stabilized platforms. The main drawback of strapdown technology is that the computational complexity is increased. An IMU does not calculate any navigation solution such as position, velocity and attitude. In general, the IMU outputs are angular rates and the specific forces (or angular and velocity increments, which corresponds to rates multiplied by the IMU sampling period) as measured by the sensors which are calibrated.

An Inertial Navigation System (INS) contains a combination of an IMU and a computer running navigation equations. An INS estimates the position, velocity and orientation of the vehicle by dead reckoning principle. The processing of navigation equations is referred to as mechanization. After a summary of the reference frames given in section 2.2.2, the principle of a 3D inertial mechanization is detailed in section 2.2.3.

2.2.2 Frames of reference

Inertial navigation involves several frames of references that are defined in this section. The Inertial Frame (i-frame) has its origin at the Earth's center of mass. Its Z-axis is parallel to the spin axis of the Earth, and its axes are non-rotating with respect to the fixed stars. The X-axis is pointing toward the mean vernal equinox, and the Y-axis completes a right handed orthogonal frame.

- The ECEF frame has its origin located at the Earth's center of mass. Its axes are fixed with respect to the Earth. The Z-axis is parallel to the spin axis of the Earth. The X-axis points towards the mean meridian of Greenwich, and the Y-axis completes a right handed orthogonal frame.
- The local navigation frame (n-frame), also known as the local-level frame or local geodetic frame, has a fixed origin with respect to the Earth, usually a point on the surface. The Z-axis is orthogonal to the reference ellipsoid pointing up. The Y-axis points towards geodetic north, and the X-axis completing a right handed orthogonal frame. If the east, north, up (ENU) system of coordinate is used in this thesis, north, east, down (NED) is also often used in the literature.
- The Body frame (b-frame) is usually centered on the center of gravity of the vehicle. The Y-axis points towards the forward direction, and corresponds to the roll angle (γ) axis. The X-axis points towards the transverse direction, and corresponds to the pitch angle (θ) axis. The Z-axis points towards the vertical direction (up) and completes a right handed orthogonal frame. It corresponds to the yaw angle (ψ) axis.

2.2.3 Principles of inertial mechanization

This section describes the process referred to as 3D mechanization for an IMU composed of 3 gyroscopes and 3 accelerometers. This mechanization operates in the navigation frame. The parametrization used for the IMU orientation plays a major role in inertial navigation. The attitude representations that are commonly used in inertial navigation are the direction cosine matrix (DCM), quaternion, rotation vector and Euler angles. Relations between these parametrizations can be found in [Shin, 2001]. A quaternion mechanization is used in this thesis. Compared to Euler angles, it enables

faster computations and avoids the problem of gimbal lock. Compare to DCM, quaternion are more numerically stable. The inputs of the algorithm are the calibrated outputs of the inertial sensors. The outputs of the mechanization are the position (x^n), velocity (v^n) (both expressed in the n-frame) and attitude (att) estimated by dead reckoning. This subsection describes the principle of the 3D mechanization that is used in this thesis and which can be summarized by Figure 7 [Groves, 2013].

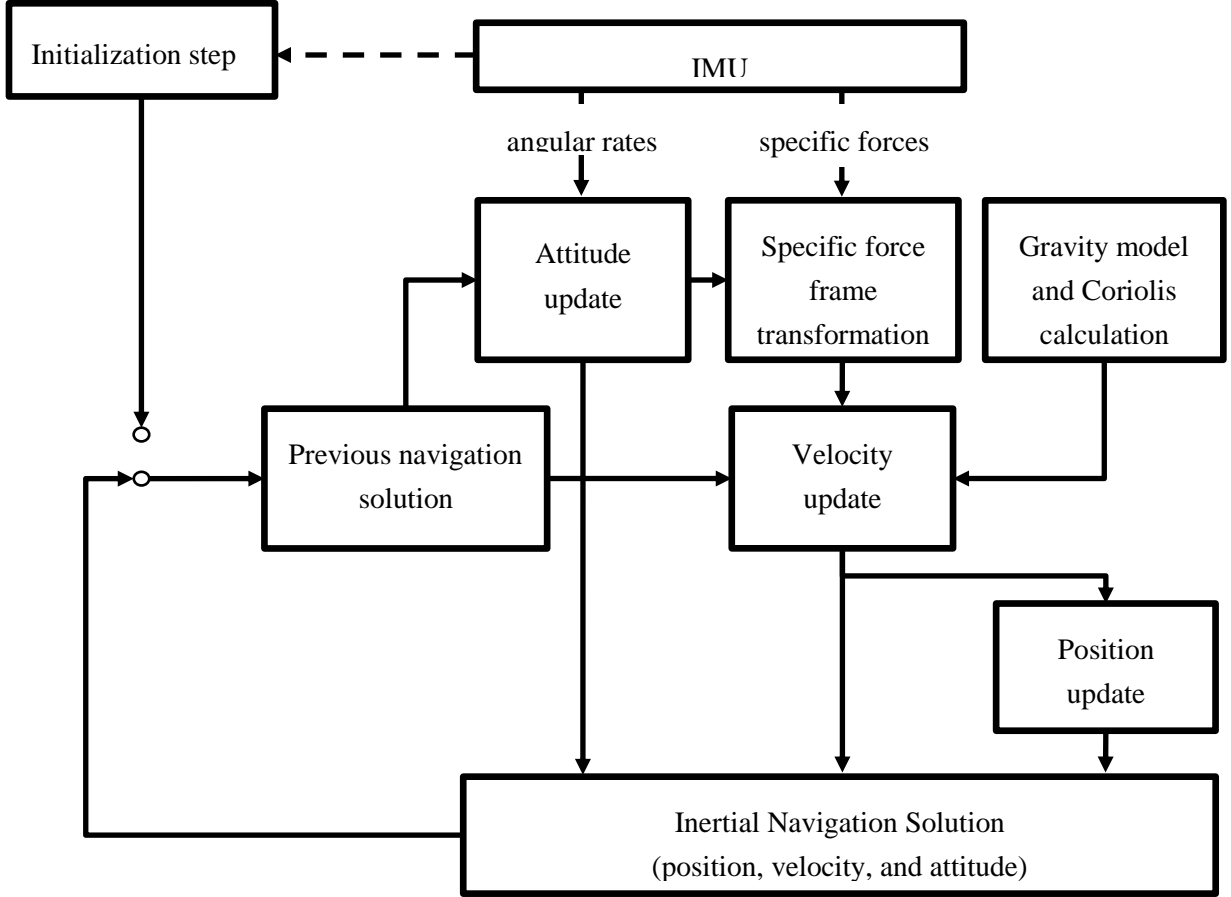


Figure 7 Principle of an inertial navigation processor, from [Groves, 2013]

Initialization step:

By principle of dead reckoning, the mechanization requires the knowledge of the initial position (x_0), velocity (v_0) and attitude of the IMU (att_0). The quaternion must be initialized by using the initial value of the attitude angles. This can be done by forming the initial C_b^n matrix, from which the quaternions can be deduced with [McGreevy, 1986]:

$$q_b^n = \begin{bmatrix} q_0 \\ q_1 \\ q_2 \\ q_3 \end{bmatrix} = \begin{bmatrix} \cos\left(\frac{\gamma}{2}\right) \cos\left(\frac{\theta}{2}\right) \cos\left(\frac{\psi}{2}\right) + \sin\left(\frac{\gamma}{2}\right) \sin\left(\frac{\theta}{2}\right) \cos\left(\frac{\psi}{2}\right) \\ \sin\left(\frac{\gamma}{2}\right) \cos\left(\frac{\theta}{2}\right) \cos\left(\frac{\psi}{2}\right) - \cos\left(\frac{\gamma}{2}\right) \sin\left(\frac{\theta}{2}\right) \sin\left(\frac{\psi}{2}\right) \\ \cos\left(\frac{\gamma}{2}\right) \sin\left(\frac{\theta}{2}\right) \cos\left(\frac{\psi}{2}\right) + \sin\left(\frac{\gamma}{2}\right) \cos\left(\frac{\theta}{2}\right) \cos\left(\frac{\psi}{2}\right) \\ \cos\left(\frac{\gamma}{2}\right) \cos\left(\frac{\theta}{2}\right) \sin\left(\frac{\psi}{2}\right) - \sin\left(\frac{\gamma}{2}\right) \sin\left(\frac{\theta}{2}\right) \cos\left(\frac{\psi}{2}\right) \end{bmatrix} \quad \text{Eq. 2-47}$$

Attitude integration step:

After having converted the IMU measurements from the sensor reference frame to the b-frame by simple rotation, it is necessary to update the quaternion based on the gyroscopes' measurements. The IMU measures the angular increment of the body frame with respect to the inertial frame expressed in the body frame ($\Delta\theta_{ib}^b$). However, the attitude corresponds to the orientation of the b-frame with respect to the n-frame. The body angular increments with respect to the navigation frame are obtained by correcting the rotation of the navigation frame with respect to the inertial frame expressed in the body frame:

$$\Delta\theta_{nb}^b = \Delta\theta_{ib}^b - \Delta\theta_{in}^b = \Delta\theta_{ib}^b - C_n^b(\omega_{ie}^n + \omega_{en}^n)\Delta t \quad \text{Eq. 2-48}$$

where:

- $C_n^b = (C_b^n)^T$, and C_b^n can be exactly calculated from the quaternion with:

$$C_b^n = \begin{pmatrix} q_0^2 + q_1^2 - q_2^2 - q_3^2 & 2(q_1q_2 - q_0q_3) & 2(q_1q_3 + q_0q_2) \\ 2(q_1q_2 + q_0q_3) & q_0^2 - q_1^2 + q_2^2 - q_3^2 & 2(q_2q_3 - q_0q_1) \\ 2(q_1q_3 - q_0q_2) & 2(q_2q_3 + q_0q_1) & q_0^2 - q_1^2 - q_2^2 + q_3^2 \end{pmatrix} \quad \text{Eq. 2-49}$$

- ω_{ie}^n is the rotation of the e-frame w.r.t the i-frame expressed in the n-frame:

$$\omega_{ie}^n = \begin{bmatrix} 0 \\ \omega_{ie} \cos(\varphi) \\ \omega_{ie} \sin(\varphi) \end{bmatrix} \quad \text{Eq. 2-50}$$

- ω_{en}^n is the rotation of the n-frame w.r.t the e-frame expressed in the n-frame:

$$\omega_{en}^n = \begin{bmatrix} -v_N/(R_N + h) \\ v_E/(R_M + h) \\ v_E \tan(\varphi)/(R_N + h) \end{bmatrix} \quad \text{Eq. 2-51}$$

where v_E and v_N corresponds to the velocity as estimated in the mechanization.

- R_N is the radius of curvature in the prime vertical, which can be calculated with:

$$R_N = \frac{R_e(1 - e^2)}{[1 - e^2 \sin^2(\varphi)]^{3/2}} \quad \text{Eq. 2-52}$$

- R_M is the meridian radius of curvature, which can be calculated with:

$$R_M = \frac{R_e}{[1 - e^2 \sin^2(\varphi)]^{1/2}} \quad \text{Eq. 2-53}$$

- e is the eccentricity of the earth, equal to 0.0818191908425
- R_e is the radius of the earth, which is equal to 6378140 m
- ω_{ie} is the earth rotation rate, which is equal to $7.2921151467 \cdot 10^{-5}$ rad/s

Let us denote $\Delta\theta_x$, $\Delta\theta_y$ and $\Delta\theta_z$ the three components of the angular increment vector. $\Delta\theta_{nb}^b$

The quaternion at the time index k is updated with:

$$q_{k+1} = q_k + \frac{1}{2} \begin{pmatrix} 0 & -\Delta\theta_x & -\Delta\theta_y & -\Delta\theta_z \\ \Delta\theta_x & 0 & \Delta\theta_z & -\Delta\theta_y \\ \Delta\theta_y & -\Delta\theta_z & 0 & \Delta\theta_x \\ \Delta\theta_z & \Delta\theta_y & -\Delta\theta_x & 0 \end{pmatrix} q_k \quad \text{Eq. 2-54}$$

The quaternion is then normalized with:

$$q_{k+1} = \frac{q_{k+1}}{\sqrt{q_{k+1}^T q_{k+1}}} \quad \text{Eq. 2-55}$$

Specific force frame transformation

The specific forces or velocity increments (Δv_f^b) measured by the accelerometers are expressed in the body frame. The corresponding velocity increment expressed in the body frame is converted to the navigation frame by multiplying the measurement vector by the DCM.

$$\Delta v_f^n = C_b^n \Delta v_f^b \quad \text{Eq. 2-56}$$

Gravity model and Coriolis force correction

The velocity increment in the navigation equation in the n-frame (Δv^n) can be obtained by adding the acceleration due to gravity and by removing the Coriolis acceleration.

$$\Delta v^n = \Delta v_f^n - (2\omega_{ie}^n + \omega_{en}^n) \wedge v^n \Delta t + \gamma^n \Delta t \quad \text{Eq. 2-57}$$

where:

- Δt is the sampling period of the IMU
- γ^n is the gravitation model (the WGS84 model has been used in this thesis)
- \wedge denotes the cross product

Velocity update

The velocity of the vehicle in the navigation frame is updated by adding the velocity increment:

$$v_{k+1}^n = v_k^n + \Delta v^n \quad \text{Eq. 2-58}$$

Position update

The position of the vehicle is updated by integrating the velocity:

$$x_{k+1}^n = x_k^n + v_{k+1}^n \Delta t \quad \text{Eq. 2-59}$$

This version of the 3D mechanization has been implemented in the thesis.

2.3 Conclusion

This chapter has firstly described the principles of GNSS, which is one of the two main technology used in this thesis. The principles of GNSS augmentations which have been developed in the context of civil aviation have been introduced. This is particularly interesting because, like the applications of interest investigated in this thesis, civil aviation is a critical application (from a safety point of view) which already integrates GNSS.

Then, the principle of inertial sensors and the way to integrate their measurements in order to estimate the navigation parameters (position, velocity and attitude) has been presented through a 3D mechanization. This algorithm has been implemented and has been used in the rest of the thesis.

2.4 References

- [Bancroft, 1985] S. Bancroft, "An Algebraic Solution of the GPS Equations," IEEE Transactions on Aerospace and Electronic Systems, vol. AES-21, no. 1, pp. 56–59, 1985
- [Blanch et al., 2012] Blanch, Juan, Walter, Todd, Enge, Per, Lee, Young, Pervan, Boris, Rippl, Markus, Spletter, Alex, "Advanced RAIM user Algorithm Description: Integrity Support Message Processing, Fault Detection, Exclusion, and Protection Level Calculation," Proceedings of the 25th International Technical Meeting of The Satellite Division of the Institute of Navigation (ION GNSS 2012), Nashville, TN, September 2012, pp. 2828-2849
- [Brenner, 1995] M. Brenner, Integrated GPS/inertial detection availability, Journal of The Institute of Navigation, Sept. 1995
- [Brown and Mc Burney, 1988] Brown R. G., P. McBurney, "Self-Contained GPS Integrity Check Using Maximum Solution Separation", Navigation: Journal of the Institute of navigation, Vol. 35, No. 1, Spring 1988
- [Curran et al., 2012] J.T. Curran, G. Lachapelle and C.C. Murphy, Improving the Design of Frequency Lock Loops for GNSS Receivers. IEEE Transactions on Aerospace and Electronic Systems , vol. 48, no. 1, pp. 850–868, January 2012
- [Diesel and Dunn, 1996] Diesel, John, Dunn, Gregory, "GPS/IRS AIME: Certification for Sole Means and Solution to RF Interference," Proceedings of the 9th International Technical Meeting of the Satellite Division of The Institute of Navigation (ION GPS 1996), Kansas City, MO, September 1996, pp. 1599-1606
- [Giremus and Escher, 2007] Giremus, Audrey, Escher, Anne-Christine, "A GLR Algorithm to Detect and Exclude up to Two Simultaneous Range Failures in a GPS/Galileo/IRS Case," Proceedings of the 20th International Technical Meeting of the Satellite Division of The Institute of Navigation (ION GNSS 2007), Fort Worth, TX, September 2007, pp.

- 2911-2923.
- [GPS SPS, 2008] Department of Defense USA, "Global Positioning Service Standard Positioning Service Performance Standard", 4th Edition, Sept. 2008
- [Foucras, 2015] Foucras, Myriam (2015) Performance Analysis of the Modernized GNSS Signal Acquisition
- [Groves, 2013] Groves, P.D. Principles of GNSS, Inertial, and Multisensor Integrated Navigation Systems; Artech House: London, UK, 2013
- [Holmes, 2000] Holmes, J.K. (2000), Code Tracking Loop Performance Including the Effect of Channel Filtering and Gaussian Interference, Proceedings of the US Institute of Navigation AM (San Diego, CA, USA, June 26-28), pp. 382-398
- [Hwang and Brown, 2006] Hwang, P. Y. and Brown, R. G. (2006), RAIM-FDE Revisited: A New Breakthrough In Availability Performance With nioRAIM (Novel Integrity-Optimized RAIM). Navigation
- [ICAO, 2006] International Civil Aviation Organization, "International Standards and Recommended Practices - Annex 10 to the Convention on International Civil Aviation - Aeronautical Telecommunications - Volume I, Radio Navigation Aids", 6th Edition (with amendment 85), July 2006.
- [Lee and O'Laughlin, 2000] Lee, Young C., O'Laughlin, Daniel G., "A Further Analysis of Integrity Methods for Tightly Coupled GPS/IRS Systems," Proceedings of the 2000 National Technical Meeting of The Institute of Navigation, Anaheim, CA, January 2000, pp. 166-174
- [McGreevy, 1986] McGreevy, J. (1986), Fundamentals of Strapdown Inertial Navigation. Litton Guidance & Control Systems. Document No. 406372, Revision A
- [Parkinson and Axelrad, 1988] B.W. Parkinson, P. Axelrad, "Autonomous GPS Integrity Monitoring using the Pseudorange Residual", NAVIGATION, Vol. 35, No. 2, Summer 1988, pp. 255-274.
- [Pervan et al., 1998] Pervan, B., Pullen, S. and Christie, J. (1998) A Multiple Hypothesis Approach to Satellite Navigation Integrity, Navigation, 45(1).
- [RTCA, 2006] RTCA Inc., "Minimum Operational Performance Standards for Global Positioning System/Wide Area Augmentation System Airborne Equipment", RTCA DO-229D, Dec. 13, 2006
- [RTKLIB] http://www.rtklib.com/rtklib_sdr.htm
- [Shin, 2001] Shin, E. (2001), Accuracy Improvement of Low Cost INS/GPS for Land Application, MSc Thesis, Department of Geomatics Engineering, University of Calgary, Canada, UCGE Report No. 20156

- [Stedman, 1997] Stedman, G. E., Ring-Laser Tests of Fundamental Physics and Geophysics, In Reports on Progress in Physics, 60 (6), 1997, pp. 615-688
- [Titterton and Weston, 1997] Titterton, D. H. and Weston, J. L. (1997). Strapdown Inertial Navigation Technology. Peter Peregrinus Ltd
- [US7219013] Method and system for fault detection and exclusion for multi-sensor navigation systems
- [US 5583774A] Assured-integrity monitored-extrapolation navigation apparatus
- [Van Graas and Farrell, 1993] F. van Graas, J. L. Farrell, "Baseline Fault Detection and Exclusion Algorithm," Proceedings of the 49th Annual Meeting of The Institute of Navigation, Cambridge, MA, June 1993, pp. 413-420.
- [Walter and Enge, 1995] Walter T., P. Enge, "Weighted RAIM for Precision Approaches", ION GPS 1995, September
- [Willisky, 1976] A Generalized Likelihood Ratio approach to the detection of mean jumps in linear systems – A.S. Willisky - IEEE Transactions on Automatic Control, pp 108-112, 1976
- [Young and McGraw, 2003] Young, Ryan S. Y., McGraw, Gary A., "Fault Detection and Exclusion Using Normalized Solution Separation and Residual Monitoring Methods", NAVIGATION, Journal of The Institute of Navigation, Vol. 50, No. 3, Fall 2003, pp. 151-170
- [Yuheng et al., 2010] H. Yuheng, R. Martin, and A. Bilgic, "Approximate Iterative Least Squares Algorithms for GPS Positioning," in IEEE International Symposium on Signal Processing and Information Technology (ISSPIT), 2010

3 OPERATIONAL REQUIREMENTS

Unlike civil aviation [ICAO, 2006] and maritime transport [IMO, 2001], no standardized operational requirements for the use of GNSS in critical terrestrial applications exist. Each country has its own systems for toll collection and train control, which slows down the process of defining common standards and requirements for the use of GNSS. Moreover, the need for interoperability is lower for terrestrial application compared to aviation and maritime as most vehicles stay within the network of one country. This tendency is evolving for train control in Europe with the development of the European Rail Traffic Management System (ERTMS) for an improved interoperability. Before ETCS, trains had to carry several control systems to travel from a country to another in Europe. However, other countries such as USA, China and Russia are already using GNSS for train control in different systems. For toll collection, countries have their own systems, therefore the On Board Units (OBU) usually includes several technologies to travel through different countries.

This chapter introduces the performance metrics that will be used to define the operational requirements for GNSS in the critical terrestrial applications of interest. The metrics and requirements used by civil aviation will be presented for references, as they are the most consolidated ones. Then, this section discusses the propositions that exist in the literature for train control. In particular, the work will focus on the use of GNSS for the European Train Control System (ETCS). The operational requirements for ETC are then discussed.

3.1 Performance requirements criterion used for civil aviation

The International Civil Aviation Organization (ICAO) is an organization that codifies the principles and techniques of international air navigation and fosters the planning and development of international air transport. For safety considerations, civil aviation requires safe, secure and high-end air navigation systems. ICAO recognizes in [ICAO, Doc 9750] the Global Navigation Satellite System (GNSS) as a key element of the Communications, Navigation, and Surveillance/Air Traffic Management (CNS/ATM) systems as well as a foundation upon which States can deliver improved

aeronautical navigation services [ICAO, Doc 9849]. Standards requirements for GNSS in civil aviation have been defined by ICAO in November 2002 in [ICAO, 2006].

The GNSS Signal-In-Space (SiS) requirements are defined in terms of accuracy, integrity, continuity and availability [ICAO, 2006]:

- **Accuracy:** GNSS position error is the difference between the estimated position and the actual position. For an estimated position at a specific location, the probability should be at least 95 per cent that the position error is within the accuracy requirement.
- **Availability:** The availability of a navigation system is defined as the ability of the system to provide the required function and performance at the initiation of the intended operation. The availability of GNSS is characterized by the portion of time the system is to be used for navigation during which reliable navigation information is presented to the crew, autopilot, or other system managing the flight of the aircraft.
- **Continuity:** The continuity of a system is the ability of the total system to perform its function without unscheduled interruption during the intended operation. More specifically, continuity is the probability that the specified system performance will be maintained for the duration of a phase operation, presuming that the system was available at the beginning of that phase operation and was predicted to operate throughout the operation.
- **Integrity:** Integrity is a measure of the trust that can be placed in the correctness of the information supplied by the total system. Integrity includes the ability of a system to provide timely and valid warnings to the user (alerts) when the system must not be used for the intended operation. Integrity requirements are defined with four parameters:
 - **Integrity risk (P_{int}):** The integrity risk is the probability of providing a position that is out of tolerance without warning the user within the time-to-alert.
 - **Alert limit (AL):** To ensure that the position error is acceptable, an alert limit is defined. It represents the largest position error allowable for a safe operation. The position error cannot exceed this alert limit without annunciation [ICAO, 2006].
 - The **Horizontal Alert Limit (HAL)** is the radius of a circle in the horizontal plane (the local plane tangent to the WGS-84 ellipsoid), with its center being at the true position, that describes the region that is required to contain the indicated horizontal position with the required probability for a particular navigation mode.
 - The **Vertical Alert Limit (VAL)** is half the length of a segment on the vertical axis (perpendicular to the horizontal plane of WGS-84 ellipsoid), with its center being at the true position, that describes the region that is required to contain the indicated vertical position with the required probability for a particular navigation mode.
 - **Time to Alert (TTA):** The TTA is the maximum allowable elapsed time from the onset of a positioning failure until the equipment annunciates the alert.

The combination of GNSS elements and a fault-free GNSS user receiver shall meet the signal-in-space requirements which are defined by ICAO in [ICAO, 2006] and are summarized in Table 2. The fault-free receiver is assumed to be a receiver with nominal accuracy and time-to-alert performance. Such a receiver is assumed to have no failures that affect the integrity, availability and continuity performance [ICAO, 2010].

The operational requirements for terrestrial applications will be understood based on the civil aviation definition of the criteria as civil aviation is the most advanced application in terms of safe GNSS-based positioning operations. The proposed operational requirements are therefore presented in the same way as in Table 2.

Operation	Accuracy-95%		Integrity				Continuity	Availability
	HA_{max}	VA_{max}	HAL	VAL	TTA	P_{int}		
En-route	3.7 km	N/A	7.4 km (oceanic) 3.7 km (continental)	N/A	5 min	$10^{-7}/h$	$1 \cdot 10^{-4}/h$ to $1 \cdot 10^{-8}/h$	0.99 to 0.99999
En-route, Terminal	0.74 km	N/A	1.85 km	N/A	15s	$10^{-7}/h$	$1 \cdot 10^{-4}/h$ to $1 \cdot 10^{-8}/h$	0.99 to 0.99999
Initial approach, Intermediate approach, NPA, Departure	220 m	N/A	556 m	N/A	10s	$10^{-7}/h$	$1 \cdot 10^{-4}/h$ to $1 \cdot 10^{-8}/h$	0.99 to 0.99999
APV I	16 m	N/A	40 m	50m	10s	$2 \cdot 10^{-7}/h$ in any approach	$1 \cdot 8 \cdot 10^{-6}/h$ in any 15 s	0.99 to 0.99999
APV II	16 m	20m	40 m	20m	6s	$2 \cdot 10^{-7}/h$ in any approach	$1 \cdot 8 \cdot 10^{-6}/h$ in any 15 s	0.99 to 0.99999
CAT I	16 m	6m to 4m	40 m	35m to 10m	6s	$2 \cdot 10^{-7}/h$ in any approach	$1 \cdot 8 \cdot 10^{-6}/h$ in any 15 s	0.99 to 0.99999

Table 2 SiS performance requirements [ICAO, 2006]

N/A: Not applicable

3.2 Derivation of performance requirements for train control

GNSS is already used for train position monitoring in the USA (Positive Train Control), China (for high velocity lines) and Russia. The present thesis focuses on the European system ETCS. In Europe, each country has its own train control system. In order to improve interoperability, the ERTMS system is being developed. ERTMS aims at replacing the different national train control and command systems in Europe. One component of ERTMS, the European Train Control System (ETCS), guarantees a common standard that enables trains to cross national borders and enhances safety. Three levels of ETCS exist:

- **ETCS level 1** can be applied as an overlay to existing signaling system. In level 1, Eurobalises radio beacons transmit track side signals to the vehicle as a Movement Authority which are permissions to cross rail sections. Route data information at fixed points is also transmitted to the vehicle. The on-board computer continuously monitors and calculates the maximum speed and the braking curve from this data. Because of the spot transmission of data, the train must travel over the Eurobalise beacon to obtain the next movement authority.
- In **ETCS level 2**, the Eurobalises are used as positions of reference and the vehicle estimates its position between two beacons by odometry. The trains report their position to the RBC (Radio Block Center) with GSM-R. The RBC monitors the train movements and transmits speed information, route data and movement authorities to the train with GSM-R. Most of the signals are displayed in the vehicle. The train detection is still ensured by track-circuits or axle counters.
- In **ETCS level 3**, the vehicle has to estimate its position as in ETCS level 2 and transmits it to the RBC. The train detection function does not rely on track circuits but on the position calculated by the onboard equipment. The possibility for frequent update of the movement authority allows trains to run closer together and the line capacity to be increased. The train also has an on-board integrity system that monitors the train.

In ETCS level 2 and 3 the vehicles have to self-monitor their position and speed, based on a combination of radiobeacons (Eurobalises) installed along the railway that provide reference positions, and odometry. An average separation between balise groups of 2 km is adopted in Europe for fast trains with speed up to 300 km/h. The possible use of GNSS in ETCS has been investigated in several European-funded projects listed in Table 3.

Project Name	Period	Funding	References
GADEROS	2002-2004	5th FP	[Bustamante and De Miguel, 2003]
INTEGRAL	2001-2004	ESA	[Bedrich and Gu, 2004]
LOCOPROL/ LOCOLOC	2001-2004	ESA-EC	[Simsy et al., 2004]
ECORAIL	2001-2005	ESA	[Wasle and Ringert, 2003]

RUNE	-2006	ESA	[Marradi et al., 2008]
GRAIL	2005-2008	6th FP, GSA	[Ballesteros, 2006]
GRAIL-2	2010-2012	7th FP, GSA	[González et al., 2012]
SATLOC	2012-	7th FP, GSA, UIC	[Barbu and Marais, 2014]
3InSat	2012-2015	ESA	[Rispoli et al., 2013]

Table 3 List of projects targeting the introduction of GNSS in ETCS

The potential use of GNSS for ETCS was discussed by the rail European authorities and it has been stated by the European Railway Association (ERA) that [MoU, 2005]: “*The Navigation Satellite System (GNSS) can play a major role in the rail sector, both for fleet management and rail safety (signalling and train control)*”. The motivation for the use of GNSS in ETCS is the reduction of the frequency of the balises distributed along the tracks that are needed to reset the train odometer error. Different realistic ways to integrate GNSS in ETCS are possible:

- The use of GNSS and sensors to enhance odometry is one of the options investigated in the projects INTEGRAIL, GRAIL and GRAIL-2. In INTEGRAIL, it is assumed that near a balise, odometry provides better precision than GNSS-based odometry. As the vehicle moves away from the balise, the GNSS odometry, at some point, becomes better than the classical one and thus replaces it. GRAIL and GRAIL-2 investigated a GNSS-based odometer to integrate and/or replace the traditional odometric systems.
- The second approach consists in using GNSS technology as a virtual balise. This provides information of absolute position. This approach enables the reduction of the frequency of balises distributed along the track line to reset the train odometer error. The integration of GNSS as a virtual balise has been studied in RUNE and the recent projects Satloc and 3InSat.

The present thesis investigates the integration of GNSS in ETCS as a virtual balise as this trend seems to be adopted by the rail community. Replacing the Eurobalise/Odometry-based train Location Determination System (LDS) by a hybridized GNSS/Sensors system is not currently realistic as it would require significant change in the system.

In any case, the operational requirements must be adapted to the way in which the GNSS is included in the system.

3.2.1 Alert limit derived from ETCS

There is no vertical requirement for GNSS in train control as the train is travelling in the horizontal plane. For train control, it is rather necessary to separate the along track and across track requirements. In ETCS, the track discrimination is done by reading Eurobalises, therefore no across track requirements exists for the existing odometry-based location system. To replace all the beacons, GNSS-based LDS should be able to discriminate the parallel tracks. According to [Hartwig et al.,

2006], the minimum separation between parallel tracks is 3.80 meters. Therefore, for tracks discrimination, an across track AL of 1.90 meters is required. In [Rispoli et al., 2013] and [Filip et al., 2008], it is said the across track confidence interval should not exceed 2.5 meters for the same reasons. The 2.5 meters across track AL is taken as a reference as it is used in most recent projects. As GNSS will be integrated in ETCS as a virtual balise, the first approach is to expect the same level of along-track accuracy as a real Eurobalise. The position accuracy requirement of the eurobalise is the following: “the location accuracy shall be within ± 1 m for each Balise, when a Balise has been passed” [UNISIG 1]. However such level of performance is not realistic for GNSS with high level of integrity. It is assumed that the determination of the railtrack on which the vehicle is driving is still determined by radiobeacons which are located after intersections. The objective is thus to use GNSS to reduce the amount of beacons and not to remove all of them.

In the along-track direction, the standard “accuracy” requirements for the LDS in ETCS are adapted to odometry and given in term of distance travelled [UIC 1]: *The minimum ETCS on-board odometer accuracy presently required for distance measurement is defined as 5 meters plus 5 % of distance travelled from the last reference point.* Assuming that the separation between two balise groups must not exceed 2.5 km [UNISIG 3], it is possible to obtain an upper bound of the maximum along-track tolerable error of 130 meter. The term “accuracy” mentioned is not clearly defined. Thus, this maximum tolerable error is not understood as a 95% confidence interval but as an along track AL (conservatively).

It will be assumed in this study that the position is propagated with odometry between two virtual balises. If it is assumed that the along-track error must not exceed 130 meters, and that the contribution of the error that is proportional to the distance travelled is assigned to the odometry, the maximum tolerable error for GNSS is related to the distance between two consecutive virtual balises with:

$$AL \leq 130 - 0.05\delta(VB_i, VB_{i+1}) \quad \text{Eq. 3-1}$$

where $\delta(\cdot)$ represents the curvilinear distance between the two consecutive virtual balises VB_i and VB_{i+1} .

Moreover, the minimum distance (δ_{min}) between two virtual balises is limited by the sampling frequency of the GNSS receiver output ($F_{s,GNSS}$) and the maximum velocity of the vehicle (v_{max}) in the area of interest. If the availability of GNSS is assumed to be 1, the minimum theoretical distance allowed between two consecutive balises is given by:

$$\delta_{min} = F_{s,GNSS}v_{max} \quad \text{Eq. 3-2}$$

Finally, we have the following upper bound for the across track:

$$AL \leq 130 - 0.05\delta(VB_i, VB_{i+1}) \leq 130 - 0.05\delta_{min} \quad \text{Eq. 3-3}$$

As the standard ETCS requirements for odometry does not make it possible to derive more than an upper bound for the GNSS along track AL , non-official requirements have been investigated in the litterature. In [Rispoli et al., 2013], it is said that on main corridor lines a 2.5 m confidence interval is required and on medium / low traffic lines the maximum confidence interval is several tens of meters or larger. [Mocek et al., 2010] gives requirements that must be fulfilled by GNSS to be used as a train location determination system for ETCS. In [Mocek et al., 2010], the along track AL is set to 25 meters for the main corridor lines and stations, from 25 m to 125 m in main and secondary lines and from 50 to 250 m in Regional and industrial lines. It can be noticed that for Regional and industrial lines the AL values may exceed the bound that have been derived in Eq. 3-3.

Finally, the along track AL will be assumed to take values between 25 and 125 meters (which corresponds to δ_{min} at a v_{max} of 300 km/h with $F_{s,GNSS}$ of 1 Hz).

3.2.2 Accuracy

Assuming the gaussianity of the along track and across track error in the nominal case, the accuracy requirement can be derived from the AL requirements with the following formula:

$$A_{max} = AL \frac{cdf_{\mathcal{N}(0,1)}^{-1}\left(1 - \frac{0.05}{2}\right)}{cdf_{\mathcal{N}(0,1)}^{-1}\left(1 - \frac{P_{int}}{2}\right)} \quad \text{Eq. 3-4}$$

where P_{int} is the integrity risk requirement (per sample).

To calculate the integrity risk requirements per sample, it is necessary to define the number of independent samples per hour. The correlation in time depends on the correlation of measurement errors, the variations of the satellite constellation geometry [Salos, 2012] (which occurs frequently in urban environment due to the variations in the configuration of the buildings) and the navigation algorithm that is used. The results that are used in civil aviation cannot be used in the case of study because the main sources of error are different, and their correlation time is different. It is proposed to define the minimum time between two independent samples in terrestrial urban/suburban environment.

Let's model the position error by a first order Gauss-Markov process. In this case, its correlation function has the following form [El-Diasty and Pagiatakis, 2009]:

$$E[\delta x(t)\delta x(t - \tau)] = \sigma_{\delta x}^2 e^{-|\tau|/T_c} \quad \text{Eq. 3-5}$$

where:

- $\delta x(t)$ is the position error
- σ_{GM} is the standard deviation of the position error
- T_c is the correlation time of the error

It is proposed to estimate T_c on the measurements collected in the campaign described later on in Chapter 5.

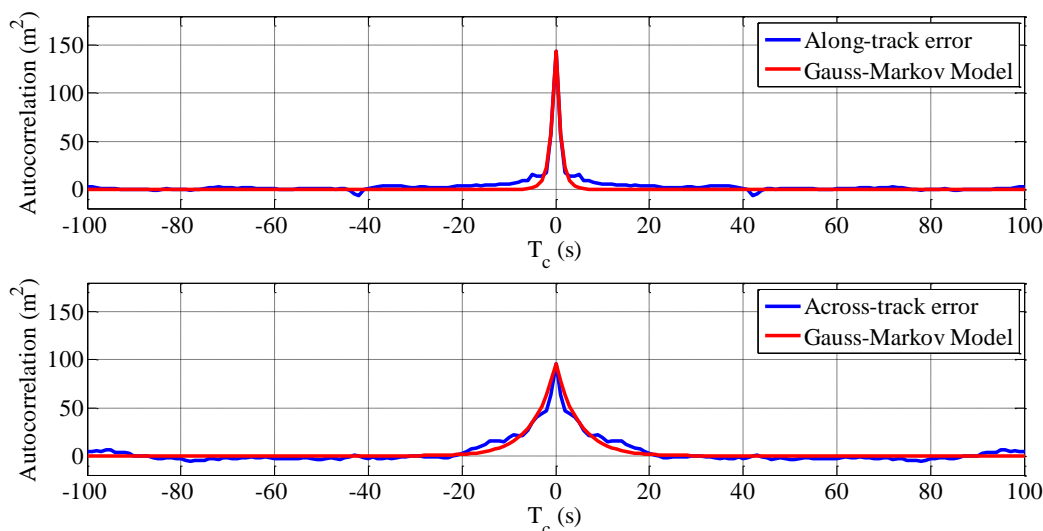


Figure 8 Correlation of position error for GPS L1 C/A receiver with Least Square position estimation algorithm

	GPS	GPS/GLO	GPS IMU/MAP	GPS/GLO/IMU/ MAP	GPS/GLO/IMU/ WSS
Algorithm	Least Square	Least Square	EKF	EKF	EKF
Along track T_c	2 s	14 s	110 s	71 s	75 s
Across track T_c	7 s	10 s	18 s	41 s	146 s

Table 4 Estimated correlation time on real data

The estimated T_c are given in Table 4 for the different architectures tested in the thesis on real data and described later on in chapter 6. The GNSS receivers that have been used only process one frequency (L1 C/A for GPS and L1 for GLONASS). The results obtained are not representative of all study cases as they have been obtained using 1-hour data collections. The organizations that are responsible for the definition of standardized requirements for terrestrial applications will have to determine these parameters on larger data collections as it has been done in civil aviation. It can be inferred from Table 4 that T_c is much larger for EKF based positioning due to the smoothing effect and the memory of the filter.

As for dual-frequency receiver, according to [Salos, 2012], (that have not been tested on real data), they present an error correlation of a few seconds which is driven by thermal noise and multipath.

Finally, it is assumed that the minimum time elapsed between two independent samples is $3T_c$, because at $3T_c$ the autocorrelation of the Gauss-Markov process is 5% of its maximum value. The decorrelation period are approximately 30 second for standalone GNSS with Least Square position estimation and approximately 300 seconds for sensor augmented GNSS with EKF position estimation.

3.2.3 Integrity risk

For train control, requirements for the maximum probability of occurrence of a failure are given in terms of Tolerable Hazard Rate (*THR*) instead of integrity risk as in civil aviation. It is necessary to find a relation between both values.

The integrity risk from the civil aviation point of view is defined as the probability of dangerous failure P_f per interval of time Δt [Filip et al., 2008]:

$$P_{int} = \frac{P_f}{\Delta t} \quad \text{Eq. 3-6}$$

Let T be the instant at which the failure occurs, T is a random variable which support is \mathbb{R}_+ . It is assumed that Δt is short enough so that the probability of multiple dangerous undetected failures in the interval is neglected. The probability that a failure occurs between t and $t + \Delta t$ can be written as:

$$P_{int} = \frac{P(t \leq T \leq t + \Delta t)}{\Delta t} \quad \text{Eq. 3-7}$$

Without loss of generality, let us set t to zero. Let's define $F(t)$ the failure distribution function of the system,

$$F(t) = P(T \leq t) \quad \text{Eq. 3-8}$$

Then P_{int} can be expressed as:

$$P_{int} = \frac{F(\Delta t)}{\Delta t} \quad \text{Eq. 3-9}$$

The risk of failure is defined as the probability that a failure occurs in a time interval $[t, t + dt]$ given that it did not occur in $[0, t]$:

$$Risk(t) = P(T \leq t + dt | T > t) \quad \text{Eq. 3-10}$$

The Hazard Rate (*HR*), also called hazard function is defined as:

$$HR(t) = \lim_{dt \rightarrow 0} \frac{Risk(t)}{dt} \quad \text{Eq. 3-11}$$

Using the conditional probability expression:

$$HR(t) = \lim_{dt \rightarrow 0} \left[\frac{P(T \leq t + dt \cap T > t) / P(T > t)}{dt} \right] \quad \text{Eq. 3-12}$$

Therefore, using the failure distribution function gives :

$$HR(t) = \frac{F'(t)}{1 - F(t)} \quad \text{Eq. 3-13}$$

If it is assumed that the failure distribution of GNSS is memoryless $HR(t) = HR$. The THR is the maximum value allowed for the HR . The failure distribution function allowed for the system is overbounded by the failure distribution obtained with HR equal to the THR is:

$$F(t) = 1 - e^{-THRt} \quad \text{Eq. 3-14}$$

This result is injected in equation and gives:

$$P_{int} = \frac{1 - e^{-THR\Delta t}}{\Delta t} \quad \text{Eq. 3-15}$$

It is assumed that $THR\Delta t$ is close to zero, therefore it is possible to apply a Taylor expansion to the exponential term around zero. At the first order, it gives :

$$P_{int} \cong THR \quad \text{Eq. 3-16}$$

As a simple relation has been found between the integrity risk and the tolerable hazard rate, it is then possible to express the failure probability requirements in the system of metric described in section 3.1. The main challenge for the introduction of the GNSS in ETCS is the very low THR , which, for the total on board ETCS, shall not be above $1.10^{-9}/\text{h/train}$ to fulfill the Safety Integrity Level 4 requirement. Therefore, this value of $1.10^{-9}/\text{h/train}$ does not apply to GNSS but to the whole positioning including GNSS and eventually other sensors.

A generic and non mandatory functional fault tree of ETCS level 2 is proposed in [UNISIG 3]. It has been stated in [GRAIL, 2008] that the gate 58 of this fault tree, which is given in Figure 9 and corresponds to the event “incorrect determination of train location ref to LRBG” (Last Relevant Balise Group) shall not exceed $1.10^{-10}/\text{h/train}$. The THR of Gate 58 has to be allocated between KERNEL-7 (Incorrect LRBG), ODO-3 (Incorrect actual physical speed direction), KERNEL-15 (Incorrect cab status) and GATE147 (Incorrect determination of distance travelled). If it is assumed that the risk is equally allocated between these events, the THR associated to GATE147 is $2.5.10^{-11}/\text{h/train}$.

Finally the THR associated to GATE147 has to be divided into KERNEL-28 (Incorrect confidence interval) and ODO-4 (Speed sensor underestimates distance). If the risk is equally allocated between these events, the THR allocated to the incorrect confidence interval event is $1.25.10^{-11}/\text{h/train}$. The introduction of GNSS in ETCS would require modifications in the functional fault tree. As in our case of study the GNSS is used to provide confidence intervals, the THR allocated to the confidence interval shall be $1.25.10^{-11}/\text{h/train}$.

The THR value obtained for GNSS by simple fault tree analysis can be compared with the reference values used in the literature and in previous projects. [Mocek et al., 2010] mentions a THR between $1.10^{-10}/\text{h}$ and $1.10^{-11}/\text{h}$ for a GNSS based Train Position Locator (TPL), [Mertens et al., 2003] mentions a THR between 1.10^{-11} and $1.10^{-12}/\text{h}$. In [Zhen et al., 2009], the authors set the integrity risk requirement (P_{int}) value to $4.10^{-12}/\text{h}$ for the use of GNSS in ETCS level. In [Rispoli et al., 2013], that describes the requirements used as a reference for the 3InSat project, it is said that “the value of $1.10^{-11}/\text{h}$ has been derived by means of the ETCS functional fault trees, but that there is an effort to allow the LDS to operate with a THR of $1.10^{-9}/\text{h/train}$ even for the most demanding initial position

determination”. The value of *THR* obtained here by simple fault tree analysis is thus relevant with respect to the state of the art. However as the *THR* for GNSS in ETCS is not standardized yet, two reference values will be considered, $1.10^{-9}/h$ and $1.10^{-11}/h$.

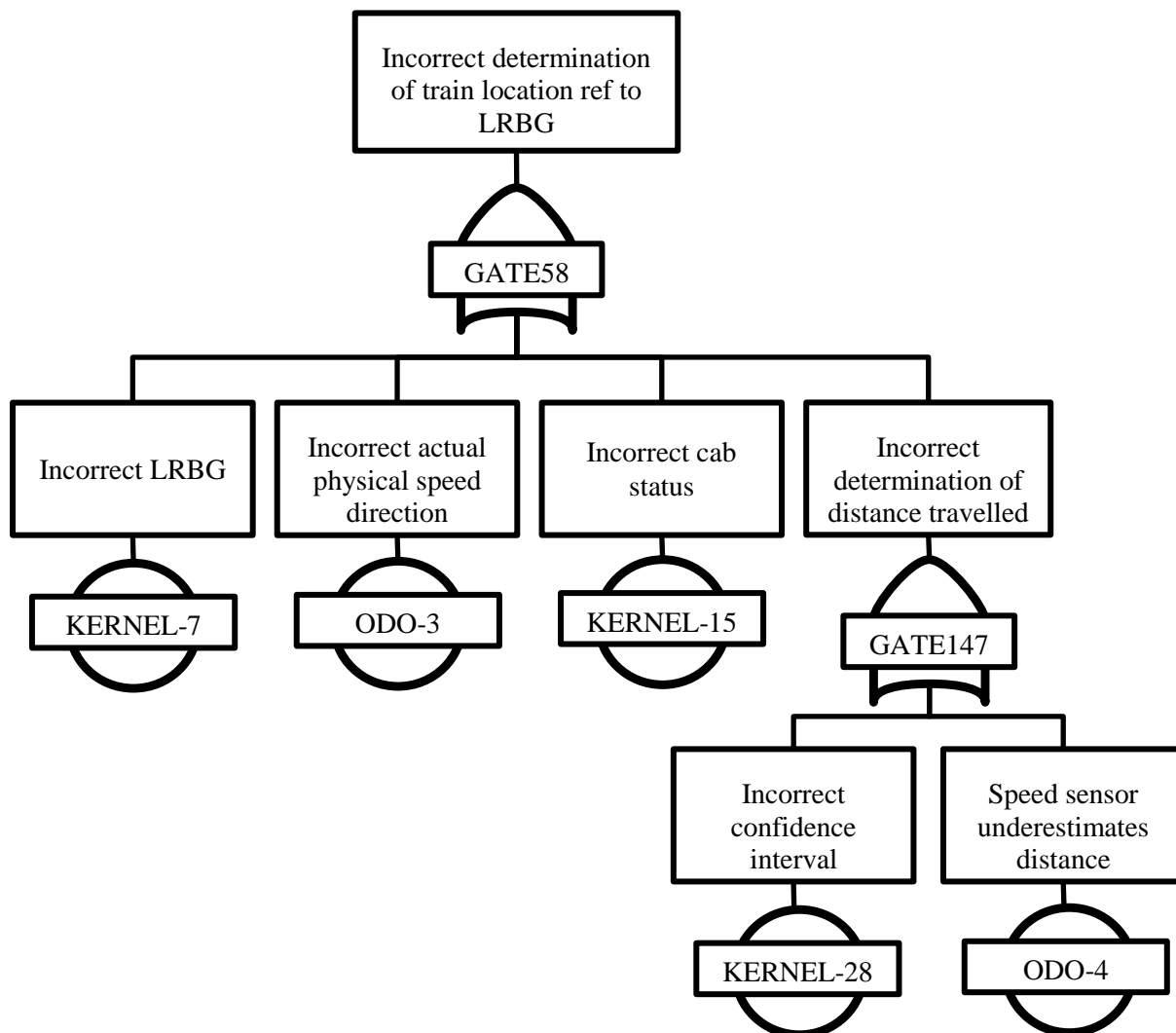


Figure 9 Generic functional fault tree of ETCS level 2 proposed in [UNISIG 3]

3.2.4 Availability

In order for the GNSS to replace Eurobalises, it has to fulfill at least the same availability requirement. The maximum unavailability for the Eurobalise is 10^{-7} according to [UIC 2]. This value is used as a reference in [Genghi et al., 2004], [Mocek et al., 2010], [Rispoli and al., 2013]. Moreover, in [Rispoli and al., 2013] an availability requirement of 2.10^{-4} is given for low traffic lines. Both values are taken as a reference in the study.

3.2.5 Continuity

No continuity requirement for GNSS in the particular case of ETCS was found in the literature. The value of 99.98% is given as an example as it was defined within the GNSS Rail Advisory Forum in 2000 [GRAF, 2000] for GNSS in train control. It shall be noted that this continuity of service requirements is not given in the same units as in civil aviation.

3.2.6 Time to alert

The *TTA* requirement for the LDS that was recommended within the GNSS Rail Advisory Forum and UIC Galileo WG is 1 s [Wiss et al., 2000]. This value is taken as a reference in recent projects such as 3InSat [Rispoli et al., 2013], and in the literature [Mocek et al., 2010].

3.2.7 Summary of the requirements of GNSS for train control

A table of non-official requirements which summarizes the analysis presented in section 3.2 is given in Table 5. The accuracies have been derived from the *AL* with Eq. 3-4. To simplify the table, the accuracy has been derived with the maximum number of independent sample (1 per 30 seconds). For main and secondary lines as well as regional and industrial lines, no across track requirement is given. It is assumed that the track on which the vehicle is located is known.

Operation	Accuracy-95%		Integrity				Continuity	Availability
	HA_{max}		HAL		TTA	P_{int}		
Main corridor lines, stations	Along track	Across track	Along track	Across track	1 s	$10^{-9}/h$ or $10^{-11}/h$	> 99.98%	$1 - 10^{-7}$
	6.6 (or 7.2) m	0.7 m	25 m	2.5 m				
Main and secondary lines	6.6 (or 7.2) m to 33 (or 36) m		25 to 125 m		1 s	$10^{-9}/h$ or $10^{-11}/h$	> 99.98%	$1 - 2 \cdot 10^{-4}$
Regional and industrial lines	13.1 (or 14.3) m to 33 (or 36) m		50 to 125 m		1 s	$10^{-9}/h$ or $10^{-11}/h$	> 99.98%	$1 - 2 \cdot 10^{-4}$

Table 5 Proposition for operational requirements to use GNSS for Train Position Locator in ETCS

3.3 Derivation of performance requirements for GNSS in Electronic toll collection

Electronic Toll Collection (ETC) consists in charging cars that drive through a road network without the necessity for them to stop at toll gates. The first objective of such system is to improve the traffic by removing the delay at toll gates. Different technologies can be used for ETC.

- For Dedicated Short Range Communications (DSRC)-based ETC, the vehicles are equipped with On Board Units (OBU) that are activated by the signal transmitted by toll gates at 5.8 or 5.9 GHz. DSRC technology is used in France in TIS PL system, in Spain in VIA-T and in Poland (viaTOLL). This technology is reliable and the cost of OBU is low as they are just tags that do not include costly sensors. The main drawback of DSRC is that it requires gantries which deployment and maintenance are costly.
- The second main technology that is being used for ETC is called Automatic Number Plate Recognition (ANPR). In ANPR, cameras are located on gantries and can detect/identify by image processing (and therefore charge) the vehicles that are driving in the road network. ANPR is, for instance, used for congestion charging in London. The main advantage of ANPR is that it does not require the vehicles to be equipped with any OBU. The drawbacks are related to reliability issues and to the dependency of gantries.
- Thirdly, GNSS is one of the recommended technologies in the EU directive for ETC [EU, 2004]. In GNSS-based ETC, the vehicle is equipped with an OBU that contains a GNSS receiver. The position information is sent to the charging authorities by GSM. GNSS based ETC systems already exists for heavy good transportation in Germany (Toll Collect) and Slovakia (MYTO). The advantage of GNSS is that it does not require any ground infrastructures. However the main drawbacks of GNSS are the high cost of the OBU and privacy (because the vehicles are tracked anywhere). Thus the GNSS technology seems more adapted for large road networks with low number of vehicle, which is typically the case for heavy good vehicle charging.

Several approaches can be adopted in order to design GNSS-based ETC systems. Three charging schemes can be distinguished according to the literature [Cosmen-Schortmann et al., 2009], [Grush et al., 2009].

- In the *discrete charging* approach, toll events are associated to the identification of objects. It includes single object charging such as bridges or tunnels, closed road charging, road segment charging, cordon charging or zone presence charging (also called congestion charging).
- In the *continuous charging* approach, the vehicles are charged as a function of the measured distance toll or in function of time in use in a predefined area.
- In the *mixed charging* approach, a combination of discrete and continuous approach is used. An example of this scheme consists in charging for cumulative distance or time considering a different price for each road segment [Toledo-Moreo et al., 2010].

Performance metrics for GNSS-based ETC have been proposed by the GNSS Metering Association for Road user charging (GMAR). The metrics are different for discrete and continuous charging approaches.

- For discrete ETC schemes, the event configurations that may occur are defined in Table 6.

The metrics proposed by GMAR for discrete ETC are the following [GPAF, 2009]:

- The *Charging Availability* is the probability that, assuming that the vehicle is using the infrastructure, a *Missed Recognition Event* does not occur
- The *Charging Integrity* is the probability that, for the vehicle that is not using the infrastructure, a False Recognition Event does not occur [GPAF, 2009].
- The metrics proposed by GMAR for continuous ETC schemes are the following [GPAF, 2009]:
 - The *Charging Availability* is the probability that the relative charging error is within the accepted charging error interval. This is the probability that the toll charger is getting sufficiently charged for road usage, and that there is an acceptable level of overcharging.
 - The *Charging Integrity* is the probability that the Relative Charging error is below the upper bound of the accepted charging error interval. This is the probability that the used is paying no more than required.

		System detects charging event	
		Yes	No
Charging event takes place	Yes	Correct Recognition	Missed Recognition (Undercharging)
	No	False Recognition (Overcharging)	Correct Rejection

Table 6 Event matrix decision: theoretic event matrix for discrete schemes [Grush et al., 2009]

The CEN (European Committee for Standardization) ISO TS 17444 1-2 norm has been created in 2012. It standardizes the performance metrics for ETC schemes defined in accordance with ISO 17573 (Electronic Fee Collection systems). The metrics in CEN ISO TS 17444 1-2 are defined at different level: End-to-End, User Account, Payment Claim, Bill Detail, Toll Declaration and Charge Report [Wedlock et al., 2012].

As proposed by [GPAF, 2009], the continuous and discrete schemes are differentiated, and metrics are proposed to each systems. Moreover, metrics for mixed charging schemes are included [Wedlock et al., 2012]. However the standard CEN ISO TS 17444 “does not propose specific numeric performance

bounds, or average or worst-case error bound in percentage or monetary units. Those decision are left to the toll charger” or to agreement between the Toll charger and the service provider.

An example of requirement for the adapted metrics is given in [Wedlock, 2012]. This example is representative of the way in which the requirements can be addressed, even if the values cannot be taken as reference.

For continuous charging scheme,

- For the vehicles not using the infrastructure, the probability that for any predefined Chargeable Event the front-end improperly detects it (false positive) shall be smaller than 10^{-5} .
- Correct charging rate shall be greater than 99%, where the Accepted Charging Error Interval is between -1% and 0.3%. This metric corresponds to the *Charging Availability* defined by GMAR.
- Overcharging rate shall be smaller than 0.1%, where the upper limit of the Accepted Charging Error Interval is 0.3%. This metric corresponds to the *Charging Integrity* defined by GMAR.

For a discrete charging scheme:

- Correct charging rate shall be greater than 99%, where the confidence interval is the one determined by the sample size of 50.000 (i.e. $< 0,2\%$ -points). This metric corresponds to the *Charging Availability* defined by GMAR
- For the vehicles not using the infrastructure, the probability that a front-end improperly detects a charging event (false positive) shall be smaller than 10^{-5} . This metric corresponds to the *Charging Integrity* defined by GMAR

Once the standard format of requirement is determined, it is necessary to find values. Requirements for the charging scheme can be found in the literature and are listed in [Salos, 2012], but most of them are not compliant with the recent CEN ISO TS 17444 metric system as they were published before 2012. However, in [EG 9, 2004], it is indicated that "*it is necessary to define a specific set of test conditions in which test geo-objects are guaranteed to be successfully recognized with a success rate of at least 99.99 %. False recognition of a geo-object should be less than 1 in 10^6* ". The requirement is equivalent to a discrete charging scheme with *Charging Availability of 99.99 % and a Charging Integrity of 10^{-6}* .

It can be inferred from this analysis of the state-of-the-art of requirements for GNSS in ETC, that the requirements depends on the charger and are given at the charging level. Nonetheless, it is necessary to define requirements at the position level. This can be done by following the methodology used by civil aviation.

3.3.1 Alert limit

The present work investigates a discrete GNSS-based event charging and it has to be stressed that the following methodology cannot be applied to continuous charging schemes. Let us define a geo-object as an area associated to a discrete charging event. The vehicles that are located in the geo-object shall be charged for the fare of the object, without consideration of travelled distance or time spent in the

area. The geo-object must be soundly designed in order to minimize the probability to erroneously charge the vehicles that are not meant to be charged and to maximize the probability to charge the vehicles that are inside the charging section. A simple way to solve this problem is to locate the geo-object boundary at an equal distance between the road section to charge and the road section that shall not be charged. It is assumed that the vehicle is charged when the estimated position is inside the geo object (actually, the decision takes into account the protection levels). Let us denote x_{true} the actual position of the vehicle in the across track direction, and \hat{x} the estimated position based on GNSS. If the vehicle is on the road to be charged, it is located in $x_{true} = 0$. If the vehicle is on the free road, it is located in $x_{true} = D$. The location of the geo object boundary is denoted G . An improved way to set the geo-object boundaries consists in choosing G in order to minimize the probability of charging error, by considering the position of the vehicle as a random variable. The probability of charging error ($P_{charging\ error}$) is given by:

$$P_{charging\ error} = P(x_{true} = 0)P(\hat{x} > G|x_{true} = 0) + P(x_{true} = D)P(\hat{x} < G|x_{true} = D) \quad \text{Eq. 3-17}$$

It is assumed that the cross track error distribution is the same on both roads. The error $\hat{x} - x_{true}$ is modelled by a centered normal distribution with a standard deviation σ_{GNSS} , which is assumed to be the same on both road segments. Thus:

$$P_{charging\ error} = \frac{P(x_{true} = 0)}{2} \operatorname{erfc}\left(\frac{G}{\sqrt{2}\sigma_{GNSS}}\right) + \frac{(1 - P(x_{true} = 0))}{2} \operatorname{erfc}\left(\frac{D - G}{\sqrt{2}\sigma_{GNSS}}\right) \quad \text{Eq. 3-18}$$

The value of G_0 that minimizes the probability of charging error is chosen so that $\frac{\partial P_{charging\ error}}{\partial G}(G_0) = 0$. The expression of the value G_0 is thus:

$$G_0 = \frac{\sigma_{GNSS}^2}{D} \ln\left(\frac{P(x_{true} = 0)}{1 - P(x_{true} = 0)}\right) + \frac{D}{2} \quad \text{Eq. 3-19}$$

If the probability of being on each road is equal, then the optimal boundaries is located at the same distance from each road segment. This result can increase the size of the geo-object when the road section within the geo object has significantly more traffic than the free road section, which is usually. The value of G_0 is plotted in Figure 10, for $D = 20$ m and $\sigma_{GNSS} = 5$ m.

The *HAL* is defined as the minimum distance between the position estimated with GNSS and the geo object boundaries. The result given in Eq. 3-19 enables to increase the *HAL* and therefore the availability of the system for dense roads.

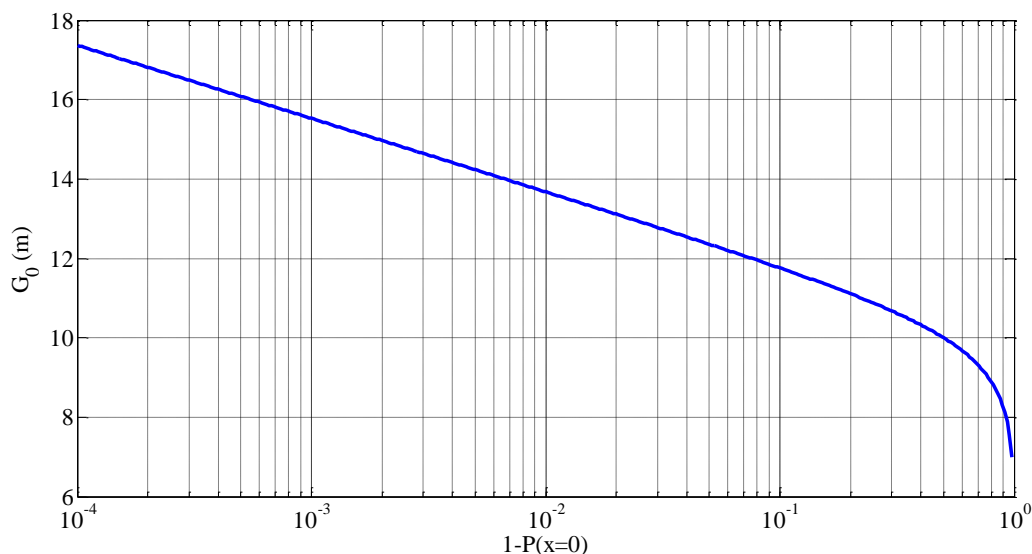


Figure 10 Example of optimal Geo-object boundary for $D = 20$ m and $\sigma_{GNSS} = 5$ m

Unlike civil aviation, the HAL value is varying over time, therefore different values are considered in the Thesis. The thesis tests different values of HAL , from 15 to 50 meters.

3.3.2 Accuracy

The accuracy requirement is obtained from the HAL , and the integrity risk (given in) by using Eq. 3-4.

3.3.3 Integrity risk

In ETC, the probability of failure is given at the charging level by the charger, therefore no standard requirement exists. It is then necessary to derive integrity risk requirements in the position domain corresponding to the definition in 3.2.2. In [Salos, 2012], a method to derive the P_{MD} of the GNSS integrity monitoring algorithm from the probabilities of missed object detection (*Charging availability*) and false object detection (*Charging integrity*) is proposed. This approach assumes that the geo-objects are charged with the same fare and assumptions on the length of the geo-objects and the velocity of the vehicles must be made. This approach consists in adapting the design of the integrity monitoring algorithm to the charging requirements, with constraints on the design of the geo-objects.

In this thesis, a different approach is preferred. Here again, the charging requirements are taken as inputs. However, the approach consists in adapting the design of the geo-objects to the charging requirements, with constraints on the design of the integrity monitoring algorithm. This approach is preferred because the requirements that are found in the literature are examples, and different chargers may require different performances. It appears simpler to change the design of the geo-objects than the integrity monitoring algorithm.

In this Thesis, it is proposed to set different values for the integrity risk of the GNSS positioning at $10^{-4}/h$, $10^{-5}/h$, and $10^{-6}/h$. Lower integrity risks are not investigated as they are associated with safety critical applications.

It is possible to design the geo-object recognition algorithm to fulfill the false object and missed object requirements. Indeed, for a given geo-object, the number of available independent GNSS position measurement (n) when driving across the geo-object is related to the length of the geo-object, the velocity of the vehicle and the minimum time between two independent samples. To decide whether the vehicle is inside the geo-object or not, the number of estimated positions that have been are inside the geo-object is compared to a defined threshold.

Let us denote N_{min} this threshold and n_i the number of estimated position that are in the geo-object, n_i is a discrete random variable. The probability of charging the vehicle that is outside the geo-object is denoted P_{FOR} (False Object Recognition) and is associated to the probability that n_i is higher than the threshold N_{min} , which is given by:

$$P_{FOR} = \sum_{i=N_{min}}^n P(n_i = i | \text{vehicle} \notin \text{geo object}) \quad \text{Eq. 3-20}$$

To wrongly decide that a vehicle outside the geo-object is charged, its estimated position and its confidence interval must be inside the geo-object. As the true position of the vehicle is assumed to be outside the geo-object, the confidence interval cannot contain the true position of the vehicle which means that there is an undetected positioning failure. However all positioning failure do not lead to a false object detection. Therefore the operational P_{FOR} can be bounded by:

$$P_{FOR} \leq \sum_{i=N_{min}}^n \binom{n}{i} P_{int}^i (1 - P_{int})^{n-i} \quad \text{Eq. 3-21}$$

where P_{int} represents the integrity risk per independent GNSS position estimation.

Finally, one has to set the value of N_{min} and n so that:

$$\sum_{i=N_{min}}^n \binom{n}{i} P_{int}^i (1 - P_{int})^{n-i} \leq P_{FOR, requirement} \quad \text{Eq. 3-22}$$

Thus the operational P_{FOR} is lower than the requirements. It has to be noted that several N_{min} and n fulfills the requirement. Indeed the term on the left in Eq. 3-22 is a decreasing function of N_{min} , thus, all values of threshold higher than N_{min} fulfills the requirement. To maximize the availability the minimum threshold has to be chosen.

3.3.4 Availability

The second requirement is the *Charging availability*. The probability of not charging the vehicle that is inside the geo-object is denoted P_{MOR} (Missed Object Recognition) is the probability that n_i is lower than the threshold N_{min} , which is given by:

$$P_{MOR} = \sum_{i=0}^{N_{min}-1} P(n_i = i | vehicle \in geo\ object) \quad \text{Eq. 3-23}$$

To decide not to charge a vehicle which true position is inside the geo object, two configurations can occur:

- If the estimated position is inside the geo-object, it means that the confidence radius exceeds the *HAL* or that there is a false alarm. The probability of the confidence radius to exceed the *HAL* or that there is a false alarm is denoted (P_u).
- If the estimated position is outside the geo-object, and the confidence radius does not exceed the *HAL*. This case is a particular case of positioning failure because the confidence interval does not include the real position of the vehicle, it is thus bounded by P_{int} .

$$P_{MOR} \leq \sum_{i=0}^{N_{min}-1} \binom{n}{i} (P_{int} + P_u)^i (1 - (P_{int} + P_u))^{n-i} \quad \text{Eq. 3-24}$$

Then it is necessary to find the value for P_u that verifies:

$$\sum_{i=0}^{N_{min}-1} \binom{n}{i} (P_{int} + P_u)^i (1 - (P_{int} + P_u))^{n-i} \leq P_{MOR,requirements} \quad \text{Eq. 3-25}$$

In the example of section 3.3.3 $N_{min} = 1$. Therefore, P_u must verify:

$$P_u \leq 1 - \sqrt[n]{P_{MOR,requirements}} - P_{int} \quad \text{Eq. 3-26}$$

If $P_{MOR,requirements}$ is set to 99.99 %, P_u must be lower than 99.99%.

3.3.5 Continuity

No continuity requirements have been found for GNSS in ETC.

3.3.6 Time-To-Alert

No Time-To-Alert requirements have been found for GNSS in ETC.

3.3.7 Summary

A table of non-official requirements that summarizes the results obtained in 3.3 is given in Table 7. The accuracy has been calculated for a time between independent samples of 30 seconds.

Operation	Accuracy-95%	Integrity			Continuity	Availability
	HA_{max}	HAL	TTA	P_{int}		
ETC	6 to 20 m	15 to 50 m	-	$10^{-4}/h$	-	Variable
	5.5 to 18 m			$10^{-5}/h$		
	5.1 to 17 m			$10^{-6}/h$		

Table 7 Proposition for operational requirements for GNSS to be used in ETC

3.4 Conclusions

There is currently no standardized requirement for the use of GNSS in the two terrestrial applications of interests. However, examples of what these requirements could be have been found in the litterature.

- For train control, it has been stated that the integrity risk requirement is extremely stringent (10^{-9} to $10^{-11}/h$) and associated with a maximum TTA requirement of 1 s. The third main issue for the introduction of GNSS in this application is the across track AL of 2.5 meters in order to identify on which track the train is located.
- For ETC, the standardization process appears to be more advanced. Metrics at the charging level have been defined so that the charging organism can emit requirements. Then these requirements can be used in order to define the requirements for the positioning system.

3.5 References

- [Ballesteros, 2006] Ballesteros, J.P., 2006. GRAIL project: GNSS introduction in the rail sector. EURNEX-Z`EL 2006. In: 14th International Symposium: Towards the Competitive Rail Systems in Europe, Z`ilina, Slovakia
- [Barbu and Marais, 2014] George BARBU, Juliette MARAIS. The SATLOC project. TRA - Transport Research Arena, Apr 2014, France. 10p
- [Bedrich and Gu, 2004] BEDRICH, S., Gu, X. (2004). GNSS-based sensor fusion for safety-critical applications in rail traffic, Galileo and EGNOS Information Catalogue
- [Bustamante and De Miguel, 2003] Bustamante, J., De Miguel, S., 2003. GADEROS – a technological approach to GNSS-aided railway traffic monitoring for conventional and low-density traffic lines – interoperability of GNSS-based location with ERTMS/ETCS on-board. Intelligent Transport Systems

and Services, Madrid, Spain.

- [Cosmen-Schortmann et al., 2009] J. Cosmen-Schortmann, B. Grush, C. Hamilton, M. Azaola-Saenz and M. A. Martínez-Olague, "The Need for Standard Performance Definitions for GNSS Road Use Metering," 16th World Congress on Intelligent Transport Systems, Stockholm, Sweden, October 2009
- [Cuadras, 2002] C. M. Cuadras, "Geometrical Understanding of the Cauchy Distribution," Elsevier, Ltd, Vol. 26, 1-2, pp 283-287, 2002
- [EG 9, 2004] Expert Group 9, "Report of Expert Group 9 Working to support the European Commission on the work on Directive 2004/52/EC: Specification of the EFC application based on satellite technologies", version 3.2, 20 February 2006
- [El-Diasty and Pagiatakis, 2009] M. El-Diasty and S. Pagiatakis, A rigorous temperature dependent stochastic modelling and testing for mems-based inertial sensor errors, published in Sensors, 2009, vol. 9, pp. 8473–8489
- [EU, 2004] European Parliament, "Directive 2004/52/EC of the European Parliament and of the Council of 29 April 2004 on the interoperability of electronic road toll systems in the Community", Official Journal of the European Union, 29 April 2004
- [Farrell and Barth, 1999] Farrell, Jay and Matthew Barth, The Global Positioning System and Inertial Navigation, McGrawHill, New York, NY, 1999
- [Filip et al., 2008] Filip, A., Mocek, H., & Suchanek, J. (2008, May). Significance of the Galileo Signal-in-Space Integrity and Continuity for Railway Signalling and Train Control. In 8 th World Congress on Railway Research (WCRR), Seoul, Korea
- [Genghi et al., 2003] Genghi, A., Marradi, L., Martinelli, L., Campa, L., Labbiento, G., Cianci, J., Venturi, G., Gennaro, G., Tossaint, M., "The RUNE Project: Design and Demonstration of a GPS/EGNOS-Based Railway User Navigation Equipment," Proceedings of the 16th International Technical Meeting of the Satellite Division of The Institute of Navigation (ION GPS/GNSS 2003), Portland, OR, September 2003, pp. 225-237.
- [GPAF, 2009] DRAFT 0.79, GPAF GMAR's Performance Assessment Framework Prepared by GMAR GNSS Metering Association for Road user charging Draft Authors: Joaquín Cosmen (GMV, Spain) Bern Grush (Skymeter, Canada) Carl Hamilton (Centre for Transport Studies, KTH, Sweden), 2009
- [González et al., 2012] E. González, C. Prados, V. Antón, and B. Kennes, "GRAIL- 2 Enhanced Odometry based on GNSS," in TRA 2012 - 4th Transport Research Arena conference, Athens, Greece, 2012, pp. 880–887.

- [GRAF, 2000] GNSS Rail Advisory Forum – Requirements of Rail Applications, European GNSS Secretariat, (2000).
- [GRAIL, 2008] Quantitative Risk Analysis of the Enhanced Odometry, 2008
- [Grush et al., 2009] B. Grush, J. Cosmen-Schortmann, C. Hamilton and M. A. MartinezOlague, “GMAR Standard Performance Definitions for GNSS Road Use Metering,” 16th World Congress on Intelligent Transport Systems, Stockholm, Sweden, October 2009.
- [Hartwig et al., 2006] K. Hartwig, M. Grimm, M. Meyer zu Hörste, K. Lemmer, “Requirements for Safety Relevant Positioning Applications in Rail Traffic – a demonstrator for a train borne navigation platform called “DemoOrt” ”, National Research Council Canada: 7th World Congress on Railway Research WCCR, Montréal, Canada, 2006
- [ICAO, Doc 9849] Global Navigation Satellite System (GNSS) Manual, 2005
- [ICAO, Doc 9750] Global Air Navigation Plan for CNS/ATM Systems. Second Edition 2002. Doc 975
- [ICAO, 2010] ICAO NSP (2010a) GBAS CAT II/III development baseline SARPs, International Civil Aviation Organization
- [ICAO, 2006] International Civil Aviation Organization, "International Standards and Recommended Practices - Annex 10 to the Convention on International Civil Aviation - Aeronautical Telecommunications - Volume I, Radio Navigation Aids", 6th Edition (with amendment 85), July 2006.
- [IMO, 2001] IMO (2001). Revised maritime policy and requirements for a future global navigation satellite system (GNSS), resolution A.915(22).
- [Marradi et al., 2008] Marradi, L., Albanese, A., Di Raimondo, S., 2008. RUNE-railway user navigation equipment, architecture and tests. In: Del Re, E., Ruggieri, M. (Eds.), Satellite Communications and Navigation Systems. Springer
- [Mertens et al., 2003] K., Mertens, P., Franckart, J.P., Starck, A., LOCPROL: A low cost Train Location and Signalling system for "Low Density" Lines, <http://www.ertico.com/download/locoprol%20documents/wccr03v3.pdf>, 2003.
- [Mocek et al., 2010] Mocek, H., Filip, A., Bazant, L., Galileo Safety-of-Life Service Utilization for Railway Non-Safety and Safety Critical Applications, (Railway Infrastructure Administration, TUDC - Laboratory of Intelligent Systems), Journal of Mechanical Systems for Transportation and Logistics, Volume 3, Issue 1, pp. 119-130, 2010
- [MoU] Memorandum of Understanding (MoU) between the European Commission, the European Railway Agency and the European Rail sector Associations (CER-UIC-UNIFE-EIM-GSM-R Industry Group-ERFA) concerning the strengthening of cooperation for the

management of ERTMS

- Rispoli et al., 2013 Rispoli, F.; Filip, A.; Castorina, M.; Di Mambro, G.; Neri, A.; Senesi, F., "Recent progress in application of GNSS and advanced communications for railway signaling," Radioelektronika (RADIOELEKTRONIKA), 2013 23rd International Conference , vol., no., pp.13,22, 16-17 April 2013
- [Rousseau and Cadet, 2006] Rousseau, M., Cadet, D., The LOCOPROL project, 7th World Congress on Railway Research (WCRR), June 4-8, 2006, Montreal, Canada
- [Salos, 2012] Salos Andrés, Carlos Daniel (2012) Integrity monitoring applied to the reception of GNSS signals in urban environments
- [Simsky et al., 2004] Simsky, A., Wilms, F., Franckart, J.-P., 2004. GNSS-based failsafe train positioning system for low-density traffic lines based on one-dimensional positioning algorithm. NAVITEC 2004, 2nd ESA Workshop on Satellite Navigation User Equipment Technologies, Noordwijk, The Netherlands.
- [Sun, 2010] Sun, D. Ultra-Tight GPS/Reduced IMU for Land Vehicle Navigation. PhD Thesis, University of Calgary: Department of Geomatics Engineering, Canada, 2010.
- [Toldedo-Moreo et al., 2010] Toledo-Moreo, R.; Ubeda, B.; Santa, J.; Zamora-Izquierdo, M.A.; Gomez-Skarmeta, A.F., "An analysis of positioning and map-matching issues for GNSS-based road user charging," Intelligent Transportation Systems (ITSC), 2010 13th International IEEE Conference on , vol., no., pp.1486,1491, 19-22 Sept. 2010
- [UIC 1] ETCS Implementation handbook, available at: http://www.uic.org/etf/publication/publication-detail.php?code_pub=190_15
- [UIC 2] EEIG : 96S126, ERTMS/ETCS RAMS Requirements Specification Chapter 2 – RAM
- [UNISIG 1] FFFIS for Eurobalise, available at: <http://www.era.europa.eu/Document-Register/Pages/UNISIGSUBSET-036.aspx>
- [UNISIG 2] Safety Requirements for the Technical Interoperability of ETCS in Levels 1 and 2, available at: <http://www.era.europa.eu/Document-Register/Pages/Set-2-Safety-Requirements-fo-the-Technical-Interoperability-of-ETCS-in-Levels-1-2.aspx>
- [UNISIG 3] ETCS Application Level 1 - Safety Analysis Part 1 - Functional Fault Tree

- [Wasle and Ringert, 2003] Wasle E, Ringert J (2003): Means of Navigation for Automatic Level Crossing Control and the Concept of the ECORAIL Project, E. Wasle and J. Ringert, *Österreichische Zeitschrift fuer Vermessung & Geoinformation (VGI)*, 1/2003, ed. by H. Schuh, F. Brunner, and H. Kahmen, pp. 61 - 67, 2003.
- [Wedlock et al., 2012] Mark Wedlock, Erich Erker, Thomas Jestädt , Joaquín Cosmen Schortmann, Standardising Charging Performance Metrics, 19th ITS world congress ,October 2012
- [Wedlock, 2012] Wedlock, Standardising Charging Performance Metrics, Presentation, ITS World Vienna, 2012
- [Wiss et al., 2000] J. M. Wiss, G. Barbu, P. Frosig, M. Schroder, C. Edwards, K. Walter, A. Filip, A. Sage and S. Forsyth, "GNSS Rail User Forum: Requirements of Rail Applications," European GNSS Secretariat, Brussels, May 2000
- [Zheng et al., 2009] Zheng, Y., Cross, P., Quddus, M., "The Effects of Railway Track Database Quality on the Performance of Tightly Coupled GNSS/Track Database Train Positioning System," Proceedings of the 22nd International Technical Meeting of The Satellite Division of the Institute of Navigation (ION GNSS 2009), Savannah, GA, September 2009, pp. 2146-215

4 POSITIONING PLATFORM DEFINITION FOR TRAIN CONTROL AND ETC

The chapter firstly proposes technical choices in terms of GNSS receiver for both terrestrial applications. As standalone GNSS may not meet the operational requirements for both applications, the sensors and information that are available on board will be used to augment GNSS. These sensors are discussed along with the possible fusion strategies. A hybridized navigation solution is proposed for each application.

4.1 GNSS receivers' architectures

This subsection discusses technical choices that have been made on the GNSS receiver characteristic for train control and ETC. The solutions proposed have to respect the primary objective of the using GNSS for monitoring the position of terrestrial vehicle: the reduction of the ground infrastructure. Therefore, this Thesis does not investigate solutions that are based on a network of ground stations such as Ground Based Augmentation Systems (GBAS) or differential GNSS. Moreover, the use of Real Time Kinematic (RTK) receivers has not been investigated in the Thesis for integrity monitoring issues due to the frequency of occurrence of cycle slips in urban environment and to the dependency with a network of ground stations. For both applications, it is proposed to use dual frequency receivers in order to cancel the ionosphere biases. In this section, the location system is assumed to use GNSS only in order to put forward the design choices related to GNSS. As it will be seen later on, the final chosen system will use other sensors.

4.1.1 Train control

Apart from the sub-meter across track accuracy requirement, the $10^{-9}/h$ to $10^{-11}/h$ integrity risk is the main challenge for using GNSS to monitor the position in train control. To design the system, it is necessary to characterize the error sources with a sufficient confidence. The very stringent integrity risk makes it impossible to use the existing error models that were developed for civil aviation because they are adapted to an integrity risk of $10^{-7}/h$ or higher. Moreover, to validate a solution with such probability, it would require a yet unavailable amount of independent data. It is thus crucial to find a way to relax this stringent integrity requirement. An example of such method is the 1D algorithm [Rousseau and Cadet, 2006] that has been proposed to fulfill the same requirements in the context of the LOCOPROL project. The 1D algorithm consists in dividing the constellation in satellite subsets of two satellites. According to [Rousseau and Cadet, 2006], the final confidence interval, which is the union of the confidence intervals of each subset, is ensured to bound the true position with a failure rate between $10^{-9}/h$ and $10^{-11}/h$. Using independent solutions to relax integrity risk is also proposed as a solution in [Rispoli et al., 2013].

4.1.1.1 Definition of the concept used to relax the integrity risk requirement

In this work, it is proposed to divide the visible satellites into two independent satellite subsets (also referred to as GNSS sub-systems in this section). It is thus necessary to work with multi-constellation receivers so that each subsystem has sufficient availability and accuracy. The choice of the independent subsystems and the hypothesis of independence to be carefully analyzed:

- The satellite faults are assumed to be independent events between satellites and thus for both subsystems (as satellites are different).
- The constellation fault, which is defined as a fault affecting several satellite of the same constellation, must be considered as a fault mode. To protect against this mode, the subsystems must use satellites taken from independent GNSS: for instance GPS and Galileo. If the constellation failures were not considered in the failure modes (or detected by other means), performances of the algorithm could be optimized by forming two hybrid constellations with optimized geometry. Currently the probability of constellation failure for GPS is assumed to be zero [Walter et al., 2013] (more recent works such as [WG-C,ARAIM] assumes that it is bounded by $10^{-7}/h$). However, for the other constellations (e.g GLONASS), it is not the case. Thus, the two sub systems will have to integrate satellites from different GNSS. A fault affecting multiple satellites from two constellations simultaneously is assumed to be negligible with respect to the integrity risk requirement (which is assumed comprised between 10^{-9} and $10^{-11}/h$).
- A failure due to abnormal ionosphere and interferences may affect both sub systems even with separated constellations. It is proposed in this thesis to use dual frequency receivers in order to remove ionosphere delay. Thus the ionosphere common mode failure is assumed removed.
- Failures due to interference or jamming are not investigated in this thesis.
- The environment, which is the same for the two subsystems, may introduce a common fault mode. As the satellites from each subsystem are at different locations with respect to the

immediate environment (in terms of elevation and azimuth) and have signals with different received power, the independency assumption between both subsystems should hold (except in deep urban canyon configuration). The validity of this subsystems' independence hypothesis against local errors shall be tested in real measurement campaigns. If the hypothesis does not hold, it is possible to decorrelate the local error sources by separating the two receivers associated to each subsystem with a sufficient distance. Such approach is possible for train control as the vehicle is long enough to separate the receivers with a sufficient distance. However, in this case, the receiver located at the back of the train will go through the same environment after a delay that depends on the velocity of the train. Thus in this case, to keep independency it may be necessary not to use any position estimation algorithm that introduces time correlation (such as Kalman filtering).

For the following of this section, let us denote \hat{x}_1 and \hat{x}_2 the position estimated by the two subsystems based on the two satellite subsets. The radius of the confidence interval associated to these positions solutions are denoted HPL_1 and HPL_2 . The combined position solution and the associated confidence intervals are respectively denoted \hat{x}_{12} and HPL_{12} .

As the sub-systems are considered independent, the integrity risk P_{int} can now be equally allocated to each subsystem ($\sqrt{P_{int}}$), provided that the confidence interval of the combined position solution is defined as the union of the confidence intervals of each sub-system. The principle consists in finding the minimum area that is sure to include both confidence intervals. Two configurations have to be taken into account.

4.1.1.1.1 First configuration

It has to be kept in mind that the integrity and accuracy requirements are given in the horizontal plane and therefore we do not investigate the vertical position.

The first configuration occurs when the confidence circle of a sub-system is included into the confidence circle of the other subsystem. This corresponds to $\|\hat{x}_1 - \hat{x}_2\| \leq |HPL_1 - HPL_2|$. In this case the combined horizontal position and confidence radius are given by:

$$\begin{aligned} \hat{x}_{12} &= \hat{x}_{\text{argmax}_i HPL_i} \\ HPL_{12} &= \max(HPL_1, HPL_2) \end{aligned} \tag{Eq. 4-1}$$

The first configuration is illustrated in Figure 11.

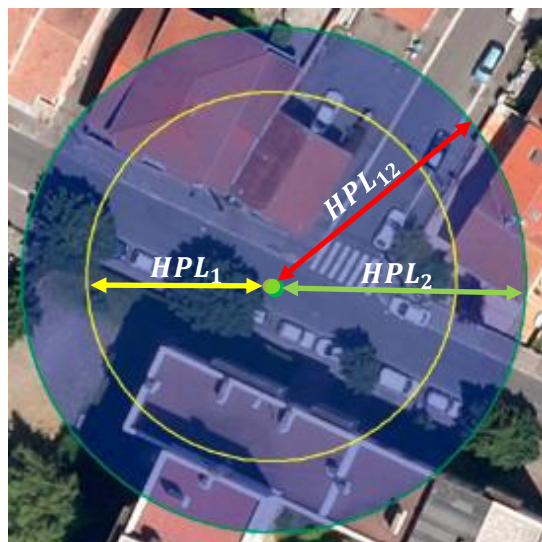


Figure 11 Definition of the confidence interval for train control, first configuration

4.1.1.1.2 Second configuration

The second configuration corresponds to $\|\hat{x}_1 - \hat{x}_2\| > |HPL_1 - HPL_2|$. In this case, the combined horizontal position and confidence radius are given by:

$$\hat{x}_{12} = \frac{1}{2} \left[\hat{x}_1 + \hat{x}_2 + \frac{\hat{x}_2 - \hat{x}_1}{\|\hat{x}_1 - \hat{x}_2\|} (HPL_2 - HPL_1) \right] \quad \text{Eq. 4-2}$$

$$HPL_{12} = \frac{HPL_1 + HPL_2 + \|\hat{x}_1 - \hat{x}_2\|}{2}$$

The second configuration is illustrated by Figure 12.

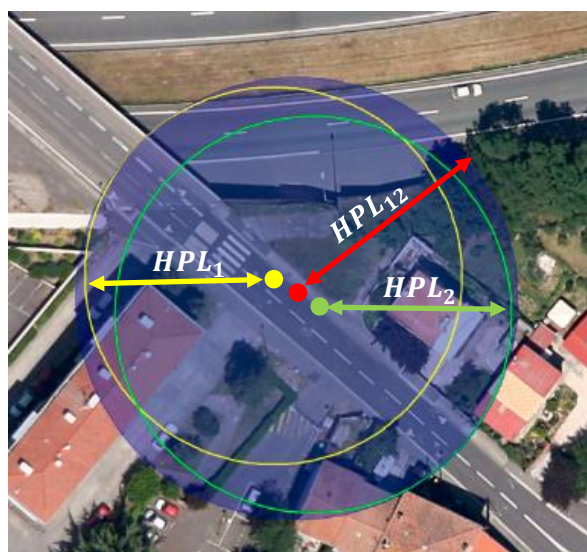


Figure 12 Definition of the confidence interval for train control, second configuration

The validity of the concept is proven in appendix A.

4.1.1.2 Theoretical performance of the concept

It has to be noted that the proposed solution based on two sub-systems will have degraded performance in terms of accuracy and availability compared to the case of single system based on all available satellite (dual constellation) even if associated with very low integrity risk.

Moreover, for the system to be available, it is necessary, but not sufficient, that each sub-system is able to provide its position estimate and the associated confidence interval. For this to happen, each sub-system requires at least 4 satellites-in-view per subsystem and thus 8 satellites. As it will be seen later, this drawback can be lifted by using Kalman filtering and hybridization with complementary sensors (in a tightly coupled architecture).

It is possible to assess the theoretical performance of the proposed method by simple modelling. The performance is assessed in terms of position error and size of confidence intervals compared to each subsystem taken independently.

To do so, let us model the GNSS errors for each subsystem (δx_1 and δx_2) by two-dimensional independent normal variables:

$$\begin{aligned}\hat{x}_1 &= x_{true} + \delta x_1 \\ \hat{x}_2 &= x_{true} + \delta x_2\end{aligned}\tag{Eq. 4-3}$$

where $\delta x_1 \sim \begin{bmatrix} \mathcal{N}(0, \sigma_1^2) \\ \mathcal{N}(0, \sigma_1^2) \end{bmatrix}$ and $\delta x_2 \sim \begin{bmatrix} \mathcal{N}(0, \sigma_2^2) \\ \mathcal{N}(0, \sigma_2^2) \end{bmatrix}$ and these random variables errors are assumed independent.

Since both errors are independent, $\|\hat{x}_1 - \hat{x}_2\|$ is Rayleigh distributed with a scale parameter $\sqrt{\sigma_1^2 + \sigma_2^2}$.

$$\|\hat{x}_1 - \hat{x}_2\| \sim \mathcal{R}\left(\sqrt{\sigma_1^2 + \sigma_2^2}\right)\tag{Eq. 4-4}$$

4.1.1.2.1 First configuration

The probability of occurrence of the first configuration is given by:

$$P(\|\hat{x}_1 - \hat{x}_2\| \leq |HPL_1 - HPL_2|) = cdf_{\mathcal{R}(\sqrt{\sigma_1^2 + \sigma_2^2})}(HPL_1 - HPL_2)\tag{Eq. 4-5}$$

The distribution of the norm of the horizontal position error is given by:

$$\begin{aligned}P(\|\hat{x}_{12} - x\| \leq u \mid \|\hat{x}_1 - \hat{x}_2\| \leq |HPL_1 - HPL_2|) \\ = \begin{cases} cdf_{\mathcal{R}(\sigma_1^2)}(U) & \text{if } HPL_1 \geq HPL_2 \\ cdf_{\mathcal{R}(\sigma_2^2)}(U) & \text{if } HPL_1 < HPL_2 \end{cases}\end{aligned}\tag{Eq. 4-6}$$

In the first configuration, the cumulative distribution function of the confidence radius HPL_{12} is given by:

$$P(HPL_{12} \leq u | \|\hat{x}_1 - \hat{x}_2\| \leq |HPL_1 - HPL_2|) = \begin{cases} 0 & \text{if } u < \max(HPL_1, HPL_2) \\ 1 & \text{if } u \geq \max(HPL_1, HPL_2) \end{cases} \quad \text{Eq. 4-7}$$

4.1.1.2.2 Second configuration

The probability of occurrence of the second configuration can be easily obtained and is equal to:

$$P(\|\hat{x}_1 - \hat{x}_2\| > |HPL_1 - HPL_2|) = 1 - cdf_{\mathcal{R}(\sqrt{\sigma_1^2 + \sigma_2^2})}(HPL_1 - HPL_2) \quad \text{Eq. 4-8}$$

Let us investigate the distribution of the norm of the horizontal position error. The combined position error is:

$$\hat{x}_{12} - x = \frac{1}{2} \left[\delta x_1 + \delta x_2 + \frac{\delta x_2 - \delta x_1}{\|\delta x_2 - \delta x_1\|} (HPL_2 - HPL_1) \right] \quad \text{Eq. 4-9}$$

The error distribution is unknown as it is the sum of correlated terms. The expectation of the position error is given by:

$$E[\hat{x}_{12} - x] = (HPL_2 - HPL_1) E \left[\frac{\delta x_2 - \delta x_1}{\|\delta x_2 - \delta x_1\|} \right] \quad \text{Eq. 4-10}$$

The expectation of $\frac{\delta x_2 - \delta x_1}{\|\delta x_2 - \delta x_1\|}$ must be determined. As it is a normalized vector, its coordinates can be written:

$$\frac{\delta x_2 - \delta x_1}{\|\delta x_2 - \delta x_1\|} = \begin{bmatrix} \cos(\theta) \\ \sin(\theta) \end{bmatrix} \quad \text{Eq. 4-11}$$

It is thus necessary to find the distribution of θ to deduce the distribution of the bi-variate vector, and then its expectation. We can form $\tan(\theta)$ in order to get rid of the norm. $\tan(\theta)$ is the ratio of the two components of $\delta x_2 - \delta x_1$, which are independent and with the same variance by definition. The ratio of two independent standard Gaussian distribution follows the standard Cauchy distribution (Unit-variance), therefore $\tan(\theta) \sim Ca(0,1)$. It is well known [Cuadras, 2002] that if a variable follows a uniform random distribution on the interval $\left[-\frac{\pi}{2}, \frac{\pi}{2}\right]$, the tangent of this variable follows a standard Cauchy distribution. However, the reciprocal may not be true. In the case of study, simulations have shown that θ is uniformly distributed over $[0, 2\pi]$. The expectation of cosine and sine of a uniformly distributed random variable over $[0, 2\pi]$ is null. Thus:

$$E[\hat{x}_{12} - x_{true}] = \begin{bmatrix} 0 \\ 0 \end{bmatrix} \quad \text{Eq. 4-12}$$

Therefore the combination of both solution does not introduce any bias on the estimated position. However, no analytical expression of the position error distribution has been established.

As for the distribution of the confidence radius, in the second configuration, it is given by (proof in appendix B):

If $u \geq \max(HPL_1, HPL_2)$,

$$P(HPL_{12} \leq u \mid \|\hat{x}_1 - \hat{x}_2\| > |HPL_1 - HPL_2|) = \frac{cdf_{\mathcal{R}(\sqrt{\sigma_1^2 + \sigma_2^2})}(2u - HPL_1 - HPL_2) - cdf_{\mathcal{R}(\sqrt{\sigma_1^2 + \sigma_2^2})}(HPL_1 - HPL_2)}{1 - cdf_{\mathcal{R}(\sqrt{\sigma_1^2 + \sigma_2^2})}(HPL_1 - HPL_2)} \quad \text{Eq. 4-13}$$

Else,

$$P(HPL_{12} \leq u \mid \|\hat{x}_1 - \hat{x}_2\| > |HPL_1 - HPL_2|) = 0 \quad \text{Eq. 4-14}$$

4.1.1.2.3 Overall performances

The distribution of the horizontal error $\|\hat{x}_{12} - x_{true}\|$ cannot be described a simple mathematical expression. In the particular case where $\sigma_1 = \sigma_2$, and assuming that the same probability is allocated to both GNSS subsystems and thus, $HPL_1 = HPL_2 = K\sigma_1$ (where K is the inverse cumulative distribution function of Rayleigh distribution with a scale parameter of one evaluated in P_{int}), the combined solution can be characterized as.

$$\hat{x}_{12} - x_{true} = \frac{1}{2}[\delta x_1 + \delta x_2] \sim \begin{bmatrix} \mathcal{N}\left(0, \frac{\sigma_1^2}{2}\right) \\ \mathcal{N}\left(0, \frac{\sigma_1^2}{2}\right) \end{bmatrix} \quad \text{Eq. 4-15}$$

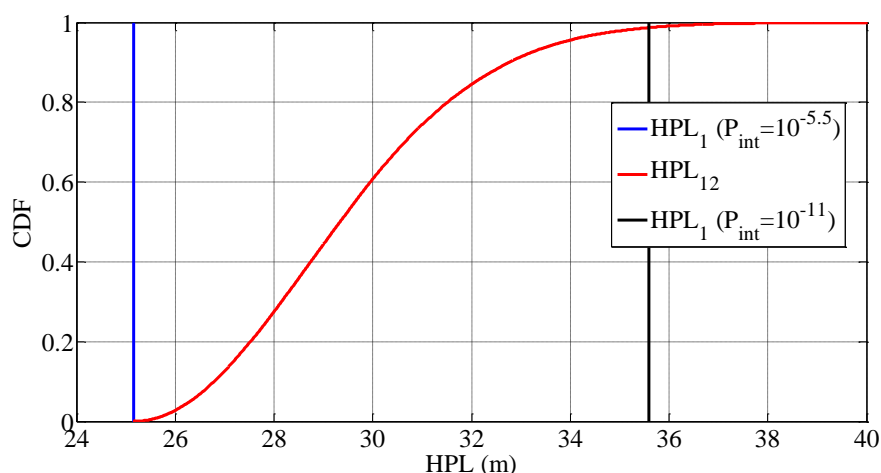
Thus the standard deviation of the combined position error on each component is attenuated by $\sqrt{2}$ compared to the standard deviation of the solution of each independent subsystem.

The cumulative distribution of HPL_{12} is given by the law of total probability:

$$P(HPL_{12} \leq u) = cdf_{\mathcal{R}(\sqrt{\sigma_1^2 + \sigma_2^2})}(2u - HPL_1 - HPL_2)H[u - \max(HPL_1, HPL_2)] \quad \text{Eq. 4-16}$$

where $H[\]$ represents the Heaviside function. This expression has been verified by simulations. By construction its minimum is the maximum of both HPL_1 and HPL_2 .

The distributions of both HPL_{12} and $HPL_1 = HPL_2$ are represented in Figure 13, in the case where $\sigma_1 = \sigma_2 = 5 \text{ m}$. HPL_{12} is associated with a probability of (e.g.) 10^{-11} whereas HPL_1 is associated with either $10^{-5.5}$ or 10^{-11} for comparison. It can be seen that the use of a scheme based on redundant constellations may improve the availability by reducing the HPL size compared to a scheme based on a single constellation with the same associated integrity risk.

Figure 13 Distribution of HPL_{12} with respect to HPL_1

4.1.1.3 Choices for the GNSS receivers

The technical choices proposed for the GNSS receivers are discussed in this section.

4.1.1.3.1 Types of receivers for train control

To ensure the independence of the two sub-system solutions, it is necessary to use two different GNSS receivers. Using one receiver would add a common-mode: a hardware failure may lead to a failure in both subsystems. The proposed configurations for the GNSS receivers in train control are the following:

- Two single frequency single constellation receivers (to ensure integrity even in case of constellation failures):
 - receiver 1 that processes GPS L1 C/A
 - receiver 2 that processes Galileo E1 OS

This solution is not expected to guarantee a sufficiently high level of integrity due to the sensitivity of both sub system to faults due to abnormal ionosphere conditions. However, this solution will be used to validate the concept and to anticipate the performances of the proposed solutions on real data.

- Two dual frequency single constellation receivers (to ensure integrity in case of constellation failures and abnormal ionosphere):
 - receiver 1 that processes GPS L1 C/A and L5 frequencies
 - receiver 2 that processes Galileo E1 OS and E5a frequencies

Even if not investigated in the thesis, the use of quad-constellation receivers would improve the performances of the solution by improving the geometry of the constellation of both sub systems.

4.1.1.3.2 Signal tracked

The characteristics of the GNSS signals that are tracked by the receivers proposed are described in this section.

The GPS L1 C/A signal has the following characteristics [IS-GPS-200-D]:

- Its carrier is located at 1575.42 MHz.
- The carrier is modulated by a pseudorandom code (PRN) and a navigation message by Binary Phase Shift Keying (BPSK) with a Non-return to zero (NRZ) waveform.
- The spreading code is 1023 chips long and is transmitted at a rate of 1.023 Mchips/s.
- The navigation message has a bit rate of 50 bit/s.

The Galileo E1 OS has the following characteristics [OS SiS ICD]:

- Its carrier is located at 1575.42 MHz.
- The signal is the sum of a data channel which waveform is CBOC(6,1,1/11,+) and a pilot channel modulated with CBOC(6,1,1/11,-).
- The spreading code is 4092 chips long and is transmitted at a rate of 1.023 Mchips/s.

The GPS L5 signal is broadcast by the Block IIF (6 operational satellites in mid-2014). It has the following characteristics [IS-GPS-705C]:

- Its carrier is located at 1176.45 MHz.
- The carrier is modulated by a pseudorandom code (PRN) and a navigation message by Binary Phase Shift Keying (BPSK) with a Non-return to zero (NRZ) waveform.
- The spreading code is transmitted at a rate of 10.23 Mchips/s.
- A pilot and data components are transmitted in quadrature

The Galileo E5a has the following characteristics [OS SiS ICD]:

- Its carrier is located at 1176.45 MHz.
- The carrier is modulated by a pseudorandom code (PRN) and a navigation message by Binary Phase Shift Keying (BPSK) with a Non-return to zero (NRZ) waveform.
- The chipping rate is 10.23Mchips/s.
- A pilot and data components are transmitted in quadrature

The spectra of the GNSS signals of interest are plotted in Figure 14.

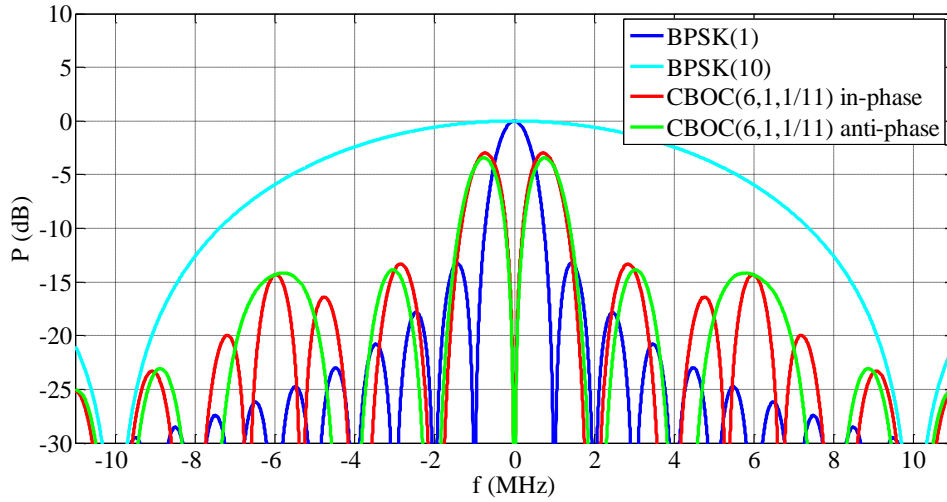


Figure 14 Spectra of GNSS signals

4.1.1.3.3 Technical characteristics of the receivers

The first two parameters that have to be selected and that will have an impact on the receiver's performances are the chip spacing between the Early and Late correlators of the DLL denoted (δ , defined in section 2.1.3.2.1), and the front-end one sided bandwidth denoted BW . The rule-of-thumb for the selection of the chip spacing is to fix $\delta = 1/BW$. Reducing δ improves the robustness of the DLL with respect to multipath and thermal noise (as detailed in chapter 5). When a data and a pilot component are available, it will be assumed that the tracking is conducted on the pilot. Finally, it is proposed to use high end wideband GNSS receivers for train control:

- To track L1 C/A or E1 OS, a wideband receiver with a double-sided ($2BW$) front end bandwidth of 16 MHz is chosen. The chosen bandwidth is large enough to take into account the contribution of the BOC(6,1) in the power spectral density of the CBOC(6,1,1/11,-). A narrow chip spacing value of 0.125 chip is used.
- To track L5 or E5a, a wideband receiver with a double-sided bandwidth of 20 MHz is proposed. It is large enough to process the main lobe of the BPSK(10) modulation. The chip spacing has been set to $\delta = 0.1$ chip.

The parameters described hereafter are the same for the different models of receiver. The loop bandwidth of the DLL was set to 1 Hz which is a typical value for this loop in a GNSS receiver. The Early Minus Late Power discriminator which expression is given in Eq. 2-14 is preferred as it is not coherent. Moreover, in order to avoid the estimation of the delay to be biased due to a Doppler shift, a second order DLL is proposed to be used.

Note: The possibility to use receivers that integrates multipath mitigation algorithms have been investigated during the thesis. Different algorithms have been tested in [Brocard et al., 2014]:

- Double-Delta ($\Delta\Delta$) algorithms [McGraw and Braasch, 1999] that use more correlators than a conventional DLL (typically 5 instead of 3), also referred to as strobe correlator (patented by Ashtech) or High Resolution Correlator (Patented by Rockwell Collins).
- Septentrio's A Posteriori Multipath Estimation (APME) [Sleewaegen and Boon, 2001] which relies on a multipath error estimation module.

These techniques have shown to improve the multipath interference level in [Brocard et al., 2014]. However, the performance improvement has not appeared to be sufficient compared to the increase in term of receiver complexity and thermal noise level. Therefore, it is chosen in the rest of the thesis not to integrate these kind of algorithm in the receiver.

An FLL is preferred over a PLL for an improved robustness of the carrier tracking at the cost of a reduced precision. The bandwidth of the second order FLL is set to 5 Hz, a typical value for such a loop in actual GNSS receivers and a non-coherent arctangent discriminator is used to estimate the frequency error based on the correlator outputs. This discriminator is defined as [Curran et al., 2012]:

$$D_{ATAN} = \frac{1}{T_I} UW \left[\arctan\left(\frac{Q_P(i)}{I_P(ki)}\right) - \arctan\left(\frac{Q_P(i-1)}{I_P(i-1)}\right) \right] \quad \text{Eq. 4-17}$$

where the function UW is defined by :

$$UW(x) = \begin{cases} x - \pi & \text{for } x \geq \pi/2 \\ x & \text{for } \pi/2 > x \geq -\pi/2 \\ x + \pi & \text{for } -\pi/2 > x \end{cases} \quad \text{Eq. 4-18}$$

4.1.2 Electronic toll collection

In ETC, the integrity risk requirements (10^{-4} , 10^{-5} and $10^{-6}/h$) are within the range of integrity risks that are already dealt with in other applications, such as civil aviation. ETC requirements are sufficiently loose not to need any separation of the positioning system into two subsystems as done for Train control. Therefore, dual constellation receiver can be used in this context.

4.1.2.1 Choices for the GNSS receivers

The technical choices proposed for the GNSS receivers are discussed in this section.

4.1.2.1.1 Types of receivers for ETC

For ETC, it is proposed to use either:

- A dual constellation single frequency GPS L1 C/A Galileo E1 OS receiver.
- A dual constellation dual frequency GPS L1 C/A, L5 and Galileo E1 OS, E5a. Indeed, GPS and Galileo signals are located in the same frequency bands L1/E1 and L5/E5a. They can thus be processed by multi-constellation devices at a lower cost.

The signals of reference have been presented in section 4.1.1.3.2. These signals have been selected because of their interoperability in dual constellation GPS/Galileo receivers.

4.1.2.1.2 Technical characteristics of the receivers

In the single frequency configuration, it is proposed to use a low end narrow band GNSS receiver for ETC to limit the cost per OBU parameter which is critical for this application.

The parameters of the DLL associated with the proposed applications are given by:

- To track L1 C/A and E1 OS, a narrowband receiver with a double-sided ($2BW$) front end bandwidth of 4 MHz is chosen. The chosen bandwidth is large enough to take into account the main lobe of BPSK(1) as well as the two main lobes of the CBOC(6,1,1/11,-). After the filtering by the front end, the CBOC(6,1,1/11,-) signal is equivalent to a BOC(1,1). A wide chip spacing value of 0.5 chip is used.
- To track L5 or E5a, a wideband receiver with a double-sided bandwidth of 20 MHz is proposed. It is large enough to process the main lobe of the BPSK(10) modulation. The chip spacing has been set to $\delta = 0.1$ chip.

The other characteristics of the tracking loops for ETC are those described in section 4.1.1.3.3.

4.1.3 Observations

For both applications, the considered vehicles are likely to operate, at least partially, in degraded conditions, creating degraded constellations due to the masking angles of the obstacles such as buildings, trees and other vehicles. This induces that the use of GNSS-only (in single- or dual-constellation configuration) would not be able to provide the required availability and/or accuracy as it will be apparent later on during measurement campaigns. As a consequence, it is necessary to complement the GNSS sensor with other complementary sensors that are present on the considered platform.

4.2 Sensor augmentation and integration strategies

To improve accuracy, availability and continuity in urban environment, it is proposed to augment the GNSS with additional sensor for both considered applications. ETC and train control are treated separately as the sensors and information that are already available on board are different. For both applications, it is proposed to couple the GNSS with a 6-axis MEMS IMU. Three coupling schemes are possible to hybridized IMU measurements with GNSS, referred to as loose, tight and ultra-tight coupling.

- **Loose coupling**, is the simplest way to hybridized GNSS and inertial sensors. In a loose scheme, the GNSS receiver and the INS are computing their own position solution independently. A final position is obtained by blending the information from both devices thanks to a fusion algorithm (Kalman Filtering for instance). In loose coupling, it is necessary to have 4 satellites-in-view to benefit from the GNSS solution and thus, to limit the drift of the IMU. For a single-constellation GNSS, in urban environment, loose coupling approach is not relevant due to the duration and the frequency of occurrence of GNSS outages. Therefore it

cannot be used for train control. The use of a dual constellation receiver makes it possible to use loose coupling because the availability of GNSS is improved.

- In **tight coupling**, GNSS pseudoranges and pseudorange rates measurements are blended with the position estimated from the inertial sensors (mechanization output). Unlike loose coupling, tight fusion scheme takes advantage of GNSS measurements when less than 4 satellites are used, which often occurs for single constellation receivers in urban environments and shadowed areas. Moreover, tightly integrated systems tend to have a more accurate navigation solution because the observables used in the blending process are not as correlated as the position and velocity solutions used in loose integration [Farrell and Barth, 1999]. The implementation of a tightly-coupled architecture requires an access to the pseudoranges and pseudorange rates of the GNSS receiver which is more and more the case. This scheme is all the more interesting for train control as this application is based on two single-constellation receivers, and therefore subject to frequent GNSS outages. Finally, tight integration enables to monitor the quality of pseudorange and Doppler measurements through the KF innovation states.
- The most complex integration scheme is referred to as **ultra-tight coupling** or deep integration in the literature. Ultra-tight GNSS/IMU integration is the process of including an IMU (and corresponding INS solution) to improve signal tracking [Petovello et al., 2007]. The receiver architecture is fundamentally different from loose or tight coupling. Indeed, compared to a classic GNSS receiver architecture, code and carrier tracking loops are replaced by a vector loop. The ultra-tight coupling scheme is said to offer the most benefits in terms of accuracy and robustness among the three integration schemes [Alban and Gebre-Egziabher, 2003]. In the present cases of study, it is preferred to not use ultra-tight coupling to keep the independence between the signal processing stage and the navigation filter. By doing so the propagation of a GNSS or INS positioning failure in the tracking loops is avoided. Moreover for implementing it, it would be necessary to modify the tracking loops, which is not possible in mass market GNSS receivers.

From the above description, the tight coupling scheme is preferred over the two other existing schemes. It is then necessary to choose between an open-loop and a closed-loop architecture.

- In the open-loop configuration, also referred to as feed-forward, the position, velocity and attitude errors estimated by the filter are used to correct the inertial solution. The errors are not corrected into the INS mechanization, which is running independently from GNSS. Moreover, in an open-loop mode, the inertial sensor outputs are not corrected before mechanization. An open-loop architecture is generally suitable for high grade IMUs as the drift of the raw inertial navigation solution is small, thus leading to low linearization errors (around the mechanization output). The main benefit of an open-loop architecture is that it ensures independence between GNSS and INS subsystems, and therefore avoids GNSS failures propagating in the INS.
- In the closed-loop scheme, inertial error estimates are fed back to the INS in order to limit the drift of the inertial solution. In a closed-loop implementation, the sensor measurement biases and scale factor errors are usually corrected before their integration in the mechanization. For

low-grade inertial sensors, only the closed-loop configuration is suitable [Groves, 2013]. Indeed for low-grade inertial sensors, the raw INS position solution is drifting very fast, which leads to large linearization errors (around the drifting position). For both considered cases of study, low- to medium-costs sensors will be used. Thus, a closed-loop architecture is chosen in this work. The main disadvantage of the closed-loop integration is that a failure will propagate into the inertial navigation solution. It is possible to run a back-up mechanization that is independent from GNSS to replace the failed inertial solution after fault detection.

The proposed fusion algorithm is thus an EKF which is adapted to the closed-loop configuration (linearization around the prediction, which is the mechanization output in this case).

4.2.1 Train control

As already discussed, the proposed architecture for positioning in train control is based on redundant independent subsystems to fulfill the very stringent integrity risks. Each sub-system will be augmented by inertial sensors. However, to avoid the introduction of common-mode failures, it is necessary that the inertial sensors used to augment the two subsystems must be different and made by different manufacturers. In this type of application, it is anticipated that mid-cost IMUs can be used (~2000 Euros).

However, a train platform also possesses other useful sources of position. It is then possible to take advantage of the knowledge of the railtrack on which the train is located. It is thus proposed to augment the GNSS/IMU hybridized system with a track database in order to improve the position, velocity and attitude estimation. As in the case of the inertial sensors, to avoid the introduction of common-mode failures it is necessary to use different track databases in each sub-system.

Finally, a train also has wheel speed sensors that are available on board. However, it is proposed not to integrate them in the solution to keep the independence between the virtual balise function and the odometry function. The position between radiobeacons will still have to be propagated with odometry. Although non optimal, this approach seems to be the most realistic way to introduce GNSS technology into ETCS without modifying the whole system architecture according to the rail community.

The architecture of the solution proposed for train position determination in train control is given in Figure 15.

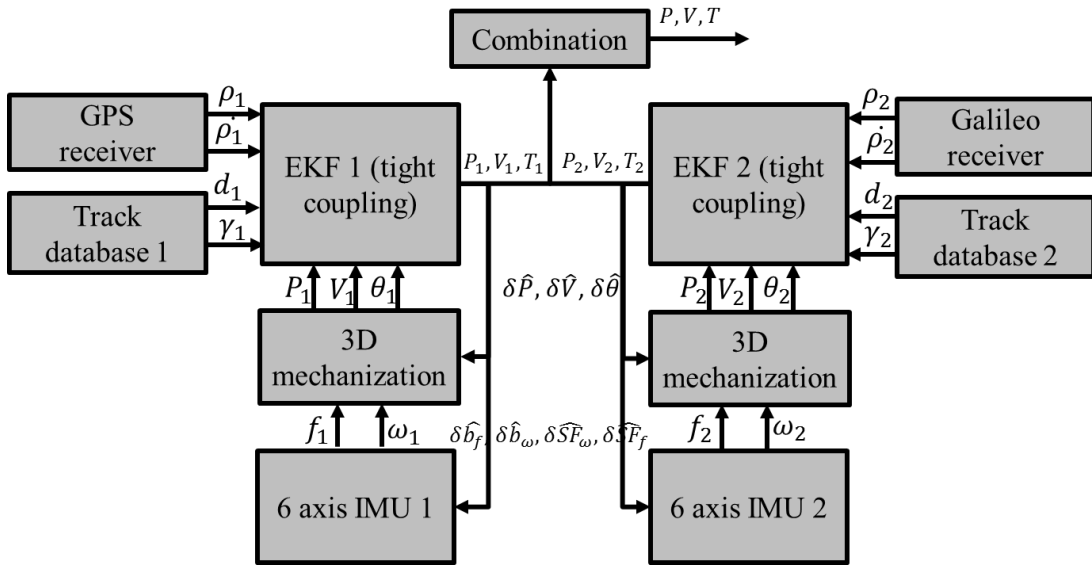


Figure 15 Basic architecture of the solution proposed for train position determination in train control

4.2.2 Electronic Toll Collection

In ETC, the cost per OBU is of particular interest for the charging organism. Therefore low-cost IMU shall be used for such application. Moreover, as most cars are equipped with wheel speed sensors, it is proposed to use the measurements from these sensors in the fusion algorithm. The architecture of the solution for ETC is given in Figure 16.

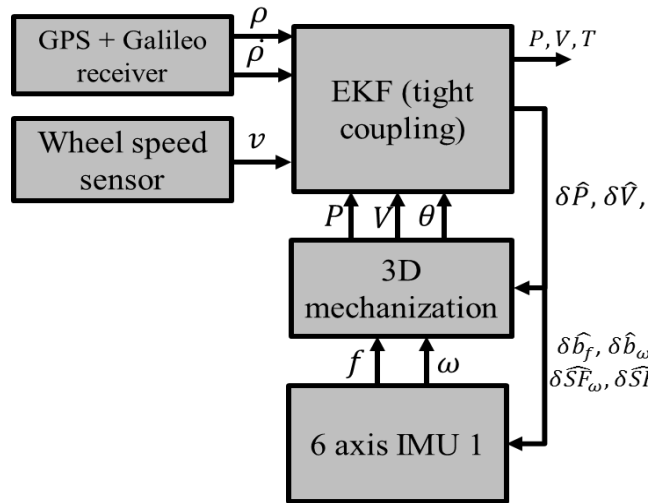


Figure 16 Basic architecture of the solution proposed for ETC

4.3 Conclusions

For train control, the solution proposed is based on two redundant EKF that each integrates measurements from different GNSS, track databases and IMUs in a tightly coupled architecture. As medium cost IMU are used, the inertial sensors are calibrated in real time prior to the inertial

mechanization. It is assumed that actual beacons are kept at crossing in order to determine on which track the train is located.

The solution developed for ETC is an EKF that integrates measurements from a dual constellation receiver, an IMU and wheel speed sensors which are already available on board. As for train control, a tightly coupled architecture operating in a closed loop scheme is preferred.

4.4 References

- [Alban and Gebre-Egziabher, 2003] Alban, S. and D. Gebre-Egziabher, "Performance Analysis and Architectures for INS-Aided GPS Tracking Loops", Proceedings of the ION NTM-03, Anaheim, CA, January 2003
- [Brocard et al., 2014] Brocard, P.; Salos, D.; Julien, O.; Mabillean, M., "Performance evaluation of multipath mitigation techniques for critical urban applications based on a land mobile satellite channel model," Position, Location and Navigation Symposium - PLANS 2014, 2014 IEEE/ION, vol., no., pp.612,625, 5-8 May 2014
- [Cuadras, 2002] C. M. Cuadras, "Geometrical Understanding of the Cauchy Distribution," Elsevier, Ltd, Vol. 26, 1-2, pp 283-287, 2002
- [Curan et al., 2012] Curran, J.T.; Lachapelle, G.; Murphy, C.C., "Improving the Design of Frequency Lock Loops for GNSS Receivers," Aerospace and Electronic Systems, IEEE Transactions on, vol.48, no.1, pp.850,868, Jan. 2012
- [Farrell and Barth, 1999] Farrell, Jay and Matthew Barth, The Global Positioning System and Inertial Navigation, McGrawHill, New York, NY, 1999
- [Groves, 2008] Groves, P. D., Principles of GNSS, Inertial and Multisensor Integrated Navigation Systems, Artech House, January 2008.
- [IS-GPS-200-D] IS-GPS-200-D: Navstar GPS Space Segment/Navigation User Interfaces, United States Department of Defense, Sep-2012
- [IS-GPS-705C] Interface Specification IS-GPS-705C. Navstar GPS Space Segment/User Segment L5 Interfaces. Sep 2012
- [McGraw and Braasch, 1999] McGraw, Gary A., Braasch, Michael S., "GNSS Multipath Mitigation Using Gated and High Resolution Correlator Concepts," Proceedings of the 1999 National Technical Meeting of The Institute of Navigation, San Diego, CA, January 1999, pp. 333-342
- [OS SiS ICD] European Commission, "European GNSS (Galileo) Open Service - Signal-in-Space, Interface Control Document Issue 1." Feb-2010.
- [Petovello et al., 2007] Petovello, M.G., Sun, D., Lachapelle, G., Cannon, M.E., "Performance Analysis of an Ultra-Tightly Integrated GPS and Reduced IMU System," Proceedings of the 20th International Technical Meeting of the Satellite Division of The Institute of Navigation (ION GNSS 2007), Fort Worth, TX,

- September 2007, pp. 602-609
- [Rispoli et al., 2013] Rispoli, F.; Filip, A.; Castorina, M.; Di Mambro, G.; Neri, A.; Senesi, F., "Recent progress in application of GNSS and advanced communications for railway signaling," *Radioelektronika (RADIOELEKTRONIKA)*, 2013 23rd International Conference , vol., no., pp.13,22, 16-17 April 2013
- [Rousseau and Cadet, 2006] Rousseau, M., Cadet, D., The LOCOPROL project, 7th World Congress on Railway Research (WCRR), June 4-8, 2006, Montreal, Canada
- [Sleewaegen and Boon, 2001] Sleewaegen, Jean Marie, Boon, Frank, "Mitigating Short-Delay Multipath: a Promising New Technique," *Proceedings of the 14th International Technical Meeting of the Satellite Division of The Institute of Navigation (ION GPS 2001)*, Salt Lake City, UT, September 2001, pp. 204-213
- [Sun, 2010] Sun, D. Ultra-Tight GPS/Reduced IMU for Land Vehicle Navigation. PhD Thesis, University of Calgary: Department of Geomatics Engineering, Canada, 2010.
- [Walter et al., 2013] Walter, Todd, Blanch, Juan, Choi, Myung Jun, Reid, Tyler, Enge, Per, "Incorporating GLONASS into Aviation RAIM Receivers," *Proceedings of the 2013 International Technical Meeting of The Institute of Navigation*, San Diego, California, January 2013, pp. 239-249
- [WG-C,ARAIM] EU-U.S. Cooperation on Satellite Navigation, Working Group C - ARAIM Technical Subgroup, Milestone 3 Report, February 25th, 2016
- [Zheng et al., 2009] Zheng, Y., Cross, P., Quddus, M., "The Effects of Railway Track Database Quality on the Performance of Tightly Coupled GNSS/Track Database Train Positioning System," *Proceedings of the 22nd International Technical Meeting of The Satellite Division of the Institute of Navigation (ION GNSS 2009)*, Savannah, GA, September 2009, pp. 2146-215

5 MEASUREMENT MODELS

The monitoring of a system as well as the verification of the compliance of a system with respect to specific requirements is always based on the accurate knowledge of the measurements that are used. Note that the level of accuracy of these models has to be adapted to the level of the requirements, which is related to the integrity risk in the case of this Thesis.

This chapter presents the measurement model that has been used to validate and assess the performances of the solutions proposed by simulations. It include GNSS and sensors error model.

The error sources are categorized between nominal errors and faults. Nominal errors are always affecting the sensor measurements. They are investigated in subsection 5.1. Faults are the errors that are not considered in the nominal case. They are punctual and characterized by their distribution and probability of occurrence. The faults are discussed in subsection 5.2. The Non-Line-Of-Sight error which affects the GNSS requirements in urban environment is of particular interest in this Thesis, and a specific subsection is dedicated to it (5.3.2).

5.1 Nominal measurement model

5.1.1 GNSS

In this thesis, a tight coupling fusion scheme is used. As explained in 4.2, in tight coupling, the GNSS pseudoranges are used as measurements. Moreover, pseudorange rates are also generally used. As a consequence, models for both of these GNSS measurements will be provided.

Note that the solutions that have been proposed in chapter 4 are based on GPS (L1 C/A and L5) and Galileo (E1 OS and E5a). To assess the performances and validate the proposed architectures on real signals for dual constellation receivers, it has been necessary to replace Galileo with GLONASS

because the number of Galileo satellite deployed is not sufficient at the time. Therefore, in this chapter, the measurement models are given for GPS, Galileo and GLONASS.

5.1.1.1 Pseudoranges error model

The GNSS code pseudorange measurement associated to the i^{th} satellite can be modelled as :

$$\rho_i = \sqrt{(x - x_i)^2 + (y - y_i)^2 + (z - z_i)^2} + c\Delta t + \varepsilon \quad \text{Eq. 5-1}$$

where:

- x, y and z design the user position
- Δt is the offset between the receiver clock and GNSS system time
- x_i, y_i and z_i design the i^{th} satellite position
- ε is the pseudorange error

In the nominal case, it is assumed that the satellite is in direct view (LOS configuration). The main sources of error that affect the GNSS measurements in this case are errors related to the estimation of the location of the transmitting satellite, to the satellite clock prediction uncertainty, the propagation in the atmosphere (ionospheric delay, troposphere delay), hardware biases, and erroneous receiver synchronization due to the presence of multipath, interference and thermal noise. These error sources are assumed to be independent.

In order to be conservative, each error is modelled as a zero-mean Gaussian distribution that overbounds the real error distribution:

The ephemeris and satellite clock errors ($\varepsilon_{Sat/Eph}$) are modelled by:

$$\varepsilon_{Sat/Eph} \sim \mathcal{N}(0, \sigma_{clk\&eph}^2) \quad \text{Eq. 5-2}$$

The error due to ionosphere (ε_{iono}) is modelled by:

$$\varepsilon_{iono} \sim \mathcal{N}(0, \sigma_{iono}^2) \quad \text{Eq. 5-3}$$

The troposphere error (ε_{tropo}) is modelled by:

$$\varepsilon_{tropo} \sim \mathcal{N}(0, \sigma_{tropo}^2) \quad \text{Eq. 5-4}$$

The error due to thermal noise (ε_{noise}) is modelled by:

$$\varepsilon_{noise} \sim \mathcal{N}(0, \sigma_{noise}^2) \quad \text{Eq. 5-5}$$

The multipath error (ε_{mp}) is modelled by:

$$\varepsilon_{mp} \sim \mathcal{N}(0, \sigma_{mp}^2) \quad \text{Eq. 5-6}$$

The total nominal error is the sum of each independent error.

$$\varepsilon = \varepsilon_{Sat/Eph} + \varepsilon_{iono} + \varepsilon_{tropo} + \varepsilon_{noise} + \varepsilon_{mp} \quad \text{Eq. 5-7}$$

The distribution of the sum of independent Gaussian distribution is normally distributed:

$$\varepsilon \sim \mathcal{N}(0, \sigma_{PSR}^2) \quad \text{Eq. 5-8}$$

with:

$$\sigma_{PSR}^2 = \sigma_{clk\&eph}^2 + \sigma_{iono}^2 + \sigma_{tropo}^2 + \sigma_{noise}^2 + \sigma_{mp}^2 \quad \text{Eq. 5-9}$$

Apart from multipath, the error models standardized for civil aviation can be used in our case of study. These models have been validated for civil aviation which is associated to an integrity risk of 10^{-7} . According to chapter 2, the integrity risk corresponding to system or sub-systems proposed in this Thesis for train control and ETC are higher than that value (after equal allocation to both subsystems for train control). Thus the civil aviation models can be used.

5.1.1.1.1 Satellite Clock and Ephemeris error

The satellite clock and ephemeris error is different for each GNSS and depends on the system infrastructure and maturity.

GPS:

The User Range Accuracy (URA) that represents the standard deviation of the range component of GPS satellite clock correction and ephemeris error is broadcast in the GPS navigation message. A nominal URA value of 3.9 meters can be found in [Have, 2003] for the GPS constellation (in 2003). Since then, it is stated in [Walter et al., 2013] that the most common GPS URA is 2.4 m in the sense of lowest possible value. However, this value is expected to decrease with the current modernization program of GPS. As a consequence, a value of 0.85 m is taken as a reference in [Salos et al., 2010], since this value is equal to the value used by Galileo.

These results are summarized by:

$$\sigma_{clk\&eph} = \begin{cases} 2.4 \text{ m} & \text{in current GPS} \\ 0.85 \text{ m} & \text{in advanced modernization stage} \end{cases} \quad \text{Eq. 5-10}$$

Galileo:

In Galileo, the Signal In Space Accuracy (SISA) is the standard deviation of a centered Gaussian distribution that overbounds the signal in space errors. The SISA bounds ephemeris and satellite clock errors. Values are specified for the SISA in nominal mode in [ESA, 2005]:

$$\sigma_{clk\&eph} = 0.85 \text{ m} \quad \text{Eq. 5-11}$$

GLONASS:

According to [Walter et al., 2013], the most common GLONASS URA is 4 m.

$$\sigma_{clk\&eph} = 4 \text{ m} \quad \text{Eq. 5-12}$$

5.1.1.1.2 Ionosphere residual error

The ionosphere is an atmosphere layer that contains partially ionised medium. The GNSS signals refraction on the ionosphere varies with its frequency, as a squared inverse relation. The ionosphere results in a code delay Δ (in m) and a phase advance of the same magnitude and opposite sign. The expression of the carrier phase delay neglecting higher order is given by:

$$\Delta = \frac{40.28}{f^2} 10^{16} STEC \quad \text{Eq. 5-13}$$

where:

- f is the frequency of the carrier in Hz
- $STEC$ (Slant Total Electron Content) represents the electron density integrated along the ionospheric path of the signal in TECU ($10^{16} \text{ e}^-/\text{m}^2$).

The ionospheric delay can be corrected by different techniques:

- Using the information provided by the GNSS itself: Klobuchar model used in GPS, NeQuick model used in Galileo,
- Using the information provided by another system complementary to GNSS, such as SBAS corrections,
- Using a GNSS dual frequency receiver which is able by itself to remove the first order ionospheric error.

5.1.1.1.2.1 Single frequency

Single frequency GPS correction:

The broadcasted GPS data contains the parameter to calculate ionospheric corrections based on Klobuchar model. The correction by Klobuchar removes about 50% of the ionospheric delay on average. The residual model for the ionosphere corrections when applying Klobuchar corrections is detailed in [Salos, 2012]. The residual standard deviation that bounds the ionosphere error is the following:

$$\sigma_{iono} = \begin{cases} Fmax(0.2\Delta_{KL,V}, 9) & 0^\circ \leq |\phi_m| < 20^\circ \\ Fmax(0.2\Delta_{KL,V}, 4.5) & 20^\circ \leq |\phi_m| \leq 55^\circ \\ Fmax(0.2\Delta_{KL,V}, 6) & 55^\circ < |\phi_m| \end{cases} \quad \text{Eq. 5-14}$$

where

- F represents the mapping function used in the Klobuchar corrections
- $\Delta_{KL,V}$ is the verical ionospheric delay estimated with the Klobuchar model
- ϕ_m is the geomagnetic latitude

The geomagnetic latitude (ϕ_m) can be obtained from the geographic latitude (ϕ) and the longitude (λ) with [Klobuchar, 1987]:

$$\sin(\phi_m) = \sin(\phi) \sin(78.3^\circ) + \cos(\phi) \cos(78.3^\circ) \quad \text{Eq. 5-15}$$

The mapping function used in the Klobuchar corrections is given by:

$$F = 1 + 16 \left(0.53 - \frac{\alpha}{180} \right)^3 \quad \text{Eq. 5-16}$$

where α represents the elevation of the satellite (in degrees)

The vertical ionospheric delay estimated ($\Delta_{KL,V}$) with the Klobuchar model is related to the ionospheric delay calculated with the Klobuchar model (T_{KL}) with:

$$\Delta_{KL,V} = cT_{KL,v} = \frac{cT_{KL}}{F} \quad \text{Eq. 5-17}$$

It is shown in [Salos, 2012], that between 1994 and 2010, the $0.2\Delta_{KL,V}$ term has never exceeded the constant terms in the expression of the maximum. Thus the model can be simplified into:

$$\sigma_{iono} = \begin{cases} 9F & 0 \leq |\phi_m| < 20^\circ \\ 4.5F & 20^\circ \leq |\phi_m| \leq 55^\circ \\ 6F & 55^\circ < |\phi_m| \end{cases} \quad \text{Eq. 5-18}$$

Single-frequency Galileo corrections:

The Galileo OS signals broadcasts the parameters to estimate the ionospheric delay with the more recent NeQuick model. NeQuick is assumed to correct 70% of the ionospheric delay when applied to E1, E5a and E5b frequencies. Civil aviation does not provide any ionospheric residual error model for single Galileo receivers. A model is proposed and justified for the NeQuick residual ionosphere error in [Salos, 2012]. The model is the following:

$$\sigma_{iono} = \begin{cases} \frac{40.3}{f^2} \cdot 0.3 \cdot 10^4 \cdot F \cdot VTEC & \text{if } F \cdot VTEC \geq 66.7 \\ \frac{40.3}{f^2} \cdot 10^4 \cdot 20 & \text{if } F \cdot VTEC < 66.7 \end{cases} \quad \text{Eq. 5-19}$$

where:

- f is the frequency of the carrier (MHz)
- $VTEC$ is the Vertical Total Electron Content

A second model independent of time is proposed in [Salos, 2012]:

$$\sigma_{iono} = F \sigma_{iono,v} \quad \text{Eq. 5-20}$$

where $\sigma_{iono,v}$ is function of the geomagnetic latitude, given in Table 8 Galileo E1.

$ \phi_m $ (°)	0	10	20	30	40	50	60	70	75
$\sigma_{iono,v}$ (m)	7.4	7.6	7.6	7	6.7	4.7	4.2	4	3.8

Table 8 $\sigma_{iono,v}$ for Galileo E1 as in function of the geomagnetic latitude [Salos, 2012]

However, there are currently uncertainties about the ability to bound the residual ionosphere error after application of the NeQuick corrections (especially for the tails).

Single-frequency GLONASS corrections:

GLONASS does not broadcast any ionosphere parameter. The Klobuchar and NeQuick can be used for GLONASS signals, but requires to be corrected by factors due to their frequency shifts. Klobuchar corrections are applied in this study.

$$\sigma_{iono,i} = \left(\frac{f_{L1}}{f_i} \right)^2 \sigma_{iono,L1} \quad \text{Eq. 5-21}$$

where f_i is the frequency of the i^{th} GLONASS satellite.

5.1.1.1.2.2 Dual frequency

The use of signals coming from the same satellite at two different frequencies has the advantage to enable removing the first order ionospheric delay by combining both pseudoranges with the following expression:

$$\rho_{iono-free} = \frac{f_A^2}{f_A^2 - f_B^2} \rho_{f_A} - \frac{f_B^2}{f_A^2 - f_B^2} \rho_{f_B} \quad \text{Eq. 5-22}$$

where ρ_{f_A} and ρ_{f_B} are the pseudorange measured on the two frequencies f_A and f_B .

Since the higher ionospheric delay orders are considered negligible for the targeted applications:

$$\sigma_{iono} \approx 0 \text{ m} \quad \text{Eq. 5-23}$$

The counterpart of such an approach is that the process to remove the ionosphere delay also amplifies the noise and multipath error components that are not correlated on the two frequencies.

5.1.1.1.3 Troposphere residual error

The troposphere induces an extra delay on the GNSS signal. This delay depends on the atmospheric conditions and receiver location. The user segment is responsible of estimating and correcting the tropospheric delay for each satellite in view. The residual error depends on the correction model used by the receiver. Assuming that the model used by the receiver is the one described in [RTCA, 2006], the residual error model is characterized by:

$$\sigma_{tropo} = F_{tropo}\sigma_{tropo,v} \quad \text{Eq. 5-24}$$

where:

- $\sigma_{tropo,v} = 0.12$ meters is the vertical error standard deviation
- F_{tropo} is the mapping function varies with the elevation of the satellite

$$F_{tropo} = \begin{cases} \frac{1.001}{\sqrt{0.002001 + \sin^2(\alpha)}} & \text{if } 4^\circ \leq \alpha \\ \frac{1.001}{\sqrt{0.002001 + \sin^2(\alpha)}} (1 + 0.015(4 - \theta)^2) & \text{if } 2^\circ \leq \alpha \leq 4^\circ \end{cases} \quad \text{Eq. 5-25}$$

This model was adopted for GPS L1 C/A and is assumed for GPS L5, Galileo E1, E5a and GLONASS L1. The tropospheric delay is not frequency dependent and thus cannot be removed by combinations of dual frequency measurements. The same model must be used for dual frequency receiver.

5.1.1.1.4 Thermal noise

The GNSS signal is affected by thermal noise which mostly depends on the front-end architecture and components according to the well-known Friis formula. This thermal noise will affect the ability of the receiver to get synchronized with the incoming signal, and will thus affect the pseudorange measurements. The variance of the synchronization error due to thermal noise depends upon a number of parameters including the modulation of the signal of interest and the key parameters of the receiver tracking loops (discriminator, correlation duration, equivalent loop bandwidth, early-late spacing).

5.1.1.1.4.1 BPSK

For a BPSK modulation, the expression of the code tracking error of a DLL using an EMLP discriminator with a BPSK modulation is given by [Van Dierendonck, 1996], [Van Dierendonck et al., 1992], assuming an infinite front-end bandwidth:

$$\sigma_{\tau}^2 = \frac{B_L \delta}{2 \frac{C}{N_0}} \left(1 + \frac{2}{(2 - \delta) \frac{C}{N_0} T_i} \right) (\text{chip}^2) \quad \text{Eq. 5-26}$$

where:

- T_i is the accumulation time

- $\frac{c}{N_0}$ is the ratio of the carrier power to the noise power spectral density in dB-Hz
- B_L is the one-sided loop bandwidth of the loop filter in Hz
- δ is the DLL chip spacing

Because GPS L1 C/A and GPS L5 and GLONASS L1 use a BPSK modulation, the above formula can be used. Galileo E5a is a side-lobe of an ALTBOC modulation, however it can be shown that it is well modeled as a BPSK modulation. As a consequence, the above expression can be used as well.

Note that all the above signals do not use the same chipping rate, and thus this has to be taken into account when converting the above formula in m^2 .

5.1.1.1.4.2 BOC modulations

The expression of the DLL error for EMLP has been extended to the case of other modulations in [Julien, 2005]:

$$\sigma_{\tau}^2 = \frac{B_L \delta}{2s \frac{C}{N_0}} \left(1 + \frac{2}{(2 - s\delta) \frac{C}{N_0} T_i} \right) (\text{chip}^2) \quad \text{Eq. 5-27}$$

where s is the absolute value of the slope of the PRN code autocorrelation in the main peak, and in particular:

- $s_{BOC(1,1)} = 3$
- $s_{CBOC(6,1,1/11,-)} = \frac{53+2\sqrt{10}}{11}$
- $s_{CBOC(6,1,1/11,+)} = \frac{53-2\sqrt{10}}{11}$

5.1.1.1.4.3 Dual frequency receivers

The dual frequency receiver combines the pseudorange measurements from each frequency to form a composite measurement, with the expression given in Eq. 5-21.

The error sources that affects ρ_{f_A} and ρ_{f_B} and are not correlated between both measurement such as noise and multipath are amplified [Salos, 2012], [Martineau, 2008]:

$$\sigma_{noise,iono-free}^2 = \left(\frac{f_A^2}{f_A^2 - f_B^2} \right)^2 \sigma_{noise,f_A}^2 + \left(\frac{f_B^2}{f_A^2 - f_B^2} \right)^2 \sigma_{noise,f_B}^2 \quad \text{Eq. 5-28}$$

where σ_{noise,f_A}^2 and σ_{noise,f_B}^2 are the variance of the noise on the pseudoranges on the two frequencies f_A and f_B .

5.1.1.1.5 Multipath

The multipath models that are used in civil aviation are not suitable for terrestrial applications that does not operates in open sky conditions. It is necessary to characterize multipath error in urban environment for the cases of study.

This section describes a way to calculate the contribution of the multipath to the nominal error model by a set of simulations based on a realistic urban channel model and a realistic GNSS tracking loop simulator. The first part describes the urban channel model and the tracking simulator. The way to connect and to validate the combination of both is then detailed. Then the parameters that are used for the simulations are detailed, as well as the results obtained.

5.1.1.1.5.1 LMS channel model

The Land Mobile Channel (LMS) model [Lehner and Steingass, 2005] which can be downloaded for free, is a generative wideband urban channel model based on a measurement campaign conducted in Munich (Germany) in 2002. Compared to a narrowband model such as the one developed in [Prieto-Cerdeira et al., 2010], a wideband model takes into account the time delays between the direct signal and the echoes. A wide-band model is preferred in here in order to realistically simulate the impact of echoes on the receivers tracking loops and therefore on the pseudorange measurements. The model simulates the signal received from a fixed satellite whose relative position to the user is characterized by its azimuth and its elevation. The LMS model simulates the channel for a vehicle moving along a street with predefined parameters. The model generates differently the direct satellite to receiver Line-of-Sight (LOS) and the multipath. The properties of the LOS are deterministically generated by simulating realistic physical phenomena. The diffraction of the LOS over the edges of the buildings, the shadowing induced by trees and the diffraction over lamp posts are considered. The echoes are statistically generated based on several distributions deduced from the measurement campaign. The number of reflections, the geometric distribution of the reflectors (from which the phase and delay are deduced), the power distribution of the echoes, their lifespan (space life duration) and the distribution of the time variation of their amplitude (fading) are used to generate the echoes. The model of the received signal sampled (at the channel sampling frequency) is:

$$r(k) = \sum_{n=1}^{N_{mp}} \alpha_n(k) d(kT_{s,c} - \tau_n(k)) c(kT_{s,c} - \tau_n(k)) \cos(\varphi_n(k)) \quad \text{Eq. 5-29}$$

where:

- $T_{s,c}$ is the channel sampling period
- α_n is the amplitude of each LOS and echoes
- τ_n is the delay of each LOS and echoes
- φ_n is the carrier phase of each LOS and echoes
- N_{mp} is number of echoes

A slight modification was added to the original LMS model in order to consider the dynamic of the mobile in the generation of the code delay. In the original model, the delay of the LOS is used as a reference for the multipath and thus remains null even when considering a moving vehicle. To model the impact of the dynamic on the delay, a delay variation corresponding to the true user/satellite dynamic was added to both the LOS and echo to LOS relative delay. This phenomenon is referred to as code Doppler which has the same origin as the carrier Doppler. The additional delay variation for two consecutive samples k and $k + 1$ is expressed by:

$$\tau(k + 1) - \tau(k) = \frac{v_r}{c} T_s \quad \text{Eq. 5-30}$$

where v_r is the derivative of the distance between the receiver and the satellite.

Moreover, the Doppler is not an explicit output of the channel model, even if it is used by the model for the phase generation. As a consequence, the echoes' Doppler has been calculated differentiating their phase measurements on two consecutive epochs.

5.1.1.1.5.2 GNSS tracking simulator

A realistic GNSS receiver simulator, developed by ENAC and referred to as GeneIQ, uses the outputs of the LMS channel model, consisting of the times series containing the amplitude, code delay, carrier phase and Doppler of each LOS and reflections. This simulator is based on the modeling of the receiver correlator outputs which expression is given in Eq. 2-7. This expression is based on the assumption that the amplitude of the signal is constant during the correlation duration and that phase variation is linear during the correlation duration. In order not to invalidate this hypothesis, the correlator outputs can be obtained by summing several partial correlations. The partial correlation duration used in the following is thus in-line with the correlator output hypothesis.

The correlation being a linear operation, the correlator outputs are obtained by summing the individual correlator associated to each component of the received signal. The expression of the In-phase and Quadra-phase partial correlator outputs are:

$$I_P(k) = \sum_{n=1}^{N_{mp}} \frac{\alpha_n(k)}{2} d(kT_{s,c} - \tau_n(k)) K_{cc}(\tau_n(k) - \hat{\tau}(k)) \text{sinc}\left(\pi \left(f_n(k) - \hat{f}(k)\right) T_s\right) \cos(\varphi_n(k) - \hat{\varphi}(k)) \quad \text{Eq. 5-31}$$

$$Q_P(k) = \sum_{n=1}^{N_{mp}} \frac{\alpha_n(k)}{2} d(kT_{s,c} - \tau_n(k)) K_{cc}(\tau_n(k) - \hat{\tau}(k)) \text{sinc}\left(\pi \left(f_n(k) - \hat{f}(k)\right) T_s\right) \sin(\varphi_n(k) - \hat{\varphi}(k)) \quad \text{Eq. 5-32}$$

where i is the integration period index.

Finally, the In-phase and Quadra phase outputs calculated by integration over $T_{s,c}$ are accumulated over T_i (it is assumed that T_i is a multiple of $T_{s,c}$).

The validation of the LMS/Receiver coupling is presented in appendix C.

5.1.1.1.5.3 Parameters used for the simulations

Parameters for the channel generation:

The first step consists in setting the parameters for the generation of the virtual street by the LMS. Even if the channel generated is a reproduction of a railtrack in urban environment, it is assumed that the model also applies to ETC in urban environment. A typical railway in downtown Toulouse +43° 35' 58.04", +1° 27' 29.82", illustrated in Fig. 3, was taken as a reference and reproduced in the simulator. In urban area, the railway is several meters wide because of the proximity with train station. The rows of trees and housefronts are respectively placed at a distance of 12 and 22 meters from the center of the railway.



Figure 17 Street model used for the channel generation

The average height of the buildings was set to 15 m and the height of the antenna was set to 4.3 m which corresponds to the standard loading gauge for trains that carry passengers (GA, GB, GB1 as defined by UIC in [UIC Leaflet 506]). The typical mask angle of the buildings for this scenario is 26° for an azimuth of 90°. According to [Perez-Fontan et al., 2001], to represent the urban environment with a sufficient time resolution, the sampling frequency shall respect the relation:

$$f_s \geq \frac{8v}{\lambda} \quad \text{Eq. 5-33}$$

The velocity tested for the vehicle in urban area has been set to 20km/h, and therefore a 1 kHz sampling frequency that verifies the relation (for L1 and L5 frequencies) was chosen for the simulations. A low velocity is preferred to avoid the reflections to be filtered by the tracking loops due to the difference between their Doppler shift and the Doppler shift of the LOS. The satellite position relative to the user is set in terms of azimuth and elevation, and will vary in order to cover most of the possible scenarios and to characterize the pseudorange error as a function of the satellite elevation.

The satellite is located at eight different elevations (10, 20, 30, 40, 50, 60, 70 and 80°) and three different azimuths (0, 45 and 90°). As the topography of the street is symmetric, it is possible to limit the study at these three azimuths. The channel is generated and processed over 1 km for each satellite position.

GNSS signals processed and receiver models:

The receiver models simulated are those presented in 4.1.1.3 and 4.1.2.1

Selection of the samples:

The aim of this section is to determine the nominal standard deviation in a representative urban scenario due to the multipath. The nominal scenario for the multipath error only occurs when the receiver is actually tracking the signal, and when the pseudorange errors are only due to the multipath interference phenomenon. The samples corresponding to the transient state of the loops, when the local replica is not locked on the LOS dynamic shall be excluded. Moreover the subsequent samples corresponding to a loss of lock shall also be removed not to impact the standard deviation. The receiver can self-monitor the effectiveness of its tracking thanks to detectors discussed in [Van Dierendonck, 1996]. As a FLL is used to track the carrier, a C/N_0 estimator is preferred over a phase lock detector:

$$\widehat{C/N_0} = A - 1 + \sqrt{A(A - 1)} \quad \text{Eq. 5-34}$$

where:

$$A = \frac{[\text{mean}(I_p^2 + Q_p^2)]^2}{\text{var}(I_p^2 + Q_p^2)} \quad \text{Eq. 5-35}$$

In Eq. 5-35, the mean and variance are computed over 1 second. When the estimator is over a set threshold that has to be determined, it is decided that the signal is tracked and the samples shall be taken into account for the nominal standard deviation evaluation. The updating rate of the C/N_0 estimation shall be sufficiently high to quickly detect any loss of lock but shall not be too low for computation issues. 0.1 second appears to be a good trade-off between sensitivity and complexity. If the estimated C/N_0 is over a set threshold, the latest 0.1 seconds of samples will be added to the “nominal case” vector by simple concatenation.

5.1.1.1.5.4 Threshold determination for the C/N_0 estimator

The nominal multipath error model has been calculated using the samples for which the GNSS receiver is tracking the signal. The C/N_0 estimator given in Eq. 5-34 has been used as tracking detector. This estimator can easily be implemented in an actual GNSS receiver. First, it is necessary to set the C/N_0 threshold at which the receiver is considered to be tracking, in presence of multipath

only. Considering four thresholds (20, 25, 30 and 35 dB-Hz), the distribution of the residual error obtained after the sample selection is studied for the specific case of the narrowband BPSK(1) receiver. For a satellite which azimuth is firstly 45° and then 90° , for each elevation, and each threshold, the residual samples have been concatenated. The mean pseudorange error is plotted in Figure 18. For elevations higher than 20° , the mean pseudorange error is sub-decimetric and does not vary with the C/N_0 threshold. For very low elevations (i.e. 20° and 10°), the distribution of the pseudorange error is not centered and its 95th percentile confidence interval is abnormally large as illustrated in Figure 19. The detector with a thresholds set to 30 and 35 dB-Hz effectively detect the loss of lock and exclude all the samples as illustrated in Figure 20. The detector with a threshold set to 20 or 25 dB-Hz detects most of the biased samples, but 3% of the samples still remain not detected and are considered relevant. The magnitude of the bias is sufficiently important (several meters) to lead to a positioning failure and jeopardize the safety of the signaling system. It can be inferred from Figure 20 that setting the threshold to 35 dB-Hz is not advisable because it reduces the availability of the satellite to less than 80 % even when the signal is tracked and that the pseudorange error is centered and has 95th percentile confidence interval lower than 2 m. The C/N_0 mask is set to 30 dB-Hz as it represents the best trade-off between the ability to detect a loss of lock and signal availability.

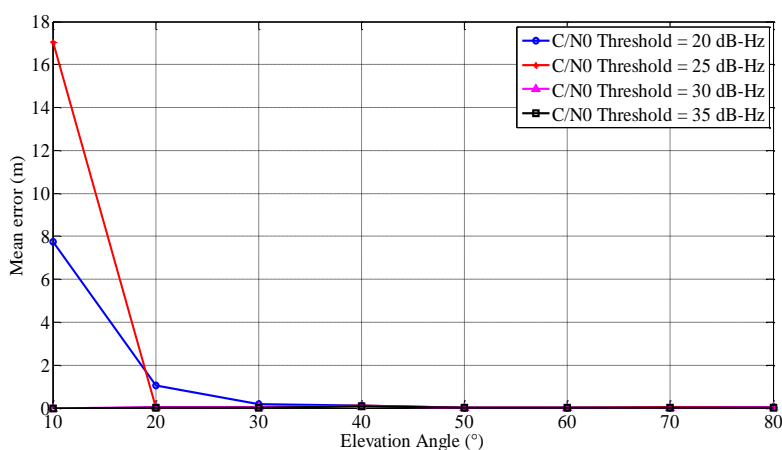


Figure 18 Mean pseudorange error for the narrowband receiver processing BPSK(1)

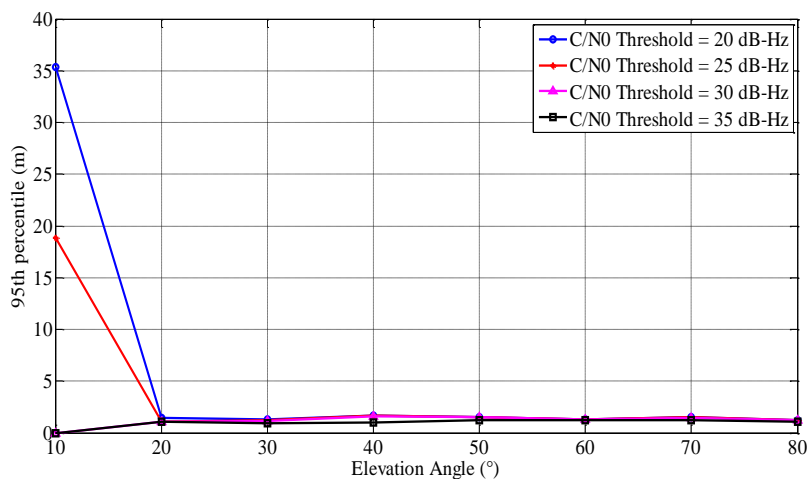


Figure 19 95th percentile of the code pseudorange error for the narrowband receiver processing BPSK(1)

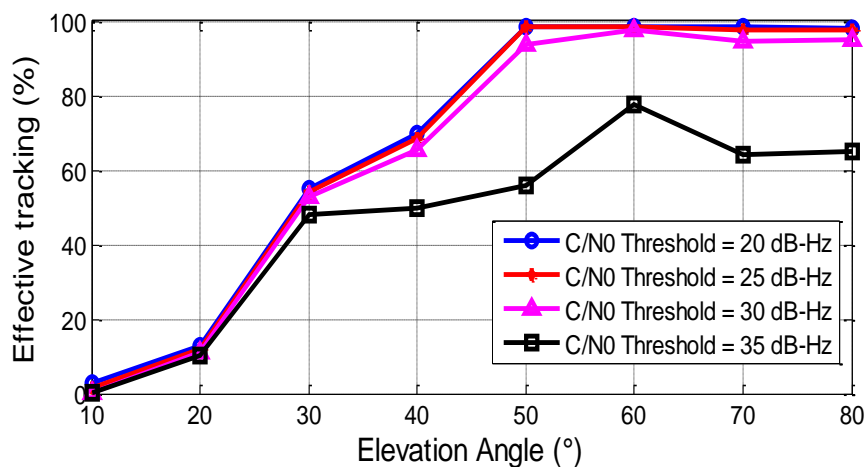


Figure 20 Percentage of time at which the receiver is actually tracking the signal generated by the LMS simulator

The case of the 0° azimuth is not taken into account for the threshold determination as the LOS is never obstructed and the receiver is tracking for the majority of the samples. The same approach has been followed for each modulation and multipath mitigation technique but is not detailed here. The same conclusion has been done for the other receivers and modulations.

In Figure 20, it can be observed that the percentage of effective tracking for nonzero azimuths decreases with decreasing elevation and is negligible for satellite elevation angles of 10° and 20° . To explain this phenomenon, the Signal to Multipath amplitude Ratios (*SMR*) histograms are plotted in Figure 21, Figure 22 and Figure 23 which respectively correspond to satellite elevations of 10° , 20° and 30° . The *SMR* is defined as the ratio between the amplitude of the LOS and the amplitude of the strongest echo. The bi modality of the *SMR* distribution is characteristic of the two configurations that occur. The mode corresponding to the low *SMR* is the consequence of the reception of a combination of a NLOS and reflections. The mode corresponding to the high *SMR* is the consequence of the reception of a LOS and reflections. The NLOS reception is characterized by very low or negative *SMR* which lead to losses of lock of the tracking loops. It can be inferred from Figure 21, Figure 22 and Figure 23 that the number of samples with very low or negative *SMR* increases as the elevation decreases. Therefore the amount of samples that are over the C/N_0 mask increases with the elevation.

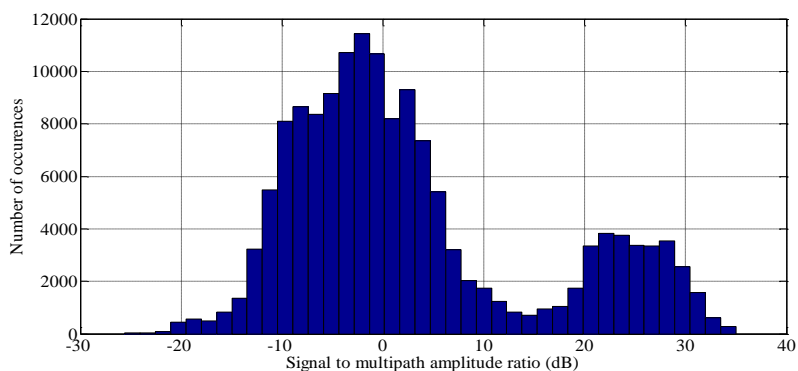


Figure 21 Signal to multipath amplitude ratio for a satellite elevation of 10°

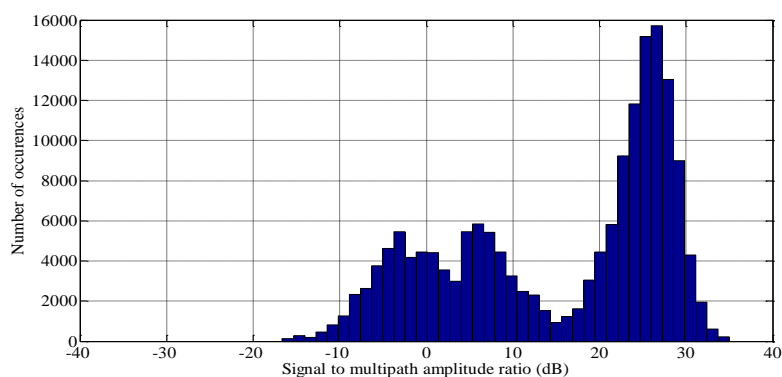


Figure 22 Signal to multipath amplitude ratio for a satellite elevation of 20°

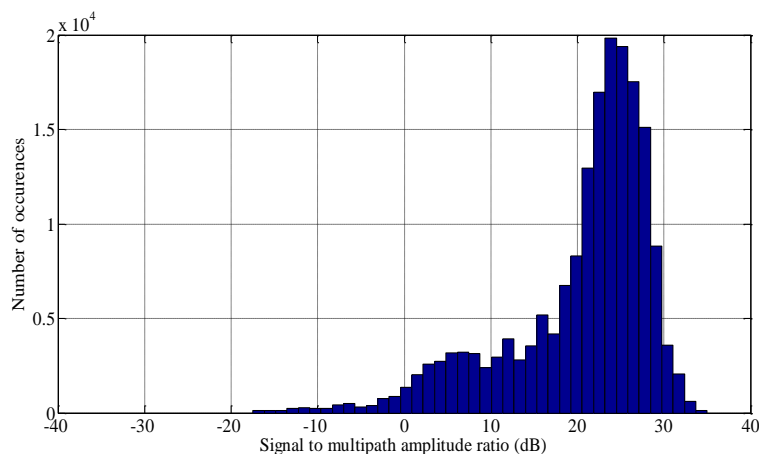


Figure 23 Signal to multipath amplitude ratio for a satellite elevation of 30°

5.1.1.1.5.5 Overbounding

The design of integrity monitoring algorithms requires the characterization of the actual error distribution by a known distribution. Integrity monitoring systems usually assume that the error follows a zero mean Gaussian distribution. The distribution of the raw multipath pseudorange error obtained by processing the LMS channel output is neither Gaussian nor centered. Thanks to the C/N_0 based selection, with a threshold of 30 dB-Hz, the mean of the residual code error is sub-decimeter as

shown in Figure 18. The centered distribution still remains not Gaussian. The well-known Cumulative Distribution Function (CDF) overbounding technique described in [DeCleene, 2000] is used here. The CDF overbounding technique requires the distribution to be unimodal, centered, and symmetric. The unimodality was checked by watching the histograms of the observed pseudorange error. All three assumptions are fulfilled after the C/N_0 discrimination.

5.1.1.1.5.6 Results

For the simulations, the channel is generated once and each receiver's architectures and signals are processed on the same channel. In real-life, the vehicle may not travel along a straight street such as what is generated in the LMS, but may face buildings when turning, or bridges, so that the satellites located in front of it can be masked. Therefore proposing a model in which the nominal multipath standard deviation is a function of the azimuth would not be relevant. For each simulated elevations, the pseudorange error from the range of possible azimuth shall be concatenated before the overbounding. The results of the CDF overbounding on the pseudorange error for the narrowband GPS L1 C/A and Galileo E1 OS receiver are given in Figure 24. It can be seen in Figure 24 that the multipath error model for BPSK(1) and BOC(1,1) is similar. For elevations lower than the mask angle of the buildings, the samples that are above the C/N_0 threshold are mainly those obtained for a null azimuth. For a null azimuth, the configuration is less favorable to multipath interference. The results of the CDF overbounding on the pseudorange error for the wideband GPS L1 C/A Galileo E1 OS receiver are given in Figure 25.

Few samples with low elevation and nonzero azimuth are effectively tracked for the wideband CBOC receiver and the overbounding process leads to a higher nominal standard deviation (as shown in Figure 26).

For elevations higher than or equal to 40° , the use of a wideband receiver instead of a narrowband one enable a significant reduction of the multipath error ($\sigma_{multipath} = 0.4$ m instead of 0.7 for BPSK(1)).

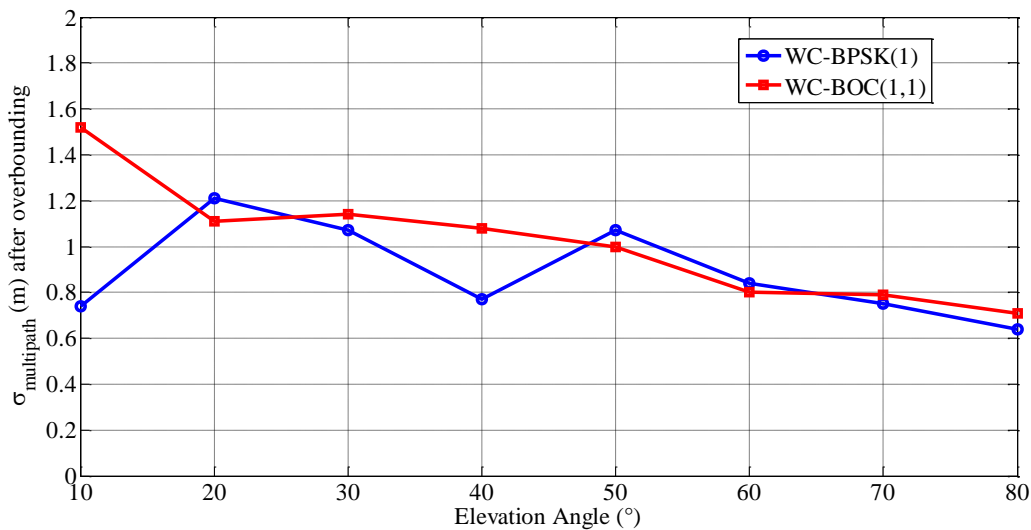


Figure 24 Nominal multipath standard deviation for the narrowband receiver obtained after CDF overbounding

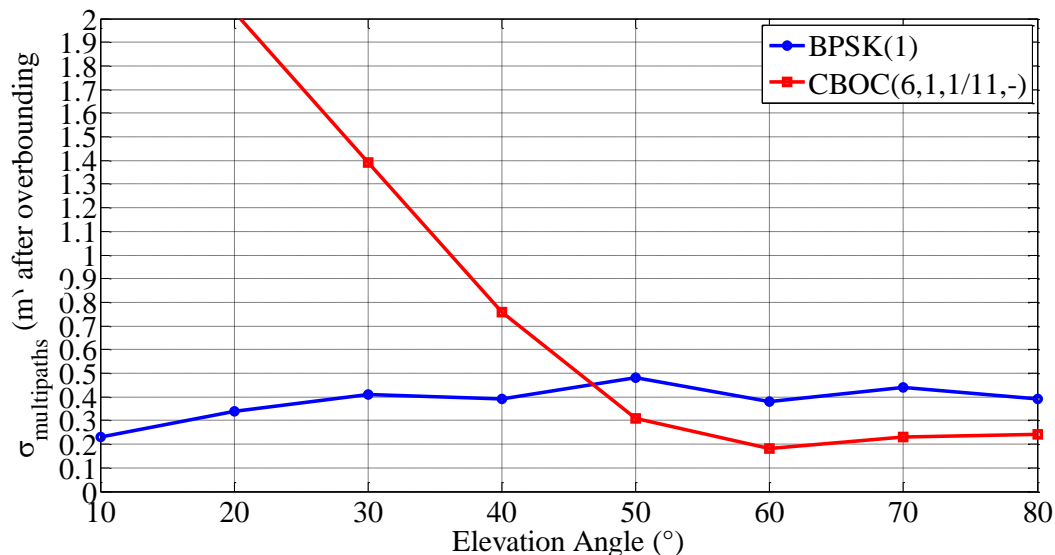


Figure 25 Nominal multipath standard deviation for the wideband receiver obtained after CDF overbounding for the BPSK(1) and CBOC(6,1,1/11,-) modulation

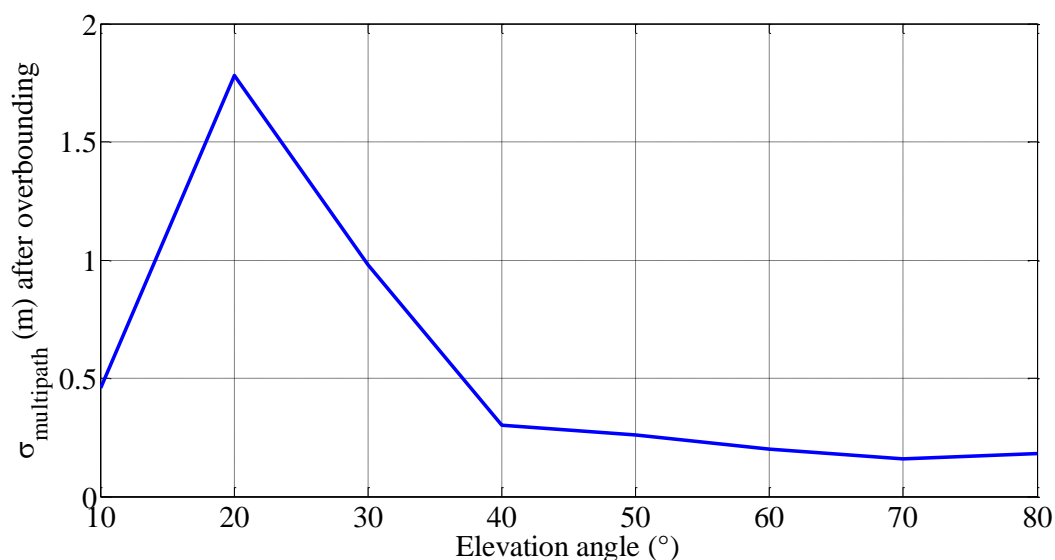


Figure 26 Nominal multipath standard deviation for the wideband receiver obtained after CDF overbounding for the BPSK(10) modulation

The lifespan of an echo is generally characterized by a distribution of distance, typically less than 5 meters for a car/train [Lehner and Steingass, 2005]. The higher is the velocity, the shorter (in terms of time) is the echo lifespan. With shorter echo lifespan, the multipath error has shorter correlation time and behaves like white noise. When distorting the correlation function, the multipath leads to a biased estimation of the delay. However, when affected by an echo with short lifespan, the DLL may not

converge to the maximum bias associated with the echo. Finally, the filtering by the carrier loop due to the Doppler shift of the echoes is all the more important as the velocity of the vehicle is high. The model that has been obtained for 20 km/h is thus conservative if applied to higher velocities. For very low velocities, the model used may not be valid for the same reasons.

It can be inferred from the results of these simulations, that, by setting a relevant C/N_0 mask, all the NLOS can be detected (and excluded). This, combined with the fact that the vehicle is moving, explains why the contribution of the multipath interference error to the nominal model is low, even in urban environment (in simulations).

However it shall be noticed, that, for very low velocities, the multipath error may reach values much higher than the proposed model. It would require significantly longer simulations to model such errors (and being representative). Moreover, the DLR model does not simulate any echoes that would be reflected on the vehicle. For a train, these echoes are likely to occur, and are not Doppler shifted compared to the direct signal as the vehicle has the same movement than the antenna.

The multipath nominal model does not account for NLOS error at all. In real environment, NLOS higher than the C/N_0 mask may remain, which makes this error source dangerous for positioning based on GNSS in urban environment.

5.1.1.1.6 Correlation time

The errors described in the previous sections are time-correlated. The time-correlated errors are usually modelled with a first order Gauss-Markov process. The discrete first order Gauss-Markov process can be generated with:

$$\varepsilon(k) = e^{-\frac{T_s}{T_c}}\varepsilon(k-1) + w(k) \quad \text{Eq. 5-36}$$

where:

- ε is the value of the process
- T_s is the sampling period
- T_c is the correlation time of the process
- w is the driven noise

The driven noise variance is given by:

$$\sigma_w^2 = \sigma_\varepsilon^2 \left(1 - e^{-\frac{2T_s}{T_c}} \right) \quad \text{Eq. 5-37}$$

As σ_ε has been given earlier in the section, it is then necessary to determine the correlation time.

The correlation of the pseudorange errors have been defined in [RTCA, 2006]:

- $T_{c,clk\&eph}$ is typically 3600 seconds according to [ICAO, 2009]
- $T_{c,iono}$ is typically 1800 seconds according to [ICAO, 2009]
- $T_{c,tropo}$ is typically 1800 seconds according to [ICAO, 2009]

- $T_{c,noise}$ is equal to $1/B_{L,DLL}$, which is equal to 1 second for the receivers modelled in chapter 4
- $T_{c,multipath}$ depends on the velocity of the vehicle. $T_{c,multipath}$ is typically lower than 5 seconds for a moving vehicle

The correlation time of the total pseudorange error depends on the magnitude and the correlation time of each error source. For single frequency receivers, ionospheric errors, thermal noise and multipath are the largest error sources and impose the general correlation time. For dual frequency receivers, the magnitude of correlation time is a few seconds because the ionospheric error has been cancelled (and noise and multipath remains).

5.1.2 Doppler error model

The pseudorange rates measurements (Doppler multiplied by the wavelength) can be integrated as additional measurements in the tight coupling scheme:

$$\dot{\rho}_i = \frac{\partial \sqrt{(x - x_i)^2 + (y - y_i)^2 + (z - z_i)^2}}{\partial t} + c\dot{\Delta}t + \varepsilon_{\dot{\rho}_i} \quad (1)$$

where $\varepsilon_{\dot{\rho}_i}$ is the error on the pseudorange rate measurement, $\varepsilon_{\dot{\rho}_i}$ is not separated into different error sources in this case.

To model the Doppler in the simulations and to characterize their covariance in the EKF, the model proposed in [Carcanague, 2013] has been used. This model, given in Table 9 assesses the standard deviation of the Doppler measurements in urban and suburban environment as a function of the vehicle speed and the C/N_0 . The model is valid for GPS L1 C/A, Galileo E1 OS and GLONASS L1 as they have approximately the same wavelength. No equivalent model has been found for L5 and E5a frequency. Even if the validity of this model for applications that requires integrity is not proven, Doppler measurements that are too far from their predicted value based on sensors will be excluded (as detailed in chapter 7), thus the impact of a wrong modelling Doppler error is reduced.

Vehicle speed	C/N_0 (dB.Hz)						
	30-33 dB.Hz	33-36 dB.Hz	36-39 dB.Hz	39-42 dB.Hz	42-45 dB.Hz	45-48 dB.Hz	48-51 dB.Hz
0-3 m/s	0.53 m/s	0.43 m/s	0.28 m/s	0.21 m/s	0.13 m/s	0.09 m/s	0.07 m/s
3-6 m/s	2.04 m/s	1.61 m/s	1.08 m/s	0.71 m/s	0.55 m/s	0.32 m/s	0.24 m/s
6-9 m/s	2.37 m/s	2.00 m/s	1.43 m/s	0.86 m/s	0.53 m/s	0.29 m/s	0.18 m/s
9-12 m/s	3.08 m/s	2.33 m/s	1.60 m/s	1.06 m/s	0.99 m/s	0.28 m/s	0.22 m/s
12-15 m/s	2.54 m/s	1.87 m/s	1.25 m/s	0.83 m/s	0.54 m/s	0.27 m/s	0.17 m/s
15-18 m/s	1.26 m/s	1.36 m/s	1.48 m/s	0.80 m/s	0.53 m/s	0.27 m/s	0.15 m/s
18-21 m/s	1.37 m/s	1.29 m/s	0.87 m/s	0.55 m/s	0.44 m/s	0.25 m/s	0.16 m/s
21-24 m/s	1.44 m/s	1.25 m/s	1.09 m/s	0.73 m/s	0.37 m/s	0.26 m/s	0.16 m/s
24-27 m/s	1.33 m/s	0.90 m/s	0.58 m/s	0.47 m/s	0.31 m/s	0.26 m/s	0.11 m/s
27-30 m/s	1.01 m/s	0.92 m/s	0.61 m/s	0.53 m/s	0.31 m/s	0.31 m/s	0.14 m/s

Table 9 Weighting scheme based on estimated Doppler measurement standard deviation as a function of velocity and C/N_0

5.1.3 Other Sensors

This section describes the nominal error models of the sensors that have been used to enhance GNSS for navigation in constrained environment. It includes the 6 axis IMU that is used for both cases of study, the track database used for train control and the wheel speed sensors used for ETC. These models have been used to simulate sensors data which have been used to validate the concepts and to weight the measurements from the sensors in the fusion algorithm.

5.1.3.1 IMU

The IMU used in the thesis is the LandMark 01 6 axis (MEMS) from Gladiator Technologies which is a medium cost inertial sensor, and therefore is adapted to the targeted applications. The specifications of this IMU are given in Table 10.

Parameter	Gyroscopes	Accelerometers
Bias (In Run Stability)	5°/hour	45 µg
Angle/Velocity Random Walk	0.003°/sec/√Hz	0.09mg/√Hz
Scale Factor Error	≤ 0.05%	

Table 10 IMU specifications [Landmark 01, datasheet]

The gyroscope and accelerometer measurement models of reference assume the presence of white noise, a scale factor and a bias [El-Diasty and Pagiatakis, 2008]:

$$x_{out} = (1 + SF_x)x_{true} + \delta b_x + n_x \quad \text{Eq. 5-38}$$

where:

- x_{out} is the sensor output
- x_{true} is the true value (angular rate or specific force)
- SF_x is the scale factor error
- δb_x is the bias that varies with time
- n_x is a white Gaussian random noise

The specifications given in Table 10 have to be converted to define the model. The objective is here to determine the distributions of the bias and white noise. The general methodology to do so is given hereafter. Specific sections are then dedicated to apply the methodology to the gyroscopes and accelerometers.

- The noise n_x is characterized by its variance which can be derived from the specifications.
- The bias instability which characterizes the time variations of δb_x can realistically be modelled by a flicker process [Strus et al., 2007] with the implementation provided by [Kasdin and Walter, 1992] or with a first order Gauss-Markov process. The first-order Gauss Markov

approach is preferred in this Thesis because it enables using the same model for the generation of the simulated sensor outputs and for the EKF equations design. In this case the variation of the bias can be modelled as:

$$\delta \dot{b}_x = -\frac{1}{\tau_{b_x}} \delta b_x + \eta_{b_x} \quad \text{Eq. 5-39}$$

where:

- τ_{b_x} is the correlation time for the process.
- η_{b_x} is the driving noise of the process with a variance σ_{b_x}

The scale factor error is modelled by a constant equal to 0.05% in simulations. In the EKF it is characterized by a first-order Gauss Markov process with long correlation time (10000 s).

5.1.3.1.1 Gyroscopes

The specifications have to be converted to determine the error characteristics necessary to define the model. The objective is here to determine the distributions of the bias and white noise.

The angular rate noisy measurements are integrated to estimate attitude. The integrated signal is affected by a zero-mean random walk error. The IMU manufacturers characterize the noise by the *ARW* value in the specifications, which must be converted into noise standard deviation.

The value given as an *ARW* in the datasheet is in fact a FFT noise density [IEEE Std 952-1997]:

$$ARW(^{\circ}/\sqrt{h}) = \frac{1}{60} FFT \left[\frac{(^{\circ})}{h} / \sqrt{Hz} \right] \quad \text{Eq. 5-40}$$

which gives for the specification of Table 2, an *ARW* of $0.18^{\circ}/\sqrt{h}$

The correspondence between *ARW* which characterize the integrated white noise and the standard deviation of the white noise given in [Woodman, 2007]:

$$\sigma_g[^{\circ}/sec] = \sqrt{\frac{1}{3600T_s} ARW(^{\circ}/\sqrt{h})} \quad \text{Eq. 5-41}$$

where:

- T_s is the sampling frequency of the sensor set (100 Hz in simulations, 10 Hz on the real campaign)

Finally $\sigma_g=0.03^{\circ}/s$ for the gyroscopes. On 10 hours long data collections in which the IMU is fixed, the standard deviations of the gyroscopes on the three axes have been estimated to 0.037, 0.033 and $0.036^{\circ}/s$ which confirms the value obtained after conversions. The process correlation time (τ_{b_g}) is set to 100 s which is a typical value for MEMS sensors [Woodman, 2007].

Finally, the variance of the driving noise of the first-order Gauss Markov process can be obtained with:

$$\sigma_{b_g} [^\circ/sec] = \sigma_{b_{s_g}} \sqrt{1 - e^{-2\frac{T_s}{\tau_b}}} \quad \text{Eq. 5-42}$$

where:

- $\sigma_{b_{s_g}}$ is the gyroscope bias stability (covariance of the process) given in Table 10

The sampling period is negligible compare to the correlation time of the sensor. Thus, at the first order:

$$\sigma_{b_g} = \sqrt{\frac{2}{\tau_{b_g}}} \sigma_{b_{s_g}} \quad \text{Eq. 5-43}$$

which gives $\sigma_{b_g} = 2.10^{-5} \text{ }^\circ/s$.

5.1.3.1.2 Accelerometers

The approach is exactly the same as for the gyroscopes. First we have to calculate the velocity random walk (VRW) with:

$$VRW [ms^{-1}/\sqrt{h}] = 60FFT [ms^{-2}/\sqrt{Hz}] \quad \text{Eq. 5-44}$$

which gives (from the specification of Table 10), $VRW [^\circ/\sqrt{h}] = 0.053 \text{ } ms^{-1}/\sqrt{h}$.

Then:

$$\sigma_a [m/sec^2] = \sqrt{\frac{1}{3600T_s}} VRW (ms^{-1}/\sqrt{h}) \quad \text{Eq. 5-45}$$

Finally, the standard deviation of the accelerometer noise is $\sigma_a = 0.0088 \text{ } ms^{-2}$. On the 10 hour data collection, the standard deviations of the three accelerometers have been measured to 0.0081, 0.0084 and $0.0085 \text{ } m/s^{-2}$ which confirms the theoretical value.

Finally, the variance of the driven noise of the first-order Gauss Markov process can be obtained with (Eq. 5-37):

$$\sigma_{b_a} = 6.2.10^{-6} \text{ } m/s^2 \quad \text{Eq. 5-46}$$

5.1.3.2 Track Database

The use of the train track data map is a way to take into account the fact that the motion of the train is limited to one axis, or equivalently one degree of freedom. In train control, it has been assumed that the railtrack on which the vehicle is located is known. In this work, it is assumed that the track database consists in a list of coordinates of track data points. These points can be close to each other (about 1.5 m [Euler et al., 1996]). Given i the index of a train track data point, its coordinates (E_i, N_i, U_i) in the ENU frame can be modeled as:

$$E_i = E_{i,true} + \delta E_i \quad \text{Eq. 5-47}$$

where:

- E_i is the true coordinate of the track point in the ENU frame
- δE_i is the mapping error
- $\delta E_i \sim \mathcal{N}(0, \sigma_{E_i}^2)$

The mapping can equivalently be done in the ECEF coordinate frame.

In this Thesis, it is assumed that:

- the errors on each axis are equally distributed and uncorrelated
- the errors on each track point follow the same distribution
- the distance between two consecutive train track data points will be denoted d_{map} and assumed constant.
- a 3D standard deviation of 20 cm on the track data points is assumed. These types of accuracies can be reached with differential phase positioning combined with post-processing and other sensors such as LIDAR.

5.1.3.3 Wheel Speed Sensors

WSS are nowadays present on-board in most vehicles and are used by the anti-lock braking system (ABS). A WSS measures the along-track velocity of the vehicle by counting the frequency of the wheel revolution and multiplying it with the wheel circumference. If the practical wheel diameter differs from the nominal wheel diameter, the distance measured by odometer will introduce an error, which is proportional to the velocity, referred to as scale factor error. The WSS error model is then:

$$v_{out} = (1 + SF)v_{true} + n_v \quad \text{Eq. 5-48}$$

where:

- SF is the scale factor error
- n_v is the noise measurement on the sensor

A constant scale factor error of 3% have been used as a reference. The variance of the noise measurement on the WSS is 0.1 m/s [Spangenberg, 2009.].

5.2 Faults

The failures are errors that are not described by the nominal error models. GNSS and other sensors can provide faulty measurements, which can lead to position larger than the alert limit. The faults are generally characterized by their probability of occurrence and signatures (amplitude, time duration). The characterization of the faults is an important step that must be done prior to the definition of an integrity monitoring algorithm.

5.2.1 Failure sources of GNSS

The GNSS faults can originate from several sources. It can be caused by satellite failure, abnormal ionosphere conditions, interference, or abnormally large local effects with respect to the nominal error model (this case is discussed in section 5.3). An exhaustive list of GNSS failure modes is given in [Bhatti, 2007]. Unfortunately, only the satellite fault has a probability of occurrence that is well characterized. The constellation faults are also introduced in this section.

5.2.1.1 Satellite faults

The GPS satellite fault which is referred to as Major Satellite Failure (MSF) is well characterized. This characterization can reasonably be applied to Galileo [Salos, 2012]. The MSF occurs when a healthy GPS satellite's ranging signal (excluding atmospheric and local errors) exceed the SIS URE not-to-exceed (NTE) tolerance. The NTE tolerance is defined as the maximum between 30 m and 4.42 times the transmitted URA. The probability of occurrence such an event provided that no MSF was present at the start of the hour is specified by the SPS SiS integrity standard:

$$P_{MSF,h} = 10^{-5}/\text{sat}/\text{h} \quad \text{Eq. 5-49}$$

After the occurrence of such an event, the GNSS will detect and alert the user within 6 hours. Realistic Maximum alert delays are around 1 hour. Thus the probability that a satellite is faulty at an instant is equal to the probability the failure occurs during the previous hour:

$$P_{MSF(1hour)} = 10^{-5}/\text{sat} \quad \text{Eq. 5-50}$$

The probability that a position calculated with N_{sat} contains n MSF is given by:

$$P_{occurrence\ of\ n\ MSF} = \binom{N_{sat}}{n} P_{MSF(1hour)}^n (1 - P_{MSF(1hour)})^{N_{sat}-n} \quad \text{Eq. 5-51}$$

There is no GLONASS equivalent to GPS MSF in terms of standard characterization. In [Walter et al., 2013], the fault is assumed to occur when the worst-case URE is greater than 50 m. This study assumes that the probability of exceedance of this threshold is 10^{-4} per satellite. The value is taken as a reference in the Thesis. Currently, the probability of occurrence of a fault that affects several satellites for GLONASS is not sufficiently low to be neglected (10^{-4} in [Walter et al., 2013]).

In general, satellite faults are classified into steps and ramps. Step errors are usually simple to detect whereas slowly growing errors (SGE), also referred to as ramps are more complex and longer to detect.

5.2.1.2 Constellation faults

Constellation faults are the faults that may affect more than one satellite within a constellation at a given time. They can be caused by control segment or by a design flaw in the satellites (e.g. in [Walter et al., 2014]). Current RAIM algorithms assume that the probability of constellation fault is equal to 0 for GPS (there is no evidence of such event in the past).

As Galileo is not yet operational, it is not possible to extrapolate the probability of constellation fault based on past observations.

The probability of occurrence of constellation faults cannot be neglected for GLONASS because such event has already been observed on April 2, 2014 where bad ephemerides were uploaded to the satellites which broadcast these corrupted information for 11 hours. The same phenomenon appeared on April 15, 2014, with eight satellites going offline. It is stated in [Walter et al., 2014] that that “ 10^{-4} is a reasonable starting place” for the probability of constellation fault for GLONASS.

5.2.2 Sensors faults

5.2.2.1 Inertial faults

The proposed solutions integrate data from an IMU, wheel speed sensors or a track database. The fault modes of these sensors have to be addressed. An exhaustive list of inertial sensors failures sources, including MEMS, is given in [Bhatti, 2007]. The failure of the inertial sensors can result in no output, null reading, repeated readings or abnormally large errors with respect to the specifications [Groves, 2013]. For inertial sensors, the only parameter related to failure occurrence that is given in the IMU datasheets is the Mean Time Between Failure (*MTBF*). The probability of failure during 1 hour of operation is given by:

$$P_{F,IMU} = 1 - e^{-\frac{1}{MTBF}} \quad \text{Eq. 5-52}$$

For the Landmark 01 IMU, the *MTBF* provided by the manufacturer is equal to 124334 hours. It corresponds to a probability of failure of $8 \cdot 10^{-6}$ per hour. However the failure events considered in the *MTBF* are not clearly defined. In particular, it remains unclear whether this value is the sum of the probability of any failure or whether it corresponds to the probability for the IMU not to be able to provide any measurement. From the safety point of view, it is much more hazardous to receive incorrect measurements than no measurement at all. As no a priori information on the probability of the IMU to provide non nominal measurements are known, $P_{F,IMU}$ derived from Eq. 5-46 will be used as a reference.

For train control, the integrity risk allocated to the IMU subsystem has to be lower than $\sqrt{P_{int}}$. With the redundant approach, the integrity risk of the subsystem is $10^{-5.5}/h$ in the most demanding case. The risk allocated to the IMU will therefore be equal to or lower than $10^{-5.5}/h$. However, $10^{-5.5}/h$ is lower than $P_{F,IMU}$ calculated for the sensor. Thus, the integrity of the IMU measurements must be monitored.

Lower grade IMU may be preferred for ETC for OBU costs considerations. Considerably shorter *MTBF* and therefore larger $P_{F,IMU}$ can be expected from these types of sensors. IMU integrity will also have to be monitored for ETC.

It is proposed in chapter 8 to protect the system against IMU faults prior to their integration in the mechanization. Moreover, the sensor nominal errors are calibrated by the EKF, therefore, it can be assumed that they do not convert into failures after their integration in the mechanization.

5.2.2.2 Other sensors faults

A fault in the track database can be manifested by an abnormally large position error on the track points or missing track points. For train control, in this thesis, the track database is assumed to be fault free.

As for ETC, the failures of the wheel speed sensors are not investigated in this thesis. Even if the vehicles are equipped with two wheel speed sensors, the dependency between the failure events of both shall be addressed before designing any failure monitoring. A possible solution consists in monitoring the variations of the velocity measurements by the WSS with the IMU as these technologies are independent.

5.3 Consideration of local effects

When the vehicle operates in suburban or urban environments, it may be affected by measurement errors that are abnormally large with respect to the nominal error model that have been presented in section 5.1. This can be due to two phenomena, multipath interference and NLOS.

5.3.1 Multipath interference

Multipath interference refers to the configuration in which the GNSS signal received is the sum of the direct signal plus reflected or diffracted rays. The errors due to this phenomenon have been integrated in the nominal error model. However, multipath interference can result, at least theoretically (as shown in chapter 7), in measurement errors that are considerably larger than what was observed during the simulations conducted on the LMS channel model. Such event has to be considered in the design of the solution. It is either possible to protect against it by modifying the nominal error model to integrate these cases, or to rely on an algorithm such as the one presented in chapter 7.1 to detect such event.

5.3.2 Non-Line-Of-Sight GNSS errors in urban environment

If the satellite is masked, the receiver may track a NLOS. NLOS are always affected by positive biases with respect to the direct signal. In the simulations that have been conducted on the LMS channel model, it has been observed that the NLOS can be excluded by using a constant C/N_0 mask at 30 dB-Hz. However, it may not be the case on real signals. The probability of occurrence of this type of event is unknown.

The nominal error model that has been presented in section 5.1 is only valid for LOS signals. For open sky to light suburban environment, not considering the possibility of tracking a NLOS may be valid to a certain extent. However, in urban environment, the distribution of the error in the NLOS case must be characterized. Then, it will either be possible to include the NLOS case in the nominal error model by inflating it sufficiently (if its probability of occurrence is high) or to include these cases in the failure modes (if it has a low probability of occurrence) and to rely on additional algorithms to protect the system from these errors.

To characterize the NLOS error, a simple statistic model is firstly proposed. Then, a measurement campaign has been conducted in order to characterize the NLOS error more precisely in actual urban environment in downtown Toulouse.

5.3.2.1 Statistic model

NLOS error has been statistically modelled for ultra-wideband signals either by a uniform [Jia and Buehrer, 2010], Gaussian [Borras et al., 1998] or exponential distribution [Guvenc, 2007]. A deterministic model for the modelling of NLOS error has been proposed in [Betaille et al., 2013], where the street is modelled by an urban canyon of infinite length with geometric characteristics that are known thanks to database. In this section a statistical distribution of the NLOS error is proposed based on statistical characterization of the street topology.

It is assumed that any GNSS signal tracked by the receiver is either:

- a direct signal
- a NLOS that is diffracted on the building edge
- a NLOS reflected on the opposite building face
- a NLOS reflected twice

Thus:

$$P(\text{direct}) + P(\text{diffracted}) + P(\text{1 reflection}) + P(\text{2 reflection}) = 1 \quad \text{Eq. 5-53}$$

These events are considered distinct, and the formula of total probability is be applied to the NLOS error cumulative distribution function and derived. The result is characteristic of a mixture density model for the NLOS error:

$$\begin{aligned} f(\varepsilon_{NLOS}) = & P(\text{direct})f(\varepsilon_{NLOS}|\text{direct}) + P(\text{diffracted})f(\varepsilon_{NLOS}|\text{diffracted}) \\ & + P(\text{1 reflection})f(\varepsilon_{NLOS}|\text{1 reflection}) \\ & + P(\text{2 reflection})f(\varepsilon_{NLOS}|\text{2 reflection}) \end{aligned} \quad \text{Eq. 5-54}$$

where $f()$ denotes the probability density function.

To determine the value of the mixture, it is proposed to

- Address the statistical models that will be used for the computation of the error distributions and the probability of occurrence of each event.
- Second, compute the four error pdf that are involved in Eq. 5-54.
- Third, determine the expressions of the four coefficients of the mixture.
- Finally provide the results.

5.3.2.1.1 Statistic modelling

The street is modelled as an urban canyon of infinite length. Let's denote $H_{building}$ the height of the building which is located on the same side of the street as the GNSS satellite. The across street distances from the antenna to the buildings are denoted L_1 and L_2 . $H_{building}$ and L (L_1 and L_2 are assumed to have same distribution) can be characterized statistically by their distributions. The log-normal distribution is commonly used to describe buildings height or street width. Some statistics can be found in the literature about the height distribution of buildings. In [Saunders, 1991], statistics are given for the area covered by the city of Westminster, which corresponds to a total area of 29.5 km². [Parsons, 1992] provides the data in a typical suburban site (Guildford, Surrey). Information on distributions of building height can be found in [Ratti et al., 2002] for several cities including Toulouse, London and Berlin based on urban Digital Elevation Models. The parameters detailed in [Ratti et al., 2002] are average building height and standard deviations:

	London	Toulouse	Berlin
$E[H_{building}]$	13.6 m	15.3 m	18.6 m
$std(H_{building})$	5 m	6.1 m	4.3 m

Table 11 Parameters of the real distribution of building heights for different cities

It is then possible to deduce the corresponding location ($\mu_{H_{building}}$) and scale ($\sigma_{H_{building}}$) parameters for the lognormal corresponding model.

$$\mu_{H_{building}} = \ln \left(\frac{E[H_{building}]^2}{\sqrt{std(H_{building})^2 + E[H_{building}]^2}} \right) \quad \text{Eq. 5-55}$$

$$\sigma_{H_{building}} = \sqrt{\ln \left(\frac{std(H_{building})^2}{m^2} + 1 \right)} \quad \text{Eq. 5-56}$$

For Toulouse downtown, it gives $\mu_{H_{building}} = 2.65$ and $\sigma_{H_{building}} = 0.38$.

Street and railway width can also be highly variable, especially in urban and suburban areas. Again, the log-normal distribution appears to be the most reasonable choice for street width [Oestges et al., 1999]. The case of train control is developed here. The same approach can be applied for ETC, and the distribution of L will be different for each geo-object.

For train control the objective is to characterize the minimum distance from the track to the buildings. In Toulouse, statistics were measured on google earth at a constant spatial frequency, in the area where the buildings are the closest to the railtrack (43°33'58.99"N, 1°29'35.88"E) to (43°36'33.33"N,

1°27'19.09"E) which corresponds to 6.16 km. Every 60 meters, for the two trailtracks that are the closest to the building, the distance to the closest building is measured. It corresponds to approximately 200 values. This distribution is conservative as the tracks in between the two that are surveyed have better visibility. The data distribution has been fitted with a lognormal distribution as illustrated in Figure 27. The parameters associated are $\mu_L = 2.9$ and $\sigma_L = 0.412$.

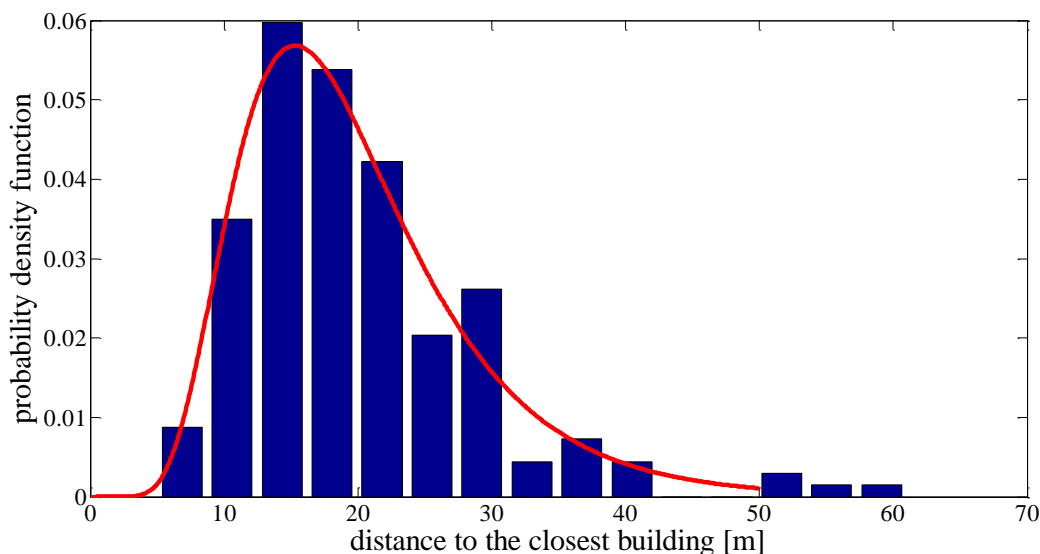


Figure 27 Distribution of the distance to the closest building

5.3.2.1.2 Determination of the probability density functions in each configuration

$H_{antenna}$ represents the height at which the GNSS antenna is located, ϑ represents difference between the satellite azimuth and the street azimuth and α represents the satellite elevation.

If the direct signal is received, the NLOS error is null:

$$f(\varepsilon_{NLOS}|direct) = 0 \tag{Eq. 5-57}$$

If the received signal is diffracted, the expression of the pseudorange error is given by:

$$\varepsilon_{NLOS}|diffracted = \frac{\sqrt{L^2 + (H - H_{antenna})^2}}{|\sin(\vartheta)|} \left\{ 1 - \sin \left[\alpha + \text{atan} \left(\frac{L}{H - H_{antenna}} \right) \right] \right\} \tag{Eq. 5-58}$$

This distribution is complex and it is not possible to characterize it well by usual distributions. Monte Carlo simulations have shown that the gamma distribution fits well this distribution, in particular the tails of the distribution as illustrated by Figure 28.

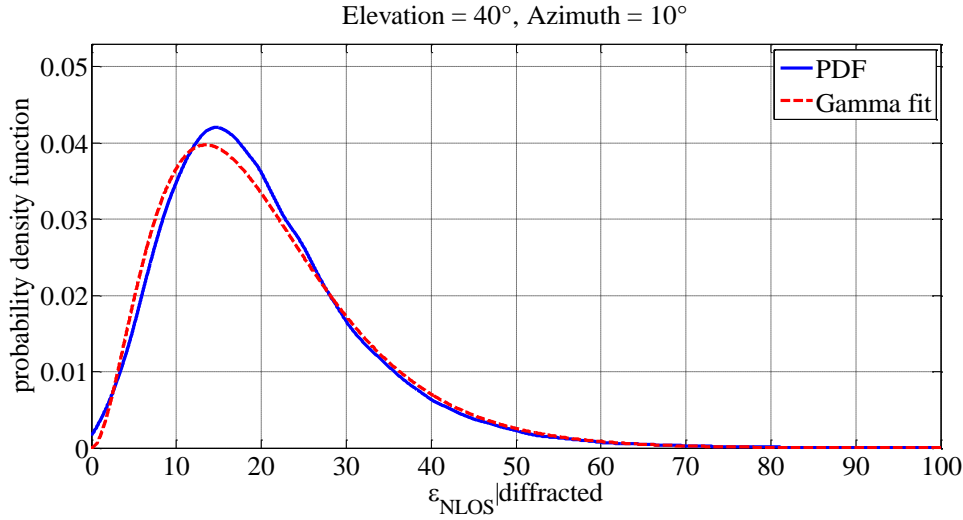


Figure 28 Probability density function for $\varepsilon_{NLOS}|diffracted$

The parameters of the Gamma fitting distribution for the example of Train control in Toulouse is given in appendix D. In the case where the NLOS is received after one reflection, the expression of the distribution is given by:

$$\varepsilon_{NLOS}|1\ reflection = 2L\sin(\vartheta)\cos(\alpha) \quad \text{Eq. 5-59}$$

This error follows a simple lognormal distribution because it is the product of a constant by a lognormal distribution:

$$\varepsilon_{NLOS}|1\ reflection \sim \log - \mathcal{N}(\mu_L + \ln(2\sin(\vartheta)\cos(\alpha)), \sigma_L^2) \quad \text{Eq. 5-60}$$

If a NLOS is received after two reflections, the expression of the NLOS error is given by [Betaille et al., 2014]:

$$\varepsilon_{NLOS}|2\ reflection = 2(L_1 + L_2)\sin(\vartheta)\cos(\alpha) \quad \text{Eq. 5-61}$$

$L_1 + L_2$ is the sum of two independent lognormal distributions. This distribution is used in many important communication problems. No exact closed form solution for the distribution is known. However there is a general agreement that a sum of independent lognormal random variable can be well approximated by another lognormal random variable. Thus:

$$L_1 + L_2 \sim \log - \mathcal{N}(\mu_{L_1+L_2}, \sigma_{L_1+L_2}^2) \quad \text{Eq. 5-62}$$

Different techniques exist to determine the parameters of the resultant lognormal distribution. Several method exists to determine these parameters and some are listed in [Beaulieu et al., 1995]. We use the Fenton-Wilkinson's method [Fenton, 1960] as it provides a better estimate of the CDF tail than other techniques. The Fenton-Wilkinson's estimation for the sum of two lognormal with the same scale and the same location gives (it is assumed that L_1 and L_2 have the same distribution):

$$\sigma_{L_1+L_2}^2 = \ln\left(\frac{1}{2}e^{\sigma_L^2} + \frac{1}{2}\right) \quad \text{Eq. 5-63}$$

$$\mu_{L_1+L_2} = \ln(2e^{\mu_L}) + \frac{\sigma_L^2}{2} - \frac{\sigma_z^2}{2} \quad \text{Eq. 5-64}$$

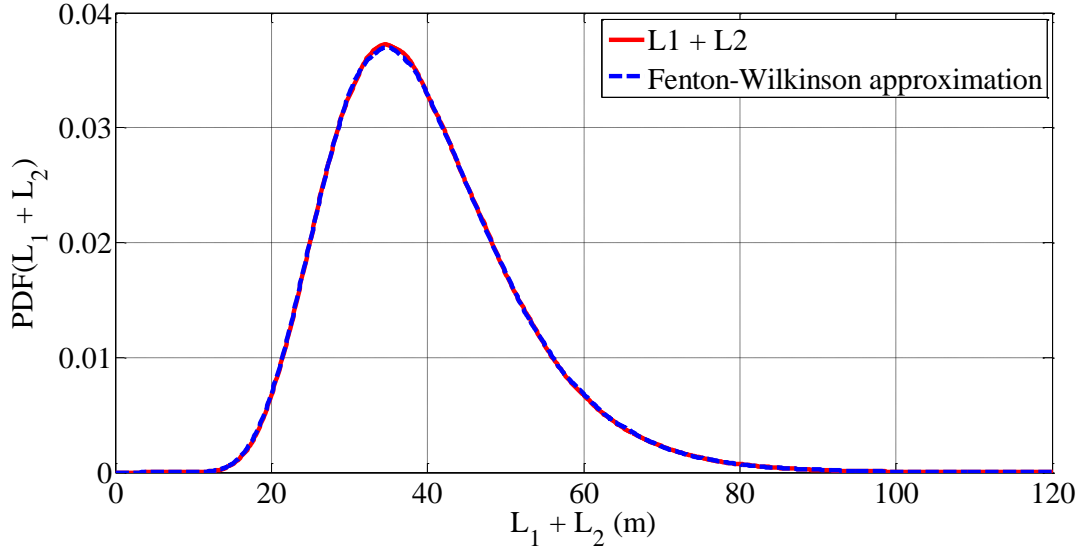


Figure 29 Fitting $L_1 + L_2$ by lognormal distribution with Fenton-Wilkinson approximation

Finally, the distribution of the pseudorange bias in this scenario is the following:

$$\varepsilon_{NLOS|2\ reflection} \sim \log - \mathcal{N}(\mu_{L_1+L_2} + \ln(2\sin(\vartheta)\cos(\alpha)), \sigma_{L_1+L_2}^2) \quad \text{Eq. 5-65}$$

The probability density functions of the NLOS errors in the four cases are well known because they are characterized in function of basic distributions.

5.3.2.1.3 Probabilities of occurrence

The next step is the characterization of the probabilities of occurrence of each configuration, i.e. the coefficients of the mixture. In [Betaille et al., 2014], the probabilities of occurrence of the reception of the direct signal, single reflected NLOS and double reflected NLOS are given as a function of the satellite elevation. This model of probabilities is characterized by two critical elevations, denoted α_{diff} and α_{ref} here. α_{diff} corresponds to the elevation mask of the buildings in the direction of the satellite. If $\alpha \leq \alpha_{diff}$, the direct signal is masked. If $\alpha \leq \alpha_{ref}$, the it is geometrically possible to receive twice reflected NLOS. The expressions of both critical elevations are:

$$\alpha_{diff} = \text{atan} \left| \frac{H_{building} - H_{antenna}}{L} \sin(\vartheta) \right| \quad \text{Eq. 5-66}$$

$$\alpha_{ref} = \text{atan} \left| \frac{H_{building} - H_{antenna}}{L_1 + 2L_2} \sin(\vartheta) \right| \quad \text{Eq. 5-67}$$

The model proposed in [Betaille et al., 2014] is slightly modified here. Firstly we have added a scenario which is the reception of a diffracted signal. It has been assumed here that the probability to track NLOS given that the elevation α is higher than the elevation of the building α_{diff} is null. Moreover the probability to track the LOS given that the satellite is masked ($\alpha \leq \alpha_{diff}$) is also null. Finally it is assumed that the probability of tracking a doubly reflected NLOS if $\alpha > \alpha_{ref}$ is null. The sum of the four probabilities has to be equal to 1 no matter the elevation. The model proposed is represented in Figure 30, and its expression is detailed in annex.

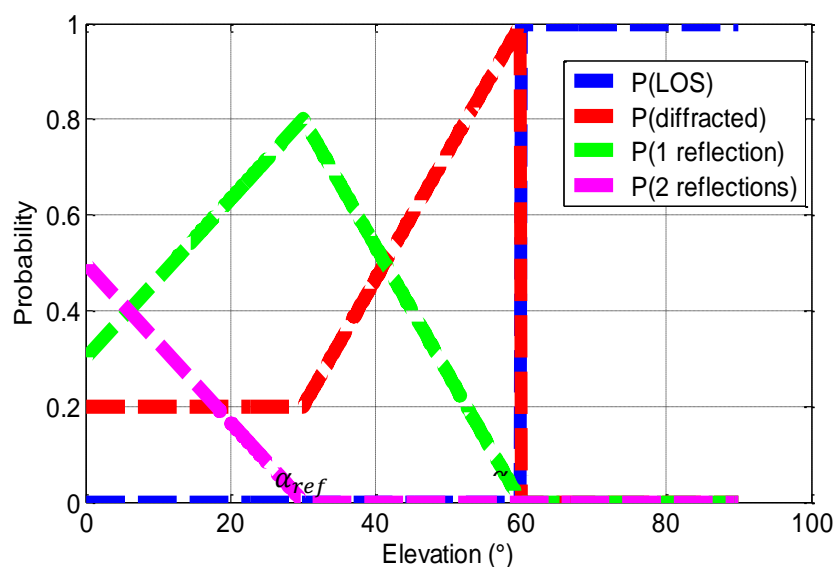


Figure 30 Probabilities of occurrence of scenarios in urban environment

In our statistical approach, α_{diff} and α_{ref} are random variables. Given the elevation of the satellite, the probability of occurrence of each scenario is in fact a random variable itself, which makes the model too complex. It is proposed to simplify it by replacing the probability of occurrence of each scenario by its expectation in the expression of the mixture (given the satellite elevation). It is then necessary to determine $E[P(direct)]$, $E[P(diffracted)]$, $E[P(1 reflection)]$ and $E[P(2 reflection)]$. These terms have been determined for the Toulouse case by Monte-Carlo simulations. The results are given in Figure 31 to Figure 34 to Y as a function of the azimuth and the elevation of the satellite.

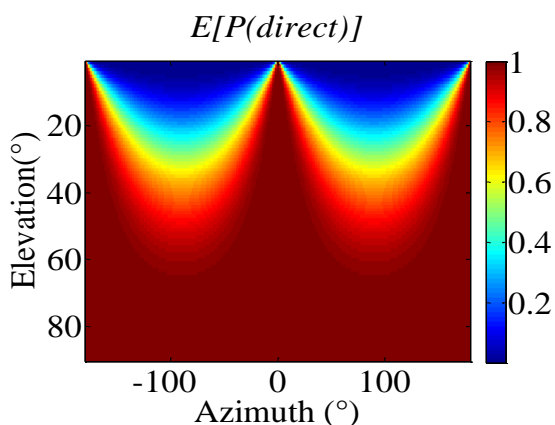


Figure 31 $E[P(\text{direct})]$ as a function of the elevation and azimuth

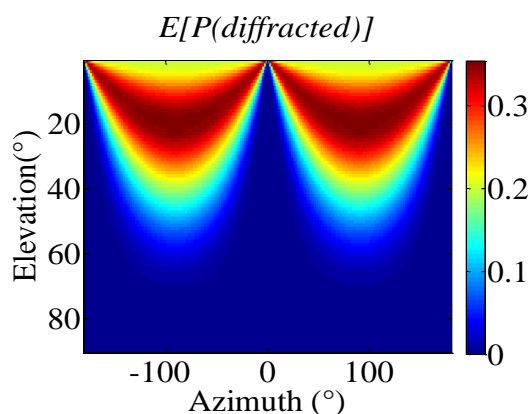


Figure 32 Value of $E[P(\text{diffracted})]$ as a function of the elevation and azimuth

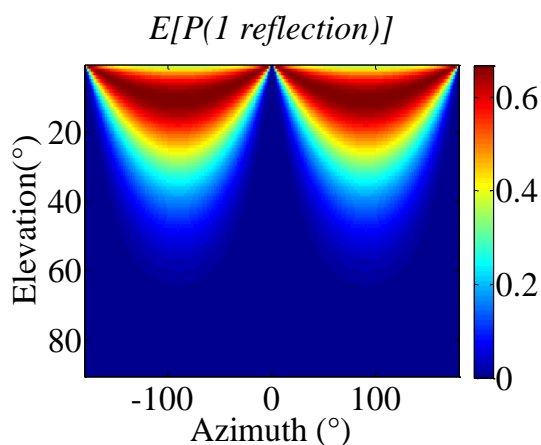


Figure 33 Value of $E[P(1 \text{ reflection})]$ as a function of the elevation and azimuth

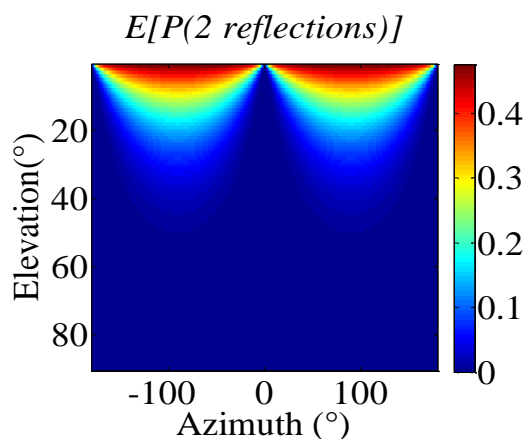


Figure 34 Value of $E[P(2 \text{ reflections})]$ as a function of the elevation and azimuth

5.3.2.1.4 Results

Once each density of the mixture has been determined, and that each coefficient is known, the density of the NLOS error resulting of all the possible configurations can be modelled. The results are given for different values of azimuth in Figure 35 to Figure 38. The probability of large NLOS errors is essentially higher for low satellite elevations and for ϑ that are close to 90° . For high elevation (60°) the NLOS error is negligible.

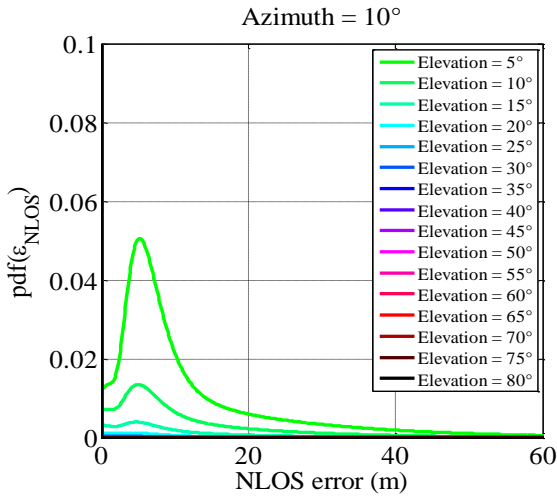


Figure 35 Distribution of NLOS error for $\vartheta = 10^\circ$

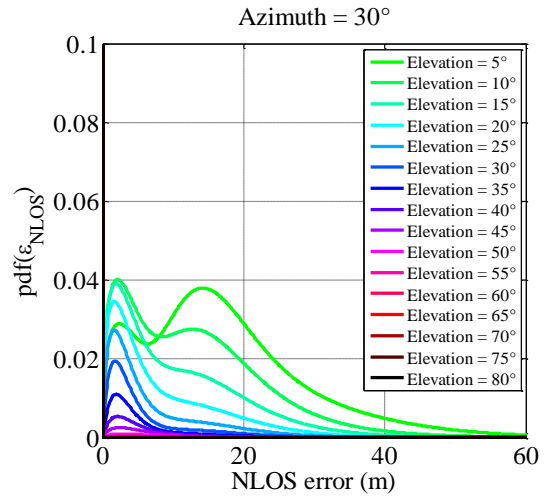


Figure 36 Distribution of NLOS error for $\vartheta = 30^\circ$

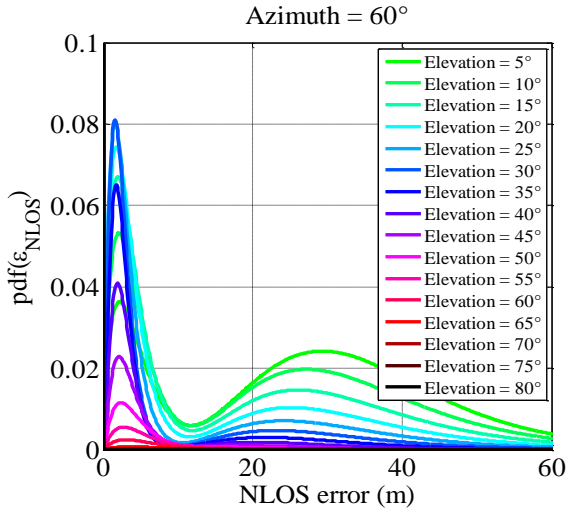


Figure 37 Distribution of NLOS error for $\vartheta = 60^\circ$

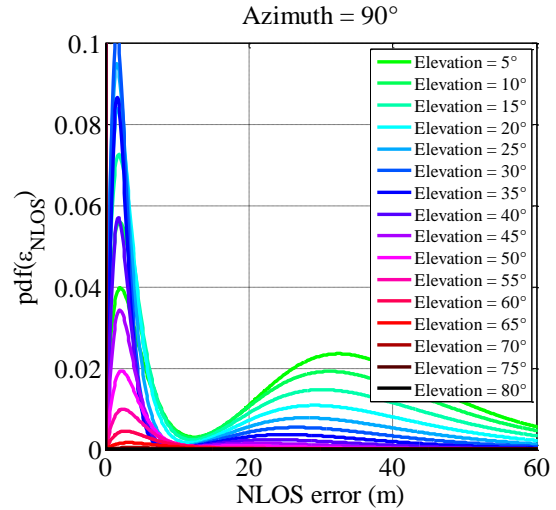


Figure 38 Distribution of NLOS error for $\vartheta = 90^\circ$

As for the time correlation, the lifespan of NLOS is highly correlated to the receiver speed. The life distance distribution of the echoes for a urban car environment is given in [Lehner and Steingass, 2005]. Most reflectors exist along a motion path that is shorter than 5 m. The train urban environment is assumed to behave the same way.

5.3.2.1.5 Conclusions

This model is very pessimistic because it does not take into account the fact that the signal has been effectively tracked, and that it is above the C/N_0 mask (if one is used). In the model, given a satellite elevation and azimuth, the probability of receiving a diffracted, once reflected and twice reflected NLOS is calculated in order to weight the terms of the mixture. Let's take the example of the twice reflected NLOS. The Bayes theorem applied to our study case gives:

$$P(2 \text{ reflections} | \text{tracked}) = \frac{P(\text{tracked} | 2 \text{ reflections})}{P(\text{tracked})} P(2 \text{ reflections}) \quad \text{Eq. 5-68}$$

Thus the probability that shall be used in the model is $P(2 \text{ reflections} | \text{tracked})$ instead of $P(2 \text{ reflections})$. It is clear that $P(\text{tracked} | 2 \text{ reflections})$ is much lower than $P(\text{tracked})$, thus $P(2 \text{ reflections} | \text{tracked})$ is much lower than $P(2 \text{ reflections})$.

Quantizing $P(\text{tracked} | 2 \text{ reflections})$ would be too complex. The statistic modelling approach may be used as an upper bound of the NLOS error distribution. A characterization based on real measurements is described in the next section.

5.3.2.2 Model based on real data

The objective of this sub-section is to refine the pseudorange error model in urban environment based on real measurements. In particular the NLOS error distribution is of particular interest in order to propose a more realistic model than the statistic model which is too conservative. The first part of the subsection is a description of the set up that has been used for the data collection. In particular the method to estimate the pseudorange error is detailed. The results of the campaign are detailed in the second part of the subsection.

5.3.2.2.1 Description of the set-up

The data collection was done on a test van owned by ENAC.

The GNSS receiver used to collect the pseudorange measurements is a U-blox 6 GPS (L1 C/A) Engine Evaluation kit (Figure 39). The receiver is connected to a U-blox active GPS antenna (Figure 40) and to a computer with a USB link. The raw GPS L1 C/A measurements have been recorded with a sampling frequency of 1 Hz.

The trajectory of reference is estimated with a SPAN system from NovAtel. The receiver is a ProPak6 receiver that process GPS L1/L2. The SPAN system combines RTK with tactical grade IMU (UIMU-LCI from Northrop-Grumman Litef GMBH). The IMU was set on the ground of the vehicle, aligned with the axis of the vehicle and with the SPAN antenna in order to reduce the lever arm error, even if it is estimated by the SPAN.



Figure 39 GNSS receiver and antenna used for the data collection



Figure 40 The U-blox antenna (left) and the NovAtel SPAN antenna (right)



Figure 41 Power supply for the set-up (battery and inverter)

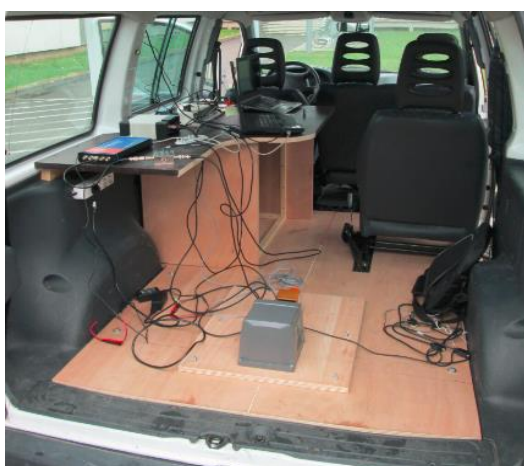


Figure 42 Picture of the set-up

The data from a dual constellation U-blox GPS/GLONASS M8 evaluation kit have also been recorded as well as the data from the LandMark 01 IMU from Gladiator that has been proposed as a reference for the cases of study. This IMU has been synchronized with the dual constellation U-blox GPS/GLONASS receiver by connecting the PPS output of the receiver to it.

5.3.2.2.2 Description of the trajectory

The data collection was done on June, 17th 2015 in Toulouse. Two separated data collections have been made and the concatenation of both trajectories is 71 km long, and corresponds to 2h40 of data. The full trajectory is given in Figure 43.

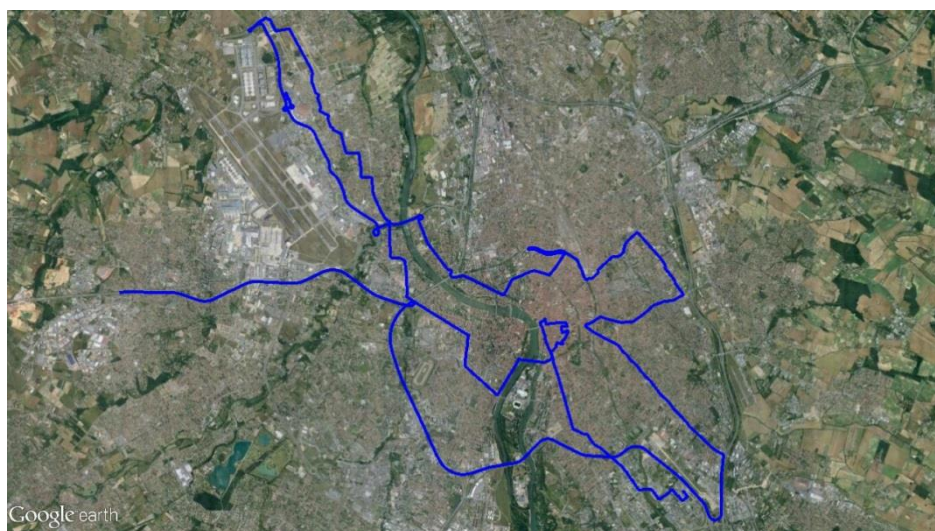


Figure 43 Data collection in Toulouse

The environments have been classified into three categories.

- The beltway environment is characterized by high velocity and open sky conditions.
- The suburban environment corresponds to areas when low buildings are presents around the receiver.
- The dense urban environment corresponds to urban canyons and important building mask angles.

In Table 12 and Table 13 these environment are respectively associated with green, yellow and red. The first trajectory lasted 1h25 approximately. It is a crossing of Toulouse represented in Table 12. After 12 minutes of suburban environment, the vehicle went through the city center during 38 minutes to do a loop in the most challenging canyons of the city, and then the vehicle drives through 37 minutes of suburban environment. In the third part of the trajectory, the trajectory follows the tramway railtracks. It is a typical environment in which rail applications operates. However, trains do not operate in narrow urban canyons.

Duration	Trajectory	Typical environment
12 min		

38 min		
37 min		

Table 12 Characterization of the first trajectory

The second trajectory was started approximately 1 hour after the end of the first one. This trajectory lasts about 1h15. The vehicle crosses a succession of different environment, including beltways Table 13.

Duration	Trajectory	Typical environment
4 min		
5 min		
17 min		
10 min		

10 min		
8 min		
17 min		

Table 13 Characterization of the second trajectory

5.3.2.2.3 Characterization of pseudorange errors

The objective here is to characterize the pseudorange error in urban environment, and in particular the NLOS error. It is proposed to differentiate the raw measurements of the receiver with the pseudoranges from a reference station (TLIA in Toulouse) to cancel the correlated errors (ionosphere, troposphere and ephemeris) which is relevant because the baseline does not exceed 20 km during the collection. The data that corresponds to the date of collection were downloaded on the IGN website. The pseudorange error models of the on board receiver (rcx) and the station of reference (sta) correspond to Eq. 5-1. The expression of the residuals after differentiating both measurements is:

$$\begin{aligned} \rho_{rcx} - \rho_{sta} = & d_{rcx} - d_{sta} + c\Delta t_{rcx} - c\Delta t_{sta} + \varepsilon_{noise,rcx} + \varepsilon_{mp,rcx} + \varepsilon_{NLOS,rcx} \\ & - \varepsilon_{noise,sta} - \varepsilon_{mp,sta} - \varepsilon_{NLOS,sta} \end{aligned} \quad \text{Eq. 5-69}$$

where d_{rcx} and d_{sta} corresponds to the true geometric distance between each receiver and the satellite. It is assumed that the station is in open sky conditions, thus $\varepsilon_{NLOS,stat}$ is null.

We have a good estimation of d_{rcx} and d_{sta} as the location of the receiver is known with decimeter level accuracy (after lever arm correction) and the location of the reference station is known. Thus to have an estimation of the term $\varepsilon_{mp,rcx} + \varepsilon_{NLOS,rcx} + \varepsilon_{noise,rcx} - \varepsilon_{noise,sta} - \varepsilon_{mp,sta}$, it is necessary to eliminate the clock offset $c\Delta t_{rcx/sta}$. The clock offset is the same for all pseudoranges differences. The first step consists in averaging all the differences from NLOS free satellites (50 °) in order to average the noise. By low pass filtering the array, it is possible to estimate the low pass components clock offset. The cut-off frequency selection must be high enough not to filter out the clock offset, but

low enough to filter out the noise and multipath terms. A first order butterworth filter with a cut off frequency of 0.1 Hz has been used to estimate $c\Delta t_{rcx/sta}$. After the corrections:

$$\begin{aligned} \rho_{rcx} - \rho_{sta} - c\Delta \hat{t}_{rcx/sta} - \hat{d}_{rcx} + \hat{d}_{sta} \\ \cong \varepsilon_{noise,rcx} + \varepsilon_{mp,rcx} + \varepsilon_{NLOS,rcx} - \varepsilon_{noise,sta} - \varepsilon_{mp,sta} \end{aligned} \quad \text{Eq. 5-70}$$

where

- \hat{d}_{rcx} and \hat{d}_{sta} are the estimated geometric ranges
- $c\Delta \hat{t}_{rcx/sta}$ is the estimated clock offset

The characterization of the pseudorange measurements can here be done according to 2 methodologies:

- The NLOS case is integrated in the nominal measurement model. For integrity purpose, it is then necessary to overbound the distribution of the LOS+NLOS case. This approach may not be rigorously adapted to the position computation algorithm (based on a Kalman filter) since it assumes that the measurement noises are white, which is not the case here. Anyways, for low elevations, the error is neither centered nor symmetric (and nor unimodal), thus, CDF overbounding cannot be applied to NLOS local errors. It is therefore not possible to overbound the CDF of the convolution of the pseudorange error sources with a centered normal distribution. However it is necessary to weight the measurements in the measurement noise covariance matrix (of the EKF here). A possible approach is to inflate empirically the nominal error model and to validate the behavior of the filter a posteriori. In this case the CDF overbound of the error distribution (that has been virtually centered) is used as the initial value prior to any inflation process.
- In the second approach, the case of NLOS reception is not included in the nominal measurement model. In this case, a mixture density model is adopted. By modelling with a mixture, we do not consider the error as the sum of NLOS error plus other errors (which lead to convolutions), but we assume that when a NLOS is received, the error density has a different expression. The model has the following expression:

$$f_{\varepsilon}(x) = P(LOS)f_{\varepsilon_{LOS}}(x) + P(NLOS)f_{\varepsilon_{NLOS}}(x) \quad \text{Eq. 5-71}$$

where $P(LOS)$ and $P(NLOS)$ are the probability of occurrence of LOS and NLOS receptions.

It is then necessary to estimate both distributions. It can be assumed that the error in the LOS configurations is centered. We isolate the LOS component based on the knowledge that the NLOS error is characterized by a positive bias on the pseudorange. Therefore the negative errors are mainly due to LOS configurations (and short NLOS). It is possible to estimate the product $P(LOS)f_{\varepsilon_{LOS}}$ with:

$$P(\widehat{LOS})f_{\varepsilon_{LOS}}(x) = \begin{cases} pdf_{\varepsilon}(x) & \text{if } x = 0 \\ H[-x]pdf_{\varepsilon}(x) + H[x]pdf_{\varepsilon}(-x) & \text{else} \end{cases} \quad \text{Eq. 5-72}$$

where $H[]$ denote the Heaviside function.

By subtracting the virtual LOS distribution, the remaining distribution is a good approximation of the error distribution contribution of the NLOS case.

$$P(\widehat{NLOS})f_{\varepsilon_{NLOS}}(x) = \max[f_{\varepsilon}(x) - P(\widehat{LOS})f_{\varepsilon_{LOS}}(x), 0] \quad \text{Eq. 5-73}$$

The norm of the whole mixture shall be one, and it is not the case due to the maximum operation (negative densities have been removed). A possible solution is to reduce the nominal region of the same negative area that have been removed by taking the maximum. Finally, the coefficients of the mixture are:

$$P(NLOS) = \int_{-\infty}^{+\infty} P(\widehat{NLOS})f_{\varepsilon_{NLOS}}(x)dx \quad \text{Eq. 5-74}$$

Then the reduced nominal model area expression is:

$$P(LOS) = 1 - P(NLOS) < \int_{-\infty}^{+\infty} P(\widehat{LOS})f_{\varepsilon_{LOS}}(x)dx \quad \text{Eq. 5-75}$$

The NLOS density is given by:

$$f_{\varepsilon_{NLOS}}(x) = \frac{P(\widehat{NLOS})f_{\varepsilon_{NLOS}}(x)}{\int_{-\infty}^{+\infty} P(\widehat{NLOS})f_{\varepsilon_{NLOS}}(x)dx} \quad \text{Eq. 5-76}$$

The LOS density must fulfill:

$$f_{\varepsilon_{LOS}}(x) = \frac{P(\widehat{LOS})f_{\varepsilon_{LOS}}(x)}{\int_{-\infty}^{+\infty} P(\widehat{LOS})f_{\varepsilon_{LOS}}(x)dx} \quad \text{Eq. 5-77}$$

It is then possible overbound $f_{\varepsilon_{LOS}}$ and $f_{\varepsilon_{NLOS}}$ separately. CDF overbounding can be used for $f_{\varepsilon_{LOS}}$, because it is, by construction, symmetric centered and unimodal. A distribution defined on \mathbb{R}_+ can be used to overbound $f_{\varepsilon_{NLOS}}$, i.e. a lognormal distribution.

An alternative approach would consist in separating the distribution into two part based on a threshold. In this case, the left part of the mixture would essentially be LOS and short NLOS (referred to as nominal). The right part would correspond to abnormal NLOS.

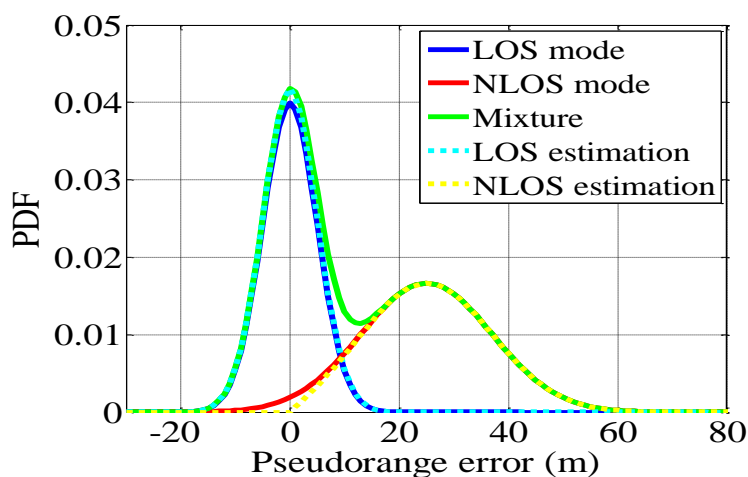


Figure 44 Principle of modelling

5.3.2.2.4 Results

The pseudorange error estimations have been concatenated by environment. The distribution functions are plotted in Figure 45, Figure 46 and Figure 47. These plots confirm that the statistic model is pessimistic, because the density of large pseudorange error due to NLOS is smaller. For low elevations ($\leq 30^\circ$) in urban environment, the mixture density model makes sense as illustrated by Figure 47. The NLOS error component is lower for suburban and even negligible in the case of beltway except for elevations between 0 and 10° . For high elevations ($> 40^\circ$), the errors due to NLOS are negligible in the three configurations.

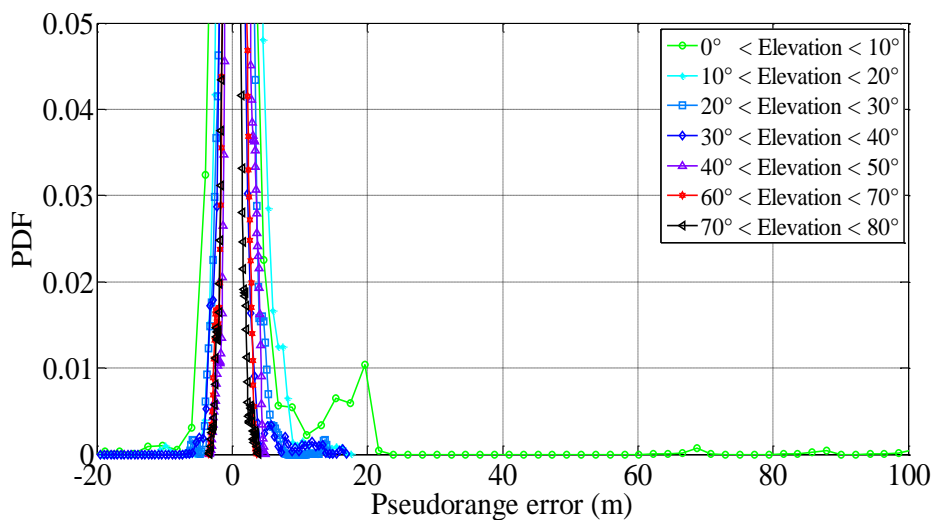


Figure 45 Pseudorange error due to local effects in beltway environment

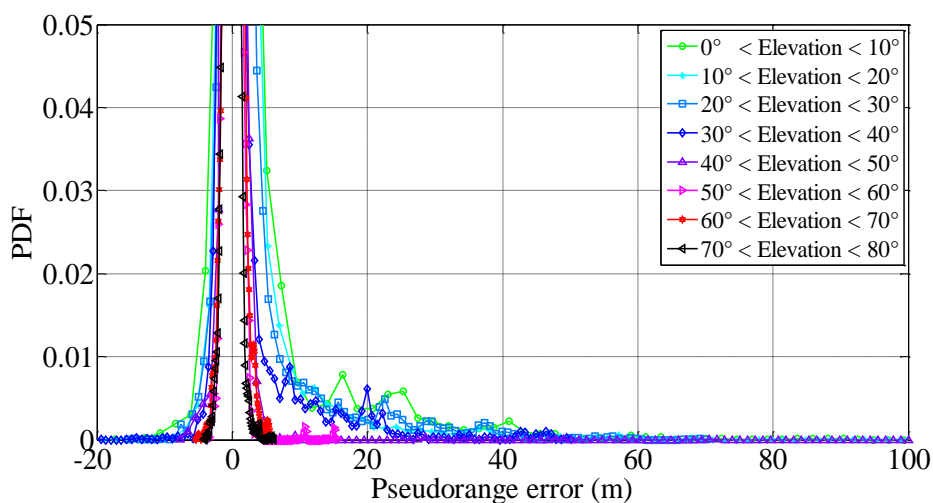


Figure 46 Pseudorange error due to local effects in suburban environment

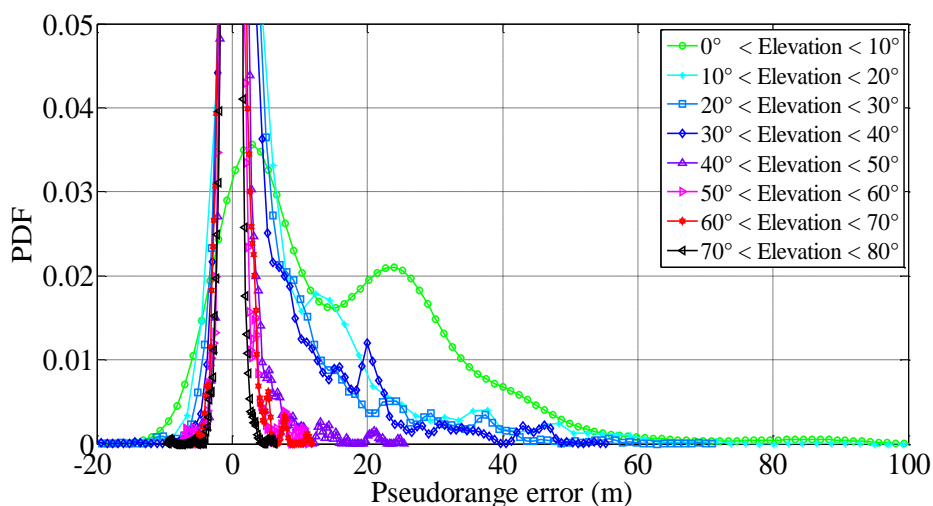


Figure 47 Pseudorange error due to local effects in urban environment

To define a nominal error model that includes NLOS error, it is necessary to overbound the pseudorange error distribution. In beltways, for elevations equal to or higher than 30° , in suburban areas, for elevations equal to or higher than 40° and in urban for elevations higher than 50° the distribution is symmetric, unimodal and its mean is less than 0.1 m. Thus for these elevation, the CDF overbounding method can be used. For low elevations, CDF overbounding is used as an initial value before any inflation. The results are summarized in Table 14. It is important to keep in mind that the model proposed is not rigorously valid for critical terrestrial applications as the number of samples is not sufficient with respect to the integrity risks. To be rigorously valid, the error model must also be representative of different cities which is not the case here. Moreover the noise and multipath error is included in the local effect contribution, which varies in function of the receiver, the modulations and the antenna.

Elevation (°)	Beltway		Suburban		Urban	
	σ_o	n_s	σ_o	n_s	σ_o	n_s
0-10	8.4	592	17	6038	30.3	537
10-20	4.9	675	16.5	11828	19.3	3255
20-30	4.2	727	16.2	6773	17	4459
30-40	2.2	1744	13.6	6557	15.6	2395
40-50	1.4	397	5.6	4705	7	2110
50-60	-	0	3.4	1456	3,1	967
60-70	1.2	418	1.6	3825	2.7	1448
70-80	1	1045	1.5	8979	2.6	3795
80-90	-	0	-	0	-	0

Table 14 Proposed weighting scheme for pseudorange errors due to local effects (including NLOS)

The second approach consists in excluding the NLOS error from the nominal model. The nominal mode and the NLOS lobe are processed independently. The nominal lobe is CDF overbounded, and the NLOS mode is fitted with a lognormal distribution. The lognormal is a good candidate because its support is positive and has an appropriate shape. The results are given in Table 15. By construction, the nominal error models have been reduced. The results also show important probabilities of NLOS reception for low elevations, especially in urban environment. However, in most cases, the high probability is due to the asymmetry of the main lobe (except for very low elevations in urban canyons). For high elevation when the probability associated to NLOS is small (for 40-50° in beltways for example), the magnitude of the NLOS errors are short.

Elevation (°)	Beltway				Suburban				Urban			
	σ_{LOS}	σ_{NLOS}	μ_{NLOS}	$P(NLOS)$	σ_{LOS}	σ_{NLOS}	μ_{NLOS}	$P(NLOS)$	σ_{LOS}	σ_{NLOS}	μ_{NLOS}	$P(NLOS)$
0-10	5.8	0.7	2.5	0.10	4.3	1.1	1.9	0.35	4.7	0.6	3	0.70
10-20	3.3	0.6	1	0.3	4.5	1.3	1.1	0.4	5.0	0.9	2.3	0.52
20-30	1.9	0.7	0.2	0.33	3.9	1.1	1.6	0.3	4.7	1	1.9	0.45
30-40	1.6	0.6	1.7	0.02	5.3	0.7	2.3	0.1	5.7	1	1.8	0.45
40-50	1.0	0.7	0	0.04	2.1	0.3	0.7	0.05	1.6	1.1	0.3	0.28
50-60	-	-	-	-	1.0	0.6	0	0.1	2.1	1	0	0.11
60-70	1	0.5	0	0.02	1.4	0.6	0	0.1	1.5	1	0	0.09

70-80	0.9	0	0	0	1.0	0	0	0	2.5	0	0	0
80-90	-	-	-	-	-	-	-	-	-	-	-	-

Table 15 Proposed mixture model for LOS and NLOS

In this case the probability of failure associated to the NLOS fault mode is the product of the probability of tracking a NLOS multiplied by the probability of failure provided that a NLOS is tracked.

5.3.3 Discussions

In urban environment, it has been proven that the pseudorange errors due to local effects (in particular NLOS) can reach more than 100 meters for elevations up to 40° . An approach to deal with NLOS errors for critical applications could consists in including these errors in the failure modes in the design of the integrity monitoring algorithm. In this case, the integrity monitoring algorithm has to protect against abnormally large NLOS. According to the statistic model and the results on real data, the probability of occurrence of large NLOS error is too high to rely on the integrity monitoring algorithm to protect from NLOS. Indeed, the integrity monitoring algorithm would have to deal with simultaneous failure which would make its design complex and leads to reduced availability. In dual constellation (ETC) the probability of occurrence of simultaneous NLOS would be even higher, and may require to design an integrity monitoring algorithms able to detect 3 or more faulty measurements simultaneously. This approach does not appear realistic, thus, two more realistic approaches are proposed and will be detailed in section 0.

First approach: inclusion of local effects in the nominal model:

The pseudorange error distribution models that have been estimated can be used, after using an appropriate overbounding technique, either to add an extra term to the nominal error model in urban environment or to inflate the covariance matrix by an empirical factor. However including NLOS error in the nominal model may increase too much the covariance matrix of the GNSS measurements, and thus would lead to large magnitudes for confidence radiuses (reducing the availability). This approach is feasible provided that the NLOS error is characterized with enough certainty.

Second approach: detection and exclusion of abnormal local effects prior to the integrity monitoring algorithm

The second approach consists in protecting the receiver against the NLOS prior to the integrity monitoring algorithm. The NLOS detection is feasible by using 3D city models [Obst et al., 2012], use of a fisheye camera [Meguro et al., 2009] located on the roof of the vehicle, by using antenna array to estimate angle of arrival [Keshvadi et al., 2011] or by applying elevation and C/N_0 masks. It has been shown in Figure 46 and Figure 47 that large NLOS biases has occurred for elevation up to 40° in urban and suburban environments. The feasibility of applying such masks elevation mask will be discussed in chapter 7.

We then investigate the correlation between the pseudorange error and the C/N_0 . All the pseudorange errors have been concatenated and have been plotted as a function of the C/N_0 in Figure 48. It can be inferred from Figure 48 that, unlike what has shown the simulations, applying a C/N_0 mask at 30 dB-Hz is not sufficient to protect against dangerous NLOS events. However, applying a higher mask (≥ 40 dB-Hz) could be sufficient.

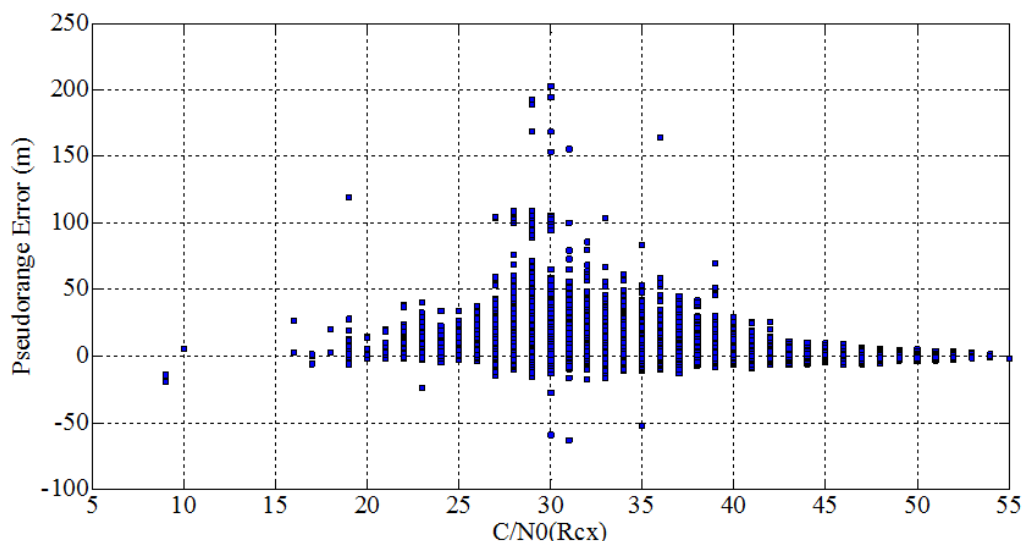


Figure 48 Pseudorange error as a function of the C/N_0 for 2h40 of data in Toulouse

Intuitively, one would be tempted to monitor the time evolution of C/N_0 to detect this sort of outliers. Intuitively, the C/N_0 should drop suddenly due to signal attenuation when a NLOS is tracked. The evolution of this metric as estimated by the mass market receiver used in the data collection (U-blox 6) is illustrated in for GPS L1 C/A on 100 seconds of the measurement campaign which corresponds to a period of time in dense urban. The satellite has an elevation of 40° during the period plotted. The fluctuations of the metric are chaotic and 5 to 10 dB-Hz drops occurs frequently between 60 and 100 second due to local effects. The C/N_0 variations over time (in Figure 49) can be compared with the norm of the residuals of the EKF that are coarse estimation of the pseudorange error by the EKF (in Figure 50).

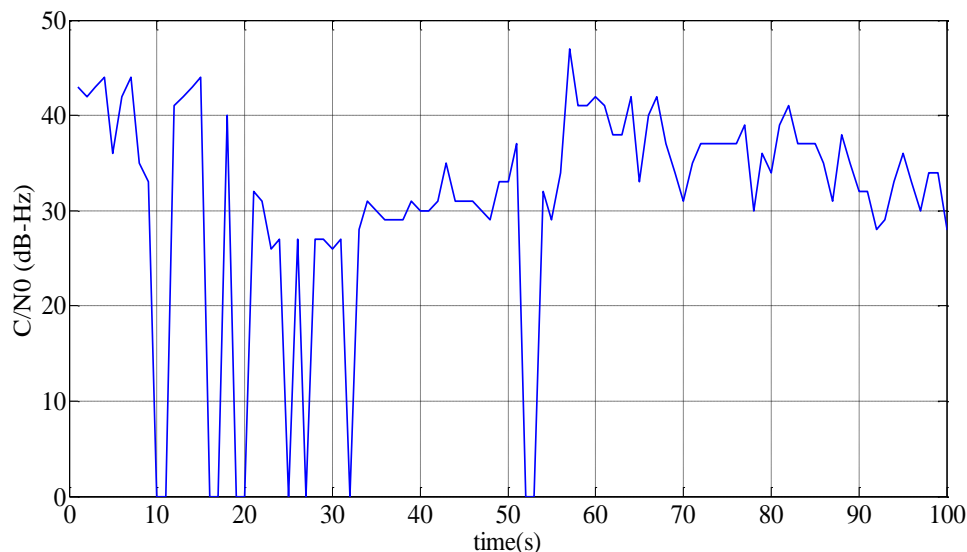


Figure 49 C/N_0 estimation in Toulouse downtown for GPS L1 C/A for Satellite 15, elevation of 40°

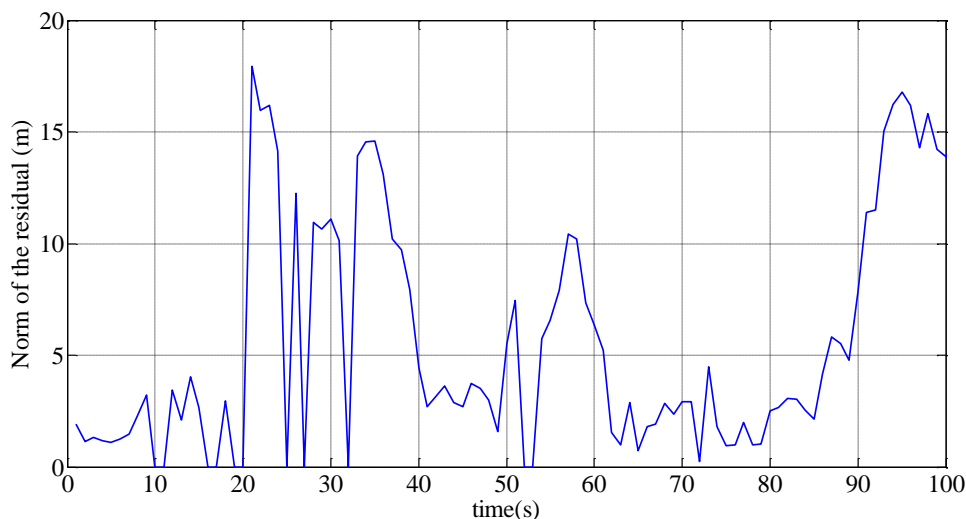


Figure 50 EKF residuals in Toulouse downtown for GPS L1 C/A for Satellite 15, elevation of 40°

Thus the detection of NLOS with C/N_0 variation monitoring does not seem feasible.

To be used for critical applications, a NLOS exclusion technique shall be associated to a probability of miss exclusion ($P_{MD,NLOS\ detector}$). For techniques such as fisheye camera based detection, the missed detection of NLOS can be caused by wrong attitude estimation, artefacts in the images and failure in image processing (due to clouds for instance). It is not feasible to associate a reliable $P_{MD,NLOS\ detector}$ to such detection method.

Anyway excluding all NLOS may degrade the accuracy in urban environment because some NLOS are affected by negligible biases, and excluding them may degrade the quality of the geometry.

5.4 Conclusions

The nominal error models of all the sensors that will be used by the proposed solutions have been firstly presented. The faults have been defined as errors that are not represented by the nominal error distributions. For GNSS, the satellite fault is the only event which is well characterized in term of magnitude and probability of occurrence. However, in suburban and urban environment, the local effects can also result in large measurement errors. These errors have been modelled statistically and observed on real measurement. Two approaches are then proposed to deal with local effects. The first approach consists in inflating the nominal error model so that it covers those large errors which are frequent. The second approach consists in selecting the measurements based on different indicators such as C/N_0 or elevation, in order to exclude these errors. Therefore, the local errors will not be included in the GNSS failure modes (which is more suitable these errors are frequent).

5.5 References

- [Beaulieu et al., 1995] Beaulieu, N.C.; Abu-Dayya, A.A.; McLane, P.J., "Estimating the distribution of a sum of independent lognormal random variables," *Communications, IEEE Transactions on*, vol.43, no.12, pp.2869,, Dec. 1995
- [Betaille et al., 2013] Betaille, D.; Peyret, F.; Ortiz, M.; Miquel, S.; Fontenay, L., "A New Modeling Based on Urban Trenches to Improve GNSS Positioning Quality of Service in Cities," *Intelligent Transportation Systems Magazine, IEEE*, vol.5, no.3, pp.59,70, Fall 2013
- [Betaille et al., 2014] Betaille, D., Peyret, F., Ortiz, M., Miquel, S., Godan, F., "Improving Accuracy and Integrity with a Probabilistic Urban Trench Modeling," *Proceedings of the 27th International Technical Meeting of The Satellite Division of the Institute of Navigation (ION GNSS+ 2014)*, Tampa, Florida, September 2014, pp. 1891-1896.
- [Bhatti, 2007] Bhatti, U. (2007). Improved integrity algorithms for integrated GPS/INS systems in the presence of slowly growing errors. Ph.D. thesis, Imperial College London
- [Borras et al., 1998] J. Borras, P. Hatrack, and N. Mandayam, "Decision theoretic framework for nlos identification," in *Vehicular Technology Conference, 1998. VTC 98. 48th IEEE*, vol. 2. IEEE, 1998, pp. 1583–1587
- [Carcanague, 2013] S. Carcanague, "Low-cost GPS/GLONASS Precise Positioning Algorithm in Constrained Environment," Ph.D. dissertation, Institut National Polytechnique de Toulouse, 2013.
- [DeCleene, 2000] DeCleene, Bruce, "Defining Pseudorange Integrity - Overbounding," *Proceedings of the 13th International Technical*

- Meeting of the Satellite Division of The Institute of Navigation (ION GPS 2000), Salt Lake City, UT, September 2000, pp. 1916-1924
- [El-Diasty and Pagiatakis, 2008] El-Diasty, M. and Pagiatakis, S. Calibration and stochastic modeling of inertial navigation sensor errors. *Journal of Global Positioning Systems*, 7, 2 (2008), 170—182
- [ESA, 2005] European Space Agency, “Galileo Integrity Concept”, Technical Note, July 2005
- [Euler et al., 1996] Euler, -. I. H.-J., Hill, C. D., AG, L., & Muller, D.-I. U. (1996). Real-Time Precise GPS for Railroad Mapping. Paper presented at the Position Location and Navigation Symposium, Atlanta, GA, USA
- [Fenton, 1960] Fenton, L., "The Sum of Log-Normal Probability Distributions in Scatter Transmission Systems," in *Communications Systems*, IRE Transactions on , vol.8, no.1, pp.57-67, March 1960
- [Groves, 2013] Groves, P.D. *Principles of GNSS, Inertial, and Multisensor Integrated Navigation Systems*; Artech House: London, UK, 2013
- [Guvenc, 2007] I. Guvenc, C. Chong, and F. Watanabe, “Nlos identification and mitigation for uwb localization systems,” in *Wireless Communications and Networking Conference, 2007. WCNC 2007. IEEE*. IEEE, 2007, pp. 1571–1576
- [Have, 2003] Have D., “Reference set of parameters for RAIM availability simulations” Working paper Sofréavia, 8-9 April, Madrid Spain, 2003
- [ICAO, 2009] ICAO, MOPS for GPS/ABAS Airborne Equipment, Apr. 2009
- [IEEE Std 952-1997] IEEE Std 952-1997, "Guide and Test Procedure for Single Axis Interferometric Fiber Optic Gyros," IEEE, 1997, p.63
- [Julien, 2005] Julien O., “Design of Galileo L1F tracking loops”, Ph.D. thesis, University of Calgary, Department of Geomatics Engineering, 2005
- [Jia and Buehrer, 2010] T. Jia and R. Buehrer, “Collaborative position location with nlos mitigation,” in *Personal, Indoor and Mobile Radio Communications Workshops (PIMRC Workshops), 2010 IEEE 21st International Symposium on*. IEEE, 2010, pp. 267–271
- [Kasdin and Walter, 1992] N.J. Kasdin and T. Walter, “Discrete Simulation of Power Law Noise”, *Proc. 1992 IEEE Frequency Control Symposium*, pp. 274-283, May 1992
- [Keshvadi et al., 2011] Keshvadi, M. H., A. Broumandan, and G. Lachapelle, “Analysis of GNSS Beamforming and Angle of Arrival Estimation in Multipath Environments,” *Proc ION ITM, San Diego, CA, January 2011*, pp. 427- 435
- [Klobuchar, 1987] Klobuchar J.A., “Ionospheric Time-Dealy Algorithm for Single-

- Frequency GPS Users?"; IEEE Transactions on Aerospace and Electronic Systems, vol AES-23, no.3, 1987
- [Landmark 01, datasheet] <http://www.gliadatorotechnologies.com/Products/LMRK/IMU/LandMark-IMU-01.html>
- [Lehner and Steingass, 2005] Lehner, Andreas, Steingass, Alexander, "A Novel Channel Model for Land Mobile Satellite Navigation," Proceedings of the 18th International Technical Meeting of the Satellite Division of The Institute of Navigation (ION GNSS 2005), Long Beach, CA, September 2005, pp. 2132-2138
- [Martineau, 2008] A. Martineau, "Performance of Receiver Autonomous Integrity Monitoring (RAIM) for Vertically Guided Approaches", PhD thesis Institut National Polytechnique de Toulouse, 2008
- [Meguro et al., 2009] Meguro, J., Murata, T., Takiguchi, J.-I., Amano, Y. and Hashizume, T. (2009). GPS Multipath Mitigation for Urban Area Using Omnidirectional Infrared Camera. IEEE Transactions on Intelligent Transportation Systems, Vol. 10, No. 1, 22–30
- [Obst et al., 2012] Obst, M., Bauer, S. and Wanielik, G. (2012). Urban Multipath Detection and mitigation with Dynamic 3D Maps for Reliable Land Vehicle Localization. Proceedings of IEEE/ION PLANS 2012, Monterey, C
- [Oestges et al., 1999] Oestges, C.; Saunders, S.R.; Vanhoenacker-Janvier, D., "Physical statistical modelling of the land mobile satellite channel based on ray tracing," Microwaves, Antennas and Propagation, IEE Proceedings , vol.146, no.1, pp.45,49, Feb 1999
- [Parsons, 1992] Parsons, D., "The mobile radio propagation channel", (Pentech Press, London, 1992)
- [Perez-Fontan et al., 2001] F.Perez-Fontan, M. Vazquez-Castro, C.E. Cabado, J.P. Garcia, E. Kubista, "Statistical modeling of the LMS channel," Vehicular Technology, IEEE Transactions on , vol.50, no.6, pp.1549-1567, Nov 2001
- [Prieto-Cerdeira et al., 2010] Prieto-Cerdeira, R., Perez-Fontan, F., Burzigotti, P., Bolea-Alamañac, A. and Sanchez-Lago, I. (2010), Versatile two-state land mobile satellite channel model with first application to DVB-SH analysis. Int. J. Satell. Commun. Network., 28:, no 5-6, pp. 291–315, 2010
- [Ratti et al., 2002] Ratti, C., S. Di Sabatino, F. Caton, R. Britter, M. Brown, and S. Burian (2002): "Analysis of 3-D urban databases with respect to pollution dispersion for a number of European and American cities". Water, Air and Soil Pollution – Focus 2, 459-469
- [RTCA, 2006] RTCA Inc., "Minimum Operational Performance Standards for Global Positioning System/Wide Area Augmentation System Airborne Equipment", RTCA DO-229D, Dec. 13, 2006

- [Salos et al., 2010] Salós, D.; Macabiau, C.; Martineau, A.; Bonhoure, B.; Kubrak, D., "Nominal GNSS pseudorange measurement model for vehicular urban applications," Position Location and Navigation Symposium (PLANS), 2010 IEEE/ION, vol., no., pp.806,815, 4-6 May 2010
- [Salos, 2012] Salos Andrés, Carlos Daniel (2012) Integrity monitoring applied to the reception of GNSS signals in urban environments
- [Saunders, 1991] Saunders, S.R., "Diffraction modelling of mobile radio wave propagation in built-up areas", PhD Dissertation, Brunel University, 1991
- [Spangenberg, 2009] M. Spangenberg. Safe navigation for vehicles. PhD thesis, Institut National Polytechnique de Toulouse, 2009
- [Strus et al., 2007] Strus, Joseph M., Kirkpatrick, Michael, Sinko, James W., "Development of a High Accuracy Pointing System for Maneuvering Platforms," Proceedings of the 20th International Technical Meeting of the Satellite Division of The Institute of Navigation (ION GNSS 2007), Fort Worth, TX, September 2007, pp. 2541-2549
- [UIC Leaflet 506] UIC Leaflet 506 - Rules governing application of the enlarged GA, GB, GB1, GB2, GC and G13 gauges
- [Van Dierendonck, 1996] Van Dierendonck, A. J., Global Positioning System: Theory & Applications, (Progress in Astronautics and Aeronautics), vol. 1. Washington, D.C.: AIAA, 1996, ch. 8; ISBN1-56347-106-X
- [Van Dierendonck et al., 1992] Van Dierendonck, A.J., P. Fenton and T. Ford (1992), Theory and Performance of Narrow Correlator Technology in GPS Receiver, NAVIGATION: Journal of The Institute of Navigation, Vol. 39, No.3, pp. 265-283
- [Walter et al., 2013] Walter, Todd, Blanch, Juan, Choi, Myung Jun, Reid, Tyler, Enge, Per, "Incorporating GLONASS into Aviation RAIM Receivers," Proceedings of the 2013 International Technical Meeting of The Institute of Navigation, San Diego, California, January 2013, pp. 239-249
- [Walter et al., 2014] Walter, T., Blanch, J., Enge, P., "Reduced Subset Analysis for Multi-Constellation ARAIM," Proceedings of the 2014 International Technical Meeting of The Institute of Navigation, San Diego, California, January 2014, pp. 89-98
- [Woodman, 2007] O. J. Woodman, "An introduction to inertial navigation", Report Number 696, University of Cambridge Computer Laboratory, August 2007

6 DESIGN OF THE FUSION ALGORITHM

This chapter describes the architecture of the hybridized solutions for the train control and ETC. For train control, a dual system approach has been proposed in chapter 4 for which both subsystems have the same integration algorithms. For ETC, a unique system using two constellations has been proposed.

The use of additional sensors to augment the GNSS is proposed to enhance the performances of the positioning system terms of accuracy, integrity, availability (in case of GNSS outage or urban canyons), and continuity. Subsection 6.1 describes the principle of the EKF based fusion algorithm. The two architectures proposed are first validated by means of realistic simulations in subsection 6.2. Indeed it is possible to model the sensors by generating ideal outputs to which we add the error models that have been described in section 5.1. This approach also enables to coarsely assess the performance of our system in the open sky configuration.

The behaviors of the proposed solutions are tested on the real data campaign conducted in Toulouse and described in section 5.3.2.2. The accuracy improvement obtained by enhancing the solution with additional measurement from motion constraints and the additional sensors is looked at.

6.1 Design of the hybridization filter

The section firstly describes the basic principle of standard and extended Kalman Filters, and then derived the theoretical expression of the elements that are involved in the fusion algorithm.

6.1.1 Kalman Filter

The Kalman Filter [Kalman, 1960] is a recursive algorithm which estimates the states of a dynamic system based on noisy observations. The Kalman Filter uses a priori knowledge of the statistical and

deterministic properties of the system to obtain optimal estimations. It is a Bayesian estimation technique that aims at minimizing a risk function: the mean square error (MSE). The model of the KF is described by two equations that are defined as the process model and the measurement model. The process model describes the temporal variations of the states over time and the observation model describes the relation between the measurements and the states. Unlike the Least-Square algorithm which estimation is only based on the measurements of the current epochs, Kalman filter estimation involves the state prediction, which is calculated from previous epochs. Thus Kalman filter introduces an additional correlation in time of the error in the states' estimations.

As an introduction, let us assume that the process and measurements models are linear. In a continuous-time Kalman filter, the time variations of the states are assumed to verify the following model:

$$\dot{x}(t) = F(t)x(t) + w(t) \quad \text{Eq. 6-1}$$

where

- $x(t)$ is the state vector
- $F(t)$ is the system dynamic matrix
- $w(t)$ is the process driving noise, its covariance matrix is denoted $Q(t)$

It is assumed that the measurements can be related to the states with the following expression:

$$z(t) = H(t)x(t) + \eta(t) \quad \text{Eq. 6-2}$$

where:

- $z(t)$ is the measurement (or observation) vector
- $H(t)$ is the observation matrix
- $\eta(t)$ is the measurement noise, its covariance matrix is denoted $R(t)$

The discretized form of the Kalman Filter can be obtained by applying Taylor expansions to the two models. Let's denote T_s the sampling period of the filter, the process model becomes:

$$x_{k+1} = F_k x_k + w_k \quad \text{Eq. 6-3}$$

where:

- $x_k = x(kT_s)$
- $F_k = e^{F(t)T_s} \cong I + F(t)T_s$ at the first order
- w_{k+1} is the process noise which covariance matrix is denoted Q_k , at the first order
 $Q_k = Q(t)T_s$

The discrete Kalman Filter measurement model corresponds to:

$$z_k = H_k x_k + \eta_k \quad \text{Eq. 6-4}$$

where:

- $z_k = z(kT_s)$
- $H_k = H(kT_s)$
- η_k is the measurement noise which covariance matrix is $R_k = R(kT_s)$

The Kalman filter algorithm is generally separated into two steps that are computed recursively.

The first step which is called prediction consists in predicting the state ($\hat{x}_{k+1|k}$) and the state error covariance ($P_{k+1|k}$) based on the previous state ($\hat{x}_{k|k}$) and error covariance ($P_{k|k}$) with the following equations:

$$\hat{x}_{k+1|k} = F_k \hat{x}_{k|k} \quad \text{Eq. 6-5}$$

$$P_{k+1|k} = F_k P_{k|k} F_k^T + Q_k \quad \text{Eq. 6-6}$$

The Kalman Gain is then computed with:

$$K_{k+1|k+1} = P_{k+1|k} H_{k+1}^T (H_{k+1} P_{k+1|k} H_{k+1}^T + R_{k+1})^{-1} \quad \text{Eq. 6-7}$$

The second step is called update, it consists in updating the state ($\hat{x}_{k+1|k+1}$) and the error estimation covariance matrix ($P_{k+1|k+1}$) a posteriori with

$$\hat{x}_{k+1|k+1} = \hat{x}_{k+1|k} + K_{k+1} (z_{k+1} - H_{k+1} \hat{x}_{k+1|k}) \quad \text{Eq. 6-8}$$

$$P_{k+1|k+1} = P_{k+1|k} - K_{k+1} H_{k+1} P_{k+1|k} \quad \text{Eq. 6-9}$$

6.1.2 Extension to the non-linear case: Extended Kalman Filter

The EKF is an extension of the Kalman Filter adapted to the case of non-linear system model. The discrete EKF state model is described by the following equations:

$$x_{k+1} = f(x_k) + w_k \quad \text{Eq. 6-10}$$

and

$$z_k = h(x_k) + v_k \quad \text{Eq. 6-11}$$

As in the linear Kalman Filter, the EKF consists in calculating the prediction with:

$$\hat{x}_{k+1|k} = f(\hat{x}_{k|k}) \quad \text{Eq. 6-12}$$

$$P_{k+1|k} = F_k P_{k|k} F_k^T + Q_k \quad \text{Eq. 6-13}$$

where:

- $F_k = \frac{\partial f}{\partial x} \Big|_{\hat{x}_{k|k}}$ is the Jacobian of the state transition function (f).

The Kalman Gain is calculated with:

$$K_{k+1|k+1} = P_{k+1|k} H_{k+1}^T (H_{k+1} P_{k+1|k} H_{k+1}^T + R_{k+1})^{-1} \quad \text{Eq. 6-14}$$

where:

- $H_{k+1} = \frac{\partial h}{\partial x} \Big|_{\hat{x}_{k+1|k}}$ is the Jacobian matrix of the observation function (h).

Finally, the update of the states and their associated covariance matrix is calculated with:

$$\hat{x}_{k+1|k+1} = \hat{x}_{k+1|k} + K_{k+1} [z_{k+1} - h(\hat{x}_{k+1|k})] \quad \text{Eq. 6-15}$$

$$P_{k+1|k+1} = P_{k+1|k} - K_{k+1} H_{k+1} P_{k+1|k} \quad \text{Eq. 6-16}$$

For fusion between GNSS and inertial measurements, the state vector usually includes the inertial position errors. In tight coupling the observations consists in the differences between the predicted pseudoranges and the observed pseudoranges. The relation between position error and pseudorange errors are non-linear. Moreover, the predicted position is estimated from IMU with the mechanization step which is a non-linear operation. Therefore it is necessary to use either a linearized Kalman filter or an EKF. A closed-loop architecture has been used in this work because of the quality of the inertial sensors. Thus, the fusion between GNSS and other sensors is done by means of an extended Kalman filter because the only position that are available to linearized the models arounds are $\hat{x}_{k|k}$ and $\hat{x}_{k+1|k+1}$.

6.1.3 Design of the basic fusion algorithm

It has been proposed to fuse GNSS and INS for the train control and ETC cases of study. The IMU measurements are processed with a 3D quaternion-based mechanization for both applications. It is proven in [Syed et al., 2007] that even if not cost effective, full-sensor configuration with 3D mechanization performs the best in terms of drift (compared to IMU with less than 6 sensors). This section describes the basic EKF that is common to both applications. Then, the ways to improve the performances of the EKF by simple means such as the inclusion of pseudorange rate measurements or the use of motion constraints are investigated. Finally, the filter is augmented to integrate data from additional sensors for the two applications in 6.1.5 and 6.1.6.

6.1.3.1 State vector

When fusing GNSS and INS, the state vector integrates the position, velocity, attitude and inertial sensors bias errors. For medium to low grade sensors such as those that are used in this thesis, the scale factor errors on the inertial measurement must be estimated as it may not be negligible. Even if not investigated in this thesis, it is also possible to include sensor misalignment in the state vector. Finally, in tight coupling, the GNSS clock bias and clock drift errors shall be estimated to predict pseudoranges. Thus, they must be included in the state vector. In this thesis, an error state EKF is used, thus the state vector (and measurements) are preceded by the term δ .

In summary, the state vector (δx) is defined here as :

$$\delta x = \begin{bmatrix} \delta P \\ \delta V \\ \delta \phi \\ \delta b_a \\ \delta b_g \\ \delta S_a \\ \delta S_g \\ \delta(c\Delta t_{offset}) \\ \delta(c\Delta t_{drift}) \end{bmatrix} \quad \text{Eq. 6-17}$$

where:

- $\delta P = \begin{bmatrix} \delta P_E \\ \delta P_N \\ \delta P_U \end{bmatrix}$ is the position error vector in the East, North, Up (ENU) navigation frame
- $\delta V = \begin{bmatrix} \delta V_E \\ \delta V_N \\ \delta V_U \end{bmatrix}$ is the velocity error in the ENU navigation frame
- $\delta \phi = \begin{bmatrix} \delta \theta \\ \delta \gamma \\ \delta \psi \end{bmatrix}$ are the errors in the estimation of the attitude angles (pitch, roll, yaw)
- $\delta b_a = \begin{bmatrix} \delta b_{a_x} \\ \delta b_{a_y} \\ \delta b_{a_z} \end{bmatrix}$ are the errors on the accelerometer biases
- $\delta b_g = \begin{bmatrix} \delta b_{g_x} \\ \delta b_{g_y} \\ \delta b_{g_z} \end{bmatrix}$ are the errors on the gyroscope biases
- $\delta S_a = \begin{bmatrix} \delta S_{a_x} \\ \delta S_{a_y} \\ \delta S_{a_z} \end{bmatrix}$ are the errors on the accelerometers scale factors
- $\delta S_g = \begin{bmatrix} \delta S_{g_x} \\ \delta S_{g_y} \\ \delta S_{g_z} \end{bmatrix}$ are the errors on the gyroscopes scale factors
- $\delta(c\Delta t_{offset})$ is the GNSS receiver clock offset.

- $\delta(c\Delta t_{drift})$ is the GNSS receiver clock drift

This basic state vector is used for single constellation GNSS and INS fusion. The extension to dual-constellations receiver is detailed in 6.1.6.

6.1.3.2 Process model

The next step consists in defining the model that describes the dynamic of the system. The F matrix is obtained by applying the perturbation method [Shin, 2001] to each state. The methodology used is derived from [Angrisano, 2010] and [Shin, 2001].

$$F = \begin{bmatrix} F_{PP} & F_{PV} & F_{P\phi} & \mathbf{0}_{3 \times 3} & \mathbf{0}_{3 \times 3} & \mathbf{0}_{3 \times 3} & \mathbf{0}_{3 \times 3} & \mathbf{0}_{3 \times 1} & \mathbf{0}_{3 \times 1} \\ F_{VP} & F_{VV} & F_{V\phi} & \hat{C}_b^n & \mathbf{0}_{3 \times 3} & \hat{C}_b^n f^b & \mathbf{0}_{3 \times 3} & \mathbf{0}_{3 \times 1} & \mathbf{0}_{3 \times 1} \\ F_{\phi P} & F_{\phi V} & F_{\phi\phi} & \mathbf{0}_{3 \times 3} & -\hat{C}_b^n & \mathbf{0}_{3 \times 3} & -\hat{C}_b^n \omega^b & \mathbf{0}_{3 \times 1} & \mathbf{0}_{3 \times 1} \\ \mathbf{0}_{3 \times 3} & \mathbf{0}_{3 \times 3} & \mathbf{0}_{3 \times 3} & \beta_{b_a} & \mathbf{0}_{3 \times 3} & \mathbf{0}_{3 \times 3} & \mathbf{0}_{3 \times 3} & \mathbf{0}_{3 \times 1} & \mathbf{0}_{3 \times 1} \\ \mathbf{0}_{3 \times 3} & \mathbf{0}_{3 \times 3} & \mathbf{0}_{3 \times 3} & \mathbf{0}_{3 \times 3} & \beta_{b_g} & \mathbf{0}_{3 \times 3} & \mathbf{0}_{3 \times 3} & \mathbf{0}_{3 \times 1} & \mathbf{0}_{3 \times 1} \\ \mathbf{0}_{3 \times 3} & \beta_{s_a} & \mathbf{0}_{3 \times 3} & \mathbf{0}_{3 \times 1} & \mathbf{0}_{3 \times 1} \\ \mathbf{0}_{3 \times 3} & \beta_{s_g} & \mathbf{0}_{3 \times 1} & \mathbf{0}_{3 \times 1} \\ \mathbf{0}_{1 \times 3} & 0 & 1 \\ \mathbf{0}_{1 \times 3} & 0 & 0 \end{bmatrix} \quad \text{Eq. 6-18}$$

where:

- $F_{PP} = \begin{bmatrix} \frac{V_U}{N+h} & \frac{V_N \sin(\varphi)}{M+h} & \frac{V_E \tan(\varphi)}{M+h} & \frac{-V_E}{N+h} \\ 0 & & \frac{V_U}{M+h} & \frac{-V_N}{M+h} \\ 0 & & 0 & 0 \end{bmatrix}$
- $F_{PV} = I_{3 \times 3}$
- $F_{P\phi} = \mathbf{0}_{3 \times 3}$
- $F_{VP} = \begin{bmatrix} 0 & \frac{2\omega_{ie}^n V_U \sin(\varphi)}{M+h} + \frac{V_E V_N}{(M+h)(N+h) \cos^2(\varphi)} & \frac{V_E V_U - V_E V_N \tan(\varphi)}{(N+h)^2} \\ 0 & \frac{-2\omega_{ie}^n V_E \cos(\varphi)}{M+h} - \frac{V_E^2}{(M+h)(N+h) \cos^2(\varphi)} & \frac{V_N V_U}{(M+h)^2} + \frac{V_E^2 \tan(\varphi)}{(N+h)^2} \\ 0 & \frac{-2\omega_{ie}^n V_E \sin(\varphi)}{M+h} & \frac{-V_E^2}{(N+h)^2} - \frac{V_N^2}{(M+h)^2} + \frac{2g}{R+h} \end{bmatrix}$
- $F_{VV} = \begin{bmatrix} \frac{V_N \tan(\varphi)}{N+h} - \frac{V_U}{N+h} & 2\omega_{ie}^n \sin(\varphi) + \frac{V_E \tan(\varphi)}{N+h} & -2\omega_{ie}^n \cos(\varphi) - \frac{V_E}{N+h} \\ -2\omega_{ie}^n \sin(\varphi) - \frac{2V_E \tan(\varphi)}{N+h} & -\frac{V_U}{M+h} & -\frac{V_N}{M+h} \\ 2\omega_{ie}^n \cos(\varphi) + \frac{2V_E}{N+h} & \frac{V_N}{M+h} & 0 \end{bmatrix}$
- $F_{V\phi} = (f^b \times) = \begin{bmatrix} 0 & f_U & -f_N \\ -f_U & 0 & f_E \\ f_N & -f_E & 0 \end{bmatrix}$
- $F_{\phi P} = \begin{bmatrix} 0 & 0 & \frac{V_N}{(M+h)^2} \\ 0 & -\frac{\omega_{ie}^n \sin(\varphi)}{M+h} & -\frac{V_E}{(N+h)^2} \\ 0 & \frac{\omega_{ie}^n \cos(\varphi)}{M+h} + \frac{V_E}{(M+h)(N+h) \cos^2(\varphi)} & -\frac{V_E \tan(\varphi)}{(N+h)^2} \end{bmatrix}$

$$\begin{aligned}
 \bullet \quad F_{\phi V} &= \begin{bmatrix} 0 & -\frac{1}{M+h} & 0 \\ \frac{1}{N+h} & 0 & 0 \\ \frac{\tan(\varphi)}{N+h} & 0 & 0 \end{bmatrix} \\
 \bullet \quad F_{\phi\phi} &= \begin{bmatrix} 0 & \omega_{ie}^n \sin(\varphi) + \frac{V_E \tan(\varphi)}{N+h} & -\omega_{ie}^n \cos(\varphi) - \frac{V_E}{N+h} \\ -\omega_{ie}^n \sin(\varphi) - \frac{V_E \tan(\varphi)}{N+h} & 0 & -\frac{V_N}{M+h} \\ \omega_{ie}^n \cos(\varphi) - \frac{V_E}{N+h} & \frac{V_N}{M+h} & 0 \end{bmatrix} \\
 \bullet \quad \beta_{b_a} &= \text{diag} \begin{bmatrix} -\frac{1}{\tau_{b_{ax}}} \\ -\frac{1}{\tau_{b_{ay}}} \\ -\frac{1}{\tau_{b_{az}}} \end{bmatrix}, \beta_{b_g} = \text{diag} \begin{bmatrix} -\frac{1}{\tau_{b_{gx}}} \\ -\frac{1}{\tau_{b_{gy}}} \\ -\frac{1}{\tau_{b_{gz}}} \end{bmatrix}, \beta_{s_a} = \text{diag} \begin{bmatrix} -\frac{1}{\tau_{s_{ax}}} \\ -\frac{1}{\tau_{s_{ay}}} \\ -\frac{1}{\tau_{s_{az}}} \end{bmatrix}, \beta_{s_g} = \text{diag} \begin{bmatrix} -\frac{1}{\tau_{s_{gx}}} \\ -\frac{1}{\tau_{s_{gy}}} \\ -\frac{1}{\tau_{s_{gz}}} \end{bmatrix}
 \end{aligned}$$

F must be discretized to obtain F_k . Then, the process noise covariance matrix (Q) is given by:

$$Q = \begin{bmatrix} q_P & 0_{3 \times 3} & 0_{3 \times 1} & 0_{3 \times 1} \\ 0_{3 \times 3} & q_V & 0_{3 \times 3} & 0_{3 \times 1} & 0_{3 \times 1} \\ 0_{3 \times 3} & 0_{3 \times 3} & q_\phi & 0_{3 \times 3} & 0_{3 \times 3} & 0_{3 \times 3} & 0_{3 \times 3} & 0_{3 \times 1} & 0_{3 \times 1} \\ 0_{3 \times 3} & 0_{3 \times 3} & 0_{3 \times 3} & q_{b_a} & 0_{3 \times 3} & 0_{3 \times 3} & 0_{3 \times 3} & 0_{3 \times 1} & 0_{3 \times 1} \\ 0_{3 \times 3} & 0_{3 \times 3} & 0_{3 \times 3} & 0_{3 \times 3} & q_{b_g} & 0_{3 \times 3} & 0_{3 \times 3} & 0_{3 \times 1} & 0_{3 \times 1} \\ 0_{3 \times 3} & q_{s_a} & 0_{3 \times 3} & 0_{3 \times 1} & 0_{3 \times 1} \\ 0_{3 \times 3} & q_{s_g} & 0_{3 \times 1} & 0_{3 \times 1} \\ 0_{1 \times 3} & q_{offset} & 0 \\ 0_{1 \times 3} & 0 & q_{drift} \end{bmatrix} \quad \text{Eq. 6-19}$$

The process noise for the position error states is caused by implementation and rounded errors [Vezinet, 2014]. The diagonal term of its covariance matrix q_P are set to 10^{-11} in this work. The process noise on the velocity and attitude error states is respectively due to the accelerometer and gyroscope noises which values are given in chapter 5:

$$q_V = \hat{C}_b^n \text{diag} \begin{bmatrix} \sigma_{a_x}^2 \\ \sigma_{a_y}^2 \\ \sigma_{a_z}^2 \end{bmatrix} (\hat{C}_b^n)^T, \quad q_\phi = \hat{C}_b^n \text{diag} \begin{bmatrix} \sigma_{g_x}^2 \\ \sigma_{g_y}^2 \\ \sigma_{g_z}^2 \end{bmatrix} (\hat{C}_b^n)^T \quad \text{Eq. 6-20}$$

The process noises of the inertial sensor biases and scale factors error corresponds to the driven noise of the first order Gauss Markov processes that model the bias stability of the sensors (given in chapter 5).

$$q_{b_a} = \text{diag} \begin{bmatrix} \sigma_{b_{ax}}^2 \\ \sigma_{b_{ay}}^2 \\ \sigma_{b_{az}}^2 \end{bmatrix}, \quad q_{b_g} = \text{diag} \begin{bmatrix} \sigma_{b_{gx}}^2 \\ \sigma_{b_{gy}}^2 \\ \sigma_{b_{gz}}^2 \end{bmatrix}, \quad q_{s_a} = \text{diag} \begin{bmatrix} \sigma_{s_{ax}}^2 \\ \sigma_{s_{ay}}^2 \\ \sigma_{s_{az}}^2 \end{bmatrix}, \quad q_{s_g} = \text{diag} \begin{bmatrix} \sigma_{s_{bx}}^2 \\ \sigma_{s_{by}}^2 \\ \sigma_{s_{bz}}^2 \end{bmatrix} \quad \text{Eq. 6-21}$$

The Q matrix must be discretized with:

$$Q_k = QT_s \quad \text{Eq. 6-22}$$

6.1.3.3 Measurement model

To simplify notations, the index k is removed in the measurement model. In tight coupling, the measurements are the pseudorange errors which are observed by subtracting the INS-based pseudoranges ($\rho_{INS,i}$) to the measured pseudoranges ($\rho_{GNSS,i}$):

$$\delta z = \begin{bmatrix} \rho_{GNSS,1} - \rho_{INS,1} \\ \vdots \\ \rho_{GNSS,n} - \rho_{INS,n} \end{bmatrix} \quad \text{Eq. 6-23}$$

Let us denote E , N and U the coordinates of the mechanization output and, $E_{s,i}$, $N_{s,i}$ and $U_{s,i}$ the coordinates of the i^{th} satellite in the navigation frame. The INS based pseudoranges are calculated based on the predicted position of the vehicle and clock bias.

$$\rho_{INS,i} = d_{0,i} + c\Delta t_{offset} \quad \text{Eq. 6-24}$$

with:

$$\bullet \quad d_{0,i} = \sqrt{(E_{s,i} - E)^2 + (N_{s,i} - N)^2 + (U_{s,i} - U)^2}$$

On real implementation, the lever arm between the IMU and the GNSS receiver antenna has to be taken into account. Let us assume that the lever arm has been measured in the body frame during the installation of the system. It can be converted into the navigation frame by using the DCM. Finally it is possible to add the lever arm vector to the position estimated at the mechanization output in the INS-based predicted pseudorange. Therefore, the INS-based pseudorange is estimated at the antenna position.

The observation matrix of the filter is:

$$H = \begin{bmatrix} H_{E,1} & H_{N,1} & H_{U,1} & 0 & \dots & 1 & 0 \\ \vdots & \vdots & \vdots & \vdots & \vdots & \vdots & \vdots \\ H_{E,N} & H_{N,N} & H_{U,N} & 0 & \dots & 1 & 0 \end{bmatrix} \quad \text{Eq. 6-25}$$

where:

$$\begin{aligned} \bullet \quad H_{E,i} &= \frac{E - E_s}{d_{0,i}} \\ \bullet \quad H_{N,i} &= \frac{N - N_s}{d_{0,i}} \\ \bullet \quad H_{U,i} &= \frac{U - U_s}{d_{0,i}} \end{aligned}$$

The expression of the observation matrix is obtained by differentiating the pseudorange measurement around the mechanization output.

In tight coupling, the measurement errors are due to the GNSS pseudorange errors which have been fully characterized in chapter 5. In Kalman filtering it is assumed that the measurement noise are centered and uncorrelated in time. It is proven in given in chapter 5, that the measurement errors are correlated in time (local effects or ionosphere for example). For local effects it has been proposed in given in chapter 5 to exclude dangerous local effects or to inflate the covariance matrix. However, the atmospheric errors (troposphere only for dual-frequency receivers) and ephemeris errors may remain. Two approaches are proposed in [Gleason and Gebre-Egziabher, 2009] to deal with this issue.

- The first approach consists in augmenting the state vector with extra states that account for the correlated errors. However, in urban environment this method may not be feasible because the satellites are frequently unavailable due to masking. Moreover it may lead to observability issues when the number of satellite in view is low. However, state augmentation enables to produce valid integrity bounds if the time correlated errors are well estimated.
- The second approach when using low cost sensors consists in inflating the noise covariance matrix according to [Gleason and Gebre-Egziabher, 2009]. This approach which is similar to the proposed technique to deal with local effect from an integrity point of view is preferred here. It is assumed that the inflation of the variance due to the overbounding of the measurement errors' CDF is sufficient (except for local effects).

Finally, the measurement noise covariance matrix R_k is given by:

$$R = \begin{bmatrix} \sigma_{\rho,1}^2 & 0 & 0 \\ 0 & \ddots & 0 \\ 0 & 0 & \sigma_{\rho,N}^2 \end{bmatrix} \quad \text{Eq. 6-26}$$

where:

- $\sigma_{\rho,i}^2$ is the variance of the pseudorange error measured with respect to the i^{th} satellite. The models used in this thesis are detailed in chapter 5.

6.1.4 Improving the solution

The accuracy of the solution can be improved by simple means that consist in adding measurements to the Kalman filter. Firstly, it is possible to use GNSS Doppler measurements that are available in most receivers. This is explained in section 6.1.4.1. It is also possible to take advantage of the a priori knowledge of the vehicle dynamics by using motion constraints referred to as Non-Holonomic Constraints in the cases of study. The Non-Holonomic Constraints are discussed in section 6.1.4.2. Finally it is possible to reduce the position error drift when the vehicle is motionless by implementing Zero Velocity Update as detailed in section 6.1.4.3.

6.1.4.1 Inclusion of Doppler measurements

Mass market receivers estimate Doppler frequency (FLL outputs). The Doppler frequency (Δf_i) is proportional to the satellite to receiver radial velocity $\dot{\rho}_{GNSS,1}$ (called pseudorange rate):

$$\dot{\rho}_{GNSS,i} = -\lambda_i \Delta f_i \quad \text{Eq. 6-27}$$

where λ_i is the wavelength of the carrier frequency of the i^{th} satellite.

Doppler measurements are quite robust and available, even in difficult environments. It is then possible to augment the measurement model of the Kalman filter to include pseudorange rates in order to improve the velocity estimation. The measurement model is thus augmented with δZ_{PRR} which expression is:

$$\delta Z_{PRR} = \begin{bmatrix} \dot{\rho}_{GNSS,1} - \dot{\rho}_{INS,1} \\ \vdots \\ \dot{\rho}_{GNSS,N} - \dot{\rho}_{INS,N} \end{bmatrix} \quad \text{Eq. 6-28}$$

where $\dot{\rho}_{INS,1}$ is calculated with :

$$\dot{\rho}_{GNSS,i} = \dot{d}_{0,i} + c\Delta t_{drift} \quad \text{Eq. 6-29}$$

with :

$$\dot{d}_{0,i} = (E - E_{s,i})(V_E - V_{E,s,i}) + (N - N_{s,i})(V_N - V_{N,s,i}) + (U - U_{s,i})(V_U - V_{U,s,i}) \quad \text{Eq. 6-30}$$

where :

- $V_{E,s,i}$, $V_{N,s,i}$ and $V_{U,s,i}$ are the satellite velocities. These velocities are obtained thanks to the ephemeris.
- V_E , V_N and V_U are the velocities estimated by the mechanization in the navigation frame.

The observation matrix must be augmented to relate these measurements to the Kalman filter state vector:

$$H_{PRR} = \begin{bmatrix} H_{PRR,E,1} & H_{PRR,N,1} & H_{PRR,U,1} & H_{PRR,VE,1} & H_{PRR,VN,1} & H_{PRR,VU,1} & 0 & \dots & 1 \\ \vdots & \vdots \\ H_{PRR,E,N} & H_{PRR,N,N} & H_{PRR,U,N} & H_{PRR,VE,N} & H_{PRR,VN,N} & H_{PRR,VU,N} & 0 & \dots & 1 \end{bmatrix} \quad \text{Eq. 6-31}$$

with:

- $H_{PRR,E,i} = \frac{V_E - V_{E,s,i}}{d_{0,i}} - \frac{(E - E_{s,i})\dot{d}_{0,i}}{d_{0,i}^2}$
- $H_{PRR,N,i} = \frac{V_N - V_{N,s,i}}{d_{0,i}} - \frac{(N - N_{s,i})\dot{d}_{0,i}}{d_{0,i}^2}$
- $H_{PRR,U,i} = \frac{V_U - V_{U,s,i}}{d_{0,i}} - \frac{(U - U_{s,i})\dot{d}_{0,i}}{d_{0,i}^2}$

- $H_{PRR,VE,i} = \frac{E-E_{s,i}}{d_{0,i}}$
- $H_{PRR,VN,i} = \frac{N-N_{s,i}}{d_{0,i}}$
- $H_{PRR,VU,i} = \frac{U-U_{s,i}}{d_{0,i}}$

The R matrix must be augmented to include the pseudorange rate error covariance matrix (R_{PRR}).

$$R_{PRR} = \begin{bmatrix} \sigma_{\rho,1}^2 & 0 & 0 \\ 0 & \ddots & 0 \\ 0 & 0 & \sigma_{\rho,N}^2 \end{bmatrix} \quad \text{Eq. 6-32}$$

The weighting scheme for R_{PRR} is described in 5.1.2. It is assumed here that GNSS receiver range and range rate errors are uncorrelated.

6.1.4.2 Non-Holonomic Constraints

Under ideal condition, terrestrial vehicles motion is straightforward. Therefore, the velocity in the across track plane is negligible. This information can be used as additional velocity measurements in the filter called Non-Holonomic Constraints (NHC). This hypothesis does not hold if the vehicle is sliding in the across track direction (which may occur during loss of grip) or if the vehicle is jumping. This situation may occur for car. On the other hand, trains are constrained by the railtracks which reinforce the relevance of this assumption. The NHC are given in the body frame. Let's denote V^b the velocity vector at the output of the mechanization expressed in the body frame. V^b can be obtained by rotating (with the DCM \hat{C}_n^b) the velocity vector expressed in the navigation frame. The measurements associated with the NHC are the following:

$$\delta Z_{NHC} = \begin{bmatrix} -V_x^b \\ -V_z^b \end{bmatrix} \quad \text{Eq. 6-33}$$

The corresponding measurement matrix is given by:

$$H_{NHC} = \begin{bmatrix} 0_{1 \times 3} & -\hat{C}_{11} & -\hat{C}_{12} & -\hat{C}_{13} & \hat{C}_{12}V_U - \hat{C}_{13}V_N & \hat{C}_{13}V_E - \hat{C}_{11}V_U & \hat{C}_{11}V_N - \hat{C}_{12}V_E & 0_{1 \times 14} \\ 0_{1 \times 3} & -\hat{C}_{31} & -\hat{C}_{32} & -\hat{C}_{33} & \hat{C}_{32}V_U - \hat{C}_{33}V_N & \hat{C}_{33}V_E - \hat{C}_{31}V_U & \hat{C}_{31}V_N - \hat{C}_{32}V_E & 0_{1 \times 14} \end{bmatrix} \quad \text{Eq. 6-34}$$

where \hat{C}_{ii} corresponds to the term at the i^{th} line and i^{th} column of the DCM \hat{C}_n^b .

The measurement noise covariance matrix corresponding to the NHC is adjusted empirically in order to account for the uncertainty into the vehicle motion.

NHC are usually included to limit the heading drift during GNSS outages. Even in tight coupling approach, this configuration may occur in tunnels. In this study, the constraints are also included when there is no GNSS outage.

6.1.4.3 Zero Velocity Update

Zero Velocity Update (ZVU or ZUPT) consists in detecting the periods of time during which the vehicle is motionless. It is then interesting to feed this information to the filter to limit the drift of the solution. It is thus necessary to define a test to detect immobility. To do so, it is possible to define a velocity threshold, under which the vehicle is assumed to be stationary. The threshold can be chosen by correlating the velocity estimation with the epochs at which the vehicle is known to be motionless during a calibration campaign. The test variable is the updated velocity estimation. It is not feasible to define a test based on the acceleration as this parameter can be negligible when the vehicle has a uniform motion. The stationarity can also be detected by means of an odometer. If the immobility is detected, a new measurement is added, similarly to the NHC (but with a zero along-track velocity):

$$\delta Z_{ZUPT} = \begin{bmatrix} -V_x^b \\ -V_y^b \\ -V_z^b \end{bmatrix} \quad \text{Eq. 6-35}$$

The corresponding measurement matrix is given by:

$$H_{ZUPT} = \begin{bmatrix} 0_{1 \times 3} & -\hat{C}_{11} & -\hat{C}_{12} & -\hat{C}_{13} & \hat{C}_{12}V_U - \hat{C}_{13}V_N & \hat{C}_{13}V_E - \hat{C}_{11}V_U & \hat{C}_{11}V_N - \hat{C}_{12}V_E & 0_{1 \times 14} \\ 0_{1 \times 3} & -\hat{C}_{21} & -\hat{C}_{22} & -\hat{C}_{23} & \hat{C}_{22}V_U - \hat{C}_{23}V_N & \hat{C}_{23}V_E - \hat{C}_{21}V_U & \hat{C}_{21}V_N - \hat{C}_{22}V_E & 0_{1 \times 14} \\ 0_{1 \times 3} & -\hat{C}_{31} & -\hat{C}_{32} & -\hat{C}_{33} & \hat{C}_{32}V_U - \hat{C}_{33}V_N & \hat{C}_{33}V_E - \hat{C}_{31}V_U & \hat{C}_{31}V_N - \hat{C}_{32}V_E & 0_{1 \times 14} \end{bmatrix} \quad \text{Eq. 6-36}$$

The measurement noise covariance matrix corresponding to the ZUPT is adjusted empirically in this work to account for possible small lateral sliding.

6.1.4.4 Zero Angular Rate Update

The Zero Angular Rate Update (ZARU) can be applied to several configuration of IMU including full IMU [Groves, 2013]. This motion constraint consists in assuming that when the angular rate should be null when the vehicle is detected as in stationary mode. Like for ZUPT, the odometer can be used to detect the stationarity. For the full IMU, the ZARU measurement is given by:

$$\delta Z_{ZARU} = \begin{bmatrix} -\omega_x^b \\ -\omega_y^b \\ -\omega_z^b \end{bmatrix} \quad \text{Eq. 6-37}$$

The measurement matrix corresponding to the ZARU constraints is given by:

$$H_{ZARU} = [0_{3 \times 3} \quad 0_{3 \times 3} \quad 0_{3 \times 3} \quad 0_{3 \times 3} \quad -I_{3 \times 3} \quad 0] \quad \text{Eq. 6-38}$$

Finally the measurement noise covariance is driven by the vibration and other disturbances. Moreover, the yaw axis is less affected by disturbances than the other two axes [Groves, 2013]. This phenomenon

must be taken into account in the weighting of these measurements. In this thesis, the ZARU measurements are used simultaneously with the ZUPT measurements.

6.1.5 Train control

As already discussed, the proposed train control positioning system is based on two redundant subsystems that use single constellation receivers. If four constellations are available, the sub-filters shall be modified to process two constellations each. The way to modify the filter for integration of two GNSS is detailed in subsection 6.1.6.

The track on which the train is located is assumed to be determined by means of radiobeacons located at strategic points (i.e. after intersections) in the proposed solution. Once the railtrack is known, it is possible to take advantage of this information to add a motion constraint and improve the positioning in the along-track dimension as well as the velocity estimation. The track database measurement (and error) model has been detailed in chapter 5. The model used, which is the same as in [Zheng et al., 2009] is a sequence of track data points, with a separation (d_{map}) that is typically 1.5 meters and on which the accuracy is negligible compared to the accuracy targeted by our solution. The proposed approach can be divided into two steps.

- As proposed in prior art [Zheng et al., 2009] (for GNSS only), it is first necessary to determine the two track data points between which the vehicle is the most likely to be.
- The position of the two track points can then be integrated in the EKF as new measurements.

6.1.5.1 Determination of the two track data points within which the train is located

An algorithm using the velocity estimated by the GNSS sensor to determine the prior and next track points is given in [Zheng et al., 2009]. It is proposed here to also take advantage of the IMU to select the two points. The method consists in finding the two points A and B that minimize the distance of the train track to the predicted position. As this optimization process can be demanding in terms of calculation for long tracks, it is necessary to restrain the potential candidates. To do so it would for instance be possible to limit the search based on the previous segment and on the estimation of the distance travelled. The proposed algorithm is summarized as the solution to a simple minimization problem.

The two points that are around the last position fix are supposed to be known (converted from ECEF to the navigation frame) and denoted $A(k)$ and $B(k)$. Let's denote the last updated position $\hat{X}_{k|k}$ and the predicted position at the mechanization output $\hat{X}_{k+1|k}$. It is firstly proposed to determine the a priori travelled distance based on INS:

$$dl = \|\hat{X}_{k+1|k} - \hat{X}_{k|k}\| \quad \text{Eq. 6-39}$$

Then it is necessary to pre select the potential candidates for $A(k+1)$ and $B(k+1)$ to limit the computation burden for the minimization problem. Let's denote P_{MAP} the bijection between the map

point index (l) and its coordinates. Let's denote $l_{k,A}$ and $l_{k,B}$ the indexes of the points of the map which corresponds $A(k)$ and $B(k)$.

The range of potential index candidates is limited to the interval:

$$Interval = \left[l_{k,A} - \left\lfloor \frac{dl}{d_{map}} \right\rfloor - margin ; l_{k,B} + 1 + \left\lfloor \frac{dl}{d_{map}} \right\rfloor + margin \right] \quad \text{Eq. 6-40}$$

where *margin* is an integer that must be high enough not to exclude the true track data points on which the vehicle is located and short enough to limit the computation burden. It is all the more necessary to work with restrained intervals to avoid wrong track points selection that might occur in case of balloon loop or spiral loops. Indeed, at "intersection" an ambiguity can occur at the overlapping region.



Figure 51 Spiral viaduct near Brusio, Switzerland [bahnbilder.ch]

This interval assumes that the direction of the motion is unknown. It is possible to reduce the size of the interval by a factor of two by determining the direction of the motion (by computing the sign of the dot product between the velocity and the trajectory).

The final step is to select l_{k+1} and $l_{k+1} + 1$ as the two indexes that minimize the Euclidian distance between their corresponding coordinates and the coordinates of the predicted position.

$$\begin{cases} l_{k+1,A} = \min_{l \in Interval} \|P_{map}(l) - \hat{X}_{k+1|k}\| \\ l_{k+1,B} = \min_{l \in Interval - \{l_{k+1,A}\}} \|P_{map}(l) - \hat{X}_{k+1|k}\| \end{cases} \quad \text{Eq. 6-41}$$

$A(k + 1)$ and $B(k + 1)$ are the coordinates of the two track data points of reference around the predicted position. The coordinates of these two points are used to augment the filter.

6.1.5.2 Integration of the track measurements into the Kalman Filter

Firstly it can be assumed that the train is located on the segment that links both points. The concept consists in adding a measurement in the measurement model that represents the Euclidean distance

between the position predicted by the mechanization and the segment $A(k+1)B(k+1)$. The vehicle position is assumed to be on this segment. Thus, the following measurement can be added:

$$\delta z_{d_{map}} = \left[0 - d \left(\hat{X}_{k+1|k}, A(k+1)B(k+1) \right) \right] \quad \text{Eq. 6-42}$$

where d refers to the Euclidean distance.

The distance is geometrically determined with the following expression:

$$d \left(\hat{X}_{k+1|k}, A(k+1)B(k+1) \right) = \frac{\kappa}{\|A(k+1)B(k+1)\|} \quad \text{Eq. 6-43}$$

where:

- $\kappa = \sqrt{\begin{aligned} &[(N - N_A)(U_B - U_A) - (U - U_A)(N_B - N_A)]^2 + \\ &[(U - U_A)(E_B - E_A) - (E - E_A)(U_B - U_A)]^2 + \\ &[(E - E_A)(N_B - N_A) - (N - N_A)(E_B - E_A)]^2 \end{aligned}}$
- $A(k+1) = \begin{bmatrix} E_A \\ N_A \\ U_A \end{bmatrix}, B(k+1) = \begin{bmatrix} E_B \\ N_B \\ U_B \end{bmatrix}$

It is then necessary to relate this measurement to the state vector. The distance to $A(k+1)B(k+1)$ expression is linearized around $\hat{X}_{k+1|k}$. The observation matrix line corresponding to the distance to the track segment is given by:

$$H_{d_{map}} = [H_{d_{map},E} \quad H_{d_{map},N} \quad H_{d_{map},U} \quad 0 \quad \dots \quad 0] \quad \text{Eq. 6-44}$$

with :

$$H_{d_{map},E} = \frac{(U_B - U_A)[(U - U_A)(E_B - E_A) - (E - E_A)(U_B - U_A)] - (N_B - N_A)[(E - E_A)(N_B - N_A) - (N - N_A)(E_B - E_A)]}{\kappa \|A(k+1)B(k+1)\|} \quad \text{Eq. 6-45}$$

$$H_{d_{map},N} = \frac{(E_B - E_A)[(E - E_A)(N_B - N_A) - (N - N_A)(E_B - E_A)] - (U_B - U_A)[(N - N_A)(U_B - U_A) - (U - U_A)(N_B - N_A)]}{\kappa \|A(k+1)B(k+1)\|} \quad \text{Eq. 6-46}$$

$$H_{d_{map},U} = \frac{(N_B - N_A)[(N - N_A)(U_B - U_A) - (U - U_A)(N_B - N_A)] - (E_B - E_A)[(U - U_A)(E_B - E_A) - (E - E_A)(U_B - U_A)]}{\kappa \|A(k+1)B(k+1)\|} \quad \text{Eq. 6-47}$$

However, the uncertainties on the coordinates of $A(k+1)$ and $B(k+1)$ must be considered to improve the measurement model. The measurement noise covariance term that model this error is thus adjusted empirically.

An additional way to integrate the knowledge of the prior and next track points consists in using them to generate a heading information . The map heading information is given by:

$$\psi_{map} = \text{atan}\left(\frac{E_B - E_A}{N_B - N_A}\right) \quad \text{Eq. 6-48}$$

The measurement added is then :

$$\delta z_{\psi_{map}} = [\psi_{map} - \hat{\psi}_{k+1|k}] \quad \text{Eq. 6-49}$$

The observation matrix H is augmented with the line corresponding to the new observation, which contains only zero except the term corresponding to the heading error state:

$$\begin{cases} H_{\psi_{map}}[i] = 1 \text{ if } i = 9 \\ H_{\psi_{map}}[i] = 0 \text{ else} \end{cases} \quad \text{Eq. 6-50}$$

The standard deviation of the error on the heading information is related to the standard deviation of the mapping error σ_{map} and the average distance between the two consecutive points d_{map} by the following expression (which proof is in appendix E):

$$\sigma_{\psi_{map}} = \sqrt{2} \frac{\sigma_{map}}{d_{map}} \quad \text{Eq. 6-51}$$

This expression can be used to weight the track heading information in the R matrix.

6.1.6 ETC

The solution proposed for ETC is based on a dual constellation receiver. To process two constellations, the filter must be modified to estimate the clock bias and clock drift of the second system. In this thesis, two states accounting for the clock offset and the clock drift of the second constellation are added to the state vector. An alternative proposed in [Angrisano, 2010], (but not used in this thesis), assumes that the time difference between the two constellations (GPS and GLONASS) is very stable and that its drift is zero. Thus only one state is added to estimate the intersystem bias.

When adding a second constellation (e.g. Galileo), the pseudorange (and pseudorange rate) measurements are integrated in the same way as in the single constellation case except the lines of the observation matrix that contain ones for the Galileo clock offset (and drift).

It is also proposed to integrate wheel speed sensor measurements in the ETC solution. WSSs provide an along-track velocity information. It is also possible to get an estimate of the yaw rate by differentiating the velocity measurements of two WSSs (on the left and right of the vehicle). The velocity gradient between the two wheels can be related to the yaw rate by geometry considerations.

This information has not been integrated in the proposed solution and is a potential improvement. Thus the WSS measurement (V_{WSS}^b) is limited to a velocity information in this thesis.

$$\delta z_{WSS} = \begin{bmatrix} 0 - V_x^b \\ V_{WSS}^b - V_y^b \\ 0 - V_z^b \end{bmatrix} \quad \text{Eq. 6-52}$$

Note that this measurement model includes the NHC, it assumes that the vehicle is moving straightforward. The WSS error model, described in chapter 5, includes a scale factor error partially due to the variations of the wheels diameter due to temperature and pressure variations. This scale factor error has to be estimated. The state vector is augmented with the WSS scale factor error (δS_{WSS}).

The corresponding observation matrix is given by:

$$H_{WSS} = \begin{bmatrix} 0_{1 \times 3} & -\hat{C}_{11} & -\hat{C}_{12} & -\hat{C}_{13} & \hat{C}_{12}V_U - \hat{C}_{13}V_N & \hat{C}_{13}V_E - \hat{C}_{11}V_U & \hat{C}_{11}V_N - \hat{C}_{12}V_E & 0 & \dots & V_x^b \\ 0_{1 \times 3} & -\hat{C}_{21} & -\hat{C}_{22} & -\hat{C}_{23} & \hat{C}_{22}V_U - \hat{C}_{23}V_N & \hat{C}_{23}V_E - \hat{C}_{21}V_U & \hat{C}_{21}V_N - \hat{C}_{22}V_E & 0 & \dots & V_y^b \\ 0_{1 \times 3} & -\hat{C}_{31} & -\hat{C}_{32} & -\hat{C}_{33} & \hat{C}_{32}V_U - \hat{C}_{33}V_N & \hat{C}_{33}V_E - \hat{C}_{31}V_U & \hat{C}_{31}V_N - \hat{C}_{32}V_E & 0 & \dots & V_z^b \end{bmatrix} \quad \begin{matrix} \text{Eq.} \\ 6-5 \\ 3 \end{matrix}$$

where the last column corresponds to the scale factor error state.

The dynamic evolution of δS_{WSS} has to be modelled to define the corresponding line in the F matrix and in the Q matrix. The scale factor error can be modelled by a first order Gauss-Markov process. Thus, the F matrix is augmented with a line that contains $-1/\tau_{S_{WSS}}$ at the column corresponding to δS_{WSS} . The Q matrix is augmented to account for the driven noise of the WSS scale factor error. This two magnitudes as well as the WSS measurement noise variance that must be included in the R matrix has to be determined with real WSS measurements.

6.2 Validation and performance assessment on simulated data

The objective of this section is to validate with simulations the EKF configurations that have been proposed and implemented during this thesis as well as to assess the performance gains that can be obtained by adding measurements (constraints and sensors) to the solution.

6.2.1 Parameters of the simulations

The simulator developed during this thesis takes a pre-defined trajectory and an along track velocity profile as an input. It generates ideal sensors measurements from this information, to which are added the realistic error models that have been described in chapter 5. The ideal measurements are generated as described:

- Provided an actual GPS almanac (giving the satellite position), the simulator generates ideal ranges. The clock offset is modelled as a linear function here and added to the true range to

form the simulated pseudorange. Multi constellation receivers (which may be used for ETC) are not simulated in this section.

- The simulator generates the ideal IMU measurements using the technique described in [Zhang et al., 2012], which is equivalent to a reverse mechanization based on Euler angles.
- For the train control application, the track points are generated by sampling the trajectory of reference with a constant step (d_{map}).
- For ETC, the wheel speed sensor ideal measurements corresponds to the velocity entered in the velocity profile. The use of dual constellations that has been proposed for ETC is not simulated in this section.

This simplified model does not simulate the lever arm between the sensors. In this section, the trajectory of reference which is given in Figure 52 is a portion of the tramway line number 3 in Montpellier France provided by Egis. Smoother trajectories that are less challenging for the navigation system can be expected for real trains on high velocity lines. This trajectory is also used to model the trajectory for ETC.

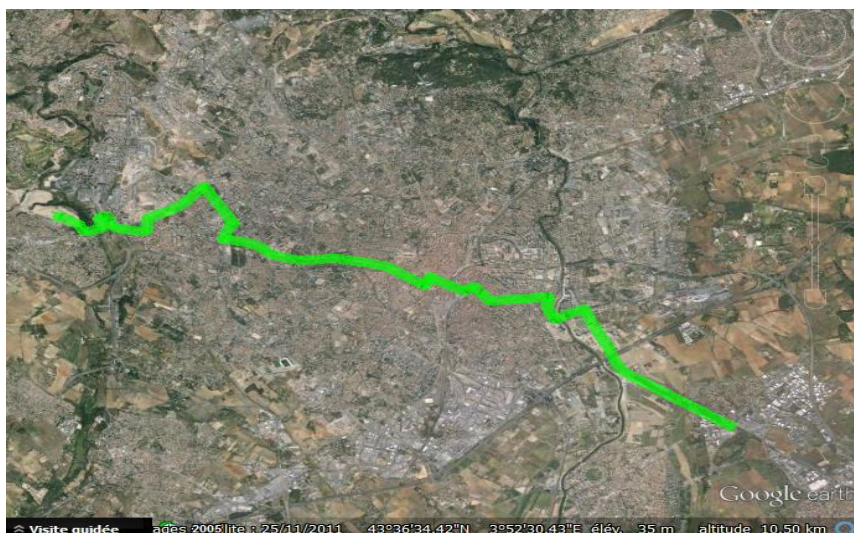


Figure 52 Portion of the tramway line number 3 in Montpellier, France

The parameters for the simulation are summarized here:

- The sampling frequency of the GPS receiver is set to 5 Hz
- The sampling frequency of the IMU is set to 100 Hz.
- The length of the trajectory is 14 km.
- The along track velocity is set to a constant value of 80 km/h
- The constellation that is used is taken from an actual GPS almanac (Yuma format) and given in Figure 2.
- The pseudorange error models of GPS are used here. The single (L1 C/A) and dual frequency (L1 C/A, L5) models presented in section 5.1.1.1 have been tested. The noise component of the pseudorange error model depends of the estimated C/N_0 . It is assumed that the C/N_0 are

30 dB-Hz which corresponds to the mask used in chapter 5. This hypothesis is conservative and very pessimistic.

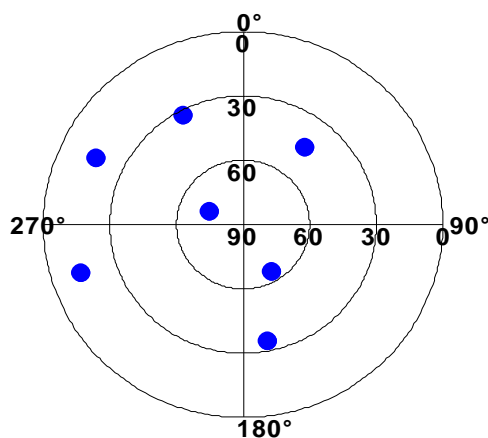


Figure 53 Skyplot of the constellation used for the simulations

6.2.2 Results: GPS/INS

A first set of simulations has been conducted to validate the basic architecture which integrates the GPS measurements (pseudorange and pseudorange rates) and the data from the IMU. The criterion used for the validation of the tuning of the EKF is the 3σ estimation of the error on the state estimation that has to bound the actual error with a sufficient probability (higher than 99%). The results in terms of position, velocity and attitude estimation errors are plotted in Figure 54, Figure 55, Figure 56 for the EKF with two different configurations of GPS receiver. The left column corresponds to the integration with a single frequency GPS L1 C/A receiver whereas the right column uses data from a dual frequency GPS L1 C/A and L5 receiver. In both cases the pseudorange rates have been integrated into the solution. It can be seen that, in both cases the velocity and attitude errors are well centered and bounded by the three sigma state error standard deviation estimation. The position error is within the bounds but not perfectly centered, especially when using a single frequency receiver. Indeed it slowly varies due to the correlated errors on the pseudorange measurements (essentially ionosphere). Much longer simulation time would be necessary for the position error to be centered because the errors are correlated over 1800 seconds or more. This phenomenon is less visible for the dual frequency receiver because the ionosphere error which is the major source of correlated component in the measurement error has been removed. In the results presented in Figure 54, Figure 55, Figure 56 the inflation factor used on the pseudorange and pseudorange rate measurement covariance matrixes is equal to 2.

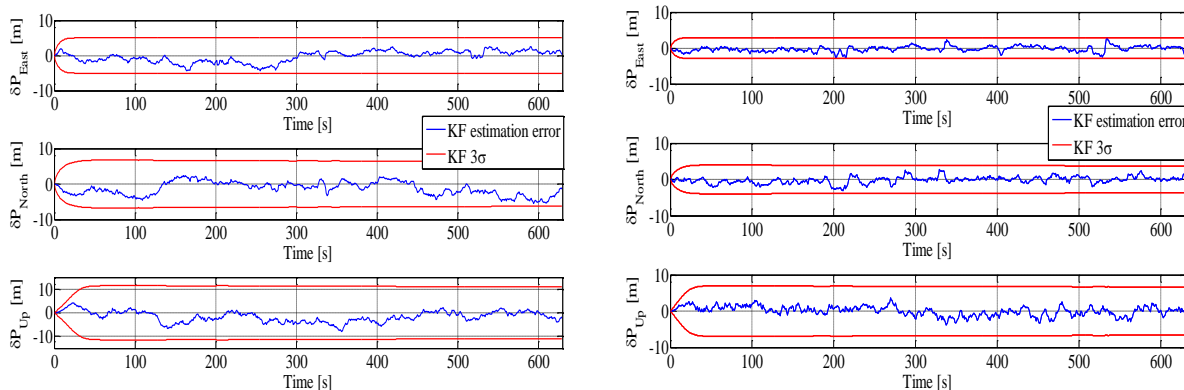


Figure 54 Position errors in the navigation frame, single frequency L1 C/A GPS receiver (left) or dual frequency L1 C/A and L5 receiver (right) and IMU

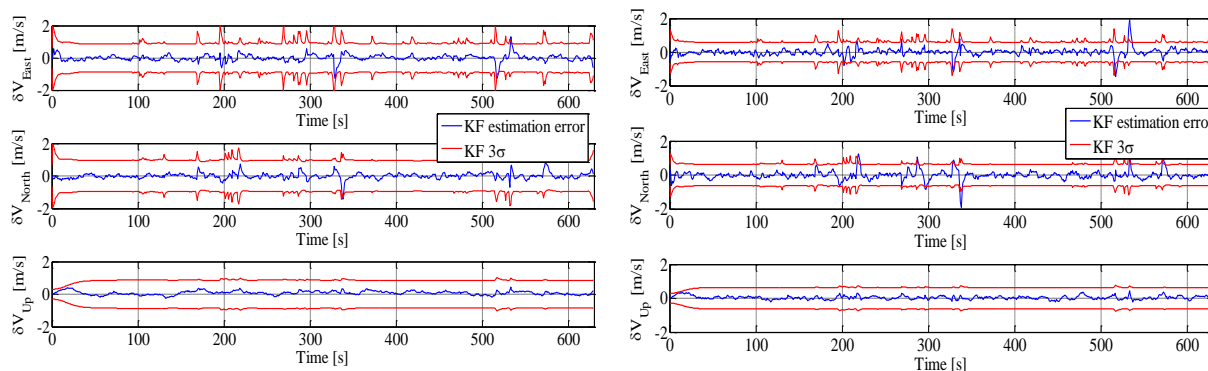


Figure 55 Velocity errors in the navigation frame, single frequency L1 C/A GPS receiver (left) or dual frequency L1 C/A and L5 receiver (right) and IMU

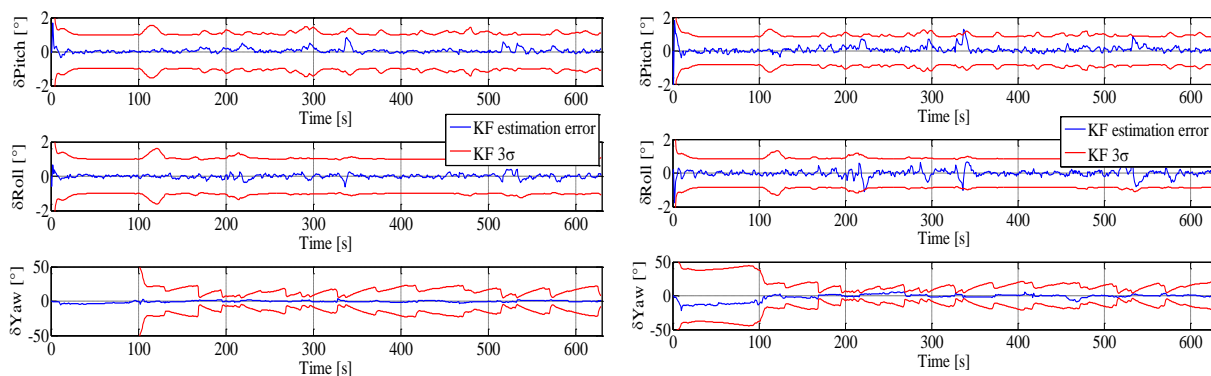


Figure 56 Attitude errors, single frequency L1 C/A GPS receiver (left) or dual frequency L1 C/A and L5 receiver (right) and IMU

The performances of different schemes in terms of position accuracy and error root mean square (RMS) are summarized in Table 16. It includes the use of single and dual frequency models (L5 has been preferred over L2C because L2C is not interoperable with Galileo). ZUPT has not been tested as the vehicle does not stop during the trajectory of reference. The accuracies are given in the horizontal plane, without differentiating into along-track and across-track direction at first. This is because the

GNSS/INS basic architecture is used for both train control and ETC and that, except for train stations or corridors in train control, the requirements are expressed in terms of horizontal accuracies.

Firstly, the use of a dual frequency receiver has improved the RMS and accuracy in all direction. Larger improvement can be expected in real condition because the C/N_0 values have been conservatively set to 30 dB-Hz for all the satellites in simulations and the noise level is increased in the iono-free measurements. The integration of the IMU has improved the horizontal accuracy and RMS with respect to the GPS only solution (with simple least square estimation). This is due to the smoothing effect of the filter. Errors which have a short correlation time (multipath and thermal noise) have been partially filtered out. The benefit of the integration of the IMU is therefore higher in the dual-frequency configuration, where the dominant sources of error have short correlation time.

Table 16 shows that the integration of pseudorange rates improves accuracy as well as introduction of non-holonomic constraints. NHC has essentially improved the vertical accuracy. It can be inferred from these simulations, that even in simulations, the basic solution cannot fulfill the accuracy requirements for track determination in train control. Indeed in the best configuration, the 2.3 m accuracy corresponds to a across-track accuracy of 1.6 m and an along-track of 1.9 m whereas the requirement is 0.7 m in the across-track direction. It reinforces the choice of keeping the radiobeacons at intersections for track selectivity.

Sensors	L1 C/A	L5	PRR	NHC	RMS/Accuracy 95% (m)	
					Horizontal	Vertical
GPS (LS)	✓				8.1/11.0	14.1/21.3
GPS (LS)	✓	✓			6.6/10.4	11.7/19.1
GPS/INS	✓				4.2/6.6	3.1/5.3
GPS/INS	✓		✓		4.0/6.3	2.9/5.0
GPS/INS	✓		✓	✓	4.1/6.3	2.0/3.6
GPS/INS	✓	✓			1.6/2.8	1.3/2.8
GPS/INS	✓	✓	✓		1.2/2.4	1.2/2.5
GPS/INS	✓	✓	✓	✓	1.2/2.3	0.5/1.2

Table 16 Position accuracy performances of the different configurations

The right estimation of inertial biases and scale factors errors can be investigated by simulations whereas it cannot in real data because the true parameters are unknown (no values of reference). Constant biases are added to the accelerometers and gyroscope measurements. These constant terms model the so called turn on bias phenomena that is due to variation in the initial conditions and physical properties of the IMU. The gyroscope and accelerometer biases are well estimated by the

EKF as illustrated in Figure 57 and Figure 58. For a better visibility, the 3σ bounds have been centered on the true bias value so that it can be seen that the filter converges to it. The estimation of the scale factor is not investigated in this set of simulations. In particular, the observability of the scale factor error states requires accelerations and rotation rates whereas only constant velocities have been simulated.

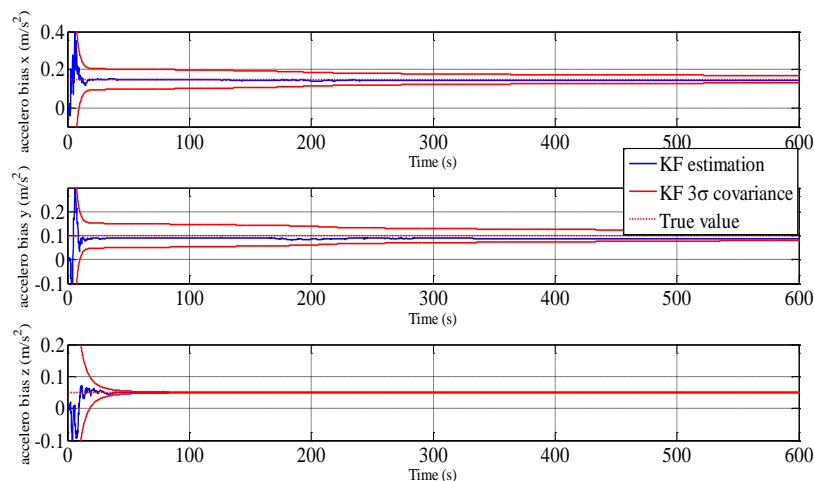


Figure 57 Accelerometer biases estimation

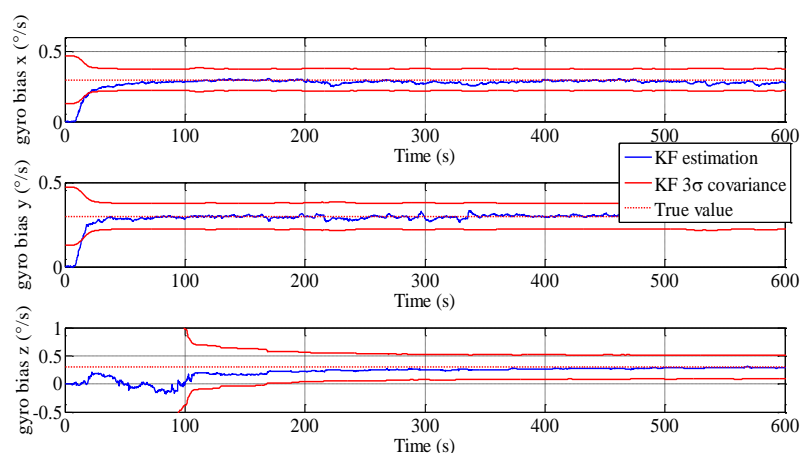


Figure 58 Gyroscopes biases estimation

6.2.3 Results: integration of the track database

In this subsection, the track database is integrated into the solution. Here, the database measurements are used to update the KF with the same frequency rate as the GNSS. However, it is possible to use map measurements to correct mechanization output with a higher rate. The position, velocity and attitude errors of the solution with integration of the track database are given in Figure 59, Figure 60 and Figure 61. The left column presents the estimation error of the EKF that uses the single frequency GPS receiver whereas in the right column, the errors of the dual frequency receiver are plotted. In

these simulations, the map distance noise covariance has been set to 10 cm^2 . Again the estimation errors are centered and within the three sigma covariance of the state estimation. It is important to notice that the integration of the track database did not lead to any biases on the state estimation. Moreover, it can be observed that the velocity and heading estimations have been improved, and the corresponding covariance estimates are lower than before the integration of the map.

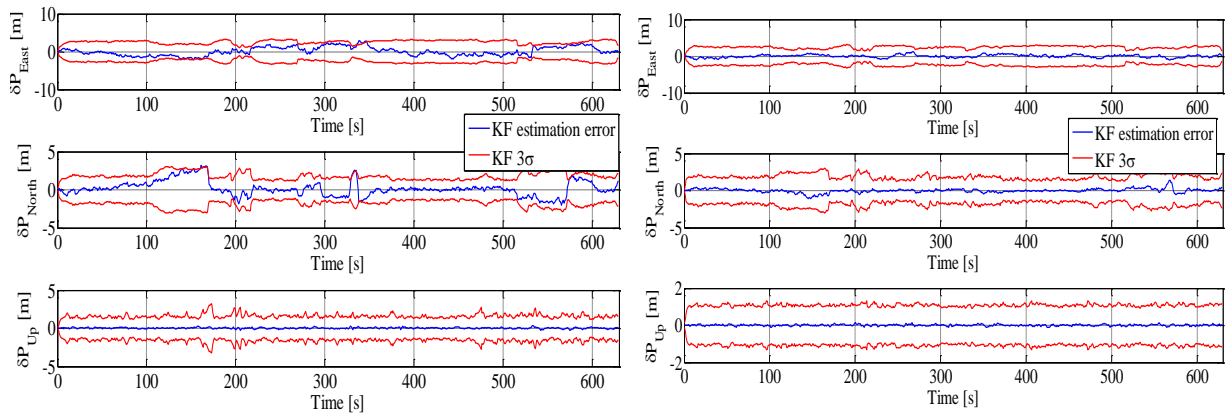


Figure 59 Position errors in the navigation frame, single frequency L1 C/A GPS receiver (left) or dual frequency L1 C/A and L5 receiver (right), IMU and track database

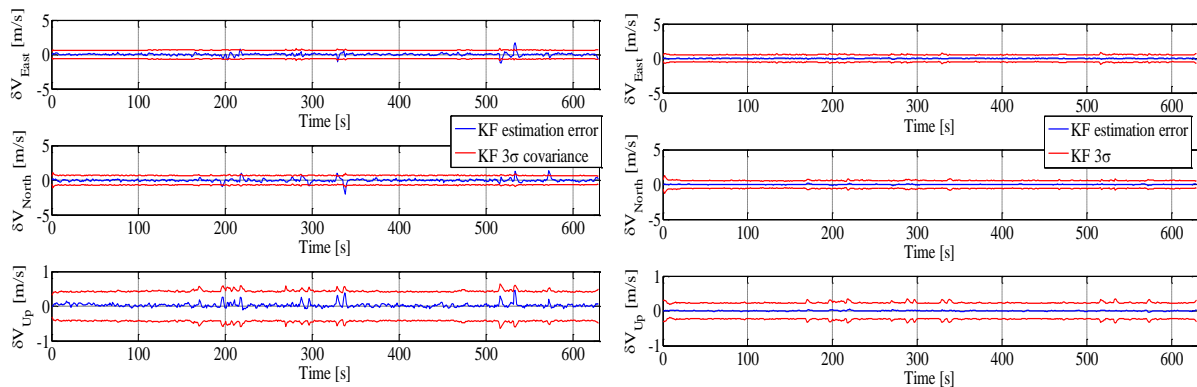


Figure 60 Velocity errors in the navigation frame, single frequency L1 C/A GPS receiver (left) or dual frequency L1 C/A and L5 receiver (right), IMU and track database

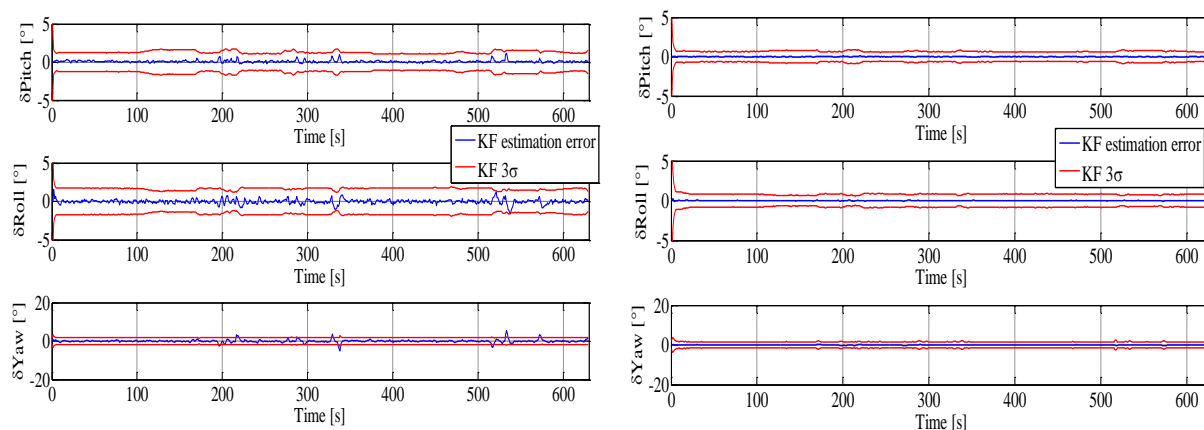


Figure 61 Attitude errors, single frequency L1 C/A GPS receiver (left) or dual frequency L1 C/A and L5 receiver (right), IMU and track database

The position accuracy of several possible configurations that integrates the track data are summarized in Table 17. The vertical accuracy is not given in Table 17 even if it has been highly improved due to the track database vertical constraint. Even if it performs a good across track accuracy due to the “projection” on the track, this solution cannot be used for track selectivity. Sub-meter along track accuracies can be reached when integrating pseudorange rates measurements to the dual frequency solution. The requirements presented in chapter 3.2 for train control in terms of along-track accuracy (6 m in the most stringent cases) are fulfilled by the subsystem in this configuration. The integration of the track database slightly improve the along track positioning by improving the velocity and heading estimation.

Sensors	L1 C/A	L5	PRR	NHC	RMS/Accuracy 95% (m)	
					Along-track	Across-track
GPS/INS/Map	✓				2.9/5.8	0.2/0.4
GPS/INS/Map	✓		✓		1.5/3.0	0.2/0.4
GPS/INS/Map	✓		✓	✓	1.4/2.8	0.2/0.4
GPS/INS/Map	✓	✓			1.0/2.1	0.1/0.3
GPS/INS/Map	✓	✓	✓		0.7/1.5	0.2/0.3
GPS/INS/Map	✓	✓	✓	✓	0.5/0.9	0.1/0.2

Table 17 Position accuracy performances of the different configurations which include track database measurements

6.2.4 Results: integration of the wheel speed sensors

It has been proposed to integrate the WSS measurements in the navigation filter for ETC application. The additional along-track velocity information is integrated in the measurements and the filter is modified as detailed in section 6.1.6. This table does not include NHC as they are implicitly contained in the odometer measurement model. It can be seen that the inclusion of wheel speed sensors has improved the horizontal accuracy by improving the velocity estimation. For single frequency L1 C/A receiver, without PRR, the horizontal accuracy has been improved by approximately 1 m. The horizontal accuracies obtained in this section with all the configurations are sufficient for the ETC application as detailed in Table 18.

Sensors	L1 C/A	L5	PRR	RMS/Accuracy 95% (m)
				Horizontal
GPS/INS/WSS	✓			3.1/5.4
GPS/INS/WSS	✓		✓	2.8/4.9
GPS/INS/WSS	✓	✓		1.6/2.8
GPS/INS/WSS	✓	✓	✓	1.1/2.1

Table 18 Position accuracy and error RMS of the different possible configurations with WSS

6.2.5 Conclusions

In all configuration, the position, velocity and attitude errors are centered and within the three sigma bounds in simulations. Therefore the implementation of the filter and its tuning are correct. However, it has been seen that the measurement covariance has to be inflated when using the single frequency receiver because the measurement white noise assumption does not hold. The accuracy improvement is higher when using the dual frequency receiver due to smoothing of uncorrelated errors. Moreover, it has been observed that inertial biases have been estimated well in this set of simulations.

The inclusion of additional measurements such as PRR or NHC has improved the position accuracy in this set of simulations. This is essentially the results of the improvement of the velocity and heading estimation. The integration of the track database did not lead to any instability of the filter or to biased state estimation. It enable to improve the velocity and attitude estimation (thanks to the yaw heading) and to slightly improve the along track accuracy thanks to it. The WSS also slightly improves the horizontal accuracy by providing a precise along-track velocity measurement as long as the attitude is well estimated.

It has been possible to validate the filter behavior and in particular the bias estimation can only be tested in simulations. However, the performances obtained in this section have a limited scope because the satellites have constant C/N_0 , the satellites are assumed to be in view. Moreover the

duration of the simulations are too short with respect to the correlation time of the ionosphere, troposphere and clock and ephemeris errors to obtain significant results, especially for the single frequency receiver. For dual frequency receivers, the major contributions are the uncorrelated errors which are partly filtered out by the EKF.

It is proposed in next section to assess the performances of the solution on the real data campaign conducted in Toulouse and described in section 5.3.2.2.

6.3 Performance assessment on real data

This section assesses the performances of the solutions in terms of position error RMS and accuracy using the test campaign presented in in section 5.3.2.2. Firstly, the performances of the basic common architecture are discussed. Finally, the solutions proposed for train control and ETC are studied as in the simulation case. In particular, the gain obtained by integrating a second constellation (GLONASS) into the solution for ETC is investigated. The receivers used are a U-blox 6 (GPS L1 C/A) and U-blox 8 (GPS L1 C/A and GLONASS L1). Only the performances of single frequency receivers have been tested on real signals in this Thesis.

6.3.1 Reference

The reference in terms of position, velocity and attitude has been estimated with a NovAtel SPAN system, described in section 5.3.2.2. The parameters of reference which are measured by the SPAN are affected by a measurement error. It is possible to assess the error done by neglecting the SPAN error by simple assumptions. Let's assume that the errors on the state estimations by the EKF ($\hat{x} - x$) and the SPAN ($\hat{x}_{ref} - x$) are centered Gaussian. The state error follows a centered Gaussian distribution:

$$\hat{x} - x \sim \mathcal{N}\left(0, \sigma_{\hat{x}-\hat{x}_{ref}}^2 + \sigma_{\hat{x}_{ref}-x}^2 + 2\text{cov}(\hat{x} - \hat{x}_{ref}, \hat{x}_{ref} - x)\right) \quad \text{Eq. 6-54}$$

The covariance term is unknown and cannot be determined without knowing $\hat{x}_{ref} - x$. Cauchy-Schwarz inequality enables to bound the covariance with:

$$\text{cov}(\hat{x} - \hat{x}_{ref}, \hat{x}_{ref} - x) < \sigma_{\hat{x}-\hat{x}_{ref}}\sigma_{\hat{x}_{ref}-x} \quad \text{Eq. 6-55}$$

Therefore the standard deviation of the state error is lower than the sum of the standard deviation of the difference between the measurement ($\sigma_{\hat{x}-\hat{x}_{ref}}$) and the reference plus the standard deviation of the state of reference ($\sigma_{\hat{x}_{ref}-x}$). An estimation of the SPAN error standard deviation is calculated in inertial explorer. For position error on the measurement campaign described in section 5.3.2.2, the SPAN error standard deviation ($\sigma_{\hat{x}_{ref}-x}$) is plotted in Figure 62. In the period of time that corresponds to suburban environment, this value is below 15 cm. For both cases of study, $\sigma_{\hat{x}-\hat{x}_{ref}}$ has a magnitude of several meters. Thus, the inaccuracy of the reference can be neglected in suburban environment. In dense urban environment, the inaccuracy of the SPAN on the horizontal east and north coordinates can

reach 50 cm due to masking and poor geometry. However, $\sigma_{\hat{x}-\hat{x}_{ref}}$ is typically around 5 meters, thus neglecting $\sigma_{\hat{x}_{ref}-x}$ makes sense. Rigorously speaking, these uncertainties should be taken into account in the representation of the state errors in urban environment.

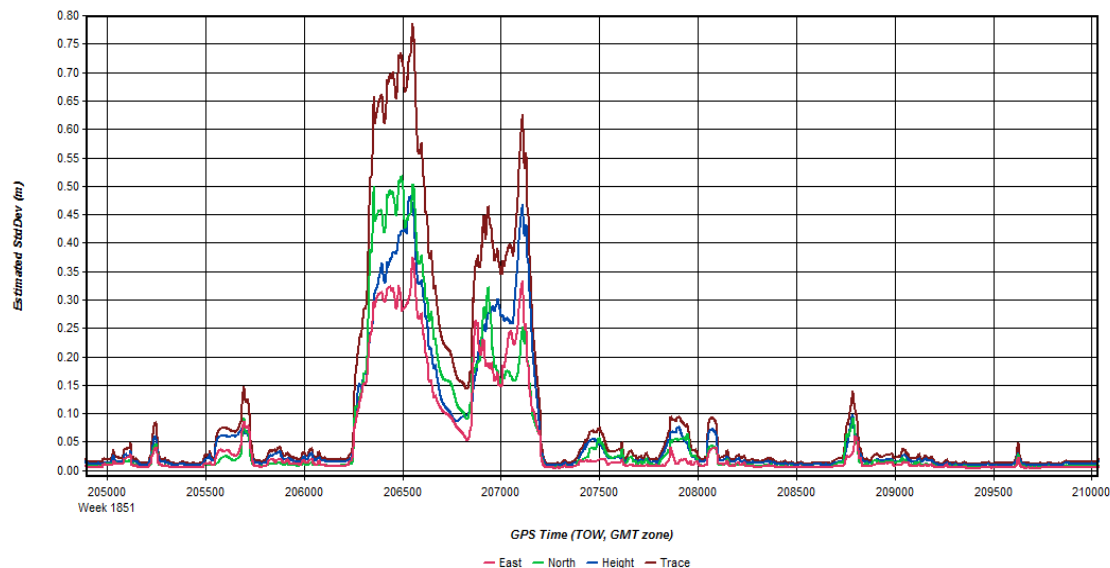


Figure 62 Standard deviation of the position error on the trajectory of reference as estimated by the SPAN system with inertial explorer

For the attitude estimation, the standard deviation of the error on the heading of reference is lower than 0.015° whereas the pitch and roll accuracy are 0.002° . The velocity accuracy is less than 0.01 m/s in suburban environment and up to 0.05 m/s in dense urban environment due to the degraded pseudorange rate measurements.

6.3.2 Results: GPS/INS

This section presents the accuracy performances of the basic architectures which integrate the measurements from the GPS receiver and the IMU. The tuning used in this section is the same than the one used in the simulations. The methods to improve the accuracy have been gradually added so that the improvement they provide can be quantized. The accuracies are given separately for the suburban and urban environments in Table 19. The statistics are given on approximately 2700 samples for suburban and 2300 for urban environment. The data collection has been conducted on June 30th, 2015. The number of GPS satellites in view as a function of time is plotted in Figure 63. Its CDF is also given for both suburban and urban environments.

- In suburban environment, the number of GPS satellites tracked is higher than 7 more than 90% of the time. A few exceptions have been encountered when crossing bridges on the motorway at 4655 seconds (3 satellites tracked, at $43^\circ 39' 20.12''\text{N}$, $1^\circ 21' 52.43''\text{E}$).
- In the environments characterized as dense urban, the number of satellite tracked is much lower on average due to building masks. 50% of the samples in urban environment are associated with 5 satellites in view or less. 10% of the time less than 4 satellites are in view

which lead to poor GPS position availability. This reinforces the benefit of using tight coupling instead of loose coupling in harsh environment.

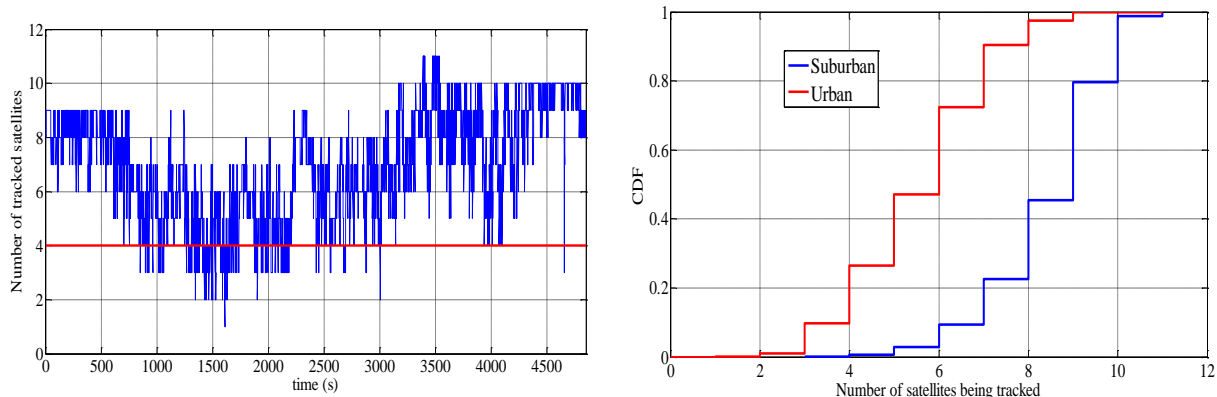


Figure 63 Number of GPS satellites being tracked as a function of time Figure 64 CDF of GPS satellites being tracked as a function of the environment

The mechanization has been initialized with a position and attitude that are different from the reference to check the ability of the filter to converge quickly. The samples corresponding to the convergence period of the filter (50 seconds) has not been included in the accuracy statistics. In these tests, a 5° elevation mask angle has been applied as well as a 30 dB-Hz C/N_0 mask.

Position RMS and accuracies are given in Table 19. According to Table 19, the coupling with the IMU measurements has improved the accuracy significantly in both the horizontal and vertical direction for all environments. These improvements are the result of the EKF filtering combined with the fact that accuracy of standalone GNSS given in Table 19 are obtained with a standard least square algorithm that equally weight every measurements which is not the case of the EKF. The coupling with the IMU with EKF enables to fulfill sub-decameter horizontal accuracy in suburban environment. The integration of PRR measurements has significantly improved the accuracy in all environments by improving the velocity estimation. Abnormally large PRR measurements have been excluded with a simple innovations check (which principle is detailed in chapter 7).

The NHC are given in the body frame. They are converted into the navigation frame by rotation, i.e. multiplication by the estimated DCM. The accuracy of these measurements is driven by the quality of the attitude estimation. Typically, when the vehicle is turning, the error on the predicted DCM is likely to increase which will lead to erroneous measurements (after conversion). However, for trains that have slow dynamics in terms of attitude, the attitude estimation is likely to be accurate. A simple test is used to detect yaw stationarity based on the z axis gyroscope output. The threshold has been set to 0.006 $^\circ/s$. When the yaw rate is lower than this threshold, the NHC are added to the measurement model, with a typical covariance of 0.001 m/s on each axis. The integration of NHC essentially improves vertical accuracy (due to the vertical velocity constraint component) which is of limited interest for most terrestrial applications that only have horizontal requirements such as ETC and train control. The same observations have been done on simulated data. Moreover, the horizontal accuracy has been slightly improved by adding NHC measurements.

The stationarity detection test variable (to trigger the ZUPT/ZARU) is the horizontal velocity as estimated by the EKF. The detection threshold is set to a value of 0.1 m.s^{-1} . This value has been derived empirically, by observing the horizontal velocity distribution when the velocity of reference is zero as depicted in Figure 65. The benefit of using ZUPT in the solution is limited because with PRR and NHC measurements, the velocity estimation is already very accurate as detailed in appendix F. The ZUPT constraint is a velocity measurement therefore it has no benefit on a solution which already estimates the velocity accurately. The ZARU mainly improves the gyro biases estimation and limits the attitude drift during stationary periods. Overall, in terms of position accuracy, these two constraints have slightly improved the performances of the solution in suburban environment.

It has to be mentioned here that no consistency checking method, or adaptive weighting scheme was used to reject outliers or minimize their impact. These outliers are mainly due to NLOS or large multipath errors. It is particularly visible when the vehicle operates in dense urban environment (between 700 and 3000 seconds). From an integrity monitoring point of view, these errors are dangerous because they are not well characterized by the error covariance estimated by the filter.

The same conclusion on the feasibility of using the proposed solution for track selectivity as the one given during the simulation test can be provided: the horizontal 95% accuracy is at best (for GPS/INS with PRR and all the constraints) 4.6 meters in suburban environment according to Table 19. Given in train control metrics, in this case, it corresponds to an along-track accuracy of 3.5 m and an across-track accuracy of 3.6 m. It is not sufficient for track selection as it is not sub-meter. For an autonomous (infrastructure free) selectivity, it would be necessary to use centimeter level positioning techniques based on carrier phase observables such as Precise Point Positioning algorithms (and precise corrections), or add a map matching algorithm (which integrity is complex to monitor).

Sensors	PRR	NHC	ZUPT ZARU	RMS/Accuracy 95% (m)			
				Horizontal		Vertical	
				Suburban	Urban	Suburban	Urban
GPS (LS)				14.0/21.6	23.4/44.3	22.3/45.8	31.3/71.2
GPS/INS				4.2/8.1	14.8/31.2	6.9/13.2	17.7/36.6
GPS/INS	✓			2.5/4.7	10.3/20.3	7.7/13.4	18.5/35.6
GPS/INS	✓	✓		2.5/4.6	8.9/19.0	6.9/12.3	15.1/28.1
GPS/INS	✓	✓	✓	2.5/4.6	8.4/17.8	6.9/12.4	14.9/25.7

Table 19 Position accuracy performances of the different configurations combining GPS and the IMU

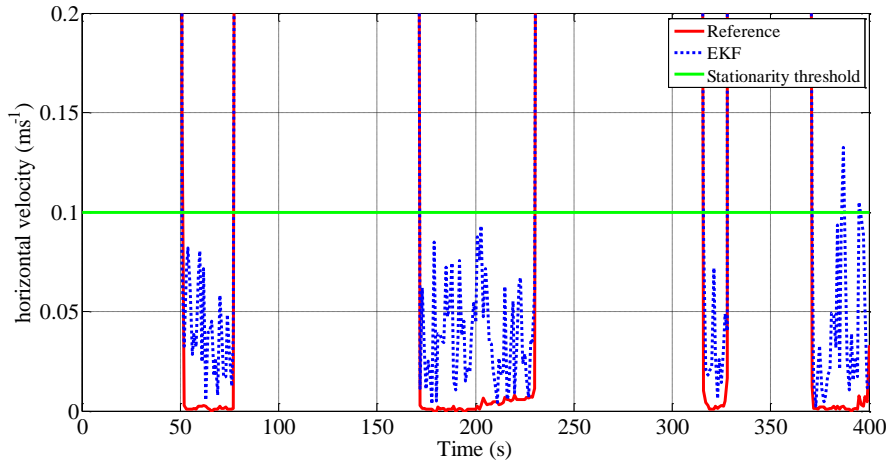


Figure 65 Selection of the Threshold for the detection of the stationarity to apply the ZUPT and ZARU constraints

Equivalently to what has been plotted for the simulations, position, velocity and attitude error estimation are represented with the estimated 3σ variance as estimated by the filter in Figure 66, Figure 67 and Figure 68. These figures correspond to the configuration augmented with the PRR. For simplicity other configurations have not been plotted. The behavior of the errors is similar to what have been observed in simulations. However, the position error sometimes exceeds the 3σ covariance, especially on the vertical axis in urban environment. Anyway, the velocity and heading estimation error are well characterized by the covariance as estimated by the EKF. In narrow urban canyons in which the vehicle is operating between 1300 and 2200 seconds, the reduction of the number of measurements available lead to an increase of the error covariance estimated by the filter, especially for the position and velocity errors.

The epochs at which the vehicle is stopped are characterized by a slowly growing heading error covariance. This can be simply explained by the fact that the measurements (especially GPS pseudoranges and pseudorange rates) do not provide any information about the attitude when the vehicle is fixed. In particular the yaw is not observable when the vehicle is stationary.

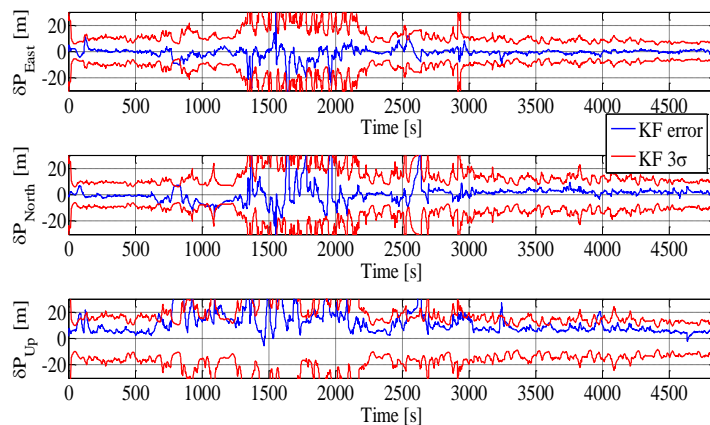


Figure 66 Position errors in the navigation frame, single frequency L1 C/A GPS receiver and IMU on real data

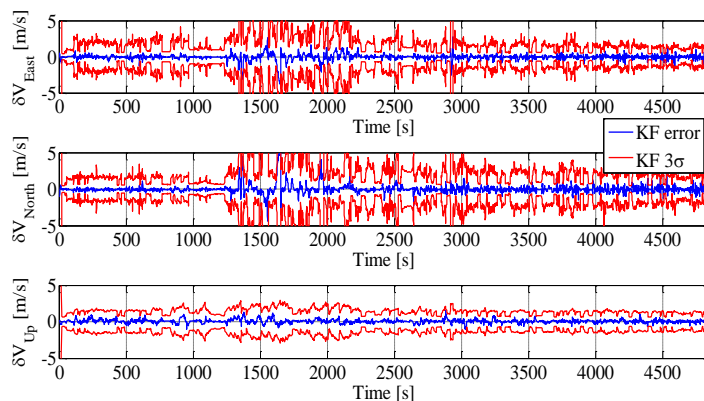


Figure 67 Velocity errors in the navigation frame, single frequency L1 C/A GPS receiver and IMU on real data

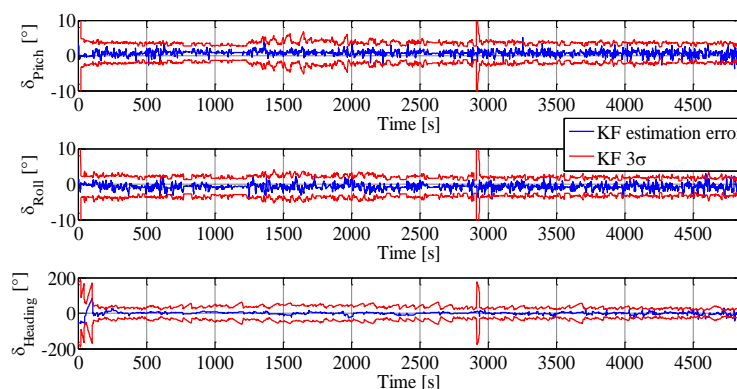


Figure 68 Attitude errors, single frequency L1 C/A GPS receiver and IMU on real data

6.3.3 Results: integration of the track database for train control

The architecture tested is composed of two subsystems. One subsystem is based on GPS and the second one is based on a second constellation. In this thesis, for the tests on real data, GLONASS has been used as a second constellation. The two subsystems are independently processed. The ionosphere delay has been corrected with Klobuchar model on the GLONASS measurements. It must not be done for an actual implementation of the solution that aims at using dual frequency receivers to remove ionosphere bias in order to avoid common mode failure. The number of GLONASS satellites being tracked is plotted in function of time in Figure 69, and its CDF is plotted in function of the environment of the vehicle in Figure 70. The elevation mask angle has been set to 5° . It can be inferred from figure that the number of GLONASS satellites being tracked in suburban environment is at least 8, 90% of the time. In urban environment this number has been higher than or equal to 5 more than 99% of the time. The number of satellite tracked in urban environment is higher for GLONASS than for GPS in urban environment.

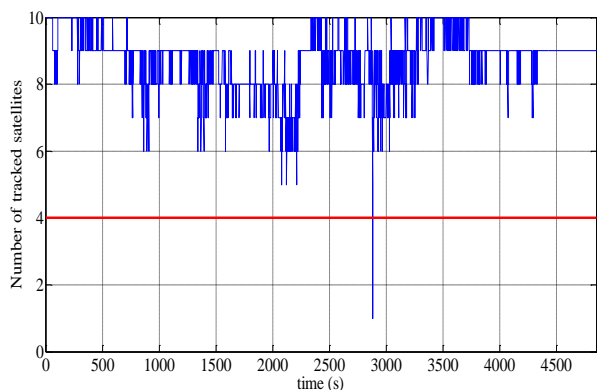


Figure 69 Number of GLONASS satellites being tracked as a function of time

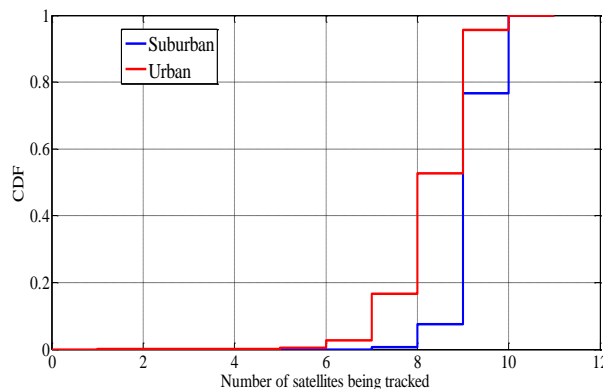


Figure 70 CDF of GLONASS satellites being tracked as a function of the environment

It appears that the receiver is more sensitive with respect to GLONASS signals than GPS signals in urban environment in the sense that it tracks weaker signals. Indeed, as illustrated in Figure 71, SV with very low C/N_0 (lower than 25 dB-Hz) are not tracked frequently on GPS compared to GLONASS. It is arguable that these degraded measurements improve the positioning, especially in case of critical applications.

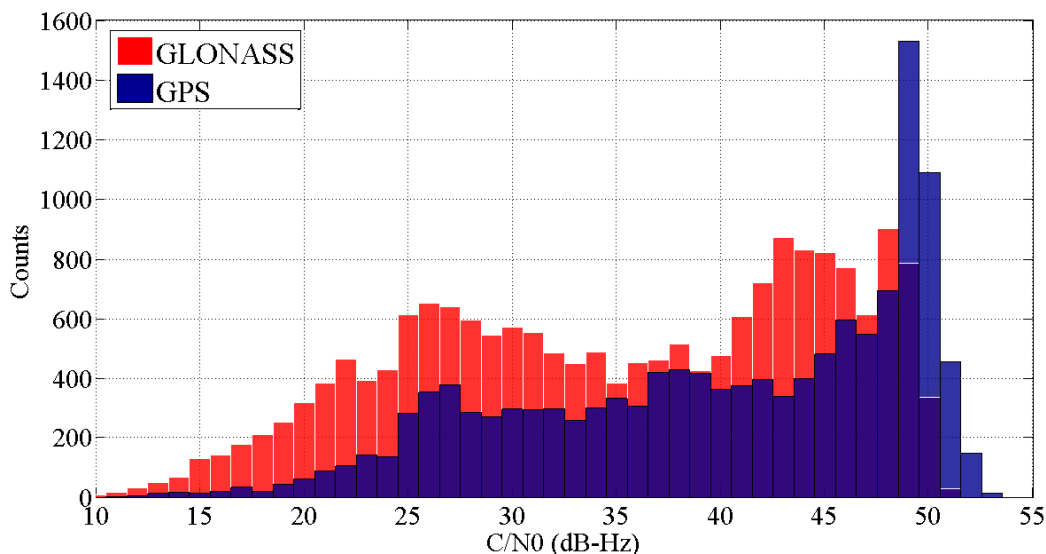


Figure 71 Histogram of C/N_0 in urban environment for GPS and GLONASS

The EKF that integrates GLONASS has the same design as the one that use GPS. The weighting scheme used for the GLONASS measurements is the one that has been presented in chapter 5 (different URA and thermal noise error model used with respect to the GPS weighting scheme). The performances presented here have been obtained by using the measurements from the same IMU. However, a real implementation requires independent devices. For each system, the track database has been generated as the true trajectory which has been sampled with a spatial step of 1.5 m. The error model described in chapter 5 has been added to the track points. Each system has its own track points. The performances of the combination of both is not given in this section because, as detailed in

chapter 4, the combined position solution involve the *HPL* of the subsystems which at not determined at this stage. As in simulations, the results are given in terms of along-track and across-track accuracy.

Sensors	PRR	NHC	ZUPT/ ZARU	RMS/Accuracy 95% (m)			
				Along-track		Across-track	
				Suburban	Urban	Suburban	Urban
GPS/INS/Map				2.8/5.2	5.6/12.5	0.2/0.4	0.7/0.8
GPS/INS/Map	✓			2.3/4.3	4.4/8.1	0.1/0.2	0.4/0.6
GPS/INS/Map	✓	✓		2.3/4.3	4.6/9.2	0.1/0.2	0.6/1.1
GPS/INS/Map	✓	✓	✓	1.8/3.6	4.1/8.3	0.1/0.2	0.4/1.1
GLO/INS/Map				2.7/5.8	9.3/18.2	0.2/0.4	0.8/0.9
GLO/INS/Map	✓			2.7/5.8	9.0/17.9	0.2/0.3	0.6/1.2
GLO/INS/Map	✓	✓		2.7/5.8	9.0/17.9	0.1/0.3	0.6/1.1
GLO/INS/Map	✓	✓	✓	2.2/5.0	8.1/16.0	0.1/0.2	0.5/1.0

Table 20 Position accuracy performances of the different configurations combining GPS or GLONASS, the IMU and the track database

The filter that integrates GLONASS measurements shows worse accuracy performances in dense urban environment. A possible explanation to this observation is that GLONASS L1 uses a BPSK(0.5) modulation, for which the multipath sensitivity is higher than for BPSK(1) used in GPS L1 C/A. Thus it is less robust to multipath error. Moreover, more satellites with high C/N_0 are visible for GPS as depicted in Figure 71.

Again, the right behavior of the filter is monitored by comparing the 3σ of the state estimation and the error. The results are plotted in Figure 72 to Figure 77 for the two EKF that use GPS L1 C/A and GLONASS L1 measurements. For both filters, the state estimation error fulfills the criterion except in a few epochs in urban environment. It is visible between 750 and 800 seconds on the north component of the position error for the GPS based EKF (encircled in black in Figure 72). This observation is characteristic of an incorrect modelling of the measurement error. This issue is addressed in chapter 7.

A direct consequence of applying the 1D constraint is the removal of the vertical error. The horizontal velocity error and its estimated variance have been reduced by integrating the track base in the solution.

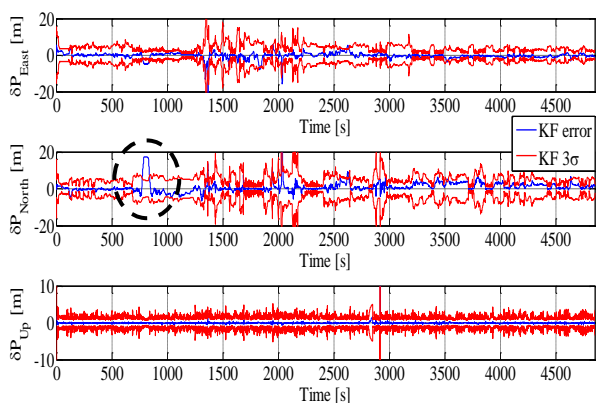


Figure 72 Position error, single frequency GPS L1 C/A receiver, IMU and track database on real data

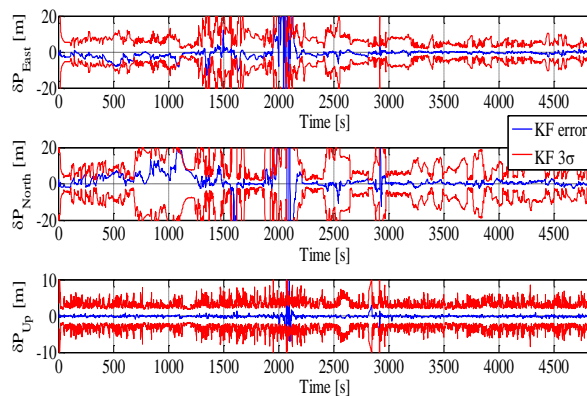


Figure 73 Position error, GLONASS L1 receiver, IMU and track database on real data

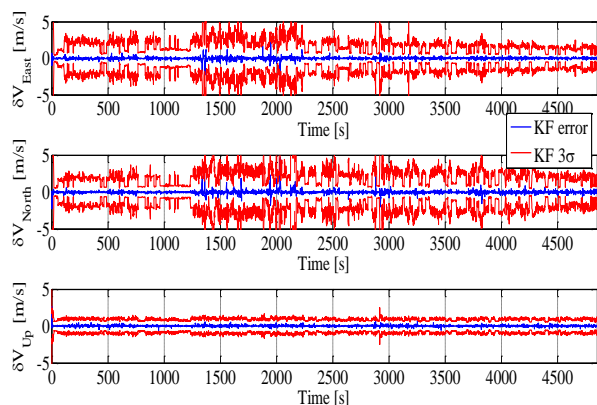


Figure 74 Velocity error, single frequency GPS L1 C/A receiver, IMU and track database on real data

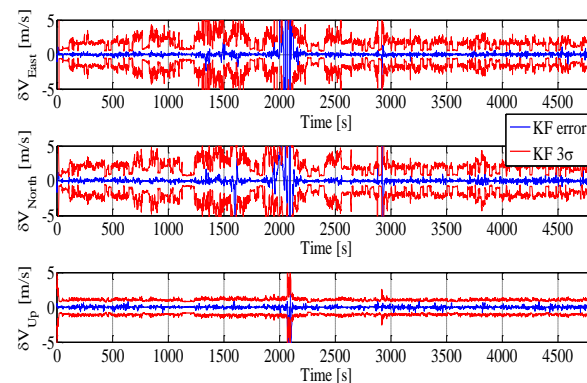


Figure 75 Velocity error, GLONASS L1 receiver, IMU and track database on real data

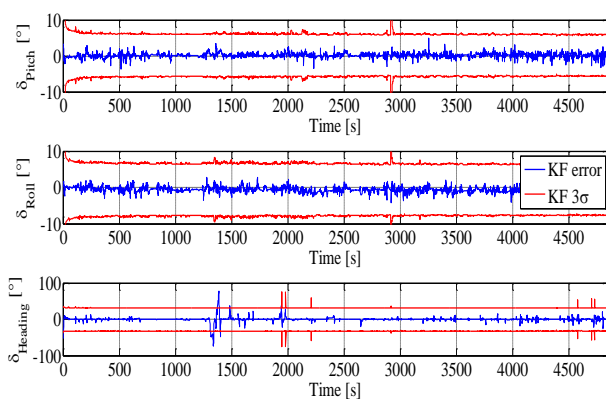


Figure 76 Attitude error, single frequency GPS L1 C/A receiver, IMU and track database on real data

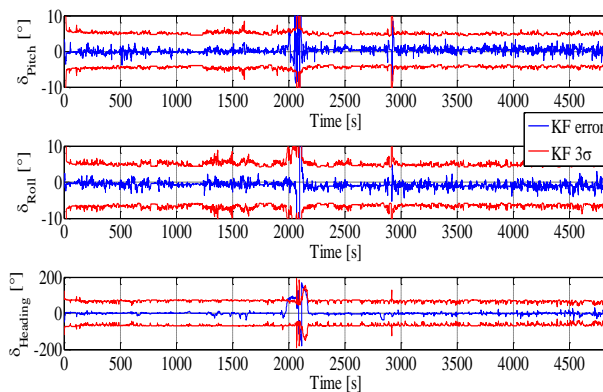


Figure 77 Attitude error, GLONASS L1 receiver, IMU and track database on real data

Essentially, the integration of the track in the solution has improved the heading and velocity estimation, and thus the along-track position estimation. The benefit of the integration of the track database cannot be observed directly from the comparison of the two tables as they are not in the same

references. However, it has been observed that the along-track position improvement is remarkable in urban environment. At best the GPS/INS configuration performs a 13 m along-track accuracy (it corresponds to a horizontal accuracy of 17.8 in Table 19) in urban environment whereas 8.3 meters have been performed when integrating the track database.

The benefit of the map is the most visible in the case of degraded constellation (i.e. less than 4 satellites), which occurs frequently in narrow urban canyons for single GNSS receiver. To verify this assertion, on the GPS based EKF, GPS Code and Doppler measurements have been removed on purpose in a portion of suburban environment (150 seconds). All satellites have been removed except SV 12 and SV 13, which elevations are 50° and 17° . The results in terms of horizontal error are plotted in Figure 78. It can be seen that the drift and the uncertainty on the estimated position are both improved by integrating the track base information. The horizontal error after integration of the map does not exceed 10 meters during the partial GPS outage whereas it reaches more than 50 meters without map. The integration of the map is equivalent to restrain the motion to one dimension. Thus 2 satellites are necessary to determine the along-track position and the clock bias. Moreover, in urban canyons, the satellites that are the least likely to be masked are those which are in the axis of the street. The satellites that are in the axis of the street are those which drive the along-track positioning accuracy.

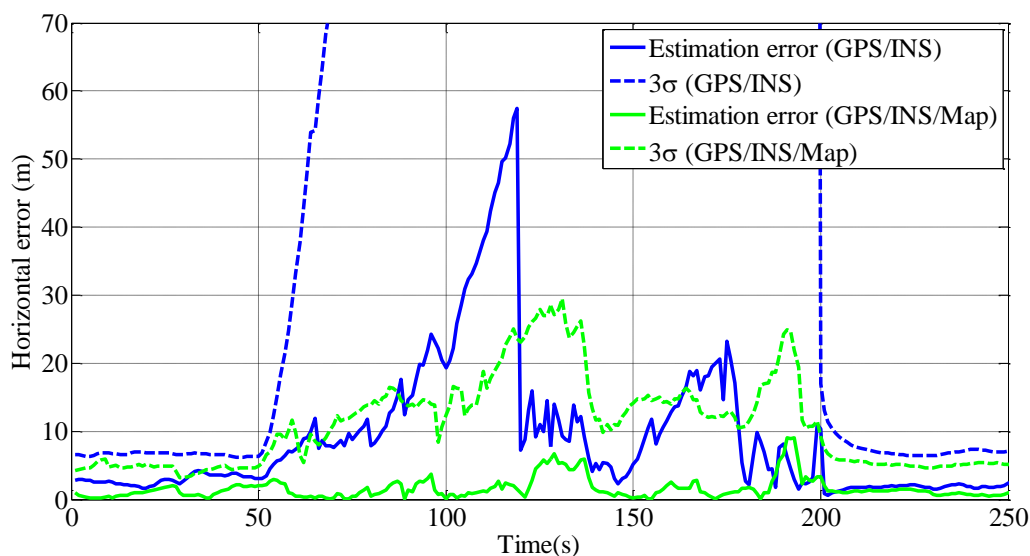


Figure 78 Position error after exclusion of all GPS satellites except SV 12 and SV 13 (from 50 to 200 seconds).

As only 2 satellites are theoretically required for the positioning with integration of the track database, it is suitable to apply very restrictive criteria for the inclusion of the measurements in the position calculation. It is feasible to apply, for instance, a 40 dB-Hz C/N_0 mask and a 50° elevation mask on the measurements, even when processing measurement from one constellation only. Doing so, it is possible to remove most NLOS signals at the cost of higher error covariance (and therefore will lead to higher *HPL*).

6.3.4 Results: dual constellation based architecture and introduction of WSS for electronic toll collection

For ETC, the architecture of the solution proposed has been detailed in chapter 4. The GPS/INS EKF has been modified to process both GPS and GLONASS simultaneously. Essentially, the state vector has been augmented with the GLONASS clock bias and clock drift. The accuracy of the GPS/GLONASS/INS EKF is given in Table 21. The benefit of adding PRR and constraints to the initial solution has also been investigated in term of horizontal position accuracy.

Most current automotive vehicles contain WSS. Therefore, the integration of WSS in the solution has been tested. Unfortunately, we had no access to these measurements in the framework of the thesis. The WSS measurements have thus been simulated from the velocity of reference to which white noise and scale factor errors have been added according to the model given in chapter 5. The results are given in Table 21. The NHC are always selected in the table when using WSS because they are contained in the WSS measurement model.

Table 21 shows that the use of a dual constellation receiver improves significantly the accuracy in urban environment (from 44 to 26 m). Moreover, as more satellites are in view, it is possible to apply restrictive C/N_0 and elevation masks to remove the measurements that are likely to be dangerous from an integrity point of view (essentially NLOS). The use of the pseudorange rates has significantly improved the accuracy in all directions urban environment as observed in the previous configurations and on simulations. The use of WSS slightly improves the horizontal accuracy in urban environment. It has to be mentioned that the accuracy in the sense of the 95% percent confidence interval does not fully represents the whole performances of the solution and may not reflect the improvement provided by additional sensors or constraints. Indeed, it has been observed by investigating the error distribution that the WSS reduces the maximum error in urban and suburban environments whereas the improvement on the accuracy/RMS is not significant. WSS have particular interest in case of long GNSS outages such as in tunnels. To prove it, a complete GNSS outage has been simulated by removing all GNSS measurements during 50 seconds when the vehicle was driving in suburban environment. This has been done on the GPS/GLONASS/INS fusion scheme which processes pseudorange rates. The results in terms of horizontal errors are given in Figure 79. In both configurations (with and without WSS), it can be observed that the horizontal error slowly drift as well as the estimated standard deviation estimated by the filter. However, the magnitude of the error drift has been reduced significantly (from 150 to 20 m) under dead reckoning mode by integrating the WSS measurement.

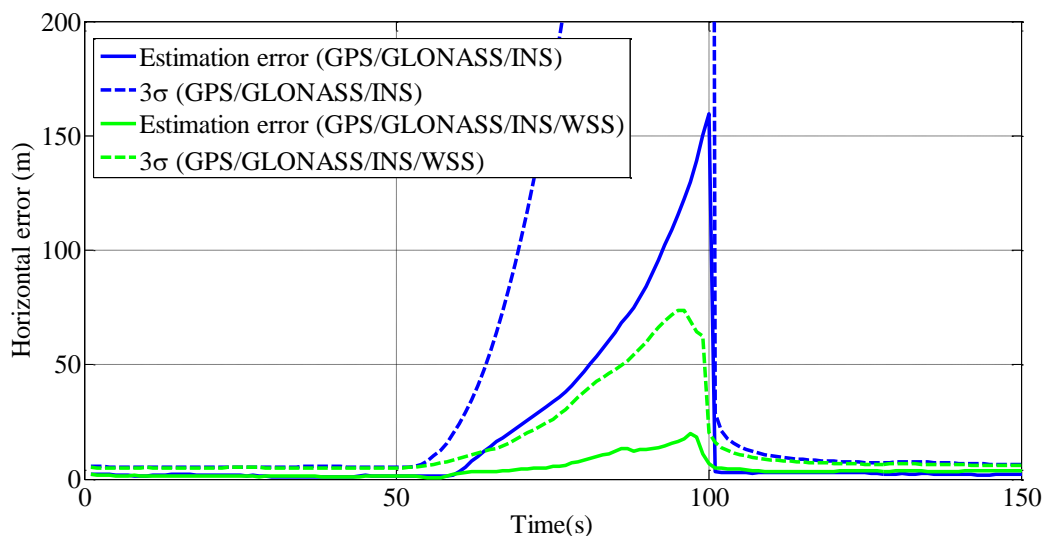


Figure 79 Horizontal position error after exclusion of all GPS and GLONASS satellites during 50 s (50 to 100 s)

Finally, the configuration that includes the WSS and the constraints provides the best position estimation, especially in urban environment.

Sensors	PRR	NHC	ZUPT ZARU	RMS/Accuracy 95% (m)			
				Horizontal		Vertical	
				Suburban	Urban	Suburban	Urban
GPS/GLO (LS)				12.0/19.5	13.5/27.6	24.6/45.6	32.8/71.5
GPS/GLO/INS				3.7/6.0	8.3/16.5	9.8/17.6	17.1/33.1
GPS/GLO/INS	✓			3.4/5.3	6.8/11.2	9.5/14.3	17.0/30.0
GPS/GLO/INS	✓	✓		3.1/5.1	6.7/12.3	8.2/13.7	12.0/21.2
GPS/GLO/INS	✓	✓	✓	2.9/4.9	6.5/12.0	7.4/11.4	12.1/20.8
GPS/GLO/INS/ WSS		✓		3.9/6.1	6.5/12.4	7.7/10.8	11.9/18.9
GPS/GLO/INS/ WSS	✓	✓		2.8/4.6	6.3/10.1	7.2/10.4	12.5/19.0
GPS/GLO/INS/ WSS	✓	✓	✓	2.8/4.7	6.8/11.7	7.1/10.2	12.6/19.3

Table 21 Position accuracy performances of the different configurations combining GPS, GLONASS, the IMU and WSS

As the WSS has been simulated, the scale factor error is known. The WSS scale factor error as estimated by the EKF is compared to the constant value that has been simulated. The results are given in Figure 80 for the configuration that integrates PRR measurement. After a transient state that lasted approximately 300 seconds, the WSS 3% scale factor error is well estimated by the EKF. The residual error is centered and within the 3σ bounds. For a real odometer, the WSS scale factor error is expected to vary with time due to slips and slide as well as variation of the diameter of the wheels due to pressure and temperature variations. In that case, the correlation time that is involved in the state transition matrix shall be adjusted as well as the covariance of the WSS scale factor driven noise.

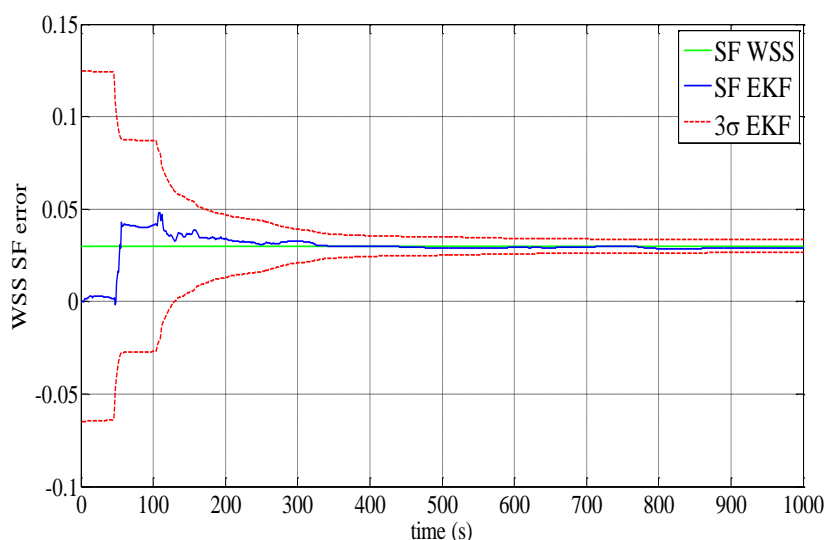


Figure 80 Estimation of WSS scale factor error

6.4 Conclusions

A GNSS/INS fusion algorithm based on EKF has been fully designed in section 6.1. From a common architecture, different possible ways to improve the navigation thanks to additional measurements and dynamic constraints have been proposed. Moreover, the algorithm has been adapted to Train control by integrating a map and to ETC by integrating two constellations and WSS. Then, for each application, different configurations of sensors and measurements can be used.

The fusion algorithms have then been validated and their performances have been assessed with simple realistic simulations in 6.2.

- Simulations have shown that, with nominal measurements errors, for train control, no solution is able to fulfill the across track sub meter accuracy requirement. However, the different configurations tested perform along-track accuracies that are lower than the 6.6 meters requirement associated to the most stringent operations for train control.

- Simulations have shown that even by integrating a single constellation, the solutions that uses PRR measurements have a better accuracy than the 5.1 m requirement (the most stringent case).

Therefore the solutions that are proposed are relevant with respect to the requirements. It was then necessary to test them on real data.

Thus, the fusion algorithms have then been tested on real data in Toulouse downtown and suburbs. The basic GPS/IMU architecture which is the part that is common to both train control and ETC architecture has been tested first. As observed in the simulations, on real data, the EKF improves the position accuracy in the horizontal and vertical plane and smooth the estimated trajectory. It has also been observed that, in most cases, the improvement obtained by using motion constraints is not significant. Therefore these measurements will not be used in the next sections.

For train control, the conclusions of this analysis are the following:

- It has been showed that even the most accurate GPS/IMU configuration is not able to perform sufficient across track accuracy for track selectivity in train control in any environment.
- The use of the track database has mainly improved accuracy in the across track direction, however, in dense urban, this motion constraint has been shown to improve the accuracy. It has also been proven that the EKF does not diverge, even with only two satellites in view if the track base is integrated. This is of particular interest for applying restrictive masks for the satellite selection and protect against local effects, which from the integrity monitoring is crucial.
- In suburban environment, the 6.6 meter along-track accuracy requirement is fulfilled for both GPS and GLONASS based EKF. The solution is not accurate enough for navigation in train stations and corridor in urban environment.

For ETC, the conclusions of this analysis are the following:

- The accuracies performed in suburban environments are lower than the worst case 5.1 m requirement for most configurations.
- The simultaneous processing of the two constellations has shown significant improvements in dense urban area (from 17 m at best, to 10 m horizontal accuracy). It is sufficient to fulfill the less stringent requirements.
- The integration of WSS has shown low benefit in terms of horizontal accuracy.
- The principal benefit of using WSS is to limit the error drift in case of long GNSS outage.

6.5 References

[Angrisano, 2010] A. Angrisano, GNSS/INS Integration Methods. PhD Thesis, "Parthenope"

- University of Naples, 2010.
- [bahnhof.ch] bahnhof.ch
- [Gleason and Gebre-Egziabher, 2009] Gleason, S., Gebre-Egziabher, D.: GNSS Applications and Methods. Artech House, Boston (2009)
- [Groves, 2013] Groves, P.D. Principles of GNSS, Inertial, and Multisensor Integrated Navigation Systems; Artech House: London, UK, 2013
- [Kalman, 1960] R. E. Kalman, , "A new approach to linear filtering and prediction problems" , Trans. ASME J. Basic Eng. , vol. 82 , pp.34 -45 , 1960
- [Shin, 2001] Shin, E. (2001), Accuracy Improvement of Low Cost INS/GPS for Land Application, MSc Thesis, Department of Geomatics Engineering, University of Calgary, Canada, UCGE Report No. 20156
- [Syed et al., 2007] Syed, Zainab, Aggarwal, Priyanka, Niu, Xiaoji, El-Sheimy, Naser, "Economical and Robust Inertial Sensor Configuration for a Portable Navigation System," *Proceedings of the 20th International Technical Meeting of the Satellite Division of The Institute of Navigation (ION GNSS 2007)*, Fort Worth, TX, September 2007, pp. 2129-2135.
- [Vezinet, 2014] J. Vezinet, Study Of Future On-Board GNSS/INS Hybridization Architectures, PhD Thesis, 2014
- [Zhang et al., 2012] Wen Zhang, Mounir Ghogho, and Baolun Yuan, "Mathematical Model and Matlab Simulation of Strapdown Inertial Navigation System," *Modelling and Simulation in Engineering*, vol. 2012, Article ID 264537, 25 pages, 2012. doi:10.1155/2012/264537
- [Zheng et al., 2009] Zheng, Y., Cross, P., Quddus, M., "The Effects of Railway Track Database Quality on the Performance of Tightly Coupled GNSS/Track Database Train Positioning System," *Proceedings of the 22nd International Technical Meeting of The Satellite Division of the Institute of Navigation (ION GNSS 2009)*, Savannah, GA, September 2009, pp. 2146-2155

7 SELECTION OF THE GNSS MEASUREMENTS

The objective of this chapter is to define a set of metrics and tests in order to select the measurements that will be integrated in the navigation algorithm. This selection process aims at removing from the PVT calculation the measurements that are unreliable in order to assist the integrity monitoring algorithm upstream so that it can focus on other types of failures. It has already been stated in Chapter 5 that the multipath interference phenomenon and the tracking of NLOS signals are the two sources of failures intrinsic to the urban/suburban environments (interference and other threats are not being investigated in the thesis).

Multipath is a phenomenon that affects radio-wave propagation in urban environment. It originates from the interaction of a travelling radio-frequency signal with urban objects present between the emitting and receiving antenna such as buildings, lamp poles or vehicles. These interactions can be reflection and diffusion by surfaces or diffraction by edges. For the GNSS case, when the direct signal (LOS) is received as well as well as multipath, the autocorrelation function is distorted which generates a bias on the estimation of the code delay by the DLL. The bias on the pseudo-range measurements in turn transforms into an error in the position domain, and may lead to positioning failures. It is therefore proposed to detect and then exclude or underweight the measurements that are affected by large non nominal multipath errors. In this chapter, the way to detect abnormally biased measurements due to multipath is investigated. In particular, a simple approach to design a multipath detection module based on the principle of detection of non-nominal distortions of the correlator function is proposed in section 7.1.

However, the tracking of a NLOS signal may not result in an abnormal distortion of the correlation function. Therefore, such an event may not be detected by monitoring the correlation function. It is necessary to detect this phenomenon by other means. It can be done by applying elevation/azimuth and/or C/N_0 masks as well as cross checking the GNSS measurements with the measurements

predicted using the sensors that are available on board (Kalman filter innovation monitoring). The ways to protect the system against biased measurements due to the tracking of NLOS signals is detailed in section 0.

7.1 Detection of measurements affected by abnormally large errors due to multipath

The contribution of multipath to the nominal error model has been characterized by simulations in chapter 5. For the different models of receivers and modulations, the error distribution has been CDF-overbounded by a zero-mean normal distribution which variance does not exceed 2 m, even for the very low elevations. This is due to the filtering effect by the carrier tracking loop (because the echoes have different Doppler frequencies than the direct signal) combined with the short lifespan of the echoes because on the simulations that have been conducted on the LMS channel, the vehicle is assumed to be moving at 20 km/h. However, larger errors due to multipath may occur in real urban environment, for instance when the vehicle is driving at lower velocities. In this case, the multipath error distribution may not be well represented by this nominal error model. It is either necessary to inflate the nominal model or to detect and exclude the measurements that are not covered by this model.

To prove that such errors are theoretically possible, let us investigate the multipath error envelope. The multipath error envelope is obtained by assuming that the signal is affected by one reflection, with a fixed attenuation, in phase or antiphase compared to the LOS. If the LOS and the echo are not in phase or antiphase, the magnitude of the resulting measurement error will be lower. Assuming the worst possible configuration, the amplitude of the specular echo is equal to the amplitude of the signal of reference. The multipath error envelopes for the two models of receiver presented in section 4.1 processing GPS L1 C/A and Galileo E1 OS are plotted in Figure 81 and Figure 82. For the narrowband receiver, the theoretical maximum tracking error is 73.2 m for L1 C/A and 55.0 m for E1 OS. For the wideband receiver model with narrow Early-Late spacing, the theoretical maximum tracking error is 15.1 m for L1 C/A and 18.3 for E1 OS. Therefore, such biases due to multipath, which are theoretically possible, are a threat for the integrity of the solution. They are all the more dangerous in case of degraded constellation conditions that occur in urban environment (because an impact of a measurement bias has a larger impact on the position error). Moreover, in Kalman filtering, the measurement errors are assumed to be centered which is an invalid assumption in such case. Additionally, at low velocities, the multipath errors are not smoothed by the EKF. Moreover it induces other problems related to the position computation based on Kalman filtering:

- the measurement errors are assumed to be centered which is an invalid assumption in such case.
- at low velocities, the multipath errors are not smoothed by the EKF.

- several large multipath errors could theoretically occur simultaneously on several measurements, especially when using dual constellation receivers such as proposed for ETC or for quad constellation based train control system

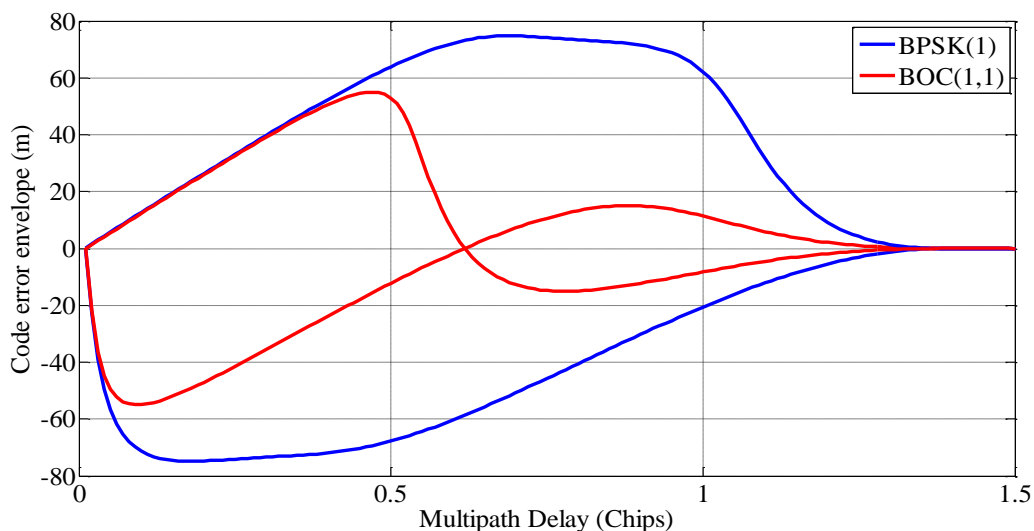


Figure 81 Code multipath envelope for the narrowband receiver model processing GPS L1 C/A and Galileo E1 OS

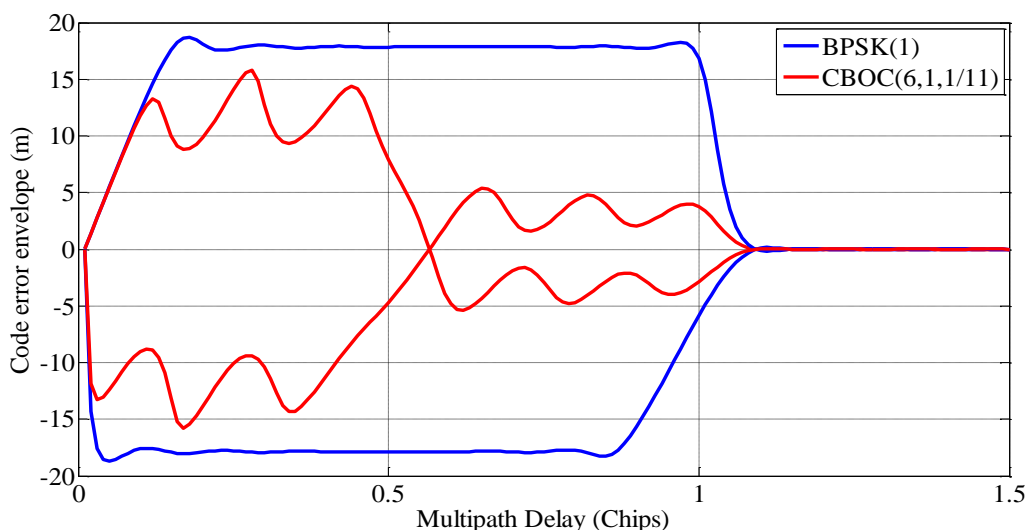


Figure 82 Code multipath envelope for the narrowband receiver model processing GPS L1 C/A and Galileo E1 OS

The approach detailed in this section consists in detecting the abnormally distorted measurements (in the LOS + NLOS configuration) and inform the integrity monitoring algorithm about their status. The aim is to measure the distortion of the correlation function due to multipath to detect abnormal measurement and exclude them prior to the integrity monitoring module. The techniques used to measure the distortion due to multipath are inspired from the research done for the detection of evil waveforms (EWF) which are anomalies on the transmitted GNSS signals [Pheltes,

2001]. Inspired from this approach, [Irsigler and Hein, 2005] proposed a technique to detect the presence of multipath by using these EWF monitors.

The approach is that of a classical hypothesis testing. A set of two hypotheses to test is defined:

- H_0 : no multipath is present
- H_1 : presence of multipath

Distortion metrics which are linear combinations of correlator outputs are used as test variables to detect multipath-induced distortions. In this thesis existing metrics and a new metric are investigated. A new rigorous approach to calculate the decision thresholds under H_0 and to adjust the Probability of False Alarm (P_{FA}) is proposed and compared to the prior art.

The P_{FA} is defined as:

$$P_{FA} = P(H_1|H_0) \quad \text{Eq. 7-1}$$

The theoretical concept of multipath sensitivity under H_1 and associated to a value of Probability of Missed Detection (P_{MD}) is defined and discussed in this thesis.

The P_{MD} is defined as:

$$P_{MD} = P(H_0|H_1) \quad \text{Eq. 7-2}$$

Then, the performances of the detection tests are assessed on time series generated by an urban channel model processed by a realistic GNSS receiver simulator.

7.1.1 Existing and proposed detection metrics

The proposed test metrics are linear combinations of correlator outputs which enable to analyze the distortion of the correlation function used by the DLL (and thus to generate the code pseudorange measurements). Usual metrics are detailed in the literature and the two that perform the best according to prior art [Irsigler and Hein, 2005] for multipath detection are the so-called simple ratio and differential ratio metrics.

Existing metrics are coherent and therefore can only be used when the carrier is tracked by a Phase Lock Loop (PLL). In urban environments, the tracking of the carrier phase by a PLL is less robust than the tracking of the carrier frequency by a Frequency Locked Loop (FLL). However, tracking only the frequency does not allow to have a carrier phase lock and thus results in an erroneous phase estimation. If this bias is close to $\pi/2$ for instance, the useful signal at the in-phase correlator output is dominated by thermal noise and computing the coherent metrics becomes meaningless. A non-coherent metrics is thus proposed in this thesis because it is compatible with the use of a FLL. The drawback of non-coherent metrics is the difficulty to accurately characterize their distribution. Coherent metrics will be studied in section 7.1.2, while non-coherent metrics will be studied in section 7.1.3.

Let us denote I_X and Q_X the in-phase and quadrature-phase correlator outputs located in X on the correlation function. The expressions of the metric of references are detailed in Table 22.

Type of test	Expression
Simple Ratio Tests (M_1)	$\frac{I_X}{I_Y}$
Differential Ratio Tests (M_2)	$\frac{I_X - I_Y}{I_Z}$
Non Coherent Simple Ratio Tests (M_3)	$\frac{I_X^2 + Q_X^2}{I_Y^2 + Q_Y^2}$

Table 22 Metrics of interest used in this thesis

Note: The A Posteriori Multipath Estimator (APME) [Sleewaegen and Boon, 2001], which has been patented by Septentrio is an open loop multipath estimation technique used for multipath mitigation and designed for GPS L1 C/A. The expression of the APME multipath error (MP) estimator is given by:

$$MP = -0.42\lambda_c \left(1 - \frac{\gamma_{+2} I_{L2}}{\gamma_0 I_P} \frac{1}{1-d} \right) \quad \text{Eq. 7-3}$$

where:

- 0.42 is an empirical likelihood factor
- I_{L2} is an additional “very late” correlator output (delayed by d chips with respect to the prompt)
- γ_{+2} and γ_0 are corrections terms that accounts for the rounding of the correlation peak due to the filtering of the incoming signal by the front-end (the way to compute these parameters is not).

This multipath estimator is equivalent to simple ratio metric (I_{L2}/I_P), which is centered (its expectation in the nominal case is equal to $\gamma_0(1-d)/\gamma_2$) and multiplied by a likelihood factor. Good multipath detection performance can be expected for such a metric as it is able to estimate correctly the multipath error according to [Sleewaegen and Boon, 2001].

7.1.2 Determination of the detection thresholds for coherent metrics

In this chapter, it is assumed that H_0 holds which means that the receiver is only affected by thermal noise. The general correlator output model at the k^{th} integration index when assuming a linear variation of the phase tracking error during the integration interval has been given in Eq. 2-9. In this chapter, the tracking is assumed to be sufficiently precise to neglect the code tracking error ($\tau - \hat{\tau}$), the phase tracking error ($\theta - \hat{\theta}$) and the frequency tracking error ($f - \hat{f}$) in the nominal case (i.e. Multipath free). The phase tracking error can only be neglected if the carrier is tracked by a PLL. The data are also not considered in the model as they have no impact when the correlator outputs are normalized by another correlator output corresponding to the same integration index, as it will be the case here. The simplified correlator output model becomes:

$$I_X(k) = \sqrt{\frac{C}{2}} K_{cc}(X) + n_X(k) \quad \text{Eq. 7-4}$$

Therefore the normalized correlator output distribution is such that $I_X \sim \mathcal{N}(\mu_X, \sigma_X^2)$ with:

- $\mu_X = \sqrt{2 C/N_0 T_i} K_{cc}(X)$
- $\sigma_X^2 = 1$
- The covariance between two correlator outputs in X and Y is $cov(n_X n_Y) = E[n_X n_Y] = K_{cc}(Y - X)$ [Irsigler and Hein, 2005] and [Sleewaegen and Boon, 2001]

The objective is now to establish the thresholds on the metric so that the receiver decide whether it is under H_0 or H_1 . In this subsection we study two different methods for the determination of the thresholds.

7.1.2.1 Threshold determination assuming that the metric is Gaussian

The first method which is the one proposed in [Irsigler and Hein, 2005] assumes that the metrics (Simple Ratio Tests and Differential Ratio Tests) follow Gaussian distributions. Let's denote M an arbitrary metric among the coherent ones, it is assumed that $M \sim \mathcal{N}(\mu_M, \sigma_M^2)$. Therefore the interval of confidence for the metrics is the interval $[\mu_M - m_{exp} \sigma_M; \mu_M + m_{exp} \sigma_M]$ where m_{exp} is an expansion factor that can be adjusted according to the desired P_{FA} . The relation between this factor and the P_{FA} can be obtained with standard tables of Gaussian tails. For instance, $m_{exp} = 2$ corresponds to an expected P_{FA} of 0.0455. The ratio of two Gaussian random variables asymptotically tends towards a Gaussian distribution when μ_M/σ_M tends towards infinity. This assumption may be relevant in the operating conditions of [Irsigler and Hein, 2005] because in this article the integration time is sufficiently high ("1000 ms") and the simulated C/N_0 values are high (40/45 dB-Hz). In a standard GNSS receiver however, the integration time is much shorter (20 ms for GPS L1 C/A at best with data bit synchronization assumed). Moreover C/N_0 values can be lower than the range of value tested in the prior art in a challenging environment, which is relevant to the application of interest. As a consequence, the distribution of the metrics has to be revisited for the present case. For each coherent metric, the bounds of the confidence interval are given hereafter, and the calculations to obtain them are given in appendix G.

For the Simple Ratio Tests (M_1), at the first order, the expression of the expectation and the standard deviation are given by:

$$E[M_1] = \frac{\mu_X}{\mu_Y} \quad \text{Eq. 7-5}$$

$$std(M_1) = \frac{\mu_X}{\mu_Y} \sqrt{\left(\frac{\sigma_X^2}{\mu_X^2} + \frac{\sigma_Y^2}{\mu_Y^2} - 2 \frac{cov_{XY}}{\mu_X \mu_Y} \right)} \quad \text{Eq. 7-6}$$

For the Differential Ratio Tests (M_2), the expression of the expectation and standard deviation are given by:

$$E[M_2] = \frac{\mu_X - \mu_Y}{\mu_Z} \quad \text{Eq. 7-7}$$

$$\text{std}(M_2) = \left(\frac{\mu_X - \mu_Y}{\mu_Z} \right) \sqrt{\frac{\sigma_Z^2}{\mu_Z^2} + \frac{\sigma_X^2 + \sigma_Y^2 - 2\text{cov}_{XY}}{(\mu_X - \mu_Y)^2} + 2 \frac{\text{cov}_{ZX} - \text{cov}_{ZY}}{\mu_Z(\mu_X - \mu_Y)}} \quad \text{Eq. 7-8}$$

7.1.2.2 Threshold determination without assuming that the metric is Gaussian

The approach which is proposed in this thesis does not assume any Gaussianity aspect of the metric (the correlator outputs are still considered Gaussian). It can thus be applied to receivers using standard integration time and for signals with low C/N_0 .

The Geary-Hinkley transformation [Geary, 1930] [Hinkley, 1969] makes it possible to form a new random variable that is Gaussian when applied to a ratio of two correlated non central Gaussian variables. If $I_X \sim \mathcal{N}(\mu_X, \sigma_X^2)$ and $I_Y \sim \mathcal{N}(\mu_Y, \sigma_Y^2)$ with a covariance cov_{XY} , then the expression of the Geary-Hinkley transform applied to $M_1 = \frac{I_X}{I_Y}$ is the following:

$$T = \frac{\mu_Y M_1 - \mu_X}{\sqrt{\sigma_Y^2 M_1^2 - 2\text{cov}_{XY} M_1 + \sigma_X^2}} \quad \text{Eq. 7-9}$$

where $T \sim \mathcal{N}(0,1)$ provided that the denominator inside de square root operator is unlikely to reach negative values.

The next step for the threshold determination is to set the desired P_{FA} on the transformed variable T . Let m_{exp} be the expansion factor that corresponds to the expected P_{FA} , the thresholds for M_1 are the roots of the associated second degree equation. For every metrics and the thresholds obtained are given hereafter.

For the Simple Ratio Tests (M_1), the expression of the lower bound (LB) and the upper bound (UB) of the metric's distribution are given by:

$$LB = \frac{-(-2\mu_X\mu_Y + 2m_{exp}^2\text{cov}_{XY}) - \sqrt{(-2\mu_X\mu_Y + 2m_{exp}^2\text{cov}_{XY})^2 - 4(\mu_Y^2 - m_{exp}^2\sigma_Y^2)(\mu_X^2 - m_{exp}^2\sigma_X^2)}}{2(\mu_Y^2 - m_{exp}^2\sigma_Y^2)} \quad \text{Eq. 7-10}$$

$$UB = \frac{-(-2\mu_X\mu_Y + 2m_{exp}^2\text{cov}_{XY}) + \sqrt{(-2\mu_X\mu_Y + 2m_{exp}^2\text{cov}_{XY})^2 - 4(\mu_Y^2 - m_{exp}^2\sigma_Y^2)(\mu_X^2 - m_{exp}^2\sigma_X^2)}}{2(\mu_Y^2 - m_{exp}^2\sigma_Y^2)}$$

For the Differential Ratio Tests (M_2), the expression of the lower and upper bounds of the metrics can be deduced from the expressions of Eq. 7-10. To do so, it is necessary to substitute the index X by the index N , and Y by the index Z (the third point on the correlation function) in the general expression of Eq. 7-10 where :

$$\mu_N = \mu_X - \mu_Y \quad \text{Eq. 7-11}$$

$$\sigma_N = \sqrt{\sigma_X^2 + \sigma_Y^2 - 2cov_{XY}} \quad \text{Eq. 7-12}$$

$$cov_{N,Z} = cov_{XZ} - cov_{YZ} \quad \text{Eq. 7-13}$$

The validity of the thresholds provided above is directly derived from the validity of the Geary-Hinkley transformation which is defined by $\mu_Y \geq m_{exp}\sigma_Y$. By replacing μ_Y and σ_Y by their expressions, the domain of validity corresponds to:

$$C/N_0 \geq \frac{1}{2T_i} \left(\frac{m_{exp}}{K_{cc}(Y)} \right)^2 \quad \text{Eq. 7-14}$$

Eq. 7-14 shows that the validity domain of the threshold depends upon the correlation function used to track the signal. It will thus be affected by the signal modulation. Indeed the slope of the correlation function is higher for BOC or CBOC signals than for a BPSK(1). This means that the range of relevant locations for the correlator at the denominator is thinner than for BPSK. This intuitive assumption is well illustrated by the domain of validity of the bounds given in Eq. 7-14. In Figure 83, the lower bound of the validity domain in term of C/N_0 is given as a function of the correlator location for the three modulations with an infinite receiver's front-end bandwidth. The expansion factor is set to a typical value of 3σ which corresponds to a P_{FA} of 0.0027. The operational range of C/N_0 constrains the choice for the monitoring correlators. In urban environment where a typical value for the C/N_0 mask is 30 dB-Hz (as shown in 5.1.1.1.5) to select the robust measurement in a multi-GNSS system, for an expansion factor of 3, the allowed values of Y for BPSK is [-0.5, 0.5] whereas it is [-0.17, 0.17] for BOC(1,1) and CBOC(6,1,1/11).

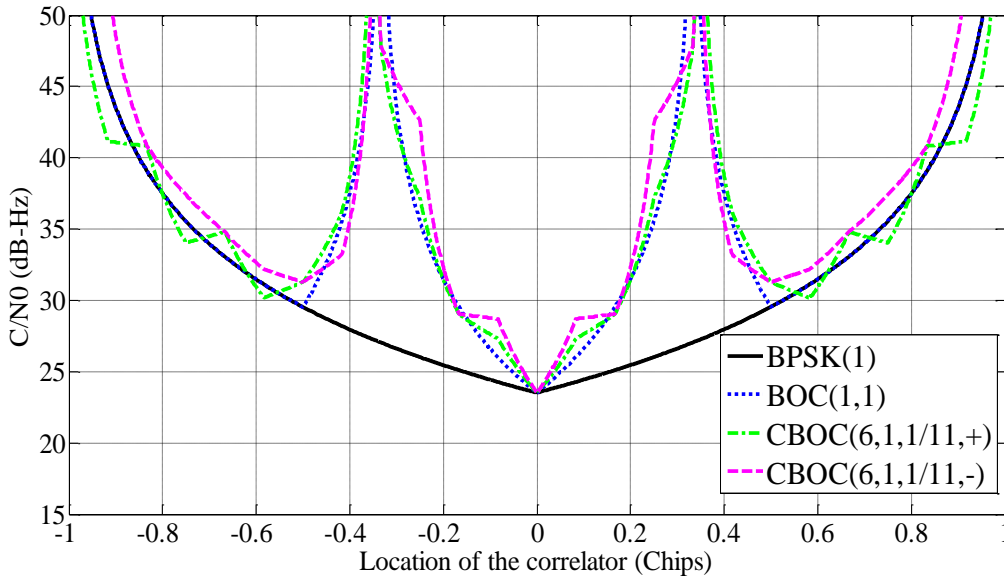


Figure 83 Locations allowed for the correlator used for the normalization of the metric correspond to the area above the curve

As the detectors studied in this thesis are likely to be implemented on standard receivers that only process three correlators outputs (prompt, early and late), this will limit the amount of possible combination to form the metric. The validity domain of the BOC imposes the condition of a chip spacing for the DLL lower than 0.34 to normalize the test by either the early or the late correlator output.

7.1.2.3 Improvement brought by the non-Gaussian approach

The performances of the thresholds based on the Gaussianity and non-Gaussianity assumptions are compared on a typical case of study in which the receiver processes GPS L1 C/A and Galileo E1 OS. The RF front-end bandwidth is assumed infinite for simplicity. Three correlator outputs are simulated according to the model presented in Eq. 7-4, in $X = 0$, $Y = 0.25$ and $Z = 0.125$. The correlation duration is set to 20 ms. The thresholds are calculated with gaussianity assumption and with the proposed method for a typical range of operating C/N_0 for an expansion factor of 3. The observed P_{FA} is plotted in Figure 84 for M_1 and in Figure 85 for M_2 on GPS L1 C/A signals.

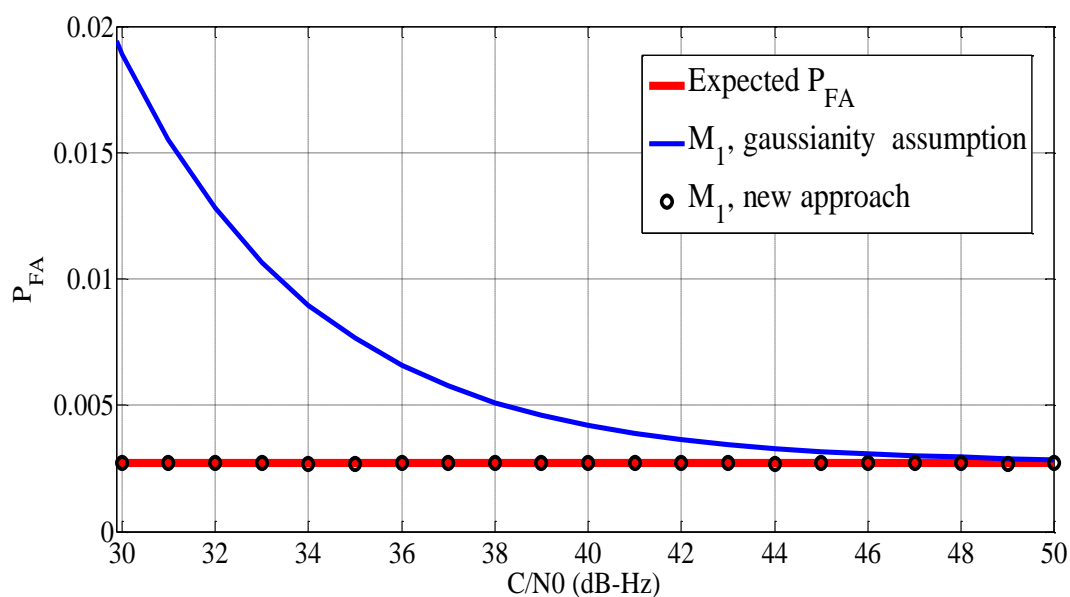


Figure 84 Comparison between the expected P_{FA} (0.0228) and the observed P_{FA} for M_1

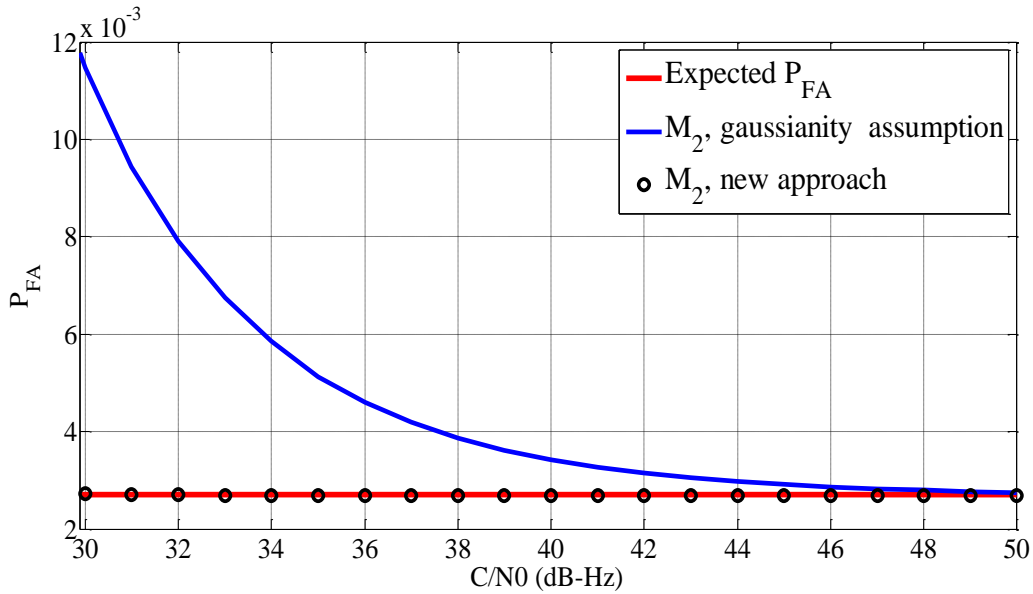


Figure 85 Comparison between the expected P_{FA} (0.0228) and the observed P_{FA} for M_2

It can be noticed that the Gaussianity of the metric distribution increases with the C/N_0 as the observed P_{FA} converge to the expected P_{FA} . The proposed thresholds enable to set the right P_{FA} , even for low C/N_0 . This observation would be all the more characteristic for lower integration times (typically 1 ms).

7.1.3 Determination of the detection thresholds for non-coherent metrics

For non-coherent metrics, it is now required to use the quadrature-phase correlator outputs that are modelled by:

$$Q_X(k) = \sqrt{\frac{C}{2}} d(k) K_{cc}(X) \sin(\varepsilon_\varphi) + n_X(k) \quad \text{Eq. 7-15}$$

The determination of the thresholds for the non-coherent metric (M_3) requires the knowledge of its distribution. The term $I_X^2 + Q_X^2$ follows a chi-square distribution with 2 degrees of freedom and a non-centrality parameter $2T_{int} C/N_0 K_{cc}(X)$. This result is classically used to form tests in the acquisition step of the receiver. The ratio of two uncorrelated non-central χ^2 distributed variables follows a doubly non-central F-distribution [Bulgren, 1971], [Scheffé, 1959], with known parameters. Few works discuss the doubly non-central F-distribution, and a way to approximate this distribution is given in [Paolella, 2007]. To test the approximation, I_X , Q_X , I_Y and Q_Y are generated without taking into account their correlation. Under these assumptions:

$$M_3 \sim F(2, 2, 2T_{int} C/N_0 K_{cc}^2(X), 2T_{int} C/N_0 K_{cc}^2(Y)) \quad \text{Eq. 7-16}$$

where F denotes the doubly noncentral F -distribution.

Eq. 7-16 has been validated by simulations. However, when considering the correlation between X and Y correlator outputs, the distribution of the non-coherent metric becomes unknown and different from the basic doubly non central F-distribution. In particular, it has been observed by simulations that the non-centrality parameters do not correctly describe the function. Simulations have shown that the distribution of M_3 (with consideration of the correlation between X and Y) can be coarsely approximated by a different doubly noncentral F -distribution:

$$M_3 \sim F \left(2, 2, 2T_{int}C/N_0 \frac{K_{cc}^2(X)}{K_{cc}(X-Y)}, 2T_{int}C/N_0 \frac{K_{cc}^2(Y)}{K_{cc}(X-Y)} \right) \quad \text{Eq. 7-17}$$

The result is given in Figure 86 for different values of C/N_0 with $X = 0$ and $Y = 0.25$ chip. The PDF of the empirical approximation coarsely fit the actual distribution even when the C/N_0 value and the X and Y locations are varying.

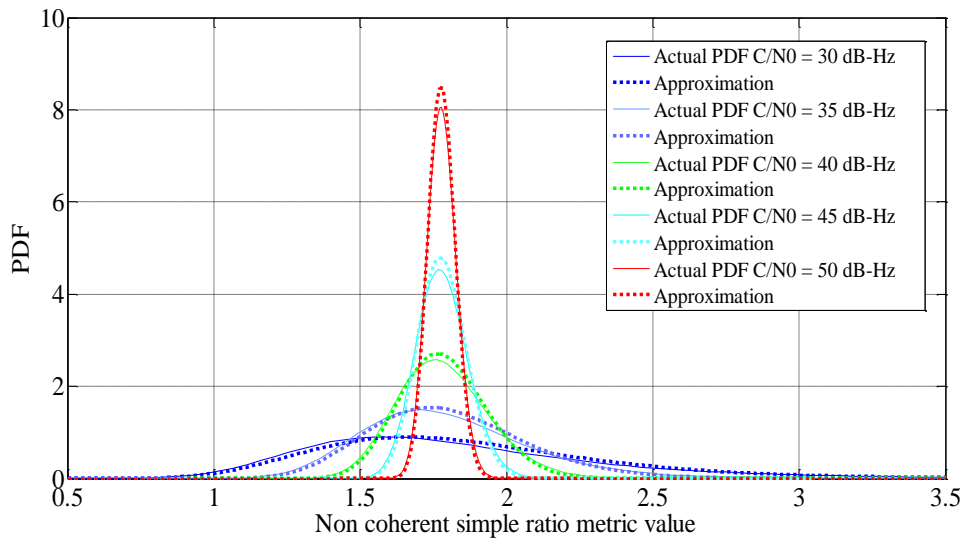


Figure 86 Approximation of the non-coherent metric probability density function with doubly non central F distribution

Due to the fact that this distribution is difficult to handle, the best approach consists in calculating the thresholds by simulation. Therefore, for non-coherent metrics, the thresholds are computed numerically. The interval of non-detection is symmetric and centered on the mean of the metric. The lack of knowledge about the distribution of the metric is the main drawback related to the use of non-coherent metrics.

7.1.4 Sensitivity of the Detection Metrics

In this subsection, the signal is assumed to be affected by one unique reflection in phase with the direct signal, which is one hypothesis generally assumed for the characterization of multipath mitigation techniques (multipath envelope) although it is not at all representative from the urban conditions with a mobile user. However, it is interesting to first test our detection metric in a simple

case. The non-coherent metrics are not studied in this section due to the lack of knowledge of their distributions. The model of the correlator output thus becomes:

$$I_{X,MP}(k) = \sqrt{\frac{C}{2}} K_{cc}(X) + \frac{1}{\sqrt{SMR}} \sqrt{\frac{C}{2}} K_{cc}(X - \tau) + n_X(k) \quad \text{Eq. 7-18}$$

where:

- τ is the relative delay of the reflection with respect to the direct signal
- SMR is the signal to multipath power ratio

The Gaussian model can be used here with:

$$\mu_{X,MP} = \mu_X + \sqrt{\frac{2 C/N_0 T_{int}}{SMR}} K_{cc}(X - \tau) = \mu_X + \alpha K_{cc}(X - \tau) \quad \text{Eq. 7-19}$$

The sensitivity is defined as the maximum Signal to Multipath Ratio (SMR) at which the test is successful providing a given allowable probability of missed detection (P_{MD}). In this subsection it is assumed that the multipath delay τ is a parameter. Figure 87 illustrates the two scenarios that can occur and can lead to a missed detection. The P_{MD} corresponds to the area (in red) in between the thresholds that were set under the H_0 hypothesis.

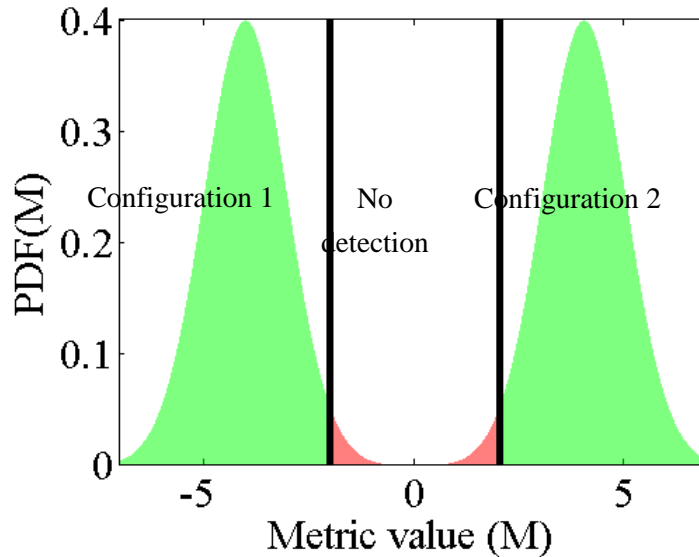


Figure 87 Possible scenarios that can lead to a missed detection

The metric affected by multipath has a new distribution, which is unknown. However the multipath only affects the mean of the metric of both numerator and denominator. The calculation of the sensitivity starts from the following statement on the metric:

- Configuration 1:

$$UB_{\exists MP} = LB_{\exists MP} \quad \text{Eq. 7-20}$$

- Configuration 2:

$$LB_{\exists MP} = UB_{\bar{\exists} MP} \quad \text{Eq. 7-21}$$

Where $LB_{\bar{\exists} MP}$ and $UB_{\bar{\exists} MP}$ are respectively the lower bound and upper bound determined in the multipath free scenario to set the P_{FA} . $LB_{\exists MP}$ and $UB_{\exists MP}$ are respectively the lower and upper bound in the presence a multipath.

The analytic expressions of $UB_{\exists MP}$ and $LB_{\exists MP}$ are obtained using the Geary-Hinkley transformation, by introducing a new expansion factor m_{md} in order to set the P_{MD} . Particular caution must be taken when setting the P_{MD} because as illustrated in Figure 87 the missed detection probability is only due to one of the two Gaussian tail (either left or right). Therefore in order to impose $P_{MD_{true}}$, the expansion factor m_{MD} shall be chosen so that it performs $P_{MD_{bilat}} = 2P_{MD_{true}}$.

Then, Configuration 1 is assumed in order to calculate the minimum SMR , which is obtained by solving the second order equation given in Eq. 7-23. The validity of the Scenario must be checked afterwards with the following possible indicator:

$$\eta = \text{sign}(E[m|\exists MP(SMR, \tau)] - E[m|\bar{\exists} MP]) \quad \text{Eq. 7-22}$$

- If η is positive, Configuration 1 is valid.
- If η is negative, Configuration 1 is not valid and the SMR shall be calculated for Configuration 2 with the corresponding equation

For the Simple Ratio Test metric, the sensitivity is obtained by calculating the minimum root (denoted α_1) of the following second order polynomial form:

Configuration 1:

$$\begin{aligned} & \alpha^2 \{ [UB_{\bar{\exists} MP} K_{cc}(Y - \tau)]^2 - 2UB_{\bar{\exists} MP} K_{cc}(Y - \tau) K_{cc}(X - \tau) + K_{cc}(X - \tau)^2 \} \\ & + \alpha \{ 2UB_{\bar{\exists} MP}^2 \mu_Y K_{cc}(Y - \tau) - 2UB_{\bar{\exists} MP} [\mu_X K_{cc}(Y - \tau) + \mu_Y K_{cc}(X - \tau)] \\ & + 2\mu_X K_{cc}(X - \tau) \} + UB_{\bar{\exists} MP}^2 (\mu_Y^2 - m_{MD}^2 \sigma_Y^2) + 2UB_{\bar{\exists} MP} (-\mu_X \mu_Y + m_{MD}^2 \text{cov}_{XY}) \\ & + \mu_X^2 - m_{MD}^2 \sigma_X^2 = 0 \end{aligned} \quad \text{Eq. 7-23}$$

Configuration 2:

$$\begin{aligned} & \alpha^2 \{ [LB_{\bar{\exists} MP} K_{cc}(Y - \tau)]^2 - 2LB_{\bar{\exists} MP} K_{cc}(Y - \tau) K_{cc}(X - \tau) + K_{cc}(X - \tau)^2 \} \\ & + \alpha \{ 2LB_{\bar{\exists} MP}^2 \mu_Y K_{cc}(Y - \tau) - 2LB_{\bar{\exists} MP} [\mu_X K_{cc}(Y - \tau) + \mu_Y K_{cc}(X - \tau)] \\ & + 2\mu_X K_{cc}(X - \tau) \} + LB_{\bar{\exists} MP}^2 (\mu_Y^2 - m_{MD}^2 \sigma_Y^2) + 2LB_{\bar{\exists} MP} (-\mu_X \mu_Y + m_{MD}^2 \text{cov}_{XY}) \\ & + \mu_X^2 - m_{MD}^2 \sigma_X^2 = 0 \end{aligned} \quad \text{Eq. 7-24}$$

Then the SMR is deduced with:

$$SMR = \frac{2 C/N_0 T_{int}}{\alpha_1^2} \quad \text{Eq. 7-25}$$

For the differential ratio test, the sensitivity is obtained with the same calculation, by substituting X by N , and Y by Z in the polynomial expression.

The sensitivity shall be taken into account in the design of the quality monitoring indicator concept. The way to calculate and interpret the sensitivity is given in this study through a realistic example. The C/N_0 is set to 40 dB-Hz, and the metric of interest is M_1 , with $X = 0.25$ and $Y = 0$. The delay of the multipath is arbitrarily set to 0.5 chip. The signal of interest is in this example BPSK(1). This example is also used to validate the results obtained by simulations. The reverse process is done as a validation, where the multipath amplitude is set to the value of the sensitivity for the corresponding P_{FA} . Random draw of the metric value affected to multipath are performed, the P_{MD} is then estimated as the proportion undetected samples. It can be inferred from Table 5 that the correspondence between the P_{MD} and the sensitivity is well characterized by the theoretical expressions according to the green cells. This table of sensitivity could have been translated into a table of maximum pseudorange error. Indeed, as an example, for a conventional DLL using a narrow correlator to track the GPS L1 C/A signal, the rule of thumb for the envelope of the pseudorange multipath error is:

$$\varepsilon_{Multipath} = \frac{1}{\sqrt{SMR}} \frac{d}{2} \quad \text{Eq. 7-26}$$

where d is the chip spacing between the early and late correlators of the DLL.

		P_{FA}			
		0.0455	0.0027	$6.33 \cdot 10^{-5}$	$5.73 \cdot 10^{-7}$
P_{MD}	0.159	10.7 dB	7.70 dB	5.21 dB	3.00 dB
		0.159	0.159	0.159	0.159
	0.0228	8.20 dB	5.77 dB	3.62 dB	1.67 dB
		0.0228	0.0228	0.0228	0.0228
	0.00135	6.26 dB	4.18 dB	2.29 dB	0.505 dB
		0.00135	0.00135	0.00135	0.00135
	$3.17 \cdot 10^{-5}$	4.68 dB	2.84 dB	1.13 dB	-0.518 dB
		$3.18 \cdot 10^{-5}$	$3.21 \cdot 10^{-5}$	$3.21 \cdot 10^{-5}$	$3.18 \cdot 10^{-5}$
	$2.87 \cdot 10^{-7}$	3.34 dB	1.68 dB	0.105 dB	-1.43 dB
		$3.05 \cdot 10^{-7}$	$3.13 \cdot 10^{-7}$	$3.03 \cdot 10^{-7}$	$3.16 \cdot 10^{-7}$

Table 23 The white cells represents the sensitivity of the test (maximum SMR for which the detection is successful given the P_{MD}) on GPS L1 C/A for M_1 with an infinite front end bandwidth. The green cells represent the observed P_{MD} .

For low P_{FA} associated with low P_{MD} , the efficiency of the test in term of sensitivity is low (at best 10.7 dB corresponds to a worst case 21.4 m error with the narrowband receiver multipath envelope processing BPSK(1)). To improve it, an intuitive idea is to narrow the distribution of the multipath-free metric. Multipath has long correlation times compared to the thermal noise which is memoryless (white). Multipath deterministically results in a translation of the distribution of the metric.

To narrow the distribution, it is either possible to low-pass filter the correlator outputs that are combined to form the metric, or to low pass filter the metric. The smoothing of the correlator outputs is preferred as the new thresholds can easily be calculated when using the proposed approach. Moreover, the filtered denominator is less likely to be null after this filtering step which enableS the extension of the domain of validity of the metrics. On the other hand, if the Gaussianity assumption has been used it is more practical to filter the metric instead. The problem relative to such a smoothing is the data term in the correlator output that can be +1 or -1. If an external mean is available to get the data message, it is possible to multiply each correlator by the corresponding sign of the data bit which is known. An alternative is to take the absolute value of each correlator outputs. This step changes the distribution of the correlator output which must then be modelled by a folded normal distribution. This distribution can still be approximated by a Gaussian provided that the correlators are unlikely to take negative values. This condition is fulfilled if all the correlators used to form the metric are under the conditions of Eq. 7-14. The general model of correlator output becomes:

$$\mu_x = \sqrt{2 \frac{C/N_0}{B_l}} K_{cc}(X) \quad \text{Eq. 7-27}$$

$$\sigma_x = 1$$

where B_l is the double-sided equivalent noise bandwidth of the low pass filter. For a noise equivalent bandwidth of 5Hz, the sensitivity is given in Table 24.

		P_{FA}			
		0.0455	0.0027	$6.33 \cdot 10^{-5}$	$5.73 \cdot 10^{-7}$
P_{MD}	0.159	21.3 dB	18.7 dB	16.6 dB	14.9 dB
		0.159	0.159	0.159	0.159
	0.0228	18.8 dB	16.7 dB	15.0 dB	13.5 dB
		0.0227	0.0227	0.0228	0.0228
	0.00135	16.9 dB	15.1 dB	13.7 dB	12.4 dB
		0.00134	0.00134	0.00135	0.00135
	3.17e-5	15.3 dB	13.8 dB	12.5 dB	11.3 dB
		3.12e-5	3.15e-5	3.11e-5	3.14e-5

2.87e-7	13.9 dB	12.6 dB	11.5 dB	10.4 dB
	2.1e-7	1.9e-7	2.3e-7	2.2e-7

Table 24 The white cells represents the sensitivity of the test (maximum SMR for which the detection is successful given the P_{MD}) on GPS L1 C/A for M1 with infinite front end BW with smoothing of the correlator. The green cells represent the observed P_{MD} .

The gain in term of sensitivity obtained by smoothing the correlator outputs with a 5 Hz equivalent noise bandwidth low pass filter is approximately 11 dB in the studied scenario at best (at best 21.3 dB corresponds to 6.3 m error with the narrowband receiver multipath envelope processing BPSK(1)). The domain of validity is also increased thanks to the smoothing of the correlator used for the normalization assuming that the navigation message is known (if the absolute value is calculated, then (6) shall be used):

$$C/N_0 \geq \frac{B_l}{2} \left(\frac{m_{exp}}{K_{cc}(Y)} \right)^2 \tag{Eq. 7-28}$$

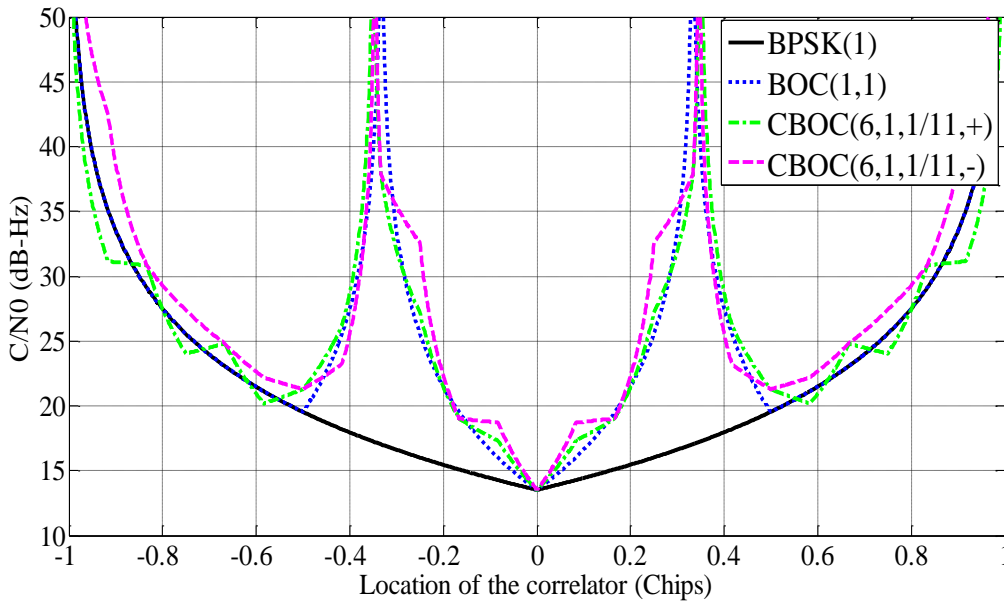


Figure 88 Allowed locations for the correlator used for the normalization of the metric after low pass filtering (5Hz)

7.1.5 Performance assessment on urban channel model

The aim of this section is to assess the performances of a test based on the multipath detection metrics to limit the filter out of abnormal pseudorange measurement in urban environment. The approach consists in coupling the wideband Land Mobile Satellite (LMS) Channel developed by the German Aerospace Center (DLR) and geneIQ as detailed in section 5.1.1.1.5. However, we chose to reformulate the test so that it is adapted to urban environment. Indeed in urban environment the

receiver is almost always affected by multipath and therefore always under H_1 . The new formulation is based on the definition of a maximum tolerable error (MTE).

The new hypotheses to test become:

- H_0' : the pseudorange error is lower than the MTE
- H_1' : the pseudorange error is higher than the MTE

The approach proposed initially, consists in setting the threshold on the metrics to fulfill a P_{FA} . The approach chosen in this section is different. Here, the MTE is set to a value (e.g. 5 meters), then the P_{MD} and P_{FA} are evaluated.

7.1.5.1 Simple ratio metric

As detailed in chapter 5 the implementation of a raw test metrics leads to poor performance in term of sensitivity. This can be illustrated by simulations on the LMS tracked by geneIQ. The channels for satellite elevations of 40, 50, 60, 70, 80° and satellite azimuths of 45 and 90° are concatenated. The LOS is not shadowed for these elevations. Each channel is 1 km long, and the velocity of the vehicle is set to 20 km/h. Thermal noise is added to the correlators assuming a C/N_0 set to 40 dB-Hz.

The simulated receiver is the wideband GPS L1 C/A receiver introduced in 4.1.2.1.2 In such a standard receiver, the available correlator outputs are located at -0.25, 0 and 0.25 chips on the correlation function. A simple ratio test with $X = 0.25$ and $Y = 0$ is used for multipath-induced error monitoring. Figure 89 illustrates the lack of correlation between the raw value of the metric and the code pseudorange error. The correlation coefficient between the two variables is - 0.19. Errors up to 8 meters are not detected.

To improve the performance, the correlator outputs are low-pass filtered with a rectangular low-pass filter with 3Hz noise equivalent bandwidth. The narrowness of the low-pass filter bandwidth is limited by the coherence time of the multipath, which in turn depends on the dynamic of the vehicle. The metric formed after filtering is shifted by a constant delay that maximizes the correlation between the metric and the code pseudorange error (e.g. 0.16 seconds for 3 Hz filtering). Figure 90 illustrates the existing correlation between the value of the metric and the code pseudorange error. The scatter is characteristic of two correlated variables. The magnitude of the coefficient of correlation between both variables is improved to - 0.53.

For a fixed maximum tolerable error and P_{FA} ($m_{exp} = 2$), the P_{MD} has decreased according to Figure 90. It reflects an improvement in sensitivity. Largest code errors are located in the right bottom region in Figure 90, which corresponds to a successful detection of abnormal error.

Table 25 contains the P_{FA} and P_{MD} as functions of the expansion factor chosen to set the thresholds. Firstly, Table 25 shows that the observed P_{FA} in urban environment is lower than the expected P_{FA} . In presence of several reflections and due to their impact on tracking loops, the distribution of the metric is different. New thresholds could be derived from these simulations to force the P_{FA} to the expected value, based on gaussianity assumption and by measuring the standard deviation of the metric. However, the validity of these thresholds would rely on too many hypotheses such as the satellite

elevation, the loop bandwidths, the chip spacing and the vehicle dynamic to name a few. Table 25 also illustrates the major improvement that can be obtained by smoothing the correlator outputs. Indeed for every expansion factor, the P_{FA} and P_{MD} are lower after low pass filtering.

Anyway, in this set of simulations, the magnitudes of the pseudorange errors are not large enough to be detected when setting a low P_{FA} (e.g. $m_{exp} = 3$).

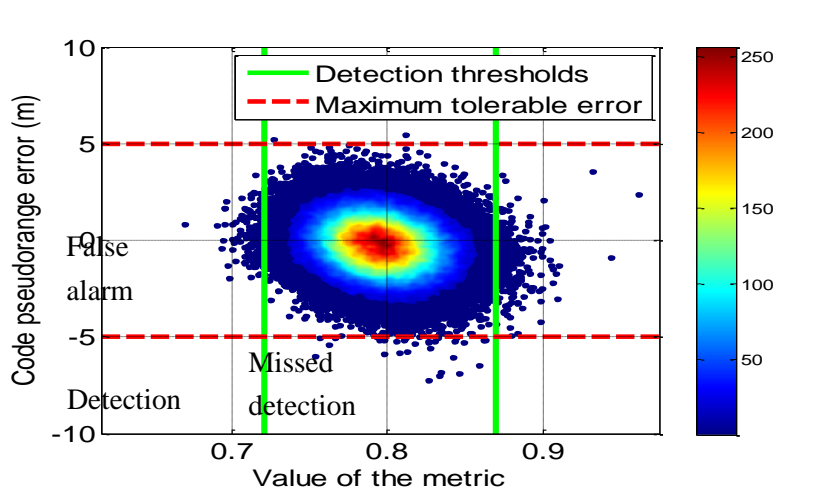


Figure 89 Correlation between code pseudorange error and value of the raw simple ratio metric (M_1) for BPSK

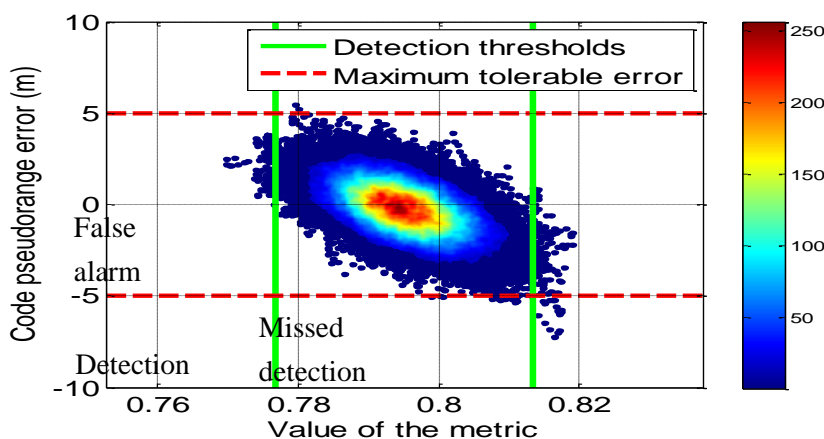


Figure 90 Correlation between code pseudorange error and value of the simple ratio metric (M_1) after smoothing the correlator outputs for BPSK

Theoretical P_{FA}	0.027	0.046	0.072	0.11	0.16
P_{FA} w/o filtering	0.0045	0.0088	0.018	0.034	0.063
P_{MD} w/o filtering	1	1	0.88	0.88	0.79
P_{FA} w/ filtering	0.0028	0.0056	0.0129	0.027	0.051

P_{MD} w/ filtering	0.52	0.52	0.30	0.17	0.090
-----------------------	------	------	------	------	-------

Table 25 Performances of the test based on the simple ratio test

The best P_{MD} presented in Table 25 after filtering is 9% which appears to be too high for such a detection algorithm. The MTE associated to this P_{MD} is equal to 5 meters. This magnitude is not sufficiently high with respect to the noise level to be detected with very low P_{MD} . The algorithm has been designed to detect errors that can lead to positioning failures (much larger than 5 meters), and it is expected to detect them with significantly lower P_{MD} .

7.1.5.2 Performance comparison with C/N_0 estimator

A conventional way for the receivers to monitor the signal quality is to estimate the C/N_0 . The objective is here to compare the ability of the C/N_0 estimation to detect error with high magnitude with the ability of a test based on the distortion metrics.

The C/N_0 estimator used hereafter is the one described in chapter 5, where the expectation and the variance terms are estimated over 1 second. We firstly compare the behavior of this estimator in presence of a 40 dB-Hz noise, with and without multipath.

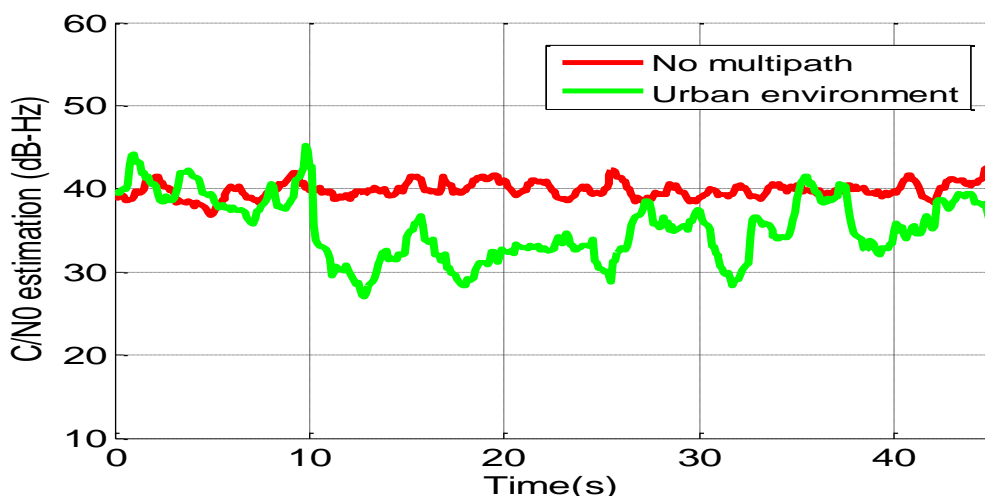


Figure 91 Estimation of C/N_0 with true C/N_0 set to 40dB-Hz

The quality of the C/N_0 estimation is degraded by the presence of multipath according to Figure 91. The C/N_0 is used for the determination of the detection threshold of the metric (in the expression of their mean). A suitable solution consists in smoothing the C/N_0 estimate over longer duration (several minutes).

Moreover, it has already been proven that the Signal to Noise Ratio (SNR) error is correlated (and in phase) with the multipath delay error [Sleewaegen, 1997]. This phenomenon can be illustrated through the simulation platform by processing the LMS output without adding any thermal noise. The shape of the scatter in Figure 92 shows that the highest multipath error occurs for low estimated C/N_0 . It is therefore relevant to define a monitoring algorithm based on this detector and it is then necessary to

set the lower bound for the detector. A typical value is 30 dB-Hz because it is a good trade-off between NLOS exclusion and availability. The efficiency of this monitoring approach is assessed on the LMS assuming a received signal with a C/N_0 of 40 dB-Hz. The code pseudorange error is plotted as a function of the estimated C/N_0 in Figure 93. Table 26 summarizes the performance of the C/N_0 based detection test for several threshold candidates.

It can be shown by comparing Table 26 to Table 25 that the SNR monitoring technique outperforms the test based on the raw metric monitoring. For instance, for a P_{FA} of 0.019, the SNR monitoring has a P_{MD} of 47% whereas the raw metric performs a P_{MD} of 88%.

However, the SNR monitoring is outperformed by the monitoring of the smoothed metric. Indeed, for an expansion factor of 1.4, the P_{FA} of the metric based monitor was 6.3%, and the P_{MD} associated was 9%. For an SNR threshold of 32 dB-Hz, the P_{FA} of the SNR monitor is equal to 8.3% and its P_{MD} is equal to 33% which is significantly higher (for an even higher P_{FA}).

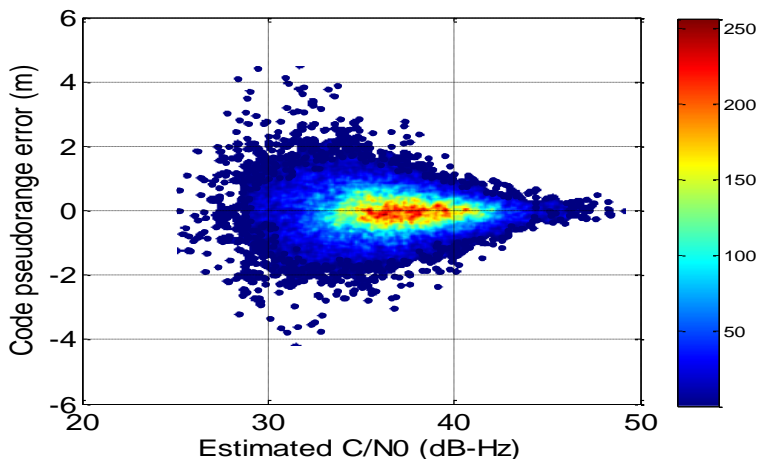


Figure 92 Correlation between code pseudorange error and estimated C/N_0 with multipath only for BPSK

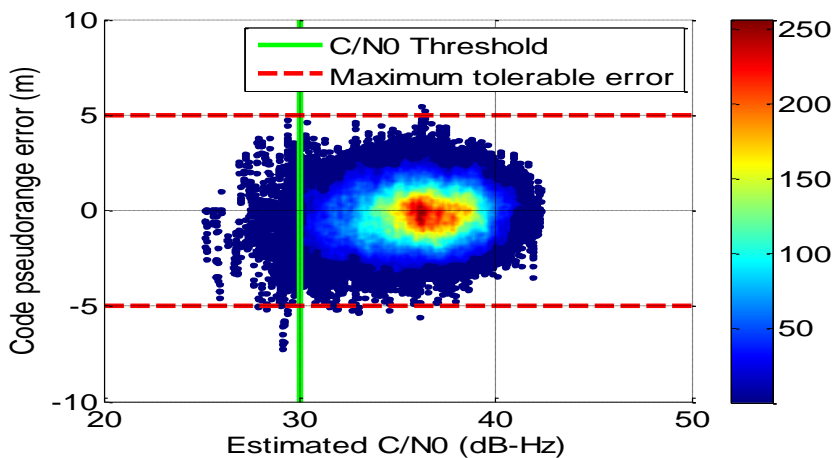


Figure 93 Correlation between code pseudorange error and estimated C/N_0 with multipath and thermal noise (40 dB-Hz) for BPSK

C/N_0 (dB-Hz) threshold	28	29	30	31	32
P_{FA}	0.0036	0.0089	0.019	0.043	0.083
P_{MD}	0.93	0.90	0.47	0.43	0.33

Table 26 Performance of the SNR monitoring

The test based on the simple ratio metric outperforms, after filtering, the test based on the C/N_0 in terms of P_{FA} and P_{MD} .

7.1.5.3 Other metrics

The same simulations were conducted for a differential ratio and non-coherent simple ratio. The differential ratio was formed by using $X = 0.25$ $Y = -0.25$ and $Z = 0$. This metric characterizes well the asymmetry of the correlation function. The correlation coefficient between the code error and this metric is 0.64 which is higher than the simple ratio metric. Table 27 summarizes the performance of this detector. No major improvement is obtained for the differential ratio compared to the simple ratio metric. Moreover the comparison in term of performance is difficult as the observed P_{FA} are not the same for both tests.

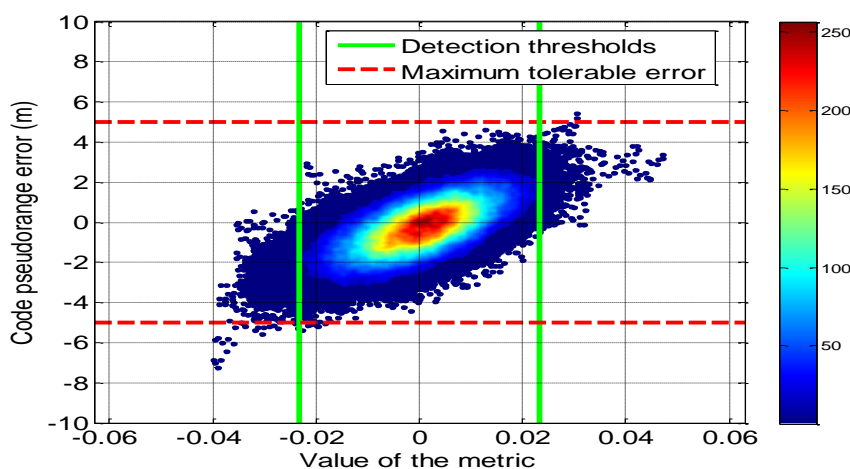


Figure 94 Correlation between code pseudorange error and differential ratio metric (M_2)

Theoretical P_{FA}	0.027	0.046	0.072	0.11	0.16
P_{FA}	0.007	0.012	0.023	0.040	0.069
P_{MD}	0.36	0.30	0.24	0.091	0.0

Table 27 P_{FA} and P_{MD} performed by monitoring the differential ratio metric

Finally a simple ratio non coherent test metric was implemented on the model of narrowband receiver, but the 3rd order PLL is replaced by a second order FLL with a 5 Hz loop bandwidth. The estimation

of the frequency error is based on the non-coherent differential arctangent discriminator. The metric is formed with $X = 0.25$ and $Y = 0$. The detection thresholds were determined a priori by simulating correlator output affected by thermal noise only. The results obtained in term of P_{FA} and P_{MD} are given in Table 10. Overall the performances of M_3 ratio are similar to the performances of M_1 and M_2 . It is therefore possible to implement a metric based test to detect the presence of multipath in a receiver using a FLL.

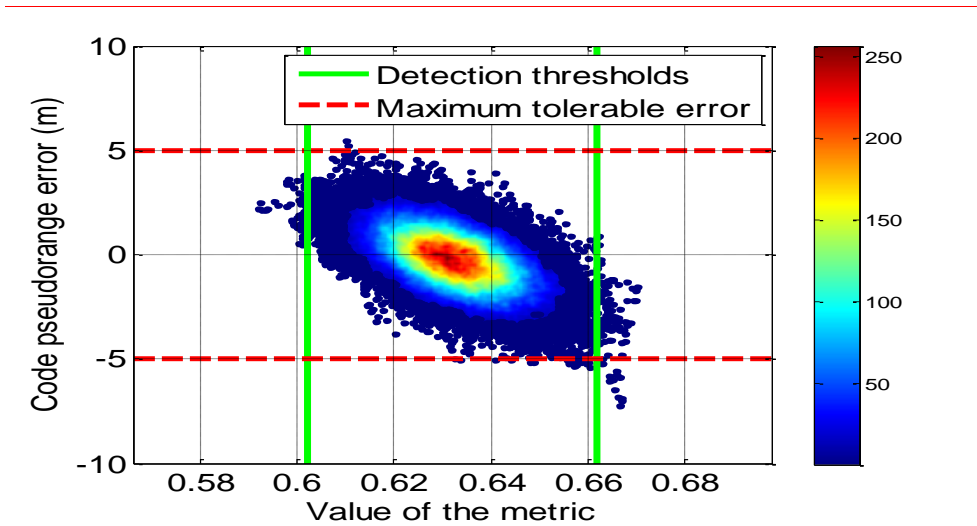


Figure 95 Correlation between code pseudorange error and non-coherent simple ratio metric (M_3)

Theoretical P_{FA}	0.027	0.046	0.072	0.11	0.16
P_{FA}	0.002	0.0054	0.012	0.025	0.047
P_{MD}	0.63	0.52	0.3	0.2	0.18

Table 28 P_{FA} and P_{MD} performed by monitoring the non coherent simple ratio metric

7.1.5.4 BOC(1,1) signal

The simple ratio metric is tested with a BOC(1,1) modulation with $X = 0.25$ and $Y = 0$. The location of Y is chosen in the validity domain according to Figure 1. Firstly, it can be inferred from Figure 11 that the magnitude of the pseudorange errors is lower for the BOC(1,1) modulation than BPSK. The maximum error does not reach 5 meters for BOC(1,1), therefore the maximum tolerable error is reduced to 3.5 meters. Table 29 shows that the metric is able to detect large errors even for BOC(1,1). Again, the errors observed do not have a sufficient amplitude to assess the performances for very low P_{FA} .

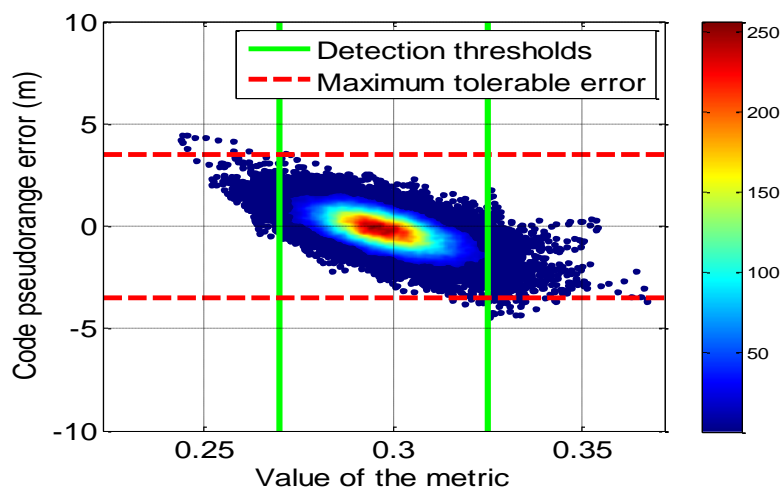


Figure 96 Correlation between code pseudorange error and simple ratio metric for BOC(1,1) modulation

Theoretical P_{FA}	0.027	0.046	0.072	0.11	0.16
P_{FA}	0.013	0.023	0.036	0.059	0.092
P_{MD}	0.32	0.18	0.054	0.036	0.018

Table 29 Performances of the simple ratio metric for BOC(1,1)

7.1.6 Conclusion

This section discusses the theoretical and simulated performance of a detection test based on correlation function distortion metrics. A new rigorous approach for the setting of the detection threshold is proposed. These thresholds enable to set the P_{FA} with a wider domain of validity. The sensitivity of the test is defined as the minimum SMR at which the test is able to detect the multipath with a fixed P_{MD} . It is then possible to theoretically assess the performances of the test metrics. It was proven in the chapter that a detector formed with the raw correlator outputs presents poor performances in term of sensitivity. However, smoothing either the correlator outputs or the metric enables narrowing the confidence interval and therefore significantly improves the sensitivity of the test.

Finally the performances of the detector were assessed by simulation on a Land Mobile Satellite channel simulator coupled with a realistic GNSS receiver simulator. The correlation between the raw metric and the actual pseudorange error is low and therefore as expected the performances of such test are low. The smoothing of the correlator outputs highly improves the sensitivity of the test provided that the bandwidth of the smoothing filter is sufficiently high not to filter out the dynamic of the multipath. Similar performances were obtained for other existing and proposed metrics and other signals.

The performances of these tests were compared with a multipath detector based on the *SNR* estimation. Even if the *SNR* estimation shows promising detection abilities, the test based on filtered correlator outputs is more efficient to detect abnormally large code error.

Finally, the test performed based on the LMS channel model did not allow generating code error with amplitude of several tenth of meter when the received signal is the sum of a LOS signal and reflections. This phenomenon is essentially due to the fact that the vehicle was moving at 20 km/h. Thus, the probability the lifespan of the reflections does not exceed a few seconds and the echoes are filtered by the carrier loop because of the difference of Doppler frequency between the direct signal and the reflections.

Future works shall be conducted to test the multipath monitoring indicators on actual measurements in urban environment. The ability of the test to detect multipath error with large magnitude thus remains to be tested.

7.2 Protection against NLOS errors and residual large multipath errors

Unlike multipath interference, there is generally no abnormal distortion of the correlation function when the receiver is tracking a reflected/diffracted ray. Thus the biased measurements must be detected by other means that are investigated hereafter.

A first possible way to protect the solution from integrating NLOS signals is to apply masks on the measurements. As train control and ETC solutions are based on different receivers and sensors they are studied separately in section 7.2.1 and section 7.2.2.

The second approach that is studied consists in taking advantage of the onboard sensors to detect inconsistency in the measurements. This technique used to detect and reject outliers is studied in section 7.2.3.

The results which are presented in this section are obtained by processing the real measurements that were collected in downtown Toulouse and surrounding. The corresponding data collection has been presented in section 5.3.2.2.

7.2.1 Application of masks in train control

The use of a track database has two main interests. Firstly it enables to estimate the position with degraded constellation as seen in chapter 6 (only two satellites are required for 1D positioning). It is therefore possible to apply masks that are very restrictive. The second interest is that it enables to store additional information into the map. It is of particular interest to inform the receiver to the environment in which it is operating. It can be used to coarsely adapt the mask with the surrounding environment, and thus, not to apply a conservative mask even in good conditions (open sky).

7.2.1.1 Elevation masks in train control

7.2.1.1.1 Constant elevation masks

It has been showed in chapter 5 that, with an appropriate elevation mask, it is possible to get rid of the NLOS phenomenon. The criterion used in chapter 5 for the selection of a mask has been based on the shape of the pseudorange error distribution function, and on the presence of outliers and large tails. It has been showed in chapter 5 that in beltways, which are typical open-sky conditions, an elevation mask of 10° is sufficient to remove measurements which distribution are heavily tailed. For constrained environments (suburban and urban), the problem is more complex as pseudorange errors from satellites with up to 30° of elevation have been observed to be following heavily tailed distributions. The objective is here to study the opportunity of using different values of elevation masks and their impact on accuracy improvement/degradation and availability.

This section firstly assesses the improvement/degradation of the statistics on the error in the position domain (RMS and 95th percentile) obtained after rejecting measurements which elevations are lower than the elevation mask. Six different solutions have been tested:

- A solution that uses GPS pseudorange measurements and the measurements from the 6 axis IMU.
- A solution that uses GPS pseudorange and pseudorange rate measurements and the measurements from the 6 axis IMU.
- A solution that integrates GPS pseudorange and pseudorange rate measurements, the measurements from the 6 axis IMU and a track database.
- A solution that uses GLONASS pseudorange measurements and the measurements from the 6 axis IMU.
- A solution that uses GLONASS pseudorange and pseudorange rate measurements and the measurements from the 6 axis IMU.
- A solution that uses GLONASS pseudorange and pseudorange rate measurements, the measurements from the 6 axis IMU and a track database.

Different elevation masks were tested (from 0 to 25°). The results are summarized in Table 30 for the GPS based solutions and Table 31 for the GLONASS based solutions. Suburban and urban environments are presented separately because these two environments are different from the building mask angle point of view. The columns that correspond to the best performances in terms of position error are highlighted in green.

Elevation threshold ($^\circ$), suburban	Elevation threshold ($^\circ$), urban
--	---

		5	10	15	20	25	0	5	10	15	20	25	0
GPS(PR)/INS	RMS along (m)	3.0	2.8	5.3	7.8	11.1	3.2	8.3	8.1	7.9	11.9	15.2	8.0
	95th along (m)	6.1	5.3	11.3	13.4	14.0	6.4	16.4	15.4	16.4	24.1	30.6	15.5
	RMS across (m)	4.0	3.1	4.5	5.1	6.3	4.0	9.0	8.6	8.4	8.8	12.3	9.1
	95th across (m)	8.1	5.9	9.7	10.8	11.6	8.5	18.5	19.0	17.9	17.1	19.6	17.9
GPS(PR and PRR)/INS	RMS along (m)	1.9	1.8	3.9	6.4	9.1	1.9	6.0	6.8	7.3	8.6	12.7	5.7
	95th along (m)	4.1	3.4	9.0	10.8	12.2	4.0	12.3	12.6	13.7	16.4	28.6	12.1
	RMS across (m)	2.3	1.8	3.1	4.1	5.2	2.3	6.5	7.1	6.9	7.0	9.1	5.8
	95th across (m)	5.0	4.4	6.6	8.5	8.9	5.1	14.0	15.5	15.1	15.7	16.0	12.6
GPS(PR and PRR)/INS/track database	RMS along (m)	1.7	1.4	1.4	1.6	1.7	1.8	4.2	10.9	5.4	4.1	4.7	4.5
	95th along (m)	3.6	2.8	3.3	3.5	3.9	3.9	7.5	12.8	11.4	7.7	9.2	8.3
	RMS across (m)	0.1	0.1	0.1	0.1	0.2	0.1	0.8	3.5	1.1	1.1	1.3	1.1
	95th across (m)	0.2	0.2	0.3	0.3	0.3	0.2	0.8	2.1	0.9	0.9	1.1	0.8

Table 30 Impact of an elevation mask on the position error for the train control solutions based on GPS

		Elevation threshold (°), suburban						Elevation threshold (°), urban					
		5	10	15	20	25	0	5	10	15	20	25	0
GLONASS/INS	RMS along (m)	3.2	3.5	3.4	4.4	17.9	3.7	9.0	8.8	9.0	10.5	21.3	9.6
	95th along (m)	6.2	6.5	6.4	8.7	50.8	7.1	17.5	16.8	17.9	21.2	49.6	21.9
	RMS across (m)	3.7	4.2	4.2	5.1	13.6	5.3	8.1	7.6	8.0	7.8	8.5	8.1
	95th across (m)	7.0	7.7	7.6	9.8	34.4	8.6	17.3	16.3	17.4	17.0	18.5	17.4
GLONASS (Doppler)/INS	RMS along (m)	3.0	3.5	3.4	4.5	16.3	3.4	8.1	7.9	7.6	9.4	21.1	8.2
	95th along (m)	5.8	6.8	7.8	8.9	46.6	6.3	17.1	17.4	14.7	16.0	51.6	16.7
	RMS across (m)	3.4	3.8	3.8	4.9	12.1	4.4	6.7	6.5	7.3	6.5	6.9	6.7
	95th across (m)	5.9	6.8	6.8	9.7	27.7	7.9	12.4	12.2	14.4	13.7	13.9	12.8
GLONASS/INS/track database	RMS along (m)	2.6	3.0	3.1	3.8	4.7	2.8	9.2	9.2	9.2	11.6	13.6	9.5
	95th along (m)	5.5	6.1	6.5	7.8	9.9	6.0	17.1	17.0	16.9	21.1	33.8	17.7
	RMS across (m)	0.3	0.3	0.3	0.4	1.2	0.3	1.0	1.0	0.9	0.9	0.8	1.0
	95th across (m)	0.5	0.5	0.5	0.6	0.7	0.5	1.1	1.1	1.1	1.1	1.4	1.1

Table 31 Impact of an elevation mask on the position error for the train control solutions based on GLONASS

Table 30 and Table 31 both shows that applying large elevation masks (20 or 25°) is not beneficial as it highly increases the along and across track error RMS and 95th percentile by degrading the quality of the geometry. As an example applying a 25° elevation mask on a GPS/INS based solution that only integrates the pseudoranges approximately increases the RMS and the accuracy of the solution by a factor 2 in the along-track direction. This property is also observed on the GLONASS based solution, where applying a 25° elevation mask also increases both the RMS and accuracy in the along-track direction by a factor 2. The elevation mask that performed the best in the different configuration tested is in the range that goes from 0° to 15°. A 10° elevation mask presents good performances in all configurations. However, from an integrity monitoring point of view, this mask does not fully protect against NLOS.

Table 30 and Table 31 also demonstrate the benefit of using the database in train control when it comes to the selection of the measurements. When applying restrictive elevation masks (e.g. 25°) the accuracy of the solution that integrates the map is slightly degraded whereas, with the same mask, the accuracy of the solutions that do not integrate the map are much more degraded (for GPS and GLONASS based solutions).

Applying an elevation mask raises the issue of the availability of the system with such a mask (even if only 2 satellites are required). The feasibility of applying such a mask has been investigated by simulating the GPS satellite positions during 14 days (starting the 16 November 2015) with a sampling period of 1 hour, from the Yuma almanacs. The GPS constellation consists of 30 healthy satellites during the tests. The distribution of the number of the satellite in view has been studied for different position of the user (across Europe), that form a grid of latitude between 25° and 80° with a step of 5° and a longitude between -20° and 45° with a step of 5°. Different elevation masks have been applied, at respectively 10°, 20°, 30° and 40°. It is necessary to have at least 2 satellites in view for positioning with the track database, and thus 3 satellites must be tracked for fault detection. 4 satellites and 5 satellites are required for positioning in respectively 2D and 3D with fault detection. Thus, the percentage of time at which the number of satellites available is higher than 3, 4 and 5 satellites is given for the four masks in Figure 97 to Figure 100. The results obtained are not authoritative but they give feasibility information. It can be inferred from Figure 97 that a 10° elevation mask is suitable for the GPS based subsystem for the train control application as the visibility of 3, 4 and 5 satellites is equal to 100%. Figure 98 shows that it is suitable to apply a 20° elevation mask in urban environment as there are 3 satellites in view at least 100% of the time. However, applying a mask of 30° to 40° does not seem feasible according to Figure 99 and Figure 100

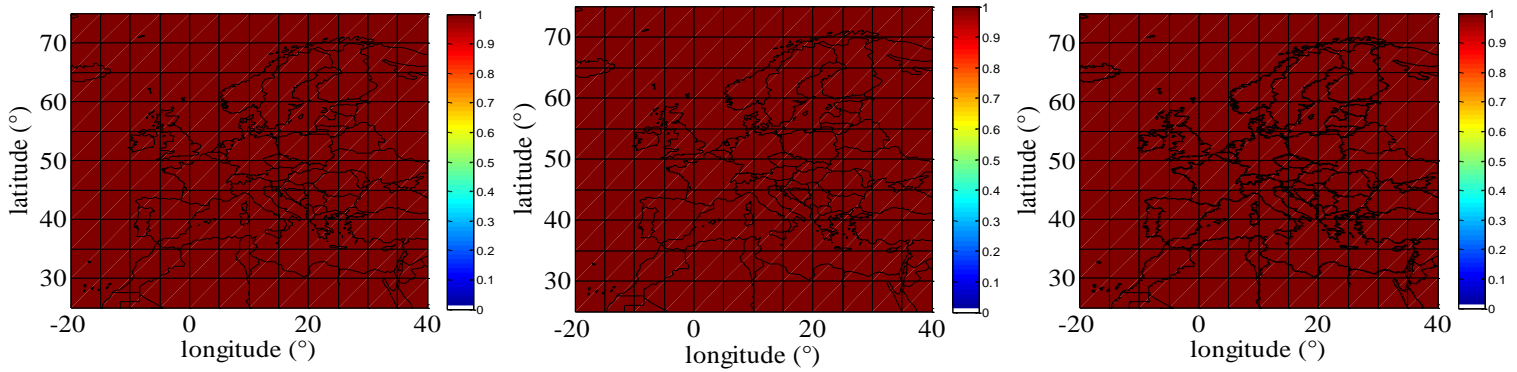


Figure 97 Percentage of time with more than 3 (left), 4 (center) and 5 (right) GPS satellites, satellite mask angle of 10°

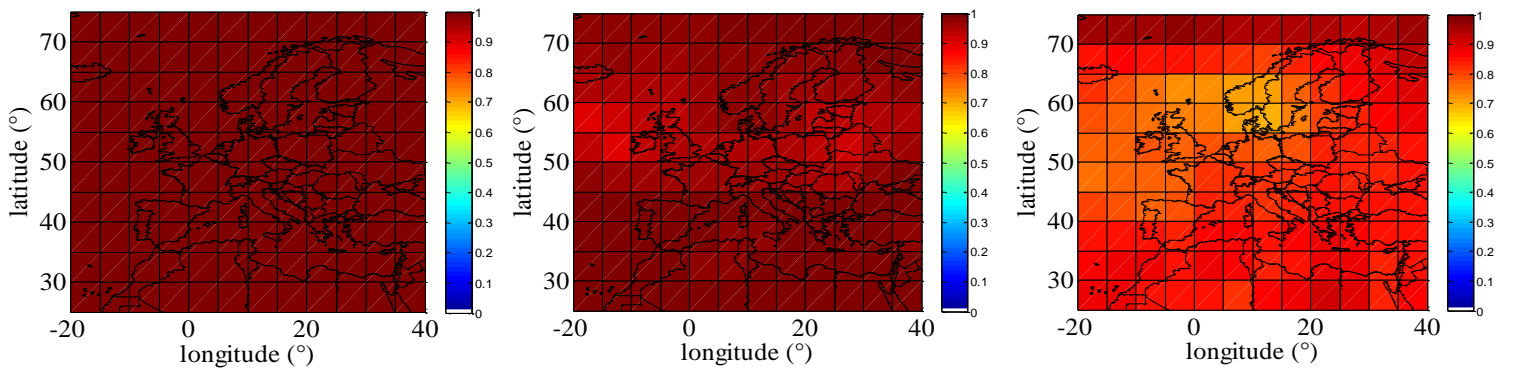


Figure 98 Percentage of time with more than 3 (left), 4 (center) and 5 (right) GPS satellites, satellite mask angle of 20°

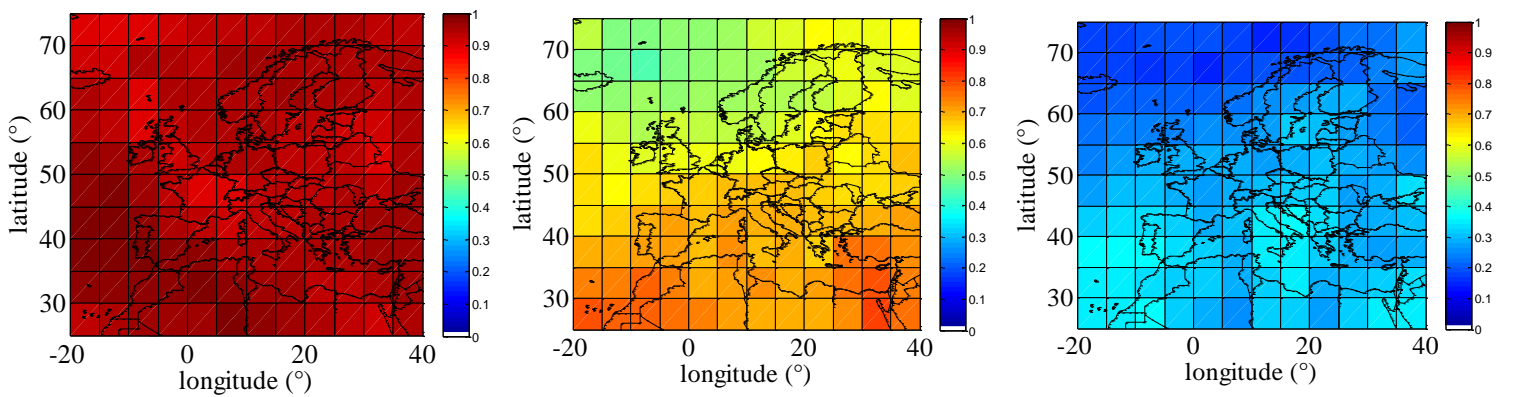


Figure 99 Percentage of time with more than 3 (left), 4 (center) and 5 (right) GPS satellites, satellite mask angle of 30°

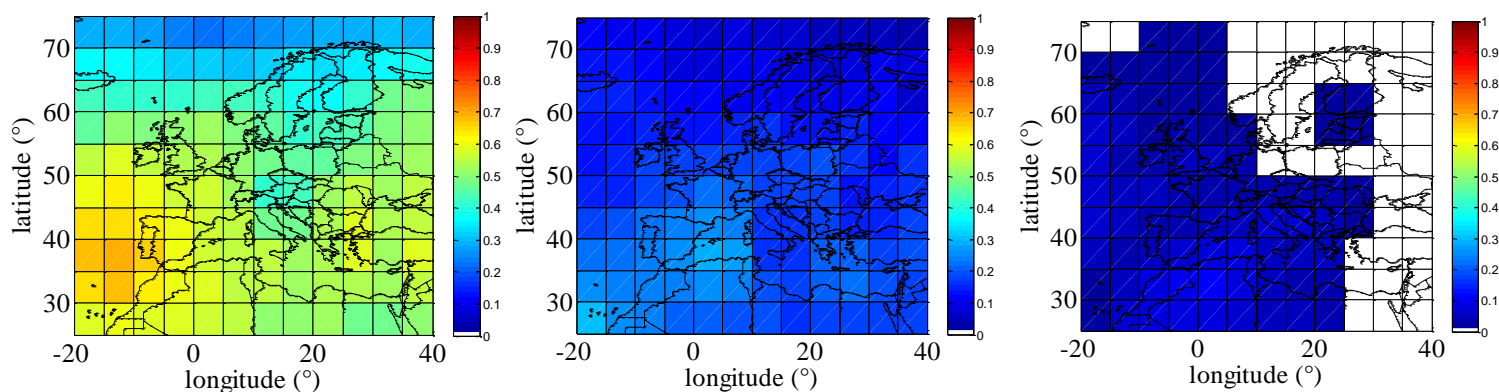


Figure 100 Percentage of time with more than 3 (left), 4 (center) and 5 (right) GPS satellites, satellite mask angle of 40°

7.2.1.1.2 Adaptive elevation masks

It is possible to take advantage of the repeatability of the trajectory in the case of a train. Indeed, the main sources of masking for a train in urban environment are the buildings on both sides of the railroad. It is possible to map the masks of the buildings and store them in the track database. This mapping can be done by using a fisheye camera in daily clear sky condition, and improved by post processing and/or with a LIDAR. The camera must be located at the same exact height as the GNSS antenna. The mask database must be updated regularly. It has to be kept in mind that this step must be done independently for the two track database (for redundancy). An important geometry improvement is expected with respect to masks with constant elevation.

Moreover, compared to a fisheye based NLOS rejection:

- the efficiency of this method is not dependent on the quality of the attitude determination.
- the trains do not have to be equipped with fisheye cameras (cost reductions)
- no image processing have to be done in real time
- the system is not sensitive to night or cloud conditions.

7.2.1.2 C/N_0 masks in train control

The possibility of detecting NLOS signals based on C/N_0 has been widely investigated in prior art. [Carcanague, 2013] has stated that non direct signals can be tracked with C/N_0 of up to 40 dB-Hz in urban environment and at maximum 34 dB-Hz in beltways and rural roads. This analysis has been based on a characterization of the mean and standard deviation of the error, but not on the shape of the distribution and the presence of outliers. The simulations conducted in chapter 5 have shown that a 30 dB-Hz C/N_0 mask is sufficient to remove all samples that corresponds to the tracking of a NLOS. This simulation result appears to be very optimistic with respect to the observations done in [Carcanague, 2013]. This is mainly due to the fact that the receiver modelled in the simulation generally loses lock when the LOS is not present.

Similar to what has been done for the elevation mask, this section assesses the improvement/degradation of the statistics on the error in the position domain obtained after rejecting measurements which C/N_0 are lower than a set threshold. The six same candidates in terms of architectures have been tested and the results are given in Table 32 and Table 33.

		C/N_0 thresholds (dB-Hz), suburban						C/N_0 thresholds (dB-Hz), urban					
		30	32.5	35	37.5	40	-	30	32.5	35	37.5	40	-
GPS(PR)/INS	RMS along (m)	3.0	2.7	2.9	3.2	4.1	3.2	10.2	13.8	12.2	14.3	21.7	8.0
	95th along (m)	5.5	5.0	5.1	6.0	8.9	6.4	23.4	25.6	25.9	33.7	46.8	15.5
	RMS across (m)	3.1	2.6	2.5	2.6	2.9	4.0	13.9	23.7	17.8	18.8	36.5	9.1
	95th across (m)	6.4	4.9	4.9	5.7	6.2	8.5	26.2	39.6	38.7	41.6	63.0	17.9
GPS(PR&PRR)/INS	RMS along (m)	1.8	1.8	1.9	2.1	2.6	1.9	7.1	10.1	11.0	13.8	19.5	5.7
	95th along (m)	3.6	3.3	3.6	3.9	5.1	4.0	13.7	16.9	16.2	21.9	24.3	12.1
	RMS across (m)	1.7	1.5	1.4	1.5	1.8	2.3	8.2	13.9	15.2	21.7	30.2	5.8
	95th across (m)	3.6	2.9	2.6	2.8	3.2	5.1	14.6	21.9	18.9	36.0	34.5	12.6
GPS(PR&PRR)/INS/track database	RMS along (m)	1.6	1.7	1.7	1.8	1.8	1.8	4.1	3.9	3.7	5.4	7.4	4.5
	95th along (m)	3.2	3.2	3.2	3.4	3.6	3.9	8.6	8.0	6.5	8.2	10.0	8.3
	RMS across (m)	0.1	0.2	0.2	0.3	0.3	0.1	1.0	0.9	1.2	4.3	4.4	1.1
	95th across (m)	0.2	0.3	0.3	0.5	0.6	0.2	0.5	0.8	0.8	1.4	1.9	0.8

Table 32 Impact of a C/N_0 mask on the position error for the train control solutions based on GPS

		C/N_0 thresholds (dB-Hz), suburban						C/N_0 thresholds (dB-Hz), urban					
		30	32.5	35	37.5	40	-	30	32.5	35	37.5	40	-
GLONASS(PR)/INS	RMS along (m)	3.5	3.5	3.6	4.3	4.4	3.7	9.7	11.2	12.0	15.8	17.6	9.6
	95th along (m)	6.5	6.3	6.4	8.2	9.2	7.1	23.1	25.6	30.8	36.7	43.9	21.9
	RMS across (m)	4.8	3.7	4.0	4.8	4.0	5.3	8.3	11.4	13.9	24.8	31.5	8.1
	95th across (m)	6.7	6.3	6.4	7.0	7.0	8.6	17.8	23.7	26.7	59.7	78.9	17.4
GLONASS (PR&PRR)/INS	RMS along (m)	3.3	3.3	3.4	3.7	3.9	3.4	7.4	10.0	10.3	11.1	14.1	8.2
	95th along (m)	6.0	6.2	6.4	7.0	7.6	6.3	14.7	20.5	21.7	21.5	28.9	16.7
	RMS across (m)	4.0	3.3	3.4	3.6	3.3	4.4	6.4	17.5	10.0	14.0	20.2	6.7
	95th across (m)	6.4	5.8	6.1	6.5	6.1	7.9	12.3	17.4	22.8	33.3	54.0	12.8
GLONASS (PR&PRR)/INS /track database	RMS along (m)	2.7	2.7	2.8	2.9	3.1	2.8	8.8	9.3	8.4	8.0	8.2	9.5
	95th along (m)	6.1	6.2	6.3	6.5	6.8	6.0	18.5	21.1	19.4	16.7	16.9	17.7
	RMS across (m)	0.3	0.4	0.5	0.5	0.3	0.3	1.0	1.8	1.2	1.0	1.0	1.0
	95th across (m)	0.5	0.5	0.5	0.8	0.7	0.5	1.1	1.3	1.6	1.6	1.4	1.1

Table 33 Impact of a C/N_0 mask on the position error for the train control solutions based on GLONASS

Table 32 and Table 33 shows that applying high C/N_0 masks (up to 40 dB-Hz) is feasible in suburban environment (for both GPS and GLONASS based solutions) as it does not lead to important deterioration in the position error statistics. However, in urban environment, applying such mask is only feasible for the solution that integrates the track database. Indeed, for the other solutions, the accuracy degradation is important. As an illustration, the accuracy in the along-track direction goes from 18 to 63 meters (line 4 in Table 32) when applying the 40 dB-Hz mask for GPS/INS without Doppler, whereas it is only goes from 8.3 to 10 meters (line 10 in Table 32) when the track database is integrated. Here again, it shows that the use of the map enables a stronger selection of the GNSS measurements.

7.2.1.3 Conclusions

To exclude NLOS from the solution, it has been proposed to select the measurements according to their elevations (signals from satellites with low elevations are likely to be NLOS), and/or their estimated C/N_0 . Tests on real data have confirmed that the integration of the track database in the solution enables an increased selectivity on the measurements which is of particular interest for the integrity of the solution (because faulty prone measurements can be excluded). The two approaches proposed for the selection of the measurements are the following:

- If the masks of the buildings are stored in the track database, the NLOS signals can be fully rejected by comparing the satellites elevation and azimuth to this mask. Unfortunately, this approach could not be tested in this thesis.
- An alternative approach consists in applying constant elevation and C/N_0 masks. The constellations simulated have shown that it is not suitable to apply a constant elevation masks higher than 20° , even when integrating the map. A 10° constant elevation mask has been chosen as it does not degrade the position accuracy. This mask is sufficient to protect against NLOS in beltways/open sky conditions (section 5.3.2.2). However, it has been proven in section 5.3.2.2 that from 10° to 40° , non-direct signals can still be tracked in suburban and urban environment. The solution proposed is to select the satellites with a threshold of 40 dB-Hz for both GPS and GLONASS. The horizontal errors on the position estimated by the solutions that integrates the track database before and after the measurement selection are represented in Figure 101 (GPS based solution) and Figure 102 (GLONASS based solution). In both cases, the selection of the measurements has reduced the position error, especially when the vehicle is operating in dense urban area (from 700 to 3000 seconds).

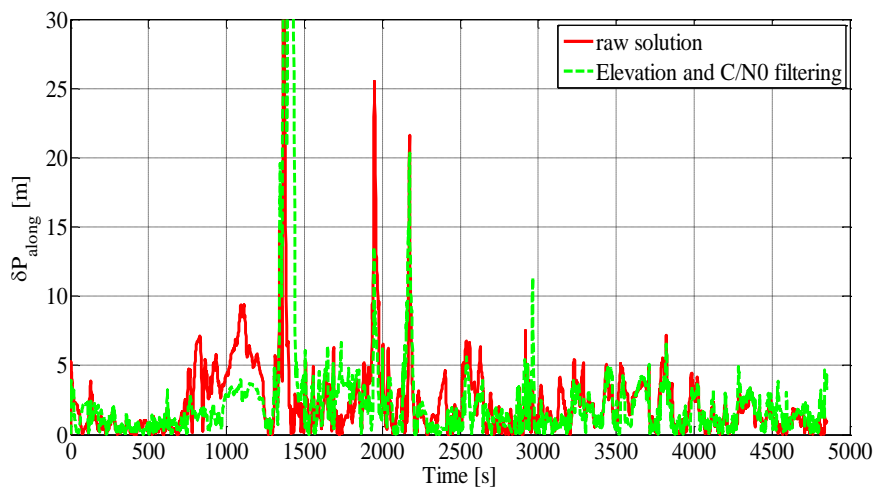


Figure 101 Impact of elevation and C/N_0 filtering on the along track error, train control (GPS/INS/Track database)

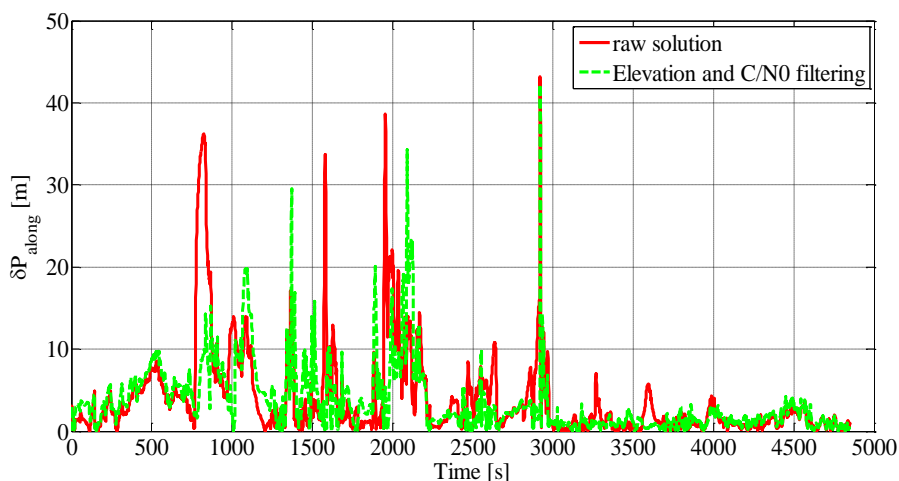


Figure 102 Impact of elevation and C/N_0 filtering on the along track error, train control (GLONASS/INS/Track database)

7.2.2 Application of masks in ETC

7.2.2.1 Elevation masks in ETC

The solution proposed for ETC integrates the measurements from a dual constellation receiver and an odometer. Unlike the track database, the odometer does not enable to navigate with only two satellites in view but only limits the drift of the inertial solution in coasting. However, the processing of measurements from two constellations increases the number of satellites in view and enables a restrictive selection of the measurements that are being integrated in the navigation filter.

The same inferences that have been done on the error distribution in the case of train control can be applied to ETC. In rural environment, a 10° elevation mask has been proven to be sufficient to exclude

the non-nominal errors due to the tracking of non-direct signals. In suburban to dense urban environment, an elevation mask of 30 to 40° is necessary to neglect this phenomenon.).

This section assesses the improvement/degradation of the statistics on the error in the position domain obtained after rejecting measurements which elevations are lower than the elevation mask. Three different solutions have been tested for ETC:

- A solution that integrates GPS and GLONASS pseudorange measurements and the measurements from the 6 axis IMU.
- A solution that integrates GPS and GLONASS pseudorange and pseudorange rate measurements and the measurements from the 6 axis IMU.
- A solution that integrates GPS and GLONASS pseudorange and pseudorange rate measurements, the measurements from the 6 axis IMU and a simulated WSS

		Elevation mask, suburban						Elevation mask, urban					
		5	10	15	20	25	0	5	10	15	20	25	0
GPS/GLO (PR)/INS	RMS horizontal(m)	4.6	4.5	4.7	4.9	5.7	5.0	9.6	9.6	9.9	10.9	12.2	9.6
	95th horizontal(m)	8.3	8.6	8.3	8.4	9.1	8.9	18.4	19.0	19.3	21.9	26.1	18.1
GPS/GLO (PR & PRR) /INS	RMS horizontal(m)	3.8	3.9	4.2	4.4	5.3	4.2	8.8	8.8	8.4	8.9	10.1	8.6
	95th horizontal(m)	6.8	6.9	7.2	7.4	8.7	7.2	14.3	14.6	14.8	5.6	18.3	14.3
GPS/GLO (PR & PRR) /INS/WSS	RMS horizontal(m)	3.4	3.6	3.6	4.2	6.0	3.7	8.1	8.3	8.1	8.4	9.6	8.0
	95th horizontal(m)	5.1	5.5	5.5	6.2	9.8	5.9	13.1	13.4	13.6	14.5	16.8	12.9

Table 34 Impact of an elevation mask on the position error for the ETC solutions based on GPS and GLONASS

The feasibility of applying these masks has been investigated by simulating the GPS and Galileo satellite positions during 14 days with a sampling period of 5 minutes (assuming a constellation of 27 Galileo satellites). The percentages of time with more than 3, 4 and 5 satellites in view are represented for elevation masks of 30° and 40°. The case of 3 satellites in view is presented here from as an informal perspective because ETC system cannot operate and ensure integrity with only 3 satellites. Processing two frequencies simultaneously enables to have 5 satellites in view 100% of the time even with a mask angle of 30° (or lower).

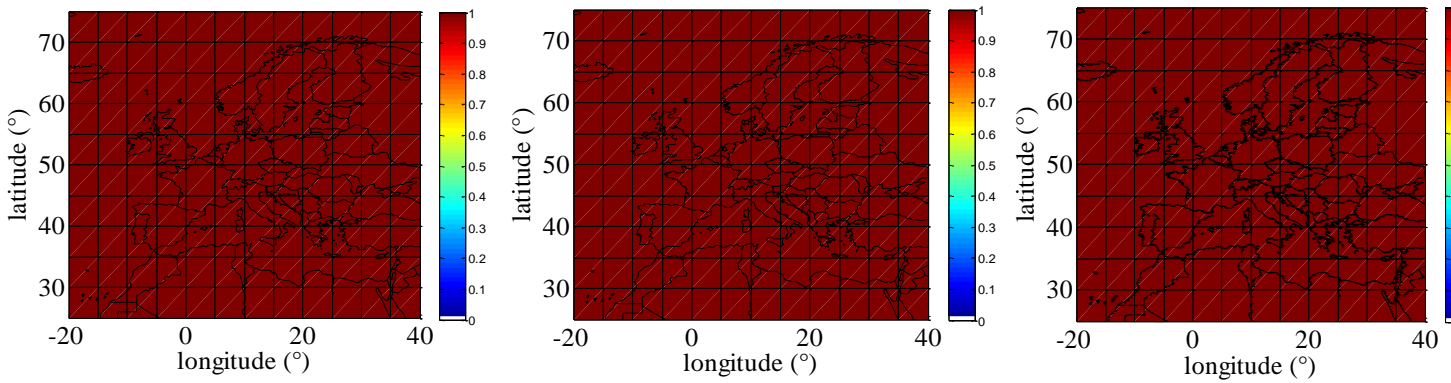


Figure 103 Percentage of time with more than 3 (left), 4 (center) and 5 (right) GPS/Galileo satellites, satellite mask angle of 30°

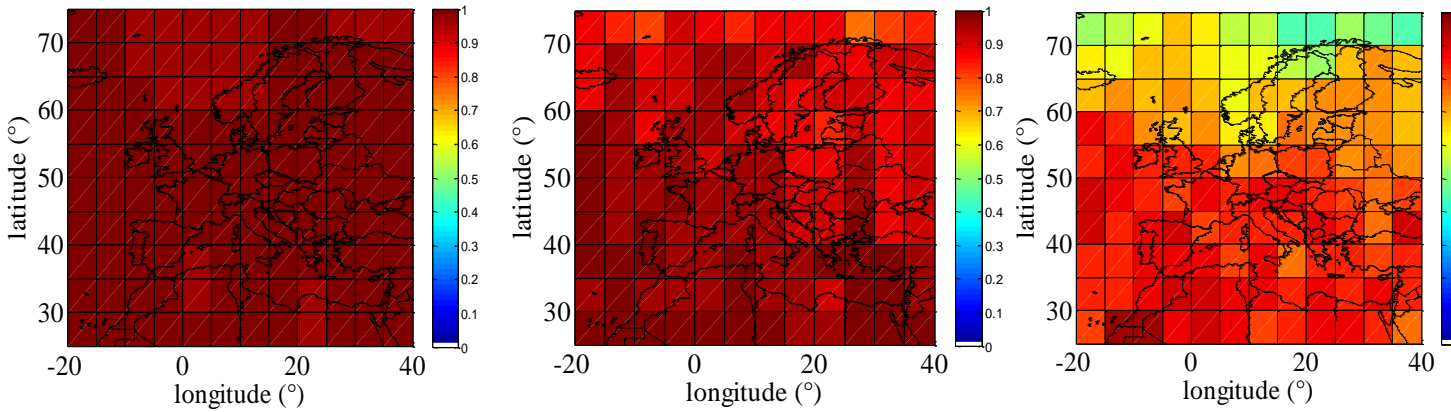


Figure 104 Percentage of time with more than 3, 4 and 5 GPS/Galileo satellites, satellite mask angle of 40°

7.2.2.2 C/N_0 mask in ETC

The conclusions that have been made for the C/N_0 masks in the case of train control can also be applied to ETC. The error statistics after applying different C/N_0 masks are presented in Table 35. The use of a dual constellation receiver in ETC enables to apply large C/N_0 masks (up to 40 dB-Hz) without degrading the accuracy of the solution. In the solution preferred for ETC, which integrates Doppler measurements and WSS, the application of such a mask has even improved the horizontal accuracy from 12.9 to 8.8 m.

		C/N_0 thresholds (dB-Hz), suburban						C/N_0 thresholds (dB-Hz), urban					
		30	32.5	35	37.5	40	0	30	32.5	35	37.5	40	0
GPS/GLO (PR)/INS	RMS horizontal(m)	3.7	3.6	3.7	3.8	4.2	5.0	8.4	8.0	8.1	8.4	10.0	9.6
	95th horizontal(m)	6.1	5.8	5.8	5.9	6.5	8.9	16.7	15.6	15.4	16.7	22.0	18.1
GPS/GLO (PR & PRR)/INS	RMS horizontal(m)	3.4	3.4	3.5	3.6	3.7	4.2	6.9	6.7	7.0	7.6	8.5	8.6
	95th horizontal(m)	5.4	5.1	5.3	5.4	5.4	7.2	11.2	9.8	10.0	12.8	14.6	14.3
GPS/GLO (PR & PRR) /INS/WSS	RMS horizontal(m)	3.1	3.1	3.2	3.4	3.9	3.7	6.3	5.7	5.8	5.8	5.9	8.0
	95th horizontal(m)	4.8	4.7	4.8	5.2	5.5	5.9	10.1	9.1	8.6	8.8	8.8	12.9

Table 35 Impact of a C/N_0 mask on the position error for the ETC solutions based on GPS and GLONASS

7.2.2.3 Conclusions

Tests on real data have confirmed that the integration of two constellations in the solution enables an increased selectivity on the measurements which is of particular interest for the integrity of the solution (because faulty prone measurements can be excluded). The approach proposed for the selection of the measurements consists in setting an elevation mask of 10° . The satellites which elevations are higher than 10° are integrated in the solution if their estimated C/N_0 is higher than 40 dB-Hz. The improvement obtained with this selection scheme is visible in Figure 105 for the solution that integrates the WSS. The benefit of the selection is particularly visible in urban environment (from 700 to 300 seconds). The maximum error value has been reduced from more than 20 meters to 12 meters.

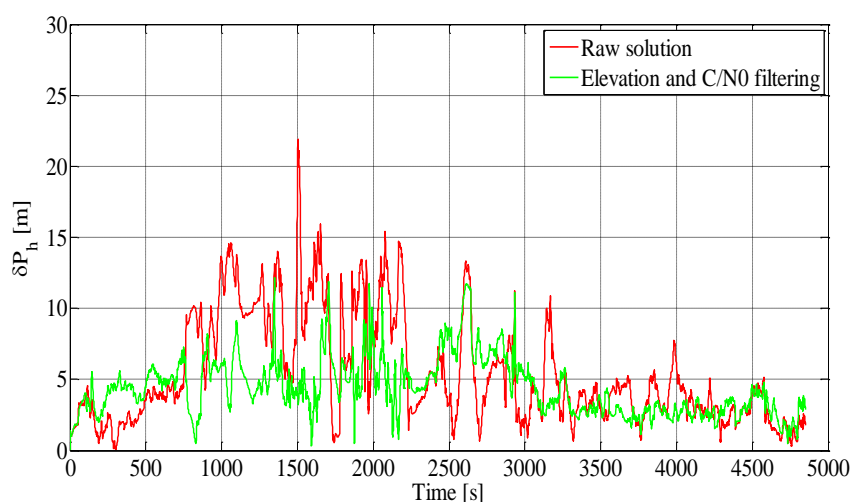


Figure 105 Impact of elevation and C/N_0 filtering, ETC (GPS/GLONASS/INS/WSS)

7.2.3 Innovation monitoring

The Kalman filter innovation is an indicator of the consistency of the actual measurements and the measurements predicated by states estimates. In tight coupling, it is then possible to detect and exclude pseudorange measurements that are too different from the predicted measurements based on the measurements from non GNSS sensors. The approach is that of a classical hypothesis testing. A set of two hypotheses to test is defined:

- H_0 : the measurement is nominal
- H_1 : the measurement is abnormal

The principle of the test is discussed in the next paragraph.

7.2.3.1 Principle of innovation monitoring

In tight coupling, the monitoring of the EKF innovation is done in the pseudorange domain and enables to detect several simultaneous biased pseudoranges. In a closed loop architecture, the predicted error state vector is set to zero. Thus the KF innovation expression is given by:

$$r_k = \rho_k - \hat{\rho}_{k,INS} \quad \text{Eq. 7-29}$$

where $\hat{\rho}_{k,INS}$ is the predicted pseudorange calculated with the position estimated by the mechanization, the satellite position, and the predicted satellite clock error.

When the signal is direct and not affected by NLOS (i.e. under H_0), the normalized innovation follows a zero-mean normal distribution:

$$\frac{r_k(i)}{\sqrt{V_k(i,i)}} \sim \mathcal{N}(0,1) \quad \text{Eq. 7-30}$$

where V_k is the covariance of the innovation that can be estimated with :

$$V_k = H_k P_k H_k^T + R_k \quad \text{Eq. 7-31}$$

where H_k is the measurement Jacobian matrix, P_k is the error covariance estimation and R_k is the noise measurement covariance matrix. The normalized innovation represents the test statistic.

Assuming an abrupt change due the DLL getting locked on a NLOS (i.e. under H_1), the innovation distribution is shifted and centered on the NLOS error (ε_{NLOS}) which is the difference between the true distance from the receiver to the satellite and the trajectory of the signal:

$$\frac{r_k(i)}{\sqrt{V_k(i,i)}} \sim \mathcal{N}\left(\frac{\varepsilon_{NLOS}}{\sqrt{V_k(i,i)}}, 1\right) \quad \text{Eq. 7-32}$$

It is possible to improve the sensitivity of the test by accumulating the innovation over time to average the noise over a sliding window. Let's denote N the size of the window used for averaging the innovation, the test $T_k(i)$ is:

$$T_k(i) = \frac{1}{N} \sum_{i=k-N+1}^k \frac{r_k(i)}{\sqrt{V_k(i,i)}} \quad \text{Eq. 7-33}$$

where $T_k(i) \sim \mathcal{N}(0, 1/\sqrt{N})$ in the nominal case and $T_k(i) \sim \mathcal{N}(\varepsilon_{NLOS}, 1/\sqrt{N})$ in the non-nominal case.

This averaging will increase the detection time. Doing so, a biased measurement can be detected after it has already corrupted the filter. This method can be referred to as innovation sequence monitoring. The best approach in this case is then to “replay” the scenario without the detected “faulty” measurement after the detection. In fact, the innovation will not stay constant, and if it does, it means that the anomaly is not affecting the state estimate.

The detection threshold for the test T_k is set by fixing the values of P_{FA} . Then, for a fixed P_{MD} , the corresponding minimum detectable biases are deduced. An alternative approach consists in fixing the P_{MD} and the minimum detectable biases to set the threshold. In this case the P_{FA} is deduced and therefore varies with time.

This test is also able to detect residual error due to abnormally large error in the LOS configuration due to multipath that would have been miss-detected by the prior test. Innovation monitoring is preferred over post-update residual monitoring method because it excludes the measurement prior to its integration in the solution. Anyway, in the proposed solution, any other NLOS exclusion technique can be used provided that it is possible to quantize the probability of occurrence of undetected dangerous NLOS.

An example of distribution of the EKF residuals observed on the measurement campaign conducted in Toulouse is given in Figure 106. The filter used for this plot integrates GPS and GLONASS PR and PRR measurements (no additional sensor). According to Figure 106, in suburban environment, the normalized innovation is approximately centered and normally distributed. However, the gaussianity of the distribution is not verified in urban environment. Figure 106 also shows that the standard deviation of the innovation has a true variance which is lower than its estimated covariance. This is a consequence of setting the measurement noise covariance with covariances of distributions that overbound the actual distribution.

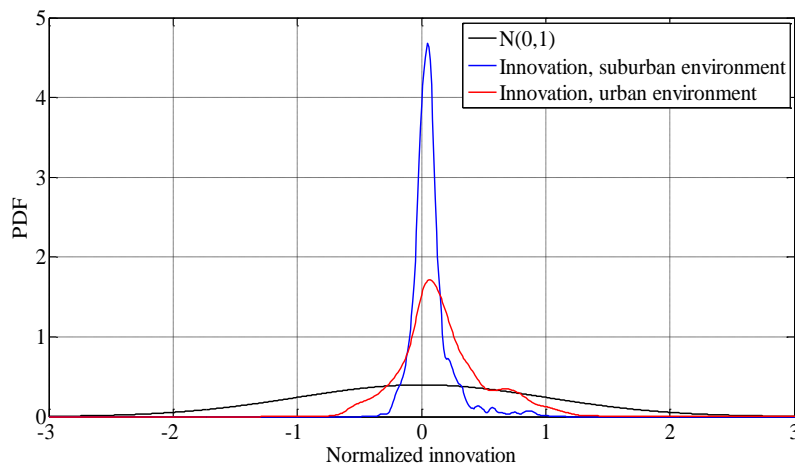


Figure 106 Distribution of pseudorange residuals for satellite 22 (elevation $\cong 20^\circ$)

7.2.3.2 Innovation filtering for train control solution

Checking the KF innovation enables to detect the measurements that are not consistent (essentially residual NLOS at this stage). In this section, the detection threshold has been set as a constant (m_{exp}) multiplied by the standard deviation of the innovation $\sqrt{V_k(i, i)}$ as estimated by the KF. Different values of m_{exp} have been tested. Results have showed that the best performances are obtained for values of m_{exp} that are between 1 and 2 (depending on the sensors integrated). It theoretically corresponds to a large P_{FA} but the normalized innovation has a variance that is significantly lower than 1. Therefore, the alarm rate is in fact much lower. Finally, the improvement obtained by rejecting inconsistent measurements is represented by Figure 107 and Figure 108 for solutions respectively based on GPS and GLONASS. This rejection method mitigates most large errors in urban environment without degrading the accuracy in suburban environment where the geometry of the constellation is much better.

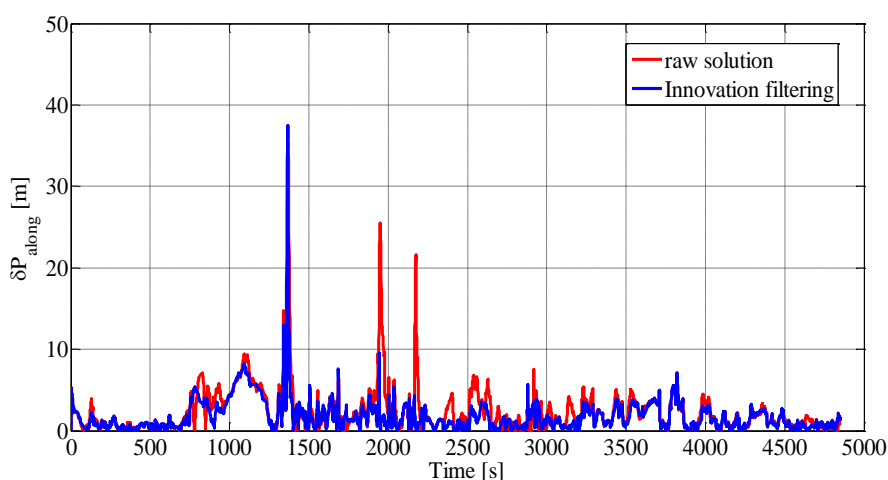


Figure 107 Impact of innovation filtering on position error, train control (GPS/INS/track database), $m_{exp}=1.5$

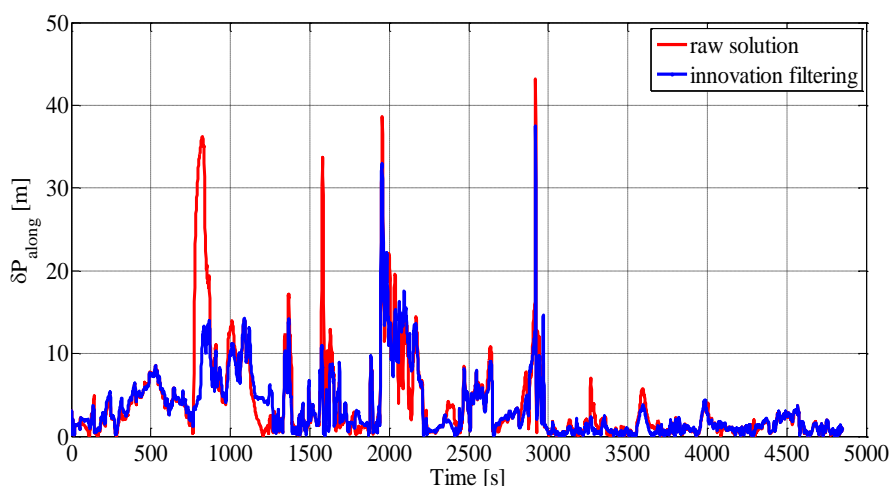


Figure 108 Impact of innovation filtering on position error, train control (GLONASS/INS/track database), $m_{exp} = 2$

7.2.3.3 Innovation filtering for ETC solution

The benefit of applying an innovation based selection scheme in the ETC solution is illustrated by Figure 109. The error reduction is essentially visible in urban environment. This technique is slightly less effective than the C/N_0 and elevation based selection on average (e.g. between 1500 and 1700 seconds). Between 2500 and 2700 seconds, innovation filtering outperforms the other selection.

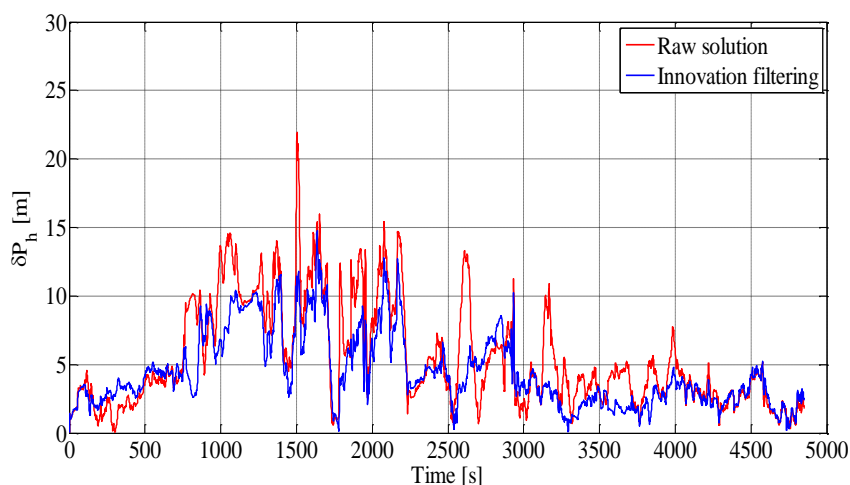


Figure 109 Impact of innovation filtering on position error, ETC (GPS/GLONASS/INS/WSS), $m_{exp} = 1.5$

7.3 Conclusion

This chapter describes a cascaded approach to improve the reliability of the navigation system when the vehicle operates in constrained environment: multipath and tracking of non-direct signals. The measurements which are affected by strong multipath shall be detected and excluded from the solution by monitoring the shape of the correlation function. An approach to design a detection test at the signal processing level has been proposed. A new way to analytically derive the decision threshold has been proposed as well as the concept of sensitivity of the test. The multipath detectors have been tested on realistic simulations and they showed promising performances even if no sufficiently large multipath error has been observed. They have not been tested on real data as the GNSS receivers used in the thesis does not provide simple access to the correlator output. Thus, these monitor are not tested in the following sections.

However, non-direct signals may not be detected by monitoring the shape of the correlation function. It has been proposed to filter out such measurements by applying elevation and stringent C/N_0 masks to the measurements as well as innovation filtering. The selection of the masks and threshold is complex as it is a trade-off between integrity, availability and accuracy. However, for rail applications, precise elevation/azimuth masks can be stored in the database to get rid of NLOS

failures. After this final measurement selection, it is assumed that the measurements provided to the hybridization filter and to the integrity monitoring algorithm are not biased due to multipath or NLOS. The measurement selection schemes have been cascaded and the results in terms of position error are plotted in Figure 110, Figure 112 and Figure 114. The number of satellites selected associated are given in Figure 111, Figure 113 and Figure 115. Apart the fact that the error has been reduced on average, these plots shows that large errors (up to 40 m in single constellations configurations) remains in the harshest urban canyon conditions, and so, even after selection of the measurements due to the poor quality of the geometry and the low number of satellites with good indicators.

If the integrity monitoring algorithm is designed correctly, at the corresponding epochs, the protection levels must be larger than the position errors. It can already be inferred from these results that the system will shows limited availability and continuity in dense urban environment for the stringent operations. As a consequence, it might be necessary to complement the navigation platform by a specific dedicated infrastructure in some areas where the proposed platform does not perform sufficiently well.

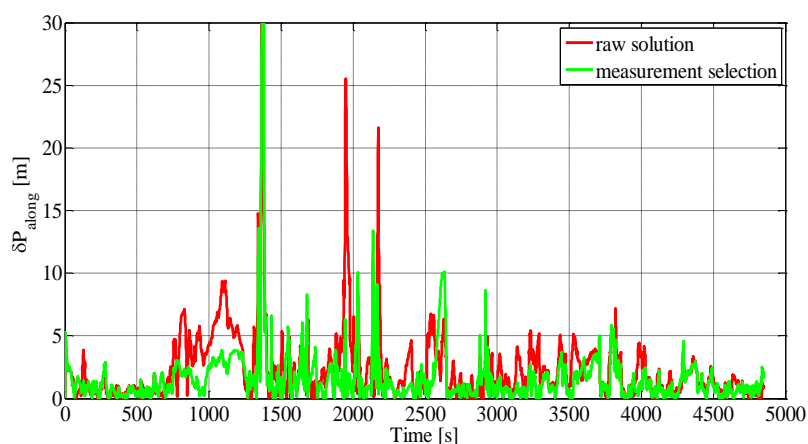


Figure 110 Reduction of the positioning error with cascaded testing, train control (GPS/INS/track database)

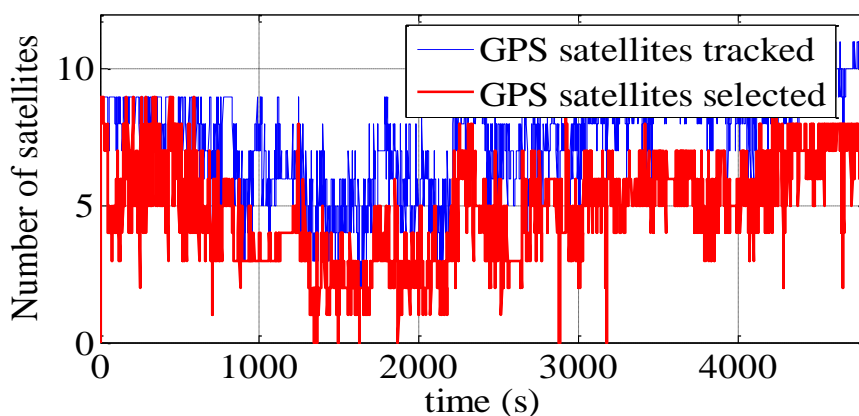


Figure 111 Number of satellite selected, train control (GPS/INS/track database)

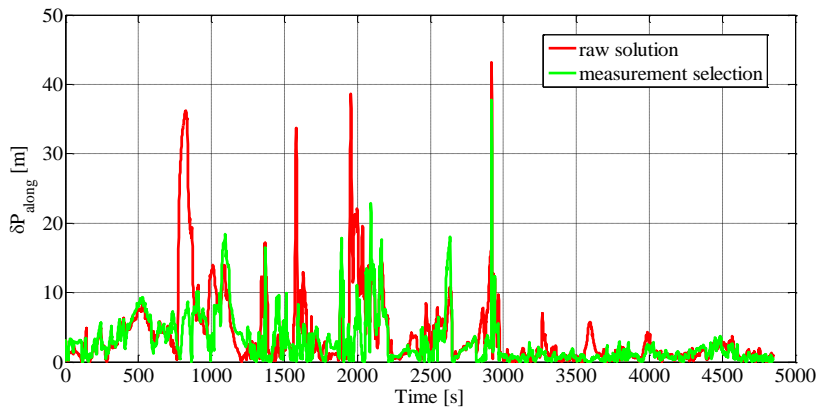


Figure 112 Reduction of the positioning error with cascaded testing, train control (GLONASS/INS/track database)

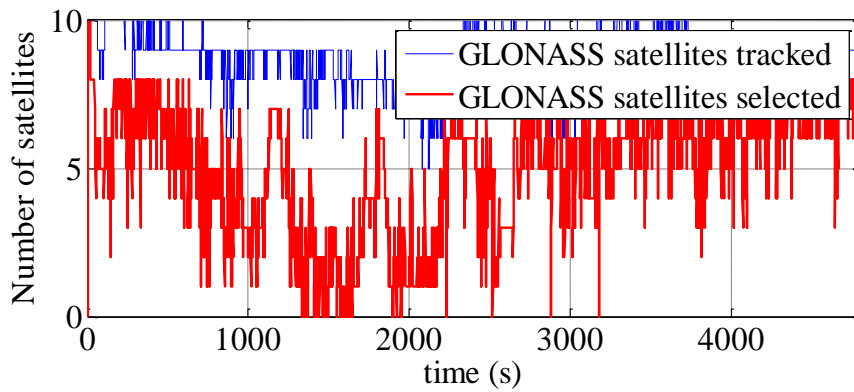


Figure 113 Number of satellite selected, train control (GLONASS/INS/track database)

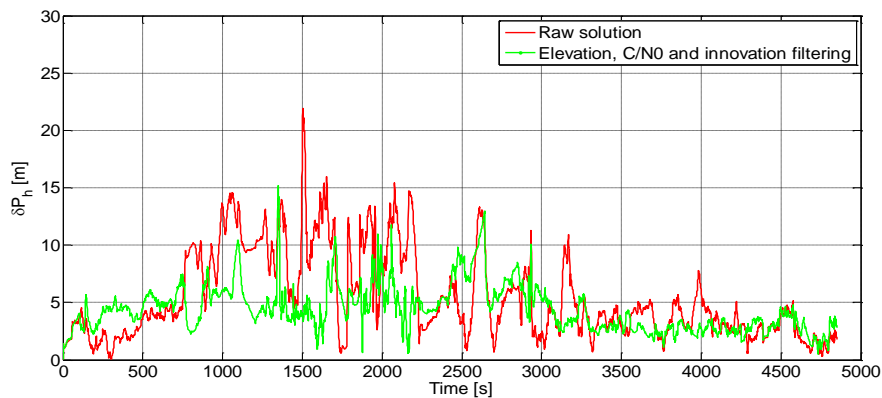


Figure 114 Reduction of the positioning error with innovation filtering, ETC (GPS/GLONASS/INS/WSS), $m_{exp} = 2$

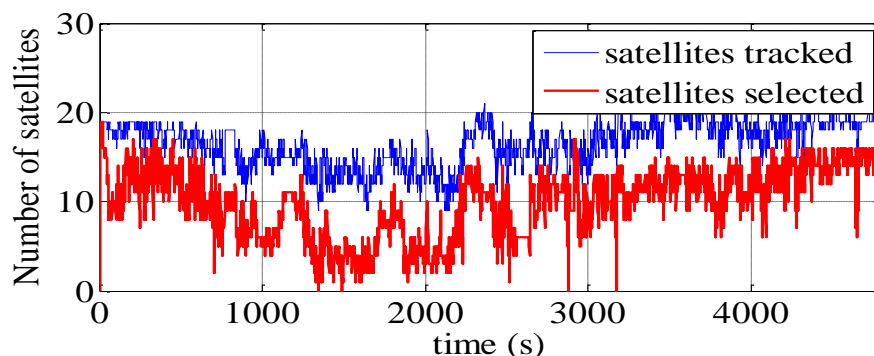


Figure 115 Number of satellite selected, ETC (GPS/GLONASS/INS/track database)

7.4 References

- [Bulgren, 1971] W. G. Bulgren, "On Representations of the Doubly Non-Central F Distribution", Vol. 66, No. 333 (Mar., 1971) , pp. 184-186
- [Carcanague, 2013] S. Carcanague, "Low-cost GPS/GLONASS Precise Positioning Algorithm in Constrained Environment," Ph.D. dissertation, Institut National Polytechnique de Toulouse, 2013
- [Geary, 1930] R. C. Geary, "The Frequency Distribution of the Quotient of Two Normal Variates", Journal of the Royal Statistical Society Vol. 93, No. 3 (1930) , pp. 442-446
- [Hinkley, 1969] D. V. Hinkley, "On the Ratio of Two Correlated Normal Random Variables", Biometrika, Vol. 56, No. 3 (Dec., 1969), pp. 635-639
- [Irsigler and Hein, 2005] Irsigler, Markus, Hein, Guenter W., "Development of a Real-Time Multipath Monitor Based on Multi-Correlator Observations," Proceedings of the 18th International Technical Meeting of the Satellite Division of The Institute of Navigation (ION GNSS 2005), Long Beach, CA, September 2005, pp. 2626-2637
- [Paolella, 2007] M. Paolella, "Intermediate Probability", 2007, page 368
- [Phelts, 2001] Phelts, R. E. (2001). Multicorrelator techniques for robust mitigation of threats to GPS signal quality (Doctoral dissertation, Stanford University).
- [Scheffé, 1959] Scheffé, H. (1959). "The Analysis of Variance". John Wiley, New York
- [Sleewaegen, 1997] Sleewaegen, Jean-Marie, "Multipath Mitigation, Benefits from using the Signal-to-Noise Ratio," Proceedings of the 10th International Technical Meeting of the Satellite Division of The Institute of Navigation (ION GPS 1997), Kansas City, MO, September 1997, pp. 531-540

[Sleewaegen and
Boon, 2001]

Sleewaegen, Jean Marie, Boon, Frank, "Mitigating Short-Delay Multipath: a Promising New Technique," Proceedings of the 14th International Technical Meeting of the Satellite Division of The Institute of Navigation (ION GPS 2001), Salt Lake City, UT, September 2001, pp. 204-213

8 MONITORING THE INTEGRITY OF THE HYBRIDIZED SOLUTIONS

Integrity monitoring for critical terrestrial applications in urban environment has encountered a growing interest over the past ten years. Most existing studies focus on liability critical applications, and in particular on ETC. Two examples of algorithms that have been developed for that purpose are:

- the Isotropy Based Protection Level (IBPL) method [Cosmen-Schortmann et al., 2008] which has been developed by GMV. IBPL is a snapshot algorithm that computes a protection level from the norm of the LS/WLS residual vector. It is not a fault detection algorithm as it does not reject measurements but only provides bounds of the position error.
- A WLSR RAIM with a variable P_{FA} has been developed in [Salos, 2012] for ETC applications in urban environment. This algorithm protects the receiver against major service failures and assumes that the local effects such as NLOS have been rejected by the receiver thanks to prior steps, which are assumed but not detailed.

As it was seen along the previous chapters of this thesis, the main challenges for the monitoring of the integrity of the position estimation in urban environment are the local effects which can lead to measurements affected by large biases, associated with unknown probabilities of occurrence. In this chapter, architectures and algorithms are proposed for monitoring the integrity of the applications of interest (train control and ETC). This chapter is constructed in the following way:

- In section 8.1, the system integrity risk is allocated between the different sources of failure at the sensors level for both applications

- In section 8.2, the integrity risk allocated to the GNSS sensor is divided between the different sources of failures in the GNSS measurements. The choice of the augmentation system that is preferred for monitoring the integrity of the solution is also discussed.
- In section 8.3, the design of the integrity monitoring algorithm is discussed. Two different algorithms are proposed. The results obtained for the solutions proposed for train control and ETC on the real measurement campaign described in section 5.3.2.2 are presented.
- SQM and innovation monitoring tests presented in chapter 7 are able to detect outliers in the range domain. A way to link the thresholds for these tests to the integrity concepts (*HAL* and integrity risk) is studied in section 8.4. A method to adjust these thresholds in real time is proposed.
- In section 8.6, the monitoring of the integrity of the IMU measurement is discussed. Results are presented for different threat models on simulated data.

8.1 Allocation of the integrity risk between the sources of failure at the sensor level

Prior to the design of any integrity monitoring algorithm, it is necessary to allocate the integrity risk between the different sensors and threats. For both train control and ETC, it has been chosen to allocate the whole risk to the GNSS sensor. It is assumed that, with adapted algorithms, the other sensors can reach a sufficient level of reliability to be considered fault free with respect to the GNSS sensor. It is assumed that the probabilities of failure of these sensors are at least 10 times lower than the total integrity risk. The way to monitor the integrity of the IMU measurements so that it fulfills this condition is discussed in section 8.6. Regarding the other sensors:

- For train control, it can be reasonably expected that the integrity of the track database (which can be monitored with advanced post processing techniques, augmentation systems, etc.) is significantly higher than the integrity level expected for the navigation system to be reached in real time.
- For ETC, it is assumed that the integrity of the WSS measurements is monitored by dedicated algorithms (not investigated in this thesis).

The fault trees for the train control and ETC are given in Figure 116 and Figure 117. The positioning failure is

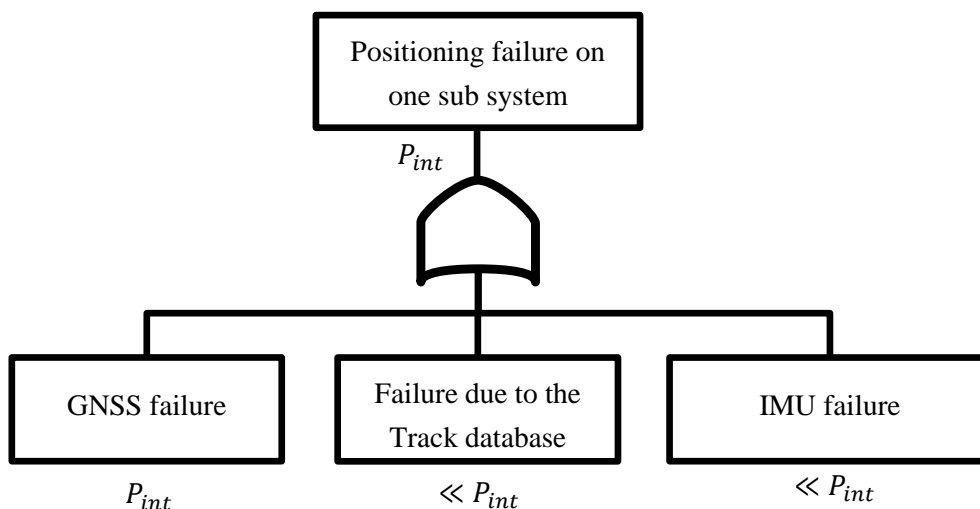


Figure 116 Allocation of the integrity risk: train control

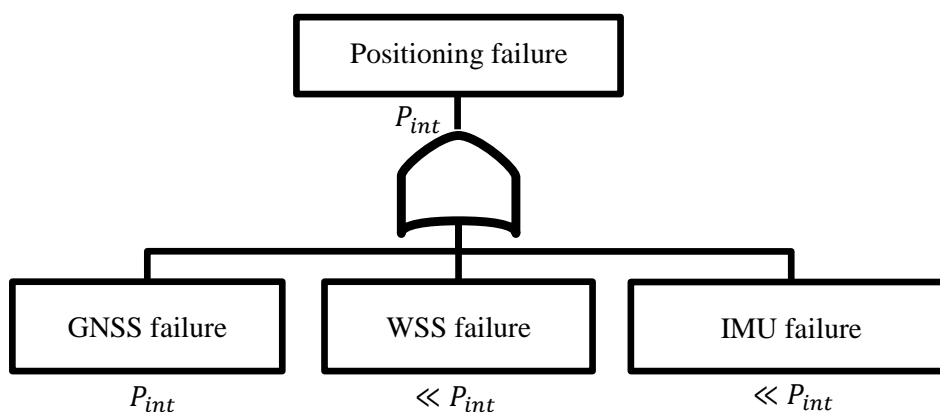


Figure 117 Allocation of the integrity risk: ETC

8.2 Allocation of the GNSS integrity risk and Selection of the augmentation system

In this section, the risk dedicated to GNSS is allocated between the different failure sources. Then, the choice of the augmentation system to monitor integrity is discussed.

8.2.1 Risk allocation between the sources of GNSS failures

The integrity risk of the GNSS sensor is allocated between the satellite faults, the failure due to abnormal measurement errors (due to the receiver's surrounding environment) and the failure under rare normal conditions.

- In this thesis, the probability of failure due to local effects are neglected in the GNSS fault tree: the NLOS and multipath-induced failures are rejected based on techniques detailed in chapter 7

- The other sources of failure such as interference, jamming, spoofing or failure of the hardware components of the receiver are assumed detected by other means.

The total allowed integrity risk is then equally allocated between the fault-free and the satellite fault modes (as in conventional RAIM [Navipedia, ARAIM]). Another possible approach would have been to allocate a significantly lower integrity risk (1% in [Lee et al., 2005]) to the fault-free case compared to the satellite fault.

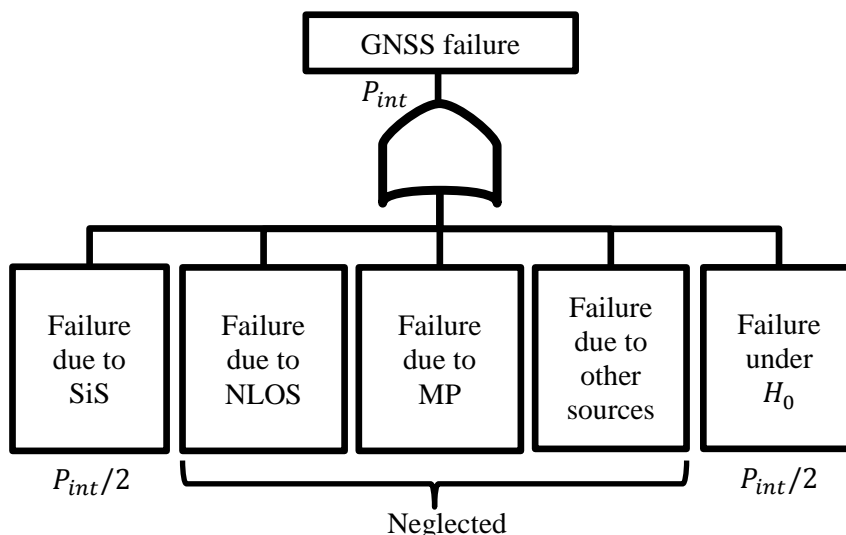


Figure 118 Allocation of the integrity risk for the ETC

8.2.2 Protection against failures of SiS

Range errors from a faulty satellite may not be bounded, and can last up to several hours. Moreover, the probability of occurrence of such satellite failures is well characterized as detailed in chapter 5. Several types of GNSS augmentation can allow the detection of satellite failures in-line with civil aviation requirements: GBAS, SBAS and ABAS. Let us analyze the opportunity to use one of these:

- It has been chosen not to use an augmentation system based on local infrastructure (GBAS like) because the main motivation for the use of GNSS in terrestrial application is to get rid of local infrastructures.
- SBAS provide information to a wide area that can protect the user from failures due to SiS. However, the architectures proposed in the Thesis do not use SBAS for fault detection for several reasons:
 - it requires such an augmentation system to be available in the area of operation. For train control, it is stated in [ERTMS factsheet 7] that ERTMS aims at being deployed widely outside Europe and that ERTMS investments outside Europe represent more than 45% of the global ERTMS investment worldwide (e.g. New Zealand, Saudi Arabia, Chile or Argentina). Some of these countries are not within any SBAS coverage. The same argument can be used for GNSS-based ETC.

- For train control, the TTA of EGNOS/WAAS is 6 seconds. It is too large compared to the operational TTA requirement for ETCS (1 second, according to chapter 3).
- The SBAS satellites can be located at low elevation angles because they have a geostationary orbit. This can cause signal masking and thus unavailability in urban canyons. This issue can be solved by using, for instance, the EDAS SiSNeT Service which uses internet as a complementary transmission link of EGNOS messages. However, the reliability of the data link must be assessed. It is also necessary to characterize the TTA when using such a link.
- Even if SBAS evolution tends to augment dual frequency, multi-constellation GNSS, current SBAS systems only augment GPS L1 signals.
- Finally, even after removal by other methods, residual abnormally large errors due to local effects may remain. These failures cannot be detected by SBAS that only monitors SiS.
- ABAS appears to be the augmentation system that is the most suitable for the two applications studied. It is the only realistic way to fulfill the 1 s TTA requirement for train control. To implement ABAS in the present cases, it is either possible to use a RAIM algorithm if the position is estimated with GNSS only, or an AAIM if additional sensors are added into the solution. As sensors have been integrated in the proposed solutions (in a tight architecture), an AAIM algorithm is to be used here. Once isolated, the faulty satellite is removed from the solution until its status is updated to healthy again. Therefore, the P_{FA} associated with this algorithm is of particular concern.

8.2.3 Considerations of local effects

The local effects can result in pseudorange errors of several tenths of meters which can then convert into large position errors. Two methods have been introduced in chapter 5 order to deal with these local effects:

- The first approach consists in adding different layers to exclude the GNSS measurements that are likely to be affected by large errors due to local effects prior to their integration in the navigation filter. In this approach, which has been studied in chapter 7, it is assumed that after rejection of the measurements by the different algorithms or masks used, the probability of failures due to local effect can be neglected.
- The second approach is to inflate the measurement nominal error model so that it covers the errors due to local effects with a sufficiently high probability (in this case the corresponding failure sources must be removed from the integrity tree as they are considered as nominal). In the context of this thesis, land vehicles can operate in a large variety of environments including open sky, suburban and urban environments. As the GNSS measurement errors distributions are highly correlated with the receiver surrounding environment, this approach calls for an adaptation of the measurement weighting scheme in the EKF to the environment in which the vehicle is operating:

- In open sky conditions, the weighting scheme accounts for the fact that all the satellites are in view (except those which elevations are lower than 10°).
- In urban canyons, the R matrix must be inflated enough so that HPL_0 bounds the position error with a sufficient probability. Different ways to inflate the measurement noise covariance are possible.

This approach has three main drawbacks. The first one is that it requires a sufficient characterization of the measurement errors (in terms of tails of distributions), and thus requires a very large amount of data. The second drawback is that this method is expected to produce large protection levels in constrained environment and therefore to provide low system availability. Finally, it requires the system to be informed about the environment in which it is operating in real time (this could be provided through the map information).

For both approaches, the integrity monitoring algorithm is designed to protect against satellite failures (even if it may have to detect residual failures due to local effects).

8.3 Integrity monitoring algorithm, principles and results

The integrity monitoring algorithm has to calculate HPL as well as to generate an alarm if the position error exceeds the HPL . As discussed, it is either assumed that the measurements with large errors due to local effects have been either rejected by the measurement selection module (if considered non nominal) or that they are covered by the (inflated) measurement nominal error model. Thus, the integrity monitoring algorithm has to protect the system against satellite failures which have a probability of occurrence that is characterized a priori (based on past observations).

8.3.1 Discussions on the algorithm and its parameters

The probability of satellite failure is assumed equal to $10^{-5}/\text{sat}/\text{h}$ for GPS (this value is extrapolated for Galileo) and $10^{-4}/\text{sat}/\text{h}$ for GLONASS [Walter et al., 2014]. The satellite failures are considered as independent events for GPS so that the probability of occurrence of simultaneous satellite failures for GPS is estimated with Eq. 5-51.

- Assuming (at maximum) 10 GPS satellites in view, based on this formula, the probability of having one faulty satellite is equal to $10^{-4}/\text{h}$, and the probability of having 2 simultaneous faulty satellites is equal to $4.5 \cdot 10^{-9}/\text{h}$. The probability of simultaneous GPS failure is thus negligible with respect to the integrity risk for train control (for the GPS based solution), which is $10^{-5.5}/\text{h}$ at minimum. These results have been extrapolated to Galileo as in [Salos, 2012]. As for GLONASS, the probability of having one faulty satellite (over 10 visible satellites) is equal to $10^{-3}/\text{sat}/\text{h}$. If the satellite failures are considered as independent, the probability of 2 simultaneous satellite faults among 10 GLONASS satellites is equal to $4.5 \cdot 10^{-7}/\text{h}$ which is also negligible with respect to the integrity risk for train control.
- For the dual constellation solution that is used in ETC, if the solution integrates 10 GPS satellites and 10 Galileo satellites, the probability of having 1 faulty satellite is equal to $2 \cdot 10^{-5}/\text{h}$.

⁴/h and the probability of having 2 faulty satellites is equal to $1.9 \cdot 10^{-8}$ /h. This event is not taken into account because its probability of occurrence is negligible with respect to the integrity risk for ETC (higher than 10^{-5} /h). If 10 GPS and 10 GLONASS satellites are used, the probability of having 1 faulty satellite (either GPS or GLONASS) is given by:

$$P(1 \text{ satellite faults}) \cong \binom{N_{GPS}}{1} P_{sat,GPS} + \binom{N_{GLONASS}}{1} P_{sat,GLONASS} \quad \text{Eq. 8-1}$$

This probability is equal to $1.1 \cdot 10^{-3}$ /h.

The probability of having 2 faulty satellites simultaneously is equal to the sum of the probability of having two simultaneous faulty GPS, two faulty GLONASS or one faulty GPS and one faulty GLONASS satellites, can be calculated with:

$$\begin{aligned} P(2 \text{ satellite faults}) & \cong \binom{N_{GPS}}{2} P_{sat,GPS}^2 + \binom{N_{GLONASS}}{2} P_{sat,GLONASS}^2 \\ & + \binom{N_{GPS}}{1} \binom{N_{GLONASS}}{1} P_{sat,GPS} P_{sat,GLONASS} \end{aligned} \quad \text{Eq. 8-2}$$

The probability of occurrence of two simultaneous satellite failures is equal to $5.5 \cdot 10^{-7}$ /h. Again, this value is negligible with respect to the integrity risk.

Note: constellation faults have been introduced in 5.2.1.2. The integrity monitoring algorithm is not designed to protect against such event. Indeed, the actual solutions are meant to integrate GPS (for which such event has not been observed) and Galileo (for which the probability of occurrence of such event is unknown). Moreover, it can reasonably be assumed that the innovation monitoring tests will detect such event.

Thus, the integrity monitoring algorithm only has to protect against single satellite faults which have an assumed known probability of occurrence (denoted P_f).

The design of the autonomous integrity monitoring algorithm (RAIM or AAIM) requires the knowledge of a P_{FA} to set the detection threshold and a P_{MD} .

- The P_{MD} of the integrity monitoring algorithm is related to the integrity risk, and has to verify:

$$P_{MD} \leq \frac{P_{int,f}}{P_f} \quad \text{Eq. 8-3}$$

where $P_{int,f}$ is the integrity risk allocated to the fault mode characterized by a probability of occurrence P_f . Half of the total integrity risk has been allocated to the satellite failure.

- The P_{FA} required for the FDE algorithm can be determined by allocating the continuity budget. Such a study has not been conducted as there are uncertainties about the continuity requirements for both applications (in particular for ETC where no continuity requirements has been derived). Therefore, in this thesis the targeted P_{FA} is considered as a parameter for which different realistic values will be tested.

The type of AAIM algorithm to be implemented to monitor the integrity of the solution had to be selected among the three possible existing candidates which are AIME, MSS and GLR. These algorithms have been introduced in chapter 2. Even if AIME provides smaller *HPL*, there is no rigorous way to confirm the detection ability based on theory according to [Lee and O’Laughlin, 2000]. Therefore, very extensive simulations (or real tests) should be used to validate the concept. As a consequence, in this thesis it has been preferred to implement a Solution Separation Method. Even if it provides larger *HPL* in comparison with AIME, Solution Separation thresholds and *HPL* formulas guarantee on an analytical basis the probability of detection regardless of the type of failure [Lee and O’Laughlin, 2000], thus no simulations are necessary. The same inference can be done about GLR. Thus, a solution separation algorithm is implemented in order to protect against residual failures and for the calculation of the protection levels. The solution separation is a snapshot algorithm that was initially developed in [Brenner, 1995]. It can be used in an open-loop or closed-loop scheme [Escher et al., 2002]. Its ability to detect ramp failures has been proven in [Escher et al., 2002].

Note: It is possible to reject a faulty satellite affected by a fault with a “jump signature” during the innovation monitoring test described in section 7.2.3. In this case, the measurement may be integrated again in the fault free solution after a sufficiently large distance has been travelled if the innovation monitoring test considers the measurement as nominal. If the innovation test is still positive after a sufficient travelled distance, it can be inferred that the measurement was not faulty due to local effects. It shall then be considered as a faulty satellite and excluded for a sufficient duration. On the other hand, the innovation monitoring algorithm may not be able to isolate SGE that will make the corrected INS position drifts. This is because the KF adapt to and incorporate any slowly varying drift as a natural dynamic state (position error state or velocity error state). For this reason, a slowly growing error (0.2 m/s or smaller) may drag off the solution and easily escape detection [Lee and O’Laughlin, 2000]. It could have been possible to add tests based on observation of the GPS measurements over longer periods such as in AIME. However, the proposed solutions rely on the MSS to detect such failures because it is ensured to detect the SGE once it has reached a sufficiently large value.

8.3.2 Principle

Two integrity monitoring algorithms which rely on solution separation principle are tested in this thesis and described in this section. The principle of the solution separation consists in running a bank of N KF in parallel that each excludes one different satellite. If the separation between any of the KF solution and the main filter exceeds a threshold, a fault is detected.

8.3.2.1 Principle of the generic solution separation monitoring algorithm

An adaptation of the original solution separation method which is proposed in [Young and McGraw, 2003] is implemented here. Initially, this algorithm was designed for an open-loop hybridization scheme. In a closed loop scheme, the closed-loop corrections are fed back from the main filter only. The sub filters are operating in open loop (their error state estimate is not reset). The principle of the algorithm (for fault detection) is presented in Figure 119. The fault isolation function can be performed by means of sub-sub filters and their separation with the corresponding parent sub-filters is

compared to an exclusion threshold or by other means as proposed in [Young and McGraw, 2003]. This thesis limits to fault detection without investigating isolation. Moreover, as we are operating in a closed loop scheme, it is necessary to run backup EKF (each excluding one satellite) and their corresponding mechanization with the corresponding closed-loop corrections. Indeed in case of SGE, once the fault is detected, it has already corrupted the main mechanization. Therefore once the faulty satellite is determined, the fault-free corresponding backup mechanization and EKF must be used as the main filter and to reinitialize the other subfilters (after exclusion). This process ensures continuity and availability. An alternative approach would consist in reinitializing the filters after exclusion.

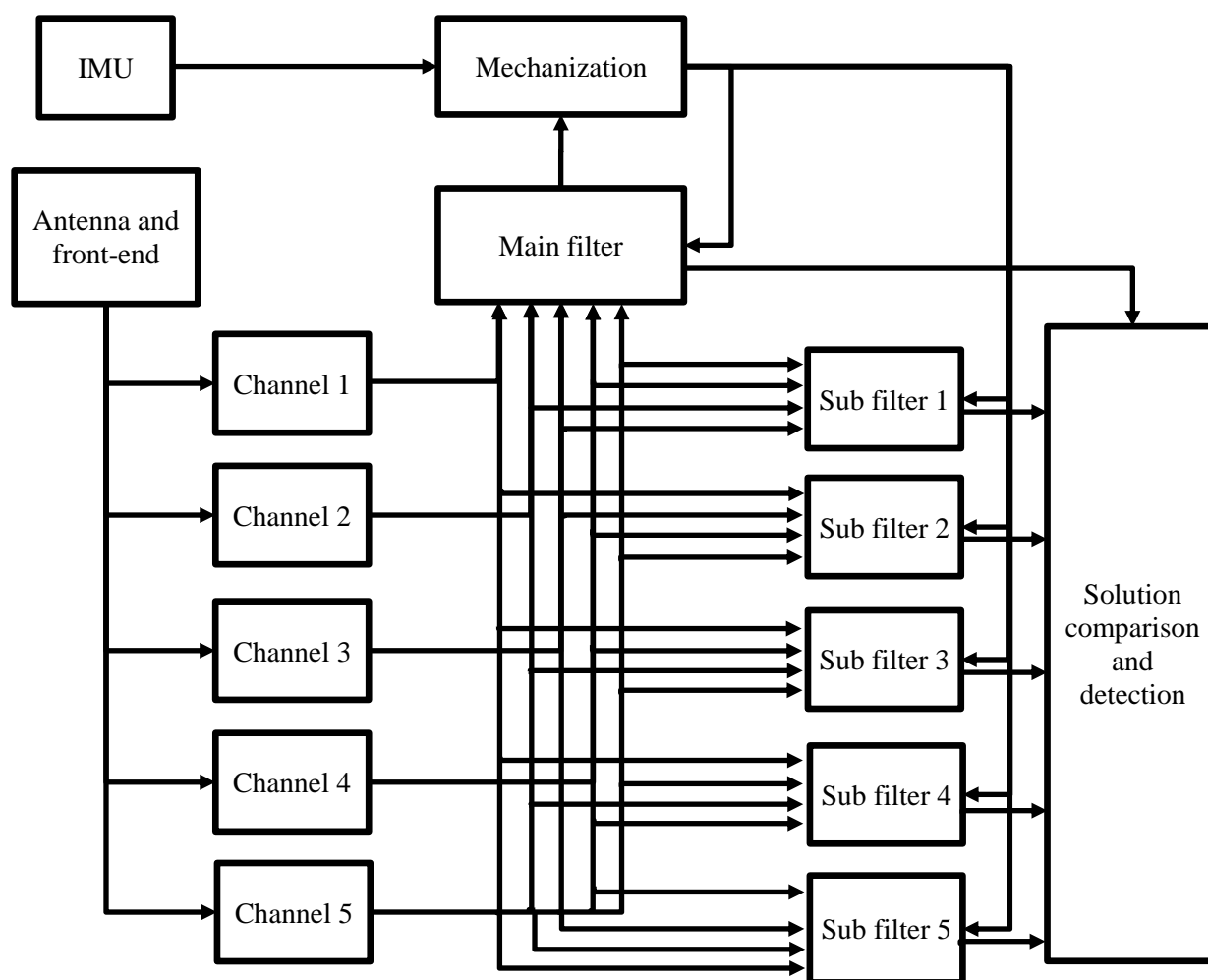


Figure 119 Principle of the solution separation algorithm in a closed loop scheme

8.3.2.1.1 Failure Detector

Let's denote $\beta_j(k)$ the separation between the horizontal position error as estimated by the main filter ($\delta\hat{x}_0^h$) and the j^{th} sub filter ($\delta\hat{x}_j^h$):

$$\beta_j(k) = \delta\hat{x}_0^h(k) - \delta\hat{x}_j^h(k) \quad \text{Eq. 8-4}$$

The covariance of the separation can be estimated by implementing a covariance propagator as detailed in [Escher, 2003]. However, it is proven in [Young and McGraw, 2003] that the covariance of the separation (B_j) can be estimated by:

$$B_j(k) = P_j^h(k|k) - P_0^h(k|k) \quad \text{Eq. 8-5}$$

where P_0^h and P_j^h are the covariance of the position error in the local tangent plane of respectively the main and the j^{th} sub filter (estimated by the KF).

The normalized solution separation test statistic is formed as:

$$\lambda_j(k) = \beta_j^T(k) B_j^\#(k) \beta_j(k) \quad \text{Eq. 8-6}$$

where $()^\#$ denotes the Moore-Penrose generalized inverse. It is also possible to work with the unnormalized test β_j as done in [Brenner, 1995].

The test statistic $\sqrt{\lambda_j(k)}$ can be used instead of $\lambda_j(k)$ as the relation between these two magnitudes is monotonic (in this case the threshold must be adapted). The test statistics $\sqrt{\lambda_j(k)}$ are compared to a detection threshold $\sqrt{\lambda}$, and a fault is declared if any of the statistics exceed the threshold.

$$\begin{cases} H_0 & \text{no failure} & \forall j \in \{1, N\}, \sqrt{\lambda_j(k)} < \sqrt{\lambda} \\ H_1 & \text{failure detected} & \exists j \in \{1, N\}, \sqrt{\lambda_j(k)} \geq \sqrt{\lambda} \end{cases}$$

The detection threshold $\sqrt{\lambda}$ is determined by fixing the P_{FA} under the fault free assumption (under H_0). As any of the several filters can cause a false alert, the detector, thresholds needs to be determined from P_{FA}/N .

In this case, the distributions of the horizontal position error of the two considered filters are Gaussians and centered, therefore the separation $\beta_j(k)$ follow a bi-dimensional centered Gaussian (with a known 2x2 covariance matrix B_j). It is shown in [Young and McGraw, 2003] that the test variable $\lambda_j(k)$ follows a chi-square distribution with two degrees of freedom. Equivalently, $\sqrt{\lambda_j(k)}$ follows a Rayleigh distribution with a parameter of 1.

8.3.2.1.2 Protection Level Computation

The horizontal protection level is calculated with:

$$HPL = \max(HPL_{H_0}, HPL_{H_1}) \quad \text{Eq. 8-7}$$

where HPL_{H_0} is associated to the rare normal fault-free hypothesis and HPL_{H_1} is associated to the fault-in-progress hypothesis.

8.3.2.1.2.1 HPL based on the rare normal Fault-Free hypothesis

Under H_0 , the position error of the main filter follows a bi dimensional centered Gaussian distribution which covariance is $P_0^h(k|k)$. HPL_{H_0} is calculated with:

$$HPL_{H_0} = K_{ff}\sigma_{1,P_0} \quad \text{Eq. 8-8}$$

where:

- σ_{1,P_0} is the maximum eigenvalue of the 2×2 covariance matrix $P_0^h(k|k)$
- K_{ff} can be determined with the circular error probable (CEP) tables [Hoover, 1984] as a function of $1 - P_{H_0}$ (the fault-free probability of integrity) and $\sqrt{\sigma_{1,P_0}/\sigma_{2,P_0}}$

With the integrity risk allocation presented in 8.2.1 the rare normal performance probability is $P_{H_0} = \frac{P_{int}}{2}$ per sample (assuming a 1 hour correlation time for the ionosphere in case of single frequency receiver).

8.3.2.1.2.2 HPL based on the fault-in-progress hypothesis

The following notation is introduced to facilitate the mathematic derivation:

$$R(\omega, P_{MD}) \text{ is the radius such that } P(\|\omega\| > R(\omega, P_{MD})) = P_{MD} \quad \text{Eq. 8-9}$$

$$R(\omega, m, P_{MD}) \text{ is the radius such that } P(\|m + \omega\| > R(\omega, m, P_{MD})) = P_{MD} \quad \text{Eq. 8-10}$$

Under H_1 , the position error of the main filter is biased, let's denote $bias_0$ this horizontal bias and ω_0 the noise vector which is zero mean (and Gaussian). The position error of the main filter is given by:

$$\delta \hat{x}_0^h(k) = bias_0(k) + \omega_0(k) \quad \text{Eq. 8-11}$$

The ideal horizontal position error bound, denoted α_H can be written as:

$$\alpha_H = \|bias_0(k)\| + R(\omega_0(k), bias_0(k), P_{MD}) \quad \text{Eq. 8-12}$$

Since $bias_0$ is unknown it shall be estimated.

It can be done by introducing the separation vector β_j , which is equal to (because the j^{th} subfilter is unbiased):

$$\beta_j(k) = bias_0(k) + \omega_0(k) - \omega_j(k) = bias_0(k) + \omega'_j(k) \quad \text{Eq. 8-13}$$

where $\omega_j(k)$ is the noise vector of the j th sub filter and $\omega'_j(k)$ is the component of ω_j independent of ω_0 .

Eq. 8-12 can be re-arranged as:

$$\alpha_H = \|bias_0(k)\| + R(\omega'_j(k), bias_0(k), P_{MD}) + R(\omega_0(k), bias_0(k), P_{MD}) - R(\omega'_j(k), bias_0(k), P_{MD}) \quad \text{Eq. 8-14}$$

The first two terms at the right side of Eq. 8-14 are due to bias and uncorrelated noise. They can be estimated with β_j . The last two terms are due to the noises $\omega_0(k)$ and $\omega'_j(k)$.

Horizontal position error due to bias and uncorrelated noise

The objective is here to bound the term $\|bias_0(k)\| + R(\omega'_j(k), bias_0(k), P_{MD})$.

It can be shown that, with an orthonormal rotation, λ_j is noncentral chi-squared distributed. Let us denote P_{bias} the non-centrality parameter which makes the probability of the noise to be inside the detection threshold equal to P_{MD} . Any bias vector with a magnitude greater than P_{bias} will be detected with a $(1-P_{MD})$ probability. This bias must then be converted from the test domain to the horizontal position domain (the corresponding bias is denoted $\gamma_{P_{bias}}(k)$).

Let us denote $Y_j(k)$ the normalized solution separation vector given by:

$$Y_j(k) = S_j^{-\frac{1}{2}}(k)V_j^T(k)\gamma_{P_{bias}}(k) \quad \text{Eq. 8-15}$$

where $V_j(k)$ and $S_j(k)$ are from the eigenvalue decomposition of $B_j(k)$:

$$B_j(k) = V_j(k)S_j(k)V_j^T(k) \quad \text{Eq. 8-16}$$

The norm of $Y_j(k)$ is bounded by P_{bias} .

The norm of $\gamma_{P_{bias}}(k)$ can be expressed using Eq. 8-15 as:

$$\|\gamma_{P_{bias}}(k)\| = \sqrt{\gamma_{P_{bias}}(k)^T \gamma_{P_{bias}}(k)} = \sqrt{Y_j^T(k)S_j(k)Y_j(k)} \quad \text{Eq. 8-17}$$

Moreover, $S_j(k)$ is diagonal and thus $\|\gamma_{P_{bias}}(k)\|$ is bounded by:

$$\|\gamma_{P_{bias}}(k)\| \leq P_{bias} \sqrt{\sigma_{1,B_j}(k)} = HPE_{B_j} \quad \text{Eq. 8-18}$$

where $\sigma_{1,B_j}(k)$ is the largest eigenvalue of $B_j(k)$.

HPE_{B_j} bounds the horizontal position error due to bias and uncorrelated noise with a probability of missed detection P_{MD} :

$$HPE_{B_j} \geq \|bias_0(k)\| + R(\omega'_j(k), bias_0(k), P_{MD}) \quad \text{Eq. 8-19}$$

Horizontal position error due to noise only

It is shown in [Young and McGraw, 2003] that Eq. 8-14 can be written:

$$\alpha_H \leq HPE_{B_j} + R(\omega_j(k), P_{MD}) - R(\omega'_j(k), P_{MD}) \quad \text{Eq. 8-20}$$

HPE_{NP_j} and HPE_{NB_j} are the terms that corresponds to the horizontal position errors due to noise only.

They can be determined with:

$$HPE_{NP_j} = R(\omega_j(k), P_{MD}) = K_{CEP,P_j}\sigma_{1,P_j} \quad \text{Eq. 8-21}$$

$$HPE_{NB_j} = R(\omega'_j(k), P_{MD}) = K_{CEP,B_j}\sigma_{1,B_j} \quad \text{Eq. 8-22}$$

where:

- σ_{1,P_j} , σ_{1,B_j} are the maximum eigenvalues of the matrix $P_j^h(k|k)$ and $B_j^h(k|k)$

- K_{CEP,P_j} and K_{CEP,B_j} are the coefficients of the circular error probable table associated to P_{MD} and respectively $\sqrt{\sigma_{1,P_j}/\sigma_{2,P_j}}$ and $\sqrt{\sigma_{1,B_j}/\sigma_{2,B_j}}$

Finally, the total estimated horizontal position error bound for the j^{th} sub-filter is computed as:

$$HPE_j = HPE_{B_j} + HPE_{NP_j} - HPE_{NB_j} \quad \text{Eq. 8-23}$$

And HPL_{H_1} is calculated with:

$$HPL_{H_1} = \max_j(HPE_j) \quad \text{Eq. 8-24}$$

8.3.2.2 Solution separation based on independent mechanizations

The implemented fusion algorithm operates in a closed loop scheme. The inertial error estimate (biases and mechanization errors) are thus fed back to the INS. In this configuration, the impact of a ramp fault affecting any pseudorange is problematic because the detection can only be done after the onset of the ramp. Prior to the detection, the mechanization and the sensors measurements are corrected with biases and errors estimated by the main filter. This correction is calculated by integrating a slowly drifting satellite. The solution separation method that has been discussed earlier assumes that the subfilter position estimation is nominal after its own update. It may still be the case as the mechanization output is corrected by a fault-free set of satellites. However, the validity of this assumption has not been addressed in the literature as the AAIM algorithms have been developed for civil aviation which operates in open-loop. It then remain unclear whether the HPL bounds the true error with a sufficiently high probability between the onset of the SGE and its detection. The SGE are all the more pernicious in the proposed solution as the innovation is monitored to remove outliers characterized by steps, frequent in urban environment. The slow drift of the INS output could lead to false exclusion of several healthy measurements by the innovation monitoring test. In this section, a solution separation version adapted to the closed-loop case is proposed. In this version, the HPL computed are sure to contain the true position error with a sufficient probability, even between the occurrence of a SGE type failure and its detection, in closed-loop. This method which is based on conservative assumptions leads to large protection levels.

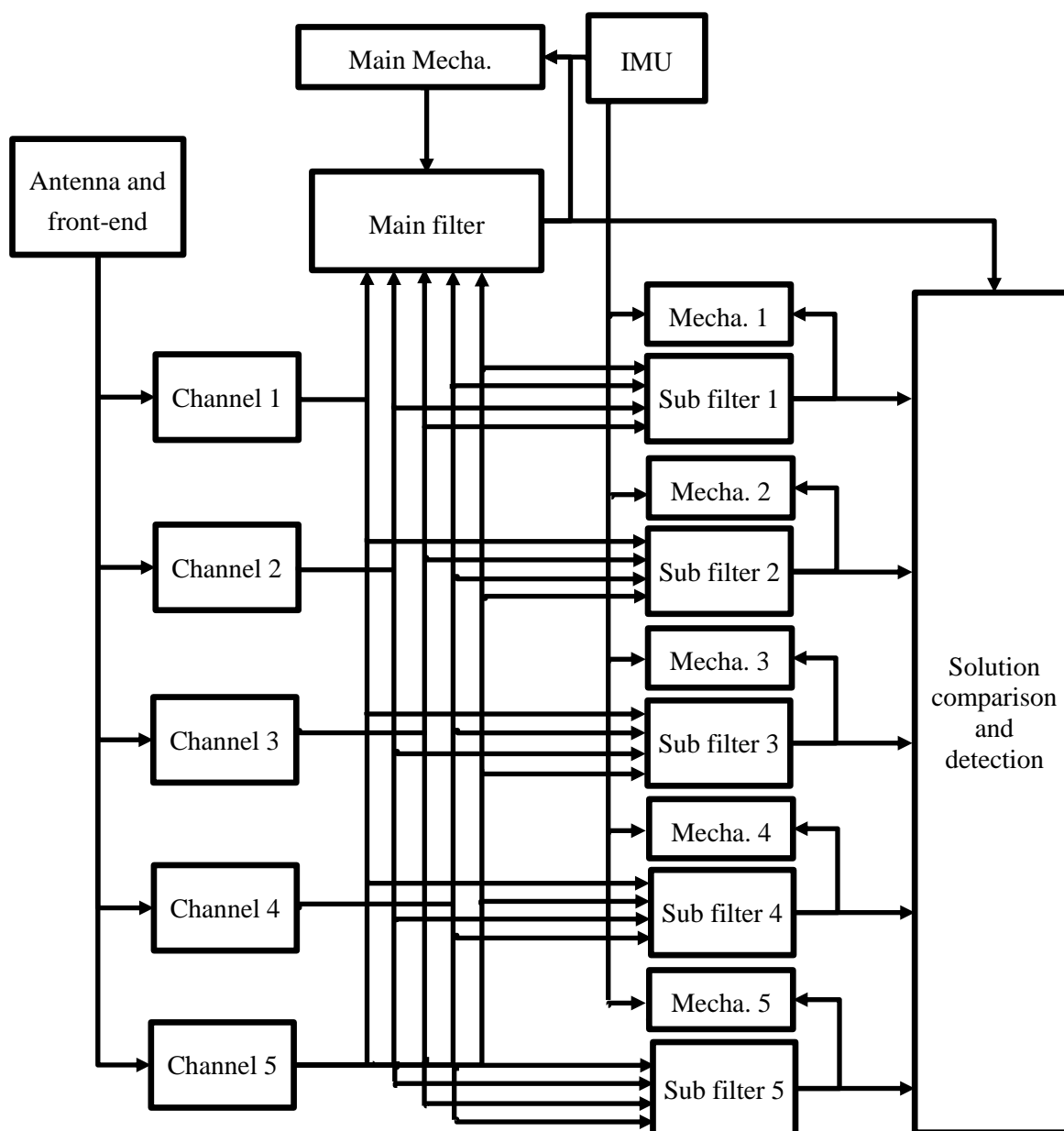


Figure 120 Algorithm proposed for solution separation in a closed loop scheme

The proposed algorithm is also based on the solution separation approach. However, unlike the solution separation algorithm presented in section 8.3.2.1, in the proposed solution, N mechanizations are run in parallel. N EKF are used to correct the N mechanizations, each excluding one satellite. Therefore even in case of SGE, it is ensured that one of the sub filters is fault-free as it completely excludes the faulty-satellite (and its mechanization is not affected).

Note that it is assumed here that the covariance of the position error due to noise only is well estimated by the main filter, even when a SGE has affected one of the measurements (it is assumed that the SGE leads to horizontal position bias). This assumption must also be valid for the HPL to bound the position error (prior to the detection) in case of SGE for a basic solution separation in an open loop scheme.

8.3.2.2.1 Test statistic

The test statistic is the separation between the positions solutions after the corrections estimated by the full-filter and the sub-filter to respectively the main and sub mechanization:

$$\beta_j(k) = \hat{x}_0^h(k) - \hat{x}_j^h(k) \quad \text{Eq. 8-25}$$

It is not possible to apply Eq. 8-5 to estimate the covariance of the separation because it is not valid in this case. Indeed, the proof of the formula (in [Young and McGraw, 2003]) assumes that the mechanization outputs are the same for the two filters, and that the matrices (observation and propagation) are linearized around the same position. The linearization points are not the same in this case (different mechanization). Moreover, the covariance propagator described in [Escher, 2003] cannot be applied here to estimate these covariances for the same reason. Unfortunately, no simple solution has been found to derive the covariance of the separation in this thesis. Therefore, we investigate a very conservative way to assess this covariance. Let us denote:

$$\hat{x}_0^h(k) = \begin{bmatrix} E_0 \\ N_0 \end{bmatrix} \text{ and } \hat{x}_j^h(k) = \begin{bmatrix} E_j \\ N_j \end{bmatrix} \quad \text{Eq. 8-26}$$

And the associated state error covariance:

$$P_0(k|k) = \begin{bmatrix} \sigma_{E_0}^2 & \sigma_{E_0N_0} \\ \sigma_{E_0N_0} & \sigma_{N_0}^2 \end{bmatrix} \text{ and } P_j(k|k) = \begin{bmatrix} \sigma_{E_j}^2 & \sigma_{E_jN_j} \\ \sigma_{E_jN_j} & \sigma_{N_j}^2 \end{bmatrix} \quad \text{Eq. 8-27}$$

Without any assumptions, it is possible to write:

$$B_j(k) = \begin{bmatrix} \sigma_{E_0}^2 + \sigma_{E_j}^2 - 2\rho_{E_0E_j}\sigma_{E_0}\sigma_{E_j} & \sigma_{E_0N_0} + \sigma_{E_jN_j} - 2\rho_{E_0N_j}\sigma_{E_0}\sigma_{N_j} - 2\rho_{N_0E_j}\sigma_{N_0}\sigma_{E_j} \\ \sigma_{E_0N_0} + \sigma_{E_jN_j} - 2\rho_{E_0N_j}\sigma_{E_0}\sigma_{N_j} - 2\rho_{N_0E_j}\sigma_{N_0}\sigma_{E_j} & \sigma_{N_0}^2 + \sigma_{N_j}^2 - 2\rho_{N_0N_j}\sigma_{N_0}\sigma_{N_j} \end{bmatrix} \quad \text{Eq. 8-28}$$

where $\rho_{E_0E_j}$ represents the correlation between the two terms in index (the two coordinates E_0 and E_j). These correlation terms can only take value within the interval $[-1,1]$. This is an application of the Cauchy–Schwarz inequality equation. The solution separation vector is a bi-dimensional random variable following a Gaussian distribution in the fault-free case. The components of the separation vector are not independent because the covariance $B_j(k)$ may not be diagonal. However, this matrix is semi positive definite, therefore it is diagonalizable and its eigenvalues are all positive or null. If the test was in one dimension, it is intuitive that the worst case for the detection (and therefore the highest PL) corresponds to the case where the noises on the two positions have a correlation value of -1. Here the problem can be formulated into a maximization problem with constraints. The cost function to maximize in this case is the maximum eigenvalue of $B_j(k)$. In particular, for a 2×2 matrix, this maximum eigenvalue (σ_{1,B_j}) can be simply calculated with by:

$$\sigma_{1,B_j}(k) = \frac{Tr}{2} + \sqrt{\frac{Tr^2}{4} - Det} \quad \text{Eq. 8-29}$$

where:

- Tr is the trace of $B_j(k)$
- Det is determinant of $B_j(k)$

Simulations have shown that the maximum value for $\sigma_{1,B_j}(k)$ is always reached for all the correlation parameters equal to -1 (the cost function is decreasing with respect to each correlation parameter). Thus the covariance of the separator can conservatively be considered equal to:

$$B_j(k) = \begin{bmatrix} \sigma_{E_0}^2 + \sigma_{E_j}^2 + 2\sigma_{E_0}\sigma_{E_j} & \sigma_{E_0N_0} + \sigma_{E_jN_j} + 2\sigma_{E_0}\sigma_{N_j} + 2\sigma_{N_0}\sigma_{E_j} \\ \sigma_{E_0N_0} + \sigma_{E_jN_j} + 2\sigma_{E_0}\sigma_{N_j} + 2\sigma_{N_0}\sigma_{E_j} & \sigma_{N_0}^2 + \sigma_{N_j}^2 + 2\sigma_{N_0}\sigma_{N_j} \end{bmatrix} \quad \text{Eq. 8-30}$$

In the nominal case, the separation follows a bi dimensional Gaussian centered distribution. The normalized solution separation test statistic is formed as:

$$\lambda_j(k) = \beta_j^T(k)B_j^\#(k)\beta_j(k) \quad \text{Eq. 8-31}$$

As in the conventional solution separation algorithm, the test statistics $\sqrt{\lambda_j(k)}$ are compared to a detection threshold $\sqrt{\lambda}$, and a fault is declared if the any of the statistics exceed the threshold. The detection threshold $\sqrt{\lambda}$ is determined by fixing the P_{FA} in the fault free case (under H_0). The test variable $\lambda_j(k)$ follows a chi-square distribution with two degrees of freedom. Equivalently, $\sqrt{\lambda_j(k)}$ follows a Rayleigh distribution with a parameter of 1.

8.3.2.2.2 Protection levels

The derivation of the protection level is the same as for the algorithm detailed in section 8.3.2.1, where the expression of $B_j(k)$ has been changed.

8.3.3 Availability results on the data set conducted in downtown Toulouse

The two autonomous integrity monitoring algorithms have been implemented on the different hybridization solutions presented in chapter 6. Their behaviors have been tested using the data collection presented in section 5.3.2.2 in suburban and urban environment. During this data collection, no satellite failure had occurred, therefore H_0 holds. It must then be proven that the HPL are sufficiently large to bound the position error when no alarm is generated. If an alarm is raised during the campaign, it is a false alarm. Finally, the objective is to check the availability of the integrity monitoring algorithm and the distribution of the HPL for the different solutions proposed. To fully validate that the solution has a probability of misleading information that is lower than or equal to the allowed integrity risk, significantly longer campaigns would be necessary. Unfortunately, the amount of data collected and processed is not sufficient. Moreover, unlike civil aviation, for terrestrial applications, it is not possible to predict the performances of the integrity monitoring algorithm because the satellites in view/masked cannot be anticipated as well as multipath error amplitude or

NLOS reception. The results presented in this section are obtained for solutions that integrate the GNSS pseudorange rates because it has been shown in chapter 6 that processing these measurements highly increases the accuracy of the solution, especially in constrained environment. For each subfilter of the integrity monitoring algorithm, the pseudorange rate measurement from the excluded satellite is also excluded.

8.3.3.1 Results: Train control

The proposed parameters for the design of the integrity algorithm in the case of train control are summarized in Table 36. These parameters are defined assuming that there is only one satellite failure at a time, and with at maximum 10 satellites in view. For GLONASS, the probability of satellite failure has been set to $10^{-4}/\text{sat}/\text{h}$. The integrity risk allocated to each GNSS is $10^{-5.5}/\text{h}$. As no continuity requirement was found for this application, different false detection rate has been tested.

	GPS based solution	GLONASS based solution
Total integrity risk (/h)	$10^{-5.5}$	$10^{-5.5}$
Missed detection probability	$0.5 \cdot 10^{-1.5}$	$0.5 \cdot 10^{-2.5}$
Rare normal performance rate (/sample)	$0.5 \cdot 10^{-5.5}$	$0.5 \cdot 10^{-5.5}$
False detection rate (/sample)	$10^{-4}/10^{-5}/10^{-6}$	$10^{-4}/10^{-5}/10^{-6}$

Table 36 Summary of the parameters of the integrity monitoring algorithm for train control

8.3.3.1.1 Approach based on the inflation of the noise measurement covariance matrix

The first approach consists in inflating the measurement error covariance matrix sufficiently so that it covers the measurement errors due to the local effects. In this approach all the pseudorange measurements are incorporated for the Kalman filter update operation. In particular, the measurement selection process described in chapter 6 is not applied here (only a 30 dB-Hz C/N_0 mask is applied here). In this case, it is assumed that all the measurements are nominal (as no satellite failure occurs during the campaign). In this case the error on the position estimated by the filter is assumed Gaussian, centered, and with a variance that is estimated by the filter. To provide sufficient integrity, HPL_{H0} shall bound the position error with the corresponding rare normal required probability. The proposed criterion that is used here is that the error magnitude shall be lower than three times the standard deviation of the position error estimated by the KF for all the data collection. For the pseudorange measurements, the weighting scheme which has been derived in section 5.3.2.2.4 to account for the local effects has been used. In dense urban environment, it has been observed that the position error exceed the 3σ bounds as estimated by the filter. It is proposed to inflate the noise standard deviation coefficients corresponding to the pseudorange (σ_ρ) and pseudorange rates ($\sigma_{\dot{\rho}}$) measurements when the receiver is located in deep urban canyons by constant multiplying factors denoted K_ρ and $K_{\dot{\rho}}$. For the filters that integrates GPS and GLONASS, K_ρ is set to 2 and $K_{\dot{\rho}}$ is set to 4. These coefficients have been determined empirically so that the criterion is fulfilled even in dense urban environment. For simplicity, the two EKF integrates the data from the same Landmark 01 IMU (but with independent mechanization). It shall not be the case for a true implementation of the proposed solution.

8.3.3.1.1.1 Standard solution separation algorithm

The solution separation algorithm presented in section 8.3.2.1 is implemented on the train control solutions. The two sub solutions that integrates GPS and GLONASS have been combined according to the method presented in section 4.1.1.1. Firstly, the performances in terms of position errors characteristic (RMS and accuracy) of the combined system are assessed and compared to the performances of each sub systems. Indeed the position of the combination is directly dependent of the protection levels of both subsystems, for this reason it has not been possible to assess the performance of the combined solution in chapter 6. Therefore different P_{MD} and P_{FA} used in the design of the integrity monitoring algorithm will result in different accuracy performances. The accuracy performance obtained with a P_{MD} at $10^{-1.5}$ and a P_{FA} at 10^{-4} are presented as an example. The along-track position error CDF is given in Figure 121. The performances of the two subsystems and the combined systems are compared in Table 37. The combined system outperforms the worst of the two subsystems for all the metrics. This result is compliant with the theoretical performances obtain by simple modelling in chapter 4. The combined solution is able to fulfill the along-track accuracy requirements (6.6 meter in the most stringent case) in order to be used in train control for all operations in suburban environment provided that the across track requirement is removed. In dense urban environment, the along-track accuracy of the combined system is sufficient to fulfil the requirements except for stations and corridors.

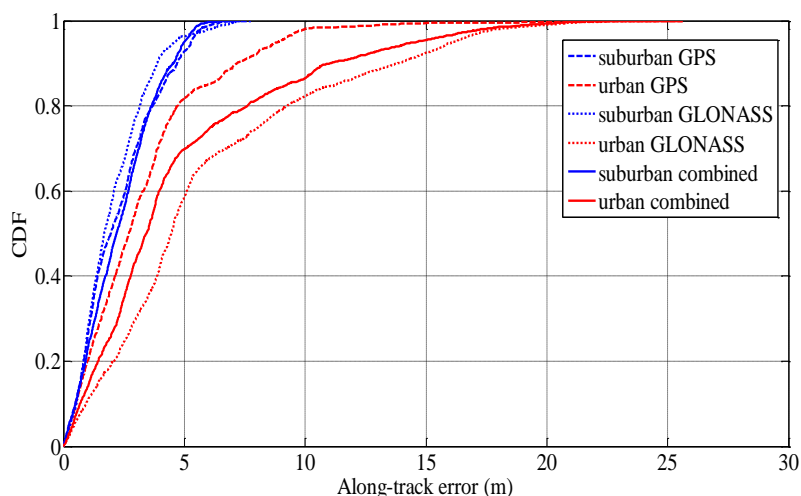


Figure 121 Distribution of the position error of the two sub solutions and their combination after inflated weighting scheme in urban environment ($P_{FA} = 10^{-4}$)

Along-track error		EKF GPS	EKF GLONASS	Combination
RMS (m)	Suburban	2.8	2.5	2.7
	Urban	4.4	7.5	6.4
Max (m)	Suburban	7.7	7.3	6.9
	Urban	25.6	24.5	25.6

95% (m)	Suburban	5.3	4.6	5.0
	Urban	8.9	16.1	14.7

Table 37 Statistics on the position error of the two sub solutions and their combination after inflated weighting schemes

For the two sub solutions as well as for the combined solution, the Stanford plots are given in appendix H. This representation consists in plotting the 2D histogram of the horizontal protection levels as a function of the horizontal error. A misleading information event does occur if the position error exceeds the protection level. These figures have confirmed that no Misleading Information occurred during the data collection for the three configurations. The distributions of *HPL* for the three subsystems are given in Figure 122 for urban and suburban environments. The results are also given in terms of availability in Table 38 and Table 39 for the different P_{FA} that have been tested. The inflated weighting scheme combined with the poor geometry leads to considerably larger protection levels in urban environment compared to suburban which leads to poor availability of the solution (even for $HAL = 125$ m). In suburban, the availability is between 99% and 100% for a HAL of 50 m. With a P_{FA} of 10^{-4} the availability is sufficient for the navigation in some main and secondary lines as well and in all the regional and industrial lines (availability higher than the requirement). It must be kept in mind here that suburban environment conditions do not correspond to open-sky conditions.

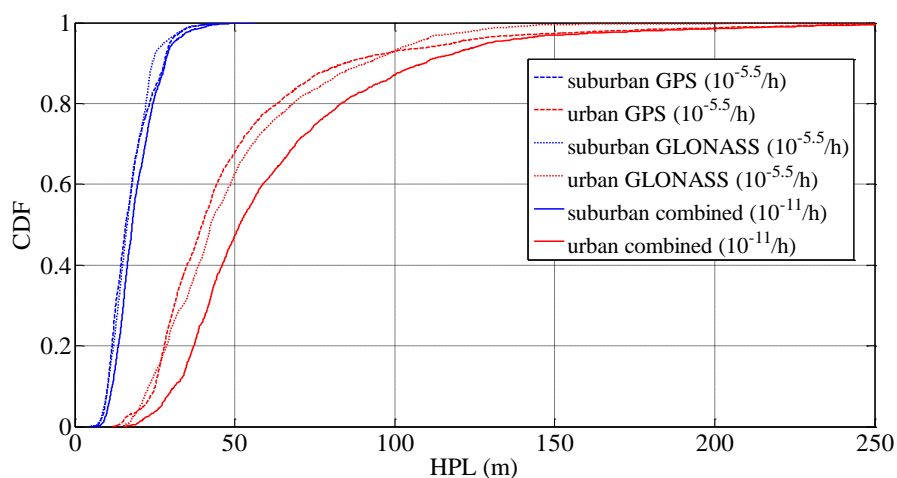


Figure 122 Distribution of the *HPL* of the two sub solutions and their combination after inflated weighting scheme in urban environment ($P_{FA} = 10^{-4}$)

Suburban	P_{FA} = 10^{-4}	P_{FA} = 10^{-5}	P_{FA} = 10^{-6}
HAL=15 m	28.8 %	24.3 %	21.1%
HAL=25 m	80.6 %	76.4 %	72.0%
HAL=50 m	99.8 %	99.6 %	99.5%

Table 38 Statistics on availability in suburban environment with inflated weighting scheme

Urban	P_{FA} = 10^{-4}	P_{FA} = 10^{-5}	P_{FA} = 10^{-6}
HAL=25 m	2.9 %	2.5 %	2.0%
HAL=50 m	46.1 %	42.1 %	38.4%
HAL=125 m	93.7 %	92.1 %	91.0%

Table 39 Statistics on availability in urban environment with inflated weighting scheme

Note: No false alarm has been observed during the data collection.

8.3.3.1.1.2 Solution separation based on sub mechanizations

The solution separation based on independent mechanization has been implemented and tested on the same data set. In this case again, the combination of GPS and GLONASS outperforms the worst of the two solutions in terms of accuracy for every environments. It has been shown that the accuracy of the combined solution is 5 meters in suburban environment and 14.7 meters in suburban environment (it is identical to what has been obtained for the standard separation algorithm). The Stanford plots are given for the two sub solutions and the combined solution in appendix H. No HMI has been observed for any solution during the campaign. However, the protection levels calculated with this algorithm are significantly larger than the position error which is damaging for the availability. It is characteristic of an ineffective integrity monitoring algorithm.

Note: The efficiency of an integrity monitoring algorithm for HPL computation can be quantized by measuring the ratio HPE/HPL . This ratio shall be as high as possible and below one to ensure integrity.

This is due to the very conservative bound that has been derived for the covariance of the separation vector (assuming anti correlated sub solutions). The cumulative distributions of the HPL for the three subsystems are given in Figure 123 for urban and suburban environments. This algorithm leads to poor availability because HPL are too conservative. It is the case in suburban environment where the availability is lower than 85% for a HAL of 50 m (Table 40). As illustrated in Table 41 urban environment, the inflation of the measurement covariance highly degrades the availability of the solution which is lower than 70%, even in sub urban environment.

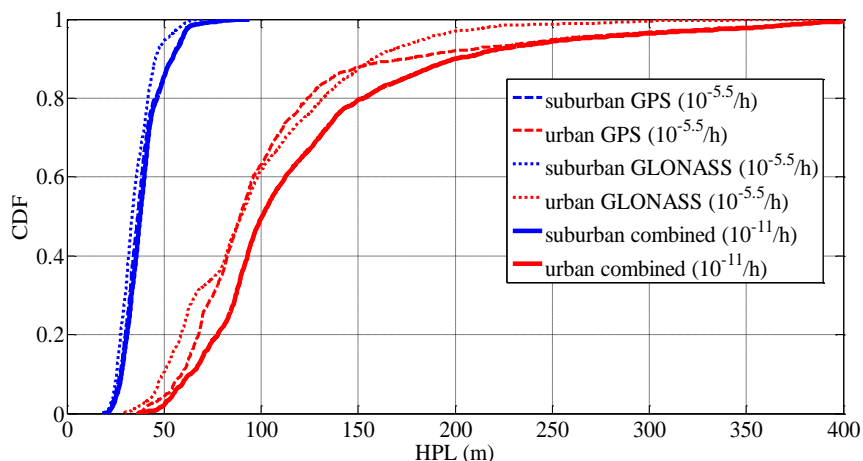


Figure 123 Distribution of the *HPL* of the two sub solutions and their combination after inflated weighting scheme in urban environment (approach based on separated mechanizations with $P_{FA}=10^{-4}$)

Suburban	$P_{FA} = 10^{-4}$	$P_{FA} = 10^{-5}$	$P_{FA} = 10^{-6}$
<i>HAL</i> = 15 m	0%	0%	0%
<i>HAL</i> = 25 m	3.8%	1.8%	0.8%
<i>HAL</i> = 50 m	84.6%	79.8%	76.1%

Table 40 Statistics on availability in suburban environment with inflated weighting scheme. (approach based on separated mechanizations)

Urban	$P_{FA} = 10^{-4}$	$P_{FA} = 10^{-5}$	$P_{FA} = 10^{-6}$
<i>HAL</i> = 25 m	0%	0%	0%
<i>HAL</i> = 50 m	0%	0%	0%
<i>HAL</i> = 125 m	66.3%	62%	57%

Table 41 Statistics on availability in urban environment with inflated weighting scheme. (approach based on separated mechanizations)

8.3.3.1.2 Approach based on the selection of the GNSS measurements

The second approach that is investigated consists in selecting the measurements prior to the integrity monitoring algorithm and excluding the measurements that are likely to be biased due to the environment of the user. In this case, the weighting scheme used to model the multipath error is based on the results obtained by simulations on the LMS and the noise error is modelled by its theoretical variance. The selection of the measurement is done according to the scheme that has been described in chapter 6 (except the multipath monitor that was not implemented on the mass market receiver used).

8.3.3.1.2.1 Standard solution separation algorithm

It can be seen in Figure 124 and Table 42 that the selection of the measurements has improved the accuracy of the solution in urban environment. As an illustration, the horizontal accuracy (95%) has

been reduced from 14.6 m to 10.9 m on the combined solution. However, the combined solution is still accurate enough for positioning in train station in urban environment due to the low accuracy of the GLONASS subsystem in this case. The accuracy requirements for the other operations are still fulfilled here.

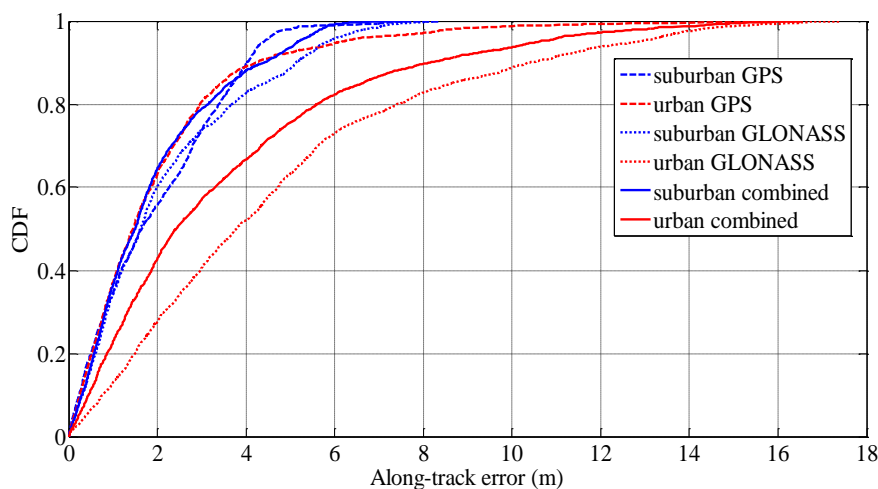


Figure 124 Distribution of the position error of the two sub solutions and their combination after innovation filtering in suburban and urban environments ($P_{FA} = 10^{-4}$)

Along-track error		EKF GPS	EKF GLONASS	Combination
RMS	Suburban	1.8	3.1	2.4
	Urban	5.4	8.0	4.8
Max	Suburban	8.3	8.2	8.3
	Urban	16.5	17.4	16.5
95 th %	Suburban	3.6	6.8	5.2
	Urban	8.2	16.7	10.6

Table 42 Statistics on the position error of the two sub solutions and their combination after measurement selection

The Stanford plots in appendix H shows that no misleading information was observed during the data collection for the sub systems and the combined solution. It can be seen in Figure 125 that the protection levels have been highly reduced in urban environment by selecting the measurements because it enables to integrate only measurements with small error covariance. The availability of the integrity monitoring algorithm is given in Table 43 and Table 44. With this approach, the system has an availability of 100 % for a HAL of 50 m in suburban environment for all the tested P_{FA} . It is sufficient for most main and secondary lines, as well as regional and industrial lines. However, it is not sufficient for corridor lines and stations. Moreover, the availability in urban environment has been significantly improved, and reaches 99% for a HAL of 125 m in urban environment. However, the tolerable unavailability associated to the HAL of 125 m shall be slightly lower. However, the epochs

corresponding to the unavailability periods do not occurs in a typical rail environment (tramway tracks) but in a very narrow urban canyon which width is about 5 meters (43°35'57.70"N, 1°26'49.13"E). This street is not wide enough to be representative of a rail track in urban environment.

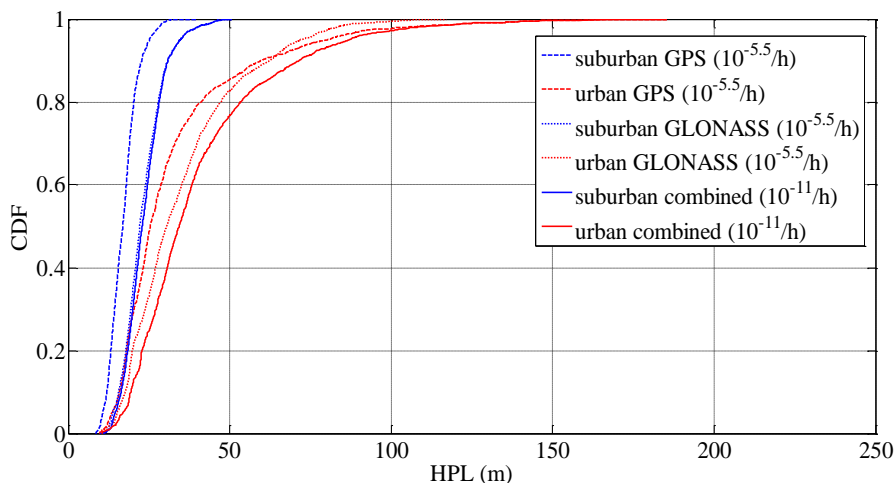


Figure 125 Distribution of the *HPL* of the two sub solutions and their combination after selection of the measurements in suburban and urban environments ($P_{FA} = 10^{-4}$)

Suburban	$P_{FA} = 10^{-4}$	$P_{FA} = 10^{-5}$	$P_{FA} = 10^{-6}$
<i>HAL</i> = 15 m	6.1%	4.9%	3.0%
<i>HAL</i> = 25 m	63.4%	56.1%	51.3%
<i>HAL</i> = 50 m	100%	99.7%	99.4%

Table 43 Statistics of availability in suburban environment with measurement selection

Urban	$P_{FA} = 10^{-4}$	$P_{FA} = 10^{-5}$	$P_{FA} = 10^{-6}$
<i>HAL</i> = 25 m	24.0%	21.8%	19.4%
<i>HAL</i> = 50 m	76.1%	73.5%	71.1%
<i>HAL</i> = 125 m	99.0%	98.6%	98.3%

Table 44 Statistics of availability in urban environment with measurement selection

8.3.3.1.2.2 Solution separation using sub mechanizations

The separation algorithm in which each sub filter corrects its own mechanization also performs large protection levels and thus low availability in urban and suburban environment. The measurement selection process has slightly reduced the size of *HPL* in urban environment. This algorithm clearly performs insufficient availability in urban environment. In suburban environment, it shall be noticed that an availability of 100% is achieved for an *HAL* of 100 m which appears sufficient for operating in low density lines.

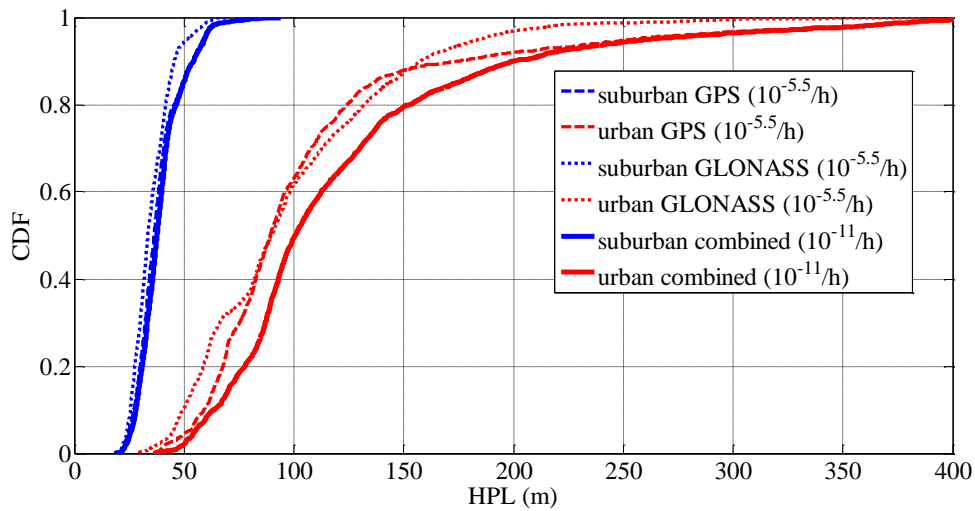


Figure 126 Distribution of the *HPL* of the two sub solutions and their combination after selection of the measurements in urban environment (approach based on separated mechanizations with $P_{FA} = 10^{-4}$)

Suburban	$P_{FA} = 10^{-4}$	$P_{FA} = 10^{-5}$	$P_{FA} = 10^{-6}$
<i>HAL</i> = 15 m	0 %	0 %	0%
<i>HAL</i> = 25 m	5.4%	2.8%	1.3%
<i>HAL</i> = 50 m	85.0%	80.7%	77.8%

Table 45 Statistics on availability in suburban environment with measurement selection. (approach based on separated mechanizations)

Urban	$P_{FA} = 10^{-4}$	$P_{FA} = 10^{-5}$	$P_{FA} = 10^{-6}$
<i>HAL</i> = 25 m	0%	0%	0%
<i>HAL</i> = 50 m	3.2%	2.3%	1.9%
<i>HAL</i> = 125 m	79.8%	75.1%	71.2%

Table 46 Statistics on availability in urban environment with measurement selection (approach based on separated mechanizations)

8.3.3.2 Results: ETC

To design the integrity monitoring algorithm, it is necessary to determine its parameters in term of P_{MD} and P_{FA} . The parameters proposed for the design of the integrity algorithm for ETC are summarized in Table 47. It is assumed that there is one satellite failure at a time, and that, at maximum, 20 satellites are in view (10 for each constellation). For GLONASS, the probability of occurrence of a satellite fault is considered equal to $10^{-4}/sat/h$. In this case, the probability of occurrence of a satellite fault for the dual constellation system is equal to $1.1 \cdot 10^{-3}/sat/h$. It has been stated in chapter 3 that the integrity risk requirements for GNSS to be used in ETC are not standardized. Therefore different GNSS integrity risk requirements can be derived depending of the

charging organism. Three typical values for the integrity risk requirement have been tested: $10^{-4}/h$, $10^{-5}/h$ and $10^{-6}/h$. It is assumed that lower integrity risks are associated with safety critical applications. Moreover, as no continuity requirement was found for this application, different false detection rate have been tested.

	GPS/GLONASS based algorithm		
Total integrity risk (/h)	10^{-4}	10^{-5}	10^{-6}
Missed detection probability	0.045	0.0045	0.00045
Rare normal performance rate (/sample)	$0.5 \cdot 10^{-4}$	$0.5 \cdot 10^{-5}$	$0.5 \cdot 10^{-6}$
False detection rate (/sample)	$10^{-4}/10^{-5}/10^{-6}$	$10^{-4}/10^{-5}/10^{-6}$	$10^{-4}/10^{-5}/10^{-6}$

Table 47 Summary of the parameters of the integrity monitoring algorithm for ETC

8.3.3.2.1 Approach based on the inflation of the noise measurement covariance matrix

The weighting scheme which has been derived in chapter 5 to account for the local effects and the thermal noise has been used. It replaces the value derived by simulations with the LMS channel model for multipath and the theoretical standard deviation of the error due to thermal noise. The noise standard deviation coefficients corresponding to the pseudorange (σ_ρ) and pseudorange rates ($\sigma_{\dot{\rho}}$) measurements have been inflated when the receiver is located in deep urban canyons by applying constant multiplying factors denoted K_ρ and $K_{\dot{\rho}}$. K_ρ has been set to 2 and $K_{\dot{\rho}}$ is set to 4.

8.3.3.2.1.1 Standard solution separation algorithm

The integration of the measurements from the two constellations enables to significantly reduce the magnitude of the protection levels in both urban and suburban environment (and thus even if there is no access any map or track base). Table 48 shows that the solution that integrates GPS GLONASS, the IMU and the WSS, achieve a good availability (more than 99%) in suburban environment for an HAL of 25 m. It may not be sufficient in some situations where the distance between parallel roads can be as low as 15 m. However, in urban environment, the degradation of the geometry and the large measurement errors lead to higher HPL (see Figure 127).

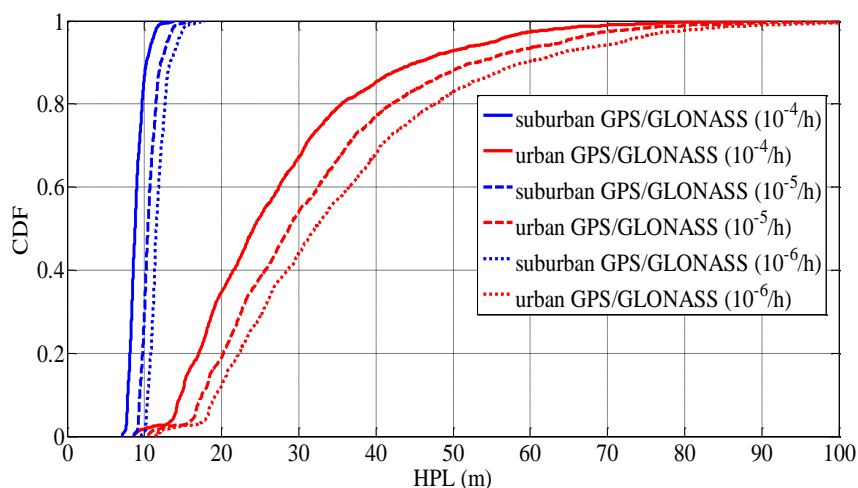


Figure 127 Distribution of the HPL for ETC ($P_{FA} = 10^{-4}$)

Suburban	$P_{int} = 10^{-4}/h$			$P_{int} = 10^{-5}/h$			$P_{int} = 10^{-6}/h$		
	$P_{FA} = 10^{-4}$	$P_{FA} = 10^{-5}$	$P_{FA} = 10^{-6}$	$P_{FA} = 10^{-4}$	$P_{FA} = 10^{-5}$	$P_{FA} = 10^{-6}$	$P_{FA} = 10^{-4}$	$P_{FA} = 10^{-5}$	$P_{FA} = 10^{-6}$
HAL = 15 m	99.4%	98.9%	98.5%	97.9%	97.6%	97.2%	96.2%	94.1%	91.9%
HAL = 25 m	100%	100%	99.9%	99.9%	99.8%	99.8%	99.8%	99.7%	99.7%
HAL = 50 m	100%	100%	100%	100%	100%	100%	100%	100%	100%

Table 48 Statistics of availability in suburban environment with measurement selection

Urban	$P_{int} = 10^{-4}/h$			$P_{int} = 10^{-5}/h$			$P_{int} = 10^{-6}/h$		
	$P_{FA} = 10^{-4}$	$P_{FA} = 10^{-5}$	$P_{FA} = 10^{-6}$	$P_{FA} = 10^{-4}$	$P_{FA} = 10^{-5}$	$P_{FA} = 10^{-6}$	$P_{FA} = 10^{-4}$	$P_{FA} = 10^{-5}$	$P_{FA} = 10^{-6}$
HAL = 25 m	51.8%	48.2%	44.8%	36.8%	34.3%	32.6%	27.3%	24.9%	23.1%
HAL = 50 m	92.6%	91.3%	90.0%	87.7%	86.1%	84.5%	82.3%	80.4%	78.8%
HAL = 75 m	99.3%	99.0%	98.6%	98.2%	97.6%	97.1%	96.2%	94.9%	94.0%

Table 49 Statistics of availability in urban environment with measurement selection

8.3.3.2.1.2 Solution separation with parallel mechanizations

The solution separation algorithm in which the subfilters are associated with different sub mechanization has been tested on the ETC solution. Again due to the conservative assumption on the covariance of the separator, the HPL are much higher than the standard solution separation algorithm. Anyway, the algorithm is able to fulfill suitable availability (99 to 100 %) in suburban environment if the alert limit is higher or equal to 50 m and the integrity risk set to 10^{-4} to $10^{-5}/h$ (associated to a false alarm rate of 10^{-4} to 10^{-5}). The availability in urban environment is very poor and not sufficient for an ETC.

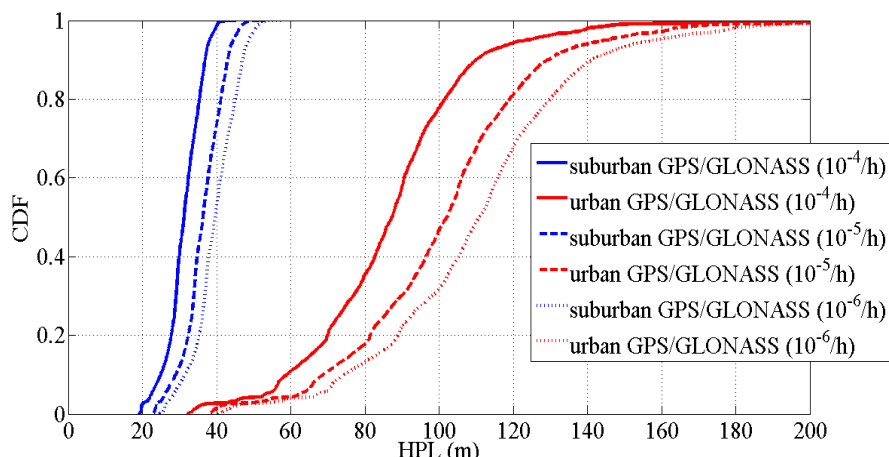


Figure 128 Distribution of the *HPL* for ETC ($P_{FA} = 10^{-4}$), solution separation using submechanizations for inflated measurement error model

Suburban	$P_{int} = 10^{-4}/h$			$P_{int} = 10^{-5}/h$			$P_{int} = 10^{-6}/h$		
	$P_{FA} = 10^{-4}$	$P_{FA} = 10^{-5}$	$P_{FA} = 10^{-6}$	$P_{FA} = 10^{-4}$	$P_{FA} = 10^{-5}$	$P_{FA} = 10^{-6}$	$P_{FA} = 10^{-4}$	$P_{FA} = 10^{-5}$	$P_{FA} = 10^{-6}$
<i>HAL</i> = 15 m	0%	0%	0%	0%	0%	0%	0%	0%	0%
<i>HAL</i> = 25 m	14.8%	10.4%	6.6%	6.2%	2.6%	0%	8.0%	0%	0%
<i>HAL</i> = 50 m	100%	100%	99.7%	99.7%	98.4%	94.5%	97.1%	90.0%	79.4%

Table 50 Statistics of availability in suburban environment with inflated measurement error model

Urban	$P_{int} = 10^{-4}/h$			$P_{int} = 10^{-5}/h$			$P_{int} = 10^{-6}/h$		
	$P_{FA} = 10^{-4}$	$P_{FA} = 10^{-5}$	$P_{FA} = 10^{-6}$	$P_{FA} = 10^{-4}$	$P_{FA} = 10^{-5}$	$P_{FA} = 10^{-6}$	$P_{FA} = 10^{-4}$	$P_{FA} = 10^{-5}$	$P_{FA} = 10^{-6}$
<i>HAL</i> = 25 m	0%	0%	0%	0%	0%	0%	0%	0%	0%
<i>HAL</i> = 50 m	1.3%	9.0%	0%	0%	0%	0%	0%	0%	0%
<i>HAL</i> = 75 m	25.6%	16.3%	12.0%	11.6%	8.3%	5.5%	7.7%	3.6%	2.0%

Table 51 Statistics of availability in urban environment with inflated measurement error model

8.3.3.2.2 Approach based on the selection of the GNSS measurements

The benefit of selecting the measurements prior to the integrity monitoring algorithm is investigated here. In this configuration, the weighting scheme used to model the multipath error is based on the results obtained by simulations on the LMS and the noise error is modelled by its theoretical variance. The scheme applied for the selection of the measurement is the one that has been described in chapter 7 (except the multipath monitor that was not implemented on the mass market receiver used).

8.3.3.2.2.1 Standard solution separation algorithm

Table 52 shows that the selection of the measurements has slightly improved the availability of the solution in urban environment (it is visible for an HAL of 25 m). Higher improvement was expected due to the ability of the selection scheme to reduce the magnitude of the HPE in the dual constellation approach. This is the result of the degradation of the geometry by excluding satellites with bad indicators. However, the drawback intrinsic to this approach is that the availability has been degraded in suburban environment.

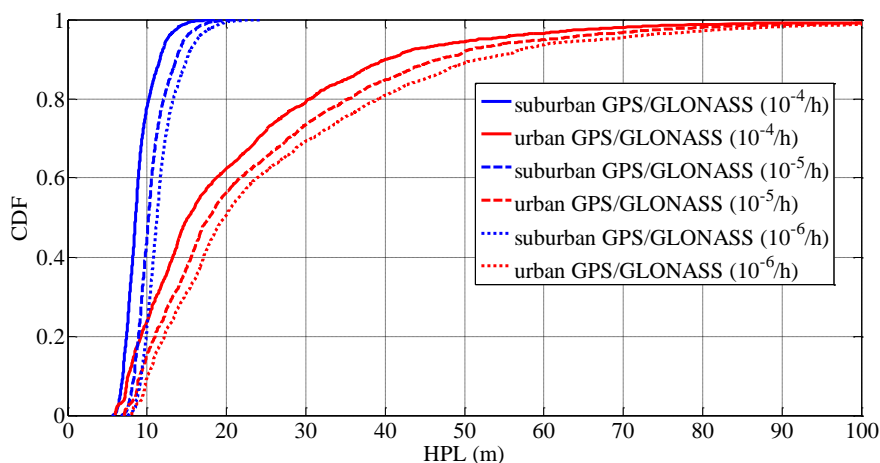


Figure 129 Distribution of the HPL for ETC ($P_{FA} = 10^{-4}$)

	$P_{int} = 10^{-4}/h$			$P_{int} = 10^{-5}/h$			$P_{int} = 10^{-6}/h$		
	$P_{FA} = 10^{-4}$	$P_{FA} = 10^{-5}$	$P_{FA} = 10^{-6}$	$P_{FA} = 10^{-4}$	$P_{FA} = 10^{-5}$	$P_{FA} = 10^{-6}$	$P_{FA} = 10^{-4}$	$P_{FA} = 10^{-5}$	$P_{FA} = 10^{-6}$
Suburban									
HAL = 15 m	98.4%	97.9%	96.9%	94.6%	92.8%	90.7%	88.8%	86.0%	83.7%
HAL = 25 m	100%	100%	100%	100%	100%	100%	100%	99.9%	99.9%
HAL = 50 m	100%	100%	100%	100%	100%	100%	100%	100%	100%

Table 52 Statistics of availability in suburban environment with measurement selection

	$P_{int} = 10^{-4}/h$			$P_{int} = 10^{-5}/h$			$P_{int} = 10^{-6}/h$		
	$P_{FA} = 10^{-4}$	$P_{FA} = 10^{-5}$	$P_{FA} = 10^{-6}$	$P_{FA} = 10^{-4}$	$P_{FA} = 10^{-5}$	$P_{FA} = 10^{-6}$	$P_{FA} = 10^{-4}$	$P_{FA} = 10^{-5}$	$P_{FA} = 10^{-6}$
Urban									
HAL = 25 m	71.2%	68.9%	66.6%	64.3%	62.8%	61.4%	60.7%	59.3%	58.1%
HAL = 50 m	94.3%	93.5%	92.8%	91.7%	90.4%	89.3%	88.7%	87.3%	85.7%
HAL = 75 m	98.4%	98.1%	97.7%	97.4%	96.9%	96.4%	96.3%	95.7%	95.3%

Table 53 Statistics of availability in urban environment with measurement selection

8.3.3.2.2 Solution separation algorithm based on sub mechanization

Finally, the sub mechanization based solution separation algorithm has been tested on the fusion algorithm that integrates GPS, GLONASS, the IMU and the WSS with selection of the measurements. A significant reduction of the protection level CDF has been obtained with the selection in urban environment. As an example, for a P_{FA} of 10^{-4} associated with an integrity risk of $10^{-4}/h$, the availability associated with an HAL of 75 meters has been improved from 25.6 to 88.6%.

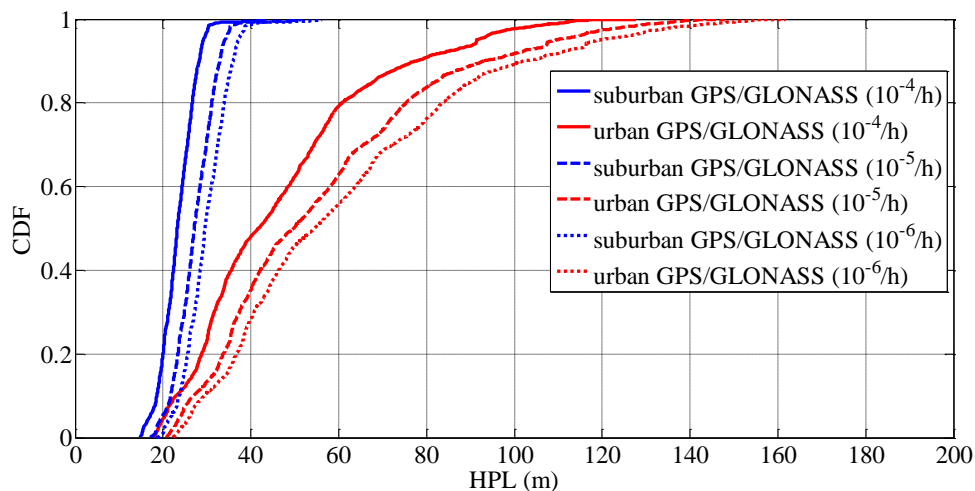


Figure 130 Distribution of the HPL for ETC ($P_{FA} = 10^{-4}$)

Suburban	$P_{int} = 10^{-4}/h$			$P_{int} = 10^{-5}/h$			$P_{int} = 10^{-6}/h$		
	$P_{FA} = 10^{-4}$	$P_{FA} = 10^{-5}$	$P_{FA} = 10^{-6}$	$P_{FA} = 10^{-4}$	$P_{FA} = 10^{-5}$	$P_{FA} = 10^{-6}$	$P_{FA} = 10^{-4}$	$P_{FA} = 10^{-5}$	$P_{FA} = 10^{-6}$
$HAL = 15$ m	2%	0%	0%	0%	0%	0%	0%	0%	0%
$HAL = 25$ m	67.9%	51.5%	34.9%	33.1%	22.2%	13.4%	18.3%	10.9%	6.9%
$HAL = 50$ m	100%	100%	99.9%	99.7%	99.5%	99.4%	99.4%	99.3%	99.3%

Table 54 Statistics of availability in suburban environment with measurement selection, approach based on parallel mechanizations

Urban	$P_{int} = 10^{-4}/h$			$P_{int} = 10^{-5}/h$			$P_{int} = 10^{-6}/h$		
	$P_{FA} = 10^{-4}$	$P_{FA} = 10^{-5}$	$P_{FA} = 10^{-6}$	$P_{FA} = 10^{-4}$	$P_{FA} = 10^{-5}$	$P_{FA} = 10^{-6}$	$P_{FA} = 10^{-4}$	$P_{FA} = 10^{-5}$	$P_{FA} = 10^{-6}$
$HAL = 25$ m	11.4%	10.3%	8.2%	7.7%	4.2%	2.0%	3.3%	1.5%	0%
$HAL = 50$ m	61.4%	55.6%	50.7%	49.0%	45.7%	41.8%	44.2%	39.6%	35.4%
$HAL = 75$ m	88.6%	85.9%	82.5%	78.9%	73.4%	69.7%	70.9%	68.2%	63.4%

Table 55 Statistics of availability in urban environment with measurement selection, approach based on parallel mechanizations

8.3.4 Detection ability

The ability of the two solution separation algorithms to detect a simulated satellite fault has been tested on real data. The solution that is used in this section uses GPS, GLONASS, the IMU of reference and the simulated WSS. The satellite failure is injected on GPS SV 15 (arbitrarily chosen), when the vehicle is driving in suburban environment. Different simulated satellite failures have been tested:

- Step jumps with magnitudes of 30 m (typical of clock jumps), 100 m
- Ramp failure with magnitudes of 0.1 m/s (as it may not be detected by monitoring the residuals), 0.5 m/s

The failure is added at 300 seconds in the data collection.

8.3.4.1 Standard solution separation algorithm

The conventional solution separation algorithm has been tested at first. It is shown in Figure 131 and Figure 132 that the algorithm is able to detect the faults characterized by a jump signature (because the separation exceed the thresholds) before the *HPE* exceeds the *HPL*. There is no misleading information in these two cases. The detection took 10 second for a 30 m jump and 2 second for a 100 m jump. The ability of the test to detect ramp failures is illustrated by Figure 133 and Figure 134. It can be inferred from Figure 133 that the ramp with a magnitude of 0.1 m/s is detected 140 seconds after having corrupted the measurement. Still, the *HPL* bound the position error prior to the detection (the misleading information occurs 40 seconds after the alarm has been raised). The ramp with a magnitude of 0.5 m/s is detected after 40 seconds and at this time the *HPE* has not exceed the *HPL*. Thus, the proposed adaptation of the solution separation algorithm to the closed loop scheme is relevant.

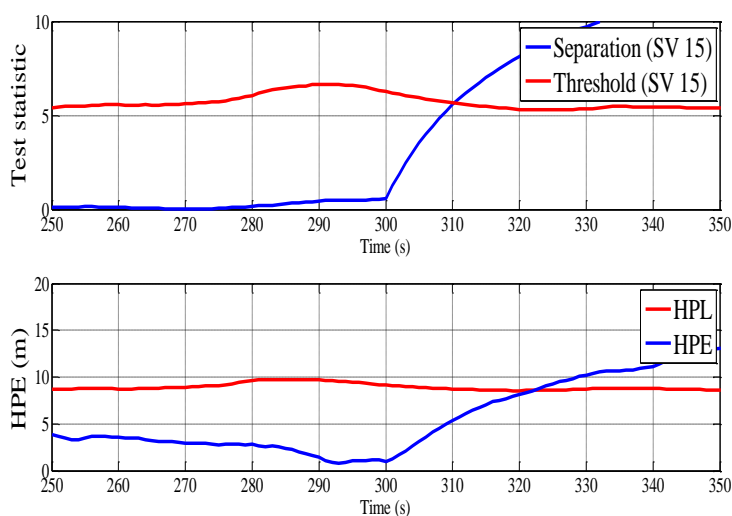


Figure 131 Detection of a step with a magnitude of 30 m

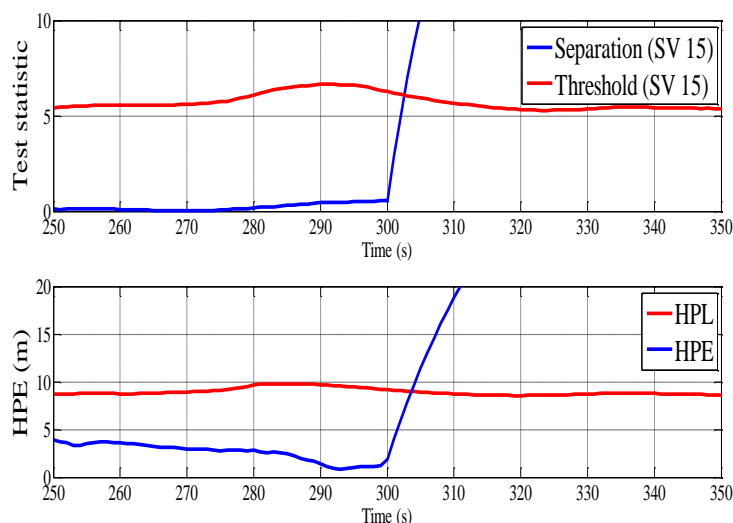


Figure 132 Detection of a step with a magnitude of 100 m

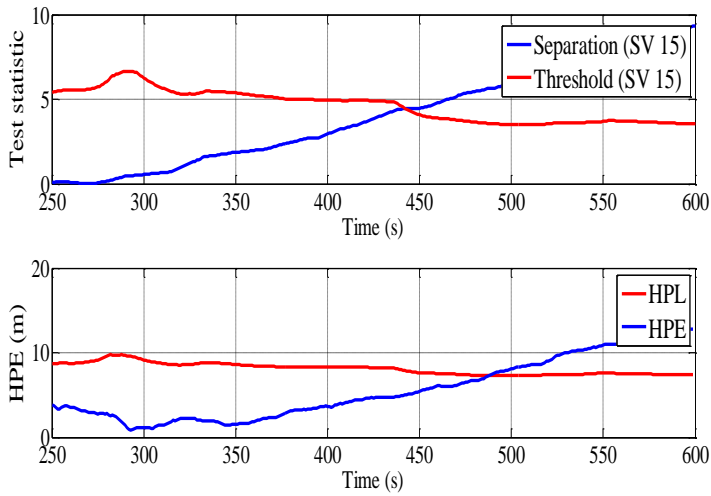


Figure 133 Detection of a ramp failure with a magnitude of 0.1 m/s

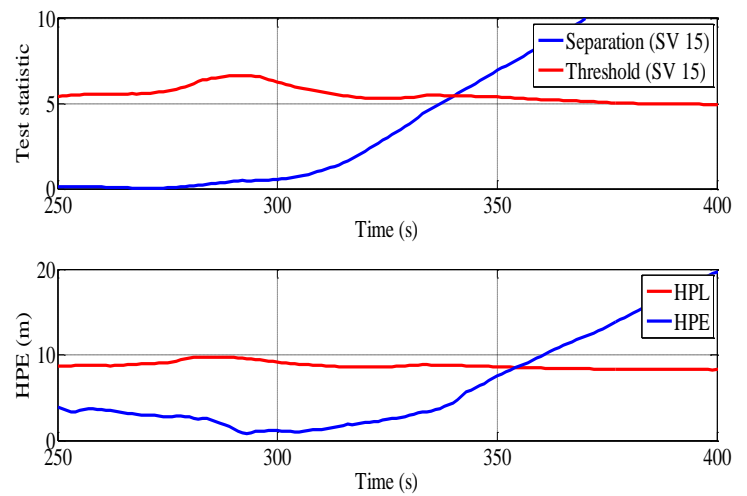


Figure 134 Detection of a ramp failure with a magnitude of 0.5 m/s

8.3.4.2 Solution separation based on parallel mechanizations

The same study has been conducted on the solution separation algorithm that uses parallel mechanizations. As shown in Figure 135 and Figure 136, the integrity monitoring algorithm is able to detect the satellite failure before the *HPE* exceeds the *HPL* in case of step failure. However, as the covariance of the separator is much larger (because of the conservative assumption), the detection is significantly longer than for solution separation with subfilters on an open loop scheme. According to Figure 135, a 30 meter jump is detected 50 seconds after its onset. The detection does not exceed 10 seconds for a jump of 100 m according to Figure 136. According to Figure 137 and Figure 138 the algorithm is also able to detect ramp failures. The 0.1 m/s ramp has been detected approximately 300 seconds after its onset. It has been observed that the *HPL* bounds the *HPE* prior to the detection. The 0.5 m/s ramp has been successfully detected after 75 seconds after its onset according to Figure 138. Thus the two solution separations algorithms are able to detect the satellite failures with jump and ramp signatures.

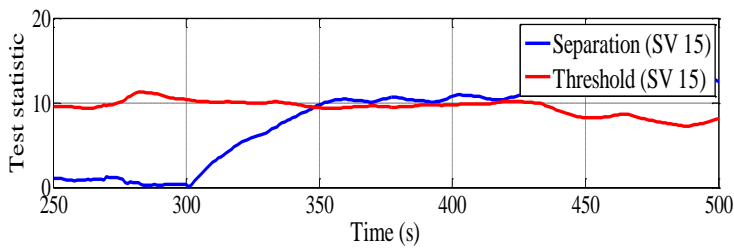


Figure 135 Detection of a step with a magnitude of 30 m, separated mechanizations

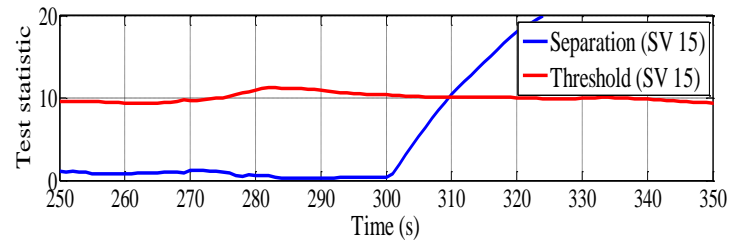
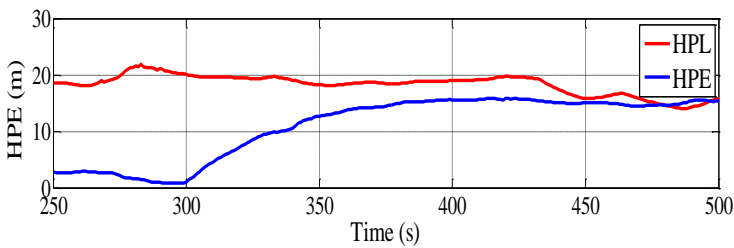


Figure 136 Detection of a step with a magnitude of 100 m, separated mechanizations

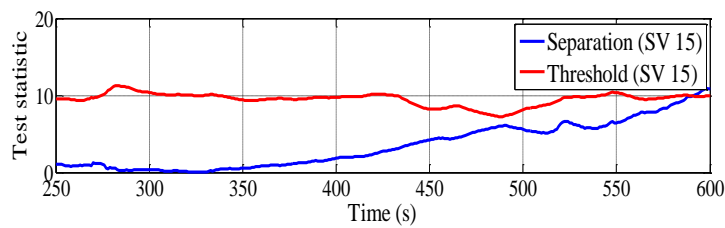
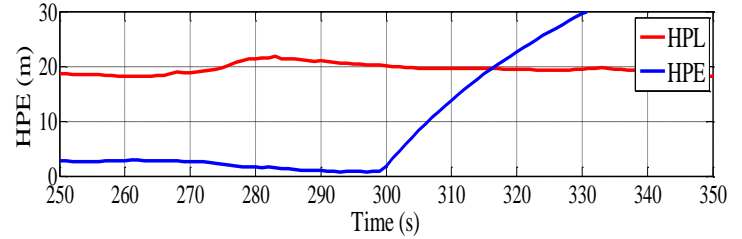


Figure 137 Detection of a ramp failure with a magnitude of 0.1 m/s, separated mechanizations

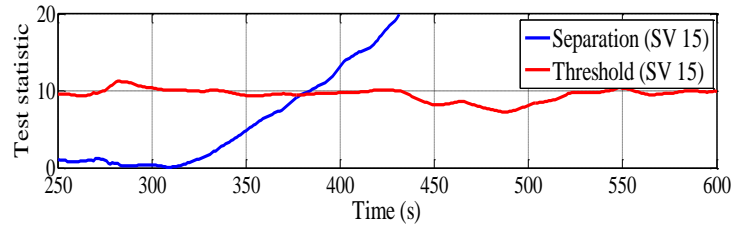
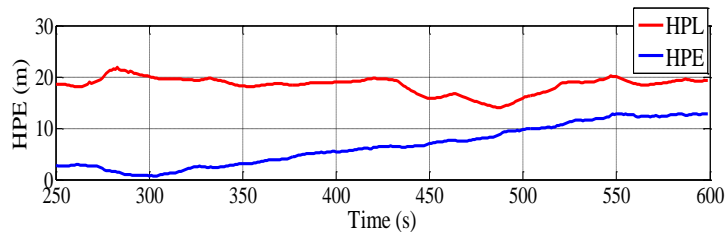
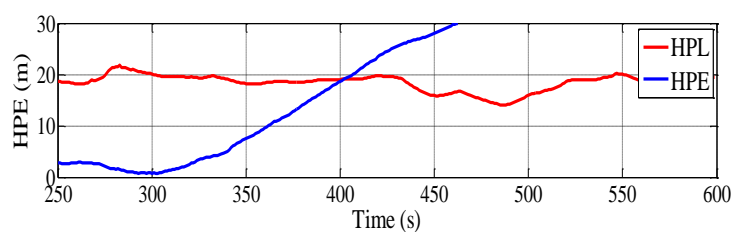


Figure 138 Detection of a ramp failure with a magnitude of 0.5 m/s, separated mechanizations



8.4 Improving the measurement selection by determining the maximum tolerable bias

The multipath detector and innovation monitoring tests that have been presented in chapter 7 have been designed following a traditional approach which consists in setting their own P_{FA} to a fixed value in order to obtain a detection threshold. A minimum detectable measurement bias can then be deduced for any value of P_{MD} .

An alternative approach investigated in this section consists in first computing the measurement biases that are dangerous for the navigation algorithm. Given this information, and knowing the the required P_{MD} for the detector, it is then possible to set the thresholds for the considered tests. The P_{FA} is then just deduced. In this case, it can be suitable to have relatively large P_{FA} for these two detectors as the

type of failure of interest (due to local effects) require the measurements to only be excluded for a short duration because local effects are known to be limited in space.

8.4.1 Concept of critical biases

Only the biases that can lead to a horizontal positioning failure need to be detected and excluded from the solution. The critical biases are defined as the smallest biases that will lead to a positioning failure with a given probability. This concept has been introduced in [Nikiforov, 2005] and is investigated in [Martineau, 2008] in the case of a WLSE position estimation algorithm. Its principle relies on the fact that small measurement biases are acceptable if, and only if, they do not lead to a probability of failure higher than the integrity risk. An illustration of the concept is given in Figure 139.

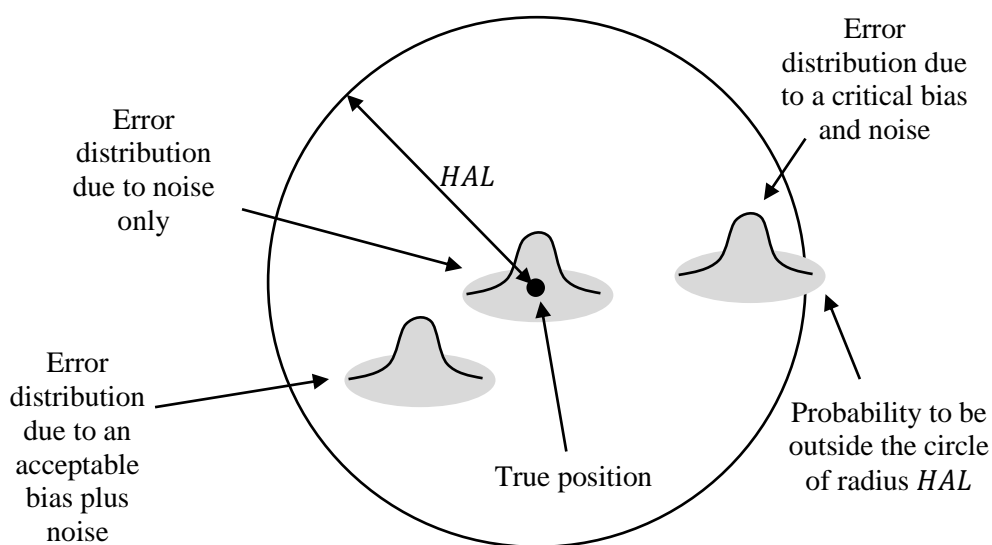


Figure 139 Principle of the critical bias concept

8.4.2 Computation of the critical bias in the single bias case

The case of a single measurement bias is first investigated. Even if the origin of the bias is not discussed, the final objective is to apply this method to NLOS and multipath biases. According to [Martineau, 2008], the critical biases values for a given user position at a given moment are obtained by computing the smallest additional range bias b_i (on satellite i) so that:

$$(1 - P_f)P_0(\|X_H - \hat{X}_H\| > HAL) + P_f P_{b_i}(\|X_H - \hat{X}_H\| > HAL) = P_{int} \quad \text{Eq. 8-32}$$

where:

- P_f is the probability of failure of one satellite
- P_0 corresponds to the fault free case
- P_{b_i} corresponds to probability of faulty case (a bias b_i on pseudorange i)

Note: P_0 and P_{b_i} are conditional probabilities.

The probability $P_{H_0}(\|X_H - \hat{X}_H\| > HAL)$ in the fault-free mode can be overbounded in real time provided that the HAL is known. Indeed, the position error follows a bi dimensional Gaussian centered distribution which covariance is estimated by the KF, and denoted $P_0(k|k)$.

$$P_{H_0}(\|X_H - \hat{X}_H\| > HAL) \leq cdf_{\mathcal{R}(\sigma_1, P_0)}(HAL) \quad \text{Eq. 8-33}$$

If this probability is higher than P_{int} , the system is not available and thus the calculation of the critical bias does not make sense. This probability can be neglected with respect to P_{int} since, in this section, the nominal error model does not include large multipath and NLOS errors (which are part of failure mode). In this case, Eq. 8-32 can be simplified and becomes:

$$P_{b_i}(\|X_H - \hat{X}_H\| > HAL) = \frac{P_{int}}{P_f} \quad \text{Eq. 8-34}$$

The approach used in [Martineau, 2008] consists in calculating the theoretical expression of the probability for the horizontal position error to be higher than the HAL , provided the value of the bias. Then it is possible to find numerically the minimum bias that leads to a position error with a given probability step by step when a LS/WLS estimation algorithm is used. This process requires an important amount of calculation because it involves integrals that can only be determined numerically. A simple way to determine a lower bound of the critical bias, which can be calculated in real time is proposed hereafter. The formula obtained can be used when a Kalman filter is used for estimating the position. The equivalent results for a position estimation with a LS/WLS algorithm are detailed in appendix J.

To determine the critical bias, it is necessary to characterize the distribution of the position error when a bias is present on one measurement. It has been proven in [Montloin, 2014] (proof given in appendix I), that for a KF, the estimation error verifies the following equation:

$$d\delta x_{k+1} = A_{k+1}d\delta x_k + K_{k+1}E_{k+1} + B_{k+1}w_{s_{k+1}} \quad \text{Eq. 8-35}$$

where:

- $d\delta x_k$ is the error on the state estimate at instant k
- $A_{k+1} = (I - K_{k+1}H_{k+1})F_k$
- $B_{k+1} = (I - K_{k+1}H_{k+1})$
- E_{k+1} is the measurement error vector
- $w_{s_{k+1}}$ is the process noise

The state estimation error at time $k + 1$ is the sum of three terms which distributions are investigated. It is assumed that, at time k the solution is fault-free, and that the filter is well implemented and tuned. In this case, the estimation error covariance is estimated by $P_{k|k}$. It is therefore assumed that:

$$d\delta x_k \sim \mathcal{N}(0, P_{k|k}) \quad \text{Eq. 8-36}$$

The measurement error vector is assumed to be a multi-dimensional Gaussian vector. The measurement errors are centered except the i^{th} measurement.

$$E_{k+1} \sim \mathcal{N}(bias, R_k) \quad \text{Eq. 8-37}$$

where $bias = [0 \quad \dots \quad b_i \quad \dots \quad 0]^T$.

The third term is the process noise, which is zero-mean normally distributed:

$$w_{s_{k+1}} \sim \mathcal{N}(0, Q_{k+1}) \quad \text{Eq. 8-38}$$

It is characterized by its covariance matrix Q_{k+1} .

The expression of the EKF error can be used to determine the critical bias. To do so, it is firstly necessary to determine the distribution of the horizontal error. The error in the horizontal plane is defined as:

$$\|d\delta x_{k+1}^H\| = \sqrt{d\delta x_{k+1,E}^2 + d\delta x_{k+1,N}^2} \quad \text{Eq. 8-39}$$

where $d\delta x_{k,E}$ and $d\delta x_{k,N}$ are respectively the east and north component of the position error.

The errors on the east and north axis are the sum of centered normally distributed terms and deterministic term due to the measurement bias. Therefore the east and north position errors are normally distributed with a non-zero mean:

$$d\delta x_{k+1}^H = b_H + n_H \quad \text{Eq. 8-40}$$

The parameters of the 2D normal distribution are given by:

$$E[d\delta x_{k+1}^H] = b_H = \begin{bmatrix} (K_{k+1})_{1,i} \\ (K_{k+1})_{2,i} \end{bmatrix} b_i \quad \text{Eq. 8-41}$$

with:

$$\text{cov}(d\delta x_{k+1}^H) = E[n_H n_H^T] = \begin{bmatrix} [\text{cov}(d\delta x_{k+1}^H)]_{1,1} & [\text{cov}(d\delta x_{k+1}^H)]_{1,2} \\ [\text{cov}(d\delta x_{k+1}^H)]_{1,2} & [\text{cov}(d\delta x_{k+1}^H)]_{2,2} \end{bmatrix} \quad \text{Eq. 8-42}$$

where the coefficients of the matrix are given by:

$$\begin{aligned} [\text{cov}(d\delta x_{k+1}^H)]_{1,1} = & \\ & \sum_{j=1}^N \sum_{l=1}^N \left\{ (K_{k+1})_{1,j} (K_{k+1})_{1,l} (R_{k+1})_{j,l} + (A_{k+1})_{1,j} (A_{k+1})_{1,l} (P_{k|k})_{j,j} \right. \\ & \left. + (B_{k+1})_{1,j} (B_{k+1})_{1,l} (Q_{k+1})_{j,l} \right\} \end{aligned} \quad \text{Eq. 8-43}$$

$$\begin{aligned}
 & [\text{cov}(d\delta x_{k+1}^H)]_{2,2} = \\
 & \sum_{j=1}^N \sum_{l=1}^N \left\{ (K_{k+1})_{2,j} (K_{k+1})_{2,l} (R_{k+1})_{j,l} + (A_{k+1})_{2,j} (A_{k+1})_{2,l} (P_{k|k})_{j,j} \right. \\
 & \quad \left. + (B_{k+1})_{2,j} (B_{k+1})_{2,l} (Q_{k+1})_{j,l} \right\}
 \end{aligned} \tag{Eq. 8-44}$$

$$\begin{aligned}
 & [\text{cov}(d\delta x_{k+1}^H)]_{1,2} = \\
 & \sum_{j=1}^N \sum_{l=1}^N \left\{ (K_{k+1})_{1,j} (K_{k+1})_{2,l} (R_{k+1})_{j,l} + (A_{k+1})_{1,j} (A_{k+1})_{2,l} (P_{k|k})_{j,j} \right. \\
 & \quad \left. + (B_{k+1})_{1,j} (B_{k+1})_{2,l} (Q_{k+1})_{j,l} \right\}
 \end{aligned} \tag{Eq. 8-45}$$

The two component of the horizontal error vector are correlated. Since $\text{cov}(d\delta x_{k+1}^H)$ is a covariance matrix, it is positive semi-definite. Therefore it is diagonalizable and its eigenvalues are positive. The matrix of the eigenvectors denoted P_{\perp} is orthogonal. Let's denote D_H the eigenvalue decomposition of $\text{cov}(d\delta x_{k+1}^H)$, it verifies:

$$P_{\perp}^T \text{cov}(d\delta x_{k+1}^H) P_{\perp} = D_H \tag{Eq. 8-46}$$

Let's multiply equation Eq. 8-40 by P_{\perp}^T . The random errors on the two components are then uncorrelated.

$$E \left[P_{\perp}^T n_H (P_{\perp}^T n_H)^T \right] = P_{\perp}^T E [n_H n_H^T] P_{\perp} = D_H \tag{Eq. 8-47}$$

Then the two components of the horizontal error are independent in this basis. Moreover, $P_{\perp}^T d\delta x_{k+1}^H$ has the same norm as $d\delta x_{k+1}^H$ because multiplying a vector by an orthogonal matrix keep the norm invariant. The bias after rotation (b'_i) is given by:

$$b'_i = P_{\perp}^T b_H = \mathcal{O}_i b_i \tag{Eq. 8-48}$$

with :

$$\mathcal{O}_i = P_{\perp}^T \begin{bmatrix} (K_{k+1})_{1,i} \\ (K_{k+1})_{2,i} \end{bmatrix} \tag{Eq. 8-49}$$

At this point, the distribution of the horizontal error in the rotated space is known: it is a 2D non central normally distributed vector which components are uncorrelated. The critical bias is the bias so that the probability for the norm of the horizontal error to exceed the *HAL*. If the two eigenvalues of $\text{cov}(d\delta x_{k+1}^H)$ were the same, the norm of the horizontal error would follows a Rice distribution (or equivalently its square would follow a non-central chi-square distribution with two degrees of freedom). It is generally not the case. However, the probability of exceeding the *HAL* for the bivariate distribution is lower than what it would be if the two normal distribution had the same variance (equal

to the maximum eigenvalue). Let's denote σ the maximum diagonal term of D_H . The following inequality can thus be written:

$$P(\|d\delta x_{k+1}^H\| \geq HAL) = P(\|P_{\perp}^T d\delta x_{k+1}^H\| \geq HAL) \leq P\left(\epsilon > \frac{HAL^2}{\sigma^2}\right) \quad \text{Eq. 8-50}$$

where ϵ follows a non-central chi square distribution with 2 degrees of freedom and with a parameter of non-centrality (λ_{b_i}) which is equal to:

$$\lambda_{b_i} = \frac{[(\mathcal{O}_{i_1})^2 + (\mathcal{O}_{i_2})^2]}{\sigma^2} b_i^2 \quad \text{Eq. 8-51}$$

The value of the non-centrality parameter λ_{b_i} is obtained from the probability of exceedance associated to the critical bias (P_{int}/P_f) and the value of the "threshold" HAL^2/σ^2 . A two degrees of freedom non central chi-square table can be used to determine it. Finally, a lower bound of the critical bias (due to the inequality in Eq. 8-50) is given by:

$$b_i = \sqrt{\frac{\sigma^2}{(\mathcal{O}_{i_1})^2 + (\mathcal{O}_{i_2})^2}} \sqrt{\lambda_{b_i}} \quad \text{Eq. 8-52}$$

The calculation of b_i can be done in real time as it only requires the calculation of the eigenvalue decomposition of a matrix and to find the non-centrality parameter in a table. The calculation of this bias requires the knowledge of the HAL , the integrity risk and the probability of occurrence of a critical bias (or higher).

8.4.3 Impact of the lifespan of the bias

The critical bias calculated is guaranteed not to make the norm of the horizontal position error exceed the HAL after the KF update. However, it is not guaranteed for the subsequent epochs. The objective is here to characterize the distribution of the position error provided that an enduring bias has been injected into the measurements. It is still assumed that $k + 1$ corresponds to the onset of the bias. Using the inductive relation Eq. 8-35, the error after n iterations can be expressed by:

$$d\delta x_{k+n} = \left(\prod_{j=1}^n A_{k+j}\right) d\delta x_k + \sum_{j=1}^n S_{j,k} [K_{k+j} E_{k+j} + B_{k+j} W_{s_{k+j}}] \quad \text{Eq. 8-53}$$

$$S_{j,k} = \begin{cases} I & \text{if } j = n \\ \left(\prod_{l=j+1}^n A_{k+l}\right) & \text{else} \end{cases} \quad \text{Eq. 8-54}$$

To simplify the problem, it is assumed that the measurement bias b_i is constant over time. As the sum of normally distributed variables and deterministic biases, the estimation error $d\delta x_{k+n}$ follows a bivariate normal distribution, which characteristics have to be determined. Firstly, its expectation is the result of the accumulation of the measurement biases:

$$E[d\delta x_{k+n}] = \sum_{j=1}^n S_{j,k} K_{k+j} b_i \quad \text{Eq. 8-55}$$

The noise on the position estimation at time k and the measurements and process noise of the subsequent epochs are assumed independent. The correlation in time of the measurements is not considered to simplify the model. Thus, the covariance of the error is driven by the measurement and process noises, as well as the initial uncertainty:

$$\begin{aligned} \text{cov}(d\delta x_{k+n}) &= \left(\prod_{j=1}^n A_{k+j} \right) P_{k|k} \left(\prod_{j=1}^n A_{k+j} \right)^T \\ &+ \sum_{j=1}^n S_{j,k} [K_{k+j} R_{k+j} K_{k+j}^T + B_{k+j} Q_{k+j} B_{k+j}^T] S_{j,k}^T \end{aligned} \quad \text{Eq. 8-56}$$

It is therefore possible to determine the critical bias with the same method as in section 8.4.2. Its value is expected to increase as n increases. Due to causality, it is not possible to determine the critical bias a priori because the matrixes which indexes exceed $k + 1$ are unknown. Therefore, the determination of the critical biases can be done a posteriori. Therefore the detection and exclusion, if it requires the critical biases as input, could only be done after the contamination. It would require to replay the scenario after the exclusion. This sequential approach is not investigated here.

However, it is expected that the biases with very short lifespans will be filtered out (smoothing effect) depending on the Kalman gain coefficients. It is typically the case for multipath or NLOS biases when the vehicle is driving with a velocity that is high compared to the lifespan of the bias. On the other hand, a persistent bias such as those generated by satellite failures is expected to make the filter converge to a biased position.

Let us determine the asymptotical critical bias that would have an infinite lifespan. If it is assumed that the constellation is frozen, the matrixes are assumed to stay constant over time (the indexes are removed).

The bias component is the sum of the terms of a geometric serie of matrices. The eigenvalues of A have a magnitude which is lower than 1, therefore the limit converges to:

$$E[d\delta x_{k+\infty}] = \lim_{n \rightarrow +\infty} \sum_{j=1}^n S_j K b_i = (I - A)^{-1} K b_i \quad \text{Eq. 8-57}$$

If it is assumed that the vehicle is not moving, the components of F that corresponds to the position error are equal to I . Thus, the bias component is equal to $(KH)^{-1}K$.

An analogy can be done with the bias component obtained when a WLS (appendix J) estimation method is used, where K substitute $H^T R^{-1}$. Simulations and tests on real data have shown that the following equality is valid:

$$(KH)^{-1}K = (H^T R^{-1} H)^+ H^T R^{-1} \quad \text{Eq. 8-58}$$

where $()^+$ denotes the Moore-Penrose pseudo inverse.

This result shows that, asymptotically (in the sense of infinite lifespan), a deterministic bias on a pseudorange has the exact same impact on the position as estimated by a KF and by a WLS. Essentially, the benefit of using the KF is that the covariance of the position error is reduced with a KF and therefore the critical bias is lower.

Then it is proposed to simplify $\text{cov}(d\delta x_{k+n})$. As the eigenvalues of A have a magnitude which is lower than 1:

$$\lim_{n \rightarrow +\infty} (A^n) P_{k|k} (A^n)^T = 0 \quad \text{Eq. 8-59}$$

The last term is so that:

$$\text{cov}(d\delta x_{k+\infty}) = \sum_{j=1}^{+\infty} S_j [K R K^T + B Q B^T] S_j^T \quad \text{Eq. 8-60}$$

Simulations have shown that the eigenvalues of the $\text{cov}(d\delta x_{k+n}^H)$ matrix has a fast convergence toward $\text{cov}(d\delta x_{k+\infty})$.

Note: the steady state covariance can also be obtained by solving the Lyapunov equation of the system.

It is therefore possible to determine the critical bias with the same method as in section 8.4.2. As an illustration, the variation of the value of the critical bias as a function of its lifespan has been studied on a real example. The HAL has been arbitrarily set to 50 m, and a fixed value of P_{int}/P_f of 10^{-5} was selected. The results are plotted in Figure 140 and Figure 141 (zoomed).

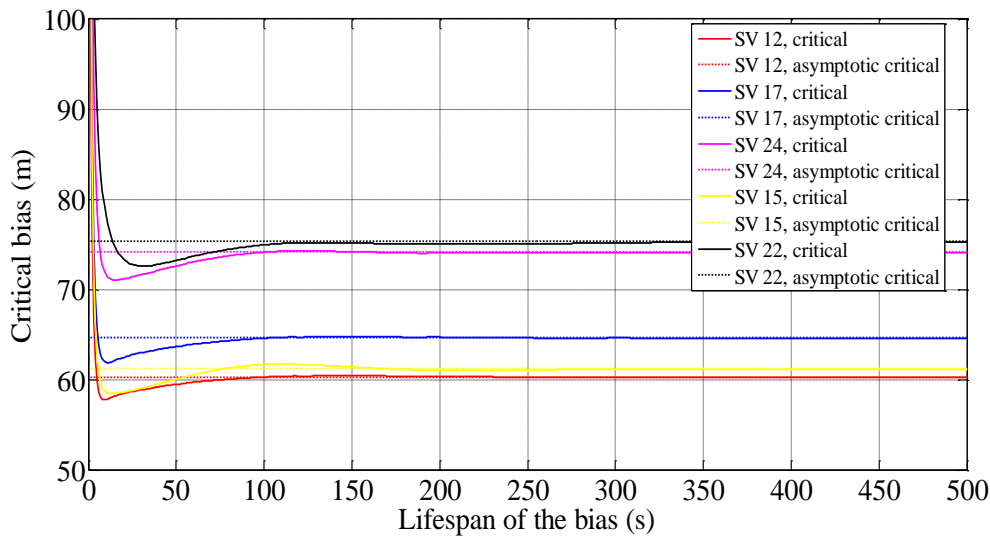


Figure 140 Convergence of critical bias assuming a frozen constellation/vehicle scenario.

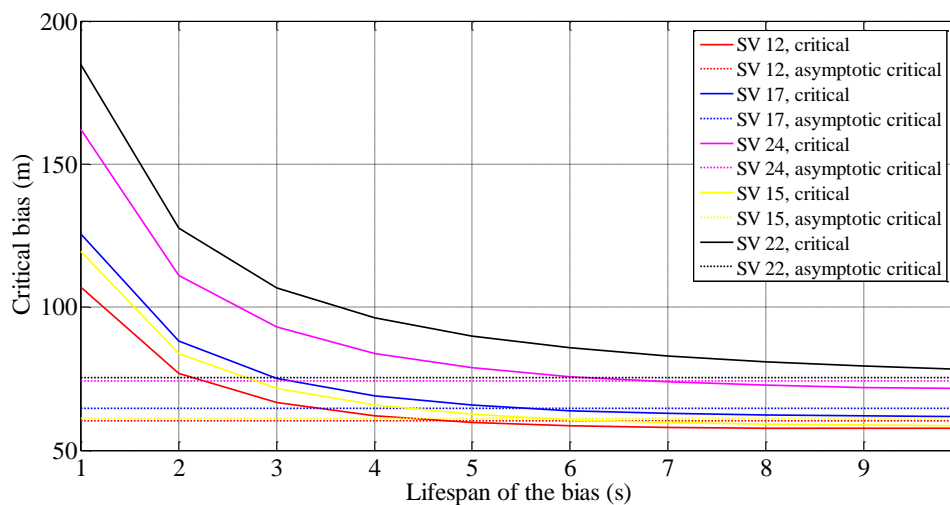


Figure 141 Convergence of critical bias assuming a frozen constellation/vehicle scenario (Zoomed).

Figure 140 shows that the critical bias actually converges toward the asymptotic critical bias (associated to the expressions Eq. 8-57 and Eq. 8-60). Figure 141 illustrates the fact that the filter is robust to biases which have a very short lifespan. It is characterized by an important decrease of the value of the critical bias in function of its lifespan. This is the illustration of the ability of the KF to filter out the measurement noise. Indeed a bias with a very short lifespans is equivalent to uncorrelated noise in this case.

8.4.3.1.1 Multiple biases

In urban environment, the probability of processing multiple simultaneously biased measurements may be too large with respect to the integrity risk to be neglected. Similar to what have been done for the determination of the critical bias in the case of a single bias, (multiple) critical biases have to be investigated. The multiple biases case is essentially a consequence of the biases generated by the environment close to the receiver. In this configuration, the measurement error vector bias component shall be rewritten:

$$Bias = [b_1 \quad \dots \quad b_n]^T \tag{Eq. 8-61}$$

It only impacts the expectation of the horizontal error. The decorrelation of the horizontal error components on the two axes requires a diagonalization step. The expectation in the rotated plane is obtained by applying the transfer matrix to the bias component. It gives the following result:

$$E[d\delta x_{k+1}^H] = P_{\perp}^T \begin{bmatrix} \sum_{i=1}^n (K_{k+1})_{1,i} b_i \\ \sum_{i=1}^n (K_{k+1})_{2,i} b_i \end{bmatrix} \quad \text{Eq. 8-62}$$

The expectation of the horizontal position error is logically a function of the biases that affect each pseudorange. The critical b_i would therefore form a surface in dimension n . To simplify the calculations, we proposed to calculate a unique critical bias b_0 . The deterministic component of the measurement error is thus written:

$$\text{Bias} = \delta_b b_0 \quad \text{Eq. 8-63}$$

where δ_b is an array which components are zero, one or minus one. For biases due to the tracking of a NLOS, the measurement biases can only be positive (thus δ_b only contains zeros or ones). This term has been introduced because the largest horizontal error does not generally correspond to situations where the measurements are all biased. Anyway, b_0 has to verify:

$$b_0^2 \leq \frac{\sigma^2 \lambda_{multi}}{\left\{ \sum_{i=1}^n [(P_{\perp}^T)_{1,1} (K_{k+1})_{1,i} + (P_{\perp}^T)_{1,2} (K_{k+1})_{2,i}] (\delta_b)_i \right\}^2 + \left\{ \sum_{i=1}^n [(P_{\perp}^T)_{2,1} (K_{k+1})_{1,i} + (P_{\perp}^T)_{2,2} (K_{k+1})_{2,i}] (\delta_b)_i \right\}^2} \quad \text{Eq. 8-64}$$

where:

- σ^2 corresponds to the maximum eigenvalue of $\text{cov}(d\delta x_{k+1}^H)$
- λ_{multi} is the non-centrality parameter associated to the *HAL* and the probability of multiple failures

Let's denote J this denominator,

$$J = \left\{ \sum_{i=1}^n [(P_{\perp}^T)_{1,1} (K_{k+1})_{1,i} + (P_{\perp}^T)_{1,2} (K_{k+1})_{2,i}] (\delta_b)_i \right\}^2 + \left\{ \sum_{i=1}^n [(P_{\perp}^T)_{2,1} (K_{k+1})_{1,i} + (P_{\perp}^T)_{2,2} (K_{k+1})_{2,i}] (\delta_b)_i \right\}^2 \quad \text{Eq. 8-65}$$

The minimum upper bound of the critical bias is obtained for the vector δ_b that maximizes the denominator of Eq. 8-65:

$$b_{critical,multi} = \sqrt{\frac{\sigma^2 \lambda_{multi}}{\max_{\delta_b} J}} \quad \text{Eq. 8-66}$$

8.5 Use of critical biases for monitoring the measurements

Eq. 8-34 which is used as a starting point to derive the calculation of the critical bias can be equivalently rewritten (in the single bias case for simplicity):

$$P(\|X_H - \hat{X}_H\| > HAL | |b| \leq |b_i|) = \frac{P_{int}}{P(|b| \leq |b_i|)} \quad \text{Eq. 8-67}$$

where b represent a bias on pseudorange i .

This equation involves the cumulative distribution function of the bias $P(|b| \leq |b_i|)$. Fortunately, the distribution of the measurement errors due to local effects has been established in chapter 5. In particular the CDF of the NLOS error has been characterized by simple modelling and on real data. These results can be used to determine the critical biases on each measurement. The methodology to do so is the following:

- The first step consists in plotting the value of the critical bias as a function of the ratio P_{int}/P_f where P_f is a parameter that varies from 0 to 1.
- The second step consists in plotting the inverse CDF of the distribution of the bias magnitude (in P_f) as a function of P_{int}/P_f .
- As long as the curve that represents the critical bias is higher than the distribution of the bias, it means that the bias is not a threat for the application. It means that the probability for the bias to exceed the critical bias is lower than the integrity risk. This case is represented in Figure 142.
- If the critical bias is lower than the distribution of the bias, it means that the source of bias is a threat for the integrity of the solution. It means that the probability for the bias to exceed the critical bias is higher than the integrity risk. The system must be protected against this bias.
- The final critical bias that shall be considered is the intersection between the two curves (the minimum bias that must be detected). The intersection gives the probability of occurrence of a failure as well as the magnitude of the associated bias. This configuration is illustrated in Figure 143. The algorithm that aims at detecting such abnormal measurement must takes as inputs the magnitude of the bias and the probability of missed detection as P_{int}/P_f . The most convenient approach is therefore not to set the P_{FA} , but to deduce it.

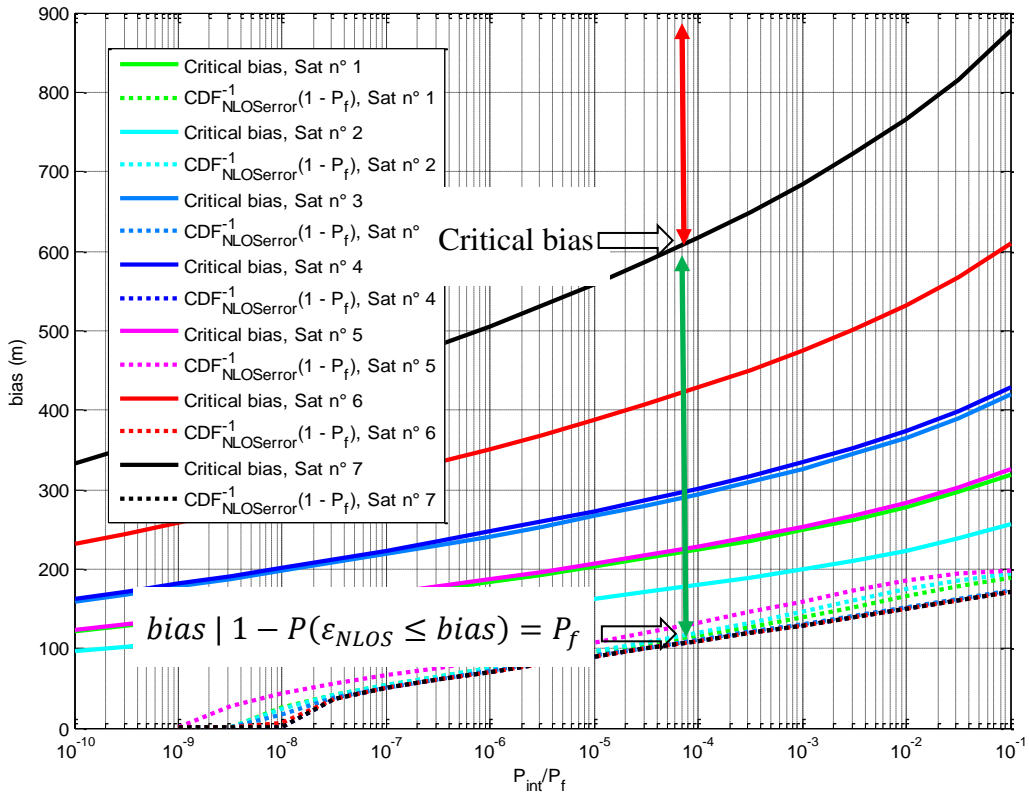


Figure 142 Calculation of the critical bias. In this example, the source of the bias is not a threat for the integrity of the solution because: $P(\epsilon_{NLOS} > bias) = P_f$ is lower than the critical bias

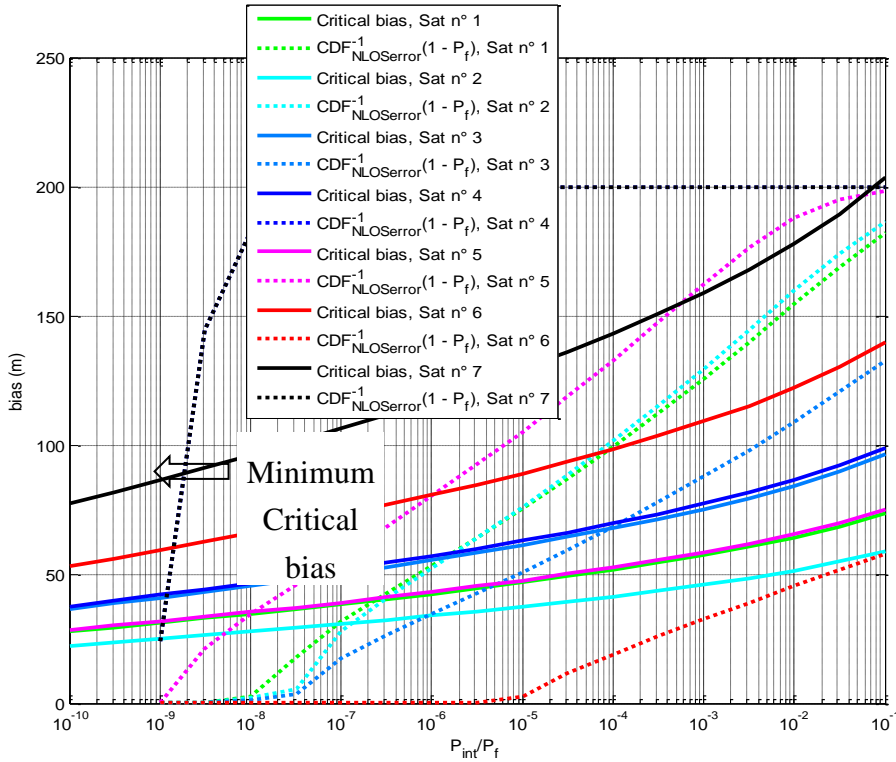


Figure 143 Calculation of the critical bias

The principle of this cascaded testing approach is summarized in Figure 144. In this case, if a measurement is excluded from the solution by the SQM or the innovation monitoring algorithm, it is necessary to update the values of the critical biases because the geometry has changed. The measurements selection process must then be reconducted with the new thresholds.

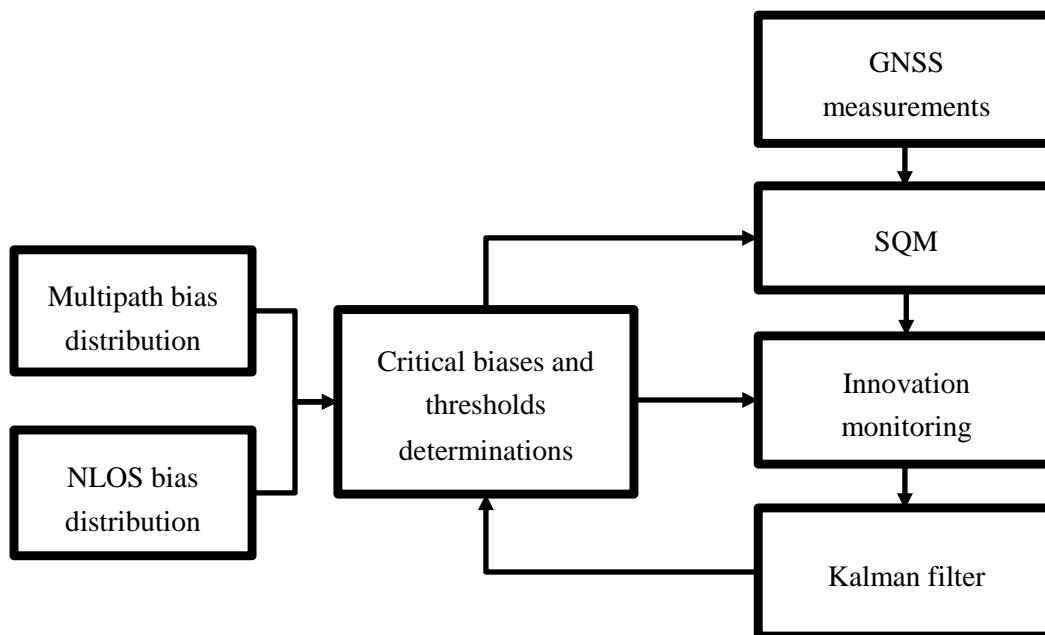


Figure 144 Principle of cascaded testing approach with real time threshold monitoring

8.5.1.1.1 Particularities of NLOS and multipath

Unlike satellite failures, measurement biases that are due to local effects are correlated in space. It will be assumed that such a bias is due to the tracking of an echo (NLOS) or an echo contaminated signal (LOS + NLOS). The distribution of the lifespan of a reflection in urban environment has been assessed in [Lehner and Steingass, 2005] and is given in Figure 145 for car applications.

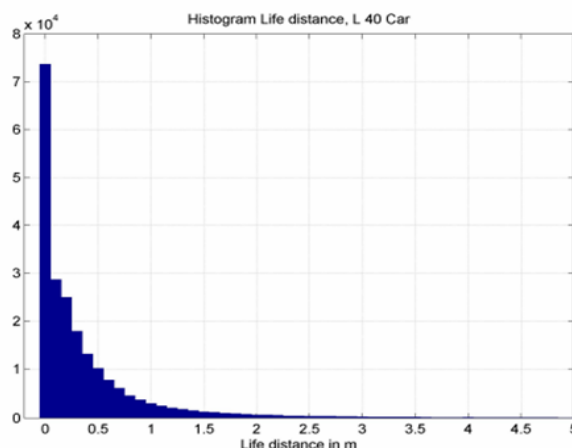


Figure 145 Distribution of the lifespan of an echo in urban environment for a car [Lehner and Steingass, 2005]

It can be seen that most reflectors exist along a motion path that is below 5 m for a urban car channel. It will be assumed that this distribution is also valid for a train channel in urban environment. Thus, the lifespan of a reflector directly depends of the velocity of the vehicle [Steingass et al., 2009], and the sampling period of the GNSS receiver. The lifespan of an echo in terms of update in the KF is given by:

$$n_{max} = \max\left(\left\lfloor \frac{l_0}{T_{s,GNSS}v} \right\rfloor, 1\right) \quad \text{Eq. 8-68}$$

where:

- l_0 is the lifespan of the echo, which is 5 m at maximum.
- $T_{s,GNSS}$ is the sampling period of the GNSS receiver. Typically, 1 Hz
- v is the horizontal velocity of the vehicle

It can be inferred from this result that a bias due to local effects will be integrated a higher amount of time if the sampling period of the receiver is high. It has been seen that biases with large lifespan are more likely to lead to positioning failures. Therefore it may seem that updating the KF with a low rate would lead to a more robust system with respect to local effects. In fact the problem is more complex because the critical bias also depends of the Kalman gain which in turns depends of the predicted estimate covariance. Between two GNSS updates, this covariance increases due to the process noises. The longer is the update period, the higher is the state error covariance. Thus the Kalman gain is lower for high update rate, and therefore the critical bias may not be lower for higher rate GNSS receivers.

The lifespan of an echo is given in Figure 146 and Figure 147. The GNSS receiver that is used in this thesis is assumed to have a 1 Hz sampling rate. It will be assumed that the lifespan of the bias is equal to the lifespan of the echo. This can be assumed because the convergence time of the DLL is approximately $1/B_l$ where B_l is the DLL loop bandwidth (typically 1 Hz), provided that the echo delay is within the discriminator linear area. In this case, except for very low velocities (lower than 10 km/h), the biased measurements are only integrated in the filter once. It is assumed that the biased on the measurement return to a value of zero once its lifespan has been exceeded. This model can be improved by involving Markov chain to account for the fact that after an echo is tracked, another echo can be tracked instead of the direct signal for NLOS.

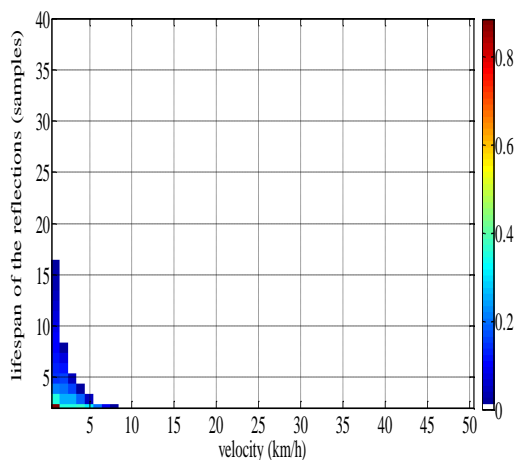


Figure 146 Distribution of the lifespan of an echo in urban environment in terms of KF updates for a 1 Hz GNSS receiver

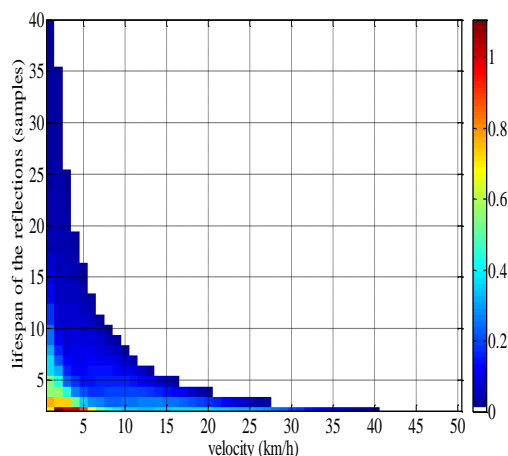


Figure 147 Distribution of the lifespan of an echo in urban environment in terms of KF updates for a 5 Hz GNSS receiver

8.6 Monitoring integrity of the IMU measurements

The integrity risk allowed by the requirements has been allocated to GNSS for both applications. Therefore, the probability of failure of the IMU must be negligible with respect to the integrity risk. It shall be at least one order of magnitude lower. From the Landmark 01 IMU *MTBF* specification, it has been stated in chapter 5 that the probability of failure of the IMU is $8 \cdot 10^{-6}$ per hour. This value is taken as a reference even if the failure events considered in the *MTBF* are not clearly defined by the manufacturer. In particular, it remains unclear whether this value is the sum of the probability of any failure or whether it corresponds to the probability for the IMU not to be able to provide any measurement. Anyway, the probability of failure of the IMU is too large to be neglected, especially for the train control application (where the integrity risk is $10^{-4.5}$ to $10^{-5.5}$ /h). The IMU is subject to hardware failures that can result in the absence of outputs, null outputs, or errors that are not covered by the nominal error model. It is stated in [Groves, 2013], that “*achieving FDR, FDI, or FDE with inertial navigation requires redundant hardware*”. The principle is to take advantage of the redundancy between the measurements to detect inconsistencies among them. Methods for FDI applied to redundant inertial measurement unit (RIMU), has been investigated in [Shim and Yang, 2004], [Sturza, 1988], [Wilcox, 1972] [Skoogh and Lennartsson, 2006]. In a hybridized system, it is possible to detect and isolate faulty inertial sensors at different level.

- The first approach is to use redundancy at system level. In this case, the GNSS is coupled with different INS individually. The fault detection is applied on the hybridized navigation solutions.
- The second approach is to use redundancy at sensor level. In this case Fault detection can be processed either before or after the mechanization. As we are in a closed-loop scheme it will be done before corrections and thus before mechanization.

Integrity monitoring of an IMU can be done either by comparing the outputs of two or more conventional IMUs or by using redundant IMU which incorporate pairs of sensors. Even if using redundant IMUs that incorporate pairs of sensors is said to be more effective [Sturza, 1988], this approach is not preferred here because such devices are not mass market. FD based on RIMU requires at least 2 IMU, and FDI/FDE/FDR requires at least 3 IMU. Only the FD process is detailed in this section. Thus, in train control, 4 IMUs are necessary for FD and 6 for FDI. If the possibility to work with several IMU is feasible for train control because medium grade sensors have been selected, it may not be suitable for ETC for which the price of the OBU is a main constraint (alternative approaches have not been investigated in this thesis). It is assumed here that the probability of failure of two sensors at the same time is negligible. It has been stated in prior art that the cone-shape redundant IMU is the optimal configuration for FDI. However, it is assumed in the method detailed hereafter that the IMUs are mounted on the same support, sufficiently close to each other and in the same orientation. It is also assumed that the missed alignment between the sensors has been calibrated a priori. The differences between the outputs of the sensors from the two IMUs are formed:

$$x_{out,i} - x_{out,j} = \delta b_{x,i} - \delta b_{x,j} + n_{x,i} - n_{x,j} \quad \text{Eq. 8-69}$$

Sensor failures can be detected by directly monitoring $x_{out,i} - x_{out,j}$. However, in this case, the sensitivity of the test may not be sufficient due to the uncalibrated biases component. To improve the sensitivity of the test, it is proposed to estimate the differential bias term component. If similar sensors are used, it is assumed that they have approximately the same correlation time (τ). Thus, the process model that characterize the differential bias term can be written:

$$\delta \dot{b}_{x,i} - \delta \dot{b}_{x,j} = -\frac{1}{\tau} (\delta b_{x,i} - \delta b_{x,j}) + \eta_{x,i} - \eta_{x,j} \quad \text{Eq. 8-70}$$

Kalman filtering can be used to estimate $\delta b_{x,i} - \delta b_{x,j}$ and to improve the sensitivity of the fault detection algorithm. Then, a fault detection algorithm based on squared residuals is proposed here. Any fault in system dynamics can be detected by a change in the weighted sum of squared residual ($WSSR_k$) measurement. This test statistic is the squared representation of the test presented in chapter 7:

$$WSSR_k = \sum_{i=k-N+1}^k r_i^T V_i^{-1} r_i \quad \text{Eq. 8-71}$$

The window length N has to be adjusted in accordance with the requirement for detection time and the false alarm. The two hypotheses to test are the following:

$$\begin{cases} H_0 & \text{no failure} & WSSR_k < \lambda \\ H_1 & \text{failure detected} & WSSR_k \geq \lambda \end{cases}$$

The test variables are formed for each of the six measurements (3 accelerometers and 3 gyroscopes). In the nominal case, for any sensor, the $WSSR_k$ is chi-squared distributed with N degrees of freedom. The detection threshold λ is set to fulfill the required P_{FA} . The P_{FA} per hour allocated to the full IMU shall be converted into a P_{FA} per sample. It is assumed that each samples are independent:

$$P_{FA}(/sample) = P_{FA}(/h) \frac{T_s}{6 * 3600} \quad \text{Eq. 8-72}$$

where $T_{s_{IMU}}$ is the sampling period of the IMU.

As no continuity risk analysis has been conducted, the P_{FA} allowed for the IMU is unknown for the two applications. To perform a $P_{FA}(/h)$ of $10^{-5}/h$ for the whole 6 axis IMU, it is necessary to set P_{FA} to $4.63 \cdot 10^{-12}$ if the IMU is sampled at 100 Hz.

8.6.1 Behavior of the test with respect to the different failure sources

In this section, the behavior of the test in case of faulty sensor is investigated. The ability of the test to detect a faulty sensor is looked at, and its sensitivity is assessed. Four fault signatures are investigated: the failure to zero, the step failure, the ramp failure and the additional noise failure.

8.6.1.1 Failure to zero

In case of failure to zero, it is assumed that one of the two redundant sensors does not sense the motion. In this case the observation becomes:

$$x_{out,i} - x_{out,j} = x_{true,i} + \delta b_{x,i} - \delta b_{x,j} + n_{x,i} - n_{x,j} \quad \text{Eq. 8-73}$$

This fault mode can be identified by the fault detection algorithm if the measurement $x_{true,i}$ is varying. The innovation is thus biased:

$$r_{k,f2z} \sim \mathcal{N}(x_{true,k}, V_k) \quad \text{Eq. 8-74}$$

If the axis of the sensor is motionless, $x_{true} = 0$ and therefore this fault cannot be detected. However, the missed detection has no impact because nothing has to be measured.

$WSSR_k$ follows a non-central χ^2 random variable, with N degrees of freedom, and a non-centrality parameter $\lambda_{k,f2z}$ which is equal to:

$$\lambda_{k,f2z} = \sum_{i=k-N+1}^k \frac{x_{true,i}^2}{V_i} \quad \text{Eq. 8-75}$$

As an illustration, if it is assumed that the $x_{true,i}$ and V_i are close to a constant over the sliding window,

$$\lambda_{k,f2z} = \frac{N}{V} x_{true}^2 \quad \text{Eq. 8-76}$$

The probability of miss detection of the failure to zero is given by:

$$P_{MD} = \int_0^\lambda f_{\chi^2(\lambda_{k,f2z_{min}}, N)}(u) du \quad \text{Eq. 8-77}$$

N is known (e.g. 40) and the detection threshold λ is set to respect the P_{FA} (depends also of N), V is also known in real time. Thus it is possible to determine the minimum $\lambda_{k,f2z_{min}}$ that ensure the required P_{MD} .

$$x_{det,f2z} = \sqrt{\lambda_{k,f2z_{min}} \frac{V}{N}} \tag{Eq. 8-78}$$

Simulations have been conducted to determine the typical sensitivity of this test. For a MEMS gyroscope that is contained in the Landmark 01 IMU, the P_{FA} of the test has been set to $4.63 \cdot 10^{-12}$ /samples, with $N = 40$ and $V = 5.013 \cdot 10^{-7}$.

P_{MD}	$x_{det,f2z}$ (°/s)
10^{-9}	0.115
10^{-6}	0.107
10^{-3}	0.096

Table 56 Sensitivity of the test with respect to failures to zero for a MEMS gyroscope (Landmark 01)

8.6.1.2 Step Failure

If a step failure occurs, it is assumed that one of the two redundant sensors is affected by a sudden additional bias. The derivation of the sensitivity and its value is the same as for the failure to zero. The Kalman filter as well as the fault detection monitor have been implemented and tested by simulation. The case of two gyroscopes of the Landmark 01 is investigated. A bias of $0.1^\circ/s$ has been added to one of the gyroscope measurement (at the 3000 sample). The test and the corresponding threshold are plotted in Figure 148. The failure detected after 15 filter updates (0.15 seconds).

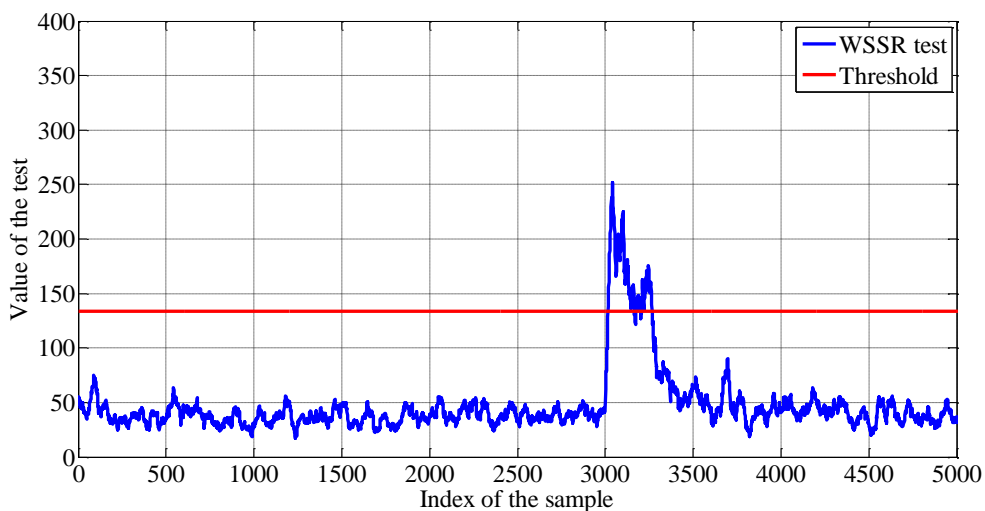


Figure 148 Detection of step failure by the WSSR monitoring algorithm (onset at the 3000 sample index)

8.6.1.3 Additional Noise

If an additional noise type failure occurs, one of the two redundant sensors is affected by an additive non nominal noise term denoted n_{an} . This noise term is assumed centered, Gaussian and with a standard deviation denoted σ_{an} (and uncorrelated with the measurement error). The distribution of the test variable becomes:

$$r_{k,an} \sim \mathcal{N}(0, V_k + \sigma_{an}^2) \quad \text{Eq. 8-79}$$

However, this is not a chi squared distribution because normalized by V (instead of $\sigma_{an}^2 + V$). If we assume that the additional noise is of constant variance and that V_k is approximately constant over the sliding window:

$$WSSR_{k,an} = \frac{V + \sigma_{an}^2}{V} \sum_{i=k-N+1}^k \frac{r_{k,an}^2}{V + \sigma_{an}^2} \quad \text{Eq. 8-80}$$

where:

$$\sum_{i=k-N+1}^k \frac{r_{k,an}^2}{V + \sigma_{an}^2} \sim \chi^2(N) \quad \text{Eq. 8-81}$$

Thus, the probability not to detect the fault is given by:

$$P\left(\sum_{i=k-N+1}^k \frac{r_{k,an}^2}{V + \sigma_{det,an}^2} \leq \frac{V}{V + \sigma_{an}^2} \lambda\right) = P_{MD} \quad \text{Eq. 8-82}$$

The sensitivity is given by:

$$\sigma_{det,an}^2 = V \left[\frac{\lambda}{cdf_{\chi^2(N)}^{-1}(P_{MD})} - 1 \right] \quad \text{Eq. 8-83}$$

The typical sensitivity of this test has been calculated for a MEMS gyroscope that is contained in the Landmark 01 IMU. The parameters are the same as those used in section 8.6.1.1. The results are given in Table 57.

P_{MD}	$\sigma_{det,an}$ (°/s)
10^{-9}	0.2
10^{-6}	0.16
10^{-3}	0.11

Table 57 Sensitivity of the test with respect to the additional noise fault for a MEMS gyroscope (Landmark 01)

An additional noise with a standard deviation of $0.2^\circ/\text{s}$ has been added to one of the gyroscope measurement (at the 3000 sample). The test and the corresponding threshold are plotted in Figure 149. The failure detected after 5 filter update (0.05 seconds).

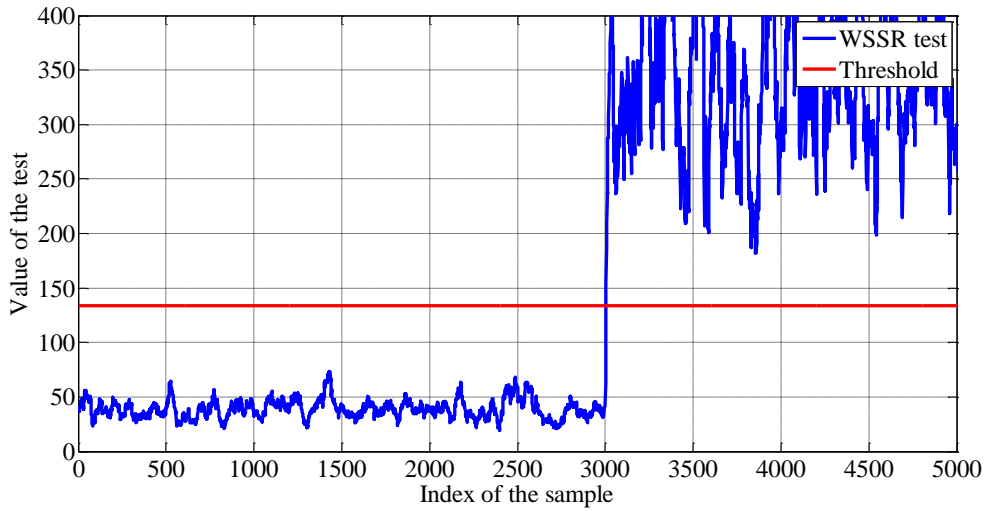


Figure 149 Detection of additional noise failure by the WSSR monitoring algorithm (onset at the 3000 sample index)

8.6.1.4 Ramp Failures

A sensor affected by a ramp failure has its measurement biased. The bias is slowly growing, and its expression in continuous time can be written:

$$\begin{aligned} ramp(t) &= 0 \text{ if } t < t_0 \\ ramp(t) &= slope(t - t_0) \text{ if } t \geq t_0 \end{aligned} \quad \text{Eq. 8-84}$$

where t_0 is the onset of the failure.

If it is assumed that the ramp appears at the beginning of the sliding window, we have $t_0 = k - W + 1$. The *WSSR* is affected by a bias which varies with time. When summed over the sliding window, this bias becomes:

$$E[WSSR_k] = \sum_{i=k-N+1}^k \frac{[slope(iT_s - t_0)]^2}{V(k)} \quad \text{Eq. 8-85}$$

If it is assumed that the innovation covariance is constant over the window

$$E[WSSR_k] \approx \frac{slope^2 T_{sIMU}^2}{V} \sum_{i=k-N+1}^k i^2 = \frac{slope^2 T_{sIMU}^2 (N-1)N(2N-1)}{6V} \quad \text{Eq. 8-86}$$

Let us denote λ_{ramp} the non centrality parameter associated with P_{MD} (for a given P_{FA}). The expression of the minimum detectable slope is given by:

$$slope_{det} = \sqrt{\frac{6V\lambda}{T_{sIMU}^2 (N-1)N(2N-1)}} \quad \text{Eq. 8-87}$$

The typical sensitivity of this test with respect to the ramp failures has been calculated for a MEMS gyroscope that is contained in the Landmark 01 IMU. The parameters are the same as those used in section 8.6.1.1. The results are given in Table 58. In particular it can be seen that only ramps with large slope can be detected fast. Moreover, very slowly errors may not be detectable because estimated in the bias. The ramp may not be distinguished from the bias. A solution may be to include a monitor on the difference of the measurement directly (without estimating the bias difference).

P_{MD}	$slope_{det}$ ($^{\circ}/s$)
10^{-9}	0.5
10^{-6}	0.46
10^{-3}	0.42

Table 58 Sensitivity of the test associated with a P_{MD} and P_{FA}

A ramp with a slope of $0.05^{\circ}/s$ has been added to one of the gyroscope measurement (at the 3000 sample). The test and the corresponding threshold are plotted in Figure 150. The failure detected after 200 filter update (2 seconds).

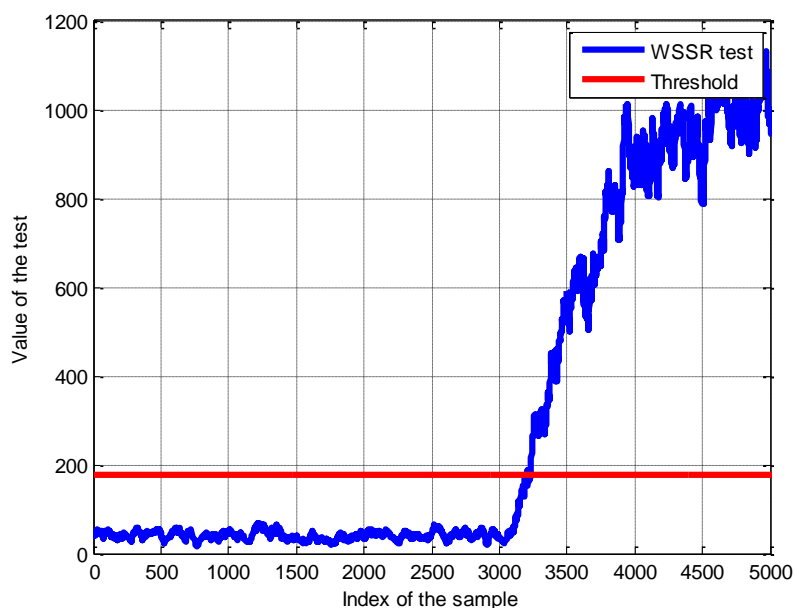


Figure 150 Detection of a ramp failure by the WSSR monitoring algorithm (onset at the 3000 sample index)

8.7 Conclusion

This chapter aims at augmenting the solutions that have been developed for each application so that they are able to fulfil the corresponding integrity requirements. Firstly, the integrity risk available for the whole system has been allocated between the different sensors integrated in the solution. The

integrity risk allocated to GNSS has been divided into the fault free mode and the satellite fault. It is thus necessary either to integrate the multipath and NLOS error in the nominal error model by inflating it or to exclude the measurements that are affected by such bias. A solution separation integrity monitoring algorithm has been designed in order to monitor the integrity of the solution. An alternative algorithm relying on separated mechanization has been developed to ensure integrity even in case of ramp failures in a closed loop scheme. However, this algorithm showed poor availability performances due to the use of a too conservative covariance of the separation vector. A way to refine the covariance of the separation shall be find so that this algorithm is suitable. The performances of the two algorithms have been studied for train control. The two approaches proposed to take into account the errors due to the local effects have been compared. The approach based on the selection of the measurements, made possible by the use of additional sensor with tight coupling or information and constellations (for ETC), outperforms the method based on the inflation of the error model. Moreover, better performances can be expected by substituting GLONASS by Galileo in the tested solutions because of the lower URA, the BOC modulations that is less sensitive to multipath than BPSK(0.5), and the probability of satellite failure which is expected to be lower. Better performances can be expected in suburban and open sky condition by processing dual frequency.

- For train control, the results have shown that it is feasible to expect an availability higher than 99% in suburban environment associated to an alert limit of 50 meters. In dense urban environment, with measurement selection, it has been possible to reach an availability of 99% for an alert limit of 125 meters. It is important to underline the fact that this environment corresponds to narrow urban canyons which are unlikely to be met by a train. The solution proposed for train control could be improved by integrating four constellations instead of two, and combining two dual constellation based sub solutions.
- For ETC, the results have shown that it is possible to perform availabilities higher than 99.5% in suburban environment for an alert limit of 25 m thanks to the use of two constellations simultaneously. In urban environment, an availability of 100% is obtained for an alert limit of 100 m.

The performances presented in the section have a limited scope and cannot be generalized because the dataset processed is not of sufficiently long.

The monitoring of the Kalman innovation and the multipath monitor algorithms are designed to detect the measurements which are biased. A method to calculate the biases that are dangerous for the solution and to adjust the thresholds of these algorithms in real time has been studied. It has been showed that the sensitivity of the KF with a bias is highly correlated with its lifespan.

Finally, a method to monitor the integrity of the IMU measurements has been studied. Its sensitivity with respect to different fault signature has been investigated by simulations.

8.8 References

- [Brenner, 1995] M. A. Brenner, "Integrated GPS/Inertial Fault Detection Availability," Proceedings of ION-GPS-95, 8th International Technical Meeting of the Satellite Division of the Institute of Navigation, Palm Springs, CA, 1995.
- [Cosmen-Schortmann et al., 2008] J. Cosmen-Schortmann, M. Azaola-Senz, M. A. Martinez-Olague and M. Toledo-Lopez, "Integrity in urban and road environments and its use in liability critical applications", Proc. IEEE Plans Conf., pp.972-983, 2008
- [Escher et al., 2002] Anne-Christine Escher, Christophe Macabiau, Benoit Roturier, Nicolas Martin. GPS/IRS hybridization : definition of exclusion radius using solution separation method. IFIS 2002, 12th International Flight Inspection Symposium, 2002, Roma, Italy. 2002
- [Escher, 2003] A. C. Escher, "Study of the contribution of gnss/ins hybridization to gnss integrity monitoring for civil aviation applications", Thesis of Toulouse University, 2003
- [ERTMS factsheet 7] http://www.ertms.net/wp-content/uploads/2014/09/ERTMS_Factsheet_7_ERTMS_deployment_outside_Europe.pdf
- [Groves, 2013] Groves, P.D. Principles of GNSS, Inertial, and Multisensor Integrated Navigation Systems; Artech House: London, UK, 2013
- [Hoover, 1984] Hoover, W. E., & Rockville, M. D. (1984). Algorithms for confidence circles and ellipses. US Department of Commerce, National Oceanic and Atmospheric Administration, National Ocean Service
- [Lee and O'Laughlin, 2000] Dr. Young C. Lee and Daniel G. O'Laughlin, "A Performance Analysis of a Tightly Coupled GPS/Inertial System for Two Integrity Monitor Methods" Proceedings of ION-GPS-2000, 13th International Technical Meeting of the Satellite Division of the Institute of Navigation
- [Lee et al., 2005] Lee, Young C., Braff, Ronald, Fernow, J. P., Hashemi, Deihim, McLaughlin, Michael P., O'Laughlin, Daniel, "GPS and Galileo with RAIM or WAAS for Vertically Guided Approaches," Proceedings of the 18th International Technical Meeting of the Satellite Division of The Institute of Navigation (ION GNSS 2005), Long Beach, CA, September 2005, pp. 1801-1825
- [Lehner and Steingass, 2005] Lehner, Andreas, Steingass, Alexander, "A Novel Channel Model for Land Mobile Satellite Navigation," Proceedings of the 18th International Technical Meeting of the Satellite Division of The Institute of Navigation (ION GNSS 2005), Long Beach, CA, September 2005, pp. 2132-2138
- [Martineau, 2008] A. Martineau, "Performance of Receiver Autonomous Integrity Monitoring (RAIM) for Vertically Guided Approaches", PhD thesis

- Institut National Polytechnique de Toulouse, 2008
- [Montloin, 2014] L. Montloin, “Impact of GNSS singular events on the integrity of airport navigation systems”, PhD thesis Institut National Polytechnique de Toulouse, 2008
- [Navipedia, ARAIM] <http://www.navipedia.net/index.php/ARAIM>
- [Nikiforov, 2005] Nikiforov I., “Autonomous Integrity monitoring of the GNSS”, Convention STNA – Astrée Final report, October 2005
- [Salos, 2012] Salos Andrés, Carlos Daniel (2012) Integrity monitoring applied to the reception of GNSS signals in urban environments
- [Shim and Yang, 2004] D.-S. Shim and C.-K. Yang. Geometric FDI based on SVD for redundant inertial sensor systems. 2004 5th Asian Control Conference, 2:1094 – 1100, 2004.
- [Skoogh and Lennartsson, 2006] D. Skoogh and A. Lennartsson, “A method for multiple fault detection and isolation of redundant inertial navigation sensor configurations,” in Proc. IEEE/ION 2006 Position, Location, And Navigation Symp., 2006, pp. 415–425.].
- [Steingass et al., 2009] Steingass, A., A. Lehner, and F. Schubert (2009) "A Location and Movement Dependent GNSS Multipath Error Model for Pedestrian Applications," in Proceedings of the IONGNSS, , Savannah,GA, pp. 2284-2296
- [Sturza, 1988] M. A. Sturza. Navigation system integrity monitoring using redundant measurement. Journal of the Institute of Navigation, 35(4), Winter 1988- 1989
- [Walter et al., 2014] Walter, T., Blanch, J., Enge, P., "Reduced Subset Analysis for Multi-Constellation ARAIM," Proceedings of the 2014 International Technical Meeting of The Institute of Navigation, San Diego, California, January 2014, pp. 89-98
- [Wilcox, 1972] J. C. Wilcox. Maximum likelihood failure detection for redundant inertial instruments. In AIAA Guidance and Control Conference, Stanford, California, August 13-16 1972
- [Young and McGraw, 2003] Young, Ryan S. Y., McGraw, Gary A., "Fault Detection and Exclusion Using Normalized Solution Separation and Residual Monitoring Methods", NAVIGATION, Journal of The Institute of Navigation, Vol. 50, No. 3, Fall 2003, pp. 151-170.

9 CONCLUSION AND RECOMMENDATIONS FOR FUTURE WORK

This chapter presents the conclusions from the research results obtain in the thesis and gives recommendations for future work.

9.1 Conclusions

The objective of this thesis was to propose, implement and assess the performance of different positioning solutions based on GNSS for critical applications which may operate in suburban and urban environments. The two applications that have been investigated in this thesis are train control and ETC.

Firstly, the performance requirements that can be expected from a GNSS based positioning system to be used in these applications have been investigated. The study of existing art has proven that, currently, no standardized requirement exists.

- Regarding train control, it has also been shown this application is more demanding in term of integrity risk ($10^{-11}/h$), *TTA* (1 s) and across track *AL* (2.5 m) requirements than civil aviation. Based on a priori knowledge of GNSS systems, it has been proposed not to rely on GNSS for the track selectivity as an *AL* of 2.5 meters does not seem currently feasible. Moreover, a solution based on redundant subsystems using different constellations (GPS and Galileo) has been proposed to reach the $10^{-11}/h$ integrity level.

- Regarding ETC, the requirements are less challenging. They have to be derived from charging metrics that are given by the charging organism. It has been proposed to use a GPS/Galileo dual constellation receiver for this application.

For train control and ETC it has been proposed to augment the GNSS with other sensors that are available on board. The hybridization scheme proposed is tight coupling as it is the most adapted to the navigation in harsh conditions. Both solutions integrate a 6 axis MEMS IMU, however different additional sensors were used for each application:

- The architecture proposed for train control integrates the data from a map of the rail tracks,
- the architecture proposed for ETC integrates WSS measurements.

The error models of the different sensors of reference have been studied. They have been divided into nominal measurements and sensor faults. The nominal error models of the inertial sensors have been derived from the datasheet of the IMU. For the GNSS measurements, the civil aviation error models can be applied for both applications, except for multipath and NLOS-induced errors. For these 2 types of errors, models based on simulations conducted on an urban channel model coupled with a realistic tracking simulator were proposed. However, statistical modelling and tests based on real measurements showed that abnormally large pseudorange errors can result from multipath or NLOS. It was thus proposed to integrate these large errors either as nominal errors (as they are frequent in urban environments) or as failure (which means that they must be detected in an efficient way).

The data fusion algorithm, based on an Extended Kalman filtering has been fully described. The way to improve the accuracy of the solution by incorporating additional measurements (motion constraints) to the solution has been discussed. The way to integrate the aiding such as a track database (for train control) or WSS (for ETC) has also been presented. After a thorough validation, their performance were assessed based on simulations using a realistic error models and on a real data collection conducted in Toulouse and surroundings. As Galileo is not currently operational, GLONASS has been used as a second constellation instead. It has been observed that the solutions tested for train control and ETC are able to fulfill the most stringent accuracy requirements in suburban environments. However, it was not the case in dense urban environments. It has also been observed that the motion constraints only slightly improve the accuracy of the solutions. On the other hand the addition of the GNSS Doppler measurements have been shown to improve the accuracy of the proposed solutions.

As mentioned earlier, one possibility was to consider the multipath- or NLOS-induced errors as measurement faults. In this case, a way to detect and exclude them prior to the integrity monitoring algorithm was investigated so that the integrity monitoring algorithm could concentrate on the detection of satellite failures.

- To detect measurements that are biased due to multipath, it has been proposed to implement monitors on the correlation function. Rigorous ways to set the thresholds for such detectors have been proposed. Moreover, a way to theoretically assess the sensitivity of these tests in terms of multipath amplitude (and thus measurement error) has been proposed. It was shown that smoothing the detection metrics significantly improved the results. Simulations on a

realistic urban channel processed by the ENAC GNSS receiver simulator (GeneIQ) have shown that these metrics enable the detection of measurements errors that exceed 5 m with a P_{MD} lower than 9% (lower P_{MD} are expected for larger errors).

- NLOS exclusion methods were also investigated. The possibility to exclude measurements affected by NLOS signals by applying elevation or C/N_0 masks have been investigated.
 - To reject NLOS based on elevation mask, it has been shown that it is necessary to apply a 40° elevation mask in urban environment which is not feasible because of the satellite availability and the resulting degradation of the accuracy. It has thus been proposed to apply a 10° elevation mask as it is sufficient to protect against NLOS errors in open sky conditions.
 - In suburban and urban environments, it appeared more suitable to apply a C/N_0 mask. It has been observed that, above 40dB-Hz, the measurements are LOS (centered distribution without outlier). Applying such a C/N_0 mask did not degrade the performance of the solutions in single constellation (train control) approach when the track database was integrated and in dual constellation (ETC).
- A monitoring of the KF innovations was added to the solution in order to protect against possible residual outliers. It enabled to detect simultaneous biased measurements.

Finally, the measurement selection process has been shown to improve the accuracy of the solution.

For train control and ETC, the total integrity risk allowed for the navigation solution has been fully allocated to the GNSS system, assuming that the measurements used from additional sensors could be considered as fault free (they thus have their own monitoring ensuring their allowed integrity risk). As an example, a way to monitor the integrity of the inertial measurement based on redundant hardware has been studied and the sensitivity of the test with respect to different types of failure has been assessed. The GNSS integrity risk was shared between the satellite failures events and the failures under nominal conditions, thus considering that large multipath- and NLOS-induced errors would be either part of the nominal case (inflation of the nominal error model) or detected and excluded. Two integrity monitoring algorithms based on the principle of normalized solution separation have been studied. Solution separation algorithms have been preferred over residual based algorithms as they were able to detect ramp failures (once it has grown sufficiently). The performances of the two algorithms have been assessed on real data. The approach based on the rejection of GNSS measurements and the inflation of the nominal error models lead to similar results in terms of availability (with a slight improvement in urban environment with the rejection approach). The observations were the following:

- For train control, the standard solution separation algorithm was able to perform an availability of 99 to 100% associated with an HAL of 25 m in suburban environment. The solution separation algorithm based on separated mechanization has shown poor availability performances due to the over-conservative assumption on the covariance of the separation vector. In dense urban environment, at best, a 99% availability has been observed for an HAL of 125 m with the standard solution separation algorithm. However, the environments

that are characterized as “dense urban” in this thesis are very unlikely to be encountered by a train (deep and narrow urban canyons).

The main problem raised is that the most stringent requirements are associated to areas such as train stations and corridors. However, train stations and corridors are the most likely to be located in urban environment where the accuracy and protection level size is higher due to local effects and poor geometry. An alternative solution thus consists in keeping the ground infrastructure (radio beacons) close to stations so that the GNSS is not used to monitor the train’s position in these sections.

- For ETC, the standard solution separation algorithm was able to perform an availability of 99 to 100% associated with an *HAL* of 25 m in suburban environment. The solution separation algorithm based on separated mechanization performed an availability of 99 to 100% associated with an *HAL* of 50 m. In very dense urban environment, it is not suitable to expect *HAL* less than 100 m with sufficient availabilities for both algorithms.

Finally, a methodology to determine the maximum tolerable bias for a solution that integrates a KF has been proposed. This tolerable bias can be used to feed the innovation monitor and the multipath detection algorithms. It has been observed that the value of the critical bias will highly depend on its lifespan.

9.2 Recommendations for future work

There are still uncertainties on the requirements for GNSS to be used in train control (in the context of ETCS). A standardization process similar to what have been done for civil aviation shall be conducted in order to better define the needs and therefore be able to propose adapted solutions for this application.

The use of Galileo instead of GLONASS and the use of dual frequency receivers instead of mono-frequency receivers is expected to improve the accuracy and the availability of the solutions (in open sky to suburban environments). Other means of improvements are the use of a higher grade IMU (tactical grade), a multipath rejecting antenna (choke ring), an antenna array (for NLOS detection) or the integration of other sensors such as magnetometers (sensitive to interferences) or laser scanner.

An alternative approach to what has been proposed in this thesis consists in not fusing the GNSS with dead reckoning sensors because it introduces correlation in time. Such approach also has the advantage of simplifying considerably the design of the integrity monitoring algorithm because a simple RAIM algorithm can be used. It would enable to predict the accuracy and availability performances in open-sky conditions.

For train control, it would be interesting to investigate the use of carrier phase positioning techniques such as PPP to try to reach the 2.5 meters across track *AL* requirements, although the reliability of such techniques might not be sufficient in urban environments (due to frequency of occurrence of cycle slips).

In the case of ETC, the measurements from the WSS were simulated in this thesis. Thus, the solution remains to be tested with the measurements from an actual WSS which is subject to varying scale factor errors and quantization errors. In order to improve the performances of the navigation system, it is not suitable to use a higher grade IMUs or a better antenna as the cost per OBU is critical.

Finally, the characterization of NLOS error distribution in urban environment could be improved by using techniques to determine which measurement actually comes from masked satellites. Significantly longer measurement collection than what has been presented in the thesis will be necessary in order to better characterize the tails of the distributions. Moreover, the multipath detectors designed in section 7.1 remain to be implemented on real data.

Appendix A

Dual constellation approach for train control: proof of concept

The validity of the approach proposed in chapter 4 to relax the integrity risk for train control is proven hereafter. The notations used hereafter have been defined in section 4.1.1.2. Moreover, the confidence circles centered in \hat{x}_1 , \hat{x}_2 and \hat{x}_{12} which radiuses are HPL_1 , HPL_2 , HPL_{12} are denoted \mathcal{C}_1 , \mathcal{C}_2 and \mathcal{C}_{12} .

Let's first prove that $\mathcal{C}_1 \subset \mathcal{C}_{12}$, as all expressions are symmetric, it will also prove that $\mathcal{C}_2 \subset \mathcal{C}_{12}$. Let's denote x , the true position of the vehicle. It is assumed that $x \in \mathcal{C}_1$, let's prove that $x \in \mathcal{C}_{12}$.

In the first configuration, as \mathcal{C}_1 is included into or equal to \mathcal{C}_{12} , $x \in \mathcal{C}_{12}$.

In the second configuration, to prove that $x \in \mathcal{C}_{12}$, one simply has to prove that the Euclidean distance between \hat{x}_{12} and x is lower than HPL_{12} .

$$\|\hat{x}_{12} - x\| = \|\hat{x}_{12} - \hat{x}_1 + \hat{x}_1 - x\| \leq \|\hat{x}_{12} - \hat{x}_1\| + \|\hat{x}_1 - x\| \quad \text{Eq. A-1}$$

$x \in \mathcal{C}_1$ therefore:

$$\|\hat{x}_1 - x\| \leq HPL_1 \quad \text{Eq. A-2}$$

Moreover by definition of \hat{x}_{12} :

$$\|\hat{x}_{12} - \hat{x}_1\| = \left\| \frac{1}{2} \left(\hat{x}_1 + \hat{x}_2 + \frac{\hat{x}_2 - \hat{x}_1}{\|\hat{x}_1 - \hat{x}_2\|} (HPL_2 - HPL_1) \right) - \hat{x}_1 \right\| \quad \text{Eq. A-3}$$

which leads to:

$$\|\hat{x}_{12} - \hat{x}_1\| = \frac{1}{2} \left\| \frac{\hat{x}_2 - \hat{x}_1}{\|\hat{x}_1 - \hat{x}_2\|} [\|\hat{x}_1 - \hat{x}_2\| + HPL_2 - HPL_1] \right\| \quad \text{Eq. A-4}$$

By simple properties of the Euclidian norm:

$$\|\hat{x}_{12} - \hat{x}_1\| = \frac{1}{2} \frac{\|\hat{x}_2 - \hat{x}_1\|}{\|\hat{x}_1 - \hat{x}_2\|} [\|\hat{x}_1 - \hat{x}_2\| + HPL_2 - HPL_1] \quad \text{Eq. A-5}$$

Thus :

$$\|\hat{x}_{12} - \hat{x}_1\| = \frac{1}{2} [\|\hat{x}_1 - \hat{x}_2\| + HPL_2 - HPL_1] \quad \text{Eq. A-6}$$

But this configuration is characterized by $\|\hat{x}_1 - \hat{x}_2\| > |HPL_1 - HPL_2|$, thus

$$\|\hat{x}_{12} - \hat{x}_1\| = \frac{1}{2}(\|\hat{x}_1 - \hat{x}_2\| + HPL_2 - HPL_1) \quad \text{Eq. A-7}$$

Finally:

$$\|\hat{x}_{12} - x\| \leq \frac{1}{2}(\|\hat{x}_1 - \hat{x}_2\| + |HPL_2 - HPL_1|) + HPL_1 = HPL_{12} \quad \text{Eq. A-8}$$

Thus:

$$x \in \mathcal{C}_{12} \quad \text{Eq. A-9}$$

Now that it has been proven that $\mathcal{C}_1 \subset \mathcal{C}_{12}$ and $\mathcal{C}_2 \subset \mathcal{C}_{12}$, it is necessary to prove that the probability for x to be outside of \mathcal{C}_{12} is the product of the probabilities to be outside of \mathcal{C}_1 and \mathcal{C}_2 . We have $\mathcal{C}_1 \subset \mathcal{C}_{12}$ and $\mathcal{C}_2 \subset \mathcal{C}_{12}$, therefore:

$$\mathcal{C}_1 \cup \mathcal{C}_2 \subset \mathcal{C}_{12} \quad \text{Eq. A-10}$$

Thus :

$$\overline{\mathcal{C}_{12}} \subset \overline{\mathcal{C}_1} \cap \overline{\mathcal{C}_2} \quad \text{Eq. A-11}$$

Moreover, the events $x \in \overline{\mathcal{C}_1}$ and $x \in \overline{\mathcal{C}_2}$ are independent as \mathcal{C}_1 and \mathcal{C}_2 are calculated from independent subsystems. Finally:

$$P(x \in \overline{\mathcal{C}_{12}}) \leq P(x \in \overline{\mathcal{C}_1})P(x \in \overline{\mathcal{C}_2}) \quad \text{Eq. A-12}$$

The probability for the true position to be outside of both confidence intervals is the product of the probabilities for the true position to be outside each interval.

Appendix B

Distribution of the protection levels in the second configuration for train control

Following the same notations which have been defined in section 4.1.1.2, in the second configuration, $\|\hat{x}_1 - \hat{x}_2\| > |HPL_1 - HPL_2|$.

The Bayes formula gives:

$$\begin{aligned} P(HPL_{12} \leq u \mid \|\hat{x}_1 - \hat{x}_2\| > |HPL_1 - HPL_2|) \\ = \frac{P(HPL_{12} \leq u \cap \|\hat{x}_1 - \hat{x}_2\| > |HPL_1 - HPL_2|)}{P(\|\hat{x}_1 - \hat{x}_2\| > |HPL_1 - HPL_2|)} \end{aligned} \quad \text{Eq. B-1}$$

Which can be written:

$$\begin{aligned} P(HPL_{12} \leq u \mid \|\hat{x}_1 - \hat{x}_2\| > |HPL_1 - HPL_2|) \\ = \frac{P(|HPL_1 - HPL_2| < \|\hat{x}_1 - \hat{x}_2\| \leq 2u - HPL_1 - HPL_2)}{P(\|\hat{x}_1 - \hat{x}_2\| > |HPL_1 - HPL_2|)} \end{aligned} \quad \text{Eq. B-2}$$

If $u < \frac{|HPL_1 - HPL_2| + HPL_2 + HPL_1}{2}$,

$$P(HPL_{12} \leq u \mid \|\hat{x}_1 - \hat{x}_2\| > |HPL_1 - HPL_2|) = 0 \quad \text{Eq. B-3}$$

Else,

$$\begin{aligned} P(HPL_{12} \leq u \mid \|\hat{x}_1 - \hat{x}_2\| > |HPL_1 - HPL_2|) \\ = \frac{cdf_{\mathcal{R}(\sqrt{\sigma_1^2 + \sigma_2^2})}(2u - HPL_1 - HPL_2) - cdf_{\mathcal{R}(\sqrt{\sigma_1^2 + \sigma_2^2})}(HPL_1 - HPL_2)}{1 - cdf_{\mathcal{R}(\sqrt{\sigma_1^2 + \sigma_2^2})}(HPL_1 - HPL_2)} \end{aligned} \quad \text{Eq. B-4}$$

Appendix C

Validation of the LMS/Receiver coupling

The simulation platform, i.e. the combination of the LMS channel model followed by the GeneIQ receiver simulator, had to be validated. In the first validation step, the LOS component of the generated received signal has been isolated from the echoes and has been processed by the simulator. This allows to check the right generation of the dynamic of the LOS signal by comparing the behavior of the tracking loops with their theoretical behavior. In this case, the received signal has been simulated for a vehicle with a constant velocity and a fixed satellite position. When the satellite to receiver distance is linearly varying, it generates a constant Doppler shift on the carrier phase and code delay, which leads to a biased estimation of the delay and phase by first orders DLL and PLL.

The code delay and carrier phase estimated by higher orders tracking loops are not biased due to a constant Doppler shift. This section describes the validation process for the DLL, the PLL and the FLL. The same method was used to validate the carrier tracking loops. The theoretical expression of the steady state error of a first order DLL is the following (in chips) [Van Dierendonck, 1996]:

$$E_{\infty, DLL} = \frac{\Delta f_c}{4B_{L, DLL}} = \frac{v_0}{4B_{L, DLL} T_c c} \quad \text{Eq. C-1}$$

where:

- v_0 is the radial speed of the receiver in m/s
- $B_{L, DLL}$ is the one-sided loop bandwidth of the DLL loop filter in Hz
- $\Delta f_c = \frac{v_0}{c T_c}$ is the code Doppler in chips/s,
- T_c is the chip duration in second

The validation has been conducted on L1 C/A signal. In the chosen scenario, the velocity of the vehicle is set to 20 km/h. The satellite has an azimuth of 40° and an elevation of 50° . Thus the radial velocity is $v_0 = 20/3.6 \cos(50) \cos(45) = 2.525 \text{ ms}^{-1}$. T_c is $0.98 \cdot 10^{-6}$ s for GPS L1 C/A. The loop bandwidth $B_{L, DLL}$ is set to 1 Hz which is a typical value for a DLL in a GNSS receiver. Using Eq. C-1, we find a steady state error of $E_{\infty, DLL} = 2.2 \cdot 10^{-3}$ chips, which corresponds to the simulation results shown in Figure 151.

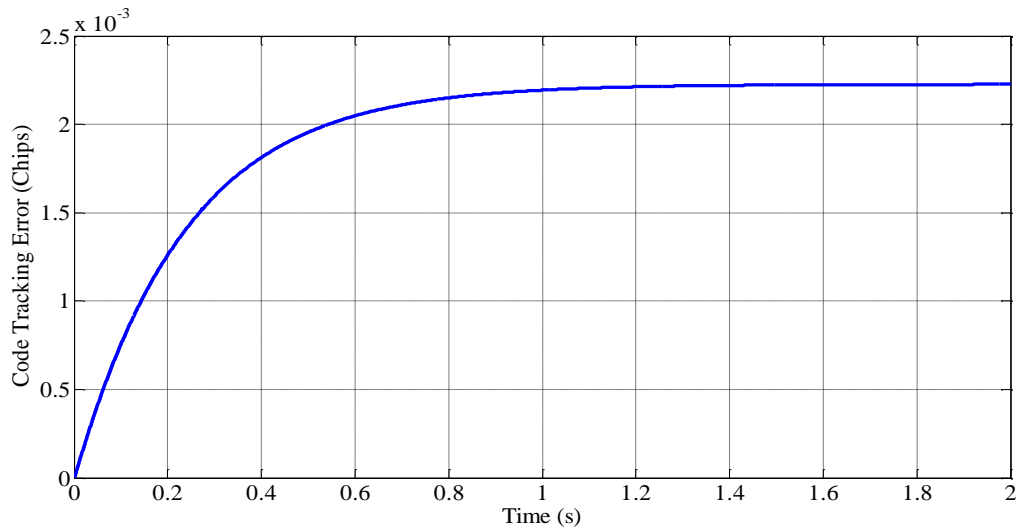


Figure 151 Steady state error of a first order DLL for a vehicle at a constant speed on the LMS

A first order PLL was run on the same channel. Eq. C-1 applied to carrier tracking gives the PLL steady state error is the following:

$$E_{\infty,PLL} = 2\pi \frac{v_0}{4B_{L,PLL}\lambda} \quad \text{Eq. C-2}$$

where:

- λ is the carrier wavelength ($\lambda = 0.19$ m for L1 C/A)
- $B_{L,PLL}$ is the one-sided loop bandwidth of the PLL loop filter in Hz (15 Hz in the simulations)

The theoretical expression gives a steady state error of - 1.473 rad, which corresponds to the steady state value obtained in Figure 152.

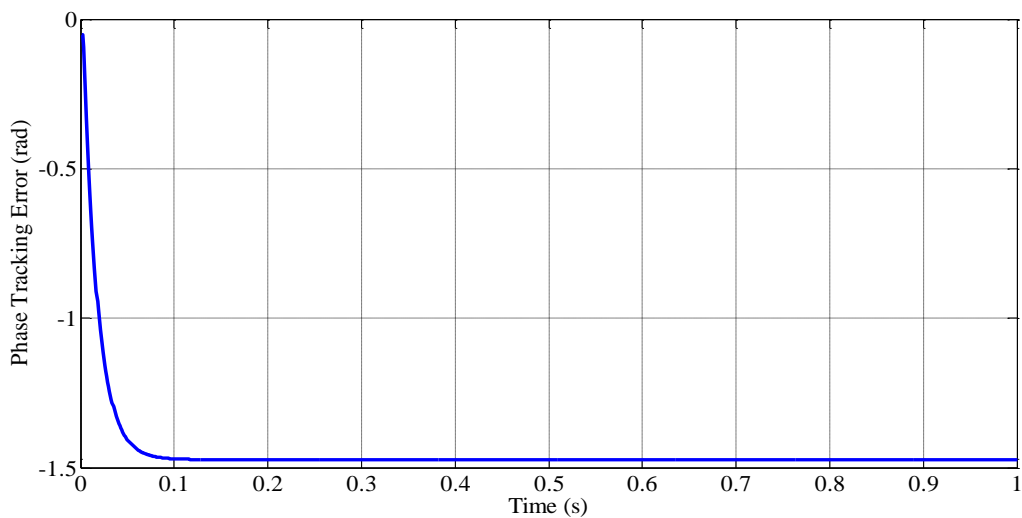


Figure 152 Steady state error of a first order PLL for a vehicle at a constant speed on the LMS

A second order FLL that tracks the Doppler shift is also tested on the channel. In this configuration, the estimation by the FLL is not affected by any steady state error. However the FLL shall track the Doppler frequency of the received signal. The Doppler frequency is given by:

$$f_{dop} = \frac{v_0}{\lambda} \quad \text{Eq. C-3}$$

In the chosen scenario, $f_{dop} = -13.3$ Hz which corresponds to the value observed in figure.

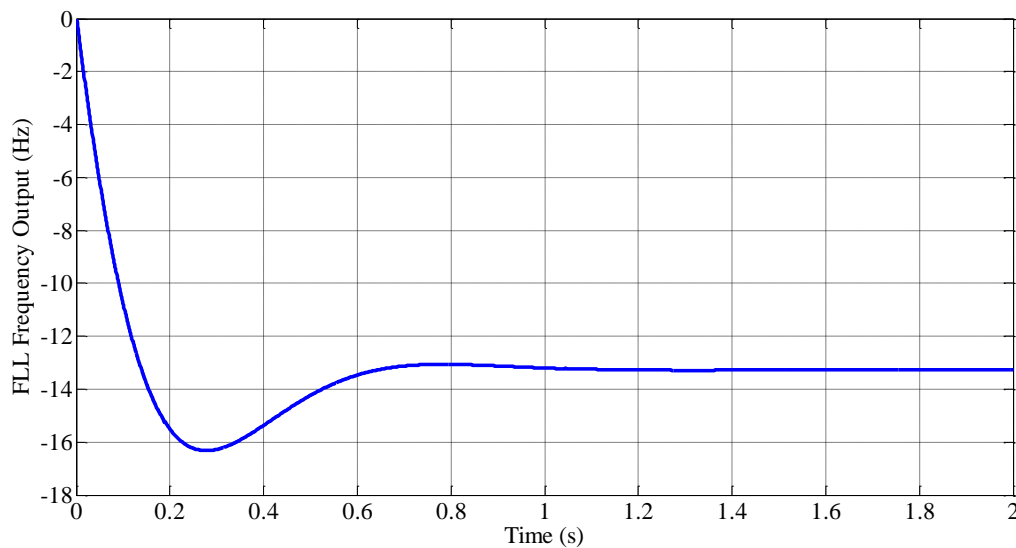


Figure 153 Steady state error of a second order FLL for a vehicle at a constant speed on the LMS

It can be inferred from this set of short simulations, that the correlator outputs are well generated from the LMS channel generator.

The right consideration of the echoes also had to be tested. To check that the reflections are well processed in the receiver, the LOS was set to zero and the LOS characteristics were injected in the multipath generation module. The same validations process has been conducted again on the LOS treated as an echo.

References:

[Van Dierendonck, Van Dierendonck, A. J., Global Positioning System: Theory & Applications, (Progress in Astronautics and Aeronautics), vol. 1. Washington, D.C.: AIAA, 1996, ch. 8; ISBN1-56347-106-X

Appendix D

Parameters for the statistic NLOS error model

In the case of a diffracted NLOS, the distribution of the pseudorange bias is approximated by a gamma distribution. The two parameters denoted k and θ of the gamma distribution are given in Table 59 and Table 60 in function of the two parameters ϑ and α .

ϑ (°)									
α (°)	10	20	30	40	50	60	70	80	90
10	0,56	0,41	0,40	0,43	0,46	0,50	0,52	0,54	0,55
20	1,23	0,63	0,52	0,47	0,45	0,44	0,44	0,44	0,44
30	2,15	0,94	0,66	0,57	0,54	0,52	0,51	0,50	0,50
40	2,98	1,45	0,91	0,70	0,61	0,57	0,55	0,55	0,54
50	3,61	2,08	1,32	0,96	0,79	0,70	0,65	0,62	0,62
60	4,07	2,71	1,88	1,4	1,13	0,97	0,88	0,83	0,82
70	4,42	3,26	2,5	2	1,68	1,47	1,34	1,27	1,25
80	4,7	3,72	3,07	2,63	2,33	2,13	2	1,93	1,91
90	4,93	4,12	3,57	3,2	2,95	2,78	2,67	2,61	2,6

Table 59 Parameters of the gamma fitting for bias due to diffraction k

ϑ (°)									
α (°)	10	20	30	40	50	60	70	80	90
10	1,26	1,34	2,23	2,95	3,41	3,69	3,85	3,93	3,96
20	3,21	2,03	1,51	1,61	1,93	2,23	2,46	2,60	2,65
30	4,91	3,97	2,92	2,19	1,84	1,71	1,69	1,69	1,70
40	6,83	5,47	4,72	3,88	3,20	2,73	2,45	2,29	2,25
50	9,15	6,57	5,89	5,33	4,77	4,30	3,96	3,76	3,69
60	11,83	7,67	6,52	5,98	5,60	5,28	5,05	4,90	4,85
70	14,76	8,92	7,07	6,20	5,70	5,38	5,18	5,07	5,03

80	17,85	10,29	7,77	6,50	5,75	5,27	4,98	4,82	4,77
90	20,98	11,7	8,56	6,96	6,01	5,41	5,03	4,83	4,76

Table 60 Parameters of the gamma fitting for bias due to diffraction θ

Appendix E

Track database heading measurement error covariance

This appendix aims at calculating the covariance of the error associated to the heading measurement that can be derived from the track database. Let us assume that the two points of the map denoted A and B are so that their coordinates in the horizontal plane are affected by errors following uncorrelated bi dimensional centered Gaussian distributions.

$$\begin{aligned} E_A &= E_{A,true} + \delta E_A \\ N_A &= N_{A,true} + \delta N_A \\ E_B &= E_{B,true} + \delta E_B \\ N_B &= N_{B,true} + \delta N_B \end{aligned} \tag{Eq. E-1}$$

with:

$$\begin{bmatrix} \delta E_A \\ \delta N_A \end{bmatrix} \sim \mathcal{N}\left(0, \begin{bmatrix} \sigma_{E_A}^2 & 0 \\ 0 & \sigma_{N_A}^2 \end{bmatrix}\right) \text{ and } \begin{bmatrix} \delta E_B \\ \delta N_B \end{bmatrix} \sim \mathcal{N}\left(0, \begin{bmatrix} \sigma_{E_B}^2 & 0 \\ 0 & \sigma_{N_B}^2 \end{bmatrix}\right) \tag{Eq. E-2}$$

The objective is then to determine the standard deviation of ψ_{MAP} where:

$$\psi_{map} = \text{atan}\left(\frac{E_B - E_A}{N_B - N_A}\right) = \text{atan}\left(\frac{E_{B,true} - E_{A,true} + \delta E_B - \delta E_A}{N_{B,true} - N_{A,true} + \delta N_B - \delta N_A}\right) \tag{Eq. E-3}$$

For simplification it has been assumed in section 5.1.3.2 that $\sigma_{E_A}^2 = \sigma_{N_A}^2 = \sigma_{E_B}^2 = \sigma_{N_B}^2 = \sigma_{map}^2$. In this particular case, the symmetry of the problem makes it possible to work with a value $\psi_{true} = \frac{\pi}{2}$ for instance and then to generalize the result by symmetry. In this particular case $E_{B,true} - E_{A,true} = 0$. If the movement is approximately plane, we have the distance between two consecutive points (d_{map}) which is equal to:

$$d_{map} \approx |N_{B,TRUE} - N_{A,TRUE}| \tag{Eq. E-5}$$

But d is a parameter of the map that is known and assumed constant. Thus:

$$\psi_{map} = \text{atan}\left(\frac{\delta E_B - \delta E_A}{d_{map} + \delta N_B - \delta N_A}\right) \tag{Eq. E-6}$$

It is assumed that the mapping error is negligible with respect to the distance between two consecutive track points ($d_{map} \gg \delta E_B - \delta E_A$). A first order Taylor serie expansion of atan gives:

$$\psi_{map} \cong \frac{\delta E_B - \delta E_A}{d_{map} + \delta N_B - \delta N_A} \cong \frac{\delta E_B - \delta E_A}{d_{map}} \quad \text{Eq. E-7}$$

In this case:

$$\psi_{map} - \psi_{true} = \psi_{MAP} = \frac{\delta E_B - \delta E_A}{d_{map}} \quad \text{Eq. E-8}$$

Thus:

$$\sigma_{\psi_{MAP}} = \sqrt{2} \frac{\sigma_{map}}{d_{map}} \quad \text{Eq. E-9}$$

Appendix F

Quality of the velocity estimation

This appendix gives the statistics of the error on the velocity estimation as done by the different architecture developed in the thesis. The thesis only has focused on the positioning error. However, the GNSS could also be used for these applications to improve the velocity estimation. This appendix, through Table 61, Table 62 and Table 63 provides the RMS of the velocity estimation error in the horizontal plane as estimated by the different filters tested.

Sensors	PRR	NHC	ZUPT ZARU	Horizontal Velocity error RMS (ms ⁻¹)	
				Suburban	Urban
GPS/INS				1.0	2.2
GPS/INS	✓			0.2	0.9
GPS/INS	✓	✓		0.2	0.8
GPS/INS	✓	✓	✓	0.2	0.7

Table 61 Quality of the velocity estimation for the different configurations combining GPS and the IMU

Sensors	PRR	NHC	ZUPT/ ZARU	Horizontal Velocity error RMS (ms ⁻¹)			
				Along-track		Across-track	
				Suburban	Urban	Suburban	Urban
GPS/INS/Map				0.6	1.2	0.3	0.4
GPS/INS/Map	✓			0.2	0.4	0.1	0.2
GPS/INS/Map	✓	✓		0.2	0.4	0.1	0.3
GPS/INS/Map	✓	✓	✓	0.1	0.4	0.1	0.3
GLO/INS/Map				0.2	0.7	0.2	0.3
GLO/INS/Map	✓			0.2	0.5	0.2	0.3
GLO/INS/Map	✓	✓		0.2	0.5	0.2	0.3

GLO/INS/Map	✓	✓	✓	0.1	0.5	0.1	0.3
-------------	---	---	---	-----	-----	-----	-----

Table 62 Quality of the velocity estimation for the different configurations combining GNSS, INS and the track database

Sensors	PRR	NHC	ZUPT ZARU	Horizontal Velocity error RMS (ms ⁻¹)	
				Horizontal	
				Suburban	Urban
GPS/GLO/INS				0.9	1.2
GPS/GLO/INS	✓			0.3	0.6
GPS/GLO/INS	✓	✓		0.2	0.4
GPS/GLO/INS	✓	✓	✓	0.2	0.3
GPS/GLO/INS/WSS		✓		0.6	0.3
GPS/GLO/INS/WSS	✓	✓		0.2	0.2
GPS/GLO/INS/WSS	✓	✓	✓	0.2	0.3

Table 63 Quality of the velocity estimation for the different configurations combining GPS, GLONASS, the IMU, and a simulated WSS.

Appendix G

Determination of the thresholds and the sensitivity for the correlator distortion metrics

This appendix provides the proofs for the formulas that are used in chapter 7 in order to set the thresholds for the multipath monitors.

The first method assumes that the metrics follows Gaussian distribution. To fully characterize a Gaussian, it is necessary to determine its mean and standard deviation. If the calculation of the expectation of the metrics is trivial, the calculation of the standard deviations is more complex. The way to calculate the theoretical expression of these standard deviations is presented in section A.

The second method does not make any gaussianity assumption on the metric. The way to derive the thresholds is given in section B.

Finally, the way to calculate the sensitivity of the tests with respect to multipath is detailed in section C.

The notations introduced in section 7.1 are used hereafter.

A. Determination of detection thresholds with gaussianity assumption

Simple ratio metric

In order to calculate the standard deviation of the simple ratio metric, the first order development in Taylor series can be used. It gives:

$$\frac{I_X}{I_Y} = \frac{\mu_X + n_X}{\mu_Y + n_Y} \approx \frac{\mu_X + n_X}{\mu_Y} \left(1 - \frac{n_Y}{\mu_Y} + \left(\frac{n_Y}{\mu_Y} \right)^2 \right) \quad \text{Eq. E-1}$$

At the second order (the zero means and higher order terms are not written):

$$E \left[\frac{I_X^2}{I_Y^2} \right] = \frac{1}{\mu_Y^2} E \left[\mu_X^2 + n_X^2 - 4 \frac{\mu_X}{\mu_Y} n_Y n_X + 3 \frac{\mu_X^2}{\mu_Y^2} n_Y^2 \right] \quad \text{Eq. E-2}$$

We also have:

$$E \left[\frac{I_X}{I_Y} \right] = \frac{\mu_X}{\mu_Y} - \frac{1}{\mu_Y^2} E[n_X n_Y] + \frac{\mu_X}{\mu_Y^3} E[n_Y^2] \quad \text{Eq. E-3}$$

Finally:

$$\sigma^2 \left(\frac{I_X}{I_Y} \right) = E \left[\frac{I_X^2}{I_Y^2} \right] - E \left[\frac{I_X}{I_Y} \right]^2 \quad \text{Eq. E-4}$$

Thus:

$$\sigma^2 \left(\frac{I_X}{I_Y} \right) = \left(\frac{\mu_X}{\mu_Y} \right)^2 \left(\frac{\sigma^2(n_X)}{\mu_X^2} + \frac{\sigma^2(n_Y)}{\mu_Y^2} - 2 \frac{\text{cov}(n_X n_Y)}{\mu_X \mu_Y} \right) \quad \text{Eq. E-5}$$

Differential ratio metric

In order to calculate the standard deviation of the differential ratio metric, the first order development in Taylor series gives:

$$\frac{I_X - I_Y}{I_Z} = \left(\frac{\mu_X + n_X - \mu_Y - n_Y}{\mu_Z} \right) \left(1 - \frac{n_Z}{\mu_Z} + \left(\frac{n_Z}{\mu_Z} \right)^2 \right) \quad \text{Eq. E-6}$$

Thus:

$$E \left[\left(\frac{I_X - I_Y}{I_Z} \right)^2 \right] = E \left[\frac{I_X^2}{I_Z^2} + \frac{I_Y^2}{I_Z^2} - 2 \frac{I_X I_Y}{I_Z^2} \right] \quad \text{Eq. E-7}$$

The previous results can be used:

$$E \left[\frac{I_X^2}{I_Z^2} \right] = \frac{1}{\mu_Z^2} E \left[\mu_X^2 + n_X^2 - 4 \frac{\mu_X}{\mu_Z} n_Z n_X + 3 \frac{\mu_X^2}{\mu_Z^2} n_Z^2 \right] \quad \text{Eq. E-8}$$

$$E \left[\frac{I_Y^2}{I_Z^2} \right] = \frac{1}{\mu_Z^2} E \left[\mu_Y^2 + n_Y^2 - 4 \frac{\mu_Y}{\mu_Z} n_Z n_Y + 3 \frac{\mu_Y^2}{\mu_Z^2} n_Z^2 \right] \quad \text{Eq. E-9}$$

$$E \left[\frac{I_X I_Y}{I_Z^2} \right] = \frac{1}{\mu_Z^2} E \left[\mu_X \mu_Y + n_X n_Y - 2 n_Z n_Y \frac{\mu_X}{\mu_Z} - 2 n_Z n_X \frac{\mu_Y}{\mu_Z} + 3 n_Z^2 \frac{\mu_X \mu_Y}{\mu_Z^2} \right] \quad \text{Eq. E-10}$$

Moreover

$$E \left[\frac{I_X - I_Y}{I_Z} \right] = \frac{1}{\mu_Z} E \left[\mu_X - \mu_Y - n_Z n_X \frac{1}{\mu_Z} + n_Z n_Y \frac{1}{\mu_Z} + n_Z^2 \frac{\mu_X - \mu_Y}{\mu_Z^2} \right] \quad \text{Eq. E-11}$$

The 4th and 3rd order terms are not written:

$$E \left[\frac{I_X - I_Y}{I_Z} \right]^2 = \frac{1}{\mu_Z^2} \left[(\mu_X - \mu_Y)^2 + E[n_Z n_Y]^2 \frac{1}{\mu_Z} + 2 \frac{(\mu_X - \mu_Y)}{\mu_Z} (E[n_Z n_Y] - E[n_Z n_X]) + 2E[n_Z^2] \frac{(\mu_X - \mu_Y)^2}{\mu_Z^2} \right]$$

Eq. E-12

Then

$$\begin{aligned} \sigma^2 \left(\frac{I_X - I_Y}{I_Z} \right) = & \frac{1}{\mu_Z^2} \left\{ \mu_X^2 + E[n_X^2] - 4 \frac{\mu_X}{\mu_Z} E[n_Z n_X] + 3 \frac{\mu_X^2}{\mu_Z^2} E[n_Z^2] + \mu_Y^2 + E[n_Y^2] - 4 \frac{\mu_Y}{\mu_Z} E[n_Z n_Y] + 3 \frac{\mu_Y^2}{\mu_Z^2} E[n_Z^2] \right. \\ & - 2 \left[\mu_X \mu_Y + E[n_X n_Y] - 2E[n_Z n_Y] \frac{\mu_X}{\mu_Z} - 2E[n_Z n_X] \frac{\mu_Y}{\mu_Z} + 3E[n_Z^2] \frac{\mu_X \mu_Y}{\mu_Z^2} \right] \\ & \left. - \left[(\mu_X - \mu_Y)^2 + 2 \frac{(\mu_X - \mu_Y)}{\mu_Z} (E[n_Z n_Y] - E[n_Z n_X]) + 2E[n_Z^2] \frac{(\mu_X - \mu_Y)^2}{\mu_Z^2} \right] \right\} \end{aligned}$$

Eq. E-13

If X and Y do not have the same value:

$$\begin{aligned} \sigma^2 \left(\frac{I_X - I_Y}{I_Z} \right) = & \left(\frac{\mu_X - \mu_Y}{\mu_Z} \right)^2 \left[\frac{\sigma^2(n_Z)}{\mu_Z^2} + \frac{\sigma^2(n_X) + \sigma^2(n_Y) - 2cov(n_X n_Y)}{(\mu_X - \mu_Y)^2} \right. \\ & \left. + 2 \left(\frac{cov(n_Z n_X) - cov(n_Z n_Y)}{\mu_Z (\mu_X - \mu_Y)} \right) \right] \end{aligned}$$

Eq. E-14

B. Determination of detection thresholds without assuming the metric Gaussian

In this section, the metric is not assumed to follow a Gaussian distribution.

Simple ratio metric

The expression of the Geary-Hinkley transform applied to $M = \frac{I_X}{I_Y}$ is the following:

$$\left| \frac{\mu_Y M - \mu_X}{\sqrt{\sigma_Y^2 M^2 - 2cov_{XY} M + \sigma_X^2}} \right| \leq m_{exp}$$

Eq. E-15

which is equivalent to

$$M^2(\mu_Y^2 - m_{exp}^2 \sigma_Y^2) + M(-2\mu_X \mu_Y + 2m_{exp}^2 cov_{XY}) + \mu_X^2 - m_{exp}^2 \sigma_X^2 \leq 0 \quad \text{Eq. E-16}$$

The expression is always positive except between the roots of the polynom then:

$$\text{Lowerbound} = \frac{-(-2\mu_X \mu_Y + 2m_{exp}^2 cov_{XY}) - \sqrt{(-2\mu_X \mu_Y + 2m_{exp}^2 cov_{XY})^2 - 4(\mu_Y^2 - m_{exp}^2 \sigma_Y^2)(\mu_X^2 - m_{exp}^2 \sigma_X^2)}}{2(\mu_Y^2 - m_{exp}^2 \sigma_Y^2)} \quad \text{Eq. E-17}$$

$$\text{Upperbound} = \frac{-(-2\mu_X \mu_Y + 2m_{exp}^2 cov_{XY}) + \sqrt{(-2\mu_X \mu_Y + 2m_{exp}^2 cov_{XY})^2 - 4(\mu_Y^2 - m_{exp}^2 \sigma_Y^2)(\mu_X^2 - m_{exp}^2 \sigma_X^2)}}{2(\mu_Y^2 - m_{exp}^2 \sigma_Y^2)} \quad \text{Eq. E-18}$$

Differential ratio metric

The expression of the threshold for the differential metric is derived from the thresholds of the simple ratio test.

C. Determination of the sensitivity

Simple ratio metric

The bounds of the biased distribution can be found the same way as they were found to set the P_{FA} . Here the P_{FA} is replaced by the P_{MD} . The new distribution is bounded (with P_{MD}) between *Lowerbound,MP* and *Upperbound,MP*. These can be obtained with the Geary-Hinkley transformation.

$$\mu_{X,MP} = \mu_X + \alpha K_{cc}(X - \tau) \quad \text{Eq. E-19}$$

$$\mu_{Y,MP} = \mu_Y + \alpha K_{cc}(Y - \tau) \quad \text{Eq. E-20}$$

The bounds of the confidence interval of the metric affected by multipath become:

$$\text{Lowerbound,MP} = \frac{-(-2\mu_{X,MP} \mu_{Y,MP} + 2m_{MD}^2 cov_{XY}) - \sqrt{(2\mu_{X,MP} \mu_{Y,MP} - 2m_{MD}^2 cov_{XY})^2 - 4(\mu_{Y,MP}^2 - m_{MD}^2 \sigma_Y^2)(\mu_{X,MP}^2 - m_{MD}^2 \sigma_X^2)}}{2(\mu_{Y,MP}^2 - m_{MD}^2 \sigma_Y^2)} \quad \text{Eq. E-21}$$

Upperbound, MP =

$$\frac{-(-2\mu_{X,MP}\mu_{Y,MP} + 2m_{MD}^2 cov_{XY})}{2(\mu_{Y,MP}^2 - m_{MD}^2 \sigma_Y^2)} + \sqrt{\frac{(2\mu_{X,MP}\mu_{Y,MP} - 2m_{MD}^2 cov_{XY})^2 - 4(\mu_{Y,MP}^2 - m_{MD}^2 \sigma_Y^2)(\mu_{X,MP}^2 - m_{MD}^2 \sigma_X^2)}{2(\mu_{Y,MP}^2 - m_{MD}^2 \sigma_Y^2)}} \quad \text{Eq. E-22}$$

Then two configurations described in section 7.1.4 are possible.

Configuration 1:

$$\text{Lowerbound, MP} = UB_{\bar{A}MP} \quad \text{Eq. E-23}$$

Where $UB_{\bar{A}MP}$ is the upper detection threshold set in order to set the P_{FA} .

Then:

$$\begin{aligned} & (-2\mu_{X,MP}\mu_{Y,MP} + 2m_{MD}^2 cov_{XY})^2 - 4(\mu_{Y,MP}^2 - m_{MD}^2 \sigma_Y^2)(\mu_{X,MP}^2 - m_{MD}^2 \sigma_X^2) \\ & = [-(-2\mu_{X,MP}\mu_{Y,MP} + 2m_{MD}^2 cov_{XY}) \\ & \quad - 2UB_{\bar{A}MP}(\mu_{Y,MP}^2 - m_{MD}^2 \sigma_Y^2)]^2 \end{aligned} \quad \text{Eq. E-24}$$

After transformation transformations it becomes:

$$\begin{aligned} & UB_{\bar{A}MP}^2 (\mu_{Y,MP}^2 - m_{MD}^2 \sigma_Y^2) + UB_{\bar{A}MP} (-2\mu_{X,MP}\mu_{Y,MP} + 2m_{MD}^2 cov_{xy}) \\ & \quad + (x^2 - m_{MD}^2 \sigma_X^2) = 0 \end{aligned} \quad \text{Eq. E-25}$$

The unknown is α , and after replacing $\mu_{X,MP}$ and $\mu_{Y,MP}$ by their expressions in function of α the equation becomes:

$$\begin{aligned} & \alpha^2 \{ [UB_{\bar{A}MP} K_{cc}(Y - \tau)]^2 - 2UB_{\bar{A}MP} K_{cc}(Y - \tau) K_{cc}(X - \tau) + K_{cc}(X - \tau)^2 \} \\ & + \alpha \{ 2UB_{\bar{A}MP}^2 \mu_Y K_{cc}(Y - \tau) - 2UB_{\bar{A}MP} [\mu_X K_{cc}(Y - \tau) + \mu_Y K_{cc}(X - \tau)] + 2\mu_X K_{cc}(X - \tau) \} \\ & + UB_{\bar{A}MP}^2 (\mu_Y^2 - m_{MD}^2 \sigma_Y^2) + 2UB_{\bar{A}MP} (-\mu_X \mu_Y + m_{MD}^2 cov_{xy}) + \mu_X^2 - m_{MD}^2 \sigma_X^2 = 0 \end{aligned} \quad \text{Eq. E-26}$$

The lowest root of this equation is the sensitivity associated with the probability of missed detection m_{MD} .

Configuration 2:

$$\text{Upperbound, MP} = LB_{\bar{A}MP} \quad \text{Eq. E-27}$$

Where $UB_{\bar{A}MP}$ is the upper detection threshold set in order to set the P_{FA} .

$$\begin{aligned}
 & \alpha^2\{[LB_{\bar{a}MP}K_{cc}(Y - \tau)]^2 - 2LB_{\bar{a}MP}K_{cc}(Y - \tau)K_{cc}(X - \tau) + K_{cc}(X - \tau)^2\} \\
 & + \alpha\{2LB_{\bar{a}MP}^2\mu_Y K_{cc}(Y - \tau) - 2LB_{\bar{a}MP}[\mu_X K_{cc}(Y - \tau) + \mu_Y K_{cc}(X - \tau)] + 2\mu_X K_{cc}(X - \tau)\} \quad \text{Eq. E-28} \\
 & + LB_{\bar{a}MP}^2(\mu_Y^2 - m_{MD}^2\sigma_Y^2) + 2LB_{\bar{a}MP}(-\mu_X\mu_Y + m_{MD}^2cov_{xy}) + \mu_X^2 - m_{MD}^2\sigma_X^2 = 0
 \end{aligned}$$

The lowest root of this 2nd order equation is the sensitivity associated with the probability of missed detection Th_{MD} .

Differential ratio metric

Substitute X by N , and Y by Z in the general expression

Appendix H

Stanford diagrams of the different solutions and algorithms tested

This appendix aims at verifying that no integrity loss has been observed on the dataset. Such an event is said to occur if the *HPE* exceed the *HPL* without detection within the *TTA*. This condition is necessary (but not sufficient) to ensure that the solution proposed perform a sufficiently high level of integrity. The Stanford plots are given for each sub solutions and solutions, augmented with the integrity monitoring algorithms of reference presented in section 8.3.

A. Train control

A. 1. Inflation of the measurement error model

A. 1. 1. Standard solution separation algorithm

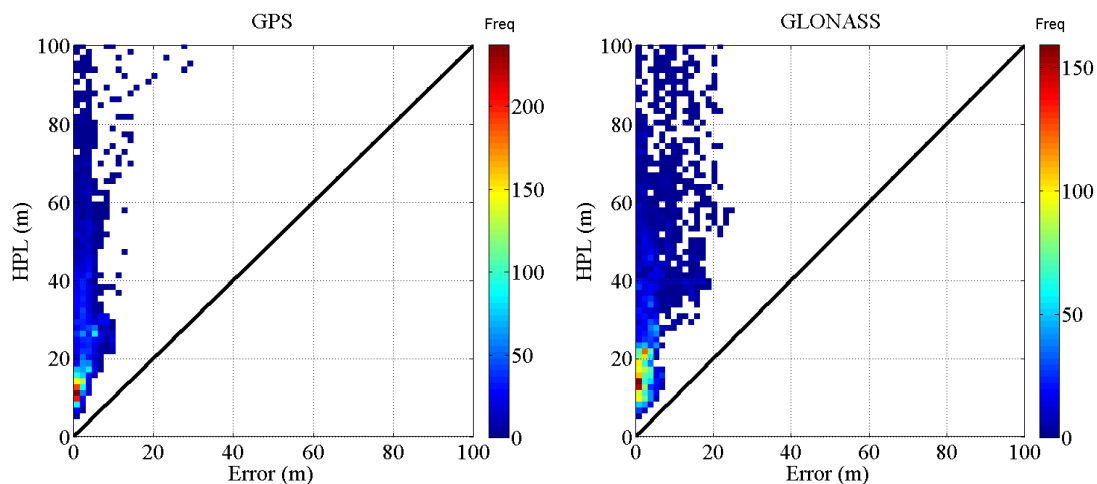


Figure 154 Stanford diagrams plotted for the two subsystems (based on GPS on the left and GLONASS on the right) after inflation of weighting scheme in suburban and urban environments. IMU and track database measurement are integrated.

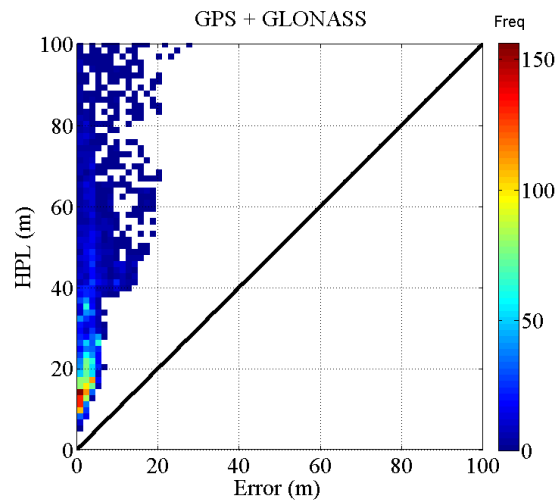


Figure 155 Stanford diagram plotted for the combined system after inflation of weighting scheme in suburban and urban environments. IMU and track database measurement are integrated

A. 1. 2. Solution separation based on sub mechanizations

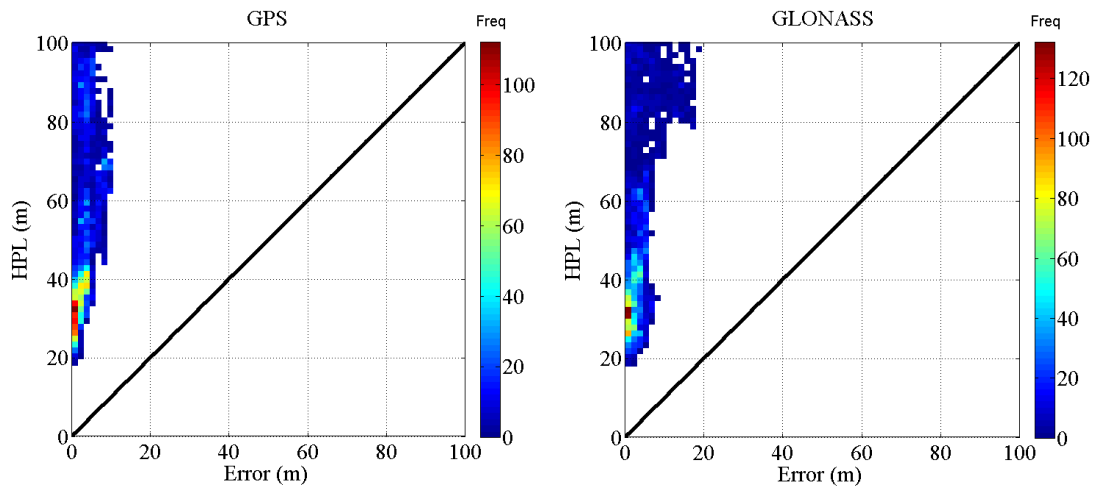


Figure 156 Stanford diagrams plotted for the two subsystems (based on GPS on the left and GLONASS on the right) after inflation of weighting scheme in suburban and urban environments (approach based on separated mechanizations). IMU and track database measurement are integrated

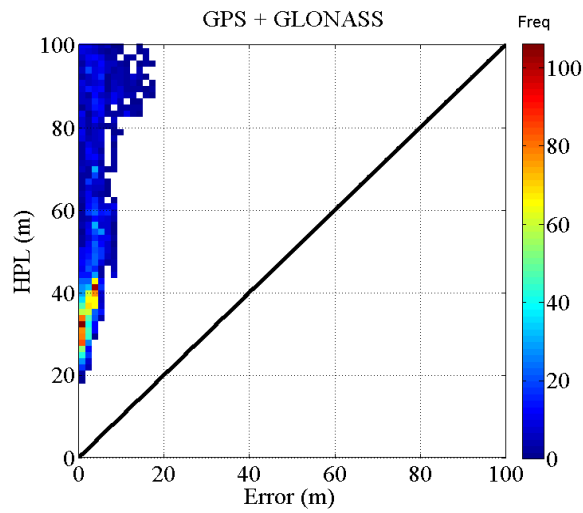


Figure 157 Stanford diagram plotted for the combined system after inflation of weighting scheme in suburban and urban environments (approach based on separated mechanizations). IMU and track database measurement are integrated.

A. 2. Approach based on the selection of the measurements

A. 2. 1. Standard solution separation algorithm

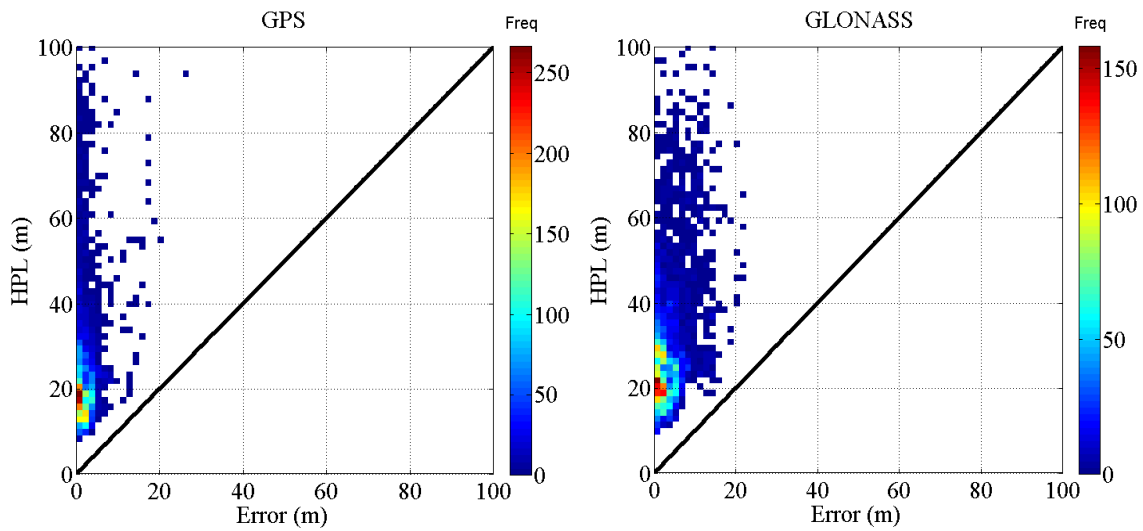


Figure 158 Stanford diagrams for each subsystem (based on GPS on the left and GLONASS on the right) after selection of the measurements. IMU and track database measurement are integrated.

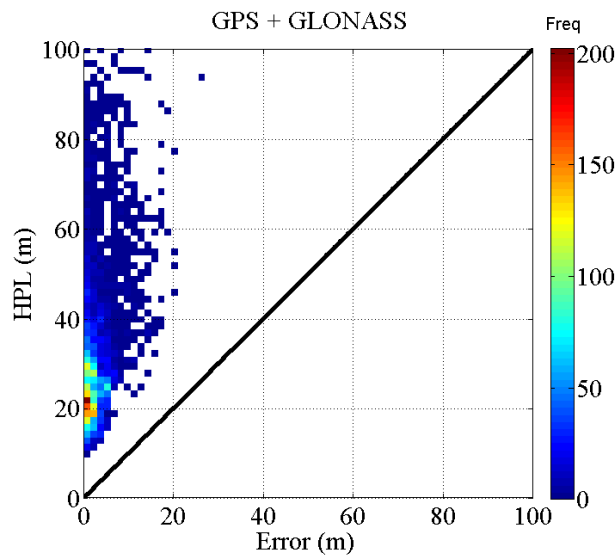


Figure 159 Stanford diagram the combined system after selection of the measurements. IMU and track database measurement are integrated.

A. 2. 2. Solution separation based on sub mechanizations

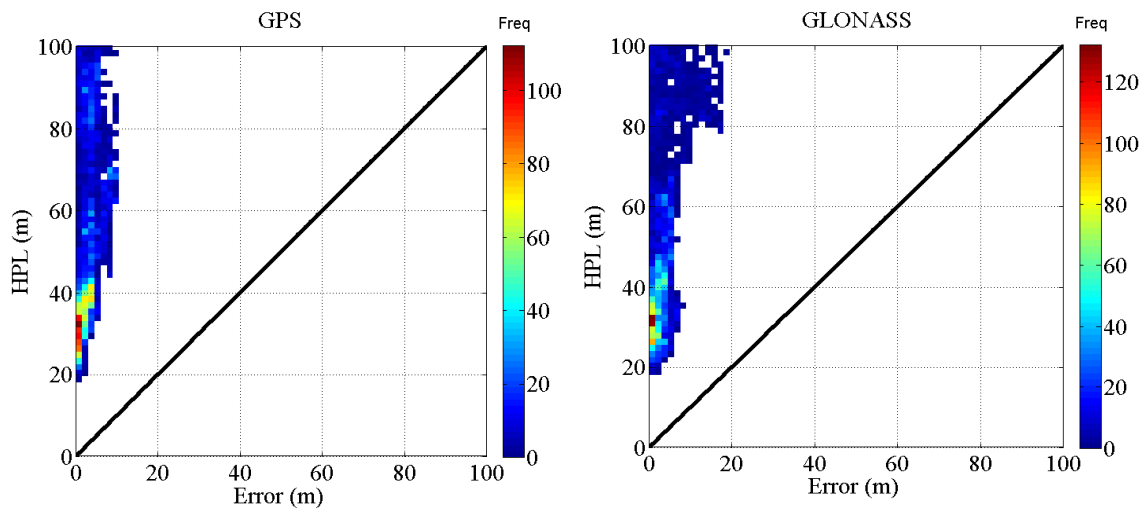


Figure 160 Stanford diagrams plotted for the two subsystems (based on GPS on the left and GLONASS on the right) after selection of the measurements in suburban and urban environments (approach based on separated mechanizations). IMU and track database measurement are integrated.

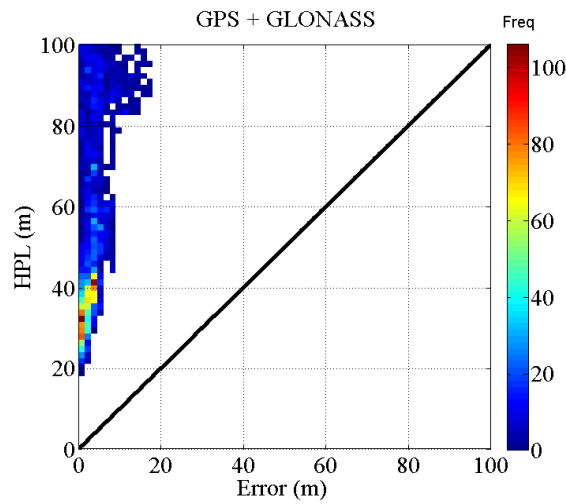


Figure 161 Stanford diagrams plotted for the combined system after selection of the measurements in suburban and urban environments (approach based on separated mechanizations). IMU and track database measurement are integrated.

B. ETC

B. 1. Inflation of the measurement error model

B. 1. 1. Standard solution separation algorithm

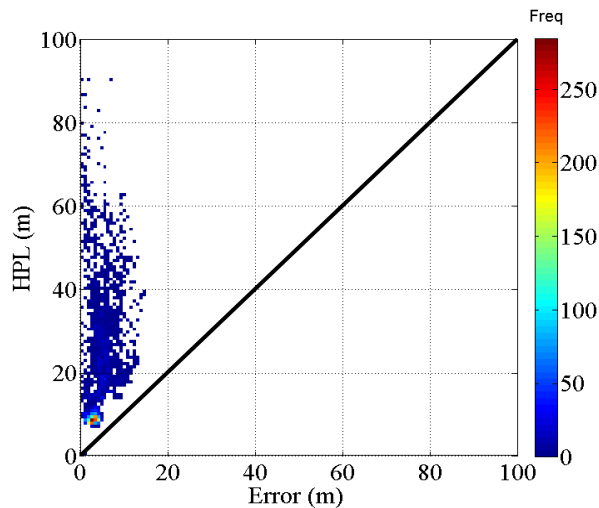


Figure 162 Stanford diagrams plotted for the GPS/GLONASS/IMU/WSS solution with conventional solution separation algorithm. Approach based on the inflation of the weighting scheme in suburban and urban environments

B. 1. 2. Solution separation based on sub mechanizations

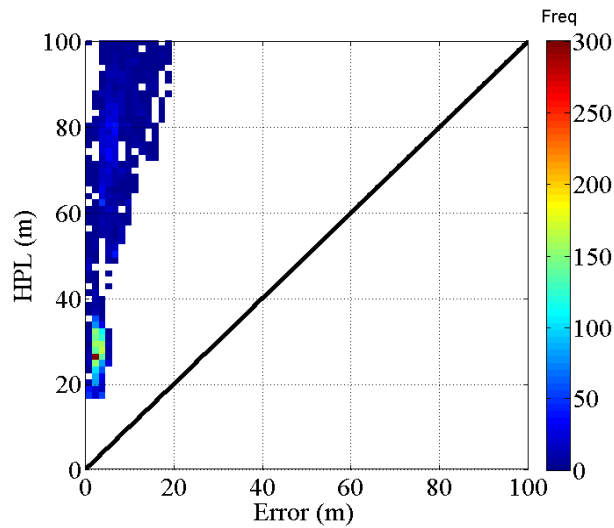


Figure 163 Stanford diagrams plotted for the GPS/GLONASS/IMU/WSS solution with solution separation using sub mechanizations. Approach based on the inflation of the weighting scheme in suburban and urban environments

B. 2. Approach based on the selection of the measurements

B. 2. 1. Standard solution separation algorithm

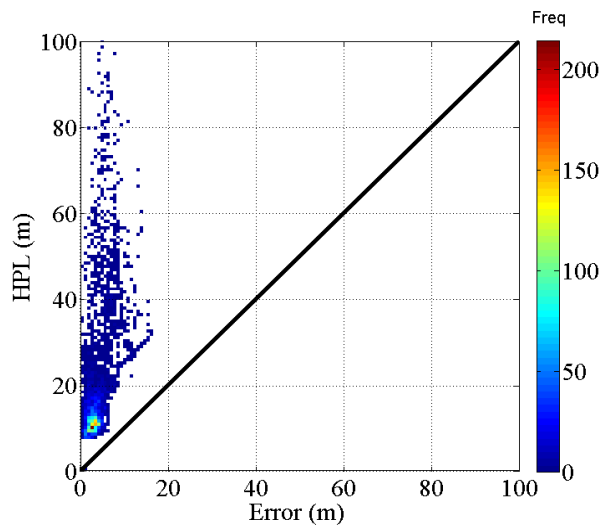


Figure 164 Stanford diagrams plotted for the GPS/GLONASS/IMU/WSS solution with conventional solution separation. Approach based on the selection of the measurements.

B. 2. 2. Solution separation based on sub mechanizations

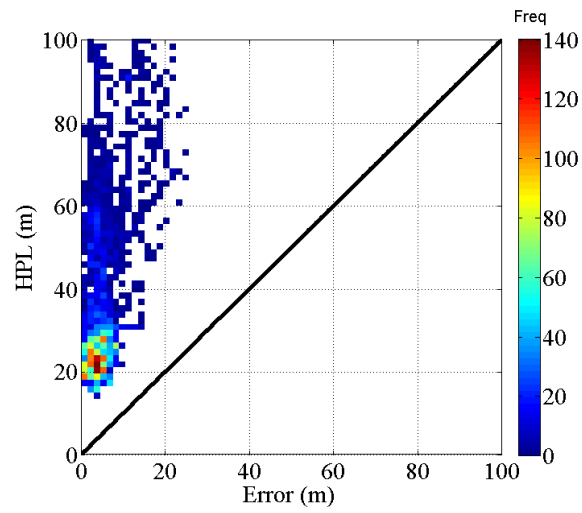


Figure 165 Stanford diagrams plotted for the GPS/GLONASS/IMU/WSS solution with solution separation using sub mechanizations. Approach based on the selection of the measurements.

Appendix I

Evaluation of the KF estimation error

This appendix justifies Eq. 8-35. In this appendix, the following assumptions are considered:

- At any time, the GNSS measurement error vectors and the process noise vector are independent each other.
- The initial prediction of the state vector is independent on the ranging error vectors
- The initial prediction of the covariance matrix of the state vector is independent of the multipath ranging error vectors.
- It is assumed that the Kalman filter contains the exact models of the transition state matrix and of the design matrix.

The position prediction is denoted $\hat{x}_{k+1|k}$. We have:

$$\hat{x}_{k+1|k} = x_{k+1} + \delta x_{k+1} \quad \text{Eq. I-1}$$

where:

- x_{k+1} the true position
- δx_{k+1} is the position error

Let us denote $\delta \hat{x}_{k+1|k+1}$ the estimation of the position error by the KF, we have:

$$\delta \hat{x}_{k+1|k+1} = \delta x_{k+1} - d\delta x_{k+1} \quad \text{Eq. I-2}$$

where:

- δx_{k+1} is the true error on the estimated position
- $d\delta x_{k+1}$ is the error on the estimation of the position error

We have:

$$\hat{x}_{k+1|k+1} = \hat{x}_{k+1|k} - \delta \hat{x}_{k+1|k+1} = x_{k+1} + d\delta x_{k+1} \quad \text{Eq. I-3}$$

Thus the position error is given by:

$$\hat{x}_{k+1|k+1} - x_{k+1} = d\delta x_{k+1} \quad \text{Eq. I-4}$$

The state vector at time $k + 1$ is given by the state propagation equation:

$$\delta x_{k+1} = F_k \delta x_k + w_{s_k} \quad \text{Eq. I-5}$$

The updated state vector is obtained in the Kalman filter as follows:

$$\delta \hat{x}_{k+1}^+ = \delta \hat{x}_{k+1}^- + K_{k+1}[\delta z_{k+1} - H_{k+1} \delta \hat{x}_{k+1}^-] \quad \text{Eq. I-6}$$

The measurement vector at time $k + 1$ is given by the observation model:

$$\delta z_{k+1} = H_{k+1} \delta x_{k+1} + w_{o_{k+1}} \quad \text{Eq. I-7}$$

The a priori state vector estimated by the mechanization at time $k + 1$ is obtained as:

$$\delta \hat{x}_{k+1}^- = F_k \delta \hat{x}_k^+ \quad \text{Eq. I-8}$$

Let's assume that the estimation of the error at time is affected by an error, it can be written:

$$\delta \hat{x}_k^+ = \delta x_k - d\delta x_k \quad \text{Eq. I-9}$$

Then by using Eq. I-8 in Eq. I-6 we have:

$$\delta \hat{x}_{k+1}^+ = F_k \delta \hat{x}_k^+ + K_{k+1}[\delta z_{k+1} - H_{k+1} F_k \delta \hat{x}_k^+] \quad \text{Eq. I-10}$$

If it is assumed that the measurements are affected by an error vector E_{k+1} :

$$\delta \hat{x}_{k+1}^+ = F_k \delta \hat{x}_k^+ + K_{k+1}[H_{k+1} \delta x_{k+1} + E_{k+1} - H_{k+1} F_k \delta \hat{x}_k^+] \quad \text{Eq. I-11}$$

Replacing $\delta \hat{x}_k^+$ by its expression Eq. I-9:

$$\delta \hat{x}_{k+1}^+ = F_k [\delta x_k - d\delta x_k] + K_{k+1}\{H_{k+1} \delta x_{k+1} + E_{k+1} - H_{k+1} F_k [\delta x_k - d\delta x_k]\} \quad \text{Eq. I-12}$$

Replacing δx_{k+1} leads to:

$$\delta \hat{x}_{k+1}^+ = F_k [\delta x_k - d\delta x_k] + K_{k+1}\{H_{k+1}\{F_k \delta x_k + w_{s_k}\} + E_{k+1} - H_{k+1} F_k [\delta x_k - d\delta x_k]\} \quad \text{Eq. I-13}$$

But $\delta x_{k+1} = F_k \delta x_k + w_{s_k}$

Then:

$$\delta \hat{x}_{k+1}^+ - \delta x_{k+1} = -F_k d\delta x(k) + K_{k+1}\{H_{k+1} w_{s_k} + E_{k+1} + H_{k+1} F_k d\delta x_k\} - w_{s_k} \quad \text{Eq. I-14}$$

It can be written:

$$\delta x_{k+1} - \delta \hat{x}_{k+1}^+ = (I - K_{k+1} H_{k+1})\{F_k [\delta x_k - \delta \hat{x}_k^+] - w_{s_k}\} - K_{k+1} E_{k+1} \quad \text{Eq. I-15}$$

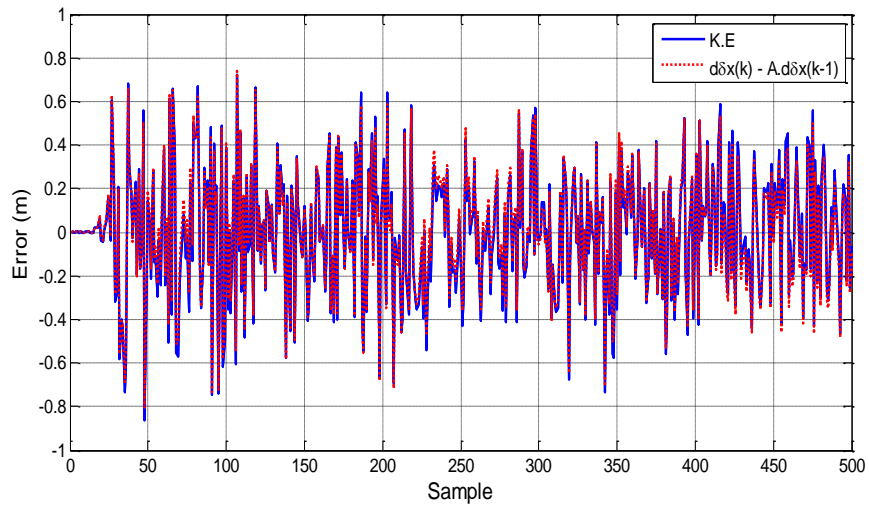


Figure 166 Validation of the relation on simulated measurements

Appendix J

Calculation of the critical bias in the case of a LS/WLS

When the position is estimated with a LS/WLS, the estimation error is given by:

$$dx = (H^T R^{-1} H)^{-1} H^T R^{-1} E \quad \text{Eq. J-1}$$

Let's assume that the measurement errors are centered except one which is biased. The error can be modelled by:

$$E \sim \mathcal{N}(\text{bias}, R) \quad \text{Eq. J-2}$$

and:

- $\text{bias} = [0 \quad \dots \quad b_i \quad \dots \quad 0]^T$
- $R = \begin{bmatrix} \sigma_1^2 & \dots & 0 \\ \vdots & \ddots & \vdots \\ 0 & \dots & \sigma_N^2 \end{bmatrix}$

As the sum of centered normally distributed terms and a deterministic term due to the bias, the position error is normally distributed. We focus on the horizontal component of the error. The parameters of the 2D normal distribution are given by:

$$E[dx^H] = \begin{bmatrix} [(H^T R^{-1} H)^{-1} H^T R^{-1}]_{1,i} \\ [(H^T R^{-1} H)^{-1} H^T R^{-1}]_{2,i} \end{bmatrix} b_i \quad \text{Eq. J-3}$$

It's covariance is given by:

$$\text{cov}(dx^H) = \begin{bmatrix} [\text{cov}(dx^H)]_{1,1} & [\text{cov}(dx^H)]_{1,2} \\ [\text{cov}(dx^H)]_{1,2} & [\text{cov}(dx^H)]_{2,2} \end{bmatrix} \quad \text{Eq. J-4}$$

where the terms of the covariance can be written by:

$$[\text{cov}(dx^H)]_{1,1} = \sum_{j=1}^N [((H^T R^{-1} H)^{-1} H^T R^{-1})_{1,j}]^2 (R)_{j,j} \quad \text{Eq. J-5}$$

$$[\text{cov}(dx^H)]_{2,2} = \sum_{j=1}^N [((H^T R^{-1} H)^{-1} H^T R^{-1})_{2,j}]^2 (R)_{j,j} \quad \text{Eq. J-6}$$

$$[\text{cov}(dx^H)]_{1,2} = \sum_{j=1}^N ((H^T R^{-1} H)^{-1} H^T R^{-1})_{1,j} ((H^T R^{-1} H)^{-1} H^T R^{-1})_{2,j} (R)_{j,j} \quad \text{Eq. J-7}$$

The two component of the horizontal error vector are correlated. Since $\text{cov}(dx^H)$ is a covariance matrix, it is positive semi-definite. Therefore it is diagonalizable and its eigenvalues are positive. The matrix of the eigenvectors denoted P_{\perp} is orthogonal. Let's denote D_H the eigenvalue decomposition of $\text{cov}(dx^H)$, it verifies:

$$P_{\perp}^T \text{cov}(dx^H) P_{\perp} = D_H \quad \text{Eq. J-8}$$

Let us multiply dx^H by P_{\perp}^T . The random errors on the two components are then uncorrelated.

$$E \left[P_{\perp}^T n_H (P_{\perp}^T n_H)^T \right] = P_{\perp}^T E[n_H n_H^T] P_{\perp} = D_H \quad \text{Eq. J-9}$$

Then the two components of the horizontal error are independent in this basis. Moreover, $P_{\perp}^T dx^H$ has the same norm as dx^H because multiplying a vector by an orthogonal matrix keep the norm invariant. The bias after rotation (b'_i) is given by:

$$b'_i = P_{\perp}^T b_H = \mathcal{O} b_i \quad \text{Eq. J-10}$$

with :

$$\mathcal{O}_i = P_{\perp}^T \begin{bmatrix} [(H^T R^{-1} H)^{-1} H^T R^{-1}]_{1,i} \\ [(H^T R^{-1} H)^{-1} H^T R^{-1}]_{2,i} \end{bmatrix} \quad \text{Eq. J-11}$$

Let's denote σ the maximum diagonal term of D_H . The following inequality can be written:

$$P(\|dx^H\| \geq HAL) = P(\|P_{\perp}^T dx^H\| \geq HAL) \leq P(\epsilon \leq HAL^2 \sigma^2) \quad \text{Eq. J-12}$$

where ϵ follows a non-central chi square distribution with 2 degrees of freedom and with a parameter of non-centrality (λ_{b_i}) that can be obtained from the probability of exceedance associated to the critical bias (P_{int}/P_f) and the value of the "threshold" $HAL^2 \sigma^2$. Finally, a lower bound of the critical bias (due to the inequality in J-12) is given by:

$$b_i = \sqrt{\frac{\sigma^2}{(\mathcal{O}_{i_1})^2 + (\mathcal{O}_{i_2})^2}} \sqrt{\lambda_{b_i}} \quad \text{Eq. J-13}$$

The expression is equivalent to what has been determined for the Kalman filter.